Nanomedicine and Nanotoxicology

Bing Yan
Hongyu Zhou
Jorge L. Gardea-Torresdey *Editors*

Bioactivity of Engineered Nanoparticles

Springer

Nanomedicine and Nanotoxicology

Series editor

V. Zucolotto, São Carlos, Brazil

More information about this series at http://www.springer.com/series/10620

Bing Yan · Hongyu Zhou
Jorge L. Gardea-Torresdey
Editors

Bioactivity of Engineered Nanoparticles

Springer

Editors
Bing Yan
School of Chemistry and Chemical Engineering
Shandong University
Jinan, Shandong
China

Jorge L. Gardea-Torresdey
Department of Chemistry
University of Texas at El Paso
El Paso, TX
USA

Hongyu Zhou
School of Environment
Jinan University
Guangzhou, Guangdong
China

ISSN 2194-0452 ISSN 2194-0460 (electronic)
Nanomedicine and Nanotoxicology
ISBN 978-981-10-5863-9 ISBN 978-981-10-5864-6 (eBook)
DOI 10.1007/978-981-10-5864-6

Library of Congress Control Number: 2017947032

Printed on acid-free paper

This Springer imprint is published by Springer Nature
The registered company is Springer Nature Singapore Pte Ltd.
The registered company address is: 152 Beach Road, #21-01/04 Gateway East, Singapore 189721, Singapore

Foreword

Among various applications of nanotechnology, exploration of biological properties of nanoparticles has drawn tremendous attention in the past decade. The biomedical impacts of nanotechnology are twofolds: applications to benefit human health, such as disease diagnosis and treatment, and the exposure-related toxicities to the human body and the pollution to environment. This book intends to give a snapshot of these important impacts.

A clear direction in the next phase of research is to expand exploration and applications of nanotechnology in medical and healthcare areas. By further understanding of unique properties of nanomaterials, novel reagents, medicines, and protocols will be developed. The advantages of this powerful technology will be further shown.

However, an even more urgent direction is to understand the impact of above applications on environment, ecosystems, and human health. Such research will assure a safe and sustainable development of nanotechnology.

Facing the challenge to cover this vast area of research, Profs. Yan, Zhou, and Gardea-Torresdey have made remarkable efforts by putting together this collection. We, therefore, recognize their dedication and efforts and warmly congratulate them for the timely publication of this book.

Beijing, China
April 2017

Guibin Jiang
Professor and Academician
of Chinese Academy of Sciences

Preface

Application of engineered nanoparticles (ENPs) in medicine has stimulated a wide range of interests in the past decades. On the other hand, the potential exposure of ENPs to humans has also been increasing with the development, manufacturing, and applications of engineered ENPs across a range of industrial and consumer products. Understanding of the bioactivity of ENPs is needed in order to better modulate their activities and regulate the potential risk. Recently, overwhelming research interests are on the investigation of bioactivities of ENPs, such as nanotoxicity, biocompatibility, ENP—biomolecule interactions, ENP—cell interactions, and cell targeting. Research papers have increased exponentially over the last decade. There is a consensus that we must have broad collaborations among chemists, engineers, toxicologists, cell biologists, and doctors in this endeavor.

This book collects papers from many international experts, who are working in diverse areas related to bioactivities of ENPs. In Chap. 1, the authors provide an overview of ENPs' ecotoxicological effects on algae to understand the underlying mechanisms of their effects on algae. Among the data available, ENPs have been shown to exert effects ranging from inhibitive to lethal due to high surface area, nanoscale size, and quantum effects. Chapters 2 and 3 discuss literatures concerning the uptake, translocation, accumulation, and physiological effects of surface-coated ENPs in vascular plants and higher plants. An important mechanism of nanotoxicity is reactive oxygen species (ROS) formation. ENPs' composition, size, shape, and surface chemistry all influence ROS generation. These are briefly discussed in Chap. 4. ENPs can enter human body through respiratory pathway, digestive tract, skin penetration, intravenous injection, and implantation. Interactions between ENPs and biomolecules, such as phospholipid, protein, DNA, and some other small biological molecules, form the chemical basis of ENPs' bioactivities. Investigation of interactions between ENPs and biomolecules is of great importance. In Chap. 5, authors discuss interactions between ENPs and biomolecules, and the effects of surface morphology, composition and modified groups on such interactions. Surface modification is a key approach to develop suitable ENP agents for disease diagnosis and drug delivery. A single and combination of surface engineering methods used for efficient delivery of nanocarriers to the requisite location are

discussed in Chaps. 6 and 7. Besides the targeting efficiency, efforts have been made in designing and improving biocompatibility, stability, safety, drug loading, delivery, imaging signals, and thermal- or photodynamic responses of ENPs. These are discussed in Chap. 8. The use of chemotherapy as one of the most conventionally therapeutic interventions in clinics results in an increasing chance of acquiring multidrug resistance. Chapter 9 highlights various aspects of Pluronic polymers, Pluronic conjugates, Pluronic nanotechnology, as well as their therapeutic implications for effective disease treatment by overcoming drug resistance. Besides laboratory synthesis, ENPs can also be formed in environmentally relevant conditions. Thermally and light-induced formation of silver ENPs and subsequent ecological effects are described in Chap. 10. Chapter 11 discusses the cytotoxicity and organ—systemic toxicity and in vivo genotoxicity of metallic ENPs. Liver is the major organ for disposition of ENPs. Chapter 12 discusses the accumulation of ENPs in liver and the induction of hepatic inflammation, DNA damage, hepatocyte death as well as liver fibrosis. Toxicity evaluation and bio-applications of silicon quantum dots synthesized by both physical and chemical methods are discussed in Chap. 13. Based on the multiple biological data from ENPs with various physicochemical properties, quantitative nanostructure—activity relationships (QNAR) modeling methods have been developed in Chap. 14 to analyze and evaluate the extent of biological activities potentially induced by various types of ENPs. Such methods are critical for both chemical risk assessment and more comprehensive evaluation of the potentially detrimental effects induced by a given ENP in a particular organism.

This book will interest a wide readership in the fields of chemical science, material science, engineering, biology, environment, and nanomedicine. We are indebted to the dedication and hard work by all authors and reviewers and the persistent convincing efforts by Dr. June Tang from Springer-Nature.

Jinan, China — Bing Yan
Guangzhou, China — Hongyu Zhou
El Paso, USA — Jorge L. Gardea-Torresdey
April 2017

Contents

Contributors

Ishaq Adisa Environmental Science and Engineering Ph.D. Program, The University of Texas at El Paso, El Paso, TX, USA

Suzanne A. Apodaca Environmental Science and Engineering, The University of Texas at El Paso, El Paso, TX, USA

Subhash C. Chauhan Department of Pharmaceutical Sciences, University of Tennessee Health Science Center, Memphis, TN, USA

Lingxin Chen Key Laboratory of Coastal Environmental Processes and Ecological Remediation, Yantai Institute of Coastal Zone Research, Chinese Academy of Sciences, Yantai, China

Seok Ki Choi Michigan Nanotechnology Institute for Medicine and Biological Sciences, and Department of Internal Medicine, University of Michigan Medical School, Ann Arbor, MI, USA

Pallabita Chowdhury Department of Pharmaceutical Sciences, University of Tennessee Health Science Center, Memphis, TN, USA

Anca Dinischiotu Department of Biochemistry and Molecular Biology, University of Bucharest, Bucharest, Romania

Denis Fourches Department of Chemistry, Bioinformatics Research Center, North Carolina State University, Raleigh, NC, USA

Jorge L. Gardea-Torresdey Environmental Science and Engineering, The University of Texas at El Paso, El Paso, TX, USA

Vladimir B. Gurvich The Ekaterinburg Medical Research Center for Prophylaxis and Health Protection in Industrial Workers, Ekaterinburg, Russia

Meena Jaggi Department of Pharmaceutical Sciences, University of Tennessee Health Science Center, Memphis, TN, USA

Yunxia Ji Key Laboratory of Coastal Environmental Processes and Ecological Remediation, Yantai Institute of Coastal Zone Research, Chinese Academy of Sciences, Yantai, China

Jianbo Jia School of Chemistry and Chemical Engineering, Shandong University, Jinan, China

Boris A. Katsnelson The Ekaterinburg Medical Research Center for Prophylaxis and Health Protection in Industrial Workers, Ekaterinburg, Russia

Santosh Kumar Department of Pharmaceutical Sciences, University of Tennessee Health Science Center, Memphis, TN, USA

Ryan Lougee Department of Chemistry, Bioinformatics Research Center, North Carolina State University, Raleigh, NC, USA

Min Lv Key Laboratory of Coastal Environmental Processes and Ecological Remediation, Yantai Institute of Coastal Zone Research, Chinese Academy of Sciences, Yantai, China

Oleg H. Makeyev The Ural State Medical University, Ekaterinburg, Russia

Tyler Malkoske College of Environmental Science and Engineering, Tongji University, Shanghai, People's Republic of China; Key Laboratory of Yangtze River Water Environment, Ministry of Education, Shanghai, People's Republic of China

Illya A. Medina-Velo Department of Chemistry, University of California Center for Environmental Implications of Nanotechnology (UC CEIN), The University of Texas at El Paso, El Paso, TX, USA

Ilzira A. Minigalieva The Ekaterinburg Medical Research Center for Prophylaxis and Health Protection in Industrial Workers, Ekaterinburg, Russia

Prashanth K.B. Nagesh Department of Pharmaceutical Sciences, University of Tennessee Health Science Center, Memphis, TN, USA

Vladimir G. Panov The Institute of Industrial Ecology, The Ural Branch of the Russian Academy of Sciences, Ekaterinburg, Russia

Jose R. Peralta-Videa Environmental Science and Engineering, The University of Texas at El Paso, El Paso, TX, USA

Larisa I. Privalova The Ekaterinburg Medical Research Center for Prophylaxis and Health Protection in Industrial Workers, Ekaterinburg, Russia

Swati Rawat Environmental Science and Engineering, The University of Texas at El Paso, El Paso, TX, USA

Muhammad Kashif Riaz School of Chinese Medicine, Hong Kong Baptist University, Kowloon Tong, Hong Kong

Virender K. Sharma Program for the Environment and Sustainability, Department of Environmental and Occupational Health, School of Public Health, Texas A&M University, College Station, TX, USA; Regional Centre of Advanced Technologies and Materials, Departments of Experimental Physics and Physical Chemistry, Faculty of Science, Palacký University in Olomouc, Olomouc, Czech Republic

Ekaterina V. Shishkina School of Natural Sciences and Mathematics, The Ural Federal University, Ekaterinburg, Russia

Vladimir Y. Shur School of Natural Sciences and Mathematics, The Ural Federal University, Ekaterinburg, Russia

Cornelia Sima Department of Laser, National Institute of Laser, Plasma and Radiation Physics, Bucharest, Magurele, Romania

Kumar Sinniah Department of Chemistry and Biochemistry, Calvin College, Grand Rapids, MI, USA

Miruna Silvia Stan Department of Biochemistry and Molecular Biology, University of Bucharest, Bucharest, Romania

Hainan Sun School of Chemistry and Chemical Engineering, Shandong University, Jinan, China

Marina P. Sutunkova The Ekaterinburg Medical Research Center for Prophylaxis and Health Protection in Industrial Workers, Ekaterinburg, Russia

Carlos Tamez University of California Center for Environmental Implications of Nanotechnology (UC CEIN), Environmental Science and Engineering Ph.D. Program, The University of Texas at El Paso, El Paso, TX, USA

Wenjuan Tan Environmental Science and Engineering, The University of Texas at El Paso, El Paso, TX, USA

Yulin Tang College of Environmental Science and Engineering, Tongji University, Shanghai, People's Republic of China; Key Laboratory of Yangtze River Water Environment, Ministry of Education, Shanghai, People's Republic of China

Deependra Tyagi School of Chinese Medicine, Hong Kong Baptist University, Kowloon Tong, Hong Kong

Irene E. Valamina The Ural State Medical University, Ekaterinburg, Russia

Anatoly N. Varaksin The Institute of Industrial Ecology, The Ural Branch of the Russian Academy of Sciences, Ekaterinburg, Russia

Shasha Wang Key Laboratory of Coastal Environmental Processes and Ecological Remediation, Yantai Institute of Coastal Zone Research, Chinese Academy of Sciences, Yantai, China

Pamela T. Wong Michigan Nanotechnology Institute for Medicine and Biological Sciences, and Department of Internal Medicine, University of Michigan Medical School, Ann Arbor, MI, USA

Huaijia Xin College of Environmental Science and Engineering, Tongji University, Shanghai, People's Republic of China; Key Laboratory of Yangtze River Water Environment, Ministry of Education, Shanghai, People's Republic of China

Murali M. Yallapu Department of Pharmaceutical Sciences, University of Tennessee Health Science Center, Memphis, TN, USA

Bing Yan School of Chemistry and Chemical Engineering, Shandong University, Jinan, China; School of Environment, Jinan University, Guangzhou, China

Guizhen Yan Lixia District People's Hospital, Jinan, China

Lily Yang Department of Surgery, Emory University School of Medicine, Atlanta, GA, USA

Zhijun Yang School of Chinese Medicine, Hong Kong Baptist University, Kowloon Tong, Hong Kong

Daqiang Yin College of Environmental Science and Engineering, Tongji University, Shanghai, People's Republic of China; Key Laboratory of Yangtze River Water Environment, Ministry of Education, Shanghai, People's Republic of China

Kun Yin Key Laboratory of Coastal Environmental Processes and Ecological Remediation, Yantai Institute of Coastal Zone Research, Chinese Academy of Sciences, Yantai, China

Radek Zboril Regional Centre of Advanced Technologies and Materials, Departments of Experimental Physics and Physical Chemistry, Faculty of Science, Palacký University in Olomouc, Olomouc, Czech Republic

Hongyu Zhou Guangdong Key Laboratory of Environmental Pollution and Health, School of Environment, Jinan University, Guangzhou, China

Zhiyang Zhou Xiangya School of Medicine, Central South University, Changsha, Hunan, China

Lei Zhu Department of Surgery, Emory University School of Medicine, Atlanta, GA, USA

Chapter 1
The Toxicity of Nanoparticles to Algae

Yulin Tang, Huaijia Xin, Tyler Malkoske and Daqiang Yin

Abstract Nanoparticles (NPs) display unique physical and chemical properties to the toxicity of algae. Among the NPs, metal oxide NPs such as titanium dioxide (nano-TiO_2), zinc oxide (ZnO NPs), and Copper oxide (CuO NPs) are the most used nanomaterials. Silver nanoparticles (Ag NPs), gold nanoparticles (Au NPs), and zero-valent iron nanoparticles (nZVI) have received considerable attention among noble metal materials. Besides, Quantum dots (QDs) and carbon-based nanoparticles are also common. To assess the ecological response of algae to NPs, we provide an overview of NPs ecotoxicological effects on algae from existing data and focus on the effect of different NPs on algae, the underlying mechanisms of NPs toxicity and their toxic effects on algae. Among the data available, NPs have been shown to exert from inhibitive to lethal effects on algae due to a high surface area, nanoscale size effects, and quantum effects.

Keywords Algae · Toxicity · Nanoparticles · Mechanisms

1.1 Introduction

Engineered nanoparticles (NPs) with sizes smaller than 100 nm in at least one dimension have received considerable attention due to their rapidly increasing application in various areas of textiles, electronics, pharmaceuticals, cosmetics, and environmental remediation [1]. At nanoscale, NPs display unique physical and chemical properties, such as a high surface area, nanoscale size effects, and quantum effects.

Y. Tang (✉) · H. Xin · T. Malkoske · D. Yin
College of Environmental Science and Engineering, Tongji University,
Shanghai 200092, People's Republic of China
e-mail: tangyulin@tongji.edu.cn

Y. Tang · H. Xin · T. Malkoske · D. Yin
Key Laboratory of Yangtze River Water Environment, Ministry of Education,
Shanghai 200092, People's Republic of China

B. Yan et al. (eds.), *Bioactivity of Engineered Nanoparticles*,
Nanomedicine and Nanotoxicology, DOI 10.1007/978-981-10-5864-6_1

Among the NPs, metal oxide NPs such as titanium dioxide (nano-TiO_2), zinc oxide (ZnO NPs), and copper oxide (CuO NPs) are the most used nanomaterials due to their attractive physicochemical properties [2]. Among noble metal materials, silver nanoparticles (Ag NPs), gold nanoparticles (Au NPs), and zero-valent iron nanoparticles (nZVI) have received considerable attention. Metal nanoparticles have a significant role in nanotechnology due to their potential utilization in nanoelcetronics, semiconductors, colorimetric techniques, DNA labeling, and development of biosensors [3–7]. Quantum dots (QDs) are a major class of semiconducting nanocrystals which possess unique optical, electrical, and chemical properties [8]. Carbonaceous NPs including graphene, fullerene, and carbon nanotubes (CNTs) are also increasingly produced and used in a variety of industrial areas [9, 10].

The production of nanomaterials is increasing dramatically with an expected resultant increase in the distribution of NPs in the environment. The risk of NPs to the ecosystem is, therefore, an increasing concern. Understanding the interactions between NPs and algae is therefore essential for assessing the ecological response to NPs. The increased use of nanomaterials in several novel industrial applications during the past decade has led to a rise in concerns about the potential toxic effects of released NPs into the environment, as their potential toxicity to aquatic organisms is just beginning to be recognized.

Microalgae, unicellular species typically found in freshwater and marine systems, which are the primary producers in the food chain, are more sensitive to contaminants than fish and invertebrates. They are important organisms for monitoring water quality and aquatic toxicity. Algae are a primary agent for global biogeochemical cycles, which justify them as a model for evaluating the ecological impact of NPs. Investigating the toxicity of NPs to algae and explaining the mechanism clearly is of great importance and can lead to strategies to remediate the potentially adverse effects of NPs on the environment [11]. Algal cells possess an additional layer of rigid, porous cell wall for modulating the entry of foreign materials, ions, and particles [12]. Among the data available, NPs have been shown to exert from inhibitive to lethal effects on algae. In addition, algal cells have been shown to produce exudates in response to the physical and chemical stresses induced by NPs [13].

In the last decade, the production of these NPs has increased considerably and the aquatic ecotoxicity studies about NPs effects on algae grow rapidly. However, data on their toxicity on microalgae remains scattered, and the comparison of multiple studies can be difficult, since experimental designs and testing conditions are rarely consistent across studies. In this chapter, we provide an overview of NPs ecotoxicological effects on algae from existing data. We also focus on the effect of different NPs on algae, the underlying mechanisms of NPs toxicity and their toxic effects on algae.

1.2 Test Methods

1.2.1 Ecotoxicological Test with Algae

Most of the ecotoxicological algae assessment studies are performed following the Organisation for Economic Co-operation and Development (OECD) and American Society for Testing and Materials (ASTM) test guidelines, and International Organization for Standardization (IOS) standards [14–16]. Freshwater and marine algae are used for NPs toxicity testing as shown in Table 1.1.

1.2.2 Algae Cell Number

The algae cell number (cell/mL) was counted using a light microscope. The optical density (OD) values were linearly proportional to the algal concentration. The algae growth curve area and inhibition rate were calculated according to OECD 201 [15] from Eq. 1.1.

$$\mathrm{A} = \frac{N_1 - N_2}{2} \times t_1 + \frac{N_1 + N_2 - 2N_0}{2} \times (t_2 - t_1) + \cdots + \frac{N_{n-1} + N_n - 2N_0}{2} \times (t_n - t_{n-1}) \tag{1.1}$$

Where A is the growth curve area; N_0 is the number of cells per milliliter at t_0; N_1 is the number of cells per milliliter at t_1; t_1 is the time of first cell count after exposure; and t_n is the time of n times the cell count after exposure.

$$I_A = \frac{A_c - A_t}{A_c} \times 100 \tag{1.2}$$

Where I_A is the inhibition rate (%) of the exposure group; A_c is the growth curve area of the control; and A_t is the growth curve area of the exposure group at time t.

Normally, the EC_{50} value, which was the actual concentration causing 50% inhibition in algal growth, was estimated by applying the logistic model. The toxicity of NPs was determined through comparisons of EC_{50} and EC_{10} values of algae [13, 17].

1.2.3 Chlorophylls

Chlorophylls, carotenoids, and phycobilin are microalgal pigments that harvest light in the process of photosynthesis. Chlorophylls are primary photosynthetic

Table 1.1 The different algae as the toxicity model

Algae	NPs	Characteristics and concentrations of NPs	Species	References
Freshwater algae	TiO_2	Hombikat UV100: <10 nm, 250–320 m^2/g, anatase, uncoated, 2.1–50 mg/L UV-Titan m212: 20 nm, 60 m^2/g, rutile, coated with Al_2O_3, 2.1–50 mg/L	*Pseudokirchneriella subcapitata*	[14]
		P25, 21 nm, white powder		[16]
		25–70 nm, 24–380 mg/mL		[21]
		Hombikat UV100: < 10 nm, 288 m^2/g, 0.6–250 mg/L Degussa P25: 30 nm, 47 m^2/g, 0.6–250 mg/L Hombitan LW-S: 300 nm, 11.5 m^2/g, 0.6–250 mg/L		[24]
		HR3: 5–10 nm DJ3: 50 nm Bulk: 600 ± 200 nm	*Chlorella*	[2]
		P25, 21 nm, 0.01, 0.1 and 1 μg/mL	*Scenedesmus*	[22]
		5, 50, 90, 350 nm	*Chlorella vulgaris Beijer*	[17]
		25, 100 nm, anatase	*Desmodesmus subspicatus*	[23]
		192 ± 0.8 nm, 274.2 m^2/g, anatase, 1–150 mg/L	*Anabaena variabilis.*	[25]
		<25 nm, anatase, 0.05–1 μg/mL	*Scenedesmus obliquus*	[26]
		P25, 21 nm, 50 ± 15 m^2/g, 0.01–100 mg/L	*Chlamydomonas reinhardtii*	[45]
		40–50 nm	*Anabaena* sp.	[70]
	ZnO		*Chlorella vulgaris*	[11]
		62 nm, coated with 3-aminopropyl triethoxysilane, 10 nM–100 mM	*Chlorella* sp.	[12]
		Nano: 20 ± 5 nm Bulk: 1000 ± 200 nm		[2]
		<100 nm, white powder	*Pseudokirchneriella subcapitata*	[16]
		30 nm, 100 mg/L		[32]
		50–70 nm, 0.04, 0.08 mg/L	*Chlorella vulgaris Bayer*	[21]
		20 nm, 0–10 mg/L		[17]
		<100 nm, 15–25 m^2/g, 0.25, 0.5 and 1 mg/L 40 nm, 80.425 m^2/g, 0.25, 0.5 and 1 mg/L	*Scenedesmus obliquus*	[28]

(continued)

Table 1.1 (continued)

Algae	NPs	Characteristics and concentrations of NPs	Species	References
	CuO	30 nm, 0.04, 0.08 mg/L	*Pseudokirchneriella subcapitata*	[21]
		Bare: 30–40 nm, 0.005–0.04 g/L Polymer-coated (CS-CuO): 81 nm, 0.005–0.04 g/L	*Chlamydomonas reinhardtii*	[35]
		30–40 nm, nearly spherical, monoclinic, 0–1000 mg/L		[34]
		<50 nm, mean 30 nm, 1–100 mg/L	*Chlorella*	[38]
			Nitellopsis	
	GO	An amber, viscous, and homogeneous solution, 0–100 mg/L	*Raphidocelis subcapitata*	[40]
		Thickness of 5 nm, 0.4 mg/mL	*Chlorella vulgaris cells*	[42]
		1 mg/L	*Scenedesmus obliquus*	[44]
		Thickness of 1–4 nm, particle size of 2 μm		[43]
		0–50 mg/L	*Microcystis aeruginosa*	[71]
	C_{60}	2 mg/L	*Scenedesmus obliquus*	[46]
	CNTs	50.0 mg CNTs/L	*Chlorella vulgaris*	[49]
		50.0 mg CNTs/L	*Pseudokirchneriella subcapitata.*	
		Outer diameters, 0–100 mg/L <10 nm (MWCNT10) 20–40 nm(MWCNT40) 60–100 nm (MWCNT100)	*Chlorella* sp.	[10]
	Au	10 nm, 1.6×10^3, 1.6×10^4, 1.6×10^5 Au NPs/cell	*Scenedesmus subspicatus*	[60]
		Non-functionalised, 10–100 mg/L Hyaluronic acid functionalized, 10–100 mg/L 12.8 ± 1.6 nm, rounded, 10–100 mg/L		[7]
		Carbonate-coated Citrate-coated: 5 nm	*Chlamydomonas reinhardtii*	[59]
	Ag	<100 nm, mean 34 ± 18 nm, spherical	*Pseudokirchneriella subcapitata*	[5]
	nZVI	Nanofer 25: pure water suspension with no additives Nanofer 25S: surface-coated with a Na-acrylic copolymer	*Desmodesmus subspicatus*	[63]
			Dunaliella salina	
			Raphidocelis subcapitata	
			Nannochloropsis limnetica	
			Trachydiscus minutus	

(continued)

Table 1.1 (continued)

Algae	NPs	Characteristics and concentrations of NPs	Species	References
	QDs	CdTe/CdS	*Chlamydomonas reinhardtii*	[66]
		CdTe, 0.01–100 mg/L		[45]
		CdTe, 1.2, 1.7, 2.5, 5.0 mg-Cd/L	*Ochromonas danica*	[67]
		CdSe/ZnS (Ex: <550 nm; Em: 570–585 nm), 0.05–5 ppm	*Chlamydomonas* sp.	[8]
Marine algae	TiO_2	21 nm, 85.4% Anatase, 14.6% rutile, 10 mg/L	*Picochlorum* sp.	[27]
		15–20 nm, semispherical, 81% anatase, 19% rutile	*Skeletonema marinoi*	[33]
			Thalassiosira pseudonana	
			Dunaliella tertiolecta	
			Isochrysis galbana	
	ZnO	50 nm, 10 mg/L	*Picochlorum* sp.	[27]
		20–30 nm, spheroid, 100% zincite, 0–1000 mg/L	*Thalassiosira pseudonana,*	[33]
		Industrial: 32.22 ± 0.68 m^2/g Sunscreen-derived: 2.29 ± 0.33 m^2/g <50 ± 5 nm		[30]
		Spherical: 6.3 ± 1.1 nm, 15.7 ± 1.3 nm, 10–80 mg/L Nanorods: 242 ± 47 nm (lengths),13.5 ± 2.7 nm (diameters), 10–80 mg/L Nanoneedle: 862 ± 301 nm (lengths), 29.5 ± 7.1 nm (diameters), 10–80 mg/L	*Chaetoceros gracilis* *Phaeodactylum tricornutum*	[29]
		20–30 nm, spheroid, 100% zincite, 0–1000 mg/L	*Skeletonema marinoi*	[33]
			Dunaliella tertiolecta	
			Isochrysis galbana	
	CuO	0.25–1 mg/L	*Acanthophora spicifera*	[36]
			Chaetomorpha antennina	
			Ulva reticulata	
		5, 10 ppm	*Gracilaria domingensis*	[37]
	GO	PGMF: 86.75 ± 20.43 nm, 0–10 mg/L GNC-1: 153.13 ± 37.80 nm, 0–10 mg/L	*Dunaliella tertiolecta*	[41]
	Ag	56 ± 5 nm, 5–20 μM	*Chattonella marina*	[61]
	nZVI	Nanofer 25: pure water suspension with no additives Nanofer 25S: surface-coated with a Na-acrylic copolymer	*Parachlorella kessleri*	[63]
		Nanofer 25 (nZVI25), Nanofer 25S (nZVI25S), Nanofer star ($nZVI_{powder}$) Mean 50 nm, 25 m^2/g; purity ~ 85%	*Pavlova lutheri*	[64]
			Tetraselmis suecica	
			Isochrysis galbana	

pigments that contain tetrapyrrole macrocycle rings and are present in various forms, such as Chl-a, Chl-b, Chl-c_1, Chl-c_2, Chl-c_3, Chl-d, and Chl-f in different algae [18]. The content of Chlorophylls was determined by the widely accepted Jeffrey and Humphrey equation [19]. The toxicity was also evaluated by measuring the culture yield and chlorophyll fluorescence parameter in relation to the control experiment. All of the chlorophyll fluorescence parameters could be measured with a Phyto-PAM fluorometer (Walz, Germany).

1.2.4 ROS Assays

When NPs entered algal cells through the cell membrane, reactive oxygen species (ROS) might be induced to generate in algal cells. At the same time, the antioxidant (e.g., ascorbate, glutathione, etc.) and antioxidant enzymes, malondialdehyde (MDA), superoxide dismutase (SOD), catalase (CAT), and glutathione (GSH), change following ROS generation to maintain the pro-oxidation/anti-oxidation balance [13]. The supernatant was collected after the interaction of algal species with NPs. The amount of protein left in the supernatant was calculated by the Lowery method [20]. A control experiment was run without NPs. SOD and CAT activities, and MDA as the end product of lipid peroxidation were detected to estimate the level of lipid peroxidation [13].

1.3 Toxicity of Nanoparticles on Algae

1.3.1 Effect of Metal Oxide Nanoparticles

1.3.1.1 Titanium Dioxide

The toxicity of nano-TiO_2 was observed by many researchers. It was found that the size and crystalline form of nano-TiO_2 determined the toxicity. Roy et al. reported that among the three tested concentrations (0.01, 0.1, and 1 μg/mL), only 1 μg/mL of P25 nano-TiO_2 showed a statistically significant damage in algae cells with respect to control. *Chlorella* was found to be more susceptible to P25 nano-TiO_2 with a higher Ti bio-uptake than *Scenedesmus* [21, 22]. Moreover, the initial toxicity of 5 nm nano-TiO_2 to *Chlorella vulgaris Beijer* was observed, then decreased with further increase in concentration. Finally, toxicity increased again reaching the maximal effect at C = 1.0 mg/L [17].

In another example, Kerstin et al. found that 25 nm nano-TiO_2 were more toxic to *Desmodesmus subspicatus* than 100 nm nano-TiO_2. The 72 h EC_{50} concentrations were 44 mg/L and >50 mg/L, and the smaller particles had a clear concentration–effect relationship, while the larger ones showed less toxicity [23]. A similar

trend was observed by Hartmann et al. Higher inhibition was detected in smaller TiO_2 particles (<10 nm) at concentrations of 2 mg/L with a 21% reduction in growth rate of *Pseudokirchneriella subcapitata*. However, 30 and 300 nm TiO_2 particles showed a slight stimulation of algal growth [24], which was in accordance with Gosteva et al. findings for 350 nm TiO_2 particles [17]. Another study showed a similar effect where nano-TiO_2 (EC_{50} = 5.83 mg Ti/L) showed significantly higher toxicity than its bulk formulations (EC_{50} = 35.9 mg Ti/L) to *P. subcapitata* [21].

The possible mechanisms for cytotoxicity are influenced by many factors. It has been suggested that nano-TiO_2 aggregates entrapping algal cells reduced the light available to algal cells and contributed to the toxicity of nano-TiO_2 [21]. Meanwhile, nano-TiO_2 was observed in many intracellular structures by Cherchi et al. and caused membrane permeability and several stress responses, such as ROS [25]. What is more, photo-induced toxicity of nano-TiO_2 was noted by Dalaia et al. As compared to dark, light conditions would induce higher cytotoxicity of nano-TiO_2 to *Scenedesmus obliquus* while producing significant ROS and increasing membrane permeability. The physical adsorption and internalization were responsible for cytotoxicity in dark conditions [26]. On the other hand, aggregation and sedimentation effects would reduce the toxicity and availability of nano-TiO_2 to marine algae [27].

1.3.1.2 Zinc Dioxide

Toxicological studies of ZnO NPs to algae can be classified into several categories: hydrodynamic particle size, type of ZnO NPs, tested matrices, exposure concentration, exposure time, solubilized Zn^{2+} ions, irradiation condition, and so on.

Bhuvaneshwari et al. reported that *S. obliquus* in the smaller sized ZnO NPs (487.5 ± 2.55 nm) were more toxic than larger sized ZnO NPs (616.2 ± 38.5 nm) in lake water medium, and significantly reduced viability, released lactate dehydrogenase (LDH), and generated reactive oxygen species [28]. Likewise, a study published by Peng et al. also showed that a more adverse effect happened with 6.3 nm than 15.7 nm ZnO spheres on marine diatoms (*Thalassiosira pseudonana*, *Chaetoceros gracilis* and *Phaeodactylum tricornutum*) [29]. Spisni et al. found that industrial ZnO NPs had higher toxicity than sunscreen-derived ZnO NPs to *T. pseudonana* ignoring concentrations, which may be due to the slightly smaller size and a larger surface area of industrial ZnO particles (24 nm, 32.22 m^2/g) compared with sunscreen ZnO NPs (31 nm, 2.29 m^2/g) [30]. The mechanism explained by Bystrzejewska et al. is that because of greater surface area, smaller sized NPs could interact, stick to or cross the cellular membrane easily and get internalized into algal cells effectively, whereas larger aggregates were less available to the algae cells [31]. It seems that the size of ZnO particles contributes to the toxicity of algae, while some other studies differ from those conclusions. Aruoja et al. discovered that there is no significant difference between bulk ZnO, ZnO NPs, and $ZnSO_4$ particles, which have different sizes, in toxicity effect (72 h EC_{50}: 0.042, 0.037 and 0.042 mg

Zn/L) for *P. subcapitata* [21]. This is consistent with findings by Franklin et al. for 72 h IC_{50} values of bulk ZnO, ZnO NPs, and ZnCl which were 0.063, 0.068, and 0.061 mg Zn/L [32]. Both attributed the toxicity of ZnO solely to solubilized Zn^{2+} ions for the near total dissolution of ZnO at low concentrations. However, the experiment results of Peng et al. were slightly different. Although a similar situation was determined for *T. pseudonana* and *C. gracilis* which had a significant decrease after exposure to ZnO regardless of the particle morphologies and initial concentration, *P. tricornutum* exhibited the capability of continuous slow growth [29]. In conclusion, there is a conflict among different researches in size and crystal structure effect of ZnO and it needs further study to verify.

As for exposure concentration, both ZnO NPs and bulk ZnO were toxic to *P. subcapitata* at low concentrations (<0.1 mg/L). For both types of particles, total inhibition was observed at 0.16 mg Zn/L [21]. Likewise, Morgalev et al. declared that the toxic effect started from 0.059 mg/L ZnO NPs (20 nm) and that concentrations of less than 0.013 mg/L caused no biological effects in *Chlorella vulgaris Bayer* [17]. Miller et al. reported that ZnO NPs (20–30 nm) at 1 mg/L could depress the algae growth rate by 50–75% for four species of marine algae (*Skeletonema marionoi*, *T. pseudonana*, *Dunaliella tertiolecta*, and *Isochrysis galbana*) [33]. Consequently, the low concentration of ZnO is enough to cause an obvious inhibition of algae growth.

Chen et al. found an interesting phenomenon, where algal cells displayed an outstanding capability of self-protection. It was found that through aggregation and exudation, *Chlorella* sp. not only minimized their surface area, but also suppressed zinc ion release. Therefore, the effects of ZnO NPs on algae were bilateral [12]. Another interesting phenomenon reported by Spisni et al. showed that the toxic effects and growth inhibition were irrelevant to the type, size, and concentration of ZnO as soon as aggregation occurred [30]. In some ways, this finding was consistent with the result of Hazeem et al. who indicated that ZnO NPs imposed a shading effect to marine algae negatively effecting algal growth and chlorophyll a concentration in early growth stages. Furthermore, aggregation and sedimentation reduced the toxicity of NPs by decreasing light availability [27].

1.3.1.3 Copper Oxide

Aruoja et al. examined the toxicity of CuO NPs to *P. subcapitata* and discovered that 30 nm CuO NPs led to more toxic effects than their bulk formulations, with EC_{50} concentrations of 0.71 and 11.55 mg Cu/L, and NOEC concentrations of 0.42 and 8.03 mg Cu/L [21]. However, the exploration of toxic concentration of CuO NPs (30–40 nm) conducted by Melegari et al. showed a significantly higher value with 150.45 mg/L CuO NPs for 72 h EC_{50} and the NOEC less than 100 mg/L CuO NPs for *Chlamydomonas reinhardtii* [34]. Thus, different algae express different sensitivity to CuO NPs. Based on the investigation of CuO NPs toxicity on the green alga *C. reinhardtii*, both bare and polymer-coated CuO NPs suspensions were toxic to *C. reinhardtii* at concentrations of 5–40 mg/L, and decreased the

photosystem II activity and formed ROS. Furthermore, it was found that coated CuO NPs were more toxic than the uncoated, which may be due to the increased penetration ability [35].

CuO NPs negatively impact several morphological, physiological, and biochemical processes for algae. It was determined that bioavailable copper ions account for the toxic effect of CuO based on yeast Cu-sensors and recombinant bacteria. The shading effect caused by CuO NPs can be negligible [21]. The Fenton reaction was utilized in the formation of ROS, which was stimulated by Cu. The production of oxidative stress led to the damage of biomolecules, such as lipids and proteins, and a reduction of glutathione reductase activity occurred [34, 36]. With increasing CuO NPs concentration, cell metabolism activity decreased [34] and resulted in photodamage of photosynthetic pigments and changes in photosynthesis [37]. Meanwhile, the degree of DNA damage increased with increasing CuO NPs concentration [36]. Additionally, a lipid peroxidation of cellular membranes was investigated and CuO NPs were present at different sites in algal cells [34, 38].

1.3.2 Toxicity Effect of Carbon-Based Nanoparticles

1.3.2.1 Graphene Nanoplatelets

Graphene-family nanomaterials (GFNs) are classified into three categories: pristine graphene, reduced graphene oxide (rGO), and graphene oxide (GO). Zhao et al. pointed out that the toxic mechanisms of GFNs at the cellular level which cause adverse impacts on aquatic species are still unclear [39].

The inhibition tests of pristine graphene, such as bulk graphite (GRP), pristine graphene monolayer flakes (PGMF), and graphene nanopowder grade C1 (GNC1), were carried out on the unicellular marine alga *D. tertiolecta* by Pretti et al. The toxicity increased with the decrease of particle size (PGMF > GNC1 > GRP). Specifically, with respect to control at concentration of 10 mg/L, GRP expressed no significant growth inhibition, while similar inhibition and toxicity were observed in PGMF (LOEC = 0.675 mg/L, 72 h EC_{50} = 1.14 mg/L) and GNC1 (LOEC = 1.25 mg/L, 72 h EC_{50} = 2.25 mg/L). The toxic effects of GO on green algae *Raphidocelis subcapitata* included oxidative stress levels and membrane damage at 10 μg/mL and EC_{50} at 20 μg/mL, which were probably because of ROS generation and mechanical damage [40]. Exposure to pristine graphene caused irreversible cell wall disruption and cell swelling [41]. Nevertheless, Wahid et al. proved that GO was nonlethal for microalgal cells with several viability tests. Moreover, his group was the first to wrap algae cells with GO layers for immobilization and the study found that GO could effectively reduce cell division rate as well as algae inhibition [42]. Graphene nanoplatelets (GNPs) concentrations of 0.5,0 1, and 5 mg/L resulted in 17 ± 7, 22 ± 2, and 34 ± 1% growth inhibition in *S. obliquus* after 96 h exposure. This indicated that the toxicity of GNPs depended on the concentration. Moreover, the total antioxidant capacity (T-AOC) was

significantly higher with increasing GNPs concentration and caused oxidative damage in the algae [43]. Likewise, previous studies have shown that oxidative stress was an important toxicity pathway in GFNs, which was produced by algae exposed to GO [40, 41, 44]. The toxic effect mechanism was due to the shading of GNP suspension. Previously, some studies have found the shading effect produced by agglomeration of carbon-based nanomaterials affect the growth of photoautotrophs. Besides, carbon nanomaterials could adsorb on cell surfaces and decrease light availability [45].

1.3.2.2 Fullerene

Chen et al. investigated the fullerene aqueous suspension (nC_{60}) uptake amounts of *S. obliquus* by dietary exposure. The absorption of nC_{60} to algae was divided into three portions: cell wall (CW), cell organelle (CO), and cell membrane (CM). The results showed that the nC_{60} distribution in *S. obliquus* was the highest in CW, followed by CO and CM [46]. The sub-lethal concentration of nC_{60} on the *S. obliquus* was 0.09 mg/L with 40% decrement of algal Mg^{2+}. Further experiments demonstrated that the photosynthetic products, such as polysaccharide, soluble protein, and total lipid, and chlorophylls contents decreased with exposure time. The key factors contributing to the mechanism of nC_{60} toxicity were that nC_{60} toxicity adsorbed and aggregated on algal surfaces blocking the Mg^{2+} channels and inducing photosynthetic toxicity [47].

1.3.2.3 Carbon Nanotubes

Functionalized multiwalled carbon nanotubes (MWNT) carboxylated by microwave-assisted acid oxidation were examined for toxicity effects of *D. tertiolecta*. Significant growth lag was observed at concentrations higher than 5 mg/L f-MWNT with up to 36% reduction in exponential growth rate and the resulting EC_{50} after 96 h was 0.82 mg/L. However, *D. tertiolecta* did not show significant cytotoxicity after large MWNT aggregates were removed by 0.2 μm filtration, which suggested that the large MWNT aggregates mainly contributed to the toxic effects [48]. The EC_{50} of carbon nanotubes (CNT) for *C. vulgaris* and *P. subcapitata* were determined by Schwab et al. in well dispersed and agglomerated suspensions (1.8 and 20 mg/L, 24 and 36 mg/L). CNTs did not affect the algae photosynthesis. Furthermore, growth inhibition was highly related to the shading of CNTs and the agglomeration of algal cells, which indicated available light reduction and different growth conditions were responsible for the reduced growth of algae [49].

As for toxicity mechanisms, Long et al. examined and quantified the contributions to algal growth inhibition by investigating the toxicity of MWCNT for *Chlorella* sp. In conclusion, the mechanisms of MWCNTs toxicity depended on the MWCNT size and concentration, which could be explained by the combined effects

of oxidative stress, agglomeration and physical interactions, and shading effects [10].

For carbon-based NPs, metal catalyst residues, the adsorption of nutrient elements, oxidative stress, agglomeration and physical interaction, and shade effects are the main five possible mechanisms to inhibition of algal growth. For metal catalyst residues, even after prolonged periods of purification by concentrated nitric acid, CNTs contain residual metal impurities of which divalent transition metals were the factor of toxicity [50, 51]. CNTs can perfectly adsorb both organic [52] and inorganic [53] compounds and sequester nutrient compounds from the culture medium leading to exhibit apparent toxicity. Some studies suggest that CNTs can provoke oxidative stress by producing ROS [54] that can threaten organisms through a variety of interrelated effects, such as lipid peroxidation and DNA damage [55]. In addition, CNTs may agglomerate with microbe cells, form hydrogen bonds between the cell surfaces and the oxygen defects of CNTs [49]. CNTs closely attached to the cell surfaces, disrupt the cell wall, interact with the biomolecules and inhibit physiological cell physically and chemically, thus present toxicity [55, 56]. The shade effects of nanoparticles result in the inhibition of growth due to adhering to algal surfaces and hence restricting light accessibility to the cells [57].

1.3.3 Toxicity Effect of Metallic Nanoparticles

1.3.3.1 Gold Nanoparticles

The toxicity of Au NPs to freshwater algae *Scenedesmus subspicatus* was researched by García-Cambero et al. For adsorption, non-functionalized Au NPs transferred to the cell wall and adsorbed onto the cellulose layer but did not penetrate into the cell. However, hyaluronic acid functionalized Au NPs did not appear around the algae as well as not interact with the cell wall. Both Au NPs showed no adverse effects and were less harmful to tested algae [58]. Similarly, the Au NPs toxicity to green algae *C. reinhardtii* examined by Behra et al. had no significant toxicity to *C. reinhardtii*, suggesting the toxicity of Au NPs on algal growth relates to particular coatings rather than to the gold core [59]. However, contradictory findings of Renault et al. showed lethal effects on *S. subspicatus* exposed to citrate-coated Au NPs (10 nm), with an LC_{50} of 1.6×10^5 Au NPs/cell [60]. Rather, the soluble salt of gold produced exerted acute toxicity in algae with an EC_{50} of 1.91 mg Au/L and LC_{50} between 1 and 2 mg/L for *S. subspicatus* [58].

In view of other toxicity studies with Au NPs, the key factors for toxicity of Au NPs can be divided into two parts, which explained both the bioavailability and toxicity of the Au NPs. One is the surface electric charge; Au NPs can exert toxicity on algae if positively charged functional groups are combined with them. The other is the particle/hydrodynamic size where smaller size particles are easier to assimilate [58].

1.3.3.2 Silver Nanoparticles

The critical factors of Ag NPs toxicity to algae are the type of silver, dosage, or concentration. He et al. examined the toxic effects of ionic silver Ag(I) and citrate-stabilized Ag NPs to marine *raphidophyte*. The dissolved Ag(I) concentration increased with the initial Ag NPs concentration, while the ratio of dissolved silver to total silver decreased (30% for 5 μM and 18% for 20 μM). This would be due to partial uptake by algae and due to the toxicity of Ag NPs. The shapes of algae cells changed from spindle to round and eventually lysed and collapsed after exposure to Ag NPs. The degree of deformation increased with the increasing dosage of Ag NPs, which caused a significant reduction in algal viability. Ionic silver exhibited higher toxicity to algae than Ag NPs [61]. Mechanisms for Ag NPs toxicity may include adhesion to membranes, altering their properties such as permeability or ion transport (eventually increasing the porosity of the cells); disturbances in the cellular phosphate management, and inhibition of DNA synthesis; ROS generation [62].

1.3.3.3 Zero-Valent Iron Nanoparticles

Pádrová et al. carried out an experiment about the effects of two different types of nZVI, Nanofer 25 (surface coated with a Na-acrylic copolymer), and Nanofer 25S (uncoated), on the growth of algae. It was observed that concentrations from 0.5 to 5.1 mg/L nZVI enhanced growth, while concentrations above 17 mg/L led to a gradual growth reduction for all treated algae. Even though both Nanofer 25 and Nanofer 25S had the same concentration range, the stimulatory effect of Nanofer 25 was more pronounced and the growth inhibition was lower compared to Nanofer 25S [63]. Other studies were conducted by Kadar et al. to analyze the effects of three types of nZVI, Nanofer 25, Nanofer 25S, and Nanfer STAR (Surface stabilized Transportable Air-stable Reactive), to three marine microalgae, unicellular algae species, which were grown in culture medium fortified with the nano-Fe compounds. Evidence showed that nZVI in equimolar concentration to Fe-EDTA in conventionally used algal growth media does not impair growth, cellular morphology, or lipid content of the three marine microalgae [64].

Nanotoxicity strongly depended on particle size. Lei et al. studied algal toxicity of 4 nZVI with claimed particle sizes of 20, 50, 80, and 100 nm (nZVI-20, nZVI-50, nZVI-80 and nZVI-100). The results illustrated a decreasing nanotoxicity with increasing particle size, and the 96 h EC_{50} concentrations were nZVI-100 (91.3 mg/L) > nZVI-80 (81.2 mg/L) > nZVI-50 (74.1 mg/L) > nZVI-20 (19.8 mg/L). Besides, nZVI-20 showed the strongest agglomeration and co-precipitation with the algae cells, maximal production of MDA content, highest level of lipid peroxidation, and greatest deformation compared with the three larger nZVIs, which accounted for algal toxicity. In conclusion, nZVI with smaller particle size can enhance the direct interaction between algae and nZVI, and lead to higher oxidative stress as a result of higher algal toxicity [65].

1.3.4 Toxicity Effect of Quantum Dots

Domingos et al. explored the bioaccumulation and effects of CdTe/CdS QDs on C. *reinhardtii*. It was found that QDs dissolution rates which accounted for bioaccumulation increased with decreasing pH, increasing QDs concentration, and decreasing particle size. Cellular Cd was increased with decreasing pH and increasing QDs concentration [66]. Another study published by Wang et al. investigated the bioaccumulation of thioglycolic acid stabilized CdTe QDs (TGA-CdTe-QDs) in freshwater alga *Ochromonas Danica*. The results showed real internalization of TGA-CdTe-QDs due to micropinocytosis and its uptake rates increased with their ambient concentration proportionally. Despite that, the uptake of TGA-CdTe-QDs had no direct acute effects on *O. Danica* [67]. The results were consistent with Lin et al. who reported there was no apparent algal cell death observed, although it was apparent that QDs adsorbed on the algae surface [8]. It was also confirmed that CdSe/ZnS QDs could be adsorbed on algal cell surfaces with a high affinity due to the porous structure of the algal cell wall affording abundant binding sites for QDs. As a result, algal photosynthesis was significantly inhibited with CO_2 depletion decreased and O_2 production declined [8].

In terms of toxic effects, physicochemical properties (size, functional groups, oxidative and photolytic stability), and environmental conditions, such as ionic strength and nutrient solution, were regarded as major determinants [68]. Similarly, Zhang et al. investigated the toxicity of functionalized (amine and carboxyl) CdSe/ZnS QDs to the marine diatom *T. pseudonana*, which showed that the nutrient conditions and surface properties of QDs influenced the interactions of QDs and algae. On one hand, both functionalized CdSe/ZnS QDs showed that the release of Cd ions was significantly higher in nitrogen-limited media compared with nutrient enriched media due to the aggregation between QDs and extracellular polymeric substances (EPS) induced by QDs. On the other hand, carboxyl-functionalized QDs dissolved mostly while amine-functionalized QDs aggregated rather than dissolved in culture [69].

1.4 Interaction of Nanoparticles with Existing Environment to Algae

Nanoparticles with their remarkably high surface may adsorb pollutants, which might change the bioavailability of both NPs and pollutants in natural systems and alter their toxicity to algae. Heavy metals including Zn, Cd, Pb, Ni, Cu, and Co have adverse effects on the growth, cell diversion, photosynthesis, and destruction of primary metabolites in algae. The metal ion speciation might be changed by NPs, therefore altering their potential toxicity to algae. At low nano-TiO_2 concentrations, the mortality increased with increasing nano-TiO_2. When the nano-TiO_2 concentration reached a certain value, the amount of Zn^{2+} dissolved and adsorbed by algae

sharply decreased. High nano-TiO_2 concentrations reduced aggregation, which decreased the mortality of *Anabaeba* sp. with increasing nano-TiO_2 [70]. The combined effects of GO and Cd^{2+} solution on *Microcystis aeruginosa* were investigated [71]. GO at low concentrations significantly enhanced Cd^{2+} toxicity. However, the concentration of GO above 5 mg/L did not increase the toxicity of the Cd^{2+}/GO system. Moreover, the significant antagonistic effects between GO and copper on the freshwater microalgae *S. obliquus* were also studied [44]. Adsorption of copper to suspended GO agglomerates, in the culture or on the algal surface, may be responsible for the decrease in copper bioavailability and contribute to the inhibition of Cu^{2+} toxicity.

Organic pollutants may interact with hydrophobic NPs such as carbon nanotubes and fullerences [72]. The toxic effects in *S. obliquus* cultures incubated with graphene nanoplatelets suspensions containing low molecular weight organic acids were related to their concentration. In addition, the influence of natural organic matter (NOM) was expected to alter materials toxicity to *M. aeruginosa* [39]. It would be essential to further elucidate if NPs could considerably interact with other common chemical pollutants by changing the form, structure, and adsorption efficiency of the chemical pollutants and eventually lead to increased additive or synergistic toxicity to algae.

At the same time, the growth of *p. subcapitata* was also found to be inhibited under visible light, UV-A (315–400 nm), and UV-B (280–315 nm) irradiation conditions, with no significant differences in results among the light conditions [16]. Moreover, the photocatalytic activity of ZnO NPs under UV-C irradiation with a wavelength less than 280 nm, enhanced the cytotoxic effects to algae *S. obliquus* [28].

So, all results underline that the potential interactions of NPs with existing environmental contaminants must be taken into account in assessing environmental risk of NPs to algae.

1.5 Summary and Future Directions

Significant progress has been made in the past decade about the toxicity of NPs on algae. The toxicity of NPs on algae has been summarized based on the currently available data. The toxic action of NPs can potentially involve some distinct mechanisms. First, NPs or their surface may interact directly with algae. Second, NPs may release toxic substances into exposure media, e.g., free heavy metal ions. Third, surface interaction of NPs with media may produce toxic substances to algae. Furthermore, the main toxicity mechanism of NPs might be different in the nature, because of their colloidal behaviors and adsorption capability. However, it is not possible to make a general conclusion on the factors determining the algal toxicity of NPs at the current state of knowledge. At the same time, there is no sufficient data on chronic effects from long term and low concentration exposure, which may be more representative for real environmental exposure.

A complete understanding of the interactions between adsorption, dispersion, and toxicity of NPs on algae warrant research in the future. Future research on the fate and transport of NPs in the subsurface environment should also address the transience and heterogeneity of the physical and chemical conditions of the porous media that influence the NPs properties, flow phenomena, and consequently, NPs transport processes. The potential interactions of engineered NPs with existing environmental contaminants must be taken into account in environmental risk assessments of NPs.

References

1. Dunphy KA, Guzmán MRT, Banfield JF (2006) Environmental risks of nanotechnology: national nanotechnology initiative funding. Environ Sci Technol 6:2000–2004
2. Ji J, Long ZF, Lin DH (2011) Toxicity of oxide nanoparticles to the green algae *Chlorella* sp. Chem Eng J 170(2–3):525–530
3. Cepoi L, Rudi L, Chiriac T, Valuta A, Zinicovscaia I, Duca G, Kirkesali E, Frontasyeva M, Culicov O, Pavlov S, Bobrikov I (2015) Biochemical changes in cyanobacteria during the synthesis of silver nanoparticles. Can J Microbiol 61(1):13–21
4. Das P, Metcalfe CD, Xenopoulos MA (2014) Interactive effects of silver nanoparticles and phosphorus on phytoplankton growth in natural waters. Environ Sci Technol 48(8): 4573–4580
5. Ksiazyk M, Asztemborska M, Steborowski R, Bystrzejewska-Piotrowska G (2015) Toxic effect of silver and platinum nanoparticles toward the freshwater microalgal *Pseudokirchneriella subcapitata*. Bull Environ Contam Toxicol 94(5):554–558
6. Chang NB, Wanielista M, Hossain F, Zhai L, Lin KS (2008) Integrating nanoscale zero-valent iron and titanium dioxide for nutrient removal in stormwater systems. NANO 3(4):297–300
7. Garcia-Cambero JP, Garcia MN, Lopez GD, Herranz AL, Cuevas L, Perez-Pastrana E, Cuadal JS, Castelltort MR, Calvo AC (2013) Converging hazard assessment of gold nanoparticles to aquatic organisms. Chemosphere 93(6):1194–1200
8. Sijie Lin PB, Rajapakse NC, Brune DE, Ke PC (2009) Effects of quantum dots adsorption on algal photosynthesis. J Phys Chem C 113(25):10962–10966
9. Lambreva MD, Lavecchia T, Tyystjarvi E, Antal TK, Orlanducci S, Margonelli A, Rea G (2015) Potential of carbon nanotubes in algal biotechnology. Photosynth Res 125(3):451–471
10. Long Z, Ji J, Yang K, Lin D, Wu F (2012) Systematic and quantitative investigation of the mechanism of carbon nanotubes' toxicity toward algae. Environ Sci Technol 46(15):8458–8466
11. Zhou H, Wang XJ, Zhou Y, Yao HZ, Ahmad F (2014) Evaluation of the toxicity of ZnO nanoparticles to *Chlorella vulgaris* by use of the chiral perturbation approach. Anal Bioanal Chem 406(15):3689–3695
12. Chen P, Powell BA, Mortimer M, Ke PC (2012) Adaptive interactions between zinc oxide nanoparticles and *Chlorella* sp. Environ Sci Technol 46(21):12178–12185
13. Li F, Liang Z, Zheng X, Zhao W, Wu M, Wang Z (2015) Toxicity of nano-TiO_2 on algae and the site of reactive oxygen species production. Aquat Toxicol 158:1–13
14. Nicolas M, Séverine LM, Anne B-N, Pascal P (2015) Effect of two TiO_2 nanoparticles on the growth of unicellular green algae using the OECD 201 test guideline: influence of the exposure system. Toxicol Environ Chem 98(8):860–876
15. Organisation for Economic Cooperation and Development (1984) Algal growth inhibition test. OECD Guidelines for Testing of Chemicals 201, Paris, France

16. Lee WM, An YJ (2013) Effects of zinc oxide and titanium dioxide nanoparticles on green algae under visible, UVA, and UVB irradiations: no evidence of enhanced algal toxicity under UV pre-irradiation. Chemosphere 91(4):536–544
17. Yu Morgalev Y, Morgaleva T, Gosteva I, Morgalev S, Kulizhskiy S, Astafurova T (2015) Effect of zink oxyde nanoparticles on the test function of water organisms of different trophic levels. In *IOP conference series: materials science and engineering*. 012005
18. Miazek K, Iwanek W, Remacle C, Richel A, Goffin D (2015) Effect of metals, metalloids and metallic nanoparticles on microalgae growth and industrial product biosynthesis: a review. Int J Mol Sci 16(10):23929–23969
19. Jeffrey SW, Humphrey GF (1975) New spectrophotometric equations for determining chlorophyll a, b, c1 and c2 in higher plants and natural phytoplankton. Biochem Physiol Pflanz 8:53–59
20. Jagadeesh E, Khan B, Chandran P, Khan SS (2015) Toxic potential of iron oxide, CdS/Ag_2S composite, CdS and Ag_2S NPs on a fresh water alga *Mougeotia* sp. Colloids Surf, B 125: 284–290
21. Aruoja V, Dubourguier HC, Kasemets K, Kahru A (2009) Toxicity of nanoparticles of CuO, ZnO and TiO_2 to microalgae *Pseudokirchneriella subcapitata*. Sci Total Environ 407 (4):1461–1468
22. Roy R, Parashar A, Bhuvaneshwari M, Chandrasekaran N, Mukherjee A (2016) Differential effects of P25 TiO_2 nanoparticles on freshwater green microalgae: Chlorella and Scenedesmus species. Aquat Toxicol 176:161–171
23. Hund-Rinke K, Simon M (2006) Ecotoxic effect of photocatalytic active nanoparticles (TiO_2) on algae and daphnids. Environ Sci Pollut Res Int 13(4):225–232
24. Hartmann NB, Von der Kammer F, Hofmann T, Baalousha M, Ottofuelling S, Baun A (2010) Algal testing of titanium dioxide nanoparticles-testing considerations, inhibitory effects and modification of cadmium bioavailability. Toxicology 269(2–3):190–197
25. Cherchi C, Chernenko T, Diem M, Gu AZ (2011) Impact of nano titanium dioxide exposure on cellular structure of *Anabaena variabilis* and evidence of internalization. Environ Toxicol Chem 30(4):861–869
26. Dalai S, Pakrashi S, Joyce Nirmala M, Chaudhri A, Chandrasekaran N, Mandal AB, Mukherjee A (2013) Cytotoxicity of TiO_2 nanoparticles and their detoxification in a freshwater system. Aquat Toxicol 138–139:1–11
27. Hazeem LJ, Bououdina M, Rashdan S, Brunet L, Slomianny C, Boukherroub R (2016) Cumulative effect of zinc oxide and titanium oxide nanoparticles on growth and chlorophyll a content of *Picochlorum* sp. Environ Sci Pollut Res Int 23(3):2821–2830
28. Bhuvaneshwari M, Iswarya V, Archanaa S, Madhu GM, Kumar GK, Nagarajan R, Chandrasekaran N, Mukherjee A (2015) Cytotoxicity of ZnO NPs towards fresh water algae *Scenedesmus obliquus* at low exposure concentrations in UV-C, visible and dark conditions. Aquat Toxicol 162:29–38
29. Peng X, Palma S, Fisher NS, Wong SS (2011) Effect of morphology of ZnO nanostructures on their toxicity to marine algae. Aquat Toxicol 102(3–4):186–196
30. Spisni E, Seo S, Joo SH, Su C (2016) Release and toxicity comparison between industrial- and sunscreen-derived nano-ZnO particles. Int J Environ Sci Technol 13(10):2485–2494
31. Bystrzejewska-Piotrowska G, Golimowski J, Urban PL (2009) Nanoparticles: their potential toxicity, waste and environmental management. Waste Manag 29(9):2587–2595
32. Franklin NM, Rogers NJ, Apte SC, Batley GE, Gadd GE, Casey PS (2007) Comparative toxicity of nanoparticles ZnO, bulk ZnO and $ZnCl_2$ to a freshwater microalgae (*Pseudokirchneriella subcapitata*) the importance of particle solubility. Environ Sci Technol 41(24):8484–8490
33. Robert J, Miller HSL, Muller EB, Tseng N, Hanna SK, Keller AA (2010) Impacts of metal oxide nanoparticles on marine phytoplankton. Environ Sci Technol 44:7329–7334
34. Melegari SP, Perreault F, Costa RHR, Popovic R, Matias WG (2013) Evaluation of toxicity and oxidative stress induced by copper oxide nanoparticles in the green alga *Chlamydomonas reinhardtii*. Aquat Toxicol 142–143(4):431–440

35. Perreault F, Oukarroum A, Melegari SP, Matias WG, Popovic R (2012) Polymer coating of copper oxide nanoparticles increases nanoparticles uptake and toxicity in the green alga *Chlamydomonas reinhardtii*. Chemosphere 87(11):1388–1394
36. Babu MY, Palanikumar L, Nagarani N, Devi VJ, Kumar SR, Ramakritinan CM, Kumaraguru AK (2014) Cadmium and copper toxicity in three marine macroalgae: evaluation of the biochemical responses and DNA damage. Environ Sci Pollut Res 21:9604–9616
37. Gouveia C, Kreusch M, Schmidt ÉC, Felix MR, Osorio LK, Pereira DT, dos Santos R, Ouriques LC, Martins Rde P, Latini A, Ramlov F, Carvalho TJ, Chow F, Maraschin M, Bouzon ZL (2013) The effects of lead and copper on the cellular architecture and metabolism of the red alga *Gracilaria domingensis*. Microsc Microanal 19(3):513–524
38. Manusadzianas L, Caillet C, Fachetti L, Gylyte B, Grigutyte R, Jurkoniene S, Karitonas R, Sadauskas K, Thomas F, Vitkus R, Ferard JF (2012) Toxicity of copper oxide nanoparticle suspensions to aquatic biota. Environ Toxicol Chem 31(1):108–114
39. Zhao J, Wang Z, White JC, Xing B (2014) Graphene in the aquatic environment: adsorption, dispersion, toxicity and transformation. Environ Sci Technol 48(17):9995–10009
40. Nogueira PF, Nakabayashi D, Zucolotto V (2015) The effects of graphene oxide on green algae *Raphidocelis subcapitata*. Aquat Toxicol 166:29–35
41. Pretti C, Oliva M, Pietro RD, Monni G, Cevasco G, Chiellini F, Pomelli C, Chiappe C (2014) Ecotoxicity of pristine graphene to marine organisms. Ecotoxicol Environ Saf 101:138–145
42. Wahid MH, Eroglu E, Chen X, Smith SM, Raston CL (2013) Entrapment of *Chlorella vulgaris* cells within graphene oxide layers. RSC Adv 3(22):8180
43. Wang Z, Gao Y, Wang S, Fang H, Xu D, Zhang F (2016) Impacts of low-molecular-weight organic acids on aquatic behavior of graphene nanoplatelets and their induced algal toxicity and antioxidant capacity. Environ Sci Pollut Res Int 23(11):10938–10945
44. Hu C, Hu N, Li X, Zhao Y (2016) Graphene oxide alleviates the ecotoxicity of copper on the freshwater microalga *Scenedesmus obliquus*. Ecotoxicol Environ Saf 132:360–365
45. Wang J, Zhang X, Chen Y, Sommerfeld M, Hu Q (2008) Toxicity assessment of manufactured nanomaterials using the unicellular green alga *Chlamydomonas reinhardtii*. Chemosphere 73(7):1121–1128
46. Chen Q, Hu X, Yin D, Wang R (2016) Effect of subcellular distribution on nC_{60} uptake and transfer efficiency from *Scenedesmus obliquus* to *Daphnia magna*. Ecotoxicol Environ Saf 128:213–221
47. Tao X, Li C, Zhang B, He Y (2016) Effects of aqueous stable fullerene nanocrystals (nC_{60}) on the food conversion from *Daphnia magna* to *Danio rerio* in a simplified freshwater food chain. Chemosphere 145:157–162
48. Wei L, Thakkar M, Chen Y, Ntim SA, Mitra S, Zhang X (2010) Cytotoxicity effects of water dispersible oxidized multiwalled carbon nanotubes on marine alga, *Dunaliella tertiolecta*. Aquat Toxicol 100(2):194–201
49. Schwab F, Bucheli TD, Lukhele LP, Magrez A, Nowack B, Sigg L, Knauer K (2011) Are carbon nanotube effects on green algae caused by shading and agglomeration? Environ Sci Technol 45(14):6136–6144
50. Hull MS, Kennedy AJ, Steevens JA, Bednar AJ, Weiss CA Jr, Vikesland PJ (2009) Release of metal impurities from carbon nanomaterials influences aquatic toxicity. Environ Sci Technol 43:4169–4174
51. Pumera M, Sánchez S, Ichinose I, Tang J (2007) Carbon nanotubes contain residual metal catalyst nanoparticles even after washing with nitric acid at elevated temperature because these metal nanoparticles are sheathed by several graphene sheets. Sens Actuators B Chem 123(2):1195–1205
52. Yang K, Xing KB (2010) Adsorption of organic compounds by carbon nanomaterials in aqueous phase: polanyi theory and its application. Chem Rev 110:5989–6008
53. Rao G, Lu C, Su F (2007) Sorption of divalent metal ions from aqueous solution by carbon nanotubes: a review. Sep Purif Technol 58(1):224–231
54. Chen CY, Jafvert CT (2010) Photoreactivity of carboxylated single-walled carbon nanotubes in sunlight: reactive oxygen species production in water. Environ Sci Technol 44:6674–6679

55. Andre Nel TX, Mädler L, Li N (2006) Toxic potential of materials at the nanolevel. Science 311(5761):622–627
56. Kang S, Herzberg M, Rodrigues DF, Elimelech M (2008) Antibacterial effects of carbon nanotubes: size does matter! Langmuir 24:6409–6413
57. Van Hoecke K, De Schamphelaere KAC, Van der Meeren P, Lucas S, Janssen CR (2008) Ecotoxicity of silica nanoparticles to the green alga *Pseudokirchneriella subcapitata*: importance of surface area. Environ Toxicol Chem 27:1948–1957
58. Garcia-Cambero JP, Nunez Garcia M, Lopez GD, Herranz AL, Cuevas L, Perez-Pastrana E, Cuadal JS, Castelltort MR, Calvo AC (2013) Converging hazard assessment of gold nanoparticles to aquatic organisms. Chemosphere 93(6):1194–1200
59. Behra R, Wagner B, Sgier L, Kistler D (2015) Colloidal stability and toxicity of gold nanoparticles and gold chloride on *Chlamydomonas reinhardtii*. Aquat Geochem 21(2–4): 331–342
60. Renault S, Baudrimont M, Mesmer-Dudons N, Gonzalez P, Mornet S, Brisson A (2008) Impacts of gold nanoparticle exposure on two freshwater species: a phytoplanktonic alga (*Scenedesmus subspicatus*) and a benthic bivalve (*Corbicula fluminea*). Gold Bull 41(2): 116–126
61. He D, Dorantes-Aranda JJ, Waite TD (2012) Silver nanoparticle-algae interactions: oxidative dissolution, reactive oxygen species generation and synergistic toxic effects. Environ Sci Technol 46(16):8731–8738
62. Klaine SJ, Alvarez PJJ, Batley GE, Fernandes TF, Handy RD, Lyon DY, Mahendra S, McLaughun MJ, Lead JR (2008) Nanomaterials in the environment: behavior, fate, bioavailability, and effects. Environ Toxicol Chem 27:1825–1851
63. Pádrová K, Lukavský J, Nedbalová L, Čejková A, Cajthaml T, Sigler K, Vítová M, Řezanka T (2014) Trace concentrations of iron nanoparticles cause overproduction of biomass and lipids during cultivation of cyanobacteria and microalgae. J Appl Phycol 27(4):1443–1451
64. Kadar E, Rooks P, Lakey C, White DA (2012) The effect of engineered iron nanoparticles on growth and metabolic status of marine microalgae cultures. Sci Total Environ 439:8–17
65. Lei C, Zhang L, Yang K, Zhu L, Lin D (2016) Toxicity of iron-based nanoparticles to green algae: effects of particle size, crystal phase, oxidation state and environmental aging. Environ Pollut 218:505–512
66. Domingos RF, Simon DF, Hauser C, Wilkinson KJ (2011) Bioaccumulation and effects of CdTe/CdS quantum dots on *Chlamydomonas reinhardtii*—nanoparticles or the free ions? Environ Sci Technol 45(18):7664–7669
67. Wang Y, Miao AJ, Luo J, Wei ZB, Zhu JJ, Yang LY (2013) Bioaccumulation of CdTe quantum dots in a freshwater alga *Ochromonas danica*: a kinetics study. Environ Sci Technol 47(18):10601–10610
68. Uyusur B, Darnault CJ, Snee PT, Koken E, Jacobson AR, Wells RR (2010) Coupled effects of solution chemistry and hydrodynamics on the mobility and transport of quantum dot nanomaterials in the vadose zone. J Contam Hydrol 118(3–4):184–198
69. Zhang S, Jiang Y, Chen CS, Creeley D, Schwehr KA, Quigg A, Chin WC, Santschi PH (2013) Ameliorating effects of extracellular polymeric substances excreted by *Thalassiosira pseudonana* on algal toxicity of CdSe quantum dots. Aquat Toxicol 126:214–223
70. Tang Y, Li S, Qiao J, Wang H, Li L (2013) Synergistic effects of nano-sized titanium dioxide and zinc on the photosynthetic capacity and survival of *Anabaena* sp. Int J Mol Sci 14 (7):14395–14407

71. Tang YL, Tian JL, Li SY, Xue CH, Xue ZH, Yin DQ, Yu SL (2015) Combined effects of graphene oxide and Cd on the photosynthetic capacity and survival of *Microcystis aeruginosa*. Sci Total Environ 532:154–161
72. Wang Z, Gao Y, Wang S, Fang H, Xu D, Zhang F (2016) Impacts of low-molecular-weight organic acids on aquatic behavior of graphene nanoplatelets and their induced algal toxicity and antioxidant capacity. Environ Sci Pollut Res 23(11):10938–10945

Chapter 2
Terrestrial Nanotoxicology: Evaluating the Nano-Biointeractions in Vascular Plants

Swati Rawat, Suzanne A. Apodaca, Wenjuan Tan, Jose R. Peralta-Videa and Jorge L. Gardea-Torresdey

Abstract The effects of engineered nanoparticles (ENPs) in living organisms are described in a myriad of articles. Most of the literature on this topic is devoted to plants of different gender and species. Studies from laboratories and greenhouse facilities highlight effects on chlorophyll production, plant growth, stress enzyme activities, phytotoxicity, cytotoxicity, and genotoxicity. With few exceptions, research reports show that toxic effects of ENPs on plants are associated with particle size, phase, surface properties, exposure concentration, and soil chemistry. ENPs have been found to be taken through roots from soilless/soil media and translocated to the aboveground organs. However, the uptake and translocation can occur in reverse if important amounts of ENPs are exposed to the foliage. This chapter includes an analysis of the most recent and relevant information about the interaction of ENPs with vascular plants. Most of the reviewed literature refers to highly produced and used ENPs. Data about exposure to carbon nanotubes (CNTs), cerium dioxide (nano-CeO_2), titanium dioxide (nano-TiO_2), zinc oxide (nano-ZnO), copper oxide (nano-CuO), gold (nano-Au), iron (nano-Fe_3O_4), silver (nano-Ag), and others ENPs are discussed.

Keywords Engineered nanoparticles · Toxicology · Uptake · Exposure pathways · Risk assessment

2.1 Introduction

Plants have evolved exposed to naturally produced particulate matter (PM). However, exposure to PM has increased since the industrial revolution due to emissions from stationary and mobile sources [1]. In current times, PM at the nanoscale is progressively released from devices, goods, personal care items,

S. Rawat · S.A. Apodaca · W. Tan · J.R. Peralta-Videa · J.L. Gardea-Torresdey (✉)
Environmental Science and Engineering, The University of Texas at El Paso,
500 West University Ave., El Paso, TX 79968, USA
e-mail: jgardea@utep.edu

B. Yan et al. (eds.), *Bioactivity of Engineered Nanoparticles*,
Nanomedicine and Nanotoxicology, DOI 10.1007/978-981-10-5864-6_2

and agriculture-intended products. Recent reports indicate that industrial facilities [2], cars, trucks, agriculture, and farming equipment [3], agricultural applications of nanotechnology [4], and the constant increase of nanomaterials in biosolids [5], have dramatically increased the risks of plant exposure to PM.

Concerns about the environmental impacts of nanotechnologies are becoming more and more voiced. US federal agencies like the National Science Foundation and the Environmental Protection Agency, governmental agencies of other countries, public and private universities, and other organizations are devoting capitals to investigate possible effects of nanotechnologies in human beings and basic resources like beneficial microorganisms, animals, and plants. So far, thousands of research and review articles (ScienceDirect.com shows more than 1,600 for 2015 and 2016 only) have described a variety of effects of nanomaterials in living organisms. This chapter includes the most recent and relevant information about the interaction of nanomaterials with vascular plants. Most of the reviewed literature refers to highly produced and used engineered nanoparticles (ENPs) including carbon-based, such as carbon nanotubes (CNTs), and metal-based, like cerium dioxide (nano-CeO_2), copper oxide (nano-CuO), titanium dioxide (nano-TiO_2), zinc oxide (nano-ZnO), gold (nano-Au), iron (nano-Fe_3O_4), silver (nano-Ag), and other ENPs. When available, information concerning micrometric particles was included. Emphasis was given to industrially produced or garden grown agricultural plants. Most of the reported studies have been performed under controlled environments (laboratory, growth chamber, and greenhouse), and to the authors' knowledge, there are no reports of field conditions.

2.2 Evidence of Uptake Accumulation and Biotransformation of ENPs and Exposure Pathways

The reported literature highlights effects of ENPs in root and shoot lengths, activity of stress enzymes, carbohydrates, sugars, amino acids, proteins, chlorophyll production, phytotoxicity, cytotoxicity, genotoxicity, and biotransformation. Analytical techniques including electron microscopy (SEM/TEM) [6], synchrotron micro X-ray fluorescence (μ-XRF) and micro X-ray absorption near edge structure (μ-XANES) [7, 8], and confocal microscopy [9], among others, have been used to study the uptake of ENPs and related ions, and to determine their location and oxidation state.

It is believed that the physiological and agronomical impacts of ENPs on plants rely on their uptake, translocation, accumulation, and biotransformation within plant systems. It is also hypothesized that impacts depend on the exposure pathway, concentration, plant species, and environment. There are reports from plants grown in liquid and solid media exposed to different concentrations of ENPs, either through the roots or the foliage. The most abundant reports correspond to root

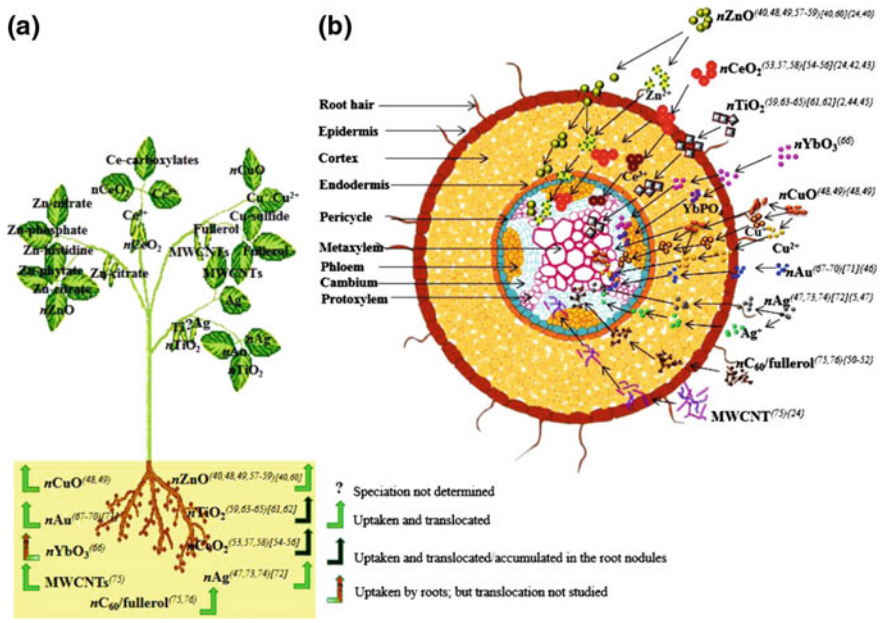

Fig. 2.1 Schematic diagram of uptake and biotransformation of nanomaterials (NMs) in plant systems, including hydroponic and soil culture. **a** Speciation of ENMs in plant tissues (roots, stems, leaves, and fruits/grains); **b** Transverse cross section of root cell illustrating biotransformation of NMs. Reference numbers in the figure correspond to the original review article and *n* stands for nano. (Reprinted with permission from Gardea-Torresdey et al. [10]. Copyright @ 2014 American Chemical Society)

exposure and only a few of them refer to foliar exposure. Figure 2.1 [10] illustrates comprehensive possible uptake routes and mechanisms. As shown in this figure, independent of the substrate, plants take up the ENPs through roots or foliage by active or passive mechanisms. Detailed information is presented in the following sections and in a critical review by Ma et al. [11].

2.2.1 Root Exposure Studies

Applications of nanoscale agricultural products such as fertilizers [4, 12], additives for soil remediation [13], growth regulators [14], and discharges of wastewater and biosolids [5, 15] could be great contributors for the uptake and accumulation of ENPs from root exposure. Studies performed in soilless or soil media have explored effects on seeds [16], seedlings [17], and tubers [18]. One of the first studies about ENPs' uptake and translocation was performed by Zhu et al. [19]. In such study, pumpkin (*Cucurbita maxima*) was exposed to magnetic nano-Fe_3O_4 through roots in an aqueous medium. After 20 days of growth, Zhu et al. measured the

concentration of ENPs in stems and leaves by busing a vibrating sample magnetometer (VSM, LakeShore 7400), demonstrating the uptake and translocation of the nano-Fe_3O_4 from roots to the aboveground plant system. Later on, Khodakovskaya et al. [16] reported that carbon nanotubes penetrated the thick seed coat of tomato (*Solanum lycopersicum* L.), affecting seed water transportation, germination, and seedling growth. More recently, Zhao et al. [9, 20] exposed corn (*Zea mays*) seedlings to fluorescein isothiocyanate (FITC)-stained CeO_2 and ZnO ENPs, and found that both penetrated the root tissues, reaching the transport system. Confocal images showed that the Casparian strip retained the stained ENPs; however, they further entered the vasculature at the emission point of lateral roots [21]. This was later confirmed by Majumdar et al. [22] in kidney bean plants (*Phaseolus vulgaris*). The images suggested that the ENPs entered the root endodermis through the apoplast, followed by the symplast [9], ultimately reaching the aboveground plant system (Fig. 2.2) [11].

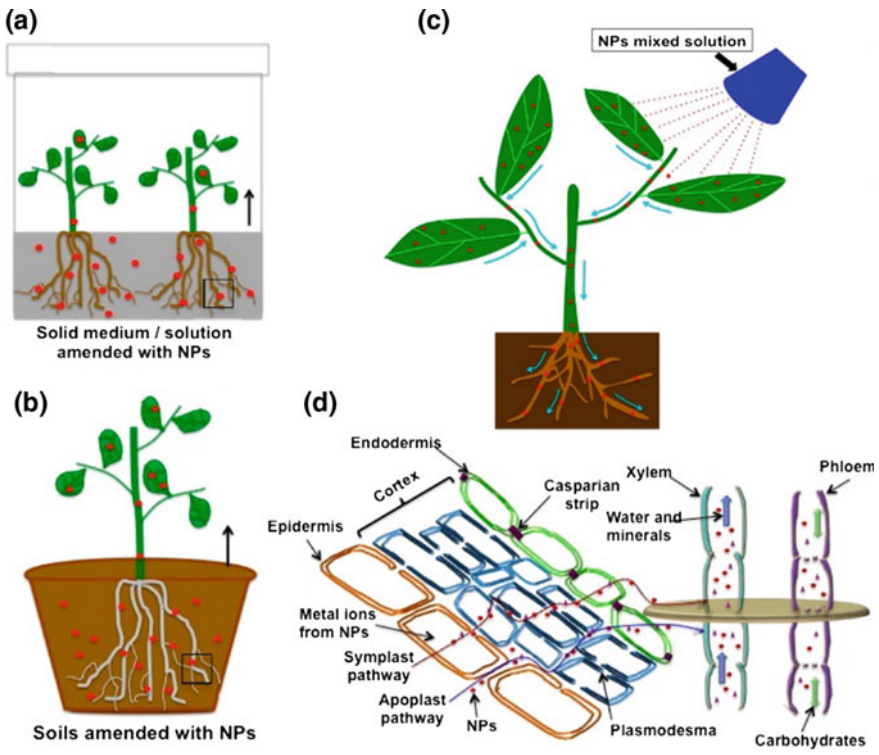

Fig. 2.2 Schematic diagram of possible pathways of ENPs uptake and translocation. **a**, **b** Plants grown in media amended with NPs. **c** ENPs exposed to plants via foliar spray. **d** ENPs entered into plants through symplastic and apoplastic regions. (Reprinted with permission from Ma et al. [11]. Copyright @ 2015 American Chemical Society)

Lopez-Moreno et al. [23] firstly reported the speciation of ZnO and CeO_2 within plant tissues. These researchers exposed soybean [23] to either ZnO or CeO_2 ENPs and through XANES analyses determined that, within the root, most of the Ce was in the same oxidation state as CeO_2, but ZnO was not present. Lopez-Moreno et al. [24] also exposed CeO_2 to alfalfa (*Medicago sativa*), corn, cucumber (*Cucumis sativus*), and tomato, and corroborated that CeO_2 ENPs were stored within the roots of the four plant species. Additionally, by using XANES and STXM, Zhang et al. [25] reported that in cucumber exposed to CeO_2 ENPs, Ce distributed in the root in nanoparticulate (NP) form and as $CePO_4$, and reached the aerial system as CeO_2 ENPs and carboxylates. Majumdar et al. [22] reported that in kidney bean (*P. vulgaris*) roots, 12% of the CeO_2 ENPs was transformed into Ce(III) and distributed to shoots time dependently. Zhao et al. [26] exposed CeO_2 ENPs to cucumber roots and detected Ce in the leaf veins. Thus, these researchers concluded that once these ENPs penetrated the roots, they were translocated to the leaves with the flow of water during transpiration. A hydroponic study with CeO_2 ENPs of different size showed significant Ce translocation from roots to shoots in plants exposed to particles of 10 nm; however, no significant Ce accumulation was observed in shoots of plants exposed to particles >20 nm [27]. Servin et al. [17] exposed cucumber to a mixture of anatase (82%)-rutile (18%) TiO_2 ENPs and analyzed the tissues with μ-XRF and μ-XANES. They found that cucumber absorbed Ti through the roots and translocated it to the leaves. Moreover, they found Ti in leaf trichomes and suggested these structures might work as sinks or excretory structures for TiO_2 ENPs. Avanasi et al. [28] cultured radish (*Raphanus sativus*) in soil amended with ^{14}C-labled C_{60}, and found that only ~7% of the C_{60} was taken up by plants, of which 40–47% was retained in roots, 22–23%, translocation to tubers, 12–16% to stems, and 18–22% to leaves. Studies with CuO and ZnO ENPs exposed to wheat (*Triticum aestivum*) through roots have shown that Cu accumulated in shoots as CuO and Cu(I)-sulfur complexes, while ZnO dissociated, leaving Zn in the form of Zn-phosphate [29]. The above-mentioned results clearly show that further studies are needed in order to fully understand the fate of ENPs absorbed through the roots. In addition, there is a lack of knowledge concerning the accumulation of ENPs in root nodules, contribution of root exudates in surface modification and uptake, retention in xylem vessels, and accumulation in organelles of the aboveground plant system.

2.2.2 Foliar Exposure

There is a long history in the use of foliar applications of micronutrients or pesticides to improve plant health. Currently, there is an increasing trend in the use of ENPs as pesticides [30], herbicides [31], and fertilizers [14]. In determined environments, plants' foliage is unintentionally exposed to ENPs from industrial fallouts [32]. In general, foliar exposure has been less investigated and remains largely

unclear. A few reports have shown physiological effects, accumulation, speciation, and have explored the uptake mechanisms.

One of the first reports about foliar exposure to ENPs was performed by Uzu et al. [33]. These researchers exposed lettuce (*Lactuca sativa*) to lead particles. After 43 days of exposure, they found aggregated Pb nanoparticles (NPs) in necrotic zones and leaf central veins. Additionally, Pb particles were detected in stomatal openings and leaf cuticles. Subsequently, Schreck et al. [34, 35] examined the impact of foliar application of Pb-containing particles in lettuce, parsley (*Petroselinum crispum*) and ryegrass (*Lolium perenne*). These researchers found Pb-rich particles in stomata, $PbCO_3$ or organic Pb crystals on the leaf surface, and $PbSO_4$ underneath leaf membranes. Larue et al. [36, 37] exposed Ag and TiO_2 (pristine and aged paint-containing) ENPs to lettuce leaves and found that some particles were retained by the cuticle and others penetrated through leaf stomata, upon which they were translocated to all plant tissues. Similarly, Hong et al. [6] exposed atmospheric (powder) CeO_2 ENPs to cucumber seedling leaves and, through ICP-OES analyses of mature plants, detected Ce in roots, stems, leaves, and flowers, demonstrating that the powdered CeO_2 reached the transport system through leaves, and remained within the plant until maturity. It seems that entrapment in the cuticle and penetration through stomata are the two main routes of ENPs entry after foliar exposure. However, Birbaum et al. [38] reported no translocation of Ce in corn plants exposed to CeO_2 ENPs, either through foliage or roots, which suggest exclusion mechanisms that deserve more in depth studies.

2.2.3 Accumulation of ENPs in Fruits and Seeds

A few studies have shown that ENPs exposed through root or foliage can be transported and accumulated in fruits and seeds and ingested by human beings. By using μ-XRF and μ-XANES, Hernandez-Viezcas et al. [7] found CeO_2 ENPs in soybean seeds harvested from plants cultivated in soil amended with such ENPs. Using the same techniques, Servin et al. [39] demonstrated that cucumber plants absorbed TiO_2 ENPs from soil and translocated them to fruits. Rico et al. [40] evaluated the Ce accumulation in grains of three rice varieties divergent in amylose content, cultivated in soil amended with CeO_2 ENPs. Results showed that Ce concentrated the most in gains of the varieties with medium and low amylose contents. More recently, Hong et al. [6] exposed CeO_2 ENPs to the foliage of 21-day-old cucumber seedlings and analyzed the fruits for Ce content. They found significantly higher Ce concentration, compared with control and the other treatments, in fruits of plants exposed to 200 mg/L of the CeO_2 ENPs. Although Rico et al. [40] and Hong et al. [6] did not use synchrotron or microscopy techniques to show the presence of CeO_2 ENPs, previous works [7, 12, 41] have demonstrated that these ENPs are very stable and undergo little transformation in soil or within plant tissues. Consequently, it is hypothesized that most of the Ce in cucumber fruits and rice grains was in nanoparticulate form. This suggests that TiO_2 and CeO_2

ENPs can reach the human body through grains and seeds of plants grown in ENPs impacted soils.

In conclusion, the uptake and accumulation of ENPs depend on the species of plant [42], particle size [27], concentration [43], and surface property [44]. The literature indicates that the exposure to ENPs through roots or foliage results in modification of enzyme activities [45], fruit quality [46], and nutrient content [47], among others. This may bring risks to human health, and even disruption of the ecological balance.

2.3 Mechanisms of Interactions Between ENPs and Plants

The literature has shown that ENPs tend to bioaccumulate and persist in plant tissue, influencing cell metabolism and development. They also tend to get deposited in aggregated or unaggregated form on subcellular sites. Figure 2.3

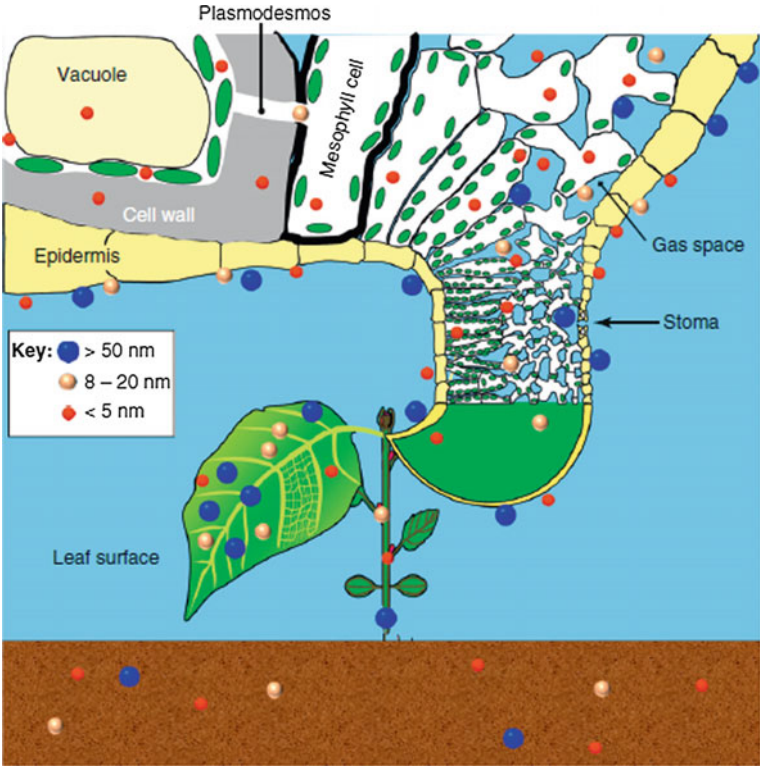

Fig. 2.3 Distribution of NPs of three different sizes in plant shoots at organ, tissue and cell level. (Reprinted with permission from Dietz et al. [48]. Copyrights @ 2011 Elsevier Ltd.)

elaborates the routes that different sized ENPs (>50, 8–20, and <5 nm) can take in the plant [48]. The ENPs translocate from the root, via stem, to the aerial parts of the plant. They enter the intercellular space and traverse to the outer apoplast, whereas only the minute ones are able to diffuse through the plant cell wall and enter the protoplast [48]. ENPs can also be taken up by roots through endocytosis [49].

There are five major mechanisms of action of ENPs on biological systems: (i) metal ions produced from the dissociation of ENPs show chemical effects in solution on dissolution. Essential heavy metals including Cu, Ni, and Zn, and toxic elements like Cd have their ionic form released from the nano forms. They biochemically bind with proteins, carboxyl, sulfhydryl, or imidazole groups hampering their normal functioning. Their meddling with cellular life processes may lead to redox imbalances and, subsequently, induce oxidative stress in plant cells [50, 51]. Metal atoms such as Cu and Fe act as oxidizing agents and give electrons to O_2 to form O_2^- or to H_2O_2 to form the reactive $OH^{\cdot}$ radical. This adds to the oxidative stress in the plant cells. (ii) Mechanical blocking of open pores that then become unavailable for biochemical transport processes. The blocking is size dependent [52]. (iii) Catalytic effect on surfaces due to ions including Ag, Pd, Au, Fe, Pt, and Co that act as catalysts for redox reactions. At very low concentration, the metal ions either bind to organic acids, inducible or constitutive chelators, like phytochelatins, metallothioneins, and ferritin [52], or they participate in transport processes [53]. Such catalytic effect enhances the toxicity of ENPs. (iv) Effects due to proteins bound to the surface of the ENPs, which could be by oxidative effects, ionic, or covalent bonds. Atoms that have an oxidic surface frequently form a layer of hydroxyl groups on the surface [48]. Being negatively charged, the layer bonds with positively charged groups of plant proteins [54]. This deteriorates the work efficiency of the proteins. If the bond between proteins and ENPs is covalent, then the toxic effect is extreme. The bond between cysteine and Au ENPs is one such example of a permanent bond. The most prominent reason for ENPs toxicity is oxidative stress caused by an excess of reactive oxygen species (ROS) [55]. (v) Changes in chemical effects like pH [49]. ENPs present in soil are influenced by variations in surrounding conditions. Factors such as temperature, pH, ionic strength, particle size, and concentration determine their surface properties that further control particle aggregation and deposition [56]. These external factors likely manifest their effect in plant roots at cellular level, via the ENPs that enter the system.

2.4 Toxicity Symptoms

Nanotechnology has experienced immense growth; by extension, plant nanotoxicology has become an emerging field of interest. Many studies on the effects of ENPs to terrestrial plants have materialized within the past few years. Table 2.1

includes an extensive list of the most recent studies, while the most notable ones are summarized in the following paragraphs.

Nano-CuO was found to be translocated from roots to shoots when exposed to maize in hydroponic culture [57]. There was no effect on germination, which was in agreement with previous literature stating that germination is an obtuse measure for phytotoxicity of ENPs [57–59]; however, root elongation was reduced by 55 and 84% at 10 and 100 mg/L of CuO ENPs. Plants also developed chlorotic symptoms, and root and shoot biomass decreased at the same CuO ENP concentrations [57]. Overall, roots of maize were found to be more susceptible to CuO ENPs' toxicity than the shoots. When Ag ENPs were exposed to mung bean (*Phaseolus radiatus*) and sorghum (*Sorghum bicolor*) in soil and agar test media, a concentration dependent-growth inhibition was discovered [60]. The bioavailability of Ag ENPs was also found to be reduced in soil, most likely explained either by changes in physiochemical properties when mixed with soil components or by the intensified aggregation that Ag experiences in the presence of clay [61].

In a comprehensive study that evaluated five commercial ENPs (MWCNTs, Al, Al_2O_3, Zn, ZnO) on seed germination and root growth of radish, rape (*Brassica napus*), ryegrass, lettuce, corn, and cucumber, the most toxic effects were produced by Zn and ZnO ENPs, which suppressed ryegrass and corn germination, respectively [59]. Root growth of five of the tested plant species was essentially terminated. When calculating dose–response curves, 50% inhibitory concentrations (IC_{50}) of 50 mg/L Zn was calculated for radish and 20 mg/L ZnO for rape and ryegrass [59]. Details about other ENPs and plant species are shown in Table 2.1.

2.5 Comparison of the Effects of Microparticles (Bulk) Versus Those of Nanoparticles

In a few studies, the effects of ENPs versus microparticles of the same metal element or compound have been compared. Hong et al. [42] exposed various copper compounds including Cu and CuO ENPs, μCu, and μCuO to lettuce and alfalfa in hydroponics. The root length was consistently affected by all the copper treatments. At 20 mg/L, both plant species absorbed more Cu from the Cu ENPs treatments, compared with both the bulk Cu and CuO treatments. Stress enzyme studies showed that the ascorbate peroxidase (APOX) activity increased at all Cu treatments in roots of both plant species, with the exception of bulk Cu in lettuce. A similar study was conducted with nano and bulk ZnO compounds in green peas (*Pisum sativum*) [91]. The ENP exposed plants resulted in significantly longer roots, whereas the bulk ZnO treatments produced significant longer roots and shoots. The chlorophyll content in leaves was diminished under both bulk and nano treatments. At all ZnO NP treatments, the catalase (CAT) activity was significantly decreased in leaves and APOX activity in roots and leaves. The bulk ZnO exposure, on the other hand, caused no changes in the CAT activity, but reduced APOX

Table 2.1 Summary of results from studies on nano-biointeractions in vascular plants

ENPs and concentration	Plant	Determination/method	Findings	Reference
Ag 25, 50, 75, 100 mg/L	Onion	Genotoxicity, cytotoxicity	Decreased mitotic index; chromosomal aberrations	[62]
Ag 100 µg/mL Au 62 µg/mL Fe_3O_4 116 µg/mL	Cucumber Lettuce	Germination	Low or no toxicity	[63]
Ag 100, 500 mg/L Cu 100, 500 mg/L	Yellow squash seeds	Toxicity induced by bulk versus nano Cu and Ag particles	Ag ENPs reduced biomass and transpiration rate by 66–84% compared to bulk Ag. Both bulk and nano Cu were toxic and brought down the two parameters by 60–70%	[64]
Al 10, 100, 1000, 10,000 mg/kg	Red kidney bean Ryegrass	Growth	Low or no toxicity	[65]
Al_2O_3, SiO_2, Fe_3O_4, ZnO 400, 2000, 4000 mg/L	Mouse-ear cress	Germination, elongation, yield	Reduced germination	[66]
Au 3.6, 7.2, 10.6, 14.0, 17.3 µM	Soybean	Chlorophyll fluorescence quenching, fluorescence spectroscopy, spectrofluorimeter	Seeds were treated with the Au ENPs. The NPs were found in plant tissues There was a chlorophyll fluorescence quenching	[67]
Au, Cu, Pd and Si 0.013 and 0.066% w/w	Lettuce seeds	Effect of ENPs exposure on seed germination and shoot to root ratio	All ENPs produced higher shoot to root ratio under the treatments (0.013% or 0.066% (w/w)), compared to controls	[68]
SWCNT 50 µg/mL QD 0.5 µg/mL SWCNT-QD 50 µg/mL	Tomato	Fluorescent and Raman-scattering 2D mapping analysis	Curtailing root development, reduced leaf life span. Decrease chlorophyll in leaves; fourfold reduction in root weight for 50 µg/mL SWCNT-QD exposure	[69]
MWCNT 50 µg/mL	Tomato	Nano-bubble amplified photothermal/photoacoustic imaging, spectroscopy, and burning method	Novel changes observed in gene expression for leaves and roots. Upregulation of genes related to stress MWCNTs observed in leaves, fruits, and root	[70]
CeO_2 100, 200, 400 mg/L	Moon trefoil	Nano vs bulk CeO_2 effects on plants, uptake of nanoceria and effect on in vitro plantlets	At low nano concentration, the root length and trifoliate leaf count increased, but the root biomass decreased. Both nano	[71]

(continued)

Table 2.1 (continued)

ENPs and concentration	Plant	Determination/method	Findings	Reference
			and bulk reduced maximum photochemical efficiency. Roots were more responsive than shoots to nanoceria	
CeO_2 100, 200, 400, 800 mg/kg	Corn (maize)	Change in CeO_2 ENPs uptake due to surface coating and the presence of organic matter, Fluorescein isothiocyanate (FITC)-stained CeO_2, confocal microscope, μ-XRF	More root Ce in organic soil, compared to low organic matter soil. Reversed results in shoots. Confocal microscopy images showed CeO_2 ENPs aggregates in cortex and epidermal cells, suggesting apoplastic route	[20]
CeO_2 100, 400 mg/kg	Wheat	Wheat lifecycle study (7 months), field lysimeter, low dose (100 mg/kg), high dose (400 mg/kg)	The chlorophyll content was lowered at the high dose along with an increase in the catalase and superoxide dismutase activities. Flowering was delayed by a week in both treatments	[72]
CeO_2 62.5, 125, 250, 500 mg/L	Red kidney bean	Biochemical assay	Reduced enzymes in roots. Enhanced enzymes in leaves	[22]
CeO_2 500, 1000, 2000, 4000 mg/L	Alfalfa Corn Tomato Onion	Germination, elongation	Reduced germination. Increased and reduced root growth. Increased root elongation	[24]
CeO_2, CuO 50, 100, 200 mg/L	Cucumber	Fruit quality	Reduced firmness	[47]
CeO_2, ZnO 400, 800 mg/kg	Cucumber	Chlorophyll, gas exchange, physiological characteristics, ICP-MS, μ-XRF	Ce and Zn bioaccumulation in fruit. μ-XRF showed Ce in the leaf vein system, hinting that Ce moved with water during transpiration	[25]
CeO_2, ZnO 500, 1000, 2000, 4000 mg/L	Soybean	Synchrotron X-ray absorption spectroscopy, random amplified polymorphic DNA assay	CeO_2 ENPs were found in the roots, but not ZnO. Both ENPs produced appearance and disappearance DNA bands, suggesting genotoxic effects	[23]
Cu 200, 400, 600, 800 mg/L	Mung bean, Wheat	Toxic effect of Cu ENPs and their bioavailability to plants, plant agar test, TEM-EDS	Mung bean was much more receptive and responsive to the toxic effect of Cu ENPs than wheat. Bioaccumulation was proportional to Cu ENPs concentration. TEM-EDS was used to visualize the ENPs agglomeration in cells	[73]

(continued)

Table 2.1 (continued)

ENPs and concentration	Plant	Determination/method	Findings	Reference
Cu, CuO 20, 80 mg/kg	Cilantro	Germination, elongation, biochemical assay, nutrient uptake	Decreased germination, impaired nutrient accumulation	[74]
Fe/Fe_3O_4, Cu/CuO 10, 20 mg/L	Lettuce	Plant health, chlorophyll content, CAT and APOX enzyme responses to ENPs exposure	No effects of Fe ENPs. Cu ENPs/ions reduced water content, dry biomass, and root length, compared with control. Cu ENPs increased Cu, Al, and S, but reduced Ca, Mg, Mn, and P	[75]
CuO 2, 5, 10, 20, 30, 40, 50, 100 mg/L	Corn	Split-root experiments, TEM-EDS, HRTEM	TEM-EDS demonstrated that CuO ENPs were translocated from roots to shoots through the xylem. HRTEM showed that the ENPs could translocate from shoots back to roots via phloem. Experiments indicate bioaccumulation and biotransformation of CuO ENPs in maize	[58]
CuO 100, 200, 400, 500 mg/L	Soybean	Root and shoot development, lignification of root cells, total chlorophyll content, H_2O_2 generation, POD enzyme activity	Root length reduced; increased ROS, lignin content, and POD activity. Total chlorophyll content, shoot growth, and weight reduction. Up regulation of POD2, POD4 and POD7 genes	[76]
CuO 0.1,1.0, 10 mg/L	Duckweed	Comparison of the inhibitory effects of CuO ENPs and bulk copper in solution	pH influenced solubility of CuO ENPs The concentration of Cu was found to be four times higher in plants exposed to CuO ENPs, compared to bulk Cu. CuO EPNs affected more morphology than growth	[77]
CuO 1.0 mg/L	Duckweed	Chlorophyll content, cell morphology, plant growth rate, electronic, scanning and light microscopic analysis	Growth inhibition at 0.6 mg/L Cu ion or 1 mg/L. CuO NPs reduced chlorophyll and growth at 1 mg/L	[78]
CuO 20, 50, 100, 200 500 mg/L	Mung bean	Effects of ENPs at physiological and molecular level	Increase H_2O_2 and lipid peroxidation in roots, deceleration of primary and lateral root growth, hampered root length and biomass. Significant curtailment of shoot length and biomass at 200 and 500 mg/L. Lignification of root cells	[79]
CuO 10, 100, 500, 1000 mg/L	Radish, perennial Ryegrass, annual Ryegrass	DNA damage in three different model plants	Marked collection of mutagenic DNA lesions due to reactive oxygen imbalances. Deterioration of plant growth in radish, annual ryegrass, and perennial ryegrass	[80]

(continued)

Table 2.1 (continued)

ENPs and concentration	Plant	Determination/method	Findings	Reference
CuO, ZnO 50, 500, 2000, 4000 mg/L	Buckwheat	Phytotoxic and genotoxic effects RAPS assays, genomic DNA isolation	Internalization of ENPs in root epidermis at high doses. Root growth hampered at 2000 mg/L ZnO and 4000 mg/L CuO ENPs. Different DNA polymorphism	[81]
CuO 625 mg/kg ZnO 640 mg/kg	Wheat	Phytotoxicity, metal speciation, oxidative stress/DLS, AFM	ENPs more toxic, compared to bulk forms. ENPs bioaccumulation in shoots, higher peroxidase and catalase activity, accelerated lipid peroxidation and oxidized glutathione in roots, reduced chlorophyll in shoots	[82]
Graphene 500, 1000, 2000 mg/L	Cabbage, Tomato, red Spinach, and Lettuce	Phytotoxicity in seedlings, morphological and physiological analysis	20 day graphene exposure significantly reduced plant growth and biomass. The leaf growth and number of leaves were reduced. There was marked increase in ROS and cell death. Little or no effects in lettuce	[83]
Pd 1–50 µmol/L	Barley	Growth	Pd uptake affected by particle size. At lower concentration reduced leaf length	[84]
Superparamagnetic iron oxide ENPs (SPIONs) 0.2, 0.4, 1, 2, mg/mL	Soybean	Soybean chlorophyll content, iron deficiency chlorosis, depletion ability in a hydroponic system	SPIONs raised the chlorophyll, levels but did not induce toxicity. Surface chemistry had different effects on chlorophyll	[85]
TiO_2 0.1, 0.2, 0.4%	long raceme Elm	Impact on the photosynthetic properties	0.1, 0.2, and 0.4% of nano-anatase TiO_2 sprayed on the leaves reduced the net rate of photosynthesis in seedlings	[86]
TiO_2 5, 25, 50 mg/L	Bell bean	Ecotoxic and genotoxic effects of TiO_2, ICP-MS, µ-XRF	ICP-MS results showed Ti in roots. µ-XRF showed Ti internalization	[87]
TiO_2 0.3, 1 g/L	Corn	Root hydraulics, growth	Physical effects: reduced hydraulic conductivity, inhibited leaf growth and transpiration. Low or no toxicity observed in long-term experiments	[52]
ZnO 10, 20, 50, 100, 200, 1000 mg/L	Ryegrass	Biomass production, plant growth	Reduced shoot and root length. Decreased biomass. Cellular vacuolation and collapse	[88]

(continued)

Table 2.1 (continued)

ENPs and concentration	Plant	Determination/method	Findings	Reference
ZnO 25, 50, 75, 100 μg/mL	Onion bulb	Genetic toxicity, mitotic index (MI), micronuclei index (MN), chromosomal aberration index, TBARS concentration, TEM, SEM	MI decreased with increasing concentration of ZnO ENPs, MN and chromosomal aberration index increased simultaneously. TEM and SEM images confirmed internalization and aggregation of the ENPs. Marked influence of ZnO ENPs on lipid peroxidation found via TBARs	[89]
ZnO 100, 200, 400, 800 mg/kg	Corn	Release of zinc ions from ZnO ENPs, uptake, translocation, TEM, confocal microscopy	Confocal microscopic images showed aggregates of ZnO ENPs diffused through root epidermis and cortex via the apoplastic route. Few ENPs aggregates were found in the xylem, indicating their passage to the endodermis via the symplastic pathway	[9]
ZnO 250, 1000 mg/k	Green pea	Protein and carbohydrate profile, plant biomass, chlorophyll levels	Plants exposed to alumina doped ZnO at 1000 mg/kg had elevated Zn concentration in roots and seeds, without influencing Si and Al uptake	[90]

Species name in order of appearance in the table: onion, *Allium cepa;* cucumber, *Cucumis sativus*; lettuce, *Lactuca sativa*; yellow squash, *Cucurbita pepo*; red kidney bean, *Phaseolus vulgaris*; perennial ryegrass, *Lolium perenne*; mouse-ear cress, *Arabidopsis thaliana*; soybean, *Glycine max*; tomato, *Solanum lycopersicum*; moon trefoil, *Medicago arborea*; corn, *Zea mays*; wheat, *Triticum aestivum*; alfalfa, *Medicago sativa*; mung bean, *Phaseolus radiatus*; cilantro, *Coriandrum sativum*; duckweed, *Landoltia punctata*; radish, *Raphanus sativus*; annual ryegrass, *Lolium rigidum*; buckwheat, *Fagopyrum esculentum*; cabbage, *Brassica oleracea*; red spinach, *Amaranthus dubius*; barley, *Hordeum vulgare*; long raceme elm, *Ulmus elongata*; bell bean, *Vicia faba*; green pea, *Pisum sativum*

activity in leaves and roots. Barrios et al. [44] performed a study with coated and uncoated CeO_2 ENPs and bulk CeO_2 in tomato plants. At the highest exposure concentration (500 mg/kg), coated and uncoated CeO_2 ENPs resulted in longer stems, while exposure to bulk reduced the shoot length. Chlorophylls *a* and *b* were markedly increased under coated ENPs' exposure, but reduced under bulk CeO_2 exposure at a lower concentration (62.5 mg/kg). In addition, bulk CeO_2 at 125 mg/kg resulted in a higher percentage of Zn and lower P in stems. Majumdar et al. [92] exposed red kidney bean plants to 1000 mg/kg of either CeO_2 ENPs or bulk CeO_2. After 36 days of exposure, they recorded 26 µg/g Ce in nano-treated roots and 19 µg/g Ce in bulk-treated roots. The translocation from roots to shoots was of 1.02 µg/g Ce in nano exposed plants and of 1.3 µg/g in bulk exposed plants. Other studies have been listed in Table 3.1.

2.6 Risk Assessment Framework for ENPs

The risk assessment of ENPs is a challenge because of the diversity of materials and the ever increasing potential industrial use [45]. It encompasses detailed characterization of the particles and their aggregates before the conventional risk assessment [46]. The risk assessment framework includes hazard identification, dose response assessment, exposure assessment, and risk characterization.

2.6.1 Hazard Identification

Hazard identification is a qualitative examination to determine the ENPs presence, or the degree of hazard that a receptor (plant) is susceptible to because of ENPs exposure. It takes note of the exposure conditions, the detrimental health effect on the plant species, and collection and analysis of the data on the types of health effects due to the exposure [87, 93–95]. It may go further into the detailed characterization of the ENP interactions with plant organs, tissues, and cells; in other words, the toxicodynamics of the ENPs [10, 96, 97].

2.6.2 Dose–Response Assessment

Dose–response assessment implies bringing forth the quantitative relationship between the exposure to the increasing amount of the xenobiotic (ENPs) and the corresponding response from the plant [98, 99]. Also known as the effect assessment, it takes into account the different kinds of hazards and the corresponding kinds of detrimental effects due to ENPs exposure, the relationship between dose, and the resultant response along with the related uncertainties [100].

2.6.3 Exposure Assessment

The exposure assessment step is used to determine the rates at which ENPs are taken up by plant tissues. It estimates the magnitude of the actual and/or any potential plant exposures to the ENPs present in the surrounding environment. The process also considers the routes of exposure to plants, the time interval and frequency of exposure, and the size of the plant population under study. Exposure assessment is performed at laboratory [25, 59] or greenhouse conditions [46, 101]. The ENP characterization prior to the risk assessment gives vital information about the chemical, physical, and other kinds of properties of ENPs. This information gives in turn, hints about the exposure characteristics of the respective ENP.

2.6.4 Risk Characterization

The risk characterization is the process of assessing the probability of a harmful effect to the plants under certain known exposure conditions. It usually puts together the outcomes from hazard identification, toxicity, and exposure assessment in order to qualitatively and/or quantitatively define the risk. It also includes a description of the uncertainties associated with the risk assessment. Another important aspect that is taken into account is the additive or synergistic effect due to exposure to mixtures of ENPs. Sufficient characterization of risk from the hazards of ENPs exposure makes way for efficient risk management and requisite corrective actions for redressal [102]. Currently, there is a lack of information concerning the risk characterization of ENPs in plants. There are no studies incorporating all exposure conditions including dissolution percentage and transformations, among others [103].

2.7 Research Needs

Most of the studies on the effects of ENPs on terrestrial plants have covered the germination and seedling stages [48]. This has limited the analysis to the juvenile phase, when organs are still in development. Very few long-term studies have shown the potential toxicity of ENPs over the complete life cycle of the plant; thus, deeper evaluation is needed. Studies at the reproductive stage offer perspective into transgenerational effects, and this knowledge is in its infancy [44, 104, 105]. A few observations on the trophic transfer of ENPs within terrestrial food chains have shown the potential for great variations [92, 106, 107]. So far, only a few, and very short, food chains have been evaluated [10, 108, 109]. Moreover, the bulk of reports corresponds to studies performed in hydroponic systems. This experimental design allows for increased aggregation of particles, which may play an important

role in their interactions with plants [110]. There is a strong tendency to use ENPs as herbicides, pesticides, and fertilizers, among other applications, within the agricultural industry; hence, soil represents a major pathway for exposure [4]. This suggests that future studies might be focused on determining the chemical, physical, and biological interactions of soil and ENPs and their effects on plants [20, 111, 112]. These studies will give a more realistic idea about the behavior of ENPs in the environment. In summary, there is much to do in order to better understand the nano-biointeractions with terrestrial plants.

Acknowledgements This material is based upon work supported by the National Science Foundation and the Environmental Protection Agency under Cooperative Agreement Number DBI-1266377. Any opinions, findings, and conclusions or recommendations expressed in this material are those of the author(s) and do not necessarily reflect the views of the National Science Foundation or the Environmental Protection Agency. This work has not been subjected to EPA review and no official endorsement should be inferred. The authors also acknowledge the USDA Grant 2016-67021-24985 and the NSF Grants EEC-1449500, CHE-0840525 and DBI-1429708. Partial funding was provided by the NSF ERC on Nanotechnology-Enabled Water Treatment (EEC-1449500). This work was also supported by Grant 2G12MD007592 from the National Institutes on Minority Health and Health Disparities (NIMHD), a component of the National Institutes of Health (NIH). J.L. Gardea-Torresdey acknowledges the Dudley family for the Endowed Research Professorship, the Academy of Applied Science/US Army Research Office, Research and Engineering Apprenticeship Program (REAP) at UTEP, and the LEER and STARS programs of the UT System.

References

1. Daresta BE, Italiano F, de Gnerao G et al (2015) Atmospheric particulate matter (PM) effect on the growth of *Solanum lycopersicum* cv. Roma plants. Chemosphere 119:37–42
2. Keller AA, Lazareva A (2014) Predicted releases of engineered nanomaterials: from global to regional to local. Environ Sci Technol Lett 1:65–70
3. Rai P (2016) Biomagnetic monitoring of particulate matter in the Indo-Burma hotspot region (Chapter 5). In: Biomagnetic monitoring of particulate pollution through plant leaves: an overview. Elsevier e-books, pp 75–109; Yeh, P.: Optical Waves in Layered Media. Wiley, New York (1988)
4. Servin AD, White JC (2016) Nanotechnology in agriculture: next steps for understanding engineered nanoparticle exposure and risk. NanoImpact 1:9–12
5. Yang Y et al (2014) Metal and nanoparticle occurrence in biosolid-amended soils. Sci Total Environ 485–486:441–449
6. Hong J, Peralta-Videa JR, Rico C et al (2014) Evidence of translocation and physiological impacts of foliar applied CeO_2 nanoparticles on cucumber (*Cucumis sativus*) plants. Environ Sci Technol 48(8):4376–4385
7. Hernandez-Viezcas JA, Castillo-Michel H, Andrews JC et al (2013) In situ synchrotron X-ray fluorescence mapping and speciation of CeO_2 and ZnO nanoparticles in soil cultivated soybean (*Glycine max*). ACS Nano 7:1415–1423
8. Lv J, Zhang S, Luo L et al (2015) Accumulation, speciation and uptake pathway of ZnO nanoparticles in maize. Environ Sci Nano 2:68–77
9. Zhao L, Peralta-Videa JR, Ren M et al (2012) Transport of Zn in a sandy loam soil treated with ZnO NPs and uptake by corn plants: Electron microprobe and confocal microscopy studies. Chem Eng J 184:1–8

10. Gardea-Torresdey JL, Rico CM, White JC (2014) Trophic transfer, transformation, and impact of engineered nanomaterials in terrestrial environments. Environ Sci Technol 48 (5):2526–2540
11. Ma C, White JC, Dhankher OP et al (2015) Metal-based nanotoxicity and detoxification pathways in higher plants. Environ Sci Technol 49(12):7109–7122
12. Naderi M, Danesh-Shahraki A (2013) Nanofertilizers and their roles in sustainable agriculture. Int J Agric Crop Sci 5:2229–2232
13. Pan B, Xing B (2012) Applications and implications of manufactured nanoparticles in soils: a review. Eur J Soil Sci 63:437–456
14. Gogos A, Knauer K, Buncheli TD et al (2012) Nanomaterials in plant protection and fertilization: current state, foreseen applications, and research priorities. J Agric Food Chem 60:9781–9792
15. Brar SK, Verma M, Tyagi RD et al (2010) Engineered nanoparticles in wastewater and wastewater sludge—evidence and impacts. Waste Manage 30:504–520
16. Khodakovskaya M, Dervishi E, Mahmood M et al (2009) Carbon nanotubes are able to penetrate plant seed coat and dramatically affect seed germination and plant growth. ACS Nano 3:3221–3227
17. Servin AD, Catillo-Michel H, Hernandez-Viezcas JA et al (2012) Synchrotron micro-XRF and micro-XANES confirmation of the uptake and translocation of TiO_2 nanoparticles in cucumber (*Cucumis sativus*) plants. Environ Sci Technol 46:7637–7643
18. Ghodake G, Seo YD, Lee DS et al (2011) Hazardous phytotoxic nature of cobalt and zinc oxide nanoparticles assessed using *Allium cepa*. J Hazard Mater 186:952–955
19. Zhu H, Han J, Xiao JQ et al (2008) Uptake, translocation, and accumulation of manufactured iron oxide nanoparticles by pumpkin plants. J Environ Monit 10:713–717
20. Zhao L, Peralta-Videa JR, Varela-Ramirez A et al (2012) Effect of surface coating and organic matter on the uptake of CeO_2 NPs by corn plants grown in soil: Insight into the up-take mechanism. J Hazard Mater 225:131–138
21. Peng C, Duan D, Xu C et al (2015) Translocation and biotransformation of CuO nanoparticles in rice (*Oryza sativa* L.) plants. Environ Pollut 197:99–107
22. Majumdar S, Peralta-Videa JR, Bandyopadhyay S et al (2014) Exposure of cerium oxide nanoparticles to kidney bean shows disturbance in the plant defense mechanisms. J Hazard Mater 278:279–287
23. López-Moreno ML, de la Rosa G, Hernandez-Viezcas JA et al (2010) Evidence of the differential biotransformation and genotoxicity of ZnO and CeO_2 nanoparticles on soybean (*Glycine max*) plants. Environ Sci Technol 44(19):7315–7320
24. López-Moreno ML, de la Rosa G, Hernandez-Viezcas JA, Peralta-Videa JR, Gardea-Torresdey JL (2010) X-ray absorption spectroscopy (XAS) corroboration of the uptake and storage of CeO_2 nanoparticles and assessment of their differential toxicity in four edible plant species. J Agric Food Chem 58(6):3689–3693
25. Zhang P, Ma Y, Zhang Z et al (2012) Biotransformation of ceria nanoparticles in cucumber plants. ACS Nano 6:9943–9950
26. Zhao L, Sun Y, Hernandez-Viezcas JA et al (2013) Influence of CeO_2 and ZnO nanoparticles on cucumber physiological markers and bioaccumulation of Ce and Zn: a life cycle study. J Agric Food Chem 61:11945–11951
27. Schwabe F, Tanner S, Schulin R et al (2015) Dissolved cerium contributes to uptake of Ce in the presence of differently sized CeO_2 nanoparticles by three crop plants. Metallomics 7:466–477
28. Avanasi R, Jackson WA, Sherwin B et al (2014) C_{60} fullerene soil sorption, biodegradation, and plant uptake. Environ Sci Technol 48:2792–2797
29. Dimkpa CO, Latta DE, McLean JE et al (2013) Fate of CuO and ZnO nano- and microparticles in the plant environment. Environ Sci Technol 47:4734–4742
30. Khot LR, Sankaran S, Maja JM et al (2012) Applications of nanomaterials in agricultural production and crop protection: a review. Crop Prot 3:64–70

31. Dubas ST, Pimpan V (2008) Humic acid assisted synthesis of silver nanoparticles and its application to herbicide detection. Mater Lett 62:2661–2663
32. Zhang Z, Kleinstreuer C, Donohue JF et al (2005) Comparison of micro- and nano-size particle depositions in a human upper airway model. J Aerosol Sci 36:211–233
33. Uzu G, Sobanska S, Sarret G et al (2010) Foliar lead uptake by lettuce exposed to atmospheric fallouts. Environ Sci Technol 44:1036–1042
34. Schreck E, Foucault Y, Sarret G et al (2012) Metal and metalloid foliar uptake by various plant species exposed to atmospheric industrial fallout: mechanisms involved for lead. Sci Total Environ 427:253–262
35. Schreck E, Dappe V, Sarret G et al (2014) Foliar or root exposures to smelter particles: consequences for lead compartmentalization and speciation in plant leaves. Sci Total Environ 476:667–676
36. Larue C, Castillo-Michel H, Sobanska S et al (2014) Foliar exposure of the crop (*Lactuca sativa*) to silver nanoparticles: evidence for internalization and changes in Ag speciation. J Hazard Mater 264:98–106
37. Larue C, Castillo-Michel H, Sobanska S et al (2014) Fate of pristine TiO_2 nanoparticles and aged paint-containing TiO_2 nanoparticles in lettuce crop after foliar exposure. J Hazard Mater 273:17–26
38. Birbaum K, Brogioli R, Schellenberg M et al (2010) No evidence for cerium dioxide nanoparticle translocation in maize plants. Environ Sci Technol 44:8718–8723
39. Servin AD, Morales MI, Castillo-Michel H, Munoz B, Zhao L, Nunez JE, Peralta-Videa JR, Gardea-Torresdey JL (2013) Synchrotron verification of TiO_2 accumulation in cucumber fruit: a possible pathway of TiO_2 nanoparticle transfer from soil into the food chain. Environ Sci Technol 47:11592–11598
40. Rico CM, Lee SC, Rubenecia R, Mukherjee A, Hong J, Peralta-Videa JR, Gardea-Torresdey JL (2014) Cerium oxide nanoparticles impact yield and modify nutritional parameters in wheat (*Triticum aestivum* L.). J Agric Food Chem 62(40):9669–9675
41. Cornelis G, Ryan B, McLaughlin MJ, Kirby JK, Beak D, Chittleborough D (2011) Solubility and batch retention of CeO_2 nanoparticles in soils. Environ Sci Technol 45(7):2777–2782
42. Hong J, Rico CM, Zhao L et al (2015) Toxic effects of copper-based nanoparticles or compounds to lettuce (*Lactuca sativa*) and alfalfa (*Medicago sativa*). Environ Sci Process Impacts 17:177–185
43. Rico CM, Barrios AC, Tan W et al (2015) Physiological and biochemical response of soil-grown barley (*Hordeum vulgare* L.) to cerium oxide nanoparticles. Environ Sci Pollut Res 22(14):10551–10558
44. Barrios AC, Rico CM, Trujillo-Reyes J et al (2016) Effects of uncoated and citric acid coated cerium oxide nanoparticles, bulk cerium oxide, cerium acetate, and citric acid on tomato plants. Sci Total Environ 563:956–964
45. Du W, Sun Y, Ji R et al (2011) TiO_2 and ZnO nanoparticles negatively affect wheat growth and soil enzyme activities in agricultural soil. J Environ Monitor 13:822–828
46. Zhao L, Sun Y, Hernandez-Viezcas JA et al (2015) Monitoring the environmental effects of CeO_2 and ZnO nanoparticles through the life cycle of corn (*Zea mays*) plants and in situ μ-XRF mapping of nutrients in kernels. Environ Sci Technol 49:2921–2928
47. Hong J, Wang L, Sun Y et al (2016) Foliar applied nanoscale and microscale CeO_2 and CuO alter cucumber (*Cucumis sativus*) fruit quality. Sci Total Environ 563:904–911
48. Dietz K, Herth S (2011) Plant nanotoxicology. Trends Plant Sci 16(11):582–589
49. Li H, Ye X, Guo X et al (2016) Effects of surface ligands on the uptake and transport of gold nanoparticles in rice and tomato. J Hazard Mater 8/15 314:188–196
50. Schutzendubel A, Polle A (2002) Plant responses to abiotic stresses: heavy metal-induced oxidative stress and protection by mycorrhization. J Exp Bot 53(372):1351–1365
51. Sharma SS, Dietz K (2009) The relationship between metal toxicity and cellular redox imbalance. Trends Plant Sci 14(1):43–50

52. Asli S, Neumann PM (2009) Colloidal suspensions of clay or titanium dioxide nanoparticles can inhibit leaf growth and transpiration via physical effects on root water transport. Plant, Cell Environ 32(5):577–584
53. Hall JL (2002) Cellular mechanisms for heavy metal detoxification and tolerance. J Exp Bot 53(366):1–11
54. Hall JL, Williams LE (2003) Transition metal transporters in plants. J Exp Bot 54 (393):2601–2613
55. Larsen MR, Thingholm TE, Jensen ON et al (2005) Highly selective enrichment of phosphorylated peptides from peptide mixtures using titanium dioxide microcolumns. Mol Cell Proteomics 4(7):873–886
56. Oberdörster G, Stone V, Donaldson K et al (2007) Toxicology of nanoparticles: a historical perspective. Nanotoxicology 1(1):2–25
57. Wang Z, Xie X, Zhao J et al (2012) Xylem- and phloem-based transport of CuO nanoparticles in maize (*Zea mays* L.). Environ Sci Technol 46(8):4434–4441
58. Navarro E, Baun A, Behra R, Hartmann NB et al (2008) Environmental behavior and ecotoxicity of engineered nanoparticles to algae, plants, and fungi. Ecotoxicology 17 (5):372–386
59. Lin D, Xing B (2007) Phytotoxicity of nanoparticles: inhibition of seed germination and root growth. Environ Pollut 150(2):243–250
60. Stampoulis D, Sinha SK, White JC (2009) Assay-dependent phytotoxicity of nanoparticles to plants. Environ Sci Technol 43(24):9473–9479
61. Lee WM, Kwak JI, An YJ (2012) Effect of silver nanoparticles in crop plants *Phaseolus radiatus* and *Sorghum bicolor*: media effect on phytotoxicity. Chemosphere 86(5):491–499
62. Kumari M, Mukherjee A, Chandrasekaran N (2009) Genotoxicity of silver nanoparticles in *Allium cepa*. Sci Total Environ 407(19):5243–5246
63. Barrena R, Casals E, Colón J et al (2009) Evaluation of the ecotoxicity of model nanoparticles. Chemosphere 75(7):850–857
64. Musante C, White JC (2012) Toxicity of silver and copper to *Cucurbita pepo*: differential effects of nano and bulk-size particles. Environ Toxicol 27(9):510–517
65. Doshi R, Braida W, Christodoulatos C et al (2008) Nano-aluminum: transport through sand columns and environmental effects on plants and soil communities. Environ Res 106 (3):296–303
66. Lee CW, Mahendra S, Zodrow K et al (2010) Developmental phytotoxicity of metal oxide nanoparticles to *Arabidopsis thaliana*. Environ Toxicol Chem 29(3):669–675
67. Falco W, Botero E, Falcão E et al (2011) In vivo observation of chlorophyll fluorescence quenching induced by gold nanoparticles. J Photochem Photobiol A 225(1):65–71
68. Shah V, Belozerova I (2009) Influence of metal nanoparticles on the soil microbial community and germination of lettuce seeds. Water Air Soil Pollut 197(1–4):143–148
69. Alimohammadi M, Xu Y, Wang D et al (2011) Physiological responses induced in tomato plants by a two-component nanostructural system composed of carbon nanotubes conjugated with quantum dots and its in vivo multimodal detection. Nanotechnology 29:295101
70. Khodakovskaya MV, de Silva K, Nedosekin DA et al (2011) Complex genetic, photothermal, and photoacoustic analysis of nanoparticle-plant interactions. Proc Natl Acad Sci 108(3):1028–1033
71. Gomez-Garay A, Pintos B, Manzanera JA et al (2014) Uptake of CeO_2 nanoparticles and its effect on growth of Medicago arborea in vitro plantlets. Biol Trace Elem Res 161(1):143–150
72. Du W, Gardea-Torresdey JL, Ji R et al (2015) Physiological and biochemical changes imposed by CeO_2 nanoparticles on wheat: a life cycle field study. Environ Sci Technol 49 (19):11884–11893
73. Lee W, An Y, Yoon H et al (2008) Toxicity and bioavailability of copper nanoparticles to the terrestrial plants mung bean (*Phaseolus radiatus*) and wheat (*Triticum aestivum*): plant agar test for water-insoluble nanoparticles. Environ Toxicol Chem 27(9):1915–1921

74. Zuverza-Mena N, Medina-Velo IA, Barrios AC et al (2015) Copper nanoparti cles/compounds impact agronomic and physiological parameters in cilantro (*Coriandrum sativum*). Environ Sci Process Impacts 17(10):1783–1793
75. Trujillo-Reyes J, Majumdar S, Botez CE et al (2014) Exposure studies of core-shell Fe/Fe_3O_4 and Cu/CuO NPs to lettuce (*Lactuca sativa*) plants: are they a potential physiological and nutritional hazard? J Hazard Mater 267:255–263
76. Nair PMG, Chung IM (2014) A mechanistic study on the toxic effect of copper oxide nanoparticles in soybean (*Glycine max* L.) root development and lignification of root cells. Biol Trace Elem Res 162(1–3):342–352
77. Lalau CM, de Almeida Mohedano R, Schmidt ÉC et al (2015) Toxicological effects of cop per oxide nanoparticles on the growth rate, photosynthetic pigment content, and cell morphology of the duckweed *Landoltia punctata*. Protoplasma 252(1):221–229
78. Shi J, Abid AD, Kennedy IM et al (2011) To duckweeds (*Landoltia punctata*), nanoparticulate copper oxide is more inhibitory than the soluble copper in the bulk solution. Environ Pollut 159(5):1277–1282
79. Nair PMG, Kim S, Chung IM (2014) Copper oxide nanoparticle toxicity in mung bean (*Vigna radiata* L.) seedlings: Physiological and molecular level responses of in vitro grown plants. Acta Physiol Plant 36(11):2947–2958
80. Atha DH, Wang H, Petersen EJ et al (2012) Copper oxide nanoparticle mediated DNA damage in terrestrial plant models. Environ Sci Technol 46(3):1819–1827
81. Lee S, Chung H, Kim S, Lee I (2013) The genotoxic effect of ZnO and CuO nanoparticles on early growth of buckwheat, *Fagopyrum esculentum*. Water Air Soil Pollut 224(9):1–11
82. Dimkpa CO, McLean JE, Latta DE et al (2012) CuO and ZnO nanoparticles: phytotoxicity, metal speciation, and induction of oxidative stress in sand-grown wheat. J Nano Res 14 (9):1–15
83. Begum P, Ikhtiari R, Fugetsu B (2011) Graphene phytotoxicity in the seedling stage of cabbage, tomato, red spinach, and lettuce. Carbon 49(12):3907–3919
84. Battke F, Leopold K, Maier M et al (2008) Palladium exposure of barley: uptake and effects. Plant Biol 10(2):272–276
85. Ghafariyan MH, Malakouti MJ, Dadpour MR et al (2013) Effects of magnetite nanoparticles on soybean chlorophyll. Environ Sci Technol 47(18):10645–10652
86. Gao J, Xu G, Qian H et al (2013) Effects of nano-TiO_2 on photosynthetic characteristics of *Ulmus elongata* seedlings. Environ Pollut 176:63–70
87. Foltête A, Masfaraud J, Bigorgne E et al (2011) Environmental impact of sunscreen nanomaterials: ecotoxicity and genotoxicity of altered TiO_2 nanocomposites on *Vicia faba*. Environ Pollut 159(10):2515–2522
88. Lin D, Xing B (2008) Root uptake and phytotoxicity of ZnO nanoparticles. Environ Sci Technol 42(15):5580–5585
89. Kumari M, Khan SS, Pakrashi S et al (2011) Cytogenetic and genotoxic effects of zinc oxide nanoparticles on root cells of *Allium cepa*. J Hazard Mater 190(1):613–621
90. Mukherjee A, Sun Y, Morelius E et al (2015) Differential toxicity of bare and hybrid ZnO nanoparticles in green pea (*Pisum sativum* L.): a life cycle study. Front Plant Sci 6:1242
91. Mukherjee A, Peralta-Videa JR, Bandyopadhyay S et al (2014) Physiological effects of nanoparticulate ZnO in green peas (*Pisum sativum* L.) cultivated in soil. Metallomics 6 (1):132–138
92. Majumdar S, Trujillo-Reyes J, Hernandez-Viezcas JA et al (2016) Cerium biomagnification in a terrestrial food chain: influence of particle size and growth stage. Environ Sci Technol 50(13):6782–6792
93. Nowack B, Ranville JF, Diamond S et al (2012) Potential scenarios for nanomaterial release and subsequent alteration in the environment. Environ Toxicol Chem 31(1):50–59
94. Praetorius A, Arvidsson R, Molander S et al (2013) Facing complexity through informed simplifications: a research agenda for aquatic exposure assessment of nanoparticles. Environ Sci Process Impacts 15(1):161–168

95. Hong J, Peralta-Videa JR, Gardea-Torresdey JL (2013) Nanomaterials in agricultural production: benefits and possible threats? In: Shamin N, Sharma VK (eds) Sustainable nanotechnology and the environment: advances and achievements. ACS symposium series, vol 1124, pp 73–90
96. Liu HH, Cohen Y (2014) Multimedia environmental distribution of engineered nanomaterials. Environ Sci Technol 48(6):3281–3292
97. Cong Y, Banta GT, Selck H et al (2011) Toxic effects and bioaccumulation of nano-, micron- and ionic-Ag in the polychaete, *Nereis diversicolor*. Aquat Toxicol 105(3–4):403–411
98. Hildebrand H, Kühnel D, Potthoff A et al (2010) Evaluating the cytotoxicity of palladium/magnetite nano-catalysts intended for wastewater treatment. Environ Pollut 158 (1):65–73
99. Hendren CO, Lowry M, Grieger KD et al (2013) Modeling approaches for characterizing and evaluating environmental exposure to engineered nanomaterials in support of risk-based decision making. Environ Sci Technol 47(3):1190–1205
100. Handy RD, van den Brink N, Chappell M et al (2012) Practical considerations for conducting ecotoxicity test methods with manufactured nanomaterials: what have we learnt so far? Ecotoxicology 21(4):933–972
101. Holden PA, Klaessig F, Turco RF et al (2014) Evaluation of exposure concentrations used in assessing manufactured nanomaterial environmental hazards: are they relevant? Environ Sci Technol 48(18):10541–10551
102. Priester JH, Ge Y, Mielke RE et al (2012) Soybean susceptibility to manufactured nanomaterials with evidence for food quality and soil fertility interruption. Proc Natl Acad Sci USA 109(37):E2451–E2456
103. Asante-Duah DK (ed) (2002) Public health risk assessment for human exposure to chemicals. Berlin, Germany
104. Hund-Rinke K, Herrchen M, Schlich K (2014) Integrative test strategy for the environmental assessment of nanomaterials. Federal Environment Agency, Project No. (FKZ) 3712(65): 409
105. Chichiriccò G, Poma A (2015) Penetration and toxicity of nanomaterials in higher plants. Nanomaterials 5(2):851–873
106. Wang Q, Ma X, Zhang W et al (2012) The impact of cerium oxide nanoparticles on tomato (*Solanum lycopersicum* L.) and its implications for food safety. Metallomics 4(10):1105–1112
107. Majumdar S, Almeida IC, Arigi EA et al (2015) Environmental effects of nanoceria on seed production of common bean (*Phaseolus vulgaris*): a proteomic analysis. Environ Sci Technol 49(22):13283–13293
108. Miralles P, Church TL, Harris AT (2012) Toxicity, uptake, and translocation of engineered nanomaterial in vascular plants. Environ Sci Technol 46(17):9224–9239
109. De La Torre-Roche R, Hawthorne J, Deng Y et al (2013) Multiwalled carbon nanotubes and C_{60} fullerenes differentially impact the accumulation of weathered pesticides in four agricultural plants. Environ Sci Technol 47(21):12539–12547
110. Handy RD, Von Der Kammer F, Lead JR et al (2008) The ecotoxicology and chemistry of manufactured nanoparticles. Ecotoxicology 17(4):287–314
111. Rico CM, Majumdar S, Duarte-Gardea M et al (2011) Interaction of nanoparticles with edible plants and their possible implications in the food chain. J Agric Food Chem 59 (8):3485–3498
112. Oberdörster G, Oberdörster E, Oberdörster J (2005) Nanotoxicology: an emerging discipline evolving from studies of ultrafine particles. Environ Health Perspect 113(7):823–839

Chapter 3
Effects of Surface Coating on the Bioactivity of Metal-Based Engineered Nanoparticles: Lessons Learned from Higher Plants

Illya A. Medina-Velo, Ishaq Adisa, Carlos Tamez, Jose R. Peralta-Videa and Jorge L. Gardea-Torresdey

Abstract Characteristics such as size, surface-to-volume ratio, and surface chemistry, among others, convey uniqueness to engineering nanoparticles (ENPs). The surface chemistry determines the stability and aggregation of ENPs and also constrains their applications, environmental fate, and interaction with living organisms. To avoid aggregation and improve stabilization, the surface chemistry of numerous ENPs has been modified through coating with several agents. However, the coating also changes their biointeractions. In this chapter we discuss literature concerning the uptake, translocation, accumulation, and physiological effects of surface-coated ENPs in economically important plants. We discussed existing information based on the type of ENP, coating agent, and species of plant. Negative and positive effects are discussed.

Keywords Nanoparticles · Surface chemistry · Crop plants · Uptake · Stress

I.A. Medina-Velo · J.R. Peralta-Videa · J.L. Gardea-Torresdey (✉)
Department of Chemistry, The University of Texas at El Paso,
500 West University Ave., El Paso, TX 79968, USA
e-mail: jgardea@utep.edu

I.A. Medina-Velo · C. Tamez · J.R. Peralta-Videa · J.L. Gardea-Torresdey
University of California Center for Environmental Implications of Nanotechnology (UC CEIN), The University of Texas at El Paso, 500 West University Ave., El Paso, TX 79968, USA

I. Adisa · C. Tamez · J.R. Peralta-Videa · J.L. Gardea-Torresdey
Environmental Science and Engineering Ph.D. Program, The University of Texas at El Paso,
500 West University Ave., El Paso, TX 79968, USA

B. Yan et al. (eds.), *Bioactivity of Engineered Nanoparticles*,
Nanomedicine and Nanotoxicology, DOI 10.1007/978-981-10-5864-6_3

3.1 Introduction

Contemporarily, nanomaterials are profusely used in many applications including products for personal care, communications, manufacture, food packaging, medicine, imaging, and remediation of soil and water, among others [1, 2]. In addition, there are strong evidences that agricultural activities like pest control and fertilization are becoming nano-enabled [3]. This suggests that nanomaterial production, which by 2010 was estimated at 260,000–309,000 t [4], will continue growing at a very rapid pace. The global production includes several metal-based ENPs, being the most produced silica, titanium dioxide, alumina, and iron and zinc oxides [4]. A side effect of the huge production and use of ENPs is the discharge into the environment after end-user applications. Estimates for the 2010 production indicated that 20,800–86,520 tons ended up in soils, 1040–21,630 in bodies of water, and 260–4635 in the air [4].

Since it seemed evident that ENPs were accumulated in the environment, the scientific community started to investigate their effects on living organisms. Different research facilities with controlled environments have been used to study the effects of ENPs in mammals, microorganisms, insects, and plants. Investigations with plants have received much attention. A simple search in ScienceDirect.com (August 20, 2016) using the keywords "effects of nanoparticles in plant growth" shows that the number of papers describing the interactions of ENPs with plants has increased exponentially during the last 12 years (Fig. 3.1).

The first publications showed effects on seed germination [5] and photosynthesis [6, 7]. In subsequent works, researchers started to explore biochemical effects [8], effects on plant growth [9–11], and molecular expression [12]. The literature covering uptake, accumulation, biotransformation, and toxicity piled up very fast. In a very popular review, Rico et al. [13] analyzed most of the existing literature produced in the first decade, concerning the effects of nanoparticles in crop plants. Five years later, several review articles analyzed different aspects of the interaction of ENPs with plants [14–16]. Some of the recent reports indicate that the interaction of the ENPs with plants is modulated by several factors including soil conditions,

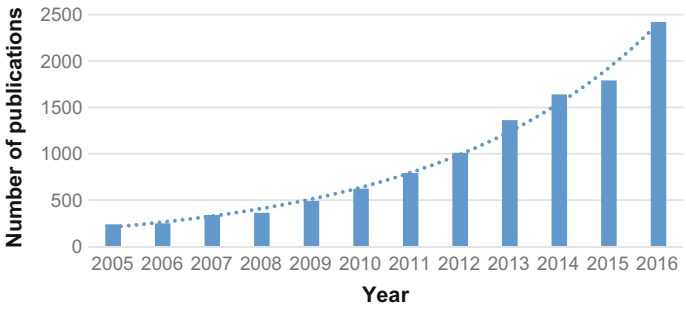

Fig. 3.1 Number of publications about the effects of nanoparticles in plants in the last 12 years

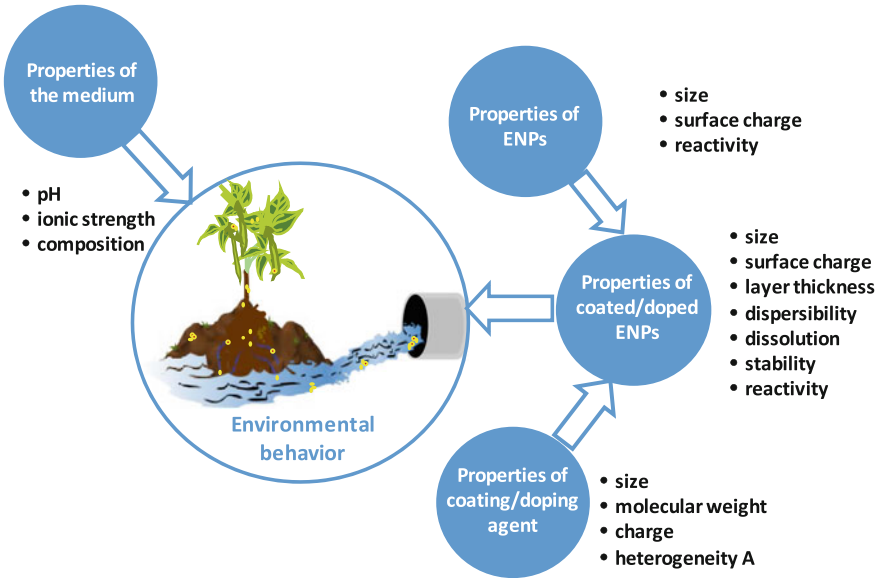

Fig. 3.2 Environmental behavior of ENPs with changes in the surface properties. Adapted from Louie et al. [18]

plant species, particle size and type, ion release from the nano forms, and surface properties [17]. Figure 3.2 shows some of the factors that can modulate the environmental impacts of ENPs. As it can be observed in Fig. 3.2, the incorporation of natural or engineered macromolecules into the surface of the nanomaterials may affect their toxicity and reactivity, as well as the way they interact with the environment, including plants [18].

Although the volume of information regarding the effects of uncoated ENPs in plants is growing very fast, very little is known about the interaction of coated/doped ENPs with them. This chapter is devoted to analyzing the effects of surface coating on the interaction of silver, gold, zinc oxide, cerium oxide, and copper oxide ENPs with plants. Effects on physiological, biochemical, and phenotypical traits are discussed. Table 3.1 summarizes the effects of surface-modified metal-based ENPs in higher plants.

3.2 Metallic ENP

3.2.1 Silver Nanoparticles (Ag ENPs)

Silver (Ag) is known to have effective antimicrobial properties and it is among the most widely used metals in the world. Prevalence applications of Ag ENPs in medical, cosmetics, and textile industries has significantly increased the release of

Table 3.1 Summary of reports about effects of surface-modified metal-based engineered nanoparticles in higher plants

Engineered nanoparticle and surface modification	Enhanced properties after modification	Plant	Uptake, translocation, and physiological effects				Ref.
			Root	Stem	Leaf	Fruit	
Gum Arabic coated Ag NPs	• Increased dissolution and greater release of Ag from AgNP	*Lolium multiflorum*	✓	✓	N/A	N/A	[19]
			Decreased root growth rate and distortion of root morphology and cell structure				
Citrated-coated Ag NPs	• Functionalization to induce a positive charge • Lower release of Ag	Mung bean (*Phaseolus radiatus*)	✓	✓	N/A	N/A	[20]
			Concentration-dependent growth inhibition of the plant and morphological distortion of the root				
		Sorghum (*Sorghum bicolor*)	✓	✓	N/A	N/A	
			Concentration-dependent growth inhibition of the plant and morphological distortion of the root				
	• Electrostatic stabilization of AgNPs • Minimized dissolution of Ag • Lower release of Ag	Maize (*Zea mays*)	✓	✓	N/A	✓	[21]
			Growth suppression; abnormal root morphology and structures at developmental stage				
		Cabbage (*Brassica oleracea* var. *capitata*)	✓	✓	N/A	✓	
			Growth suppression; abnormal root morphology and structures at developmental stage				

(continued)

Table 3.1 (continued)

Engineered nanoparticle and surface modification	Enhanced properties after modification	Plant	Uptake, translocation, and physiological effects				Ref.
			Root	Stem	Leaf	Fruit	
Au NPs coated with TTMA[a]	• Functionalization to induced a positive charge	Rice (*Oryza sativa*)	✓	✓	✓	N/A	[22]
			Functional group coating affected Au uptake. Highest Au uptake observed in TTMA in root tissues				
Au NPs coated with TEGOH	• Functionalization to induce a neutral charge		✓	✓	✓	N/A	
			LA-ICP-MS reveals heterogeneous distribution of Au ions in leaf tissues				
Au NPs coated with TEGCOOH	• Functionalization to induce a negative charge		✓	✓	✓	N/A	
			Au concentration highest in shoots treated with TEGCOOH				
Au NPs coated with citrate	• Coated to simulate low molecular weight organic acids in soil	Tobacco (*Nicotiana tabacum*)	✓	✓	✓	N/A	[23]
			Accumulation of Au in leaf				
		Wheat (*Triticum aestivum*)		✗	✗	N/A	
			No evidence of Au accumulation in any tissues				
Au NPs coated with tannate	• Coated to simulate low molecular weight organic acids in soil	Tobacco (*Nicotiana tabacum*)	✓	✓	✓	N/A	[23]
			Au uptake between 2 and 50 mg/kg				
		Wheat (*Triticum aestivum*)	✗	✗	✗	N/A	
			No evidence of Au accumulation in any tissues				

(continued)

Table 3.1 (continued)

Engineered nanoparticle and surface modification	Enhanced properties after modification	Plant	Uptake, translocation, and physiological effects				Ref.
			Root	Stem	Leaf	Fruit	
Au NPs capped with citrate	• Functionalization to provide electrostatic stabilization	Onion (*Allium cepa*)	N/A	N/A	N/A	N/A	[24, 25]
			Oxidative stress increased with increasing concentration and particle size				
Aluminum-doped ZnO	• Broadening of optical band gap	Green pea (*Pisum sativum*)	✓	✓	✓	✓	[26, 27]
			Increased weight of fresh plant tissues at 1000 mg/kg Chlorophyll and carotenoids increased at 250 mg/kg Nutrient content and carbohydrate profile (sucrose) changed				
Iron-doped ZnO	• Reduced dissolution • Reduced toxicity to bronchial and macrophage cells • Stabilization of material crystal structure	Green pea (*Pisum sativum*)	✓	✓	✓	✓	[28, 29]
			Chlorophyll content and H_2O_2 production decreased Doped ZnO ENPs resulted less toxic than uncoated ZnO ENPs				
ZnO coated with γ-aminopropyltriethoxysilane (KH550)	• Functionalization with organic groups • Improved dispersibility and shape • Improved UV absorption	Green pea (*Pisum sativum*)	✗	✓	✓	✓	[27, 30, 31]
			Increased weight of fresh plant tissues at 1000 mg/kg				
Alginate-coated CeO_2	• Better interactions in water/soil environment	Corn (*Zea mays*)	✓	✓	✓	N/A	[32, 33]
			Different behavior of alginate-coated CeO_2 ENPs with the plant and soil when compared to uncoated ENPs				

(continued)

Table 3.1 (continued)

Engineered nanoparticle and surface modification	Enhanced properties after modification	Plant	Uptake, translocation, and physiological effects				Ref.
			Root	Stem	Leaf	Fruit	
Citric acid-coated CeO_2	• Hydrophilic characteristics with a carboxylic group that can be further functionalized • Less agglomeration • Better interactions with the environment	Radish (*Raphanus sativus*)	Seedlings ✓	[34]			[34–36]
			Citric acid-coated CeO_2 ENPs at 1:7 molar ratio showed increased root biomass, water content, and reduced Ce uptake Decreased toxicity when compared to uncoated ENPs				
		Tomato (*Solanum lycopersicum*)	✗	✗	✗	✗	
			Increased chlorophyll Enhanced catalase activity and reduced ascorbate peroxidase activity Carbohydrates affected				

[a]Thioalkyl tetra(ethyleneglycol)ated trimethylammonium (TTMA); tetraethylene glycol (TEGOH), and tetraethylene glycol acetic acid ligand (TEGCOOH); laser ablation inductively coupled plasma mass spectroscopy (LA-ICP-MS)

the element into the environment [37–39]. In the last decade, several studies have shown that Ag NPs have a wide variety of applications [16]. In addition, these ENPs, at the appropriate concentration, are considered nontoxic and non-carcinogenic [U. S. EPA, www.epa.gov/IRIS/subst/0099.htm].

Various forms of Ag ENPs, with diverse physical and surface properties, portend contamination of the ecosystem [40]. Thus, there is a need to understand the stability, mode of interaction, translocation, aggregation, and effects of this important nanomaterial at various levels of ecosystems [38]. Silver ENPs are synthesized by several methods but the synthesis is generally done in organic solvents or by the use of capping agents to avoid its aggregation [41–53]. Organic coating of Ag ENPs primarily stabilizes them against aggregation, while the capping agent, concomitantly, reduces Ag^{+} ions to Ag^{0}.

Various sizes and shapes of Ag ENPs have been synthesized by several methods. Shapes, as shown in Fig. 3.3, include quasi-spheres, nanotubes, rods, discs, cubes, prisms, octahedral, and triangular nanoplates [54–57]. Capping agents such as citrate, polysaccharides, surfactants, proteins, polymers, and natural organic matter can be used in the synthesis of Ag ENPs [56–61]. Ag ENPs can also be synthesized by using inorganic ligands such as borate, carbonate, chloride, and sulfide to produce inorganic-coated Ag ENPs [62, 63]. The fate of Ag ENPs in the ecosystem is determined by size, shape, as well as the core shell surrounding the Ag atom [64].

There are few reports describing the response of plants to surface-coated Ag ENPs. A study showed negative effects of gum Arabic (GA)-coated Ag ENPs on *Lolium multiflorum*. There was a significant decrease in the growth rate of the root

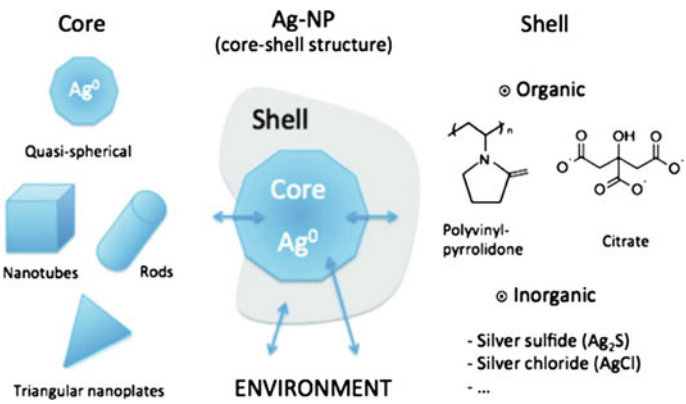

Fig. 3.3 Typical core–shell structure of an Ag ENP that might be released in the environment. *Double arrows* represent the reactions that might occur between the shell or the core with the environment and also at the interface between core and shell. Note that the shell is usually not a continuous impermeable layer but rather is a discontinuous layer allowing the interaction between the core and the surrounding environment. The discontinuity arises from steric and electrostatic forces between the macromolecules attached to the surface. Reprinted with permission from Levard et al. [55]. Copyright 2012 America Chemical Society

and a distortion in the root morphology and cell structure [19]. At a concentration of 40 mg/L of GA-coated Ag ENPs, light microscopy revealed that the seedling growth was inhibited, the root hair failed to develop, the cortical cells were highly vacuolated, and the epidermis and root cap were collapsed. Compared with exposure to equivalent concentrations of ionic silver, the seedlings showed no such effects. There was a significant decrease in root growth rate and distortion of root morphology and cell structure [19]. Seedlings exposed to ionic Ag did not show such effects. Since the effects were observed at high concentrations of Ag ENPs over a short period of time, it is not known if the plants recovered at longer developmental stages. Moreover, by comparing cysteine binding GA-coated Ag ENPs and supernatant components of the GA-coated Ag ENP suspension, it was demonstrated that the toxicity of GA-coated Ag ENPs might not be only due to the released Ag from the ENPs [19]. The Ag concentration in the root might result from the Ag ions adsorbed to the root surface, while the concentration in the shoot could result from the adsorption of Ag ENPs and the translocation of both the ENPs and Ag ions, similar to plants treated with CeO_2 [19, 65]. The root growth inhibition and cell damage may result from the nanomaterial itself, the Ag ions released from the ENPs, or both [19].

Phytotoxicity studies of citrated-coated Ag ENPs were performed in *Phaseolus radiatus* and *Sorghum bicolor*. Experiments were carried out in both agar and soil media. Transmission electron microscopy (TEM) images showed that Ag ENPs were spherical in shape (Fig. 3.4a) and evenly distributed in the agar medium (Fig. 3.4b). TEM images also showed that the plants took up the ENPs from both media but the growth rate was inhibited in both plants only in the agar medium, in a dose-dependent manner. At the higher concentration, the citrate-coated Ag ENPs inhibited the growth of seedlings in agar medium; however, none of the concentrations affected soil grown seedlings.

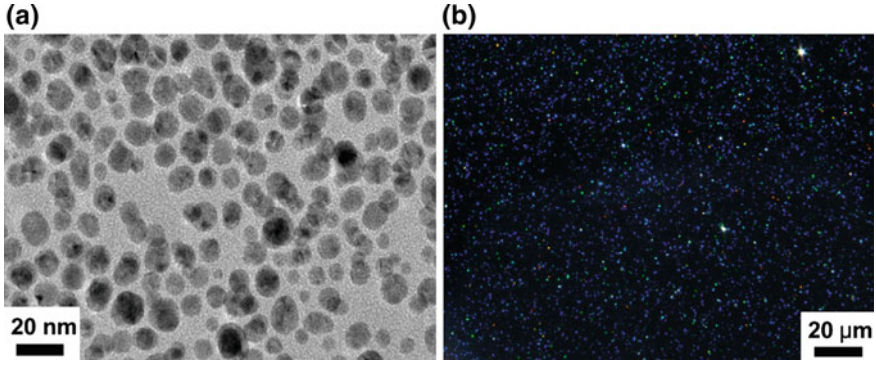

Fig. 3.4 **a** Transmission electron micrograph of silver nanoparticles; **b** high-resolution microscopic image of silver nanoparticle distributed in agar medium of 40 mg/L. Reprinted from Lee et al. [20]. Copyright 2011, with permission from Elsevier

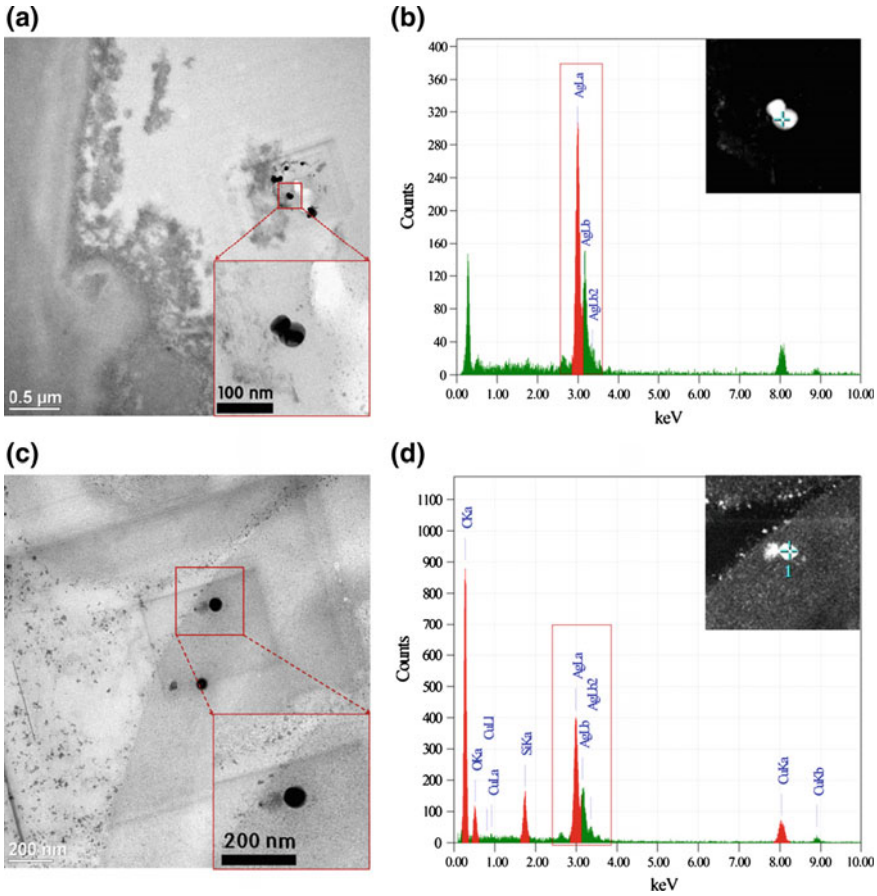

Fig. 3.5 Transmission electron micrographs of the roots of *Phaseolus radiatus and Sorghum bicolor* exposed to Ag NPs in agar medium of 100 and 40 mg/L, respectively: **a** *Phaseolus radiatus*, **b** spectrum of energy-dispersive spectroscopy (EDS) of dense spot for TEM scan in (**a**), **c** *Sorghum bicolor*, and **d** spectrum of EDS of dense spot for TEM scan in **c**. Reprinted from Lee et al. [20] Copyright 2011, with permission from Elsevier

Figure 3.5 shows further TEM and energy-dispersive spectroscopy (EDS) images of the root tissue of *P. radiatus* and *S. bicolor* exposed to Ag ENPs in agar medium at 100 and 40 mg/L. The EDS scan showed the penetration of particulate Ag into the root [20]. The study showed that toxicity was species dependent, since *P. radiatus* and *S. bicolor* showed 13 and 26 mg/L EC_{50} values, respectively. It is noteworthy that citrate, at 3 mg/L, may have no significant effect on the growth of *P. radiatus* [66]. Pokhrel and Dubey [21] reported that citrate-coated Ag ENPs imposed toxicity to the early growth and development of both maize (*Zea mays* L.) and cabbage (*Brassica oleracea* var. capitata L.). The toxic potential of Ag ENPs was more pronounced in both plants than the

corresponding ionic salts. Both plants revealed abnormal root morphology and structures under exposure to citrate-coated Ag ENPs. However, germination and root elongation were less affected by the ENPs, compared to free ions [21]. In addition, maize absorbed less Ag from citrate-coated Ag ENPs, compared with $AgNO_3$ [21].

3.2.2 Gold Nanoparticles (Au ENPs)

Although many coatings are currently being utilized on Au ENPs [67–72], research investigating the implications of their exposure to agricultural crops is extremely lacking. Koelmel et al. [22] explored the effects of Au ENPs coated with thioalkyl tetra(ethyleneglycol)ated trimethylammonium (TTMA), tetraethylene glycol (TEGOH), and tetraethylene glycol acetic acid ligand (TEGCOOH). These coatings gave the ENPs a positive, neutral, and negative charge, respectively. Hydroponically grown rice (*Oryza sativa*) plants were studied by using a laser ablation inductively coupled plasma mass spectroscopy (LA-ICP-MS) to track the uptake of the coated ENPs and determine how surface charge affected the spatial distribution of Au [22]. LA-ICP-MS analysis revealed that functional groups on the Au ENP coatings did affect uptake, with roots showing a preference for the positively charged TTMA coating, followed by the neutral TEGOH coating, and then the negatively charged TEGCOOH coating. Gold concentrations were highest in the shoots with the TEGCOOH (–) coating. Examination of rice leaves revealed heterogeneous distribution of Au based on charge/surface coating. Leaves from rice treated with Au ENPs and coated with TEGOH (neutral) contained higher concentrations of gold on the left side of the blade, while rice treated with TEGCOOH (–) showed gold concentrated in the midsection of the leaf.

The effects of Au ENPs coated with citrate and tannate have also been evaluated [23]. Both tobacco (*Nicotiana tabacum*) and wheat (*Triticum aestivum*) were grown hydroponically and exposed to Au ENPs coated with either citrate or tannate at sizes of 10, 30, or 50 nm. At the 30 mg/kg treatment concentration tested, the authors found no gold uptake in wheat with any of the size/coating combinations. In addition, synchrotron micro X-ray fluorescence (μ-XRF) analysis revealed no uptake of gold into the root tissues. Gold uptake in tobacco was measured between 2 and 50 mg/kg at all treatments. Synchrotron experiments indicated the accumulation of gold from 30-nm citrate-coated Au ENPs in the mid-rib of tobacco leaves. However, with the exception of the above-mentioned treatment, the majority of tobacco leaves tested contained Au concentrations below the μ-XRF detection limit of 1 mg/kg.

A recently published study examined the biological effects of Au NPs capped with citrate in onion (*Allium cepa*) [24]. These researchers measured the generation of reactive oxygen species (ROS) in roots exposed to increasing concentrations of capped Au ENPs at sizes of 15, 30, and 40 nm. The authors found that generation of O_2^-, H_2O_2, and ^-OH radicals increased with increasing nanoparticle exposure, but

the trend decreased with increased nanoparticle size. This trend was mirrored with the production of malondialdehyde (MDA) production, with the most MDA production occurring in onions treated with 15 nm Au ENPs at the highest concentration.

It is clear from the number of published articles, and from the scope of these studies, that research into the effects that coatings may have on Au ENPs is still in its infancy. Research in this area must intensify, if it is to keep pace with the demand for Au ENPs with a seemingly endless list of coatings.

3.3 Metal Oxide ENPs

3.3.1 Zinc Oxide Nanoparticles (ZnO ENPs)

Among the ENPs, zinc oxide is subjected to surface modification to enhance its properties, including conductivity, dispersion, shape, photoluminescence, and reflectance, among others. The growing application in electronics and optics has increased the number of coated/doped ZnO ENPs. However, their release into the environment is unquantified and its implications are still unknown. Table 3.1 shows literature reports on the synthesis of surface-modified ZnO nanoparticles whose biocompatibility with plants has been studied.

To the best of the authors' knowledge, there are only a couple of studies evaluating the effects of coated/doped ZnO ENPs in plants. Mukherjee et al. [29] performed a soil study in green pea (*Pisum sativum* L.) plants exposed to iron-doped ZnO ENPs (Fe@ZnO) and uncoated ZnO ENPs. Plants were grown in soil amended with either 10% Fe@ZnO or uncoated ZnO at 0, 125, 250, and 500 mg/kg. Root and stem Zn was enhanced after exposure to the Fe-doped ENPs, but the Fe absorption remained unaffected after comparison to control treatments. In addition, chlorophyll content and production of H_2O_2 decreased. Authors concluded that Fe@ZnO ENPs resulted less toxic than uncoated ZnO ENPs. In a further study, Mukherjee et al. [27] exposed green pea for 65 days to soil amended uncoated ZnO, 2 wt% alumina (Al_2O_3)-doped ZnO, and 1% KH550-coated ZnO at 250 and 1000 mg ENP/kg. Results showed increased weight of fresh plant tissues at 1000 mg/kg. Higher concentrations of Zn were found in roots and seeds under aluminum-doped ZnO at 1000 mg/kg, compared with other ZnO ENPs and macrosized ZnO. Authors attributed the result to the high positive surface charge due to Al doping as well as high Zn^{2+} dissolution. Increased seed Zn was found in both doped and coated ZnO treatments at 250 mg/kg, attributed to the alumina doping and the negative surface charge of the KH550-coated that promotes Zn uptake due to the repulsion from the negatively charged root surface. Chlorophyll and carotenoids were increased by the alumina-doped treatment at 250 mg/kg, compared to the rest of the treatments. The seed quality was affected the most by the doped NPs at 1000 mg/kg, where nutrient content and carbohydrate profile

(sucrose) changed. Alumina-doped particles had larger size (15 nm) than bare-ZnO ENPs (10 nm); authors hypothesized this had greater effects on plant and seed quality. The authors highlighted the importance of the surface modification in the behavior of ENPs in edible plants, since the aluminum-doped ZnO showed more negative effects in green pea plants than KH550-coated and uncoated ZnO ENPs.

3.3.2 Cerium Dioxide Nanoparticles (CeO_2 ENPs)

One of the first studies on the effects of coated CeO_2 ENPs in plants was reported by Zhao et al. [32]. Alginate-coated CeO_2 ENPs interaction with corn (*Zea mays*) plants was evaluated in natural (sandy loam) and organic (1:1 natural soil:commercial potting soil) soils at concentrations of 100, 200, 400, and 800 mg/kg, and compared to uncoated CeO_2 ENPs. Alginate was selected as a coating agent, since it is naturally produced by algae and some bacteria found in soil [33]; thus, the interaction between alginate and the ENPs can occur naturally in water or soil environments. Authors reported that the surface coating modified the interaction of CeO_2 ENPs with the plant and soils. Authors also stated that the behavior of the coated ENPs depends on the type of soil and its organic matter content. In this specific study, Ce content increased in plants grown in organic soil amended with uncoated and coated CeO_2 ENPs at concentrations of 400 and 800 mg/kg, compared with plants grown in natural soil under the same conditions. This confirms that the behavior of both uncoated/coated ENPs is highly dependent on the medium properties.

Trujillo-Reyes et al. [34] modified CeO_2 ENPs with a surface coating of citric acid (CA) at molar ratios of 1:2, 1:3, 1:7, and 1:10 CeO_2:CA. Citric acid was previously reported as a coating agent for silver [73] and iron oxide [74] ENPs. Citric acid was added as a coating material due to its biocompatibility with Fe_2O_3 ENPs and its adsorption onto the ENPs surface [74]. Coating with CA also adds to the surface at least one carboxylic group exposed (that can be even further functionalized), gives hydrophilic characteristics to the ENPs, and avoids agglomeration [74]. In addition, similarly to alginate, CA can be naturally found in the environment, representing a potential path of interaction with ENPs. In the study performed by Trujillo-Reyes et al. [34], they evaluated the toxicity of CA-coated and uncoated CeO_2 ENPs into radish (*Raphanus sativus*) seedlings at concentrations of 50, 100, and 200 mg/L. Water and CA at 100 mg/L were used as controls. The results did not show any changes in seed germination. However, at all concentrations, CA-coated CeO_2 ENPs at 1:7 molar ratio showed increased root biomass, water content, and reduced Ce uptake. According to the authors, citric acid coating decreased the toxicity of CeO_2 ENPs.

CA-coated CeO_2 ENPs were also evaluated in tomato (*Solanum lycopersicum* L.) plants, along with uncoated CeO_2, micron-sized CeO_2, ionic Ce (cerium acetate), and citric acid. Barrios et al. [36] exposed tomato plants for 210 days to commercial potting soil amended with each of the five different chemicals at concentrations of

62.5, 125, 250, and 500 mg/kg. None of the treatments increased stem and leaf Ce, but CA-coated CeO_2 ENPs reduced the Ce uptake by roots and increased levels of chlorophyll, in comparison to control. Neither uncoated nor coated particles affect the accumulation of micro and macronutrients in roots, stems, and leaves. However, at 500 mg/kg, CA-coated CeO_2 enhanced catalase activity, which represents the plant's response to modifications in the environmental conditions [75]. Additionally, both coated and uncoated CeO_2 ENPs reduced the activity of ascorbate peroxidase, enzyme responsible for hydrogen peroxide and hydroxyl radicals scavenging, which could damage cell constituents [76].

Finally, Barrios et al. [35] performed a nutritional assessment in the fruit obtained from tomato plants exposed to the previously mentioned materials. The study included quantification of elements (Ce, Al, B, Ca, Cu, Fe, K, Mg, Mn, P, and Zn) along with total and reducing sugars, starch, and lycopene. The authors concluded that all Ce compounds (macrosized, uncoated, and coated nano CeO_2) affected the physiology and nutrient composition of the tomato fruits. However, it was evident that the surface coating plays an important role in the effects of the ENPs on the biochemistry of the plant, since the uncoated CeO_2 ENPs affected mainly the nutritional elements, while the CA-coated CeO_2 ENPs disturbed the carbohydrates.

3.3.3 Copper Oxide ENPs

Although the scope of this chapter is limited to higher plants, a comprehensive search yielded no published work dealing with terrestrial vascular plants. However, some work has been done looking at polymer coated CuO in duckweed and green algae. Saison et al. [77] investigated the effects of polystyrene(poly (styrene-co-butyl acrylate)-coated CuO nanoparticles (CS-CuO ENPs) on ROS generation in green algae. Measurements of lipid peroxidation indicate a 350% increase in ROS production in algae treated with CS-CuO ENPs at 20 mg/L, compared to control. There was no significant increase in ROS observed in algae treated with bare CuO or with polystyrene alone. The authors attributed high ROS production to photocatalytic processes induced by CuO semiconductor properties and light exposure, as plants treated with CS-CuO ENPs in the absence of light produced low levels of ROS. Chlorophyll content decreased by half and photosynthesis II (PS II) electron transport was significantly reduced, after six hours of exposure to CS-CuO NPs. These results were supported by a later study that found CS-CuO ENPs produced a 390% increase in ROS generation, and caused a reduction in PS II activity to 13% of control levels [78]. In the same study, green algae treated with uncoated CuO ENPs saw ROS levels of only 160% of controls, while PS II activity remained at 78% of controls.

Perreault et al. [79] recently conducted studies looking at CS-CuO ENPs, this time using duckweed instead of green algae. CS-CuO ENPs were found to be 10 times more toxic than bare CuO. The coated CuO also reduced duckweed's growth

rate by 50%, while the bare CuO ENPs required over 10 times the concentration to achieve the same effect. Perreault et al. [78] also reported that ROS generation was 400% higher in CS-CuO ENPs compared to CuO ENPs, citing unique characteristics caused by the surface coating, as the polymer alone did not produce similar results.

3.4 Conclusions

Although the number of reports concerning the effects of surface-coated ENPs on plants is limited (a dozen of species), they have covered growth stages from germination to fruit production and, in the case of Au NPs [22], the compartmentalization of particles as affected by the type of surface coating. Practically, no effects have been observed in germination; however, some effects have been shown in root growth and ROS production [20, 24]. Attempts have also been made to evaluate the effects of surface modification on the quality of seeds [27] and fruit [35]. Alumina-doped ZnO ENPs increased chlorophyll, carotenoids, and seed Zn in green pea [27], while citric acid-coated CeO_2 disturbed carbohydrates in tomato [35]. The above information clearly shows that more studies are needed in order to generalize the effects of surface coating in the interaction of NPs with plants. Very few long-term studies have shown possible effects of seeds and fruits. Only a study has evaluated the tissue distribution of coated NPs [22] and there is no idea about the effects on trophic transfer. Only one report has evaluated the interaction of coating $\times$ soil properties [32]. This suggests that future research has to be performed in soils with different properties and with plants of different species. In addition, future studies have to determine the biotransformation of surface-coated ENPs within plants, possible trophic transfer and the transgenerational effects. In summary, there is a long way to run in order to have a clear idea about the environmental effects of surface modification of ENPs.

Acknowledgements This material is based upon work supported by the National Science Foundation and the Environmental Protection Agency under Cooperative Agreement Number DBI-1266377. Any opinions, findings, and conclusions or recommendations expressed in this material are those of the author(s) and do not necessarily reflect the views of the National Science Foundation or the Environmental Protection Agency. This work has not been subjected to EPA review and no official endorsement should be inferred. The authors also acknowledge the USDA grant 2016-67021-24985 and the NSF Grants EEC-1449500, CHE-0840525 and DBI-1429708. Partial funding was provided by the NSF ERC on Nanotechnology-Enabled Water Treatment (EEC-1449500). This work was also supported by Grant 2G12MD007592 from the National Institutes on Minority Health and Health Disparities (NIMHD), a component of the National Institutes of Health (NIH). J.L. Gardea-Torresdey acknowledges the Dudley family for the Endowed Research Professorship, the Academy of Applied Science/US Army Research Office, Research and Engineering Apprenticeship program (REAP) at UTEP, and the LEER and STARs programs of the UT System. I.A. Medina-Velo thanks the support of Consejo Nacional de Ciencia y Tecnologia of Mexico (CONACyT).

References

1. Roco MC, Bainbridge WS (2013) The new world of discovery, invention, and innovation: convergence of knowledge, technology, and society. J Nanopart Res 15(9):1–17
2. Peralta-Videa JR, Huang Y, Parsons JG et al (2016) Plant-based green synthesis of metallic nanoparticles: scientific curiosity or a realistic alternative to chemical synthesis? Nanotechnol Environ Eng 1:4
3. Servin AD, White JC (2016) Nanotechnology in agriculture: next steps for understanding engineered nanoparticle exposure and risk. NanoImpact 1:9–12
4. Keller AA, McFerran S, Lazareva A, Suh S (2013) Global life cycle releases of engineered nanomaterials. J Nanopart Res 15:1–17
5. Lu CM, Zhang CY, Wen JQ et al (2002) Research of the effect of nanometer materials on germination and growth enhancement of *Glycine max* and its mechanism. Soybean Sci 21:168–172
6. Zheng L, Hong F, Lu S, Liu C (2005) Effect of nano-TiO(2) on strength of naturally aged seeds and growth of spinach. Biol Trace Elem Res 104:83–92
7. Hong F, Yang F, Liu C et al (2005) Influences of nano-TiO_2 on the chloroplast aging of spinach under light. Biol Trace Elem Res 104:249–260
8. Gao F, Hong F, Liu C et al (2006) Mechanism of nano-anatase TiO_2 on promoting photosynthetic carbon reaction of spinach: inducing complex of rubisco-rubisco activase. Biol Trace Elem Res 111:239–253
9. Yang L, Watts DJ (2005) Particle surface characteristics may play an important role in phytotoxicity of alumina nanoparticles. Toxicol Lett 158:122–132
10. Lin D, Xing B (2007) Phytotoxicity of nanoparticles: inhibition of seed germination and root growth. Environ Pollut 150:243–250
11. Yang F, Liu C, Gao F et al (2007) The improvement of spinach growth by nano-anatase TiO_2 treatment is related to nitrogen photoreduction. Biol Trace Elem Res 119:77–88
12. Linglan M, Chao L, Chunxiang Q et al (2008) Rubisco activase mRNA expression in spinach: modulation by nanoanatase treatment. Biol Trace Elem Res 122:168–178
13. Rico CM, Majumdar S, Duarte-Gardea M et al (2011) Interaction of nanoparticles with edible plants and their possible implications in the food chain. J Agric Food Chem 59:3485–3498
14. Tripathi DK, Gaur S, Singh S et al (2017) An overview on manufactured nanoparticles in plants: uptake, translocation, accumulation and phytotoxicity. Plant Physiol Biochem 110:2–12
15. de la Rosa G, García-Castañeda C, Vázquez-Núñez E et al (2017) Physiological and biochemical response of plants to engineered NMs: implications on future design. Plant Physiol Biochem 110:226–235
16. Zuverza-Mena N, Martínez-Fernández D, Du W et al (2016) Exposure of engineered nanomaterials to plants: insights into the physiological and biochemical responses—a review. Plant Physiol Biochem 110:236–264
17. Pachapur VL, Larios AD, Cledon M et al (2016) Behavior and characterization of titanium dioxide and silver nanoparticles in soils. Sci Total Environ 563–564:933–943
18. Louie SM, Tilton RD, Lowry GV (2016) Critical review: impacts of macromolecular coatings on critical physicochemical processes controlling environmental fate of nanomaterials. Environ Sci Nano 3:283–310
19. Yin L, Cheng Y, Espinasse B et al (2011) More than the ions: the effects of silver nanoparticles on *Lolium multiflorum*. Environ Sci Technol 45:2360–2367
20. Lee WM, Kwak JI, An YJ (2012) Effect of silver nanoparticles in crop plants *Phaseolus radiatus* and *Sorghum bicolor*: media effect on phytotoxicity. Chemosphere 86:491–499
21. Pokhrel LR, Dubey B (2013) Evaluation of developmental responses of two crop plants exposed to silver and zinc oxide nanoparticles. Sci Total Environ 452–453:321–332

22. Koelmel J, Leland T, Wang H et al (2013) Investigation of gold nanoparticles uptake and their tissue level distribution in rice plants by laser ablation-inductively coupled-mass spectrometry. Environ Pollut 174:222–228
23. Judy JD, Unrine JM, Rao W et al (2012) Bioavailability of gold nanomaterials to plants: importance of particle size and surface coating. Environ Sci Technol 46:8467–8474
24. Rajeshwari A, Suresh S, Chandrasekaran N, Mukherjee A (2016) Toxicity evaluation of gold nanoparticles using an *Allium cepa* bioassay. RSC Adv 6:24000–24009
25. Brewer SH, Glomm WR, Johnson MC et al (2005) Probing BSA binding to citrate-coated gold nanoparticles and surfaces. Langmuir 21:9303–9307
26. Suwanboon S, Amornpitoksuk P, Haidoux A, Tedenac JC (2008) Structural and optical properties of undoped and aluminium doped zinc oxide nanoparticles via precipitation method at low temperature. J Alloys Compd 462:335–339
27. Mukherjee A, Sun Y, Morelius E et al (2015) Differential toxicity of bare and hybrid ZnO nanoparticles in Green Pea (*Pisum sativum* L.): a life cycle study. Front Plant Sci 6:1242
28. George S, Pokhrel S, Xia T et al (2010) Use of a rapid cytotoxicity screening approach to engineer a safer zinc oxide nanoparticle through iron doping. ACS Nano 4:15–29
29. Mukherjee A, Pokhrel S, Bandyopadhyay S et al (2014) A soil mediated phyto-toxicological study of iron doped zinc oxide nanoparticles (Fe at ZnO) in green peas (*Pisum sativum* L.). Chem Eng J 258:394–401
30. Abdolmaleki A, Mallakpour S, Borandeh S (2012) Effect of silane-modified ZnO on morphology and properties of bionanocomposites based on poly(ester-amide) containing tyrosine linkages. Polym Bull 69:15–28
31. Mallakpour S, Madani M (2014) The effect of the coupling agents KH550 and KH570 on the nanostructure and interfacial interaction of zinc oxide/chiral poly(amide–imide) nanocomposites containing l-leucine amino acid moieties. J Mater Sci 49:5112–5118
32. Zhao L, Peralta-Videa JR, Varela-Ramirez A et al (2012) Effect of surface coating and organic matter on the uptake of CeO_2 NPs by corn plants grown in soil: insight into the uptake mechanism. J Hazard Mater 225–226:131–138
33. Chen KL, Mylon SE, Elimelech M (2006) Aggregation kinetics of nanoparticles in monovalent and divalent electrolytes. Environ Sci Technol 40:1516–1523
34. Trujillo-Reyes J, Vilchis-Nestor AR, Majumdar S et al (2013) Citric acid modifies surface properties of commercial CeO_2 nanoparticles reducing their toxicity and cerium uptake in radish (*Raphanus sativus*) seedlings. J Hazard Mater 263:677–684
35. Barrios AC, Medina-Velo IA, Zuverza-Mena N et al (2016) Nutritional quality assessment of tomato fruits after exposure to uncoated and citric acid coated cerium oxide nanoparticles, bulk cerium oxide, cerium acetate and citric acid. Plant Physiol Biochem 110:100–107
36. Barrios AC, Rico CM, Trujillo-Reyes J et al (2016) Effects of uncoated and citric acid coated cerium oxide nanoparticles, bulk cerium oxide, cerium acetate, and citric acid on tomato plants. Sci Total Environ 563–564:956–964
37. Morones JR, Elechiguerra JL, Camacho A, Holt K, Kouri JB, Ramirez JT, Yacaman MJ (2005) The bactericidal effect of silver nanoparticles. Nanotechnology 16(10):2346–2353
38. Navarro E, Baun A, Behra R et al (2008) Environmental behavior and ecotoxicity of engineered nanoparticles to algae, plants, and fungi. Ecotoxicology 17:372–386
39. Asharani PV, Lian WuY, Gong Z, Valiyaveettil S (2008) Toxicity of silver nanoparticles in zebrafish models. Nanotechnology 19:255102
40. Panyala NR, Pena-Mendez EM, Havel J (2008) Silver or silver nanoparticles: a hazardorous threat to the environment and human health? J Appl Biomed 6:117–129
41. Phenrat T, Saleh N, Sirk K et al (2008) Stabilization of aqueous nanoscale zerovalent iron dispersions by anionic polyelectrolytes: adsorbed anionic polyelectrolyte layer properties and their effect on aggregation and sedimentation. J Nanopart Res 10:795–814
42. Sharma VK, Yngard RA, Lin Y (2009) Silver nanoparticles: green synthesis and their antimicrobial activities. Adv Colloid Interface Sci 145:83–96
43. Hotze EM, Phenrat T, Lowry GV (2010) Nanoparticle aggregation: challenges to understanding transport and reactivity in the environment. J Environ Qual 39:1909–1924

44. Dallas P, Sharma VK, Zboril R (2011) Silver polymeric nanocomposites as advanced antimicrobial agents: classification, synthetic paths, applications, and perspectives. Adv Colloid Interface Sci 166:119–135
45. Nadagouda MN, Speth TF, Varma RS (2011) Microwave-assisted green synthesis of silver nanostructures. Acc Chem Res 44:469–478
46. Narayanan KB, Sakthivel N (2011) Green synthesis of biogenic metal nanoparticles by terrestrial and aquatic phototrophic and heterotrophic eukaryotes and biocompatible agents. Adv Colloid Interface Sci 169:59–79
47. Rafey A, Shrivastavaa KBL, Iqbal SA, Khan Z (2011) Growth of Ag-nanoparticles using aspartic acid in aqueous solutions. J Colloid Interface Sci 354:190–195
48. Sintubin L, Verstraete W, Boon N (2012) Biologically produced nanosilver: current state and future perspectives. Biotechnol Bioeng 109:2422–2436
49. Šišková K, Bečička O, Mašek V et al (2012) Spacer-free SERRS spectra of unperturbed porphyrin detected at 100 fM concentration in Ag hydrosols prepared by modified Tollens method. J Raman Spectrosc 43:689–691
50. Upert G, Bouillère F, Wennemers H (2012) Oligoprolines as scaffolds for the formation of silver nanoparticles in defined sizes: correlating molecular and nanoscopic dimensions. Angew Chemie Int Ed 51:4231–4234
51. Ashraf S, Abbasi AZ, Pfeiffer C et al (2013) Protein-mediated synthesis, pH-induced reversible agglomeration, toxicity and cellular interaction of silver nanoparticles. Colloids Surf B Biointerfaces 102:511–518
52. Faramarzi MA, Sadighi A (2013) Insights into biogenic and chemical production of inorganic nanomaterials and nanostructures. Adv Colloid Interface Sci 189–190:1–20
53. Ravindran A, Chandran P, Khan SS (2013) Biofunctionalized silver nanoparticles: advances and prospects. Colloids Surf B Biointerfaces 105:342–352
54. Wiley B, Sun Y, Xia Y (2007) Synthesis of silver nanostructures with controlled shapes and properties. Acc Chem Res 40:1067–1076
55. Levard C, Hotze EM, Lowry GV, Brown GE (2012) Environmental transformations of silver nanoparticles: impact on stability and toxicity. Environ Sci Technol 46:6900–6914
56. Ringe E, Zhang J, Langille MR et al (2012) Correlating the structure and localized surface plasmon resonance of single silver right bipyramids. Nanotechnology 23:444005
57. Liu G, Eichelsdoerfer DJ, Rasin B et al (2013) Delineating the pathways for the site-directed synthesis of individual nanoparticles on surfaces. Proc Natl Acad Sci USA 110:887–891
58. Dahl JA, Maddux BLS, Hutchison JE (2007) Toward greener nanosynthesis. Chem Rev 107:2228–2269
59. Sal'nikov D, Pogorelova A, Makarov S (2009) Silver ion reduction with peat fulvic acids. Russ J Appl Chem 82:545–548
60. Sanghi R, Verma P (2009) Biomimetic synthesis and characterisation of protein capped silver nanoparticles. Bioresour Technol 100:501–504
61. Gigault J, Hackley VA (2013) Differentiation and characterization of isotopically modified silver nanoparticles in aqueous media using asymmetric-flow field flow fractionation coupled to optical detection and mass spectrometry. Anal Chim Acta 763:57–66
62. Delay M, Dolt T, Woellhaf A et al (2011) Interactions and stability of silver nanoparticles in the aqueous phase: Influence of natural organic matter (NOM) and ionic strength. J Chromatogr A 1218:4206–4212
63. Piccapietra F, Sigg L, Behra R (2012) Colloidal stability of carbonate-coated silver nanoparticles in synthetic and natural freshwater. Environ Sci Technol 46:818–825
64. Sharma VK, Siskova KM, Zboril R, Gardea-Torresdey JL (2014) Organic-coated silver nanoparticles in biological and environmental conditions: fate, stability and toxicity. Adv Colloid Interface Sci 204:15–34
65. Ravel B, Newville M (2005) ATHENA, ARTEMIS, HEPHAESTUS: data analysis for X-ray absorption spectroscopy using IFEFFIT. J Synchrotron Radiat 12:537–541
66. Lee W-M, An Y-J, Yoon H, Kweon H-S (2008) Toxicity and bioavailability of copper nanoparticles to the terrestrial plants mung bean (*Phaseolus radiatus*) and wheat (*Triticum*

aestivum): plant agar test for water-insoluble nanoparticles. Environ Toxicol Chem 27:1915–1921
67. Mandal TK, Fleming MS, Walt DR (2002) Preparation of polymer coated gold nanoparticles by surface-confined living radical polymerization at ambient temperature. Nano Lett 2:3–7
68. Mine E, Yamada A, Kobayashi Y et al (2003) Direct coating of gold nanoparticles with silica by a seeded polymerization technique. J Colloid Interface Sci 264:385–390
69. Kim D, Park S, Jae HL et al (2007) Antibiofouling polymer-coated gold nanoparticles as a contrast agent for in vivo X-ray computed tomography imaging. J Am Chem Soc 129: 7661–7665
70. Alric C, Taleb J, Le DG et al (2008) Gadolinium chelate coated gold nanoparticles as contrast agents for both X-ray computed tomography and magnetic resonance imaging. J Am Chem Soc 130:5908–5915
71. Zhang G, Yang Z, Lu W et al (2009) Influence of anchoring ligands and particle size on the colloidal stability and in vivo biodistribution of polyethylene glycol-coated gold nanoparticles in tumor-xenografted mice. Biomaterials 30:1928–1936
72. Chew CKT, Salcianu C, Bishop P et al (2015) Functional thin film coatings incorporating gold nanoparticles in a transparent conducting fluorine doped tin oxide matrix. J Mater Chem C 3:1118–1125
73. Tejamaya M, Römer I, Merrifield RC, Lead JR (2012) Stability of citrate, PVP, and PEG coated silver nanoparticles in ecotoxicology media. Environ Sci Technol 46:7011–7017
74. Li L, Mak KY, Leung CW et al (2013) Effect of synthesis conditions on the properties of citric-acid coated iron oxide nanoparticles. Microelectron Eng 110:329–334
75. Mhamdi A, Queval G, Chaouch S et al (2010) Catalase function in plants: a focus on Arabidopsis mutants as stress-mimic models. J Exp Bot 61:4197–4220
76. Asada K (1992) Ascorbate peroxidase–a hydrogen peroxide-scavenging enzyme in plants. Physiol Plant 85:235–241
77. Saison C, Perreault F, Daigle JC et al (2010) Effect of core-shell copper oxide nanoparticles on cell culture morphology and photosynthesis (photosystem II energy distribution) in the green alga, *Chlamydomonas reinhardtii*. Aquat Toxicol 96:109–114
78. Perreault F, Oukarroum A, Melegari SP et al (2012) Polymer coating of copper oxide nanoparticles increases nanoparticles uptake and toxicity in the green alga *Chlamydomonas reinhardtii*. Chemosphere 87:1388–1394
79. Perreault F, Popovic R, Dewez D (2014) Different toxicity mechanisms between bare and polymer-coated copper oxide nanoparticles in *Lemna gibba*. Environ Pollut 185:219–227

Chapter 4
Nanoparticles-Induced Oxidative Stress

Hainan Sun, Guizhen Yan and Hongyu Zhou

Abstract With the growing usage of nanoparticles (NPs) in industry, biomedicine, and daily life, an increasing chance for humans to be exposed to NPs has been issued. However, the basis of toxicity of most manufactured NPs is not fully understood. An important mechanism of nanotoxicity is reactive oxygen species (ROS) formation, which could cause oxidative stress, inflammation, and consequent cell death. NPs can interact with H_2O or O_2 in the physiological environment, resulting in the direct production of ROS, or affect the function of mitochondria and NADPH oxidase, resulting in the indirect production of ROS. ROS generation and oxidative stress were depicted by the hierarchical oxidative stress model. Critical determinants that can affect the generation of ROS, including NPs' composition, size, shape, and surface chemistry, are briefly discussed in this review.

Keywords Oxidative stress · Nanoparticles · Nanotoxicity · Reactive oxygen species · Physicochemical properties

4.1 Introduction

Nanotechnology is a rapid developing field that encompasses the production and usage of particles at the nanoscale (1–100 nm). Due to the excellent optical, electronic, and biological properties, nanoparticles (NPs) are widely used in industry, biomedicine, and over 1800 consumer products [1, 2]. For example,

H. Zhou (✉)
Guangdong Key Laboratory of Environmental Pollution and Health,
School of Environment, Jinan University, Guangzhou 510632, China
e-mail: hyzhou001@jnu.edu.cn

H. Sun
School of Chemistry and Chemical Engineering, Shandong University,
Jinan 250100, China

G. Yan
Lixia District People's Hospital, Jinan 250014, China

B. Yan et al. (eds.), *Bioactivity of Engineered Nanoparticles*,
Nanomedicine and Nanotoxicology, DOI 10.1007/978-981-10-5864-6_4

carbon nanotubes (CNTs) are used in energy field due to its electronic properties [3]. Various NPs have also been used in the area of biotechnology, biosensors, and nanomedicine [4–7].

The application of NPs enhances their contact probability with humans. Humans may be exposed to NPs through different pathways, such as inhalation, ingestion, skin contact, and injection. For example, NPs in plants, animal bodies, and microbes could transfer into human body through food chain [8, 9]. Airborne NPs could easily enter into respiratory tract by inhalation [10]. NPs in cosmetics and personal care products could enter into human body through skin penetration [11]. In addition, theronostic NPs could also be intravenously injected into human body for imaging and drug delivery [12]. The small size of NPs makes them easily to pass through cell membranes and penetrate into living organisms and consequently cause cellular dysfunction. In addition, the great surface area to volume ratio of NPs increases their chemical or catalytic activity, resulting in increased toxicity through different mechanisms. Thus, understanding and assessing of NPs' toxicity is necessary for the safety usage of NPs.

Reactive oxygen species (ROS) formation is one of the mechanisms of nanotoxicity, which could lead to cellular oxidative stress, inflammation, and cell death. NPs with specific properties could interact with H_2O or O_2 in the physiological environment, resulting in the direct production of ROS. Furthermore, NPs may affect the function of mitochondria and NADPH oxidase, resulting in the indirect production of ROS. The elevated ROS level leads to hierarchical oxidative stress [13]. The physicochemical properties of NPs, such as chemical composition, size, shape, and surface chemistry have been found to dictate oxidative stress level and their toxicity. In this review, we focus on introducing molecular mechanisms underlying NP-induced oxidative stress and hierarchical oxidative stress models used to study the oxidative stress-related mechanism. We also review the recent progress on regulation of oxidative stress and nanotoxicity through NPs' physicochemical properties.

4.2 Molecular Mechanisms Underlying Nanoparticle-Induced Oxidative Stress

The generation of ROS and related oxidative stress is considered as the main cause of nanotoxicity. The level of ROS generation depends on the physicochemical nature of NPs, including their composition, size, shape, and surface chemistry. Different NPs can induce the ROS generation through direct and indirect mechanisms.

4.2.1 Direct Mechanisms of ROS Generation

NPs could donate or receive electrons from intracellular and extracellular molecules, such as H_2O and O_2, resulting in the production of abiotic ROS. The composition, surface structure, and photosensitivity are key determinants to the direct production of abiotic ROS.

The composition of NPs affects the abiotic ROS level. Nel et al. demonstrated that when particles' concentration was 0.5 μg/mL, titanium dioxide (TiO_2) NPs induced the highest abiotic ROS level, followed by ambient ultrafine particles and fullerol, while carbon black (CB) and polystyrene (PS) NPs did not induce abiotic ROS [14]. In another paper, the induction ability of abiotic ROS was in the following order: ZnO > CeO_2 > TiO_2 > NH_2-PS (10 μg/mL) [15]. The abiotic ROS level was also screened in 24 metal oxide NPs. Co_3O_4, Mn_2O_3, CuO, Ni_2O_3, and CoO induced abiotic ROS in a dose dependent manner, while the rest NPs did not induce abiotic ROS [16]. PdO doping on Co_3O_4 NPs (200 μg/mL) dictates abiotic ROS. The abiotic ROS level is positively correlated to PdO content [17].

Specific surface structure could catalyze the production of abiotic ROS. For example, fumed silica NPs induced higher ROS level compared to colloidal silica due to the strained three-membered rings (3MRs) on the surface. 3MRs on fumed silica could be cleaved to release radicals, which further react with oxygen-containing molecules, such as water, to generate ROS [18].

NPs could induce abiotic ROS under photocatalysis. After irradiated by light with energy greater than band gap, NPs' electrons transform to the conduction band, leaving a hole in the valence band. Electrons in conduction band could react with O_2 to generate superoxide anion. Holes in the valence band could react with H_2O to produce hydroxyl radicals. For example, TiO_2 NPs (10, 20, 100 nm) induced abiotic ROS after photoactivation. Smaller TiO_2 NPs induced higher ROS level due to more photoactivated electrons and holes formed on NPs' surface and more H_2O and O_2 molecules were absorbed [19]. Under solar radiation, ZnO NPs induce the production of ROS in a dose-dependent manner [20]. Due to the local surface plasmon resonance (SPR), ROS generated on the surface of Ag NPs under UV-365 irradiation could be regulated by surface decoration of Ag NPs. Citrate-decorated Ag NPs could induce highest ROS level, followed by bare Ag NPs, while PVP-decorated Ag NPs did not elicit a detectable amount of ROS under UV-365 irradiation [21].

4.2.2 Indirect Mechanisms of ROS Generation

Besides ROS production and oxidative stress induced by direct reaction with NPs, ROS and oxidative stress could also be elicited through mitochondria and NADPH oxidase pathways, which are the main resources of ROS generation in cell. It was first reported in 1966 that the respiratory chain in mitochondria could produce ROS

[22]. The follow-up work demonstrated that the electron leakage in respiratory chain was captured by oxygen, resulting in ROS generation [23]. Previous papers demonstrated extracellular stimulus, such as hypoxia, cytokines, and grow factors, could stimulate the production of ROS through mitochondrial respiration [24]. NADPH oxidase is a plasma membrane-associated enzyme found in both phagocytic and non-phagocytic cells. Some of its subunits are located on the cell membrane and the rest parts are in cytoplasm in quiescent condition. When NADPH oxidase is activated, subunits in cytoplasm migrate to cell membrane and all the subunits are assembled [25]. Previous research confirmed NPs could induce ROS production by affecting the function of mitochondria and NADPH oxidase.

4.2.2.1 Mitochondrial Respiration

The toxicity of Ag NPs was investigated to find the possible molecular mechanisms associated with their toxic effects. When Ag NPs were exposed to NIH3T3 cells, ROS was produced through mitochondrial pathway and subsequent activation of the JNK and P53 pathway and apoptosis were found [26]. Plate-shaped Ag NPs induced high level of ROS than sphere Ag NPs [27]. TiO_2 NPs are widely used in human products such as sunscreen and paints. The impact of TiO_2 NPs on mitochondrial function isolated from lung tissue was investigated. TiO_2 NPs elevated ROS level in short exposure time, resulting in the decrease of the mitochondria membrane potential [28]. Besides TiO_2 NPs, hydroxyapatite (HA) NPs are also widely used in human life, such as the additives of oral hygiene products to resist dental decay. Both TiO_2 NPs and nano-HA were able to stimulate ROS production through mitochondrial pathway in TR146 epithelial cells and subsequently induced inflammation and apoptosis [29]. ZnO NPs could induce ROS in mitochondria, while CeO_2 NPs did not induce any ROS at the same dose [15].

Besides the daily use of NPs, they have also been used in biomedical field, The dendrimer phthalocyanine (DPc)-encapsulated polymeric micelle, which was designed for photodynamic therapy, could induce ROS in mitochondria and induce damages to the mitochondria [30].

4.2.2.2 NADPH Oxidase Pathway

Ambient ultrafine particles can pass from the lungs to the blood circulation after inhalation because of their small size, and subsequently induce lung oxidative stress. The ROS producing mechanism of ambient ultrafine particles exposed to mouse pulmonary microvascular endothelial cells was investigated. The result showed ROS induced by ambient ultrafine particles could be inhibited by DPI, a NADPH oxidase inhibitor, while the mitochondria respiratory chain inhibitor did not influence the ROS induced by ambient ultrafine particles [31]. The data confirmed that ambient ultrafine particles induced ROS through activation of NADPH oxidase. Carbon nanomaterials, which are widely used, arise concerns for their

possible harmful healthy effects. The inflammatory response induced by CNTs in human primary macrophages was conducted, with results showing CNTs induced ROS through NADPH oxidase and subsequently induced NLRP3 activation and IL-1β secretion [32, 33]. CeO_2 NPs are widely used in industry as fuel additives, catalysts, semiconductors, and oxygen sensors. The safety evaluation of CeO_2 NP showed that ROS induced by CeO_2 could be hampered by DPI, indicating CeO_2 NPs induced ROS through NADPH oxidase pathway [34].

4.3 The Hierarchical Oxidative Stress Model

ROS induced by NPs results in oxidative stress. To elucidate the oxidative stress-related mechanism, the hierarchical oxidative stress model was proposed, which contains three parts: antioxidant defense, inflammation, mitochondrial perturbation, and cell death (Fig. 4.1) [13].

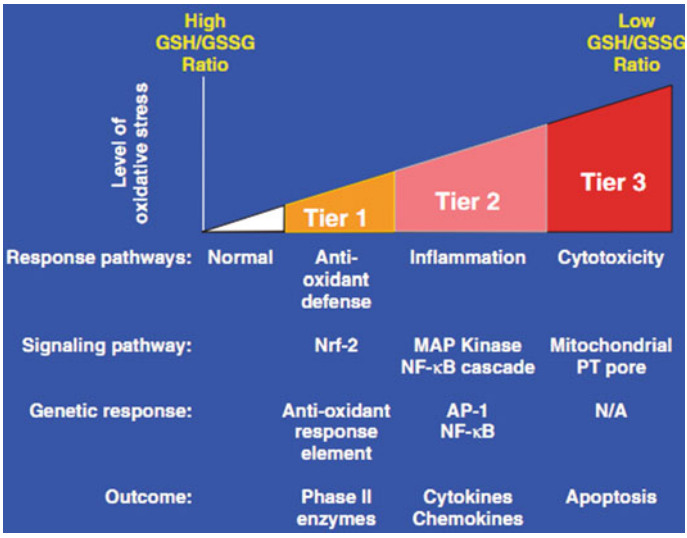

Fig. 4.1 The hierarchical oxidative stress model. At a lower amount of oxidative stress (tier 1), phase II antioxidant enzymes are induced via transcriptional activation of the antioxidant response element by Nrf-2 to restore cellular redox homeostasis. At an intermediate amount of oxidative stress (tier 2), activation of the MAPK and NF-kB cascades induces pro-inflammatory responses. At a high amount of oxidative stress (tier 3), perturbation of the mitochondrial PT pore and disruption of electron transfer results in cellular apoptosis or necrosis. From [13], Reprinted with permission from AAAS

4.3.1 Antioxidant Defense

Low levels of oxidative stress induce antioxidant defense, in which stage Keap1-Nrf2-ARE pathway plays an important role. The transcription factor Nrf2 is captured by the actin-anchored protein Keap1 in quiescent conditions, inducing the low expression of Nrf2-regulated genes. When cells are exposed to oxidative molecules, Nrf2 is detached from Keap1, translocates to nuclear and activates the ARE-responsive genes, which subsequently activates a lot of antioxidative enzyme, such as heme oxygenase 1 (HO-1), glutathione-*S*-transferase isoenzymes, NADPH quinone oxidoreductase, superoxide dismutase and glutathione peroxidase [35].

Among these enzymes, HO-1 is usually used as an antioxidant defense marker. ROS induced by NPs can promote the expression of HO-1. For example, when ambient ultrafine particles and NH_2-PS were exposed to RAW 264.7 cells, the intracellular ROS level increased as indicated by the enhancement of HO-1 expression, while other NPs, such as CB, TiO_2, and COOH-PS, did not affect the HO-1 expression [14]. The antioxidant response induced by TiO_2, ZnO, and CeO_2 were screened in RAW 264.7 and BEAS-2B cells. Among these NPs, ZnO NPs enhanced the intracellular HO-1 level, while TiO_2 NPs and CeO_2 NPs did not affect [15]. The HO-1 level in lung tissue of mice was enhanced by Co_3O_4, Cr_2O_3, and CuO NPs, while NiO, Fe_2O_3, and Fe_3O_4 NPs did not influence the HO-1 level [36].

4.3.2 Inflammation

Under moderate level of oxidative stress, the protective antioxidant defense is overtaken by inflammation. MAPK and NF-κB pathway, which is sensitive under redox condition, is activated at high level of oxidative stress condition, and eventually induces the release of cytokines and chemokines.

Several papers have discussed inflammation induced by oxidative stress. Although both ambient ultrafine particles and NH_2-PS could induce ROS and antioxidant defense, only ambient ultrafine particles can activate JNK pathway and induce the release of TNF-α [14]. ZnO NPs was also found to activate the JNK pathway and induce the release of TNF-a [15]. IL-6 secretion was investigated by a series of metal oxide NPs. Co_3O_4, Cr_2O_3, CuO, Mn_2O_3, CoO, and Ni_2O_3 NPs induced a higher level of IL-6 than NiO, Fe_2O_3, Fe_3O_4, Y_2O_3, ZrO_2, CeO_2, HfO_2, and In_2O_3 NPs [36]. Oxidative stress induced by nano-HA and TiO_2 NPs activated the NF-κB pathway and induced the release of TNF-α and IL-6 [29]. ROS induced by pristine graphene activated MAPK pathway, including JNK, ERK and p38 MAPK, promoted the release of TNF-α [37]. To evaluation the potential harmful effects of Ag NPs on immune system, oxidative stress-related toxicity assay was conducted, with results showing ROS induced by Ag NPs activated both MAPK and NF-κB pathways [38].

4.3.3 Mitochondrial Perturbation and Cell Death

The high level of oxidative stress also affects the mitochondrial membrane potential, inducing the release of pro-apoptotic factors and cell death.

An investigation was conducted to compare the effect of Fe_2O_3, Fe_3O_4, and CuO NPs on mitochondrial perturbation. Results showed Fe_2O_3 and CuO NPs induced mitochondrial depolarization in A549 cells while Fe_3O_4 did not affect the mitochondria membrane potential [39]. ROS induced by ambient ultrafine particles, NH_2-PS and ZnO NPs resulted in mitochondria membrane potential decrease and cell apoptosis [14, 15]. Nano-HA and TiO_2 NPs also induced the production of ROS and inflammation, and eventually cell apoptosis. It is interesting that TiO_2 NPs induced a higher percentage of early apoptosis than nano-HA, while nano-HA induced a higher percentage of late apoptosis [29]. ROS induced by Ag NPs on human Jurkat T cells resulted in a time-dependent apoptosis, in which both early and late apoptosis were observed [38]. PVP-decorated Ag NPs were observed to induce apoptosis and necrosis in THP-1 monocytes in a time-dependent manner [40]. ROS induced by pristine graphene in murine RAW 264.7 macrophages activated MAPK pathway, resulting in cell apoptosis. In addition, late apoptosis and necrosis increased in a dose-dependent manner while early stage apoptosis was not affected [37]. The impact of size on oxidative stress induced apoptosis was conducted, with results showing the percentage of early apoptosis was not affected by NPs' size. Silica NPs with a diameter of 19 nm induced higher percentage of late apoptosis than silica NPs with diameters of 43 and 68 nm [41].

4.4 Nanoparticles' Physicochemical Properties Regulate Oxidative Stress and Nanotoxicity

Although the induction of oxidative stress by NPs may proceed through a variety of mechanisms, the oxidative stress formation from a particular NP depends on the physicochemical properties of the NPs. The critical physicochemical properties that lead to the induction of oxidative stress and nanotoxicity include composition, size, shape, and surface chemistry.

4.4.1 Composition

The toxicity of spherical metal oxides NPs with different chemical composition [Fe_2O_3 (29 nm), Fe_3O_4 (20–30 nm), TiO_2 (63 nm) and CuO (42 nm)] has been compared [39]. CuO NPs were found to be the most toxic ones in A549 human lung cancer cells by inducing DNA damage and DNA lesions. A lot of polymer and inorganic nanomaterials can induce oxidative stress by generation of ROS.

For example, the widely used Ag NPs were reported to induce apoptosis by generation of ROS and inducing DNA damage in Jurkat T Cells [38]. Magnetite NPs, which can be used as contrast agents for MRI imaging, induced high level of ROS in A549 cells [42]. Previous results showed graphene oxide (GO) (thickness of about 1 nm and the size of 1–2 μm) induced ROS production in J774A.1 and RAW264.7 cells [43].

Some studies were conducted to investigate the impact of composition of NPs on ROS induction. Four types of nanomaterials with different compositions [CB (sphere, 12.3 ± 4.1 nm), single-walled carbon nanotubes (SWCNTs) (rope-shaped, diameters: 8 nm length: <5 μm), SiO_2 NPs (crystal structure, 20.2 ± 6.4 nm) and ZnO NPs (crystal structure, 19.6 ± 5.8 nm)] induced different levels of cytotoxicity on primary mouse embryo fibroblast cells [44]. ZnO NPs induced the highest cell death and oxidative stress among all NPs. However, SWCNTs exhibited highest genotoxicity, which might be attributed to particle shape. A high-throughput screening approach was used to analyze the toxicology of Au (sphere, 12 nm), Ag (sphere, 13 nm), Pt (sphere 13 nm), Al_2O_3 (sphere 12 nm), SiO_2 (sphere 19 nm), ZnO (sphere 10 nm), and CdSe/ZnS (QD) (dot, 6.5 nm) NPs in RAW 264.7 and BEAS-2B cells. The results showed QD and ZnO trigger the highest ROS level, while Au, Ag, Pt, Al_2O_3, and SiO_2 did not induce ROS [45]. The relation between intracellular ROS level and NPs' properties related to their composition, such as conduction band energy, was investigated among 24 MOx NPs (10–100 nm, except for Cr_2O_3 and Ni_2O_3 of 193 ± 90.0 and 140.6 ± 52.5 nm, respectively). NPs could induce high level of ROS when NPs' band energy was between cellular redox potential (−4.12 to −4.84 eV) (Fig. 4.2) [36]. Using this method, Nel et al. demonstrated that Co_3O_4 NPs induce high level of ROS and PdO doping could dictate the band energy of Co_3O_4 NP (11.1 ± 2.8–13.3 ± 3.7 nm), which could tune the oxidative stress level. The intracellular ROS level was positively correlated to percentage of PdO doping [17].

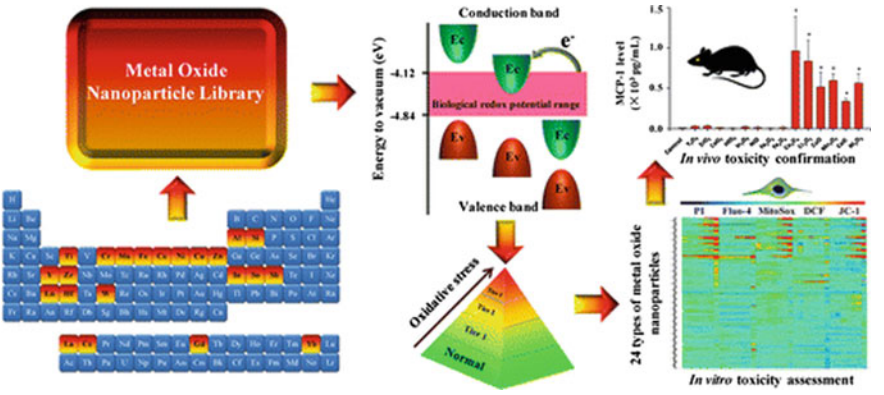

Fig. 4.2 Use of metal oxide nanoparticle band gap to develop a predictive paradigm for oxidative stress. Reprinted with the permission from [36]. Copyright 2012 American Chemical Society

4.4.2 Size

The toxicity is regularly negatively related to NPs' size. The cytotoxicity of Ag NPs with different sizes from 10 to 75 nm was evaluated in BEAS-2B cells [46]. Small NPs (10 nm) were found to be more toxic. In another paper, size-dependent toxicity of Ag NPs (15, 30, and 55 nm) has been reported. Smaller Ag NPs could induce higher apoptosis in macrophages than larger NPs at the same dose (10 μg/mL) [47]. Smaller ZnO NPs induced higher cell cytotoxicity in human $CD4^+$ T cells [48]. Silica NPs have been used in gene delivery and biomedical imaging. The hemolytic activity was investigated using silica NPs with different diameters. Smaller nano-silica induced higher percentage of hemolysis of red blood cells [49]. The interaction between NPs and biomolecules, such as protein and DNA, takes place on the nano-bio interface, and sequentially affects NPs' toxicity. NPs' curvature and surface area are crucial parameters for NP-biomolecule interactions and are determined by NPs' size. Therefore, small-sized NPs have great potential in inducing cell death. The toxicity of nano- and micrometer particles of CuO after exposure of A549 cells confirmed the above conclusion [39]. CuO NPs were more toxic in terms of cytotoxicity, mitochondrial damage, DNA damage and oxidative DNA lesions in A549 cells than micrometer particles.

The impacts of NPs' size on oxidative stress and ROS have also been investigated by several research groups. Because of the tiny size of NPs, they can easily penetrate cell membranes and other biological barriers into living organisms, so the intracellular ROS level is in general negatively correlated to NP's size. For example, Ag NPs was used to investigate the influence of size on intracellular ROS level in macrophage, indicating that Ag NPs with a diameter of 15 nm induced higher ROS level in alveolar macrophages than NPs with a diameter of 30–55 nm. The enhanced ROS was caused by the decrease of mitochondria membrane potential [47]. In another paper, the impact of Ag NPs' size on ROS in non-phagocyte was investigated, showing that small sized Ag NPs induced highest ROS level in hepG2 cells [50]. Silica NPs with a diameter of 19 nm induced higher ROS level than that of 43 and 68 nm in hepG2 cells. Cell apoptosis and necrosis were also found when incubated with silica NPs with a diameter of 19 nm [41].

4.4.3 Shape

Previous papers have demonstrated that the shape of NPs affects their nanotoxicity. Hemolytic activity of SiO_2 nanorods with aspect ratio of 2, 4, and 8 were investigated [51]. Spherical SiO_2 showed highest hemolysis activity, while mesoporous SiO_2 with high aspect ratio had lower hemolysis activity than mesoporous SiO_2 with low aspect ratio. TiO_2 nanomaterial with a fiber structure of longer than 15 nm showed higher toxicity when compared with TiO_2 nanospheres with a diameter of 5 nm [52] because that long TiO_2 nanobelts induced inflammasome activation and

release of inflammatory cytokines. The shape of Ni NPs also dramatically affected the toxicity upon exposure to zebrafish embryos. Dendritic clusters consisting of aggregated 60 nm particles resulted in higher toxicity than spherical Ni NPs [53].

The cytotoxicity, DNA oxidative damage, and apoptosis in HeLa cells were investigated when they were incubated with wire-shaped NPs and alpha-MnO_2 nanowires, respectively. Long nanowires in cultured fibroblasts cause failed cell division, DNA damage, and increased ROS, while vertical nanowire arrays induce cell motility and proliferation rate [54]. NPs' aspect ratio is negatively correlated to ROS level. For example, ROS in HCT116 cells was evaluated after exposed to CTAB-decorated gold nanorods (GNRs). GNRs with lowest aspect ratio induced the highest intracellular ROS [55]. In another paper, ROS induced by spherical gold nanoparticles (GNPs) and GNRs was investigated in MDCK II cells. Spherical GNPs with diameter of 43 nm induced higher ROS level than GNRs with a size of 38 nm $\times$ 17 nm [56]. The impact of mesoporous silica NPs' shape on intracellular ROS was investigated in A375 cells. Spherical NPs induced highest ROS level, while long rod-like NPs possess low intracellular ROS level [57]. Y_2O_3 NPs could be used in biological imaging and photodynamic therapy. Spherical Y_2O_3 NPs induced higher ROS level than rod-like NPs [58]. The aforementioned properties may be useful for design new NPs with expected biocompatibility and low toxicity.

Besides aspect ratio, other factors of NPs could also dictate ROS level. For example, our lab found that PS nano-disk did not induce ROS generation, while PS nanosphere elicited intracellular ROS production in BJ and jurkat cells. In addition, ROS level induced by PS NPs is correlated with cellular uptake [59]. Hexagonal plate-like ZnO nanocrystals were also reported to display significantly higher activity in ROS induction than rodshaped crystals [60].

4.4.4 Surface Chemistry

A wide variety of synthetic and natural ligands could be attached to NPs to tune the surface physicochemical properties of the NPs. Surface chemistry modification can be divided into non-covalent and covalent method. The non-covalent decoration is usually achieved by non-covalent interactions between NPs and ligands, including hydrophobic interactions [61, 62], ionic interactions [63, 64] and π–π interactions [65, 66]. Ligands can also be covalently linked to the surface of NPs through certain chemical reactions. Compared to non-covalent methods, covalent methods could afford more versatile decoration to NPs through stable chemical bonds. Different chemical reagents and linking methods can be used in chemical modifications of NPs. With strong oxidative acid treatment, abundant carboxylic groups can be introduced onto the surfaces of CNTs [67], thus providing the possibility of further immobilization of functional molecules on the nanotubes by reacting with carboxylic groups. Surface functionality of NPs with poly (ethylene glycol) (PEG) could effectively prevent NP agglomerations and protein adsorption, leading to the extended circulation time of NPs in biological systems. The chemical

couplings of PEG onto GNPs are often performed by Au-S bond or copolymerization of PEG with the bulk materials of NPs to form the PEGylated NP systems [68, 69].

The decoration on NPs may also alter NPs' surface charge density, resulting in the variation of nanotoxicity. NPs initially interact with plasma membranes when exposed to cells. The damage of model cell membranes was evaluated by GNPs and TiO_2 NPs with different surface charges [70]. Both kinds of NPs with positive charges on surface induced strong leakage (>80%), whereas only marginal leakage, was found for negatively charged NPs. When a human keratinocyte cell line (HaCaT) was exposed to three different GNPs (positively charged, neutral, and negatively charged), cell morphology was disrupted by all GNPs and charged GNPs displayed a lower LD_{50} than neutral GNPs. More oxidative stress was founded in cells treated with charged GNPs than neutral ones [71]. In addition, charged GNPs and neutral GNPs caused cell death through different mechanisms. Charged GNPs promoted the expression of p53 and caspase-3 in nuclear, while the neutral GNPs caused an increased expression of p53 in both nuclear and cytoplasm. Lin and Zhang et al. also investigated the effect of GNPs' surface charge on cytotoxicity [72]. They found that positively charged GNPs can be attracted by the cell membrane due to electrostatic interaction, while negatively charged GNPs were rejected. Increasing GNPs' surface charge density promoted cellular uptake and increased cytotoxicity. However, the level of penetration and membrane disruption were in different manner, with low charge densities inducing high penetration and high charge densities resulting in membrane disruption. Besides GNPs, it was also found that SWCNT coated with negatively charged ligands caused a minimal leakage of liposomes [73]. Meso-2,3-dimercaptosuccinic acid (DMSA) was used to modified Fe_2O_3 NPs for reducing cytotoxicity and genotoxicity [74]. Auffan et al. found that DMSA-Fe_2O_3 NPs caused lower toxicity in fibroblasts, which might be due to that the negative charge on the surface of DMSA-Fe_2O_3 NPs prevented cell contact and reduced the toxic effect. When superparamagnetic iron oxide NPs (SPIONs) were coated with different surface ligands [75], Mahmoudi et al. found that bare SPIONs were more toxic than charged SPIONs in three cell lines (HCM, BE-2-C, and 293T), while the SPIONs-COOH showed lower toxic than SPIONs-NH_2. The result was consistent with the alteration of genes expression levels. In conclusion, surface charge also plays an important role on intracellular ROS level, with positively charged NPs inducing higher intracellular ROS level than negatively charged and neutral NPs [14]. A similar phenomenon was found when positively and negatively charged silicon NPs were exposed to macrophage NR8383 cells [76]. The intracellular ROS level in HeLa cells was detected after exposure to a GNP library decorated with cationic ligands of different length. The results showed that intracellular ROS level was positively correlated with ligand length [77]. Poly(methacrylic acid) (PMAA) and oleic acid (OA) were used to decorate ZnO NP, resulting low level of ROS induction of PMAA and OA decorated ZnO NPs compared to undecorated ZnO NPs [78].

The cytotoxicity of NPs can also be modulated by altering the hydrophobicity. Our lab synthesized a GNP library with a continuous change in hydrophobicity. It was found that cell viability was negatively correlated with hydrophobicity [79].

The cytotoxicity of GNRs coated with CATB and PEG has been compared [80]. It showed that GNRs coated with CTAB resulted in more cell death than PEG-GNRs in Hela cell. The cytotoxicity of unmodified and PEG functionalized SWNTs in neuronal PC12 cells has been compared at cell and molecular level [81]. Unmodified SWCNTs showed higher cytotoxicity than PEG-SWCNTs because of the ROS level. Phospholipid-PEG (Pl-PEG)- coating CNTs was also found to enhance cell viability and proliferation [82].

Other polymers were also used for decorating NPs. Various layer-by-layer polyelectrolytes (PE) were used for surface decoration of GNRs. The cellular uptake, toxicity, and gene expression in HeLa cells could be regulated by PE density [83]. The cytotoxicity of uncoated and poly(vinyl alcohol) (PVA)-coated SPIONs in mouse fibroblasts has been compared in another report [84]. Cell viability of bare SPION was lower than PVA-coated SPIONs at the same concentration. Significant apoptosis could be found in cells treated with bare SPIONs at high concentration while PVA-coated SPIONs induced no apoptosis. In another paper, Poly(*N*,*N*-dimethylacrylamide) (DMAAm) was used for Fe_2O_3 NP functionality [85]. It was found that the cell viability of DMAAm-Fe_2O_3 NPs was higher than dextran-modified and unmodified Fe_2O_3 NPs.

4.5 Concluding Remarks

Production of manufactured NPs for commercial usage in various fields has been growing exponentially, therefore, the toxicity of NPs has become an urgent issue to the public. ROS generation and oxidative stress are usually considered to be the starting points of toxicology induced by NPs. Nanotoxicity such as inflammation and cell death has been recognized as the downstream effects to the ROS formation and oxidative stress. Oxidative stress can be directly induced by NPs or indirectly through mitochondrial respiration and activation of NADPH oxidase. NPs' physicochemical properties, such as composition, size, shape, and surface chemistry, have been found to affect the generation of ROS and oxidative stress.

Besides nanotoxicity, oxidative stress is also related to aging and diseases, such as cancer and neurodegeneration. For example, DNA damage induced by oxidative stress is responsible for cancer induction. Under high level of oxidative stress, cancer cells will be killed. Therefore, precise regulation of oxidative stress is important for both prevention of NP-induced toxicity and treating diseases. However, previous studies generally attempted to explore the correlations on a case-by-case basis, looking at one parameter while keeping others constant. In addition, the complex formation of NPs in biological systems (such as adsorption of serum proteins) further aggravates the difficulty in precise regulation of oxidative stress. Therefore, examining the collective impact of combined parameters of NPs on oxidative stress and nanotoxicity will be crucial for systemically understanding the interactions between NPs and biological systems and will also be helpful for design of new NPs with better safety profiles.

References

1. Weir A, Westerhoff P, Fabricius L, Hristovski K, Von GN (2012) Titanium dioxide nanoparticles in food and personal care products. Environ Sci Technol 46(4):2242–2250
2. Weiss J, Takhistov P, Mcclements DJ (2006) Functional materials in food nanotechnology. J Food Sci 59(6):274–275
3. Tans SJ, Verschueren AR, Dekker C (1998) Room-temperature transistor based on a single carbon nanotube. Nature 393(6680):49–52
4. Peer D, Karp JM, Hong S, Farokhzad OC, Margalit R, Langer R (2007) Nanocarriers as an emerging platform for cancer therapy. Nat Nanotechnol 2(12):751–760
5. Boisselier E, Astruc D (2009) Gold nanoparticles in nanomedicine: preparations, imaging, diagnostics, therapies and toxicity. Chem Soc Rev 38(6):1759–1782
6. Moghimi SM, Hunter AC, Murray JC (2005) Nanomedicine: current status and future prospects. FASEB J 19(3):311–330
7. Cho K, Wang X, Nie S, Chen ZG, Shin DM (2008) Therapeutic nanoparticles for drug delivery in cancer. Clin Cancer Res 14(5):1310–1316
8. Judy JD, Unrine JM, Bertsch PM (2010) Evidence for biomagnification of gold nanoparticles within a terrestrial food chain. Environ Sci Technol 45(2):776–781
9. Werlin R, Priester JH, Mielke RE, Krämer S, Jackson S, Stoimenov PK, Stucky GD, Cherr GN, Orias E, Holden PA (2011) Biomagnification of cadmium selenide quantum dots in a simple experimental microbial food chain. Nat Nanotechnol 6(1):65–71
10. Song Y, Li X, Du X (2009) Exposure to nanoparticles is related to pleural effusion, pulmonary fibrosis and granuloma. Eur Respir J 34(3):559–567
11. Pietroiusti A (2012) Health implications of engineered nanomaterials. Nanoscale 4(4): 1231–1247
12. De Jong WH, Borm PJ (2008) Drug delivery and nanoparticles: applications and hazards. Int J Nanomed 3(2):133–149
13. Nel A, Xia T, Mädler L, Li N (2006) Toxic potential of materials at the nanolevel. Science 311(5761):622–627
14. Xia T, Kovochich M, Brant J, Hotze M, Sempf J, Oberley T, Sioutas C, Yeh JI, Wiesner MR, Nel AE (2006) Comparison of the abilities of ambient and manufactured nanoparticles to induce cellular toxicity according to an oxidative stress paradigm. Nano Lett 6(8):1794–1807
15. Xia T, Kovochich M, Liong M, Mädler L, Gilbert B, Shi H, Yeh JI, Zink JI, Nel AE (2008) Comparison of the mechanism of toxicity of zinc oxide and cerium oxide nanoparticles based on dissolution and oxidative stress properties. ACS Nano 2(10):2121–2134
16. Kaweeteerawat C, Ivask A, Liu R, Zhang H, Chang CH, Low-Kam C, Fischer H, Ji Z, Pokhrel S, Cohen Y (2015) Toxicity of metal oxide nanoparticles in *Escherichia coli* correlates with conduction band and hydration energies. Environ Sci Technol 49(2): 1105–1112
17. Zhang H, Pokhrel S, Ji Z, Meng H, Wang X, Lin S, Chang CH, Li L, Li R, Sun B (2014) PdO doping tunes band-gap energy levels as well as oxidative stress responses to a Co_3O_4 p-type semiconductor in cells and the lung. J Am Chem Soc 136(17):6406–6420
18. Zhang H, Dunphy DR, Jiang X, Meng H, Sun B, Tarn D, Xue M, Wang X, Lin S, Ji Z (2012) Processing pathway dependence of amorphous silica nanoparticle toxicity: colloidal vs pyrolytic. J Am Chem Soc 134(38):15790–15804
19. Xiong S, George S, Ji Z, Lin S, Yu H, Damoiseaux R, France B, Ng KW, Loo SCJ (2013) Size of TiO_2 nanoparticles influences their phototoxicity: an in vitro investigation. Arch Toxicol 87(1):99–109
20. Ma H, Wallis LK, Diamond S, Li S, Canas-Carrell J, Parra A (2014) Impact of solar UV radiation on toxicity of ZnO nanoparticles through photocatalytic reactive oxygen species (ROS) generation and photo-induced dissolution. Environ Pollut 193:165–172

21. Li Y, Zhang W, Niu J, Chen Y (2013) Surface-coating-dependent dissolution, aggregation, and reactive oxygen species (ROS) generation of silver nanoparticles under different irradiation conditions. Environ Sci Technol 47(18):10293–10301
22. Jensen P (1966) Antimycin-insensitive oxidation of succinate and reduced nicotinamide-adenine dinucleotide in electron-transport particles I pH dependency and hydrogen peroxide formation. Biochim Biophys (BBA) Acta Enzymol Biol Oxid 122(2): 157–166
23. Murphy M (2009) How mitochondria produce reactive oxygen species. Biochem J 417:1–13
24. Hamanaka RB, Chandel NS (2010) Mitochondrial reactive oxygen species regulate cellular signaling and dictate biological outcomes. Trends Biochem Sci 35(9):505–513
25. Bedard K, Krause K-H (2007) The NOX family of ROS-generating NADPH oxidases: physiology and pathophysiology. Physiol Rev 87(1):245–313
26. Hsin Y-H, Chen C-F, Huang S, Shih T-S, Lai P-S, Chueh PJ (2008) The apoptotic effect of nanosilver is mediated by a ROS-and JNK-dependent mechanism involving the mitochondrial pathway in NIH3T3 cells. Toxicol Lett 179(3):130–139
27. George S, Lin S, Ji Z, Thomas CR, Li L, Mecklenburg M, Meng H, Wang X, Zhang H, Xia T (2012) Surface defects on plate-shaped silver nanoparticles contribute to its hazard potential in a fish gill cell line and zebrafish embryos. ACS Nano 6(5):3745–3759
28. Freyre-Fonseca V, Delgado-Buenrostro NL, Gutiérrez-Cirlos EB, Calderón-Torres CM, Cabellos-Avelar T, Sánchez-Pérez Y, Pinzón E, Torres I, Molina-Jijón E, Zazueta C (2011) Titanium dioxide nanoparticles impair lung mitochondrial function. Toxicol Lett 202(2): 111–119
29. Tay CY, Fang W, Setyawati MI, Chia SL, Tan KS, Hong CHL, Leong DT (2014) Nano-hydroxyapatite and nano-titanium dioxide exhibit different sub-cellular distribution and apoptotic profile in human oral epithelium. ACS Appl Mater Interfaces 6(9):6248–6256
30. Nishiyama N, Nakagishi Y, Morimoto Y, Lai P-S, Miyazaki K, Urano K, Horie S, Kumagai M, Fukushima S, Cheng Y (2009) Enhanced photodynamic cancer treatment by supramolecular nanocarriers charged with dendrimer phthalocyanine. J Control Release 133(3):245–251
31. Mo Y, Wan R, Chien S, Tollerud DJ, Zhang Q (2009) Activation of endothelial cells after exposure to ambient ultrafine particles: the role of NADPH oxidase. Toxicol Appl Pharmacol 236(2):183–193
32. Palomäki J, Välimäki E, Sund J, Vippola M, Clausen PA, Jensen KA, Savolainen K, Matikainen S, Alenius H (2011) Long, needle-like carbon nanotubes and asbestos activate the NLRP3 inflammasome through a similar mechanism. ACS Nano 5(9):6861–6870
33. Ye S, Wang Y, Jiao F, Zhang H, Lin C, Wu Y, Zhang Q (2011) The role of NADPH oxidase in multi-walled carbon nanotubes-induced oxidative stress and cytotoxicity in human macrophages. J Nanosci Nanotechnol 11(5):3773–3781
34. Culcasi M, Benameur L, Mercier A, Lucchesi C, Rahmouni H, Asteian A, Casano G, Botta A, Kovacic H, Pietri S (2012) EPR spin trapping evaluation of ROS production in human fibroblasts exposed to cerium oxide nanoparticles: evidence for NADPH oxidase and mitochondrial stimulation. Chem Biol Interact 199(3):161–176
35. Kensler TW, Wakabayashi N, Biswal S (2007) Cell survival responses to environmental stresses via the Keap1-Nrf2-ARE pathway. Annu Rev Pharmacol Toxicol 47:89–116
36. Zhang H, Ji Z, Xia T, Meng H, Low-Kam C, Liu R, Pokhrel S, Lin S, Wang X, Liao Y-P (2012) Use of metal oxide nanoparticle band gap to develop a predictive paradigm for oxidative stress and acute pulmonary inflammation. ACS Nano 6(5):4349–4368
37. Li Y, Liu Y, Fu Y, Wei T, Le Guyader L, Gao G, Liu R-S, Chang Y-Z, Chen C (2012) The triggering of apoptosis in macrophages by pristine graphene through the MAPK and TGF-beta signaling pathways. Biomaterials 33(2):402–411
38. Eom H-J, Choi J (2010) p38 MAPK activation, DNA damage, cell cycle arrest and apoptosis as mechanisms of toxicity of silver nanoparticles in Jurkat T cells. Environ Sci Technol 44 (21):8337–8342

39. Karlsson HL, Gustafsson J, Cronholm P, Möller L (2009) Size-dependent toxicity of metal oxide particles—a comparison between nano-and micrometer size. Toxicol Lett 188(2):112–118
40. Foldbjerg R, Olesen P, Hougaard M, Dang DA, Hoffmann HJ, Autrup H (2009) PVP-coated silver nanoparticles and silver ions induce reactive oxygen species, apoptosis and necrosis in THP-1 monocytes. Toxicol Lett 190(2):156–162
41. Li Y, Sun L, Jin M, Du Z, Liu X, Guo C, Li Y, Huang P, Sun Z (2011) Size-dependent cytotoxicity of amorphous silica nanoparticles in human hepatoma HepG2 cells. Toxicol In Vitro 25(7):1343–1352
42. Könczöl M, Weiss A, Stangenberg E, Gminski R, Garcia-Käufer M, Gieré R, Merfort I, Mersch-Sundermann V (2013) Cell-cycle changes and oxidative stress response to magnetite in A549 human lung cells. Chem Res Toxicol 26(5):693–702
43. Qu G, Liu S, Zhang S, Wang L, Wang X, Sun B, Yin N, Gao X, Xia T, Chen J-J (2013) Graphene oxide induces toll-like receptor 4 (TLR4)-dependent necrosis in macrophages. ACS Nano 7(7):5732–5745
44. Yang H, Liu C, Yang D, Zhang H, Xi Z (2009) Comparative study of cytotoxicity, oxidative stress and genotoxicity induced by four typical nanomaterials: the role of particle size, shape and composition. J Appl Toxicol 29(1):69–78
45. George S, Xia TA, Rallo R, Zhao Y, Ji ZX, Lin SJ, Wang X, Zhang HY, France B, Schoenfeld D, Damoiseaux R, Liu R, Lin S, Bradley KA, Cohen Y, Nal AE (2011) Use of a high-throughput screening approach coupled with in vivo zebrafish embryo screening to develop hazard ranking for engineered nanomaterials. ACS Nano 5(3):1805–1817
46. Gliga AR, Skoglund S, Wallinder IO, Fadeel B, Karlsson HL (2014) Size-dependent cytotoxicity of silver nanoparticles in human lung cells: the role of cellular uptake, agglomeration and Ag release. Part Fibre Toxicol 11(11):1–17
47. Carlson C, Hussain SM, Schrand AM, Braydich-Stolle LK, Hess KL, Jones RL, Schlager JJ (2008) Unique cellular interaction of silver nanoparticles: size-dependent generation of reactive oxygen species. J Phys Chem B 112(43):13608–13619
48. Hanley C, Thurber A, Hanna C, Punnoose A, Zhang J, Wingett DG (2009) The influences of cell type and ZnO nanoparticle size on immune cell cytotoxicity and cytokine induction. Nanoscale Res Lett 4(12):1409–1420
49. Lin Y-S, Haynes CL (2010) Impacts of mesoporous silica nanoparticle size, pore ordering, and pore integrity on hemolytic activity. J Am Chem Soc 132(13):4834–4842
50. Liu W, Wu Y, Wang C, Li HC, Wang T, Liao CY, Cui L, Zhou QF, Yan B, Jiang GB (2010) Impact of silver nanoparticles on human cells: effect of particle size. Nanotoxicology 4(3):319–330
51. Yu T, Malugin A, Ghandehari H (2011) Impact of silica nanoparticle design on cellular toxicity and hemolytic activity. ACS Nano 5(7):5717–5728
52. Hamilton R, Wu N, Porter D, Buford M, Wolfarth M, Holian A (2009) Particle length-dependent titanium dioxide nanomaterials toxicity and bioactivity. Part Fibre Toxicol 6(1):35
53. Ispas C, Andreescu D, Patel A, Goia DV, Andreescu S, Wallace KN (2009) Toxicity and developmental defects of different sizes and shape nickel nanoparticles in zebrafish. Environ Sci Technol 43(16):6349–6356
54. Persson H, Kobler C, Molhave K, Samuelson L, Tegenfeldt JO, Oredsson S, Prinz CN (2013) Fibroblasts cultured on nanowires exhibit low motility, impaired cell division, and DNA damage. Small 9(23):4006–4016
55. Wan J, Wang J-H, Liu T, Xie Z, Yu X-F, Li W (2015) Surface chemistry but not aspect ratio mediates the biological toxicity of gold nanorods in vitro and in vivo. Sci Rep 5:11398
56. Tarantola M, Pietuch A, Schneider D, Rother J, Sunnick E, Rosman C, Pierrat S, Sönnichsen C, Wegener J, Janshoff A (2011) Toxicity of gold-nanoparticles: synergistic effects of shape and surface functionalization on micromotility of epithelial cells. Nanotoxicology 5(2):254–268
57. Hao N, Yang H, Li L, Li L, Tang F (2014) The shape effect of mesoporous silica nanoparticles on intracellular reactive oxygen species in A375 cells. New J Chem 38(9): 4258–4266

58. Andelman T, Gordonov S, Busto G, Moghe PV, Riman RE (2010) Synthesis and cytotoxicity of Y_2O_3 nanoparticles of various morphologies. Nanoscale Res Lett 5(2):263–273
59. Zhang Y, Tekobo S, Tu Y, Zhou Q, Jin X, Dergunov SA, Pinkhassik E, Yan B (2012) Permission to enter cell by shape: nanodisk vs nanosphere. ACS Appl Mater Interfaces 4 (8):4099–4105
60. McLaren A, Valdes-Solis T, Li G, Tsang SC (2009) Shape and size effects of ZnO nanocrystals on photocatalytic activity. J Am Chem Soc 131(35):12540–12541
61. Redhead H, Davis S, Illum L (2001) Drug delivery in poly(lactide-co-glycolide) nanoparticles surface modified with poloxamer 407 and poloxamine 908: in vitro characterisation and in vivo evaluation. J Control Release 70(3):353–363
62. Neal JC, Stolnik S, Garnett MC, Davis SS, Illum L (1998) Modification of the copolymers poloxamer 407 and poloxamine 908 can affect the physical and biological properties of surface modified nanospheres. Pharm Res 15(2):318–324
63. Xian Y, Hu Y, Liu F, Xian Y, Wang H, Jin L (2006) Glucose biosensor based on Au nanoparticles–conductive polyaniline nanocomposite. Biosens Bioelectron 21(10):1996–2000
64. Lin Y, Lu F, Tu Y, Ren Z (2004) Glucose biosensors based on carbon nanotube nanoelectrode ensembles. Nano Lett 4(2):191–195
65. Artyukhin AB, Bakajin O, Stroeve P, Noy A (2004) Layer-by-layer electrostatic self-assembly of polyelectrolyte nanoshells on individual carbon nanotube templates. Langmuir 20(4):1442–1448
66. Islam M, Rojas E, Bergey D, Johnson A, Yodh A (2003) High weight fraction surfactant solubilization of single-wall carbon nanotubes in water. Nano Lett 3(2):269–273
67. Zhang B, Xing Y, Li Z, Zhou H, Mu Q, Yan B (2009) Functionalized carbon nanotubes specifically bind to α-chymotrypsin's catalytic site and regulate its enzymatic function. Nano Lett 9(6):2280–2284
68. Moghimi SM, Hunter AC, Murray JC (2001) Long-circulating and target-specific nanoparticles: theory to practice. Pharmacol Rev 53(2):283–318
69. Otsuka H, Nagasaki Y, Kataoka K (2003) PEGylated nanoparticles for biological and pharmaceutical applications. Adv Drug Del Rev 55(3):403–419
70. Moghadam BY, Hou W-C, Corredor C, Westerhoff P, Posner JD (2012) Role of nanoparticle surface functionality in the disruption of model cell membranes. Langmuir 28(47):16318–16326
71. Schaeublin NM, Braydich-Stolle LK, Schrand AM, Miller JM, Hutchison J, Schlager JJ, Hussain SM (2011) Surface charge of gold nanoparticles mediates mechanism of toxicity. Nanoscale 3(2):410–420
72. Lin J, Zhang H, Chen Z, Zheng Y (2010) Penetration of lipid membranes by gold nanoparticles: insights into cellular uptake, cytotoxicity, and their relationship. ACS Nano 4 (9):5421–5429
73. Hirano A, Uda K, Maeda Y, Akasaka T, Shiraki K (2010) One-dimensional protein-based nanoparticles induce lipid bilayer disruption: carbon nanotube conjugates and amyloid fibrils. Langmuir 26(22):17256–17259
74. Auffan M, Decome L, Rose J, Orsiere T, De Meo M, Briois V, Chaneac C, Olivi L, J-l Berge-lefranc, Botta A, Wiesner MR, J-y Bottero (2006) In vitro interactions between DMSA-coated maghemite nanoparticles and human fibroblasts: a physicochemical and cyto-genotoxical study†. Environ Sci Technol 40(14):4367–4373
75. Mahmoudi M, Laurent S, Shokrgozar MA, Hosseinkhani M (2011) Toxicity evaluations of superparamagnetic iron oxide nanoparticles: cell "vision" versus physicochemical properties of nanoparticles. ACS Nano 5(9):7263–7276
76. Bhattacharjee S, de Haan LH, Evers NM, Jiang X, Marcelis AT, Zuilhof H, Rietjens IM, Alink GM (2010) Role of surface charge and oxidative stress in cytotoxicity of organic monolayer-coated silicon nanoparticles towards macrophage NR8383 cells. Part Fibre Toxicol 7(1):25

77. Chompoosor A, Saha K, Ghosh PS, Macarthy DJ, Miranda OR, Zhu ZJ, Arcaro KF, Rotello VM (2010) The role of surface functionality on acute cytotoxicity, ROS generation and DNA damage by cationic gold nanoparticles. Small 6(20):2246–2249
78. Yin H, Casey PS, McCall MJ, Fenech M (2010) Effects of surface chemistry on cytotoxicity, genotoxicity, and the generation of reactive oxygen species induced by ZnO nanoparticles. Langmuir 26(19):15399–15408
79. Li S, Zhai S, Liu Y, Zhou H, Wu J, Jiao Q, Zhang B, Zhu H, Yan B (2015) Experimental modulation and computational model of nano-hydrophobicity. Biomaterials 52:312–317
80. Niidome T, Yamagata M, Okamoto Y, Akiyama Y, Takahashi H, Kawano T, Katayama Y, Niidome Y (2006) PEG-modified gold nanorods with a stealth character for in vivo applications. J Control Release 114(3):343–347
81. Zhang Y, Xu Y, Li Z, Chen T, Lantz SM, Howard PC, Paule MG, Slikker W, Watanabe F, Mustafa T, Biris AS, Ali SF (2011) Mechanistic toxicity evaluation of uncoated and PEGylated single-walled carbon nanotubes in neuronal PC12 Cells. ACS Nano 5(9): 7020–7033
82. Hadidi N, Hosseini Shirazi SF, Kobarfard F, Nafissi-Varchehd N, Aboofazeli R (2012) Evaluation of the effect of PEGylated single-walled carbon nanotubes on viability and proliferation of jurkat cells. Iran J Pharm Res 11(1):27–37
83. Hauck TS, Ghazani AA, Chan WCW (2008) Assessing the effect of surface chemistry on gold nanorod uptake, toxicity, and gene expression in mammalian cells. Small 4(1):153–159
84. Mahmoudi M, Simchi A, Vali H, Imani M, Shokrgozar MA, Azadmanesh K, Azari F (2009) Cytotoxicity and cell cycle effects of bare and poly(vinyl alcohol)-coated iron oxide nanoparticles in mouse fibroblasts. Adv Eng Mater 11(12):B243–B250
85. Babič M, Horák D, Jendelová P, Glogarová K, Herynek V, Trchová M, Likavčanová K, Lesný P, Pollert E, Hájek M, Syková E (2009) Poly(*N*,*N*-dimethylacrylamide)-coated maghemite nanoparticles for stem cell labeling. Bioconj Chem 20(2):283–294

Chapter 5
The Interactions Between Engineered Nanomaterials and Biomolecules

Shasha Wang, Yunxia Ji, Kun Yin, Min Lv and Lingxin Chen

Abstract With the development and wide applications of engineered nanomaterials (ENMs), their impacts on human health have received increasing concerns. ENMs can enter human body through respiratory pathway, digestive tract, skin penetration, intravenous injection, and implantation, and then they are carried to distal organs via bloodstream and lymphatic functions to perturb physiological systems. It is very important to investigate the interactions between ENMs and biomolecules (the basic building blocks of the human body) such as phospholipid, protein, DNA, and some other small biological molecules. The chapter intends to discuss the chemical basis of interactions between ENMs and biomolecules, and the effects of the differences in surface morphology, composition, and modified groups of ENMs. The in-depth understanding of interactions between ENMs and biomolecules could lay foundations for further elucidating the effects of ENMs on human cells, organs, and physiological systems, which paves the way for human and environmental friendliness in the production and usage of ENMs.

Keywords Engineered nanomaterials (ENMs) · Biomolecules · Phospholipid · Protein · DNA

5.1 Brief Introduction of Interactions Between Engineered Nanomaterials and Biomolecules

5.1.1 Engineered Nanomaterials (ENMs)

Nanomaterial is defined as a material with at least one dimension in the size range between 1 and 100 nm (the usual definition of nanoscale) in principle, and it is an aggregate or agglomerate based on nanoscale units. Engineered nanomaterials

S. Wang · Y. Ji · K. Yin · M. Lv · L. Chen (✉)
Key Laboratory of Coastal Environmental Processes and Ecological Remediation, Yantai Institute of Coastal Zone Research, Chinese Academy of Sciences, Yantai 264003, China
e-mail: lxchen@yic.ac.cn

B. Yan et al. (eds.), *Bioactivity of Engineered Nanoparticles*,
Nanomedicine and Nanotoxicology, DOI 10.1007/978-981-10-5864-6_5

(ENMs) refer to nanomaterials which are intentionally manufactured in contrast to natural ones. ENMs possess many unique optical, electronic, chemical, and biological features compared with bulk materials. In addition, all features could be influenced by surface, small size, quantum size, macroscopic quantum tunnel, and dielectric confinement effect [1–3]. For example, gold nanoparticles (Au NPs) exhibit a characteristic absorption peak in UV–Vis absorption spectrum [4], quantum dots (QDs) display strong fluorescence emission [5], and graphene has excellent mechanical property [6]. All these distinctive and advanced characteristics endow ENMs with fast-growing applications in medicine, pharmacy, chemical/biological sensing, manufacturing, optics, and national defense [7–10].

Most compositions of ENMs include carbon, silica, polymer, metal, and metal oxide (with shapes of sphere, rod, wire, tube, prism, sheets, and so on). The size of ENMs is often designed to be coordinate with major cellular machines and their components, so ENMs can interact with biological molecules to exert biochemical functions. Currently, the detailed chemical compositions of ENMs could be acquired by elemental analysis [11], X-ray photoelectron spectroscopy (XPS) [12], auger electron spectroscopy (AES) [13], and time-of-flight mass spectrometry (TOF-MS) [14]. Transmission electron microscopy (TEM), scanning electron microscopy (SEM), and atomic force microscopy (AFM) could characterize the morphology of ENMs [15]. And dynamic light scattering (DLS) could offer information on the hydrodynamic radii of nanoparticles in solution [16].

The surface properties of ENMs mainly refer to the surface charge and hydrophobicity, depending on different chemical modification groups. Generally, the chemical groups on the surface of nanoparticles are determined by the synthetic process. Furthermore, the group can be altered via ligand exchange or other chemical bonding methods [17]. Multiple methods have been reported to characterize the physical and chemical properties of ENMs. Zeta-potential measurements could provide information of the surface charge properties of nanoparticles [18]. Ligands or adsorbed molecules on the surfaces could be identified by Fourier-transform infrared spectroscopy (FTIR) [19], liquid chromatography–mass spectroscopy (LC–MS) [20], and magic angle spinning nuclear magnetic resonance (MAS NMR) [21]. In addition, surface-enhanced Raman scattering (SERS) spectroscopy is another frequently used method for fingerprint identification of chemical groups [22].

5.1.2 Interaction Between ENMs and Biological Molecules

With the expanding production volume and applications of ENMs, the health and environmental effects of ENMs have attracted wide attention. The major portals of human body exposed to ENMs are skin, gastrointestinal tract, lung, nasal cavity, and eyes [23]. ENMs could then be translocated to other human organs which are distal to the site of uptake by absorbing into the bloodstream [24, 25]. In biological

fluids or systems, ENMs are surrounded by excessive amounts of biological molecules, and inevitably interact with various biomolecules.

Figure 5.1 schematically illustrates the comparison of sizes and shapes between common ENMs and more familiar chemical/biological materials [24]. Materials shown for comparison are below, within or above the nanoscale range, aiming to put ENMs' size in perspective. As seen, the sizes of biomolecules, such as lipids, proteins, and DNA, are also in nanoscale range. ENMs have super-large specific surface area and high surface energy. As a result, pristine nanoparticles are nearly nonexistent since they prefer to adsorb various molecules in order to reduce their surface energy. The driving forces for the adsorption of biomolecules by ENMs involve hydrophobicity, hydrogen bonding capability, π bonds, and stereo chemical interactions, which are related to the composition, size, shape, and surface properties of ENMs [26].

Besides, the interactions between ENMs and biomolecules are also driven by the characteristics of biological settings. For instance, phospholipid, which is the main components of cell membranes, consists of a hydrophobic carbon chain (tail) and a hydrophilic phosphate group (head). The surface hydrophobicity of ENMs indicates the interaction with the hydrophilic head or the hydrophobic tail [26]. At physiological pH, proteins fold into different sizes, shapes, and net charges, and their hydrophobicity are largely dependent on the exposed amino acid residues. When ENMs encounter proteins in biological fluids, the spontaneous adsorption could occur and the stoichiometry and orientation of the combination are affected by the

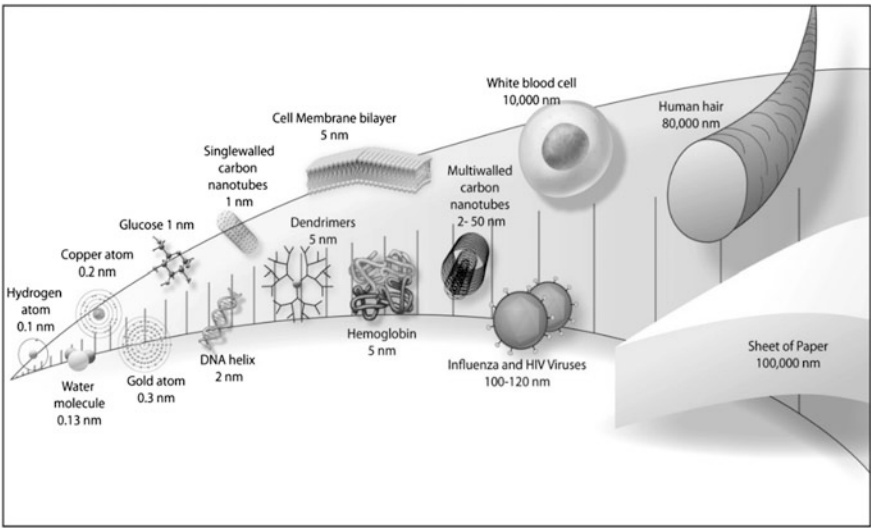

Fig. 5.1 The sizes and shapes of some ENMs compared to more familiar materials. Materials shown for comparison are below, within or above the nanoscale range, aiming to put ENMs' size in perspective. Reproduced with permission from Ref. [24]. Copyright © 2011 Yokel and MacPhail; licensee Bio Med Central Ltd. All rights reserved

properties of proteins [27]. Possessing phosphate groups and base π systems, DNA molecules can bind nanoparticles through electrostatic, π–π stacking, and hydrophobic interactions [28]. Moreover, ENMs could also adsorb other small biological molecules such as amino acids [30, 35, 36], nucleobases [37, 38], and vitamins [39, 40].

Generally speaking, the morphology and surface properties of ENMs are crucial in determining the nature or the interactions between ENMs and biological molecules [31, 32]. Therefore, the primary objective of the chapter is to perform systematic summary on the interactions between ENMs and biomolecules with the diversity in morphology, composition, and modified groups of ENMs. These observations not only provide powerful evidence to understand the fundamental chemical interactions of nanoparticles and biological systems, but also provide practical approaches to produce "safe-by-design" ENMs for various industrial or medicinal applications, which would pose minimal hazard potential to human health and the environment.

5.2 The Interactions Between Engineered Nanomaterials and Small Biological Molecules

A great variety of small biological molecules play tremendous roles in various metabolic processes, and the significant reduction of their contents has been shown to elicit adverse effects in cellular functions, as evidenced of incurring injuries and illnesses [33, 34]. Due to the extremely large surface area of ENMs, small biological molecules can be adsorbed onto nanoparticles with the help of hydrophobic interactions, π–π stacking, and electrostatic interactions. For the moment, the most studied molecules include amino acids [30, 35, 36], nucleobases [37, 38], and vitamins [39, 40].

5.2.1 Amino Acids

The combination of ENMs with amino acids, the basic unit of proteins, can lead to the impairment in amino acid structure, the dysfunction of amino acids, and even the abnormal metabolism, which will perturb the intrinsic biological behaviors of biomolecules. Based on this, related researches on the interaction between ENMs and amino acids are particularly important.

For example, in Roswell Park Memorial Institute (RPMI) cell culture medium, single-walled carbon nanotubes (SWCNTs) could adsorb a variety of amino acids, vitamins, and phenol red [35]. The driving forces for adsorption were ascribed to π-π interactions and electrostatic interactions. Using the depleted media to culture HepG2 cells, their viability was reduced obviously and could be largely restored by

replenishment of folate. Moreover, Casey et al. utilized spectrographic technique to demonstrate the interactions of SWCNTs and components in cell culture medium [41]. Afterward, this research group also investigated indirect cytotoxicity accounted for micronutrient depletion incurred by SWCNTs incubating A549 lung cells [36]. As seen, SWCNTs have enough large specific surface area to alter micronutrient in culture medium by adsorbing small-molecule solutes. Meanwhile, the combined data demonstrated that a broad range of small-molecule solutes, such as amino acids, vitamins, and indicator/probe dyes, is frequently influenced by nonspecific binding of physical adsorption.

Due to the excellent electrical conductivity, structure and mechanical properties of carbon nanotubes (CNTs) [42–44], numerous studies have focused on their applications in biological and biomedical fields. As is well known, computational chemistry has provided comprehensive information for the interaction between amino acids and nanomaterials. The binding of collagen amino acids (glycine, proline, and hydroxyproline) to graphene and Ca-doped graphene has been studied by density functional theory calculations and Ab initio molecular dynamics (AIMD) simulations [30]. The obtained data revealed that the doping calcium atoms on carbon surface dramatically enhanced the collagen amino acids binding to graphene, which was due to the electronic charge transfer from Ca to graphene and the carboxyl group of the amino acid. Rajesh et al. investigated the effect of curvature on the non-covalent interaction by comparing the interaction of amino acids with graphene and SWCNTs [45]. Figure 5.2 schematically shows a

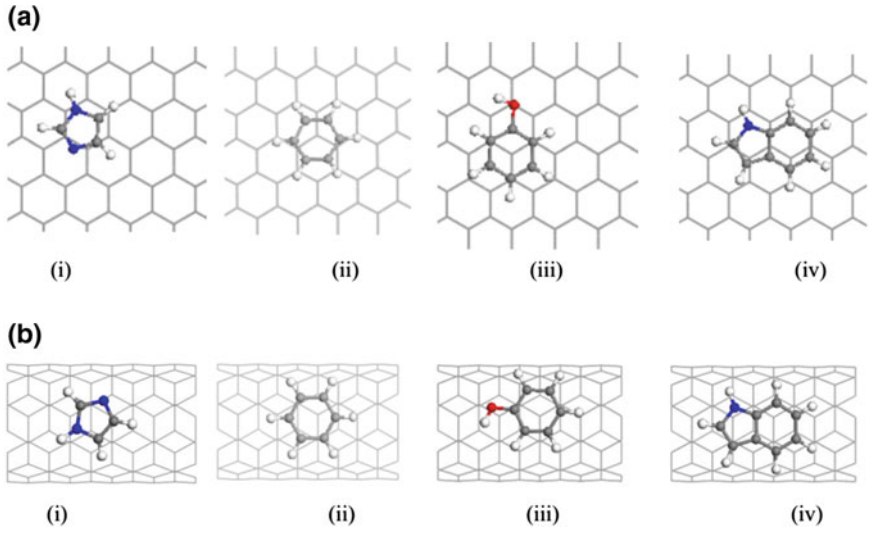

Fig. 5.2 Scheme for a comparison of interactions between the graphene (planar) or CNT (*curved*) and four aromatic amino acids: Equilibrium geometry of the rings of the aromatic amino acids on top of graphene (**a**) and on top of (5, 5) CNT (**b**), including (*i*) histidine, (*ii*) phenylalanine, (*iii*) tyrosine, and (*iv*) tryptophan. Reproduced with permission from Ref. [45]. Copyright © 2009 American Institute of Physics. All rights reserved

comparison of interactions between the graphene (planar) or CNT (curved) and four aromatic amino acids [45]. The binding energy followed the same trend between the planar graphene and rolled nanotube structure, but differed in the absolute magnitude. As a result, the binding strength between amino acids and CNT was weaker than that of amino acids and graphene sheet, due to the deviations of the π–π stacking resulting in the case of planar substrates. This observation indicated that the surface curvature of nanomaterials could be a key influence factor on the interactions between nanomaterials and amino acids. Besides, Mukhopadhyay and coworkers found molecular polarity could also affect the interaction of a boron nitride nanotube (BNNT) with amino acids [46]. Governed by electrostatic interactions, polar amino acid molecules exhibited easier binding with the tubular surface of BNNT. Related research results have provided fundamental insights into the interactions between ENMs and amino acids and contributed greatly to the applications of ENMs to biological and biomedical fields.

5.2.2 Nucleobases

Nucleic acid bases, also named genetic molecules, are key components of deoxyribonucleic acid (DNA) and ribonucleic acid (RNA), since they carry the information storage component of every cell in every plant or animal, and play a crucial role in life system, and has become a hot research focus over the past 5 years. Recently, there has been a profound insight in understanding the interaction between nucleobases and ENMs. This interaction not only depends on the individual susceptibility of nucleotide bases but also on the intrinsic physicochemical properties of ENMs.

Zhong et al. explored the adsorption of nucleic acid bases [adenine (A), guanine (G), cytosine (C), thymine (T), and uracil (U)] on hydrogen-passivated silicon nanowire (SiNW) by density functional theory [37]. Figure 5.3 depicts the equilibrium configurations of different nucleobases interacting with a hydrogen-passivated SiNW [37]. As shown, the calculated binding energy of the bases with SiNW was nearly the same, except that of G was higher than others. What's more, further study indicated that the nature of bonding between a nucleobase and proposed passivated SiNW was dominated by electrostatic interactions. By using the same calculations, Akdim and coworkers calculated the adsorption energy of nucleobases on chiral C (6, 5), C (9, 1), and C (8, 3) SWCNTs [47]. And the trend of calculation was consistent with related computations and experimental work on graphitic surfaces. The interactions between nucleic acid bases with graphene [48, 49] and CNTs [50] were determined by van der Waals force, and the binding energy increased with the polarizability of nucleobases. For single-walled BNNT, the order of calculated binding energy was $G > A \approx C \approx T \approx U$, indicating the similar interaction strength of nucleobases except for G [51]. Related structural analysis of the adsorbed nucleic acid bases has suggested that the

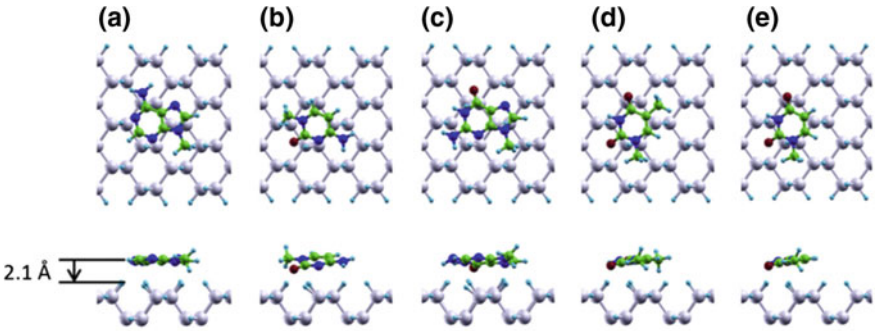

Fig. 5.3 Scheme for interactions between ENMs and different nucleases: top and side views of the equilibrium configurations of different nucleobases interacting with a hydrogen-passivated SiNW: **a** A, **b** C, **c** G, **d** T and **e** U. Silicon *gray*, hydrogen *light blue*, nitrogen *dark blue*, carbon *green*, oxygen *red*. Reproduced with permission from Ref. [37]. Copyright 2012 Elsevier B. V. All rights reserved

dispersion forces with a marginal contribution from electrostatic forces could provide the stability of the bioconjugated complexes.

Furthermore, Saha et al. theoretically investigated the interactions of different nucleotide bases (A, G, C, T, and U) and four ZnO nanomaterials (ZnO nanowires, ZnO nanotubes, ZnO quantum dots, and ZnO surface) by the self-consistent charge density functional tight binding (SCC-DFTB) method to optimize the complex systems [38]. The site-specific binding nature and the adsorption strength of these nucleobases with different ZnO nanoparticles were calculated in detail. The results manifested the binding energy order and the interaction strength of nucleobases was much dependent on the surface properties of the nanoparticles.

5.2.3 Vitamins

Vitamins are one of the organic materials required to sustain life, which plays a pivotal role in maintaining cell interstitial normal structure, enhancing blood circulation, promoting wound healing, and so on, and they are also important active substrates to keep system alive and healthy. The vitamins adsorbed by ENMs are very important in food industry and biomedical fields. For example, some ENMs with mesoporous structures, such as CNTs, are widely used for vitamin adsorption. The improvement of ENMs in uniformity and specific mesoporous properties has been seen in recent years.

Lu and coworkers added different amounts of CNTs into phenolic resin to synthesize composite spheres by suspension polymerization [40]. Then porous CNTs/activated carbon composite spheres were obtained by carbonizing above composite sphere at 600 °C and steam activating at 850 °C for more than 90 min.

After being characterized by nitrogen adsorption–desorption isotherms, the pore size distribution of the obtained porous spheres was "multi-peak", especially within 20–100 nm pores due to the aggregated pores of CNT bundles. Moreover, the amount of vitamin B12 adsorbed on porous CNTs/activated carbon composite spheres (45 wt% CNT) could be as high as 32.38 mg/g, indicating the application potential of the materials as adsorbents for middle-molecular-weight toxins or large molecules in hemoperfusion.

Shih et al. synthesized mesoporous titania (TiO_2) nanocrystallite powders by means of titanium chloride and tri-block nonionic surfactant as starting materials [52]. After investigation, the distribution of pore size was in the range of 2–50 nm, and the surface area of the mesoporous material was 301 m^2/g. The adsorption isotherms of vitamin E on TiO_2 mesoporous nanocrystals revealed a high affinity between the vitamin E molecule and the adsorbent surface, and the results of XRD and nitrogen adsorption proved the tight packing of the vitamin E molecule inside the mesopores of TiO_2 nanocrystals.

Due to the importance of vitamin to metabolism, growth, development, and health, the adsorption characteristics of nanomaterials to vitamin can be utilized in slow-release formulation. In 2015, Golubeva and coworkers investigated adsorption and in vitro release of vitamin B_1 by synthetic nanoclays with montmorillonite (Mt) structure [53]. The synthetic Mt structures, with varying compositions $Na_{2x}(Al_{2(1-x)}Mg_{2x})Si_4O_{10}(OH)_2 \cdot nH_2O$ (where $0 < x < 1$), were prepared by hydrothermal synthesis. Modeling release of vitamin B1 was performed in simulated gastric fluid (SGF) and simulated intestinal fluid (SIF). It revealed that the adsorption of vitamin B_1 depended mainly on the composition and cation-exchange capacity of Mt, and on the pH of the solution to a lesser extent. For the release of vitamin B1, the maximum amounts could reach 54 and 19 wt% in SGF and SIF, respectively, which were higher than that in natural Mt K10. Meanwhile, the data provided information on the optimal Mt compositions for further development of drug delivery systems.

5.2.4 Other Small Biological Molecules

Besides the abovementioned amino acids, nucleobases, and vitamins, other small biological molecules have also been investigated on their interactions with ENMs, such as glucose, and hormones related small biological molecules.

Ganji and coworkers studied the adsorption mechanism of glucose on intrinsic and Pt-decorated SWCNTs by using first-principles van der Waals density functional (vdW-DF) calculations [54]. Due to the higher binding energy, higher net charge transfer values, and shorter connecting distances, Pt-decorated (8, 0) SWCNT could strongly adsorb glucose molecule at the most stable state. Furthermore, the density of states demonstrated the orbital hybridization between the glucose and Pt-decorated nanotube. Therefore, Pt-decorated SWCNT is expected to be a good candidate for the design of glucose biosensors.

Because of the porous, layered structure and large surface area, soluble CNTs can be used to adsorb many environmental pollutants. Among these, the adsorption ability of CNTs for the hormones of bisphenol A (BPA) altered the properties of both BPA and CNTs, leading to different toxicities to human and living systems when BPA and CNTs were used alone. Wang et al. utilized the interactions between BPA and CNTs to investigate the endocrine disrupting effect in mice male offspring [55]. In comparison with oral exposure of BPA alone during gestation and lactation period, the male offspring suffered decreased reproductive toxicity when the mice were exposed to BPA/MWCNT–COOH (carboxylated multi-walled carbon nanotubes). BPA/MWCNT–COOH could effectively decrease malondialdehyde (MDA) level in testis and follicle-stimulating hormone (FSH) in serum, and increase the level of serum testosterone in male offspring. Their results have broadened the knowledge in nanotoxicity and provided important information on the safe application of CNTs.

In summary, ENMs have good application prospects in biomedical and pharmaceutical industry because of their small volume, high surface-activity, and easier interaction with various small biomolecules. However, the potential toxicity of ENMs has become the major constraint to their applications. Thus, it is particularly important to get insights into the impacts of nanoparticles on organisms, elaborate the mechanisms of interaction, and explore ways to minimize toxic effect. Understanding the interactions between ENMs and biomolecules would ensure us to apply the ENMs in more fields safely and effectively taking full advantages of their unique physical and chemical properties.

5.3 The Interactions Between Engineered Nanomaterials and Phospholipids

5.3.1 Current Understanding of the Interactions Between ENMs and Phospholipids

The cell membrane is mainly composed of phospholipids and proteins, and ENMs are capable to perform their functions on organisms only by entering cells through the membrane. Therefore, investigating the interactions between ENMs and phospholipids plays important roles in further studying drug delivery and reducing hazard potential of ENMs. Generally, nanoparticles can pass through cell membranes in two ways: one is direct piercing, and the other is endocytosis.

Shi et al. theoretically studied the interaction mechanisms between CNTs and lipid bilayer by coarse-grained molecular dynamics (CGMD) [56]. An analysis of the structures revealed that the van der Waals force and hydrophobic effect controlled the CNT–cell membrane interaction. As shown in Fig. 5.4, because of small diffusion distance and large curvature energy, small tubes preferred directly piercing through the membrane; on the contrary, larger tubes tended to wrapping

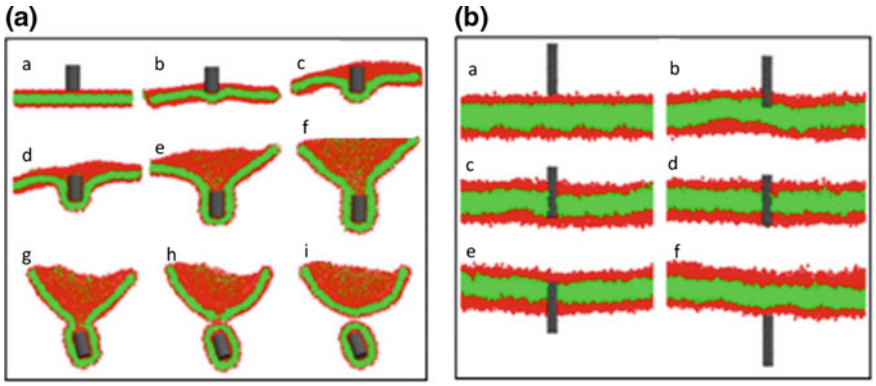

Fig. 5.4 Time-sequenced snapshots of a MWCNT (**a**) and SWCNT **b** passing through membrane. **a** *a–f* Time sequence of six snapshots of a MWCNT entering a membrane via a wrapping process driven by the van der Waals force; (*g*, *h*) fusion of the membrane neck; (*i*) separation of the lipid covered tube from the membrane. **b** (*a–f*) Time sequence of six snapshots of a SWCNT piercing through a membrane driven by the van der Waal force. The *red particles* indicate the head group of lipid molecules. Reproduced with permission from Ref. [56]. Copyright © Springer-Verlag 2008. All rights reserved

into the cell membrane due to larger diffusion distance and lower curvature energy [56]. Wallace and coworkers also employed CGMD to simulate the phospholipid–CNT interaction [57]. When SWCNTs penetrated the dipalmitoylphosphatidylcholine (DPPC) bilayers, lipids were detected to extract and reside on the outer and the inner tube surfaces. In addition, lipids binding on the CNT interior wall could block the tube by spreading out. And the tube penetration velocity was a key influence factor for the degree of lipid lining of the inner surface.

The interactions between ENMs and phospholipids can change the structures and properties of cell membrane. Jing and coworkers found that the binding of semihydrophobic nanoparticles could disrupt supported lipid bilayers (SLBs) [58]. When semihydrophobic nanoparticles reached a critical concentration, the disruption of SLBs, as well as the formation and rapid growth of lipid-poor regions which could be controlled by the concentration, size, and surface hydrophobicity of nanoparticles, was observed. Bothun investigated the effects of aqueous lipid/nanoparticle assemblies on bilayer phase and fluidity [59]. In this research, hydrophobic decanethiol-modified silver nanoparticles were embedded in DPPC bilayers as a model. It was observed that increasing nanoparticle concentration in bilayer-embedded nanoparticles could suppress the lipid pretransition temperature, reduce the melting temperature, and disrupt gel phase bilayers. And the characteristic surface plasmon resonance (SPR) peak of the embedded nanoparticles was independent of the bilayer phase; however, the SPR absorbance was related to vesicle aggregation.

5.3.2 Factors of ENMs Influencing the ENM–Phospholipid Interactions

The interaction of ENMs and phospholipids is mainly affected by the physicochemical properties of nanomaterials, such as size, shape, surface charge, hydrophobic/hydrophilic effect, crystallinity, and concentration. In a real biological system, either one or multiple above mentioned factors play dominant roles in ENM–phospholipid interactions. Moreover, to uncover the mechanisms of these influence factors, many efforts have been devoted to studying their behaviors and integrated forms in vitro and in vivo, which can facilitate the development of ENMs with high biocompatibility for safer biological applications. Here, we center on discussing a series of factors which are recognized to be major contributors that could affect the interactions of ENMs and phospholipids.

Using computer simulations, Yang and coworkers investigated the effect of ENMs with a series of shapes (spheres, ellipsoids, rods, discs, and pushpin-like particles) and volumes on the physical translocation processes [60]. It was revealed that the interaction between the nanoparticle and lipid bilayer was related to the shape anisotropy and initial orientation of ENMs, and the contact area of the particle and lipid bilayer, and the local curvature of the particle at the contact point determined the penetrating capability of a nanoparticle across a lipid bilayer. Moreover, the volume of nanoparticles could influence the translocation indirectly, and the complication of penetration process was determined by particle rotation. L-cysteine and L-glutathione capped Au NPs and gold nanorods (Au NRs) have been synthesized to discuss particle size effects on ENM–phospholipid interaction by determining surface pressure of a preformed model membrane [61]. For Au NPs of 10 and 15 nm average diameter, incorporation rate of smaller Au NPs was higher than those larger counterparts. Meanwhile, the size effect of Au NRs elicited internalization mainly but not exclusively due to longer wrapping time.

To further explore the effect of surface charge, CGMD simulations were employed to observe the interaction between charge-neutral phospholipid membranes and three kinds of nanoparticles with different surface charge densities (the uncharged one, the positively charged one, and the negatively charged one) [62]. The obtained data proved that the adhesion of a charged nanoparticle to the membrane was enhanced by the electrostatic attraction, and a full wrapping to a charged ENM occurred accompanied with the increase of electrostatic energy. At the same time, the structural transitions of fluid bilayers were induced by the adhesion of a charged nanoparticle. Furthermore, the gain in electrostatic energy drove the wrap at the cost of the elastic energy of biomembranes. Kettiger et al. compared the interaction of anionic silica nanoparticles (SNPs) and amine-modified cationic SNPs with phospholipid membranes [63]. The results from dye leakage assay and isothermal titration calorimetry (ITC) illustrated that negatively charged SNPs could react with phospholipids and made phosphatidylcholine (POPC)-based phospholipid bilayers unstable, which was driven by van der Waals forces at the level of the hydration layer on the vesicles surface.

The hydrophilic/hydrophobic property of nanoparticles is another key factor that affects the ENM–phospholipid interactions [64]. Two kinds of nanoparticles (hydrophobic and semihydrophilic) and DPPC bilayer were used as an example to simulate the interactions. Due to the difference in system-free energy, the hydrophobic nanoparticles were included into the bilayer; on the contrary, semihydrophilic nanoparticles were only adsorbed onto the membrane, which indicated that endocytosis-like mechanism was an energy-mediated process. Qiao et al. compared the translocation of fullerene C_{60} and its derivative $C_{60}(OH)_{20}$ across a model cell membrane [65]. Based on the molecular dynamics (MD) study, pristine C_{60} could translocate the membrane within a few milliseconds driven by the hydrophobic interactions. The surface functionalization rendered the hydrophilicity of fullerene, and thereby $C_{60}(OH)_{20}$ preferred to be adsorbed onto the membrane rather than the bilayer.

In short, investigating the interactions between ENMs and phospholipids, as well as considering the structure and properties of membrane and nanoscale materials, will uncover the mechanisms and elaborate the regulation strategies. It is beneficial to the amelioration of drug delivery system, decryption of its toxicological mechanisms, and development of safer nanomaterials.

5.4 The Interactions Between Engineered Nanomaterials and Proteins

Due to the active surface chemistry of ENMs, proteins in biofluids can be bound on the surfaces of nanoparticles to form bionano interfaces when ENMs are introduced into the biological settings [66]. Investigating the interactions between ENMs and proteins would expand our understanding of molecular mechanisms responsible for nanoparticles and nanoparticle–protein complexes, and would provide information for tailoring physicochemical properties to prepare “safety by design” ENMs.

5.4.1 Experimental Study of ENM–Protein Interactions

5.4.1.1 Thermodynamic and Kinetic Aspects of ENM–Protein Interactions

The thermodynamics and kinetics of the formation of ENM–protein complex are of great importance to investigate the adsorption process. De et al. used ITC to quantify the binding thermodynamics of L-amino acid-terminated monolayers functionalized Au NPs with R-chymotrypsin (ChT), histone, and cytochrome c (Cyt c) [67]. It was revealed that the changes of enthalpy and entropy for the complex formation were dependent on both physiochemical properties of nanoparticles and the intrinsic characteristics of the protein.

The effects of physiochemical properties of the specific nanoparticles on the protein adsorption can also be estimated by investigating the thermodynamics and kinetics. By using ITC, adsorption of human serum albumin (HSA) to N-iso-propylacrylamide/N-tert-butylacrylamide copolymer nanoparticles with varying size and hydrophobicity was studied [68]. It was found that a higher surface coverage occurred for the more hydrophobic particles, and lower degree of surface coverage was observed for smaller nanoparticles (70 nm) than larger counterparts (200–400 nm). Boulos and coworkers explored the adsorption of bovine serum albumin (BSA) on nanoparticles with different shapes, sizes, and surface charges using steady-state fluorescence quenching titration and affinity capillary electrophoresis (ACE) [69]. The obtained results indicated that similar binding constants were observed, which were independent of the shape and surface charge of gold nanomaterials. The limitations of these two present methods mean we are in urgent need of establishing new methods to investigate the ENM–protein interactions.

5.4.1.2 Conformational Change of Proteins Bound on ENMs

The binding of proteins on the surfaces of nanomaterials is usually accompanied by the conformational change of proteins. A significant conformational alteration at both secondary and tertiary structures of BSA upon interaction with Au NPs had been identified by various spectroscopic techniques [70]. Further fluorescence and circular dichroism studies had demonstrated that a higher pH was more inclined to elicit conformational change.

Besides the pH of the system, the size and shape of nanoparticle can affect the conformational change of the bound proteins. As shown in Fig. 5.5, the loss in α-helices content was elevated with the increase of nanoparticle size, and the

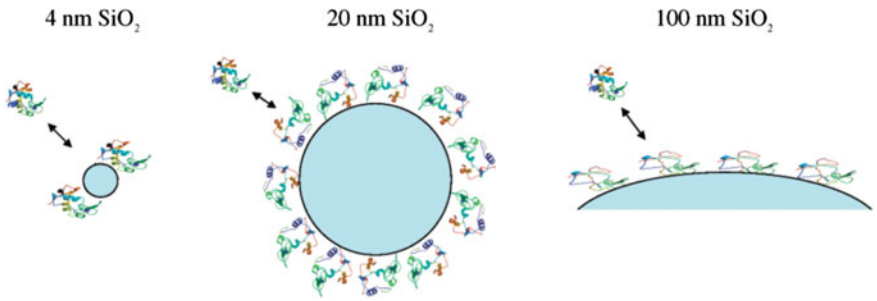

Fig. 5.5 Schematic illustration of lysozyme adsorption on silica nanoparticles with different diameters. As the size of the nanoparticle decreases, the curvature of the silica surface increases leading to a greater distance between the approaching protein molecule and the silica surface, and, thus, less interaction between the protein and smaller nanoparticles would be expected. Reproduced with permission from Ref. [71]. Copyright © 2008 American Chemical Society. All rights reserved

activity of the fixed lysozyme was lower than that of the free one [71]. Gagner et al. investigated the effect of gold nanomaterials morphology on the structure and function of adsorbed proteins (lysozyme and α-chymotrypsin) [72]. Under saturating conditions, a higher surface density of adsorbed proteins was found on Au NRs than that of Au NPs. The adsorption of lysozyme on Au NPs and Au NRs led to a 10 and 15% loss of secondary structure, respectively. Besides, a significant diminished enzymatic activity was also observed. At low surface coverage, α-chymotrypsin could maintain most of its secondary structure and activity when binding the two kinds of gold nanomaterials; however, the losses of secondary structure and activity could reach to 40 and 86% in an approached monolayer condition, respectively.

In addition, the surface properties of nanoparticles also influence ENM–protein interactions. By altering the ratio of the hydrophobic to hydrophilic ligands, a series of monolayer-protected metal nanoparticles (MPMN) were used to examine their interactions with Cyt c [73]. With the exaggeration of polar ligand content, adsorption of Cyt c was generally increased, indicating hydrophilic interactions between Cyt c and MPMN played a dominant role. Due to the amphipathic character of the lysine side chain, no significant structural disruption happened to Cyt c when bound to various MPMN. Moreover, the results from computational MD simulations were in qualitative agreement with experimental assay. Furthermore, the secondary and tertiary conformational changes of lysozyme relied on a higher or lower surface concentration as well [74].

5.4.2 Simulation of ENM–Protein Interactions

Though experimental methods can offer information on dynamics, thermodynamics, and conformational changes of proteins binding to ENMs, the detailed investigation of individual nanoparticle–protein conjugate is still limited. As an alternative, computer simulation could solve this problem in spite of its shortcoming that could not fully represent the situation in complex biofluids. According to the reported literatures, the nanomaterials used in simulations could be divided into two kinds: one is solid nanoparticles such as metals and their oxides, expressed by plane or solid sphere; the other is carbon-based nanomaterials with the structures of 5- and 6-member rings composed of carbon atoms.

By using discontinuous MD simulations with coarse-grained protein models, three proteins (Trp, WW, and GB3) at concentrations from 0.5 to 5 mM were adsorbed on nanoparticles with diameters ranging from 5 to 20 nm [75]. The simulation results delineated that Langmuir, Freundlich, Temkin, and Kiselev adsorption models performed well with the adsorption of Trp and WW on 10 nm nanoparticles, and provided two positive signals for developing a generalized adsorption model for a series of ENM–protein systems. Voicescu et al. employed the conformation of HSA on functionalized silver nanoparticles (Ag NPs) by the Monte Carlo simulations [76]. When interacted with Ag NPs, the α-helices of HSA

diminished, and Trp residue would prefer to locate toward the proteins boundary rather than binding onto the surface of nanoparticles. Tavanti and coworkers simulated the competitive binding of insulin and fibrinogen, two of the most abundant proteins in the plasma, on citrate-coated Au NPs with a diameter of 5 nm [77]. When binding a layer of proteins, a maximum of 20 insulins could be bound and only 3 fibrinogens were able to make contemporaneous interactions with the Au NPs. The binding site of insulin was specific and mainly consisted of the C-terminal residues of the two dimer chains, whereas that of fibrinogen was less specific and generally located at the boundary between the α-nodule and the β-nodule. Once the two proteins were added simultaneously, a competitive binding process for Au NPs could be observed.

Similar to solid nanoparticles, carbon-based nanomaterials could also cause conformational changes of adsorbed proteins. Due to the structure particularity of carbon-based nanomaterials, diverse impacts could occur depending on the structure and adsorption aspects of proteins. Using the sub-domain of HSA as an example, its adsorption behaviors and features on the surfaces of CNTs were explored by MD simulation [78]. It was found that the stepwise conformation and orientation of the model protein was decided by the properties and the texture of surfaces. During its adsorption process, the secondary structures of α-helices and the random coils connecting them were slightly and strongly affected, respectively. Adopting the same simulation method, Noon and coworkers investigated the buckyball (C_{60})-antibody complex in detail [79]. The simulation results indicated that the complementary shape and extensive side chain interactions led to the high binding affinity and specificity between C_{60} and antibody molecule, and π–π stacking interaction was the regular mode for π–electron-rich carbon nanoparticles to combine biomolecules. After the tight binding of antibody, there was still 17% of the surface area of buckyball exposed to the solvent, leaving enough room for further manipulation. The adsorption of insulin on graphene with different sizes was also conducted by MD simulation [80]. Polar and charged residues and phenyl rings in the proteins could bind graphene surfaces via the van der Waals interaction and π–π stacking interaction, respectively. In addition, it is also demonstrated that the final conformation of protein was affected by the sizes of graphene and whether the graphene was fixed. Some α-helices in insulin could be protected in non-fixed graphene but not in fixed system. And when the size of graphene was smaller than protein, the interaction energy and the number of adsorption residues would increase as a function of the width of graphene.

When preparing nanomaterials, a basic and strict requirement is to obtain a good dispersion of nanoparticles. However, the adsorption of the peptide chains on the surfaces of nanoparticles can prevent nanoparticles from agglomeration; this finding offers new ways for the synthesis of nanomaterials. Containing hydrophobic valine, aromatic phenylalanine residues, hydrophilic glutamic acid, and lysine residues, the designed amphiphilic helical peptide nano-1 by Chiu et al. [81] was used to investigate its characteristics in different water/hydrophobic interfaces (water/oil, water/graphite, and water/SWCNT) by atomistic MD simulations. Compared with the other two interfaces, nano-1 curved on the SWCNT surface was in α-helical

conformation, which maximized its hydrophobicity to contact with the SWCNTs and its hydrogen to bind with water. Also, Chiu et al. studied the properties of the pentamer/(6,6) SWCNT complex and the hexamer/(8, 8) SWCNT complex [82]. As observed in Fig. 5.6, the adsorbed peptides still kept α-helical conformation and formed inter-peptide H-bonds through their Lys and Glu residues [82]. Just like the single peptide system, the peptides in the multipeptide/SWCNT complexes also had as much contact with the SWCNTs, indicating nano-1 was an excellent dispersal agent for SWCNTs.

In a word, there are various factors influencing the interactions between ENMs and proteins, including physicochemical properties of nanoparticles (size, shape, and surface modification) and environmental factors (the concentrations of proteins and nanoparticles) [66, 83, 84]. Confirming these factors contributes to the understanding of the relationships between synthetic chemistry and biological sciences. Modification of ENMs could prevent the unexpected interactions or enhance the desirable interactions, which will facilitate rapid development of

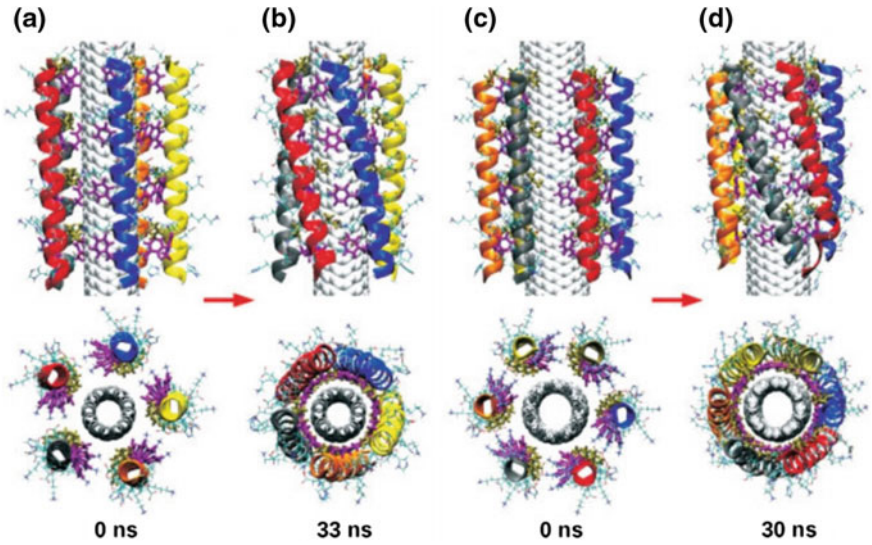

Fig. 5.6 Snapshots from MD simulations for pentamer/(6, 6) SWCNT (**a**, **b**) and hexamer/(8, 8) SWCNT (**c**, **d**) systems. **a** and **c** illustrate the initial conformations, whereas **b** and **d** illustrate the final conformations after 33 ns of simulation. The *upper panels* display views perpendicular to the SWCNT long axis, and the *lower panels* display perspectives to the SWCNT long axis. SWCNTs are represented using the vdW model, and peptide backbones are visualized using ribbons. Side chains are shown with a stick model, where Phe and Val residues are emphasized using *thicker lines* colored in *purple* and *tan*, respectively. The peptides are marked as P0 (*blue*), P1 (*red*), P2 (*gray*), P3 (*orange*), and P4 (*yellow*) for both systems, and in addition P5 (tan) for the hexamer/(8,8) SWCNT system. The P1 peptide in (**d**) has slightly unfolded at its C-terminus and uses its His residue to interact with the SWCNT sidewall. Reproduced with permission from Ref. [82].

nanotechnology-based drug delivery and rational nanotoxicity reduction, and safer ENMs design for biomedical applications.

5.5 The Interactions Between Engineered Nanomaterials and DNA

As one of the basic macromolecules in organisms, DNA with different sequences of base pairs stores a large amount of genetic information. DNA is the polymer of deoxynucleotides which is consisted of a pentose, a phosphate, and a base. All the deoxynucleotides are linked by phosphodiester bond, and two single-stranded DNA (ssDNA) with specific base pairing could form double helix structure [double-stranded DNA (dsDNA)] by hydrogen bonding. Due to the particularity of molecular structure, DNA could strongly interact with ENMs. The interaction between DNA and nanomaterials is related to the properties of both the DNA molecules and the nanoparticles. According to the reported literatures, gold nanoparticles (Au NPs), carbon-based nanomaterials, and quantum dots (QDs) are the hot spots in this research area.

5.5.1 Gold Nanoparticles (Au NPs)

The binding of DNA on the surfaces of Au NPs is attributed to electrostatic interactions. A kinetic study of the interaction of dsDNA with N-(2-mercaptopropionyl) glycine capped Au NPs was investigated by Prado-Gotor and coworkers [85]. The obtained kinetic curves revealed that the interaction involved a simple three-step series mechanism reaction scheme: the first step is fast and involves diffusion-controlled formation of a precursor complex; the second step is the formation of compound (DNA/Au NPs) I dependent on the binding affinity; and the third step is the conformational change from the compound (DNA/Au NPs) I to a more complex form (DNA/Au NPs) II. Komarov et al. employed computer simulation to study the metallization of DNA fragments by the assembly of Au NPs [86]. Due to electrostatic attraction and the short-range attraction between the metallic nanoparticles, Au NPs could aggregate on template DNA. As illustrated in Fig. 5.7, at $D = 1\sigma$, the thickness of Au NPs aggregated monolayer covering was close to the diameter of the nanoparticles, and the distribution of the nanoparticles on the template surface was similar to the charge distribution of the template (Fig. 5.7a); however, at $D = 2\sigma$, the number of aggregated nanometers was the same as the smaller nanoparticles, indicating that nanoparticles at $D = 2\sigma$ could aggregate until the negative charge of the DNA fragment was almost compensated (Fig. 5.7b); at $D = 3\sigma$, most of the aggregated nanoparticles were in direct contact with the surface of the template (Fig. 5.7c); and, the final aggregation was formed

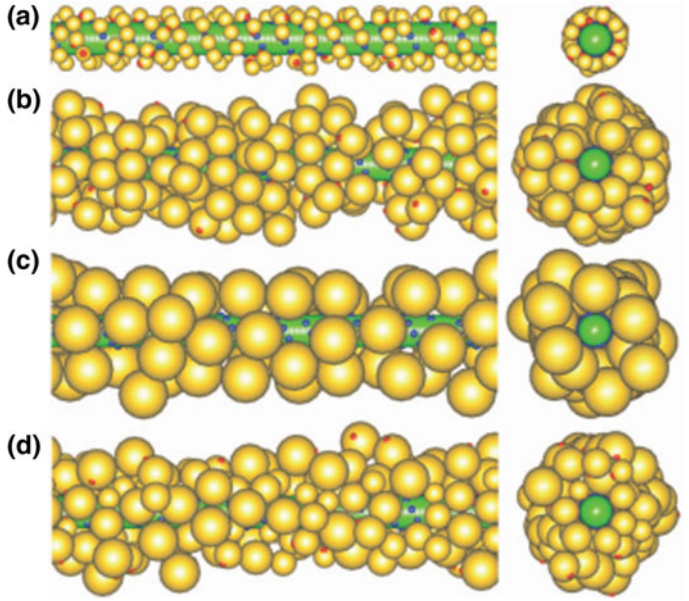

Fig. 5.7 Typical snapshots of two different projections of the final aggregate formed by monodisperse nanoparticles. *Green* represents DNA and *yellow* represents nanoparticles. **a** $D = 1\sigma$, the nanoparticles do form the monolayer covering of the thickness not much larger than the diameter of a nanoparticle, the distribution of the nanoparticles on the template surface roughly duplicates the charge distribution of the template. **b** $D = 2\sigma$, the thickness of metallic covering is about two times larger than the diameter of a nanoparticle, a considerable number of nanoparticles do not contact with the template surface immediately. **c** $D = 3\sigma$, the metallic coat in this case is still more uneven than at $D = 2\sigma$, the aggregation number does not depend on the charge of the nanoparticles because the diameter of the nanoparticles becomes larger than the electrostatic screening length. **d** A typical snapshot of the final aggregate formed by polydisperse nanoparticles, the distribution of the nanoparticles is less even in comparison with the case of monodisperse nanoparticles at $D = 2\sigma$. $\sigma = 10$ Å is the unit of length.

by polydisperse nanoparticles, and the distribution of the nanoparticles was less even in comparison with the case of monodisperse nanoparticles of 2σ size. It was manifested that the size of Au NPs and the charge of the DNA fragment influenced the structure of metallic coat on template DNA. What's more, the adsorption constants and the number of binding sites on the surfaces of Au NPs were obtained by analyzing adsorption isotherms via model-based Scatchard and Langmuir methods [87].

Au NP–DNA interactions are mainly affected by the characters of DNA, nanoparticles, and the microenvironment. The binding ability of unmodified DNA to colloidal and surface-confined Au NPs has been investigated by colorimetric and electrochemical technologies [88]. Only ssDNA rather than dsDNA can be

adsorbed by colloidal and naked surface-confined Au NPs, and the binding mode was electrostatic interaction and covalent interaction, respectively. To explore the variables which influenced the coverage of DNA on Au NPs, a series of factors, including nanoparticle size, salt concentration, spacer composition, and degree of sonication, had been discussed in detail [89]. Compared to Au NPs with small particle size (13–30 nm), the amount of DNA loading for larger nanoparticles (250 nm) was two orders of magnitude higher. For a particular Au NPs with a diameter of 15 nm, DNA loading can be increased by using 0.7 M NaCl for salt aging and PEG as spacer instead of common nucleobase (A or T) spacers. Lazarus and coworkers found Au NPs functionalized with cationic polyelectrolytes (poly-ethyleneimine and poly-L-lysine) presented a higher electrophoretic mobility when bound to linear DNA than the supercoiled and nicked configuration [90]. In addition, the binding affinities of DNA to Au NPs varied with the change of pH, which could be used to distinguish human p53 gene from sequences with single-base mismatch [91].

The interactions of DNA and Au NPs also elicit alterations in DNA molecules. For example, the relaxation of supercoiled DNA (scDNA) was enhanced when bound to the surfaces of trimethylammonium (TMA) C12 capped Au NPs, which promoted the potency of Au NPs in the treatment of diseases [92]. Yang et al. found small Au NPs inhibited the hybridization of ssDNA with complementary DNA sequences [93]. The nonspecific binding was strong enough to break pre-existing hydrogen bonds in short dsDNA and weakened with the increase of the particle size. The assembly of small metal nanoparticles by DNA hybridization also has provided new ideas for synthesizing larger nanoparticles via core–shell assisted growth method. Octanethiol and 11-trimethylammonium-undecanethiol functionalized Au NPs (2 nm) displayed high binding ability toward DNA driven by electrostatic attraction, and the Au NPs–DNA complex possessed sufficient affinity to inhibit recognition and transcription of T7 RNA polymerase from producing RNA products, indicating the useful application of ENMs to biological researches [94].

5.5.2 Carbon-Based Nanomaterials

In recent years, molecular interactions between carbon-based nanomaterials and DNA have attracted special attention owing to the excellent properties and promising applications carbon-based nanomaterials. The driving forces for the binding of DNA on carbon-based nanomaterials mainly include hydrophobic effect, π–π stacking, and electrostatic force [95]. The adsorption of DNA could alter not only the properties of carbon-based nanomaterials but also the conformations changes of DNA molecules.

5.5.2.1 Carbon Nanotubes (CNTs)

In order to explore the self-assembly mechanisms, structure, and energetic properties of SWCNTs–ssDNA, classical all-atom MD simulations have been adopted [96]. As shown in Fig. 5.8, a random 14-base DNA was initially in a helical-stacked conformation (Fig. 5.8a), and a conformational change of nucleobases within the first 500 ps enabled individual nucleobases when bound on the sidewall of SWCNTs in radial direction via the π–π stacking interaction; Afterward, the additional nucleobases were bound to the sidewall within 5.5 ns accompanied with the approach of entire ssDNA backbone to SWCNTs (Fig. 5.8b). Over the next 16 ns, ssDNA spontaneously wrapped around SWCNTs into a compact right- or left-handed helices, which was driven by electrostatic and torsional interactions

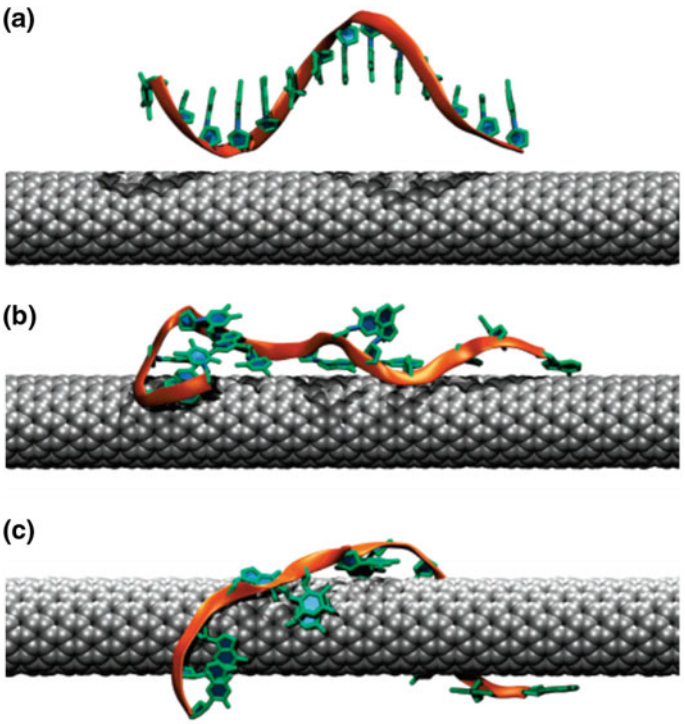

Fig. 5.8 The configuration changes of ssDNA in self-assemble DNA–carbon nanotube hybrid in aqueous solution. **a** Initial configuration. A simulation was performed on a random 14-base oligonucleotide initially separated from a (11, 0) SWCNT by about 1.5 nm. ssDNA was initialized in a helical-stacked conformation. **b** Configuration after 5.5 ns. Within 5.5 ns, the entire ssDNA backbone is drawn close to SWCNT, which permits additional nucleobases to bind to the side wall. **c** Final configuration after 21 ns. Over the next 16 ns, many of the remaining unbound nucleobases adsorb and ssDNA spontaneously warps around SWCNT into a left-handed helix. Reproduced with permission from Ref. [96].

(Fig. 5.8c). Using the method of replica exchange molecular dynamics (REMD), Roxbury et al. found that the ordered structures of ssDNA on SWCNTs were dependent on DNA sequence and SWCNT size [97]. Experimental measurements manifested that DNA sequence (TAT)4 on smaller diameter (6,5)-SWCNT and larger diameter (8,7)-SWCNT formed an ordered right-handed helical strand and a small loop configuration, respectively, indicating the selectivity of SWCNT size. In addition, homopolymer $(T)_{12}$ formed a left-handed wrap on the (6,5)-SWCNT via intrastrand hydrogen bonding, showing the effect of DNA sequence. Albertorio and coworkers quantified the base-dependent ssDNA–SWCNT interactions by probing the specific base dissociation temperatures of homo-oligonucleotide/SWCNT hybrids [98]. Qiu et al. proved that the interaction of DNA–CNT was also governed by the monovalent salt concentration in aqueous solutions [99]. Besides the interaction of ssDNA–SWCNT, the binding of fragmented double-stranded (fds-) DNA (100–500 base pairs, containing both double- and single-stranded regions) to SWCNT should be considered as well [100]. Compared with ssDNA, the interaction of fds-DNA–SWCNT was less efficient. And the formation of hybrids started from the binding of untwisted ss-regions of DNA, and then the whole polymer could wrap on the wall of the tube.

A number of studies have documented the genotoxicity of CNTs in vivo and vitro. There is also a possible interruption of genetic integrity, because DNA could readily insert into CNTs. The MD simulations have proved that the insertion is a spontaneous process, and the van der Waals and hydrophobic forces play dominant roles in the interaction [101]. MD simulations have verified that external electric field could regulate and control the translocation of ssDNA through polarized CNTs [102]. When the electric field strength is inferior to the critical field strength, the translocation event could be inhibited. The translocation process is related not only to the electric field strength, but also to the tube size and nonbonded interactions. Similar to electric field, gravitational acceleration field also has a significant influence on the DNA translocation process [103]. Figure 5.9 shows that DNA could translocate through (10, 10)–(14, 14) CNTs under the gravitational field, and an existing energy barrier indicated that DNA translocation inside a CNT channel was different from DNA translocation into a CNT from outside. Alshehri et al. explored interaction of ssDNA inside SWCNTs, and obtained that the minimum and optimum radiuses of SWCNTs to enclose ssDNA were 12.30 and 12.8 Å [104].

5.5.2.2 Graphene Oxide (GO)

The complex DNA–GO has been widely used in biosensing and biomedicine. However, the cognition of GO-mediated genotoxicity is still scarce; thus far, exploring the interaction between DNA and GO is very meaningful. Xu et al. adopted SPR technique to explore DNA–GO binding [105]. In comparison with dsDNA, the binding of ssDNA toward GO was much stronger, which was driven by hydrogen bonding. As a result, an ultra-sensitive sensor for the detection of

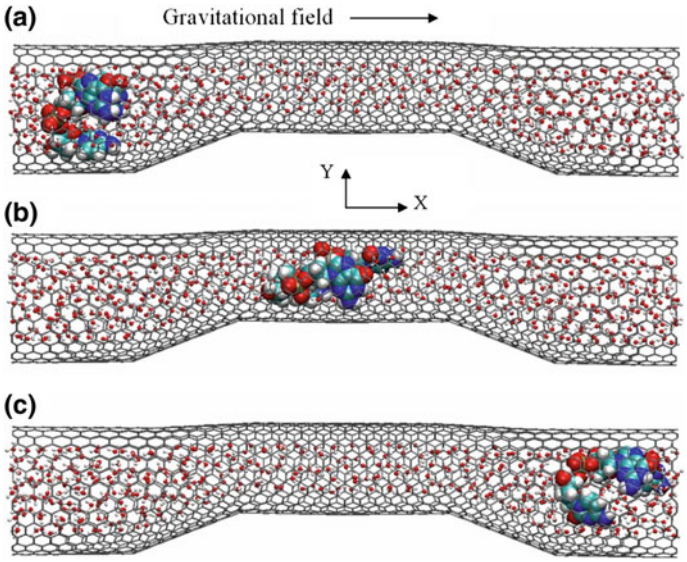

Fig. 5.9 Schematic diagrams for effect of the gravitational field: Snapshots of DNA translocation through (10, 10)–(14, 14) CNTs under the gravitational field of ag = 2.6×10^{13} m/s^2 at **a** time = 0 ps, **b** time = 330 ps, and **c** time = 600 ps. Reproduced with permission from Ref. [103]. Copyright © 2008 American Institute of Physics. All rights reserved

ssDNA could be established based on the ssDNA/dsDNA discrimination ability of GO. And a homogenous fluorescence polarization assay for the measurement of the DNA of HIV A T7 was also exploited by using the binding difference between dsDNA and ssDNA [106]. Though ssDNA can be bound to GO more easily, the binding force is also connected with the length of DNA. In order to explain the difference caused by DNA length, he and coworkers deeply investigated the binding mechanism of ssDNA with GO by using fluorescence spectroscopy [107]. After calculation, the binding constant of short ssDNA with GO was much lower than that of long ssDNA. According to this conclusion, a novel sensing strategy for determination of S1 nuclease and its inhibitor has been developed. Similarly, Zhang et al. reported a turn-on fluorescence-sensing technique for glucose determination [108]. Additionally, the adsorption kinetics of nano-sized GO (NGO) to shorter DNA was proved faster than that of micro-sized large GO by Lee and coworkers [109].

5.5.3 *Quantum Dots (QDs)*

Possessing unique properties of emitting narrow and symmetric fluorescence peak, high fluorescence intensity, and excellent anti-photobleaching ability, QDs have

been widely used in contaminant and biomolecule sensing, bio-labeling, and immunoassay. Investigating the interactions between QDs and DNA is of great importance for the further application in biology, and a series of methods have been used to study it. Wang and coworkers adopted UV–vis adsorption spectroscopy and electrochemical method to explore the interaction of CdSe/CdS QDs with herring sperm DNA (hs-DNA) [110]. Deduced from the changes of UV–vis adsorption spectroscopy, the apparent association constants of dsDNA–QDs and ssDNA–QDs were 4.94×10^3 and 2.39×10^2 M^{-1}, respectively. The high affinity of hs-DNA toward QDs is attributed to electrostatic force, hydrogen bonds, and van der Waals interactions. Xu et al. investigated the interaction between dsDNA and CdTe QDs by an indirect electrochemical method with the help of $Co(phen)^{33+/2+}$ (phen = 1,10-phenanthroline) [111]. It was found that the presence of CdTe QDs accelerated the dissociation of $Co(phen)^{33+/2+}$ from dsDNA modified gold electrode. The results indicated that the major groove of dsDNA was probably the binding site of CdTe QDs, and the same conclusion was also obtained by capillary electrophoresis with laser-induced fluorescence detection and gel electrophoresis [112]. Besides experimental methods, a prototypical model consisting of a capped CdSe QDs and a DNA molecule has also been chosen to compute the interaction by Ab initio electronic structure (based on density functional theory) calculations [113].

The nature of QD surface cations can exert an influence on the interaction with DNA [114]. For instance, the fluorescence of surface-activated CdS QDs by Cd^{2+}, Mg^{2+}, and Zn^{2+} could be remarkably quenched after binding DNA with straight, bent, and linked structures. And CdS QDs activated with harder Mg^{2+} and Zn^{2+} showed higher affinity to different DNAs than those activated with softer Cd^{2+} ions; however, the ability to distinguish different oligonucleotide shapes was lower because Mg^{2+} and Zn^{2+} could cause DNA bending. The complex QDs–DNA could also be used to evaluate the interaction and conformational change of DNA. Employing electrochemiluminescence resonance energy transfer (ECRET), Li et al. [115] and Hu et al. [116] successfully determined them by using luminol-DNA-CdSe/ZnS QDs and CdSe/ZnS QDs-DNA-Cy5 systems, respectively.

Due to the distinctive structure of the DNA molecule that can be connected through the strict principle of base pairing, DNA molecules can combine with metal nanoparticles or graphene to synthesize self-assembly nanomaterials. In addition, exploring the interactions between ENMs and DNA has important practical significance on disease treatment and genetic detection.

5.6 Conclusions and Outlook

Possessing outstanding properties of diverse morphologies, large specific surface area and strong surface reactivity, ENMs have good application prospect in biomedical field. Due to the high affinities to biomolecules, the toxic and side effects of ENMs on organisms impose restrictions on their wide usages. In recent

years, remarkable progress has been witnessed in the investigation between nanomaterials and biomolecules by a fair amount of theoretical and experimental research. Current results have revealed that the binding ability of ENMs is related to their size, shape, and surface properties when they react with small biological molecules, phospholipid, protein, and DNA. Meanwhile, the nature of biomolecules is also affected, such as the change of protein structure and DNA conformation.

However, the interaction mechanisms between ENMs and biomolecules are still far from clear understanding, which need further investigations. In-depth understanding of the ENM–biomolecule interactions can do help to explore the interaction mechanisms of ENMs–organelle and ENMs–cell, which contribute to proposing new methods to effectively reduce the toxicity of nanoparticles. In addition, investigating the binding of biomolecules on the surfaces of ENMs also makes people realize the characteristics of the materials more clearly. As a result, we can make more safe and effective use of ENMs with excellent physical and chemical properties in more fields.

References

1. Liang WZ, Wang XJ, Yokojima S, Chen GH (2000) Electronic structures and optical properties of open and capped carbon nanotubes. J Am Chem Soc 122:11129–11137
2. Eychmuller A (2000) Structure and photophysics of semiconductor nanocrystals. J Phys Chem B 104:6514–6528
3. Leroueil PR, Hong SY, Mecke A, Baker JR, Orr BG, Holl MMB (2007) Nanoparticle interaction with biological membranes: does nanotechnology present a janus face? Acc Chem Res 40:335–342
4. Ray PC (2010) Size and shape dependent second order nonlinear optical properties of nanomaterials and their application in biological and chemical sensing. Chem Rev 110:5332–5365
5. Jin T, Yoshioka Y, Fujii F, Komai Y, Seki J, Seiyama A (2008) Gd^{3+}-functionalized near-infrared quantum dots for in vivo dual modal (fluorescence/magnetic resonance) imaging. Chem Commun 44:5764–5766
6. Zhang YY, Wang CM, Cheng Y, Xiang Y (2011) Mechanical properties of bilayer graphene sheets coupled by sp^3 bonding. Carbon 49:4511–4517
7. Bobo D, Robinson KJ, Islam J, Thurecht KJ, Corrie SR (2016) Nanoparticle-based medicines: a review of FDA-approved materials and clinical trials to date. Pharm Res 33:2373–2387
8. He H, Pham-Huy LA, Dramou P, Xiao DL, Zuo PL, Pham-Huy C (2013) Carbon nanotubes: applications in pharmacy and medicine. Biomed Res Int 2013:578290
9. Islam MS, Deng Y, Tong LY, Faisal SN, Roy AK, Minett AI, Gomes VG (2016) Grafting carbon nanotubes directly onto carbon fibers for superior mechanical stability: towards next generation aerospace composites and energy storage applications. Carbon 96:701–710
10. Zheng TY, Bott S, Huo Q (2016) Techniques for accurate sizing of gold nanoparticles using dynamic light scattering with particular application to chemical and biological sensing based on aggregate formation. ACS Appl Mater Interfaces 8:21585–21594
11. Nagao A, Higashimine K, Huaman JLC, Iwamoto T, Matsumoto T, Inoue Y, Maenosono S, Miyamura H, Jeyadevan B (2015) Formation of Pt decorated Ni-Pt nanocubes through low

temperature atomic diffusion—time-resolved elemental analysis of nanoparticle formation. Nanoscale 7:9927–9934
12. Powell CJ, Werner WSM, Shard AG, Castner DG (2016) Evaluation of two methods for determining shell thicknesses of core-shell nanoparticles by X-ray photoelectron spectroscopy. J Phys Chem C Nanomater Interfaces 120:22730–22738
13. Chao LC, Yang SH (2017) Growth and Auger electron spectroscopy characterization of donut-shaped ZnO nanostructures. Appl Surf Sci 253:7162–7165
14. Chhoden T, Clausen PA, Larsen ST, Norgaard AW, Lauritsen FR (2015) Interactions between nanoparticles and lung surfactant investigated by matrix-assisted laser desorption/ionization time-of-flight mass spectrometry. Rapid Commun Mass Spectrom 29:1080–1086
15. Rao CNR, Biswas K (2009) Characterization of nanomaterials by physical methods. Annu Rev Anal Chem 2:435–462
16. Zimbone M, Calcagno L, Messina G, Baeri P, Compagnini G (2011) Dynamic light scattering and UV–vis spectroscopy of gold nanoparticles solution. Mater Lett 65:2906–2909
17. Ding Y, Wang S, Li J, Chen L (2016) Nanomaterial-based optical sensors for mercury ions. TrAC Trends Anal Chem 82:175–190
18. Chen LX, Fu XL, Li JH (2013) Ultrasensitive surface-enhanced Raman scattering detection of trypsin based on anti-aggregation of 4-mercaptopyridine-functionalized silver nanoparticles: an optical sensing platform toward proteases. Nanoscale 5:5905–5911
19. Yao H, Dai QL, You ZP (2015) Fourier transform infrared spectroscopy characterization of aging-related properties of original and nano-modified asphalt binders. Constr Build Mater 101:1078–1087
20. Zhao PY, Huang BY, Gu KJ, Zou N, Pan CP (2015) Analysis of triallate residue and degradation rate in wheat and soil by liquid chromatography coupled to tandem mass spectroscopy detection with multi-walled carbon nanotubes. Int J Environ Anal Chem 95:1413–1423
21. Kim HJ, Lee HC, Lee JS (2007) Al-27 triple-quantum magic-angle spinning nuclear magnetic resonance characterization of nanostructured alumina materials. J Phys Chem C 111:1579–1583
22. Lang XF, You TT, Yin PG, Tan EZ, Zhang Y, Huang YF, Zhu HP, Ren B, Guo L (2013) In situ identification of crystal facet-mediated chemical reactions on tetrahexahedral gold nanocrystals using surface-enhanced Raman spectroscopy. Phys Chem Chem Phys 15:19337–19342
23. Schwerha JJ (2010) Fantastic voyage and opportunities of engineered nanomaterials: what are the potential risks of occupational exposures. J Occup Environ Med 52:943–946
24. Yokel RA, MacPhail RC (2011) Engineered nanomaterials: exposures, hazards, and risk prevention. J Occup Med Toxicol 6:7
25. Kapralov AA, Feng WH, Amoscato AA, Yanamala N, Balasubramanian K, Winnica DE, Kisin ER, Kotchey GP, Gou PP, Sparvero LJ, Ray P, Mallampalli RK, Klein-Seetharaman J, Fadeel B, Star A, Shvedova AA, Kagan VE (2012) Adsorption of surfactant lipids by single-walled carbon nanotubes in mouse lung upon pharyngeal aspiration. ACS Nano 6:4147–4156
26. Mu QX, Jiang GB, Chen LX, Zhou HY, Fourches D, Tropsha A, Yan B (2014) Chemical basis of interactions between engineered nanoparticles and biological systems. Chem Rev 114:7740–7781
27. Ambike A, Rosilio V, Stella B, Lepêtre-Mouelhi S, Couvreur P (2011) Interaction of self-assembled squalenoyl gemcitabine nanoparticles with phospholipid–cholesterol monolayers mimicking a biomembrane. Langmuir 27:4891–4899
28. Xu JW, Yang LL, Han YY, Wang YM, Zhou XM, Gao ZD, Song YY, Schmuki P (2016) Carbon-decorated TiO_2 nanotube membranes: a renewable nanofilter for charge-selective enrichment of proteins. ACS Appl Mater Interfaces 8:21997–22004

29. Munk M, Ladeira LO, Carvalho BC, Camargo LSA, Raposo NRB, Serapiao RV, Quintao CCR, Silva SR, Soares JS, Jorio A, Brandao HM (2016) Efficient delivery of DNA into bovine preimplantation embryos by multiwall carbon nanotubes. Sci Rep 6:33588
30. Cazorla C (2010) Ab initio study of the binding of collagen amino acids to graphene and A-doped (A = H, Ca) graphene. Thin Solid Films 518:6951–6961
31. Albanese A, Tang PS, Chan WC (2012) The effect of nanoparticle size, shape, and surface chemistry on biological systems. Annu Rev Biomed Eng 14:1–16
32. Baer DR, Gaspar DJ, Nachimuthu P, Techane SD, Castner DG (2010) Application of surface chemical analysis tools for characterization of nanoparticles. Anal Bioanal Chem 396:983–1002
33. Shan CS, Yang HF, Song JF, Han DX, Ivaska A, Niu L (2009) Direct electrochemistry of glucose oxidase and biosensing for glucose based on graphene. Anal Chem 81:2378–2382
34. McCallum EA, Hyung H, Do TA, Huang CH, Kim JH (2009) Adsorption, desorption, and steady-state removal of 17 beta-estradiol by nanofiltration membranes. J Membr Sci 319:38–43
35. Guo L, Von Dem Bussche A, Buechner M, Yan AH, Kane AB, Hurt RH (2008) Adsorption of essential micronutrients by carbon nanotubes and the implications for nanotoxicity testing. Small 4:721–727
36. Casey A, Herzog E, Lyng FM, Byrne HJ, Chambers G, Davoren M (2008) Single walled carbon nanotubes induce indirect cytotoxicity by medium depletion in A549 lung cells. Toxicol Lett 179:78–84
37. Zhong XL, Slough WJ, Pandey R, Friedrich C (2012) Interaction of nucleobases with silicon nanowires: a first-principles study. Chem Phys Lett 553:55–58
38. Saha S, Sarkar P (2014) Understanding the interaction of DNA-RNA nucleobases with different ZnO nanomaterials. Phys Chem Chem Phys 16:15355–15366
39. Shen WZ, Wang H, Guan RG, Li ZJ (2008) Surface modification of activated carbon fiber and its adsorption for vitamin B1 and folic acid. Colloid Surface A 331:263–267
40. Lu YM, Gong QM, Lu FP, Liang J (2014) Synthesis of porous carbon nanotubes/activated carbon composite spheres and their application for vitamin B12 adsorption. Sci Eng Compos Mater 21:165–171
41. Casey A, Davoren M, Herzog E, Lyng FM, Byrne HJ, Chambers G (2007) Probing the interaction of single walled carbon nanotubes within cell culture medium as a precursor to toxicity testing. Carbon 45:34–40
42. Geim AK, Novoselov KS (2007) The rise of graphene. Nat Mater 6:183–191
43. Zhang Y, Tan YW, Stormer HL, Kim P (2005) Experimental observation of the quantum Hall effect and Berry's phase in graphene. Nature 438:201–204
44. Abanin DA, Lee PA, Levitov LS (2006) Spin-filtered edge states and quantum Hall effect in graphene. Phys Rev Lett 96:176803
45. Rajesh C, Majumder C, Mizuseki H, Kawazoe YA (2009) Theoretical study on the interaction of aromatic amino acids with graphene and single walled carbon nanotube. J Chem Phys 130:124911
46. Mukhopadhyay S, Scheicher RH, Pandey R, Karna SP (2011) Sensitivity of boron nitride nanotubes toward biomolecules of different polarities. J Phys Chem Lett 2:2442–2447
47. Akdim B, Pachter R, Day PN, Kim SS, Naik RR (2012) On modeling biomolecular-surface nonbonded interactions: application to nucleobase adsorption on single-wall carbon nanotube surfaces. Nanotechnology 23:165703
48. Ortmann F, Schmidt WG, Bechstedt F (2005) Attracted by long-range electron correlation: adenine on graphite. Phys Rev Lett 95:186101
49. Le D, Kara A, Schröder E, Hyldgaard P, Rahman TS (2012) Physisorption of nucleobases on graphene: a comparative van der Waals study. J Phys Condens Mater 24:424210
50. Gowtham S, Scheicher RH, Pandey R, Karna SP, Ahuja R (2008) First-principles study of physisorption of nucleic acid bases on small-diametercarbon nanotubes. Nanotechnology 19:125701

51. Mukhopadhyay S, Gowtham S, Scheicher RH, Pandey R, Karna SP (2010) Theoretical study of physisorption of nucleobases on boron nitride nanotubes: a new class of hybrid nano-biomaterials. Nanotechnology 21:165703
52. Shjh CJ, Lin CT, Wu SM (2010) Adsorption of vitamin E on mesoporous titania nanocrystals. Mater Res Bull 45:863–869
53. Golubeva OY, Pavlova SV, Yakovlev AV (2015) Adsorption and in vitro release of vitamin B-1 by synthetic nanoclays with montmorillonite structure. Appl Clay Sci 112:10–16
54. Ganji MD, Skardi FSE (2014) Adsorption of glucose molecule onto platinum-decorated single-walled carbon nanotubes: a dispersion-corrected DFT simulation. Fuller Nanotub Carbon Nanostruct 23:273–282
55. Wang WW, Jiang CJ, Zhu LD, Liang NN, Liu XJ, Jia JB, Zhang CK, Zhai SM, Zhang B (2014) Adsorption of bisphenol A to a carbon nanotube reduced its endocrine disrupting effect in mice male offspring. Int J Mol Sci 15:15981–15993
56. Shi XH, Kong Y, Gao HJ (2008) Coarse grained molecular dynamics and theoretical studies of carbon nanotubes entering cell membrane. Acta Mech Sin 24:161–169
57. Wallace EJ, Sansom MSP (2008) Blocking of carbon nanotube based nanoinjectors by lipids: a simulation study. Nano Lett 8:2751–2756
58. Jing BX, Zhu YX (2011) Disruption of supported lipid bilayers by semihydrophobic nanoparticles. J Am Chem Soc 133:10983–10989
59. Bothun GD (2008) Hydrophobic silver nanoparticles trapped in lipid bilayers: size distribution, bilayer phase behavior, and optical properties. J Nanobiotechnol 6:13
60. Yang K, Ma YQ (2010) Computer simulation of the translocation of nanoparticles with different shapes across a lipid bilayer. Nat Nanotechnol 5:579–583
61. Ábrahám N, Csapó E, Bohus G, Dékány I (2014) Interaction of biofunctionalized gold nanoparticles with model phospholipid membranes. Colloid Polym Sci 292:2715–2725
62. Li Y, Gu N (2010) Thermodynamics of charged nanoparticle adsorption on charge-neutral membranes: a simulation study. J Phys Chem B 114:2749–2754
63. Kettiger H, Québatte G, Perrone B, Huwyler J (2016) Interactions between silica nanoparticles and phospholipid membranes. BBA Biomembr 1858:2163–2170
64. Li Y, Chen X, Gu N (2008) Computational investigation of interaction between nanoparticles and membranes: hydrophobic/hydrophilic effect. J Phys Chem B 112:6647–16653
65. Qiao R, Roberts AP, Mount AS, Klaine SJ, Ke PC (2007) Translocation of C60 and its derivatives across a lipid bilayer. Nano Lett 7:614–619
66. Mahmoudi M, Lynch I, Ejtehadi MR, Monopoli MP, Bombelli FB, Laurent S (2011) Protein-nanoparticle interactions: opportunities and challenges. Chem Rev 111:5610–5637
67. De M, You CC, Srivastava S, Rotello VM (2007) Biomimetic interactions of proteins with functionalized nanoparticles: a thermodynamic study. J Am Chem Soc 129:10747–10753
68. Lindman S, Lynch I, Thulin E, Nilsson H, Dawson KA, Linse S (2007) Systematic investigation of the thermodynamics of HSA adsorption to *N*-iso-propylacrylamide/*N*-tert-butylacrylamide copolymer nanoparticles. Effects of particle size and hydrophobicity. Nano Lett 7:914–920
69. Boulos SP, Davis TA, Yang JA, Lohse SE, Alkilany AM, Holland LA, Murphy CJ (2013) Article-protein interactions: a thermodynamic and kinetic study of the adsorption of bovine serum albumin to gold nanoparticle surfaces. Langmuir 29:14984–14996
70. Shang L, Wang Y, Jiang J, Dong S (2007) pH-dependent protein conformational changes in albumin: gold nanoparticle bioconjugates: a spectroscopic study. Langmuir 23:2714–2721
71. Vertegel AA, Siegel RW, Dordick JS (2004) Silica nanoparticle size influences the structure and enzymatic activity of adsorbed lysozyme. Langmuir 20:6800–6807
72. Gagner JE, Lopez MD, Dordick JS, Siegel RW (2011) Effect of gold nanoparticle morphology on adsorbed protein structure and function. Biomaterials 32:7241–7252
73. Hung A, Mwenifumbo S, Mager M, Kuna JJ, Stellacci F, Yarovsky I, Stevens MM (2011) Ordering surfaces on the nanoscale: implications for protein adsorption. J Am Chem Soc 133:1438–1450

74. Wu X, Narsimhan G (2008) Effect of surface concentration on secondary and tertiary conformational changes of lysozyme adsorbed on silica nanoparticles. BBA Proteomics 1784:1694–1701
75. Shao Q, Hall CK (2016) Protein adsorption on nanoparticles: model development using computer simulation. J Phys Condens Mater 28:414019
76. Voicescu M, Ionescu S, Angelescu DG (2012) Spectroscopic and coarse-grained simulation studies of the BSA and HSA protein adsorption on silver nanoparticles. J Nanopart Res 14:1–13
77. Tavanti F, Pedone A, Menziani MC (2015) Competitive binding of proteins to gold nanoparticles disclosed by molecular dynamics simulations. J Phys Chem C 119:22172–22180
78. Shen JW, Wu T, Wang Q, Kang Y (2008) Induced stepwise conformational change of human serum albumin on carbon nanotube surfaces. Biomaterials 29:3847–3855
79. Noon WH, Kong YF, Ma JP (2002) Molecular dynamics analysis of a buckyball-antibody complex. Proc Natl Acad Sci USA 99:6466–6470
80. Lj Liang, Wang Q, Wu T, Shen JW, Kang Y (2009) Molecular dynamics simulation on stability of insulin on graphene. Chin J Chem Phys 22:627–634
81. Chiu CC, Dieckmann GR, Nielsen SO (2008) Molecular dynamics study of a nanotube-binding amphiphilic helical peptide at different water/hydrophobic interfaces. J Phys Chem B 112:16326–16333
82. Chiu CC, Dieckmann GR, Nielsen SO (2009) Role of peptide-peptide interactions in stabilizing peptide-wrapped single-walled carbon nanotubes: a molecular dynamics study. Biopolymers 92:156–163
83. Shvedova AA, Kagan VE, Fadeel B (2010) Close encounters of the small kind: adverse effects of man-made materials interfacing with the nano-cosmos of biological systems. Annu Rev Pharmacol Toxicol 50:63–88
84. Moghimi SM, Hunter AC, Andresen TL (2012) Factors controlling nanoparticle pharmacokinetics: an integrated analysis and perspective. Annu Rev Pharmacol Toxicol 52:481–503
85. Prado-Gotor R, Grueso E (2011) A kinetic study of the interaction of DNA with gold nanoparticles: mechanistic aspects of the interaction. Phys Chem Chem Phys 13:1479–1489
86. Komarov PV, Zherenkova LV, Khalatur PG (2008) Computer simulation of the assembly of gold nanoparticles on DNA fragments via electrostatic interaction. J Chem Phys 128:124909
87. Akhlaghi Y, Kompany-Zareh M, Ebrahimi S (2015) Model-based approaches to investigate the interactions between unmodified gold nanoparticles and DNA strands. Sensor Actuators B Chem 221:45–54
88. Wu Y, Liu LK, Liang ZQ, Shen ZM, Zhu XL (2011) Colorimetric and electrochemical study on the interaction between gold nanoparticles and unmodified DNA. Curr Nanosci 7:359–365
89. Hurst SJ, Lytton-Jean AKR, Mirkin CA (2006) Maximizing DNA loading on a range of gold nanoparticle sizes. Anal Chem 78:8313–8318
90. Lazarus GG, Revaprasadu N, Lopez-Viota J, Singh M (2014) The electrokinetic characterization of gold nanoparticles, functionalized with cationic functional groups, and its' interaction with DNA. Colloids Surf B 121:425–431
91. Sun LP, Zhang ZW, Wang S, Zhang JF, Li H, Ren L, Weng J, Zhang QQ (2009) Effect of pH on the interaction of gold nanoparticles with DNA and application in the detection of human p53 gene mutation. Nanoscale Res Lett 4:216–220
92. Foley EA, Carter JD, Shan F, Guo T (2005) Enhanced relaxation of nanoparticl-bound supercoiled DNA in X-ray radiation. Chem Commun 3192–3194
93. Yang J, Lee JY, Too HP, Chow GM (2006) Inhibition of DNA hybridization by small metal nanoparticles. Biophys Chem 120:87–95
94. McIntosh CM, Esposito EA, Boal AK, Simard JM, Martin CT, Rotello VM (2001) Inhibition of DNA transcription using cationic mixed monolayer protected gold clusters. J Am Chem Soc 123:7626–7629

95. Wang Z, Fang H, Wang S, Zhang F, Wang DG (2015) Simulating molecular interactions of carbon nanoparticles with a double-stranded DNA fragment. J Chem 2015:1–6
96. Johnson RR, Johnson ATC, Klein ML (2008) Probing the structure of DNA-carbon nanotube hybrids with molecular dynamics. Nano Lett 8:69–75
97. Roxbury D, Mittal J, Jagota A (2012) Molecular-basis of single-walled carbon nanotube recognition by single-stranded DNA. Nano Lett 12:1464–1469
98. Albertorio F, Hughes ME, Golovchenko JA, Branton D (2009) Base dependent DNA-carbon nanotube interactions: activation enthalpies and assembly-disassembly control. Nanotechnology 20:395101
99. Qiu XY, Ke FY, Timsina R, Khripin CY, Zheng M (2016) Attractive interactions between DNA-carbon nanotube hybrids in monovalent salts. J Phys Chem C 120:13831–13835
100. Gladchenko GO, Karachevtsev MV, Leontiev VS, Valeev VA, Glamazda AY, Plokhotnichenko AM, Stepanian SG (2006) Interaction of fragmented double-stranded DNA with carbon nanotubes in aqueous solution. Mol Phys 104:3193–3201
101. Gao HJ, Kong Y, Cui DX, Ozkan CS (2003) Spontaneous insertion of DNA oligonucleotides into carbon nanotubes. Nano Lett 3:471–473
102. Xie YH, Kong Y, Soh AK, Gao HJ (2007) Electric field-induced translocation of single-stranded DNA through a polarized carbon nanotube membrane. J Chem Phys 127:225101
103. Pei QX, Lim CG, Cheng Y, Gao HJ (2008) Molecular dynamics study on DNA oligonucleotide translocation through carbon nanotubes. J Chem Phys 129:125101
104. Alshehri MH, Cox BJ, Hill JM (2012) Interaction of double-stranded DNA inside single-walled carbon nanotubes. J Math Chem 50:2512–2526
105. Xue TY, Cui XQ, Guan WM, Wang QY, Liu C, Wang HT, Qi K, Singh DJ, Zheng WT (2014) Surface plasmon resonance technique for directly probing the interaction of DNA and graphene oxide and ultra-sensitive biosensing. Biosens Bioelectron 58:374–379
106. Wang LJ, Tian JN, Huang Y, Lin XW, Yang W, Zhao YC, Zhao SL (2016) Homogenous fluorescence polarization assay for the DNA of HIV A T7 by exploiting exonuclease-assisted quadratic recycling amplification and the strong interaction between graphene oxide and ssDNA. Microchim Acta 183:2147–2153
107. He Y, Jiao BN, Tang HW (2014) Interaction of single-stranded DNA with graphene oxide: fluorescence study and its application for S1 nuclease detection. RSC Adv 4:18294–18300
108. Zhang H, Huang H, Lin ZH, Su XG (2014) A turn-on fluorescence-sensing technique for glucose determination based on graphene oxide-DNA interaction. Anal Bioanal Chem 406:6925–6932
109. Lee J, Yim Y, Kim S, Choi MH, Choi BS, Lee Y, Min DH (2016) In-depth investigation of the interaction between DNA and nano-sized graphene oxide. Carbon 97:92–98
110. Wang QS, Yang L, Fang TT, Wu S, Liu P, Min XM, Li X (2011) Interactions between CdSe/CdS quantum dots and DNA through spectroscopic and electrochemical methods. Appl Surf Sci 257:9747–9751
111. Xu Q, Wang JH, Wang Z, Yin ZH, Yang Q, Zhao YD (2008) Interaction of CdTe quantum dots with DNA. Electrochem Commun 10:1337–1339
112. Stanisavljevic M, Chomoucka J, Dostalova S, Krizkova S, Vaculovicova M, Adam V, Kizek R (2014) Interactions between CdTe quantum dots and DNA revealed by capillary electrophoresis with laser-induced fluorescence detection. Electrophoresis 35:2587–2592
113. Anandampillai S, Zhang X, Sharma P, Lynch GC, Franchek MA, Larin KV (2008) Quantum dot-DNA interaction: computational issues and preliminary insights on use of quantum dots as biosensors. Comput Methods Appl Mech Eng 197:3378–3385
114. Mahtab R, Sealey SM, Hunyadi SE, Kinard B, Ray T, Murphy CJ (2007) Influence of the nature of quantum dot surface cations on interactions with DNA. J Inorg Biochem 101: 559–564

115. Li MY, Li J, Sun L, Zhang XL, Jin WR (2012) Measuring interactions and conformational changes of DNA molecules using electrochemiluminescence resonance energy transfer in the conjugates consisting of luminol, DNA and quantum dot. Electrochim Acta 80:171–179
116. Hu XF, Zhang XL, Jin WR (2013) Applications of electrochemiluminescence resonance energy transfer between CdSe/ZnS quantum dots and cyanine dye (Cy5) molecules in evaluating interactions and conformational changes of DNA molecules. Electrochim Acta 94:367–373

Chapter 6
Surface Engineering: Incorporation of Bioactive Compound

Muhammad Kashif Riaz, Deependra Tyagi and Zhijun Yang

Abstract Surface engineering facilitates incorporation of various bioactive compounds and provides unique advantages for the specific delivery of imaging and therapeutic agents. Several molecules with imaging, diagnostic, prognostic, sensing, and therapy can be incorporated in the bioformulations with the help of different surface engineering techniques. This chapter reviews drug carriers which were surface engineered for targeted drug delivery at the requisite location. A single or combination of surface engineering has been used for efficient delivery of carriers. The carriers reviewed here were divided into two categories: lipid-based carriers (liposomes and solid lipid nanoparticles) and non-lipid-based carriers (niosomes, polymeric nanoparticles, hydrogels, dendrimers, quantum dots, gold nanoparticles, and mesoporous silica nanoparticles). Various kinds of bioactive compounds along with the involvement of surface engineering techniques in incorporation were also discussed. This chapter focuses on recent advances in the surface engineering of nanocarriers for therapeutic applications.

Keywords Surface engineering · Lipid carriers · Non-lipid carriers · Liposomes · Active targeting · Solid lipid nanoparticles · Niosomes · Polymeric nanoparticles · Hydrogels · Dendrimers · Quantum dots · Gold nanoparticles · Mesoporous silica nanoparticles

6.1 Introduction

Surface engineering plays a pivotal role in preparation of nanocarriers. It involves the utilization of synthetic or natural biomaterials for advancement and amenability of biological function, i.e., targeted drug delivery system. The need for new biological materials and novel technologies arises the requirement of surface engi-

M.K. Riaz · D. Tyagi · Z. Yang (✉)
School of Chinese Medicine, Hong Kong Baptist University,
7 Baptist University Road, Kowloon Tong, Hong Kong
e-mail: yzhijun@hkbu.edu.hk

B. Yan et al. (eds.), *Bioactivity of Engineered Nanoparticles*,
Nanomedicine and Nanotoxicology, DOI 10.1007/978-981-10-5864-6_6

neering. It helps in construction of molecular design, easy synthesis, and tailoring broad range of applications. Surface engineering has the ability to manipulate biological interfaces and precise the arrangement with the modification of surface according to the need and requirement, for the development of well-controlled bioformulations.

Three most important approaches for surface modifications are: direct deposition, incorporation, and encapsulation. Direct deposition means the filming of a bioactive compound directly on the surface of a nanocarrier. Whereas, in incorporation various bioactive compounds are integrated in between the surface layer of the nanocarrier using suitable surface modification techniques. Though, enclosing a bioactive compound in a nanocarrier, i.e., the addition of a bioactive compound inside a nanocarrier is called encapsulation. Therefore, the encapsulation of a bioactive compound in a nanocarrier means to encapsulate/surround a bioactive compound inside a nanocarrier, i.e., liposomes. Here in this chapter, we focused on the incorporation of bioactive compound in nanocarriers for drug delivery.

In current healthcare practice, especially in chemotherapy drug toxicity is an important factor for consideration. A conventional drug given to a patient affects both normal and diseased tissues. To decrease the adverse effects on normal tissues, targeting of the diseased tissues can be achieved via surface engineered targeted drug carriers. Many drug carriers, i.e., liposomes, solid lipid nanoparticles (SLNs), niosomes, polymeric nanoparticles (PNPs), hydrogels, dendrimers, quantum dots, gold nanoparticles (AuNPs), and mesoporous silica nanoparticles (MSNPs) have been developed, which include surface engineering for controlled release with enhancement of drug potency [1–4].

Here, we have categorized drug carriers into two classes, i.e., lipid-based and non-lipid-based carriers and further describes the surface engineering involved in the incorporation of bioactive compounds in these carriers. The difference between these two carriers is explained as follows. Lipid carriers are made up of lipid molecules and form a vesicle or certain structure to carry the desired biomolecules load. Liposomes and solid lipid nanoparticles are the examples of lipid-based carriers. Liposomes have phospholipid bilayers and contain incorporated drugs. Solid lipid nanoparticles have a solid lipid matrix with drug embedded in the matrix or adsorbed on the surface [2]. Non-lipid nanocarriers are those carriers which are composed of materials other than lipids such as nonionic surfactants, polymers, etc. Niosomes have nonionic surfactant bilayers and contain incorporated drugs. Polymeric nanoparticles are composed of natural or synthetic polymers and hydrogels are gels made of hydrophilic polymers. Dendrimers are synthetic polymeric macromolecules. Quantum dot is composed of a semiconductor material.

Applications of lipid-based nanocarriers have an advantage of least toxicity and drug safety. Lipid-based delivery systems include micelles, liposomes, solid lipid nanoparticles, nanoemulsions, and nanosuspensions. Lipid-based nanocarriers are a class of biocompatible and biodegradable vehicles. It provides advanced delivery of therapeutic and imaging agents, with improved pharmacokinetics. In this category, the most extensively studied drug carrier is liposome. A number of non-lipid-based nanocarrier formulations have also been described in terms of incorporation of

bioactive compound and their formulation with respect to surface engineering. Most of the non-lipid-based carriers are studied to improve the oral, intranasal, and central nervous system delivery of analgesic agents. This part includes niosomes, polymeric nanoparticles, hydrogels, dendrimers, quantum dots, gold nanoparticles, and mesoporous silica nanoparticles.

6.2 Lipid-Based Nanocarriers

6.2.1 Liposomes

Alec Bangham, the father of liposomes described them for the first time in 1965. First they were called as Banghasomes [5] but later were called as liposomes [6]. Phospholipid is ampiphilic in nature and has hydrophilic head with two hydrophobic fatty acid chains. They form multilamellar vesicles (MLVs) on the hydration of phospholipid film and the hydration is done above the phase transition temperature of the phospholipid. Cholesterol is added to lipid mixture to toughen the liposomes. The presence of charge on the liposomes provides physical stability to liposomes. The addition of DOTAP (1,2-dioleoyl-3-trimethylammoniuum-propane chloride) to lipid mixture provides +ve charge to liposomes. Cationic liposomes are used for the loading of −ve charged nucleic acids. Liposomes can be giant unilamellar vesicles (GUVs), multilamellar vesicles (MLVs), large unilamellar vesicles (LUVs), and small unilamellar vesicles (SUVs). The size range is >1000, >500, >100, and 20–100 nm for GUVs, MLVs, LUVs, and SUVs respectively. LUVs are now used for the drug delivery studies [7, 8].

The extrusion of MLVs through polycarbonate filters generates LUVs. The sonication of MLVs gives SUVs. LUVs are obtained by solvent injection, detergent removal, reverse phase evaporation [7]. The following techniques can be used for the large-scale production of liposomes [7, 9]:

- Microfluidization [10, 11]
- Spray drying [12]
- Freeze drying/lyophilisation [13]
- Super critical reverse phase evaporation (SCRPE) method [14]

Liposomes applications for targeted drug delivery include the incorporation of bioactive compounds, i.e., anticancer, antibiotic, antifungal, and anti-inflammatory drugs and genes where comes the role of surface engineering. Figure 6.1 illustrates the role of surface engineering to formulate different types of liposomes. In general, biomaterials can be incorporated in liposome by active or passive loading. The surface properties of bioactive materials dictate the final application of liposomes.

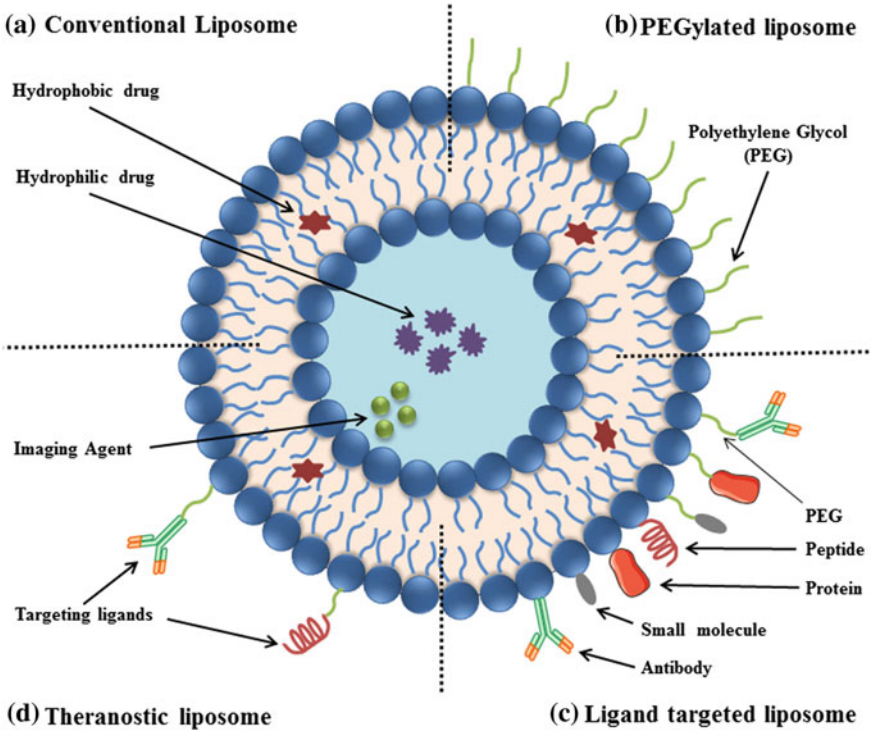

Fig. 6.1 Different types of liposomes. **a** Conventional liposome. **b** PEGylated liposome. **c** Ligand-targeted liposome for specific targeting (ligands may be antibodies, peptides, etc). **d** Theranostic liposome contains an imaging agent such as Gd-DOTA-DSPE for MRI and a therapeutic drug such as paclitaxel which is a hydrophobic anticancer drug

6.2.1.1 Stealth Liposomes/PEGylated Liposomes

Stealth liposomes are the liposomes which show extended blood circulation time while reducing mononuclear phagocyte system uptake. Advancement of liposomal preparation based on lipid composition, size, and charge of the vesicle modulate it into long-circulating liposomes. Inclusion and incorporation of the synthetic polymer poly-(ethylene glycol) (PEG) in liposome composition has developed stealth liposomes (see Fig. 6.1). Further, by synthetic modification of the terminal PEG molecule, stealth liposomes can also be actively targeted with monoclonal antibodies or ligands and incorporation of these active molecules provide high target efficiency and activity. PEG is the universally used polymer for improvement of circulation time among the different polymers investigated to data.

Different surface engineering are involved in the incorporation of PEG on the liposomal surface but the most widely used method is the use of cross-linked lipid, i.e., PEG-distearoyl-phospha-tidylethanolamine (DSPE). Poly(ethylene glycol)-linked phospholipids such as DSPE-PEG 2000 or methoxy PEG 2000-DSPE are

commercially available for the preparation of stealth liposomes. DSPE is a synthetic amphiphilic phospholipid. The role of phospholipid portion in poly(ethylene glycol)-linked phospholipid needs to be investigated. Therefore, non-phospholipid-PEGs such as Cholesteryl-PEG (Chol-PEG) are also being developed for the preparation of stealth liposomes [15]. An FDA approved liposomal doxorubicin preparation Doxil® contains stealth liposomes composed of cholesterol, hydrogenated soybean phosphatidylcholine (HSPC), and methoxy PEG 2000-DSPE [16].

Other surface modifications involved are: physical adsorption of the polymer onto the surface of the vesicles, incorporating of PEG-lipid conjugate during liposome preparation, or by covalently attaching reactive groups onto the surface of preformed liposomes.

6.2.1.2 Immunoliposomes

Immunoliposomes are liposomes in which antibodies or their fragments are conjugated onto the surface. The surface modification with antibody increases the therapeutic index of many drugs via targeted drug delivery and controlled release of drugs. Two strategies are involved in coupling of antibody to the liposome surface. One involves covalent cross-linking with a liposomal lipid while another involves incorporation of chemically modified antibody into the bilayer by increasing hydrophobicity of the antibody. These approaches can attach a wide variety of antibodies to various types of liposomes.

For covalent cross-linking, first derivatization of the free amino group of phosphatidlyethanolamine (PE) with amino reactive bifunctional crosslinking molecules have been employed. This modified PE is combined with the bulk lipid to form liposomes. Later approach requires chemical modification of the antibody molecule with a hydrophobic substituent which increases the hydrophobicity of the antibody and hence, increases the affinity for the liposomal bilayer.

Nowadays, PEGlyated antibodies are used for targeted delivery. The lipid is usually cationic such as DOTAP (1,2-dioleoyl-3-trimethylammoniuum-propane chloride) which is added to lipid mixture to provide +ve charge to liposomes. See Fig. 6.2 for structure of DOTAP. A solution of +ve charged lipid along with a helper neutral lipid such as dioleoylphosphatidylcholine (DOPC) is mixed with gene material/nucleic acid which have −ve charge such as DNA. A +ve charged complex between nucleic acid and lipid is formed which is called as lipoplex. Cationic lipids are usually used in the delivery of genes but anionic lipids such as phosphatidic acid can also be used in the presence of divalent metal ions such as Ca^{2+} [17]. Due to risk of inactivation of whole antibody during the chemical conjugation process, fragment antigen-binding (Fab′) or single-chain fragment variable (scFv) are used to get imunoliposomes. The latter are the smallest fragment of an antibody containing the complete antigen-binding site [18]. Immunoliposomes are used for the delivery of genes which include DNA [19, 20], plasmid-DNA [21, 22], and RNA-based therapeutics such as antisense oligonucleotides and small interfering ribonucleic acid (siRNA) [23, 24].

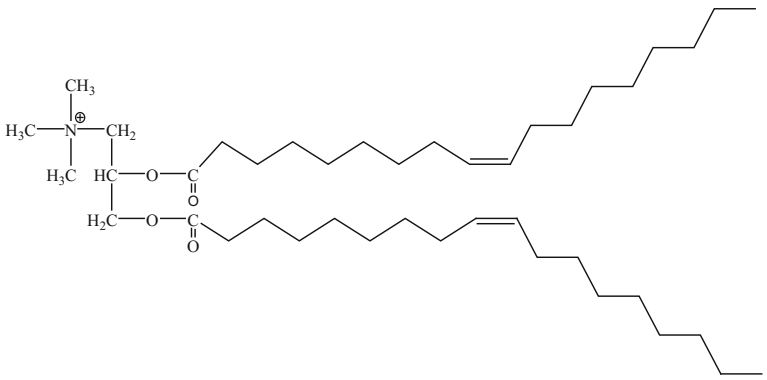

Fig. 6.2 Structure of DOTAP

Immunoliposomes are now extensively used to treat cancer cells in animal models. The targeting of immunoliposomes containing anticancer drugs at the overexpressed receptors in cancer cells resulted in the treatment of cancer. Transferrin receptors (TfRs) are overexpressed in cancers. An improved therapeutic activity was observed using TfR-targeted stealth immunoliposomes against liver cancer [25]. Cationic liposomes are used in the delivery of drugs to brain through blood–brain barrier [26, 27].

6.2.1.3 Multifunctional Liposomes: Theranostic Liposomes

Surface engineering plays a significant role in preparation of multifunctional liposomes and these are the advanced formulations of nanotechnology having simultaneous functions of diagnostics and therapeutics (theranostics) (see Fig. 6.1). Preparation of theranostic liposome requires the engagement of therapeutic, diagnostic, and imaging agent for defined targeted delivery of drugs which are toxic in free form. Theranostic liposomes are formed by correct utilization of surface engineering of the bilayers [28].

Surface engineered multifunctional liposomes containing UCNPs (lanthanide-doped up converting nanoparticles) and doxorubicin were prepared. UCNPs consisting of Er^{3+} and Yb^{3+} co-doped $NaGdF_4$ upon exposure to an excitation wavelength of 890 nm showed a decrease in emission signals (a quenching effect). This allows the monitoring of drug release and drug loading. It was suggested that these prepared liposomes have a potential as theranostic nanocarriers [29]. A theranostic liposomal drug delivery system was reported with paclitaxel, carboplatin loaded as therapeutic agents and Gd-DTPA-BMA as contrast agent for MRI. These liposomes have prolonged circulation time and 36 times higher T_1 relaxation-rate as compared to a commercial MRI contrast agent (Omniscan). These theranostic liposomes can carry both hydrophilic and hydrophobic drugs for lung cancer treatment with significant reduction in toxicity. The biodistribution of drugs was imaged via

T_1-weighted MRI in real time while drug delivery was achieved by the use of targeted tandem chemotherapy. The study offers new possibilities such as the evaluation of therapeutic response by in vivo imaging via T_1-weighted MRI [30].

6.2.1.4 Active Loading or Remote Loading of Bioactive Compounds in Liposomes

Passive drug loading in liposomes means loading of drug in the process of formation of liposomes. Conventional liposomes usually have low encapsulation efficiency. Active drug loading requires the modification of surface to enhance the encapsulation efficiency and drug loading was done on preformed liposomes which had a pH gradient. This is known as active or remote drug loading. For desired biomedical application of liposomes, covalent immobilization of bioactive compounds onto the surface plays a significant role. Active loading have several advantages, i.e., high specificity and efficiency. The method of surface functionalization varies according to the final application of liposome formulation. By using surface functionalization, several types of liposomes were prepared and each of them have distinct functions.

In this pH gradient was developed by adding amine solution or basic drug to liposomes in pH 4.0 citrate buffer. To generate a pH gradient, the pH of the external medium was raised to pH 8 [31]. This helps in the incorporation of therapeutic agent in liposomes. The loading of amphiphilic amines (catecholamines), amphipathic (amphiphilic) weak base drugs having amine groups, i.e., anthracyclines were incorporated by pH gradient. In liposomes formulation, i.e., Myocet®, DaunoXome®, doxorubicin drug was loaded by using pH gradient [31–34]. Ammonium sulfate gradient is another kind of gradient and here liposomes were prepared in 300 mM ammonium sulfate solution (pH 4.0). To create a gradient, the liposomes were dialyzed against pH 7.5 HEPES buffer or diluted in pH 7.5 HEPES buffer [33, 34].

6.2.1.5 Incorporation of Targeting Agents

Targeted delivery is the utmost requirement of today's research for effective chemotherapy. The aim is to provide required drug to the affected tissues. It is called active targeting of drugs. It involves the attachment of a ligand to the surface of drug carrier which detects and binds to the diseased cells [35]. Active targeting of drug leads to enhanced drug level at targeted site [36]. In active targeting, nanocarriers, i.e., liposomes are surface modified with specific targeting ligands. The ligand binds to overexpressed receptors on target cell surface. Commonly used ligands for active targeting of liposomes include antibodies, peptides, and small molecules [37, 38].

Nanocarriers can be incorporated covalently or non-covalently with a targeting ligand due to their flexible surface chemistry [39]. Ligands for active targeting have

been attached directly to lipids or attached covalently to distal end of PEG-chain [40]. Targeting ligand's optimal density on nanocarrier is also an important aspect of surface modification. High targeting ligand density in optimum range may increase binding at the target site. Issues like aggregation or raised cost may arise by increasing the ligand density beyond optimum range [41].

Targeting ligands provide better internalization of nanocarriers in tumor cells [39]. Ligand-mediated endocytosis plays a vital role in delivery of drugs and genetic materials, i.e., siRNA and oligonucleotide [41]. Active drug targeting has an added advantage of declining the nonspecific distribution to undesired tissues [36]. Therefore, active targeting plays an important role in efficacy and safety of treatment. Table 6.1 describes some examples of targeting ligands and their targeting sites along with their category and drug delivered with the site and type of cancer.

Peptides as Targeting Ligand

Peptides are short chains made up of amino acid monomers. Peptides are also used as targeting ligands for active drug targeting. A peptide, vasoactive intestinal peptide (VIP) has been used in active drug targeting [53]. A VIP-receptor is relatively a new target for active drug targeting. VIP-receptors are overexpressed in human breast and lung cancer cells [54, 55].

^{99}Tc-HMPAO encapsulated liposomes conjugated with VIP as targeting ligand has been developed for theranostic application. ^{99}Tc-HMPAO is a radiopharmaceutical and used as a diagnostic agent in liposomal formulation. Targeted delivery of VIP-conjugated ^{99}Tc-HMPAO in breast tumor model has shown significantly better uptake in breast cancer cells as compared to non-targeted liposomes [42]. VIP has shown no adverse effect on normal tissues mainly due to the fact that VIP-conjugated-carriers extravasates out at only leaky vasculature on disease site [56].

SP94 is another targeting peptide, used on a nanocarrier based on surface modified liposome called protocell. In protocell, a nanoporous silica core is encapsulated by lipid bilayer. The targeting peptide resulted in 10,000 folds higher binding affinity for hepatocellular carcinoma as compared to normal hepatocytes, in vitro [57].

Folate/Folic Acid as Targeting Ligand

Folate (folic acid) is a small-molecule targeting agent [36]. Folate receptors are overexpressed in various human tumors such as lung, breast, brain, colon, kidney, and ovarian cancers [58–60]. Folic acid exhibits high affinity for folate receptors and demonstrated better internalization in tumor cells [61]. Another important feature is folate-receptor location. They are located on apical-membrane of epithelial cells reducing the chances for entry of targeted nanocarrier into normal cells [58, 62].

Folic acid being a small molecule has several advantages over antibody ligands. The advantages include non-immunogenicity, nontoxicity, low cost, small size, and higher stability in preparation, storage, and circulation [63]. In folate receptor targeting of nanocarriers, off-target effect should also be considered [36].

Doxorubicin loaded folate-targeted liposomes have been formulated demonstrating 45-folds higher uptake as compared to non-targeted liposomes. Surface modified targeted liposomes demonstrated 85-folds higher cytotoxicity than

Table 6.1 Targeting ligands and targets for ligand-targeted liposomes in cancer treatment

Targeting moiety/ligand	Example	Diagnostic/therapeutic agents	Targeting site	Type of cancer	Refs.
Peptide	Vasoactive intestinal peptide (VIP)	^{99}Tc-HMPAO	Vasoactive intestinal peptide receptor (VIP-R)	Breast cancer	[42]
Small molecule	Folate	Doxorubicin	Folate receptors	Ascitic tumor	[43]
Small protein	HER2-specific affibody	Calcein	Human Epidermal Growth Factor Receptor 2 (HER2)	Breast cancer	[44]
	EGFR-specific affibody	Mitoxantrone	Epidermal growth factor receptor (EGFR)	Breast cancer	[45]
Aptamer	sgc8 aptamer	FITC-Dextran	protein tyrosine kinase 7 (PTK7)-receptor	Leukemia	[46]
	AS1411 derived aptamer	Cisplatin	Nucleolin (NCL)	Breast cancer	[47]
Antibody (fragment)	Fab′ fragments of cetuximab	Doxorubicin	Epidermal growth factor receptor (EGFR)	Breast cancer	[48]
	Anti-MT1-MMP Fab	Doxorubicin	Matrix metalloproteases (MMPs)	Cancer cells expressing MT1-MMPs i.e. fibrosarcoma	[49]
Antibody	Cetuximab	Oxaplatin	Epidermal growth factor receptor (EGFR)	Colorectal cancer	[50]
	Trastuzumab	Doxorubicin	Human Epidermal Growth Factor Receptor 2 (HER2)	Cancer cells over-expressing HER2 i.e. breast cancer	[51]
	Carbonic anhydrase IX (CA IX) Antibody	Docetaxel	Carbonic anhydrase IX (CA-IX)	Lung cancer	[52]

non-targeted liposomes [43, 64]. Folate conjugated liposomes having 5-fluorouracil or doxorubicin encapsulated have shown improved biodistribution as compared to unconjugated liposomes [65, 66].

Affisomes as Targeting Ligand

Affibody is a small molecule which has been considered as antibody mimics and used as targeting ligand for nanocarriers, i.e., liposomes. Affibodies are small proteins (approximately 8 kDa) having high stability and solubility. Affibodies are expressed in a bacterial system or produced by peptide synthesis. Affibodies have relatively higher binding affinity as compared to corresponding antibodies [67].

A research group has reported formulation of affisomes by surface modification of thermosensitive liposomes for breast cancer treatment. HER2-specific affibody having 8.3-kDa mass was conjugated to thermosensitive liposomes surface [44]. Similarly, EGFR-specific affibody having 14-kDa mass has been conjugated to PEGylated liposomes for the formulation of affisomes targeted at EGFR-expressing cells. Mitoxantrone loaded affisomes has shown increased cytotoxicity against EGFR-expressing cells [45].

Affibodies have different receptor-binding domains than antibodies that may result in altered outcome. Thus, further research is required to establish the advantage of using affibodies as targeting ligands for nanocarriers, i.e., liposomes [67].

Aptamers as Targeting Ligand

Aptamers are RNA or ssDNA oligonucleotides. They show high affinity and recognize target molecules by hydrogen bonding, electrostatic and hydrophobic interactions [68]. Aptamers have several advantages in their application as targeting ligand due to following reasons: smaller size, higher stability, simple synthesis method, easy modification and show high antigen recognition as compared to other ligands, i.e., nucleotide sequence which can be easily altered for better selectivity [69].

sgc8 aptamer-conjugated liposomes have been developed for leukemia. Liposomes were covalently linked to the aptamer using a PEG spacer. Aptamer-conjugated liposomes bound target cells and released the drug within 30 min after cell incubation [46]. A research group has reported aptamer-conjugated multifunctional liposomes encapsulating cisplatin as a therapeutic agent. AS1411 derived aptamer was used as a targeting ligand for cisplatin encapsulated multifunctional liposomes for targeted delivery in breast cancer. AS1411 derived aptamer due to its high binding affinity to nucleolin (NCL) has exhibited anti-proliferative activity in many tumor cell lines such as MCF-7. Therefore, AS1411 derived aptamer is a promising ligand for targeting of breast cancer [47].

Antibody as Targeting Ligand

Monoclonal antibody (mAb) is a promising ligand for active targeting of drugs using a nanocarrier. The surface modification of a nanocarrier can be done with whole antibody or fragment of mAb, enhancing cellular uptake at the diseased site [36]. Use of antibody fragments i.e. Fab (antigen-binding fragment) and ScFv

(single-chain variable fragment) not only reduces immunogenicity but also results in substantial size reduction of ligand favoring development of ligand-targeted nanocarriers [41].

Certain configuration should be maintained for antibody and peptide ligands to have the desired binding affinity. So, a high temperature or organic solvent during preparation should be used with caution [41].

The targeting moiety is attached to PEGylated liposomes to target overexpressed surface receptors, e.g., EGFR, HER 2, carbonic anhydrase IX or receptors in tumor vasculature such as VCAM 1, MT1-MMP.

Epidermal Growth Factor Receptor (EGFR)

EGFR immunoliposomes to target EGFR were prepared. The regression in breast cancer was observed compared to nontargeted liposomes [48]. EGFR targeted liposomes containing two anticancer drugs (oxaliplatin, a platinum derivative and cetuximab, a monoclonal antibody) were prepared. In a colorectal cancer (CRC) xenograft model, an increased drug delivery was observed for targeted formulation as compared to non-targeted liposomes [50].

Human Epidermal Growth Factor Receptor 2 (HER2)

HER2-targeted liposomes containing doxorubicin were developed. The liposomes also contained trastuzumab which targets signaling pathway of HER2. The results showed increased anti-tumorigenesis (inhibition of the development of a neoplasm) with no cardiotoxicity or cardiac dysfunction, while on the other hand conventional anthracycline based cancer therapy is associated with cardiac toxicity [51].

Carbonic Anhydrase IX (CA IX)

CA IX is overexpressed due to hypoxia in cancers such as lung cancer [70]. In a study, anti-carbonic anhydrase immunoliposomes containing docetaxel showed growth inhibition in CA IX positive lung cancer cells as compared to free drug or non-targeted drug containing liposomes. The prepared liposomes have an encapsulation efficiency of $\sim$85% and $\sim$144 nm size [52]. In a review, the potential of targeted CA IX immuoliposomes to deliver anticancer drugs to cancer cells in vivo has been discussed [70].

Vascular Cell Adhesion Molecules (VCAMs)

VCAMs play roles in atherosclerosis (cholesterol or fatty deposition in the arteries) and inflammation. VCAM 1 is overexpressed on cancer vessels [68]. In a study the delivery of anti-inflammatory drugs by liposomes was investigated. Anti-VCAM 1 liposomes were prepared by the coupling of 'Fab' with liposomes containing celecoxib (used to treat inflammation) [71].

Matrix Metalloproteases (MMPs)

Several MMPs (enzymes) particularly membrane-type MT1-MMP are involved in angiogenesis (formation of new blood cells) [72]. MT1-MMPs are expressed on cancer cells and angiogenic endothelium cells. Doxorubicin liposomes with 'Fab' fragments were prepared. The fragments were used as targeting ligands against

MT1-MMP. An enhanced uptake of the liposomes was observed in HT 1080 cancer cells with highly expressed MT1-MMP compared with non-targeted liposomes [49]. In another study, MMP sensitive liposomes were prepared containing: (a) PEG coating, (b) monoclonal antibody (mAb 2C5) for specific targeting to cancer cells, (c) matrix metalloprotease 2-sensitive bond which cleaves in tumor, and (d) cell penetrating peptide such as TATp [73].

6.2.1.6 Stimuli-Sensitive Surface Engineered Liposomes and Their Benefits in Drug Release

Stimuli or triggers have been used to release drugs. The stimuli may be external such as magnetic field or local such as pH. The latter utilizes the local environment of the target/tumor site while the former use an external stimulus such as heat, ultrasound or light [74].

pH Sensitive Liposomes

These liposomes release their drug loads at the acidic environments of tumors. The tumor tissues and inflamed areas have low pH than normal tissues [75].

Various approaches were tried to get pH-sensitive liposomes. In one approach, a pH-sensitive bond (hydrazone bond; $=C=N-NH_2$) was inserted between PEG and bilayer. Such liposomes are stable at neutral pH but release their contents in the acidic environments [75]. In a second approach, fusogenic peptides such as glutamic acid-alanine-leucine-alanine (GALA) were incorporated in liposomes. Such liposomes do not fuse to cells at pH 7.4 but at lower pH fuse into cells and release their contents [76, 77]. In another approach, poly 2-propylacrylic acid (PPAA) based cationic (DOTAP) liposomes were prepared for the delivery of antisense oligonucleotides. PPAA is pH-sensitive hydrophobic polymer. The aim was to silence genes in A2780 human ovarian cancer cells. It was hoped that this system could also be used for the delivery of plasmid-DNA, aptamer, or siRNA [78].

Liposomes containing overexpressed hyaluronic acid (HA) receptors and doxorubicin were reported. These liposomes were also pH-sensitive. In vitro studies showed a higher release in mild acidic conditions than at pH 7.4. Further enhanced antitumor activity was observed in cancer cells with high levels of CD44 than non-targeted liposomes [79].

Temperature Sensitive Liposomes

Thermosensitive liposomes are stable at body temperature but release their contents when temperature is raised. The presence of lysolipids increase permeability in the bilayers. Doxorubicin liposomes containing a lysolipid (10%) were prepared. An increased drug release was observed on producing mild hyperthermia (39–40 °C) [80].

These can be prepared by use of a temperature sensitive polymer. In a study, doxorubicin loaded liposomes containing both temperature sensitive polymer poly (*N*-isopropylacrylamide) pNiPAAm and pH sensitive polymer 2-propylacrylic acid

(PAA) were prepared. The drug was released in the acidic environment of tumors. The drug release was further enhanced by the use of heat which was generated by focussed ultrasound at the specific (cancer) site [81]. Temperature sensitive liposomes containing gadolinium (Gd-DTPA) for MRI and an aptamer (TSLs-AS1411) for specific targeting against cancer cells were developed. At 42 °C, liposomes released gadolinium at the cancer site which was easily detected by MRI. It was suggested that these liposomes could be used for the early detection of cancer [82]. In a study, paclitaxel loaded temperature sensitive liposomes were prepared. The particle size was ~100 nm and encapsulation efficiency was ~95%. The phase transition temperature of the liposomes was 42 °C which was determined by differential scanning calorimetry. At 42 °C, the drug release was higher than at 37 °C [83].

Magnetic Liposomes

These become magnetized on the application of an external magnetic field. This produces instability in the bilayers resulting in the release of drug. In a study, liposomes containing magnetite (Fe_3O_4, ferriferous oxide) and doxorubicin showed enhanced release of the drug in the tumor due to the application of an external magnetic field of 0.4 T strength [84]. Folate receptor targeted magnetic liposomes loaded with doxorubicin were prepared. The site-specific drug release was observed on the application of alternating magnetic field due to the presence of magnetized particles and hyperthermia produced [85]. Super magnetic cationic liposomes containing anticancer drug paclitaxel showed enhanced drug delivery to the brain of rats. The vesicles were of uniform diameter (20 nm). It was concluded that cationic magnetic liposomes are potential vehicles for the delivery of drugs to the brain [27].

6.2.2 Solid Lipid Nanoparticles (SLNs)

The nanoparticle has a solid lipid matrix. The drug is in the matrix or adsorbed on the surface of the nanoparticle [2]. For hydrophilic drugs, cold homogenization technique is usually used to get SLNs. This technique is also suitable for thermosensitive drugs by dispersing of lipids in the cold aqueous dispersion medium. Hot homogenization technique is used for lipophilic and insoluble drugs. High pressure homogenization at a temperature above the lipids melting point gives o/w emulsion, which gives SLNs after cooling at room temperature [86]. They can also be prepared by supercritical fluid (SCF) technology. SLNs are carriers for drugs, peptides (i.e., cyclosporine A—a cyclic peptide which is an immunosuppressant), proteins (i.e., bovine or human serum albumin BSA/HAS), and antigens (i.e., hepatitis B surface antigen). They are usually administered by IV route and can also be delivered by other routes, i.e., oral, pulmonary, and nasal and transdermal [87].

Their surface can be PEGylated to increase blood circulation time. PEGylated SLNs (having stearic acid lipid core) formulations of methotrexate (MTX) has been

reported. The formulations were further evaluated with the help of 99mTc radionuclide. The kinetic studies showed longer blood circulation times for the formulations. SPECT imaging showed efficient tumor uptake of SLNs. The characterization of these nano particles was also done. The particle size found was about 130 nm (via TEM and AFM) and zeta potential was about −34 mV [88]. In another study, paclitaxel (PTX) loaded SLNs (with trimyristin as a solid lipid core and pegylated phospholipid as a stabilizer) were evaluated for biodistribution in organs such as kidneys, heart, and lungs. It was found that the prepared PEGylated SLNs (containing paclitaxel) are similar to Taxol® (a commercial preparation for paclitaxel) because both showed similar biodistribution and circulation times [89].

SLNs have limitations which include low drug entrapment efficiency and possibility of drug degradation during hot dispersion technique. A new generation of SLNs is also known as nanostructured lipid carriers (NLCs) which are free from low drug entrapment efficiency. These have solid matrix with oil nano-compartments containing drug surrounded by a lipid shell. Due to the presence of the nano-compartments, NLCs have high drug loading capacity [2]. Docetaxel-loaded NLCs were produced where the anticancer drug was held in core. These NLCs showed more cytotoxicity than free docetaxel [90].

SLNs have several advantages. They can be called as alternate drug carriers because they can be used in place of liposomes. They can be sterilized by autoclaving or by γ irradiation. Surface modifications can be made to make SLNs site-specific. The ease of scale up to industrial scale production (particularly by hot dispersion technique) is due to the availability of the homogenization production lines for the production of emulsions in pharmaceutical industry. The cost of excipients is low. They can be lyophilized and also spray dried [86].

6.3 Non-lipid Nanocarriers

6.3.1 Niosomes

Niosomes are nonionic surfactant vesicles and, like liposomes, have bilayers. The nonionic surfactant has a polar head and a nonpolar chain (amphiphile). They are formed by the hydration of a nonionic surfactants film. Cholesterol (as rigidizing/stabilizing agent for the bilayer) is added to the nonionic surfactant. The surfactants are biodegradable, inexpensive, and relatively nontoxic. Niosomes are used as an alternate to liposomes as a drug delivery system. Like liposomes, they are multilamellar vesicles (MLVs), large unilamellar vesicles (LUVs), and small unilamellar vesicles (SUVs) and their methods of preparations are similar to those in liposomes. The preparation methods include thin film hydration, ether/alcohol injection, and reverse phase evaporation. The size reduction by extrusion is used to get LUVs.

Proniosomes as a dry product have been prepared which on hydration gives niosomes.

$$\text{Proniosomes} \xrightarrow{\text{Hydration}} \underset{\text{(aqueous dispersion)}}{\text{Niosomes}}$$

There are some differences between niosomes and liposomes. A phospholipid has two nonpolar chains while nonionic surfactant has one nonpolar chain. Liposomes may be charged or neutral while niosomes are uncharged. Phospholipids can undergo oxidation and hydrolysis. Nonionic surfactants are comparatively chemically stable [86, 91–93].

The surface charge is important for the physical stability of niosomes. A charge is produced at the surface of neutral niosomes by the addition of −ve charged dicetyl phosphate, dihexadecyl phosphate or by the +ve charged stearylamine and cetyl pyridinium chloride. The surface charge is measured by zeta potential. As a rough rule, a value greater than 30 mV indicates electrostatic stability while 5–15 mV values indicate limited flocculation and 3–5 mV indicate maximum aggregation. Cationic niosomes containing DC-Cholesterol (+ve charged cholesterol) showed good physical stability and were used for the delivery of genes. A complex is formed between cationic niosomes and −ve charged genes, which helps in the gene transfer [92, 94].

Niosomes have been used for the treatment of various diseases [92]. They are readily taken up by the RES system. They have been successfully used to treat leishmaniasis where parasites attack liver and spleen. Niosomes containing sodium stibogluconate (an antileishmaniasis agent) successfully treated leishmaniasis in mice [95]. Metformin (an oral hypoglycaemic agent) loaded niosomes using Span 40 and Span 60 nonionic surfactants were prepared for oral administration. The best sustained release formulation contained cholesterol and surfactant in equal molar ratio. It was suggested that the sustained release metformin niosomes are useful for the treatment of Type II diabetes [92]. Isoniazid containing niosomes were prepared for the treatment of tuberculosis. The −ve charge was given to niosomes by the use of dicetylphosphate. The drug uptake (about 62%) by macrophage J744 A was observed. The formulations showed decreased drug toxicity and better patient compliance [96]. Niosomes containing paclitaxel (anticancer drug) were prepared for oral administration. The formulations were slow released and formulation with span 40 showed stability against trypsin, chymotrypsin, and pepsin (GIT enzymes) [97]. Niosomes have been used as a topical drug delivery system because of increased drug penetration, sustained drug release, and increased drug stability. In a review, the role of niosomes in dermatology has been discussed [98].

All surface modifications done on liposomes to achieve the goal of targeted drug delivery can be easily done on niosomes. PEGylation of niosomes increase their circulation times. Niosomes containing PEG 4400 and glucose conjugates were used for targeting overexpressed glucose receptors in a carcinoma model. Improved targeting of encapsulated paramagnetic agent such as gadolinium was observed using MRI [99]. Niosomes containing anticancer mitoxantrone and pH sensitive PEG-PMMI-CholC6 copolymer were prepared. The niosomes were more cytotoxic against cancer cell lines (ovarian and breast) than conventional niosomes [100].

6.3.2 *Polymeric Nanoparticles*

The nanoparticle has a polymeric matrix. The drug is dissolved or dispersed in the matrix or adsorbed on the surface of polymeric nanoparticles (PNPs) [2]. See Fig. 6.3 schematic differences between solid lipid nanoparticle (SLN), polymeric nanoparticle (PNP), nanocapsule and nanostructured lipid carrier (NLC). Solid lipid nanoparticle (SLN) and polymeric nanoparticle (PNP) have different matrix, i.e., lipid solid and polymeric matrix. Similarly, nanocapsule and nanostructured lipid carrier (NLC) have different composition of shell, i.e., polymeric and lipid shell. They are made of natural hydrophilic polymer (proteins such as albumin, gelatin, lectins, and polysaccharides such as chitosan, dextran, and alginate) or synthetic hydrophobic polymers. The synthetic polymers are either pre-polymerized polymer such as poly lactic acid (PLA), poly E-caprolactone (PECL) or a polymer which is further polymerized during the process of nanoparticle formation. The latter compounds include poly isobutylcyanoacylate (PICA) which is a monomer [86].

Since few synthetic polymers are nontoxic, this limits their use as drug carriers. Poly alkyl cyanoacrylate (PACA) is a biodegradable and nontoxic monomer [86].

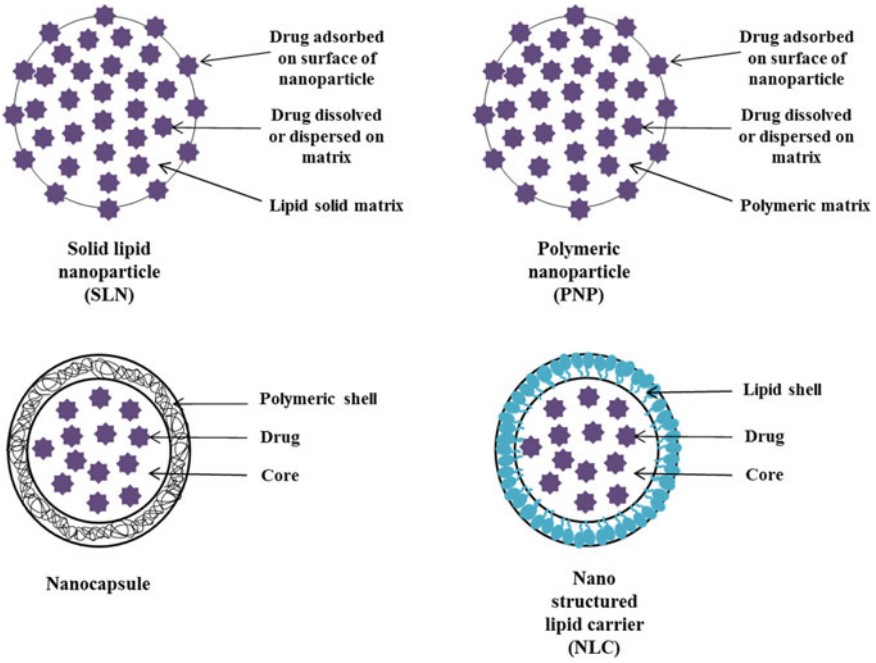

Fig. 6.3 Schematic differences between solid lipid nanoparticle (SLN), polymeric nanoparticle (PNP), nanocapsule and nanostructured lipid carrier (NLC). Solid lipid nanoparticle (SLN) and polymeric nanoparticle (PNP) have different matrix i.e. lipid solid and polymeric matrix. Similarly, nanocapsule and nanostructured lipid carrier (NLC) have different composition of shell i.e. polymeric and lipid shell

Depending upon the polymerization medium, PACA monomers can be polymerized to give various types of nanocarriers such as nanoparticles, nanospheres, and nanocapsules. These can carry a variety of drugs. PACA first appeared in 1979. A review on PACA nanoparticles was published 33 years later (in 2012) by Georgi Yordanov to show their importance as drug carriers. It was suggested to prepare multifunctional PACA-based nanoparticles (for improved drug action) containing a drug, a contrast agent for biodistribution imaging study and a drug stabilizer. These nanoparticles should be decorated with targeting moieties for active drug targeting at the overexpressed receptors [101]. Polysaccharide conjugated PACA nanoparticles have been formulated in aqueous-medium through redox-radical-emulsion polymerization. Drugs, i.e., doxorubicin can be loaded on surface of such nanoparticles by adsorption [102]. PACA nanospheres have been prepared by zwitterionic polymerization. PACA nanospheres were covalently attached with PEG-chains. Polymerization was done at low pH in the presence of PEG or methoxy PEG [103]. Further clinical trials should be initiated for already developed PEGylated nanoparticles particularly for oral and topical use because of lesser danger of systemic toxicity by these routes [101].

PACA nanoparticles containing doxorubicin showed better drug uptake by cancer cells than free drug. It was also found that these doxorubicin containing PACA nanoparticles were also effective in multidrug resistant (MDR) cancer [104]. Stealth/PEG-coated injectable PACA nanoparicles can be prepared by the use of poly (MePEG cyanoacrylate-*co*-alkyl cyanoacrylate) copolymer [105]. By modifying PACA nanoparticles surface with polysorbate 80 surfactant, the particles can be targeted into brain because these surface modified particles first adsorb apolipoproteins from plasma and then cross brain endothelium through endothelial cells [101]. Nanoparticle-mediated drug delivery to brain is based on coating of nanoparticles with polysorbates, i.e., polysorbate-80. Drugs may be adsorbed or chemically attached to the nanoparticle surface [101]. Another research group has used polylactic acid (PLA) instead of PACA and reported formulation of PLA (Polylactic acid) nanoparticles coated with polysorbate-80 for targeted delivery to brain. Suspension of surfactant-free nanoparticles (SFNPs) was prepared by modified nano-precipitation method. Suspension was prepared by dissolving PLA in acetonitrile and then transferring the solution slowly into 50% ethanol. Suspension was slowly transferred to water with shaking. Surplus water and organic solvents were removed in a vacuum evaporator. Addition of FITC-dextran was done in formulation of SFNPs and incubation was done for 24 h. After this step, Polysorbate-80 was added into formulation and incubation was done for another 24 h. The weight ratio between Polysorbate-80, FITC-dextran, and nanoparticles was 10:1:10. The experimentation involved preparation of two controls, FITC-dextran-loaded nanoparticles and polysorbate-coated nanoparticles. The controls were prepared in similar way as PLA-nanoparticles, only without addition of Polysorbate-80 and FITC-dextran, respectively [106].

Inhalable effervescent doxorubicin containing nanoparticles based on polybutyl cyanoacrylate (monomer) have been reported for curing lung cancer in mice and it

was suggested that this noninvasive route for the administration of anticancer drugs might be useful in the treatment of lung cancer [107].

Polyethylene glycol 100 stearate (PEG-100S) coated SLNs containing levothyroxine (a drug to treat hypothyroidism) were reported with development of an oral drug delivery system for hydrophobic drugs. Electron microscopy showed that the coated SLNs were spherical while photon correlation spectroscopy showed a size of about 187 nm. Differential Scanning Calorimetry (DSC) showed that the nanoparticles were in amorphous state, a state that is appropriate for drug delivery. A reduction in zeta potential from −40 to −23 mV occurred due to PEG coating. A controlled drug release from these nanoparticles was observed due to surface modification by PEG. A comparison of drug release from PEG-coated SLNs and uncoated SLNs has been illustrated in in vitro drug release plot. The plot has shown slow drug release from PEG-coated SLNs due to covering effect of coating layer. PEG coating reduces burst release effect because levothyroxine adsorbed on lipid surface was slowly released from PEG-coated SLNs. In fact, coating layer of PEG provides resistance against diffusion of levothyroxine leading to reduced drug release [108].

6.3.3 Hydrogels

Natural or synthetic hydrophilic polymers in water form a three-dimensional cross-linked mesh or network which can entrap drugs, proteins, peptides, monoclonal antibodies, etc. Due to high affinity for water absorption, they have soft consistency. The cross-links help to keep their physical integrity in the presence of water [109]. Physical integrity of hydrogels is maintained by physical and/or chemical cross-links. Physical crosslinks include tie-points and junctions; while, chemical cross-links includes entanglements and crystallites. Chemical crosslinks provide integrity and network structure to hydrogels [109, 110]. Hydrogels, particularly stimuli-sensitive, (pH and enzyme sensitive) are used as an oral drug delivery system because of the controlled release of entrapped drug to a specific site within GIT [109]. Recently, multi-responsive hydrogels have also been developed which release their contents on the application of more than one stimulus (temperature, electric or magnetic field, pH, etc). Hydrogels are finding use in targeted drug delivery, controlled drug release and soft contact lens, wound repair, targeted cell growth/tissue engineering [111]. By the use of osteoblasts (cells from which bone develops) and alginate hydrogel, an improved bone formation was observed [112].

Hydrogels may be classified on the basis of charge as neutral, amphiphilc, cationic, or anionic. They are also classified on the basis of source such as synthetic, natural, or hybrid made from both natural and synthetic polymers. Another classification is based on the bonding such as covalent bonding or non-covalent bonding. The latter are usually weak attraction forces like hydrogen bonding. pH-responsive hydrogels may be cationic or anionic hydrogels [109].

Natural polymers, alginate, and chitosan have been extensively used for the oral delivery of drugs using hydrogels. Alginate, a linear polysaccharide (anionic

polymer from sea weed) forms a mesh or gel due to reaction between −ve charged G blocks of the polymer (the polymer is made of alternate G blocks and M Blocks) and Ca^{2+} ions. Chitosan (cationic polymer) has amino groups on the polymer which are pH sensitive. At low pH, groups are protonated and are dissolved easily. Due to pH response, chitosan hydrogels have been used for the delivery of drugs to stomach [109].

Paclitaxel-loaded chitosan-based temperature-sensitive hydrogel system was developed for the local treatment of cancer by Biosyntech Inc., Canada. The system consists of chitosan-solution neutralized with b-glycerophosphate, liquid at room temperature but becomes gel at the body temperature. Hydrogel containing paclitaxel was formulated by pouring chitosan-solution on sterilized paclitaxel powder and stirring for 4 h. The mixture was then mixed with glycerophosphate solution. The hydrogel formulated contained 6.4% (w/v) paclitaxel. One intratumoral injection of the hydrogel showed controlled drug delivery for a period of over 30 days and was effective as four Taxol® IV injections against cancer cells (EMT-6) in mice [113]. In another study insulin containing chitosan hydrogels were developed. The sustained release of insulin was observed over a period of 21 days. The gel forming material chitosan/glycerol-phosphate was solution at room temperature, but once injected inside the body by injection it becomes gel [114].

β-Cyclodextrin (*β*-CD, a biopolymer) based multifunctional supramolecular (supramolecular chemistry is based on weak interaction forces to hold groups of molecules together) hydrogel was prepared where *β*-CD acts as a host by forming a cavity where guest molecule PNIPAAm binds. It contained *β*-CD dimmers and PNIPAAm whose chains were modified with light-sensitive azobenzene groups. *β*-CD is commonly used as a host molecule in supramolecular hydrogel formation while other compounds such as crown ethers can also be used for this purpose [111, 115]. Poly(*N*-isopropyl acrylamide) (PNIPAAm or pNIPAAM or PNIPAm) is a temperature-sensitive polymer which is hydrophilic below 32 °C [116, 117]. See Fig. 6.4 for temperature sensitive hydrogel.

6.3.4 Dendrimers

Dendrimers are synthetic polymeric macromolecules that have three main parts: a small central core to which are attached branches or shells and the outermost shell/part is composed of surface groups. Overall, dendrimers have tree-like structure.

Polyamidoamine or PAMAM dendrimers are the most common dendrimers and have also been extensively studied. These were first introduced in 1978 by Fritz Vogtle. Their generations (G0 to G10) are now commercially available such as Starburst® dendrimers. They have akyl-diamine internal core such as ethylene diamine (2 carbon core) and 1, 4-diaminobutane (4 carbon core) and with repetitive amidoamine branches or tertiary amine branches and primary amine surface groups. They are becoming spherical and by fourth generation they are three-dimensional

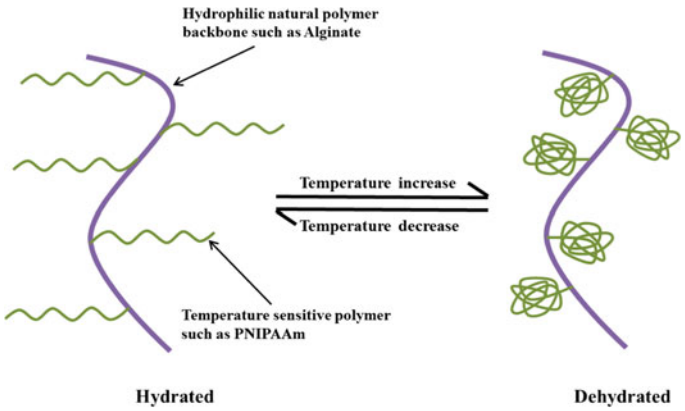

Fig. 6.4 Temperature sensitive hydrogel where a temperature sensitive polymer i.e. PNIPAAm (poly(*N*-isopropyl acrylamide) is grafted on hydrophilic natural polymer i.e. alginate backbone. On heating at >32 °C, the hydrogel collapses due to phase transition of PNIPAAm from swollen to shrunken state

spheres. They are synthesized by repetitive polymerization and after fourth generation their dimensions can be precisely controlled. When we go to next generation, an increase in size, molecular weight, and number of end groups occurs, e.g., number of end groups increases from 4, 8, 16, 32, and 64 respectively when we go from G0 to G1, G2, G3, and G4. The end groups may be same such as amine group. Dendrimers with different functional end groups such as hydroxyl, carboxyl, etc., are also available. A second generation means two shells outside the central core with more surface groups than first generation. Dendrimers, because of the void spaces, has been used as vehicles/carriers for nano drug delivery. Various routes of administration such as oral, parenteral, local have been tried [118–124].

The increased bioavailability of pilocarpine was observed when the drug containing PAMAM dendrimer (with carboxyl or hydroxyl surface groups) eye drops were instilled to the eyes of New Zealand albino rabbit. The study showed the ability of surface modified dendrimers as ocular controlled drug delivery vehicle [125]. Lee et al. [126] conjugated doxorubicin with biodegradable polystyrene dendrimers and found to be effective in the treatment of C-26 colon carcinoma in mice. The long circulation time (half life about 16 h) was achieved through PEGylation. The antitumor effect was similar to equal dose of liposomal doxorubicin injection Doxil® [126]. Amphotericin B (AmB) is an antifungal agent but its use is limited due to its poor water solubility and nephrotoxicity. In a study, its solubility increased in the presence of a third-generation PAMAM dendrimer. The study showed that the drug binding inside dendrimers is responsible for its sustained release [127]. Dendrimers have the ability to cross blood–brain barrier. In a review, the latest research opportunities and challenges in the production of various dendrimers (PAMAM, PPI, and PLL) for the diagnosis and treatment of brain tumor have been discussed [128]. A multifunctional dendrimer may contain one

anticancer drug, targeting ligands for overexpressed receptors such as EGFR and a diagnostic agent say for MRI imaging (gadolinium) or gamma imaging(a radionuclide) [121].

6.3.5 Quantum Dots

Quantum dot is composed of a semiconductor material. For medical applications, commonly used quantum dots (QD's) are cadmium selenide (CdSe), zinc sulfide (ZnS), cadmium telluride (CdTe), indium phosphide (InP), and indium arsenide (InAs). They are fluorescent, spherical nanoparticles or nanocrystals of 2–10 nm size which emit light strongly than fluorescent compounds (organic dyes such as eosin). The surface of QD's can be PEGylated to increase circulation times. They can be made site-specific by linking suitable ligands [129].

A single quantum dot conjugated to HER2 MAb (monoclonal antibody) has helped in the location of tumors in mice. In vivo, QD's were followed by the use of confocal microsocope fitted with a high-speed camera [130, 131]. Quantum dots can be incorporated in nano-drug-carriers such as liposomes but long term toxicity particularly in disease state needs to be addressed [132].

QD's as drug carriers have been reported. QD's surface is coated with an amphiphilic polymer. The hydrophobic compound, i.e., QD capping compound tri-*n*-octylphosphine oxide (TOPO) can be placed between quantum dot internal core and the polymer. The hydrophilic therapeutics, i.e., oligodeoxynucleotide (ODN), siRNA are attached to the polymer surface. To the polymer surface, various ligands (aptamers, antibody, and peptide) can also be attached for site-specific targeting. Targeting moieties can be immobilized on hydrophilic portion of amphiphilic polymer by covalent or non-covalent bond. siRNA and peptide have been conjugated to QDs in parallel manner. Targeting ligands, e.g., peptides were prepared and simultaneously linked to QD-surface.

Small interfering RNA containing QD's have been used to silence genes. The co-transfection of quantum dot and siRNA was done by the use of lipofectamine (a transfection reagent) [133, 134]. In a review, quantum dot preparation, their toxicity, quantum dots as probes and as carriers for targeted delivery have been discussed [135].

6.3.6 Gold Nanoparticles

Gold nanoparticles of different sizes can be prepared by reduction of gold salts in presence of suitable stabilizing agents. Stabilizing agent prevents agglomeration of gold nanoparticles. Many research groups have reported formulation of gold nanoparticles with functional moieties. Functional moieties are anchored with thiolinkers in monolayers of gold nanoparticles. Gold sol (colloidal suspension)

containing gold nanoparticles is prepared by the reduction of gold salt such as chloroauric acid ($HAuCl_{4)}$ by a reducing agent such as sodium borohydride ($NaBH_4$) in the presence of appropriate stabilizing agent such as a surfactant, cetyl trimethylammonium bromide (CTAB). In the absence of a stabilizing agent, agglomeration of nanoparticle occurs. Since CTAB is toxic, a thiol capping agent dodecanethiol (a capping agent prevents the growth of nanoparticle) is generally used in its place which also attaches thiol (–SH) groups to the surface of gold particles by forming stable Au:S bonds. Gold particles obtained by this method has 1.5–6 nm diameter and are soluble in nonpolar solvents. The reduction with sodium citrate gives particles of 15–150 nm size [136, 137].

Gold nanoparticles can successfully deliver large biomolecules such as nucleic acids, i.e., RNA or DNA, proteins and peptides, etc [136]. A research group has fabricated DNA-binders through anchoring β-cyclodextrin on periphery of modified oligo(ethylenediamino) gold nanoparticles. The modified gold nanoparticles successfully delivered plasmid-DNA into MCF-7 breast tumor cells [138]. Thiol (–SH) modification of nucleic acid strands has been done for grafting on nanoparticles. A research group has reported conjugation of thiolated-siRNA (SH-siRNA) with gold nanoparticles for cellular delivery [139]. A study has demonstrated gold nanoparticles as carriers of insulin. Gold nanoparticles were stabilized with chitosan. Chitosan-coated gold nanoparticles adsorb insulin on the surface and have been effective in oral delivery of insulin [140].

Based on the surface modification requirement, gold nanoparticle formulations vary in shape and size for different therapeutic applications. Depending upon the method of preparation, various gold nano-forms are produced such as nanospheres, nanorods, nanoshells, and nanocages. Gold nanoshells (50–150 nm) usually have silica core with thin layer of gold, however, pure gold nanoshell can also be prepared. Gold nanorods are 25–45 nm long. Gold nanorods are prepared from chloroauric acid with a gold-seed and a stabilizer, i.e., cetyltrimethylammonium bromide (CTAB). It was found that gold particles with less than 5–6 mm size show enhanced kidney clearance. For drug delivery use, spherical gold nanoparticles are used. The drug is conjugated to the nanoparticles [136, 137]. Further gold cores are nontoxic and biocompatible. Gold nanoparticles can be incorporated into a larger drug carrier such as liposomes for increased diagnostic, therapeutic, and imaging applications. Multifunctional gold particles have also been developed.

To prepare functional nanoparticles, gold nanoparticles are PEGylated to increase circulation times and then various ligands can be attached via thiol-PEG monolayer [141]. Covalent grafting of thiolated-polyethylene glycol (mPEG-SH) was done on gold nanoparticle surface. Thiolated-polyethylene glycol solution was added to citrate-capped gold nanoparticles solution with stirring. Stirring of solution was done for approximately 1 h allowing exchange of citrate-ligands with mPEG-SH. Centrifugation at 15,000 rpm was done for approximately 45 min to remove excessive mPEG-SH. PEG covalently attaches to gold nanoparticles because thiol groups have strong affinity for gold. Colloidal solution obtained was stable for many months [142].

Gold particles have enhanced absorption and scattering of light in near infrared range (NIR), 650–950 nm upon exposure to a near NIR laser source. This property of gold particle is finding use in the diagnosis and treatment of cancer. On exposure to laser source, the scattered light produces hyperthermia in cancer cells due to surface plasmon resonance effect [143]. In a study, a mouse was implanted subcutaneously with colon cancer cells. After IV administration of gold nanoshell-PEG conjugates, the accumulation of gold nanoshells within cancer cells resulted. On exposure to an 808 nm NIR laser, cancer was ablated due to heat [144]. The combined use of NIR laser thermal therapy and MRI imaging via gold nanoshells was effective in the treatment of breast cancer [145]. Since breast cancer is near the skin, the cancer can be easily treated by the limited use of NIR laser. It was concluded that gold particles provide an opportunity/commitment in the treatment of breast cancer [137].

Gold particles as a contrast agent in X-ray CT scans have been extensively studied. Gold nanoparticles provide superior images. They have longer circulation times than conventional iodine based contrast agents enabling prolonged imaging of specific cells [141]. In a study, PEG-coated AuNPs were injected to mice for X-ray CT scan. The scan could be recorded even after 24 h [146]. Gold nanoparticles coated with a Gadolinium chelator Gd-DTDTPA provided images for both CT scan and MRI [147]. van Schooneveld et al. [148] prepared gold/silica nanoparticles for CT scan, MRI, and fluorescent imaging.

6.3.7 Mesoporous Silica Nanoparticles

Mesoporous silica nanoparticles (MSNPs) have emerged as drug delivery devices around two decades ago. They have unique properties: large surface areas, large pore volumes, high loading capacity, biocompatibility, and tunability regarding size and pore diameter. First MSNP was Material MCM-41 (Mobil Composition of Matter no. 41) which was synthesized in Japan and later in the USA at Mobil Corporation. It had 2D hexagonal pore structure, ~60–100 nm size, pore diameter ~1.5–3.5 nm, surface area ~1000 $m^2\ g^{-1}$ and pore volume ~1 $cm^3\ g^{-1}$. The well-studied MSNPs include MCM-41 and SBA-15. The latter were produced at University of California, Santa Barbara and had pore size ~5–30 nm. MSNPs have surface silanol groups, i.e., free silanol group (≡Si–OH) and geminal silanol group ($=S(OH)_2$) which have affinity for head groups of phospholipids. Thus affinity for adsorbing on cell surfaces that finally leads to endocytosis (transport of substances into cells). The strong silicon-oxygen bonds provide stability to silica nanoparitcles and these are mechanically stable as compared to liposomes.

Surface modification of MSNPs is done by three methods: co-condensation, grafting, and imprint-coating method [149–152]. They are PEGylated to avoid uptake by the RES system. A research group has reported PEGylation of MSNPs. 25 mg MSNPs was dispersed in 30 ml of pH 4 HCl solution of ethyl-alcohol and water (volume ratio 1:2) with stirring. The solution was termed as solution-A.

Dissolution of 100 mg PEGxk-silane was done in 30 ml of ethyl-alcohol. The solution was termed as solution-B. A specific volume of solution-B was added dropwise in solution-A. The mixture of both solutions was vigorously stirred for 24-h and then dried at 100 °C for 12-h in vacuum. The experimentation gave covalently-PEGylated MSNPs [153]. Different ligands can be conjugated to the surface of MSNPs for site-specific targeting of drugs against overexpressed receptors such as Epidermal Growth Factor Receptors (EGFRs) in cancer cells. They are made of constituents such as tetraethyl orthosilicate (ETOS), a silica source and C16TAB (a surfactant) which are not costly. They are used for the controlled release of antibiotics, anti-inflammatory agents, etc. [149–152].

Stimuli-sensitive MSNPs have been developed for the delivery of drugs at specific sites. The stimuli include external (temperature, electric field, magnetic field, light) and internal (pH, redox potential, enzymes). The stimuli make drug carrier leaky, thereby drug is released at the desired site [154]. In a study, it was found that the combined use of photodynamic therapy using a photosensitizer (porphyrin) and lectin-targeted MSNPs containing anticancer drug (camptothecin) was very effective in the treatment of cancer [155]. Further the combined use of doxorubicin and siRNA employing MSNPs against the target (the P-glycoprotein drug transporter), showed more than 50% efficiency in treating multidrug resistant breast cancer than free drug alone in a xenograft model in mice [156].

6.4 Challenges and Limitations

The drug carriers are not without challenges and limitations. For example, liposomal preparations are advised to be stored at refrigeration temperature, not in a freezer to avoid disruption of lipid bilayers [157]. Solid lipid nanoparticles have low entrapment efficiency [2]. Quantum dots can be incorporated in nano drug carriers such as liposomes but long-term toxicity issue needs to be addressed [132]. A lot of research has been carried out on nanocarriers but more research is required for optimization of nanocarriers using cutting edge surface engineering techniques to tailor a nanocarrier for treatment of fatal diseases, i.e., cancer. In this regard, multifunctional nanocarriers obtained by surface modification of a nanocarrier with a targeting ligand, pro-drug, and imaging agent is the latest approach. Research on multifunctional nanocarriers should be focused for more efficient treatment of diseases. Each nanocarrier should be considered unique and must be individually evaluated. Systematic studies on various aspects of nanocarrier's surface modification need to be carried out before proceeding to clinical trials [158].

PEGylation has significantly improved circulation time of liposomes. PEGylation has reduced the liposomal uptake by RES but it does not completely inhibit liposomal uptake [159]. Liposomal uptake is also possible through pathways which are independent of opsonization suggesting more research on surface modification of liposomes for further increment in circulation time [160, 161]. Modification of liposomes by various synthetic components may lead to antibody

production against various components of liposomes, if recognized as a foreign particle by the body [162–164]. Some liposomal formulations trigger innate immune-response leading to hypersensitivity syndrome called complement activation-related pseudoallergy (CARPA) [165]. Development of new surface modification techniques can resolve the issues and have the potential to decrease immunogenic-reactions to liposome based treatment preventing their loss of efficacy, altered pharmacokinetics, and toxicity.

Impressive-progress has been made in preparation and targeting of nanoparticles for treatment of diseases but only few nanoparticle-based drugs are commercially available. This is due to following main reasons. Nanoparticles have low drug loading capacity, i.e., less than 5% drug with respect to nanocarrier weight. Burst release of drug after administration is another challenge, needs to be addressed. Burst release is rapid drug-fraction release of adsorbed or anchored drug from nanocarrier's surface leading to lower therapeutic response [166].

Hydrogels typically have higher water content resulting in rapid drug release from gel-matrix especially hydrophilic drugs. The drug release profile of hydrogels is usually shorter than some other nanocarriers. Sensitive molecules, e.g., antibody, proteins, and nucleic acid are deactivated by interaction with hydrogel. Similarly, hydrogel mediated delivery of hydrophobic drugs also requires improvement. Complexation or pre-encapsulation of biomolecules may be helpful in addressing these challenges [167].

Gold nanoparticle is a promising nanocarrier. However, challenges such as toxicity, biodistribution, and pharmacokinetics needs to be addressed [158]. Biodistribution of gold- nanoparticles is often affected by the route of administration. Therefore, nanomaterials should be properly characterized and in vivo studies can be carried out in animal models with apt statistical analysis [168]. Gold nanoparticles have low inherent toxicity [169]. More research on interaction of gold nanoparticles with tumor microenvironment should be done to reduce their toxicity by adapting suitable surface engineering techniques. Detection of toxicity of gold nanoparticle, i.e., core, capping agents and ligands is another research area, needs to be explored. Certain ligands attached to gold nanoparticles cause toxicity, e.g., cationic ligands leads to moderate toxicity [170].

Surface engineering has played a vital role in formulation and optimization of nanocarriers for better targeting, cellular-internalization (endocytosis), and therapeutic response. Surface engineering aided in addressing the challenges and limitations associated with nanocarriers. It can provide multifunctional properties to these nanocarriers, i.e., imaging, prognosis, diagnosis, and additionally theranostics. Research on surface modification and engineering based on the incorporation of desired bioactive compound to get anticipated results will lead to achieve a targeted drug and gene delivery with enhanced drug loading capacity and better cellular uptake for prolonged duration of action.

References

1. Khodabandehloo H, Zahednasab H, Hafez AA (2016) Nanocarriers usage for drug delivery in cancer therapy. Iran J cancer Prev 9(2):e3966
2. Calixto G, Fonseca-Santos B, Chorilli M, Bernegossi J (2014) Nanotechnology-based drug delivery systems for treatment of oral cancer: a review. Int J Nanomed 9:3719
3. Ruiz ME, Gantner ME, Talevi A (2014) Applications of nanosystems to anticancer drug therapy (Part II. Dendrimers, micelles, lipid-based nanosystems). Recent Pat Anticancer Drug Discov 9:99–128
4. Drbohlavova J, Chomoucka J, Adam V et al (2013) Nanocarriers for anticancer drugs–new trends in nanomedicine. Curr Drug Metab 14:547–564
5. Bangham AD, Standish MM, Watkins JC (1965) Diffusion of univalent ions across the lamellae of swollen phospholipids. J Mol Biol 13:238–252
6. Sessa G, Weissmann G (1968) Phospholipid spherules (liposomes) as a model for biological membranes. J Lipid Res 9:310–318
7. Pattni BS, Chupin VV, Torchilin VP (2015) New developments in liposomal drug delivery. Chem Rev 115:10938–10966
8. Madni MA, Sarfraz M, Rehman M et al (2014) Liposomal drug delivery: a versatile platform for challenging clinical applications. J Pharm Pharm Sci 17:401–426
9. Patil YP, Jadhav S (2014) Novel methods for liposome preparation. Chem Phys Lipids 177:8–18
10. Vemuri S, Yu C-D, Wangsatorntanakun V, Roosdorp N (1990) Large-scale production of liposomes by a microfluidizer. Drug Dev Ind Pharm 16:2243–2256
11. http://www.microfluidicscorp.com. Accessed 6 Apr 2016
12. Sollohub K, Cal K (2010) Spray drying technique: II. Current applications in pharmaceutical technology. J Pharm Sci 99:587–597
13. Chen C, Han D, Cai C, Tang X (2010) An overview of liposome lyophilization and its future potential. J Control Release 142:299–311
14. Karn PR, Cho W, Park HJ et al (2013) Characterization and stability studies of a novel liposomal cyclosporin a prepared using the supercritical fluid method: comparison with the modified conventional Bangham method. Int J Nanomed 8:365–377
15. Nag OK, Awasthi V (2013) Surface engineering of liposomes for stealth behavior. Pharmaceutics 5:542–569
16. http://www.rxlist.com/doxil-drug.htm
17. Balazs DA, Godbey W, Balazs DA, Godbey W (2011) Liposomes for use in gene delivery. J Drug Deliv 2011:1–12
18. Mirafzali Z Immunoliposomes. http://www.liposomes.org/2011/09/immunoliposomes.html
19. Fraley R, Subramani S, Berg P, Papahadjopoulos D (1980) Introduction of liposome-encapsulated SV40 DNA into cells. J Biol Chem 255:10431–10435
20. Fraley R, Straubinger RM, Rule G et al (1981) Liposome-mediated delivery of deoxyribonucleic acid to cells: enhanced efficiency of delivery related to lipid composition and incubation conditions. Biochemistry 20:6978–6987
21. Tan Y (2001) Sequential injection of cationic liposome and plasmid DNA effectively transfects the lung with minimal inflammatory toxicity. Mol Ther 3:673–682
22. Hoekstra SAD (2001) Cationic lipid-mediated transfection in vitro and in vivo. Mol Membr Biol 18:129–143
23. Straubinger RM, Papahadjopoulos D (1983) [32] Liposomes as carriers for intracellular delivery of nucleic acids. Methods Enzymol 101:512–527
24. Wyrozumska P, Meissner J, Toporkiewicz M et al (2015) Liposome-coated lipoplex-based carrier for antisense oligonucleotides. Cancer Biol Ther 16:66–76
25. Li X, Ding L, Xu Y et al (2009) Targeted delivery of doxorubicin using stealth liposomes modified with transferrin. Int J Pharm 373:116–123
26. Masserini M (2013) Nanoparticles for brain drug delivery. ISRN Biochem 2013:1–8

27. Zhao M, Chang J, Fu X et al (2012) Nano-sized cationic polymeric magnetic liposomes significantly improves drug delivery to the brain in rats. J Drug Target 20:416–421
28. Li S, Goins B, Zhang L, Bao A (2012) Novel multifunctional theranostic liposome drug delivery system: construction, characterization, and multimodality MR, near-infrared fluorescent, and nuclear imaging. Bioconjug Chem 23:1322–1332
29. Huang Y, Hemmer E, Rosei F, Vetrone F (2016) Multifunctional liposome nanocarriers combining upconverting nanoparticles and anticancer drugs. J Phys Chem B 120(22):4992–5001
30. Ren L, Chen S, Li H et al (2016) MRI-guided liposomes for targeted tandem chemotherapy and therapeutic response prediction. Acta Biomater 35:260–268
31. Mayer LD, Bally MB, Cullis PR (1986) Uptake of adriamycin into large unilamellar vesicles in response to a pH gradient. Biochim Biophys Acta Biomembr 857:123–126
32. Gubernator J (2011) Active methods of drug loading into liposomes: recent strategies for stable drug entrapment and increased in vivo activity. Expert Opin Drug Deliv 8:565–580
33. Fenske DB, Cullis PR (2007) Encapsulation of drugs within liposomes by pH-gradient techniques. In: Gregoriadis G (ed) Liposome technol. Entrapment drugs other mater into liposomes, 3rd edn. Informa Healthcare, New York, pp 27–50
34. Haran G, Cohen R, Bar LK, Barenholz Y (1993) Transmembrane ammonium sulfate gradients in liposomes produce efficient and stable entrapment of amphipathic weak bases. Biochim Biophys Acta 1151:201–215
35. Torchilin VP (2010) Passive and active drug targeting: drug delivery to tumors as an example. Springer, Berlin Heidelberg, pp 3–53
36. Lim SB, Banerjee A, Önyüksel H (2012) Improvement of drug safety by the use of lipid-based nanocarriers. J Control Release 163:34–45
37. Torchilin VP (2007) Micellar nanocarriers: pharmaceutical perspectives. Pharm Res 24:1–16
38. Joshi MD, Müller RH (2009) Lipid nanoparticles for parenteral delivery of actives. Eur J Pharm Biopharm 71:161–172
39. Benhabbour SR, Luft JC, Kim D et al (2012) In vitro and in vivo assessment of targeting lipid-based nanoparticles to the epidermal growth factor-receptor (EGFR) using a novel Heptameric Z EGFR domain. J Control Release 158:63–71
40. Patel JD, O'Carra R, Jones J et al (2007) Preparation and characterization of nickel nanoparticles for binding to his-tag proteins and antigens. Pharm Res 24:343–352
41. Feng L, Mumper RJ (2013) A critical review of lipid-based nanoparticles for taxane delivery. Cancer Lett 334:157–175
42. Dagar S, Krishnadas A, Rubinstein I et al (2003) VIP grafted sterically stabilized liposomes for targeted imaging of breast cancer: in vivo studies. J Control Release 91:123–133
43. Gabizon A, Tzemach D, Gorin J et al (2010) Improved therapeutic activity of folate-targeted liposomal doxorubicin in folate receptor-expressing tumor models. Cancer Chemother Pharmacol 66:43–52
44. Puri A, Kramer-Marek G, Campbell-Massa R et al (2008) HER2-specific affibody-conjugated thermosensitive liposomes (Affisomes) for improved delivery of anticancer agents. J Liposome Res 18:293–307
45. Beuttler J, Rothdiener M, Müller D et al (2009) Targeting of epidermal growth factor receptor (EGFR)-expressing tumor cells with sterically stabilized affibody liposomes (SAL). Bioconjug Chem 20:1201–1208
46. Kang H, O'Donoghue MB, Liu H, Tan W (2010) A liposome-based nanostructure for aptamer directed delivery. Chem Commun (Camb) 46:249–251
47. Cao Z, Tong R, Mishra A et al (2009) Reversible cell-specific drug delivery with aptamer-functionalized liposomes. Angew Chem Int Ed 48:6494–6498
48. Mamot C, Drummond DC, Noble CO et al (2005) Epidermal growth factor receptor-targeted immunoliposomes significantly enhance the efficacy of multiple anticancer drugs in vivo. Cancer Res 65:11631–11638
49. Hatakeyama H, Akita H, Ishida E et al (2007) Tumor targeting of doxorubicin by anti-MT1-MMP antibody-modified PEG liposomes. Int J Pharm 342:194–200

50. Zalba S, Contreras AM, Haeri A et al (2015) Cetuximab-oxaliplatin-liposomes for epidermal growth factor receptor targeted chemotherapy of colorectal cancer. J Control Release 210:26–38
51. Reynolds JG, Geretti E, Hendriks BS et al (2012) HER2-targeted liposomal doxorubicin displays enhanced anti-tumorigenic effects without associated cardiotoxicity. Toxicol Appl Pharmacol 262:1–10
52. Chi B, Wong K, Qin L (2014) Carbonic anhydrase IX-directed immunoliposomes for targeted drug delivery to human lung cancer cells in vitro. Dovepress, Auckland, pp 993–1001
53. Önyüksel H, Jeon E, Rubinstein I (2009) Nanomicellar paclitaxel increases cytotoxicity of multidrug resistant breast cancer cells. Cancer Lett 274:327–330
54. Moody TW, Gozes I (2007) Vasoactive intestinal peptide receptors: a molecular target in breast and lung cancer. Curr Pharm Des 13:1099–1104
55. Gespach C, Bawab W, De Cremoux P, Calvo F (1988) Pharmacology, molecular identification and functional characteristics of vasoactive intestinal peptide receptors in human breast cancer cells. Cancer Res 48:5079–5083
56. Koo OM, Rubinstein I, Onyuksel H (2005) Role of nanotechnology in targeted drug delivery and imaging: a concise review. Nanomed Nanotechnol Biol Med 1:193–212
57. Ashley CE, Carnes EC, Phillips GK et al (2011) The targeted delivery of multicomponent cargos to cancer cells by nanoporous particle-supported lipid bilayers. Nat Mater 10:389–397
58. Low PS, Antony AC (2004) Folate receptor-targeted drugs for cancer and inflammatory diseases. Adv Drug Deliv Rev 56:1055–1058
59. Elnakat H, Ratnam M (2004) Distribution, functionality and gene regulation of folate receptor isoforms: Implications in targeted therapy. Adv Drug Deliv Rev 56:1067–1084
60. Alexis F, Basto P, Levy-Nissenbaum E et al (2008) HER-2-targeted nanoparticle-affibody bioconjugates for cancer therapy. ChemMedChem 3:1839–1843
61. Leamon CP, Pastan I, Low PS (1993) Cytotoxicity of folate-Pseudomonas exotoxin conjugates toward tumor cells: contribution of translocation domain. J Biol Chem 268:24847–24854
62. Low PS, Kularatne SA (2009) Folate-targeted therapeutic and imaging agents for cancer. Curr Opin Chem Biol 13:256–262
63. Wu J, Liu Q, Lee RJ (2006) A folate receptor-targeted liposomal formulation for paclitaxel. Int J Pharm 316:148–153
64. Lee RJ, Low PS (1995) Folate-mediated tumor cell targeting of liposome-entrapped doxorubicin in vitro. BBA Biomembr 1233:134–144
65. Shmeeda H, Mak L, Tzemach D et al (2006) Intracellular uptake and intracavitary targeting of folate-conjugated liposomes in a mouse lymphoma model with up-regulated folate receptors. Mol Cancer Ther 5:818–824
66. Gupta Y, Jain A, Jain P, Jain SK (2007) Design and development of folate appended liposomes for enhanced delivery of 5-FU to tumor cells. J Drug Target 15:231–240
67. Puri A, Loomis K, Smith B et al (2009) Lipid-based nanoparticles as pharmaceutical drug carriers: from concepts to clinic. Crit Rev Ther Drug Carrier Syst 26:523–580
68. Deshpande PP, Biswas S, Torchilin VP (2013) Current trends in the use of liposomes for tumor targeting. Nanomedicine (Lond) 8:1509–1528
69. Edwards KA, Wang Y, Baeumner AJ (2010) Aptamer sandwich assays: human α-thrombin detection using liposome enhancement. Anal Bioanal Chem 398:2645–2654
70. Helena Ng HL, Lu A, Lin G et al (2014) The potential of liposomes with carbonic anhydrase IX to deliver anticancer ingredients to cancer cells in vivo. Int J Mol Sci 16:230–255
71. Il KD, Lee S, Lee JT et al (2011) Preparation and in vitro evaluation of anti-VCAM-1-Fab'-conjugated liposomes for the targeted delivery of the poorly water-soluble drug celecoxib. J Microencapsul 28:220–227
72. Handsley MM, Edwards DR (2005) Metalloproteinases and their inhibitors in tumor angiogenesis. Int J Cancer 115:849–860

73. Zhu L, Kate P, Torchilin VP (2012) Matrix metalloprotease 2-responsive multifunctional liposomal nanocarrier for enhanced tumor targeting. ACS Nano 6:3491–3498
74. Bibi S, Lattmann E, Mohammed AR, Perrie Y (2012) Trigger release liposome systems: local and remote controlled delivery? J Microencapsul 29:262–276
75. Torchilin VP (2014) Multifunctional, stimuli-sensitive nanoparticulate systems for drug delivery. Nat Rev Drug Discov 13:813–827
76. Li W, Nicol F, Szoka FC (2004) GALA: a designed synthetic pH-responsive amphipathic peptide with applications in drug and gene delivery. Adv Drug Deliv Rev 56:967–985
77. Yao L, Daniels J, Wijesinghe D et al (2013) PHLIP®-mediated delivery of PEGylated liposomes to cancer cells. J Control Release 167:228–237
78. Peddada LY, Garbuzenko OB, Devore DI et al (2014) Delivery of antisense oligonucleotides using poly(alkylene oxide)-poly(propylacrylic acid) graft copolymers in conjunction with cationic liposomes. J Control Release 194:103–112
79. Paliwal SR, Paliwal R, Agrawal GP, Vyas SP (2016) Hyaluronic acid modified pH-sensitive liposomes for targeted intracellular delivery of doxorubicin. J Liposome Res 2104:1–12
80. Mills JK, Needham D (2006) Temperature-triggered nanotechnology for chemotherapy: rapid release from lysolipid temperature-sensitive liposomes. Small 2:5–8
81. pH and Temperature Sensitive Polymer Modified Liposomes. http://www.bu.edu/medal/research/chemotherapy/. Accessed 11 May 2016
82. Zhang K, Liu M, Tong X et al (2015) Aptamer-modified temperature-sensitive liposomal contrast agent for magnetic resonance imaging. Biomacromolecules 16:2618–2623
83. Wang Z-Y, Zhang H, Yang Y et al (2016) Preparation, characterization, and efficacy of thermosensitive liposomes containing paclitaxel. Drug Deliv 23:1222–1231
84. Nobuto H, Sugita T, Kubo T et al (2004) Evaluation of systemic chemotherapy with magnetic liposomal doxorubicin and a dipole external electromagnet. Int J Cancer 109:627–635
85. Pradhan P, Banerjee R, Bahadur D et al (2010) Targeted magnetic liposomes loaded with doxorubicin. In: Weissig V (ed) Liposomes, vol 605. Methods molecular biology. Humana Press, New Jersey, pp 279–293
86. Vyas SP, Khar RK (2002) Nanoparticles. In: Targeted & controlled drug delivery. CBS Publishers & Distributors, New Delhi, pp 331–386
87. Almeida AJ, Souto E (2007) Solid lipid nanoparticles as a drug delivery system for peptides and proteins. Adv Drug Deliv Rev 59:478–490
88. Kakkar D, Dumoga S, Kumar R et al (2015) PEGylated solid lipid nanoparticles: design, methotrexate loading and biological evaluation in animal models. Med Chem Commun 6:1452–1463
89. Li R, Eun JS, Lee MK (2011) Pharmacokinetics and biodistribution of paclitaxel loaded in pegylated solid lipid nanoparticles after intravenous administration. Arch Pharm Res 34:331–337
90. Liu D, Liu Z, Wang L et al (2011) Nanostructured lipid carriers as novel carrier for parenteral delivery of docetaxel. Colloids Surf B Biointerfaces 85:262–269
91. Kuotsu K, Karim K, Mandal A et al (2010) Niosome: a future of targeted drug delivery systems. J Adv Pharm Technol Res 1:374
92. Sankhyan A, Pawar P (2012) Recent trends in niosome as vesicular drug delivery system. J Appl Pharm Sci 2:20–32
93. Niosome. https://en.wikipedia.org/wiki/Niosome
94. Huang Y, Yu F, Liang W (2010) Niosomal delivery system for macromolecular drugs. In: Fanun M (ed) Colloids in drug delivery. CRC Press, Boca Raton, pp 355–364
95. Baillie AJ, Coombs GH, Dolan TF, Laurie J (1986) Non-ionic surfactant vesicles, niosomes, as a delivery system for the anti-leishmanial drug, sodium stibogluconate. J Pharm Pharmacol 38:502–505
96. Singh G, Dwivedi H, Saraf SK, Saraf SA (2011) Niosomal delivery of isoniazid—development and characterization. Trop J Pharm Res 10:203–210

97. Taylor MJ, Tanna S, Sahota T (2010) In vivo study of a polymeric glucose-sensitive insulin delivery system using a rat model. J Pharm Sci 99:4215–4227
98. Hamishehkar H, Rahimpour Y, Kouhsoltani M (2013) Niosomes as a propitious carrier for topical drug delivery. Expert Opin Drug Deliv 10:261–272
99. Luciani A, Olivier J-C, Clement O et al (2004) Glucose-receptor MR imaging of tumors: study in mice with PEGylated paramagnetic niosomes. Radiology 231:135–142
100. Tila D, Yazdani-Arazi SN, Ghanbarzadeh S et al (2015) PH-sensitive, polymer modified, plasma stable niosomes: promising carriers for anti-cancer drugs. EXCLI J 14:21–32
101. Yordanov G (2012) Poly (alkyl cyanoacrylate) nanoparticles as drug carriers: 33 years later. Bulg J Chem 1:61–73
102. Alhareth K, Vauthier C, Gueutin C et al (2011) Doxorubicin loading and in vitro release from poly(alkylcyanoacrylate) nanoparticles produced by redox radical emulsion polymerization. J Appl Polym Sci 119:816–822
103. Zhang Y, Zhu S, Yin L et al (2008) Preparation, characterization and biocompatibility of poly(ethylene glycol)-poly(n-butyl cyanoacrylate) nanocapsules with oil core via miniemulsion polymerization. Eur Polym J 44:1654–1661
104. Vauthier C, Dubernet C, Chauvierre C et al (2003) Drug delivery to resistant tumors: the potential of poly(alkyl cyanoacrylate) nanoparticles. J Control Release 93:151–160
105. Peracchia MT, Desmae D, Couvreur P, Angelo J (1997) Synthesis of a novel poly (MePEG cyanoacrylate-co-alkyl cyanoacrylate) amphiphilic copolymer for nanoparticle technology. Macromolecules 30:846–851
106. Sun W, Xie C, Wang H, Hu Y (2004) Specific role of polysorbate 80 coating on the targeting of nanoparticles to the brain. Biomaterials 25:3065–3071
107. Roa WH, Azarmi S, Al-Hallak MHDK et al (2011) Inhalable nanoparticles, a non-invasive approach to treat lung cancer in a mouse model. J Control Release 150:49–55
108. Kashanian S, Rostami E (2014) PEG-stearate coated solid lipid nanoparticles as levothyroxine carriers for oral administration. J Nanoparticle Res 16(3):1–10
109. Sharpe LA, Daily AM, Horava SD, Peppas NA (2014) Therapeutic applications of hydrogels in oral drug delivery. Expert Opin Drug Deliv 11:901–915
110. Peppas NA, Bures P, Leobandung W, Ichikawa H (2000) Hydrogels in pharmaceutical formulations. Eur J Pharm Biopharm 50:27–46
111. Knipe JM, Peppas NA (2014) Multi-responsive hydrogels for drug delivery and tissue engineering applications. Regen Biomater 1:57–65
112. Augst AD, Kong HJ, Mooney DJ (2006) Alginate hydrogels as biomaterials. Macromol Biosci 6:623–633
113. Ruel-Gariépy E, Shive M, Bichara A et al (2004) A thermosensitive chitosan-based hydrogel for the local delivery of paclitaxel. Eur J Pharm Biopharm 57:53–63
114. Khodaverdi E, Tafaghodi M, Ganji F et al (2012) In vitro insulin release from thermosensitive chitosan hydrogel. AAPS PharmSciTech 13:460–466
115. Guan Y, Zhao H-B, Yu L-X et al (2014) Multi-stimuli sensitive supramolecular hydrogel formed by host–guest interaction between PNIPAM-Azo and cyclodextrin dimers. RSC Adv 4:4955–4959
116. Poly(N-isopropylacrylamide). https://en.wikipedia.org/wiki/Poly(N-isopropylacrylamide
117. Sun J, Tan H (2013) Alginate-based biomaterials for regenerative medicine applications. Materials (Basel) 6:1285–1309
118. Arseneault M, Wafer C, Morin J-F (2015) Recent advances in click chemistry applied to dendrimer synthesis. Molecules 20:9263–9294
119. Hannah H (2008) The role of dendrimers in topical drug delivery. Pharm Technol 32:88–98
120. Abbasi E, Aval S, Akbarzadeh A et al (2014) Dendrimers: synthesis, applications, and properties. Nanoscale Res Lett 9:247–256
121. Leiro V, Garcia JP, Tomás H, Pêgo AP (2015) The present and the future of degradable dendrimers and derivatives in theranostics. Bioconjug Chem 26:1185–1197
122. PAMAM Dendrimers. http://www.dendritech.com/pamam.html

123. PAMAM Dendrimers. http://www.sigmaaldrich.com/materials-science/material-science-products.html?TablePage=9539880
124. PAMAM Dendrimers. http://www.andrewschemservices.com/
125. Vandamme TF, Brobeck L (2005) Poly(amidoamine) dendrimers as ophthalmic vehicles for ocular delivery of pilocarpine nitrate and tropicamide. J Control Release 102:23–38
126. Lee CC, Gillies ER, Fox ME et al (2006) A single dose of doxorubicin-functionalized bow-tie dendrimer cures mice bearing C-26 colon carcinomas. Proc Natl Acad Sci USA 103:16649–16654
127. Jose J, Rn C (2016) Prolonged drug delivery system of an antifungal drug by association with polyamidoamine dendrimers. Int J Pharm Investig 6:123
128. Dwivedi N, Shah J, Mishra V et al (2016) Dendrimer-mediated approaches for the treatment of brain tumor. J Biomater Sci Polym Ed 5063:1–24
129. Krishnan SR, George SK (2014) Nanotherapeutics in cancer prevention, diagnosis and treatment. In: Gowder S (ed) Pharmacology and therapeutics. InTech, Rijeka. doi:10.5772/58419
130. Singh R, Lillard JW (2009) Nanoparticle-based targeted drug delivery. Exp Mol Pathol 86:215–223
131. Tada H, Higuchi H, Wanatabe TM, Ohuchi N (2007) In vivo real-time tracking of single quantum dots conjugated with monoclonal anti-HER2 antibody in tumors of mice. Cancer Res 67:1138–1144
132. Ghaderi S, Ramesh B, Seifalian AM (2011) Fluorescence nanoparticles "quantum dots" as drug delivery system and their toxicity: a review. J Drug Target 19:475–486
133. Qi L, Gao X (2008) Emerging application of quantum dots for drug delivery and therapy. Expert Opin Drug Deliv 5:263–267
134. Chen AA, Derfus AM, Khetani SR, Bhatia SN (2005) Quantum dots to monitor RNAi delivery and improve gene silencing. Nucleic Acids Res 33(22):e190
135. Yong KT, Wang Y, Roy I et al (2012) Preparation of quantum dot/drug nanoparticle formulations for traceable targeted delivery and therapy. Theranostics 2:681–694
136. Ghosh P, Han G, De M et al (2008) Gold nanoparticles in delivery applications. Adv Drug Deliv Rev 60:1307–1315
137. Lee J, Chatterjee DK, Lee MH, Krishnan S (2014) Gold nanoparticles in breast cancer treatment: promise and potential pitfalls. Cancer Lett 347:46–53
138. Wang H, Chen Y, Li X-Y, Liu Y (2006) Synthesis of oligo(ethylenediamino)-beta-cyclodextrin modified gold nanoparticle as a DNA concentrator. Mol Pharm 4:189–198
139. Oishi M, Nakaogami J, Ishii T, Nagasaki Y (2006) Smart PEGylated gold nanoparticles for the cytoplasmic delivery of siRNA to induce enhanced gene silencing. Chem Lett 35:1046–1047
140. Bhumkar DR, Joshi HM, Sastry M, Pokharkar VB (2007) Chitosan reduced gold nanoparticles as novel carriers for transmucosal delivery of insulin. Pharm Res 24:1415–1426
141. Mieszawska AJ, Mulder WJM, Fayad ZA, Cormode DP (2013) Multifunctional gold nanoparticles for diagnosis and therapy of disease. Mol Pharm 10:831–847
142. Rahme K, Chen L, Hobbs RG et al (2013) AuNP92-PEGylated gold nanoparticles: polymer quantification as a function of PEG lengths and nanoparticle dimensions. RSC Adv 3:6085
143. Huang X, Jain PK, El-Sayed IH, El-Sayed MA (2007) Gold nanoparticles: interesting optical properties and recent applications in cancer diagnostics and therapy. Nanomedicine (Lond) 2:681–693
144. O'Neal DP, Hirsch LR, Halas NJ et al (2004) Photo-thermal tumor ablation in mice using near infrared-absorbing nanoparticles. Cancer Lett 209:171–176
145. Hirsch LR, Stafford RJ, Bankson JA et al (2003) Nanoshell-mediated near-infrared thermal therapy of tumors under magnetic resonance guidance. Proc Natl Acad Sci USA 100:13549–13554

146. Cai Q-Y, Kim SH, Choi KS et al (2007) Colloidal gold nanoparticles as a blood-pool contrast agent for X-ray computed tomography in mice. Invest Radiol 42:797–806
147. Alric C, Taleb J, Le DG et al (2008) Contrast agents for both X-ray computed tomography and magnetic resonance imaging. J Am Chem Soc 130:5908–5915
148. Van Schooneveld MM, Cormode DP, Koole R et al (2010) A fluorescent, paramagnetic and PEGylated gold/silica nanoparticle for MRI, CT and fluorescence imaging. Contrast Media Mol Imaging 5:231–236
149. Slowing II, Vivero-Escoto JL, Wu C-W, Lin VSY (2008) Mesoporous silica nanoparticles as controlled release drug delivery and gene transfection carriers. Adv Drug Deliv Rev 60:1278–1288
150. Roggers R, Kanvinde S, Boonsith S, Oupický D (2014) The practicality of mesoporous silica nanoparticles as drug delivery devices and progress toward this goal. AAPS PharmSciTech 15:1163–1171
151. Kwon S, Singh RK, Perez RA et al (2013) Silica-based mesoporous nanoparticles for controlled drug delivery. J Tissue Eng 4(1):2041731413503357
152. Mesoporous silica. https://en.wikipedia.org/wiki/Mesoporous_silica
153. He Q, Zhang J, Shi J et al (2010) The effect of PEGylation of mesoporous silica nanoparticles on nonspecific binding of serum proteins and cellular responses. Biomaterials 31:1085–1092
154. Martínez-carmona M, Colilla M, Vallet-regí M (2015) Smart mesoporous nanomaterials for antitumor therapy. Nanomaterials 5:1906–1937
155. Gary-Bobo M, Hocine O, Brevet D et al (2012) Cancer therapy improvement with mesoporous silica nanoparticles combining targeting, drug delivery and PDT. Int J Pharm 423:509–515
156. Meng H, Mai WX, Zhang H et al (2013) Codelivery of an optimal drug/siRNA combination using mesoporous silica nanoparticles to overcome drug resistance in breast cancer in vitro and in vivo. ACS Nano 7:994–1005
157. JOINT FORMULARY COMMITTEE (2014) Section 8: malignant disease and immunosuppression. In: British National Formulary, 68th edn (Sep 2014–Mar 2015). BMJ Group and Pharmaceutical Press, London, pp 562–645
158. Arvizo R, Bhattacharya R, Mukherjee P (2010) Gold nanoparticles: opportunities and challenges in nanomedicine. Expert Opin Drug Deliv 7:753–763
159. Ishida T, Harashima H, Kiwada H (2001) Interactions of liposomes with cells in vitro and in vivo: opsonins and receptors. Curr Drug Metab 2:397–409
160. Laverman P, Carstens MG, Storm G, Moghimi SM (2001) Recognition and clearance of methoxypoly(ethyleneglycol)2000-grafted liposomes by macrophages with enhanced phagocytic capacity: Implications in experimental and clinical oncology. Biochim Biophys Acta Gen Subj 1526:227–229
161. Sawant RR, Torchilin VP (2012) Challenges in development of targeted liposomal therapeutics. AAPS J 14:303–315
162. Dams ET, Laverman P, Oyen WJ et al (2000) Accelerated blood clearance and altered biodistribution of repeated injections of sterically stabilized liposomes. J Pharmacol Exp Ther 292:1071–1079
163. Ishida T, Masuda K, Ichikawa T et al (2003) Accelerated clearance of a second injection of PEGylated liposomes in mice. Int J Pharm 255:167–174
164. Ishida T, Ichihara M, Wang X et al (2006) Injection of PEGylated liposomes in rats elicits PEG-specific IgM, which is responsible for rapid elimination of a second dose of PEGylated liposomes. J Control Release 112:15–25
165. Moghimi SM, Hunter C (2001) Capture of stealth nanoparticles by the body's defences. Crit Rev Ther Drug Carr Syst 18:24
166. Couvreur P (2013) Nanoparticles in drug delivery: past, present and future. Adv Drug Deliv Rev 65:21–23

167. Hoare TR, Kohane DS (2008) Hydrogels in drug delivery: progress and challenges. Polymer (Guildf) 49:1993–2007
168. Hillyer JF, Albrecht RM (2001) Gastrointestinal persorption and tissue distribution of differently sized colloidal gold nanoparticles. J Pharm Sci 90:1927–1936
169. Shukla R, Bansal V, Chaudhary M et al (2005) Biocompatibility of gold nanoparticles and their endocytotic fate inside the cellular compartment: a microscopic overview. Langmuir 21:10644–10654
170. Goodman CM, McCusker CD, Yilmaz T, Rotello VM (2004) Toxicity of gold nanoparticles functionalized with cationic and anionic side chains. Bioconjug Chem 15:897–900

Chapter 7
Riboflavin-Conjugated Multivalent Dendrimer Platform for Cancer-Targeted Drug and Gene Delivery

Pamela T. Wong, Kumar Sinniah and Seok Ki Choi

Abstract Riboflavin receptors (RFRs) are overexpressed in several malignant cells, and have been characterized as an emerging tumor surface biomarker. In this article, we discuss the design principles of a RFR-targeted nanoparticle system and illustrate its applications with studies performed in our laboratories. This system is based on a poly(amidoamine) (PAMAM) dendritic polymer which is modified on the surface by conjugation with riboflavin (RF) as the targeting ligand. First, we discuss the application of this system for targeted drug delivery by its conjugation with methotrexate as an antitumor payload. In cell-based experiments performed in vitro, this drug conjugate displayed RF-dependent, potent inhibition of cell growth in RFR(+) KB carcinoma cells. Second, the use of the RF-conjugated dendrimer for gene delivery applications through the formation of polyplexes with plasmid DNA is described. The ability of this targeted system to significantly enhance gene transfection in epithelial cells points to its potential as a promising new class of nonviral vectors. Third, the tunability of the functional properties of the dendrimer through modular integration is illustrated with an optically active gold nanoparticle (AuNP). The resultant dendrimer-coated AuNPs have a unique capability for tumor cell imaging via surface plasmon resonance scattering. Finally, we discuss the biophysical basis of the multivalent mechanism involved in the tight and specific binding of a RF-conjugated multivalent dendrimer to RFRs on the cell surface. The design principles and proof of concept studies presented here are

P.T. Wong (✉) · S.K. Choi (✉)
Michigan Nanotechnology Institute for Medicine and Biological Sciences,
and Department of Internal Medicine, University of Michigan Medical School,
Ann Arbor, MI 48109, USA
e-mail: ptw@med.umich.edu

S.K. Choi
e-mail: skchoi@med.umich.edu

K. Sinniah (✉)
Department of Chemistry and Biochemistry, Calvin College,
3201 Burton St. SE, Grand Rapids, MI 49546, USA
e-mail: ksinniah@calvin.edu

B. Yan et al. (eds.), *Bioactivity of Engineered Nanoparticles*,
Nanomedicine and Nanotoxicology, DOI 10.1007/978-981-10-5864-6_7

strongly supportive of the promising potential of RF-conjugated nanoparticles for delivery and imaging applications in tumors.

Keywords Riboflavin · Tumor surface marker · PAMAM dendrimer · Targeted delivery · Multivalent avidity · Surface plasmon resonance · Imaging cavity

Abbreviations

AFM	Atomic force microscopy
BSA	Bovine serum albumin
DAPP	3,8-Diamino-6-phenylphenanthridinium
DLS	Dynamic light scattering
EPR	Enhanced permeation and retention
EGFR	Epidermal growth factor receptor
FGFR	Fibroblast growth factor receptor
FAD	Flavin adenine dinucleotide
FMN	Flavin mononucleotide
FITC	Fluorescein isothiocyanate
FAR	Folate receptor
G5	Generation 5
AuNP	Gold nanoparticle
HPMA	*N*-(2-hydroxypropyl)methacrylamide
ITC	Isothermal titration calorimetry
MTX	Methotrexate
NP	Nanoparticle
pDNA	Plasmid DNA
PAMAM	Poly(amidoamine)
PSMA	Prostate-specific membrane antigen
RF	Riboflavin
RFBP	Riboflavin binding protein
RFR	Riboflavin receptor
SPR	Surface plasmon resonance

7.1 Introduction

Identification of tumor-associated surface markers plays a fundamental role in the design strategy for tumor-targeted nanoparticles (NPs) [1]. NP conjugation with a ligand molecule of high specificity for the particular biomarker of interest constitutes the basis for the mechanism of active tumor targeting [2, 3]. Optimal ligand conjugation design confers these NPs with a greater ability to facilitate tumor-specific NP binding and payload uptake than passive targeting mechanisms which rely solely on the enhanced permeation and retention (EPR) effect in which NPs accumulate in the tumor through the enhanced leakiness of tumor vasculature [4].

Several classes of tumor biomarkers have already been identified and used in the development of targeted NPs [1–3, 5]. These include: (1) receptors for vitamin uptake such as the folate receptor α, β (FAR_{α}, FAR_{β}) [6, 7], biotin receptor [8, 9]; (2) an integrin family of receptors such as $\alpha_v\beta_3$ [10]; (3) prostate-specific membrane antigen (PSMA) receptor [11, 12]; (4) growth factor receptors including HER2 [13], epidermal growth factor receptor (EGFR) [14], fibroblast growth factor receptor (FGFR) [15]; insulin receptors [16]; and (5) the transferrin receptor [17]. Each of these tumor biomarkers is overexpressed in one or more types of tumors and engages in receptor-mediated endocytosis [18], which serves as the specific route for the internalization of targeted NPs.

Riboflavin receptors (RFRs) belong to the class of vitamin uptake receptors which show promising potential for tumor-targeted applications [19, 20]. In an earlier study, Low et al. [21] investigated the cellular uptake mechanism of riboflavin (RF)-conjugated bovine serum albumin (BSA) in several human tumor cell lines. Uptake of this conjugate occurred at a rate greater than that of unmodified BSA, and the process was RFR-dependent and specific. Such facilitated protein uptake was attributed to RFR-mediated endocytosis, and highlighted the potential of using a RFR-targeted strategy for enhancing specific delivery. A research group led by Swaan, P.W. later also demonstrated the receptor-mediated uptake of a RF-rhodamine dye conjugated form [22, 23] in human cell lines.

Recently, we [24–28] and others [29–32] have started the development of RFR-targeted delivery platforms, and have conducted several proofs of concept studies in vitro and in vivo for their validation in tumor-targeted delivery. In this review article, we aim to describe our approaches in the design of RF-conjugated NPs, and provide several lines of evidence supportive of their significance and potential as a novel platform for tumor-targeted delivery. The purpose of this chapter is primarily to address the current lack of reviews and perspectives focused on RFR-targeted applications. Other established tumor biomarkers such as FARs [33, 34], integrin $\alpha_v\beta_3$ [10], PSMA receptor [35], HER2 [13, 36], and EGFR [14, 37] are already extensively reviewed elsewhere and thus are introduced only minimally here. We believe that this review provides a timely coverage of the various aspects important to RFR-targeted drug and gene delivery, and will serve as an invaluable resource in the design of RFR-targeted nanoplatforms.

7.2 Riboflavin Receptors and Ligands

In cellular metabolism, RF (vitamin B2) is required in the biosynthesis of flavin-based redox cofactors including flavin mononucleotide (FMN) and flavin adenine dinucleotide (FAD). However, its hydrophilicity ($\log P = -1.46$; P = partition coefficient = $[RF]_{octanol}/[RF]_{water}$) makes it unable to passively diffuse across hydrophobic cell membranes [38]. Thus, its cellular availability depends on the uptake mechanism mediated by its receptors.

Table 7.1 Properties of riboflavin receptors (RFRs)

Isoform	Biochemistry [40, 41]	Ligand	Tissue distribution
Soluble: riboflavin binding/carrier protein [45] Membrane-bound: riboflavin uptake transporter [23, 39, 40]	Glycosylated 219–469 Amino acids 27.5–40 kD_a	RF [41] Lumiflavin, Roseoflavin [47] Quinacrine [25]	Placenta [40], Small intestine [40], Breast [19, 39], Prostate [20], Liver [17], Cancer stem cells [43]

7.2.1 RFRs

A group of multiple proteins is involved in the cellular uptake of RF, consisting of RF carrier, RF transporter, and RF binding protein (RFBP). In this article, these proteins are collectively referred to as riboflavin receptors (RFRs) (Table 7.1). They are expressed as both soluble and membrane-bound isoforms [23, 39–41], and are involved primarily in cellular trafficking and uptake of RF. RFRs display high RF affinity as illustrated by RFBP ($K_D \approx 1$ nM) [41]. Recent studies suggest that RFRs are overexpressed in certain malignant cells including human breast and prostate tumors, which implicate RFRs as a class of tumor biomarkers [19, 20, 32]. Thus, these cells displayed the unique ability to take up riboflavin or its macromolecular conjugates, which is indicative of their expression of RFRs [20, 21, 26, 32, 42]. These cells include KB carcinoma [21, 26, 42], LnCap (prostate cancer) [20, 32], SK-LU-1 and A549 (lung cancer) [21], and SK-OV (ovarian cancer) [21]. In addition, a class of ATP-dependent RF transporters is involved in the subcellular accumulation of RF in certain cancer stem cells which are resistant to anticancer chemotherapeutic agents, suggesting their potential as a biomarker for these cells [43].

RFRs share several structural and functional similarities with FARs. Both RFRs and FARs belong to the family of folate binding proteins which are glycosylphosphatidylinositol-anchored surface receptors [38]. The receptors exhibit a high degree of homology in their amino acid sequences [44] and have similar secondary structure [45] in their ligand binding domains. RFRs, like FARs are taken up along with their bound ligand by the cell through endocytosis [21, 23, 46], the mechanism responsible for the uptake of NPs following their cell surface binding to the receptor.

Despite such similarities between these two important vitamin uptake receptors, RFRs play a distinct role in RF transport and cellular uptake and exist as more diverse forms such as soluble carriers, transporters, and membrane-bound proteins [23, 39, 40, 45]. As summarized in Table 7.1, RFRs also show clear differences in their tissue distribution and the types of malignant cells they are associated with including cancer stem cells [43]. Such distinct features of RFRs suggest an important opportunity for targeting specific malignant cells which are otherwise not addressable by use of other tumor biomarkers. In addition to their ligand role,

certain types of RF analogs display potent cytotoxic activity due to their ability to competitively interfere with the cellular functions of flavin cofactors [48], and offer additional benefits in the therapeutic applications of RF ligand-conjugated nanoplatforms [25].

7.2.2 *Riboflavin Ligands*

The primary targeting ligand for RFR-targeted platform design is RF which is the endogenous ligand for these receptors. It is made up of two structural units—an isoalloxazine and a (D)-ribose, each modifiable for ligand conjugation (Fig. 7.1). In addition, there are a number of structural homologues to RF which are referred to as RF antagonists or antimetabolites. These include roseoflavin, cofactor F_{420} [47], and 2(4)-imino-4(2)-amino-2,4-dideoxyriboflavin [25, 47–49]. Each of these retains the ability to bind RFRs, but lacks the requisite functional activity required for the biosynthesis of RF-associated cofactors.

To be considered ideal for the design of RFR-targeted platforms, the ligand should provide certain sites amenable for linker installation, allow easy synthetic modification, and lack any functional activity for stimulating cell growth. In an effort to identify such ligands, we searched RF-mimicking small molecules in the SciFinder® database, and identified a set of candidate molecules that include

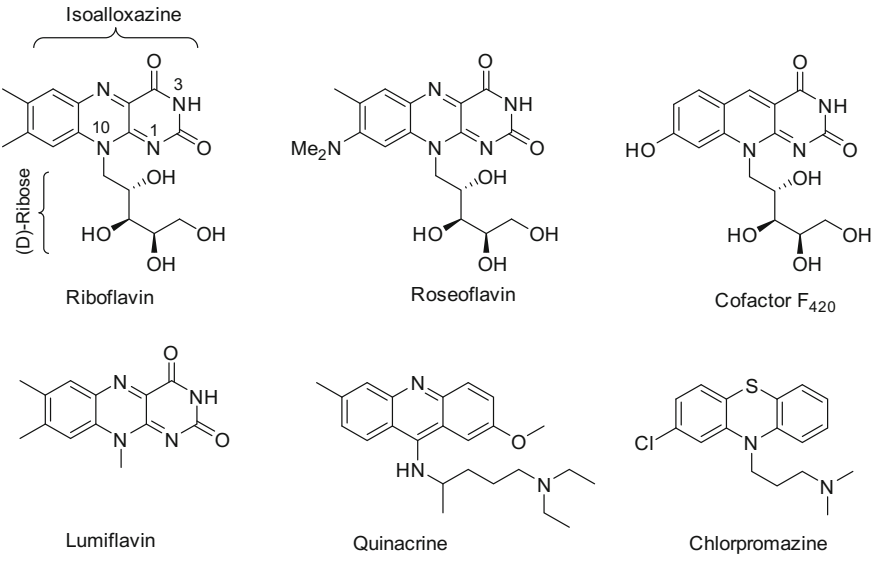

Fig. 7.1 Riboflavin and selected riboflavin antagonists which are either naturally occurring (roseoflavin, cofactor F_{420}, lumiflavin) or synthetic (quinacrine, chlorpromazine)

Table 7.2 Binding affinity and thermodynamic parameters of RF antagonists to riboflavin binding protein (RFBP) in PBS buffer, pH 7.4

RF antagonists	n^a	K_D (nM)	ΔH^a (kJ mol^{-1})	ΔG (kJ mol^{-1})	ΔS (kJ mol^{-1} K^{-1})
Riboflavin	0.78 ± 0.02	5.0	−91.2 ± 5.7	−47.5	−0.15
Lumiflavin	1.08 ± 0.07	61	−48.2 ± 7.2	−41.2	−0.02
Quinacrine	0.90 ± 0.04	264	−51.6 ± 3.9	−37.5	−0.05
Chloroquine	1.06 ± 0.04	2100	−40.4 ± 2.9	−32.4	−0.03
Perphenazine	No binding observed				
Chlorpromazine	No binding observed				

Adapted with permission from [25]. Copyright © 2011, American Chemical Society
[a]n = binding stoichiometry of ligand to receptor. Reported errors (SD) are from fitting data

perphenazine, chlorpromazine, quinacrine, and chloroquine (Fig. 7.1) [25]. Each of these is structurally less complex than RF but contains a flat tricyclic heterocycle that mimics the isoalloxazine head of RF.

We investigated the binding interaction of these small molecules with chicken RFBP using isothermal titration calorimetry (ITC), and determined their dissociation constants (K_D) as summarized in Table 7.2. In general, these molecules bound with lower affinity than RF in the order of RF (5.0 nM) > lumiflavin (61 nM) > quinacrine (264 nM) > chloroquine (2100 nM). Two other tested compounds, perphenazine and chlorpromazine, lacked detectable binding affinity despite their structural similarities based on the tricyclic heterocycle. Both lumiflavin and quinacrine do not cause undesired positive trophic effects as those associated with the function of RF which has been shown to stimulate tumor cell growth. Despite their lower affinity, it is anticipated that NPs conjugated with this lower affinity ligand will still have the ability to bind RFRs on the cell surface with high avidity constants via multivalent binding interactions [50–52]. Use of these RF-mimicking molecules in the design of RFR-targeted platforms constitutes a subject of follow-up studies.

7.3 Application of RF-Conjugated Dendrimers

7.3.1 Linker Design

An X-ray crystal structure was determined for RF in complex with chicken RFBP at a resolution of 2.5 Å [45]. This serves as the basis for rational linker design by providing several insights on the position and orientation of the linker needed in the design of a RF-linker construct. First, the xylene domain of its isoalloxazine unit is stacked between aromatic planes in the ligand binding cleft and is not ideal for linker attachment. However, the opposite face (*N*-3 position) of the same isoalloxazine head is relatively open for linker modifications. This is illustrated by an earlier study, in which 3-carboxymethylriboflavin (**1**, Fig. 7.2) [25, 53, 54], a RF derivative with a carboxylic acid extended out from the *N*-3 position, retained its

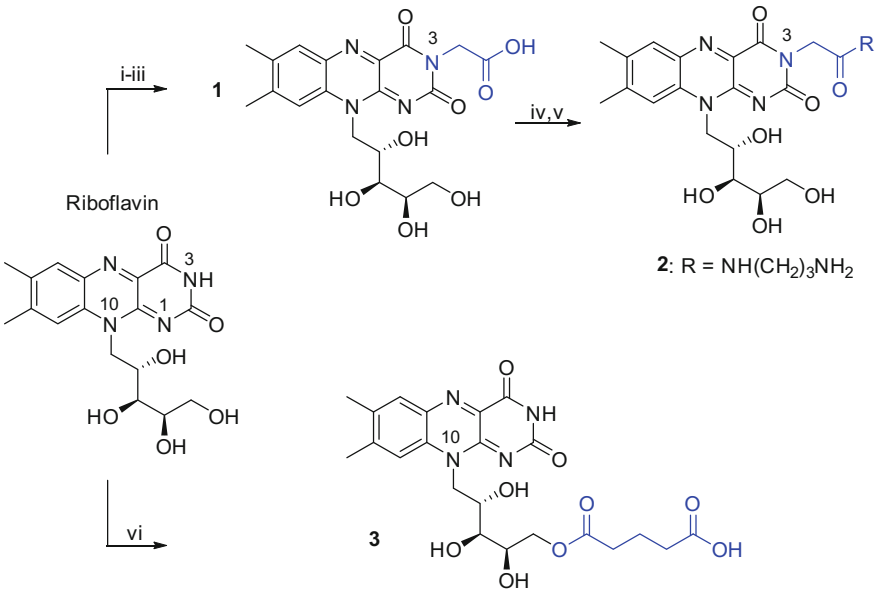

reagents and conditions: i) Ac_2O, AcOH,65°C, 6 h; ii) Ethyl bromoacetate (3 eq), K_2CO_3 (3 eq), DMF, 85°C; iii) 6 M HCl, 90°C, 6 h; iv) EDC, NHS, DMAP, DMF, rt; then N-Boc 1,3-diaminopropane; v) TFA, CH_2Cl_2, rt; vi) glutaric anhydride (2 eq), pyridine, DMSO.85°C, 12 h. rt = room temperature

Fig. 7.2 Synthesis of riboflavin linker constructs. Each linker (in *blue*) is installed at the *N*-3 (**1**, **2**) or *N*-10 position through the terminal hydroxyl group of (D)-ribose (**3**)

affinity for RFBP which allowed its use in the detection of RFBP in milk products [53, 54]. Synthesis of this riboflavin linker construct at the *N*-3 position (**1**) as described in literature [25, 53, 54] is conveniently achieved in three consecutive steps that comprise of the exhaustive acetylation of (−)-riboflavin, the *N*-alkylation of 2′,3′,4′,5′- tetra-*O*-acetylriboflavin to the ethoxycarbonyl methyl derivative, and complete removal of ester protecting groups by acidic hydrolysis (Fig. 7.2).

In order to further validate 3-carboxymethylriboflavin as the linker construct in RFR-targeted delivery platforms, we investigated its binding affinity to RFBP by surface plasmon resonance (SPR) spectroscopy using a biosensor chip prepared by immobilization with **2** which contains a spacer (3-aminopropyl) at the carboxylic acid terminus of 3-carboxymethylriboflavin. This amine-terminated riboflavin derivative **2** was prepared by the EDC-mediated amide conjugation of 3-carboxymethylriboflavin **1** with a mono *N*-Boc protected propanediamine (Fig. 7.2). RFBP bound to the surface in a dose-dependent manner (Fig. 7.3). Its binding was also ligand-specific, as the RFBP adsorption was competitively blocked by co-injecting RF, quinacrine and **2**. This SPR study validated the compatibility of the linker installation made at the *N*-3 position of RF.

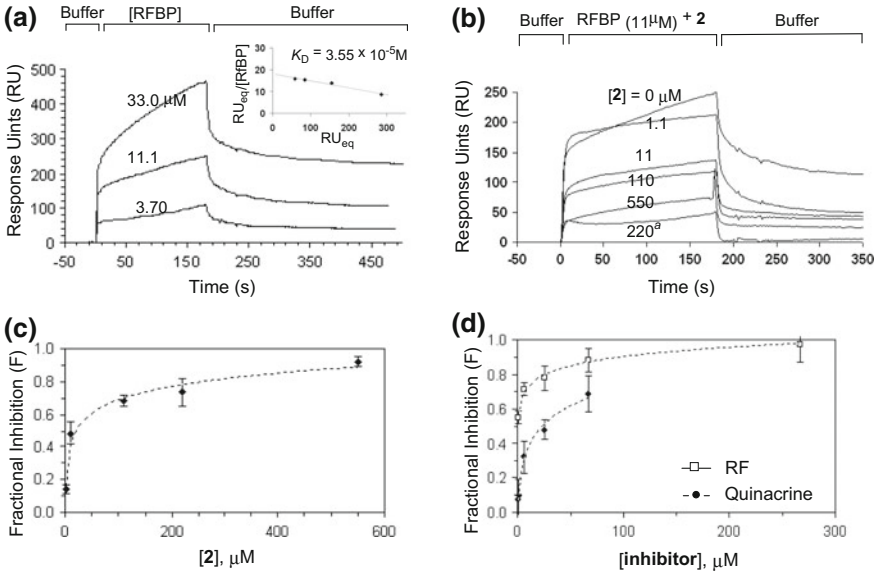

Fig. 7.3 Surface plasmon resonance (SPR) spectroscopy using a riboflavin (**2**)-immobilized CM5 sensor chip. **a** Binding of RFBP in PBS (pH 7.4). *Inset* a Scatchard plot; **b** Competitive binding experiments of riboflavin binding protein (RFBP) with **2**. [a]Injection of **2** alone (220 μM) without RFBP; **c**, **d** Plot of fractional inhibition ($F = 1 - (RU_{[I]}/RU_{[I]=0})$) as a function of the ligand (RF, **2**) or competitive inhibitor (quinacrine). Adapted with permission from [25]. Copyright © 2011, American Chemical Society

Second, the (D)-ribose unit is largely exposed to the aqueous medium and makes a minimal contribution to receptor binding. Thus, its external accessibility in combination with its flexible configuration makes the sugar unit suitable for linker installation as illustrated by a glutarate linker attached at the terminus of the (D)-ribose through an ester linkage (**3**, Fig. 7.2). This riboflavin derivative **3** contains a glutarate moiety attached through an ester linkage at its hydroxyl group of the (D)-ribose unit. It was prepared by heating a mixture of riboflavin and glutaric anhydride in a mixture of pyridine and DMSO. This coupling reaction might occur regioselectively at the primary hydroxyl group as suggested by other similar conjugation reactions of riboflavin reported elsewhere [21, 46], possibly because the primary terminal position is sterically less hindered than those secondary alcohols located adjacent to the bulky isoalloxazine head.

7.3.2 *Dendrimer Conjugates Designed for RFR-Targeted Drug Delivery*

We developed RF-targeted delivery platforms with a generation 5 (G5) poly(amidoamine) (PAMAM) dendrimer (diameter 5.4 nm) [55]. This PAMAM dendrimer

has a globular shape with a large number of dendritic branches (theoretically 128 for G5), each terminated with a primary amine which is amenable to conjugation with a targeting ligand or a drug molecule. The use of this G5 dendritic polymer provides several key benefits for biomedical applications [56, 57] as it displays biocompatibility, is characterized by favorable pharmacokinetic properties such as extended duration of circulation, and lacks immunogenicity [58–61].

Two types of conjugates were designed that include $G5(RF)_{6.3}(FITC)_{1.3}$ **5** and $G5(RF)_{2.5}(MTX)_{3.9}$ **6** (Fig. 7.4). First, $G5(RF)_{6.3}(FITC)_{1.3}$ is a fluorescently labeled conjugate that has a mean of 6.3 RF molecules and 1.3 fluorescein isothiocyanate (FITC) molecules attached on the dendrimer surface prepared for confocal microscopic imaging of its cellular uptake. Here, the ligand attachment was made conveniently through an ester bond formed between a primary hydroxyl group on the (D)-ribose unit of RF and a glutaric acid spacer presented on the dendrimer surface. Second, $G5(RF)_{2.5}(MTX)_{3.9}$ **6** is a drug conjugate that carries covalently attached

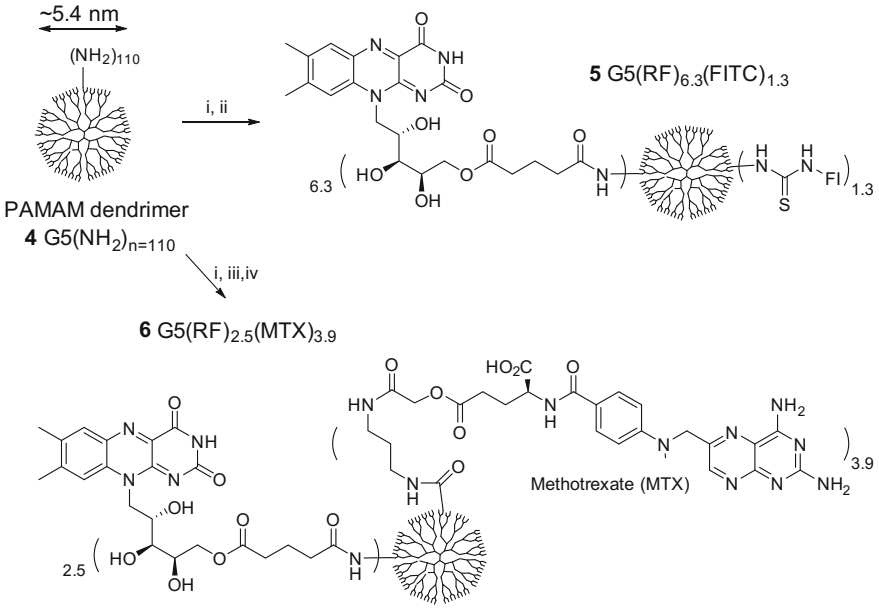

Reagents and conditions: (i) glutaric anhydride, Et_3N, MeOH, rt, 3 days; (ii) riboflavin, FITC-$NH(CH_2)_4NH_2$, EDC, DMAP, DMF, rt; (iii) EDC, 4-dimethylaminopyridine (DMAP), riboflavin, DMF, rt, 24 h; (iv) MTX-C(=O)O$(CH_2)_3NH_2$, EDC, DMAP, DMF, rt, 24 h

Fig. 7.4 Structure of a fifth generation (G5) poly(amidoamine) dendrimer $G5(NH_2)$ (**4**), and synthesis of two representative riboflavin (RF)-conjugated dendrimers, $G5(RF)_{n=6.3}(FITC)_{p=1.3}$ (**5**) and $G5(RF)_{n=2.5}(MTX)_{m=3.9}$ (**6**). *n*, *m* and *p*: each refers to a mean number of RF, methotrexate (MTX) or fluorescein isocyanate (FITC) covalently attached to the dendrimer polymer, respectively

methotrexate (MTX) as the payload. MTX potently inhibits dihydrofolate reductase in the cytoplasm with a K_i value of 4.8 pM [62], leading to strong inhibition of cell growth.

Assessment of the cellular binding and uptake of conjugate **5** was performed in RFR(+) KB cells. These cells belong to a subline of cervical tumor cells that showed receptor-mediated uptake of RF and RF-dye conjugates [21, 46]. Our flow cytometry analysis showed dose- and incubation time-dependent binding of the conjugate (Fig. 7.5) [26]. When incubated with other human cancer cell lines, this RF conjugate also showed significant fluorescence intensity in these cell lines including IGROV-1 (ovarian) and SCC15 (head and neck) like in KB cells. This is supportive of conjugate binding and uptake by these tumor cells, some of which have been validated earlier for their overexpression of RFR on the cell surface [21].

In a subsequent study, we investigated the effectiveness of this RFR-targeted conjugate for drug delivery using $G5(RF)_{2.5}(MTX)_{3.9}$ **6**. The cytotoxic effect of **6** was determined in KB cells in vitro using an XTT assay (Fig. 7.5b). This conjugate showed potent inhibition of tumor cell growth at low nM doses, and its inhibition activity was incubation time- and dose-dependent. The IC_{50} value estimated from

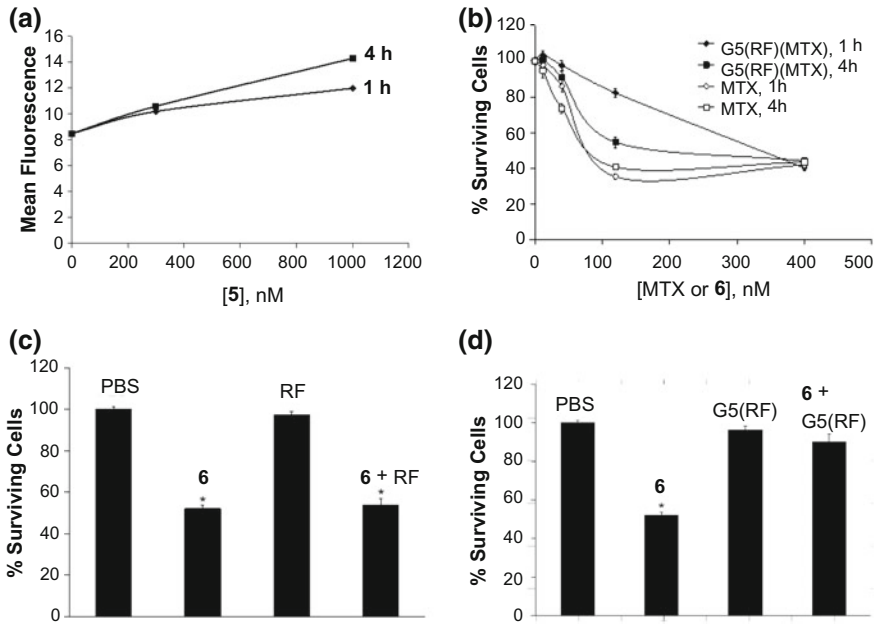

Fig. 7.5 **a** Dose-dependent binding and uptake of **5** $G5(RF)_{6.3}(FI)_{1.3}$ in KB cells (incubation time = 1, 4 h); **b** Dose-dependent cytotoxicity of **6** $G5(RF)_{2.5}(MTX)_{3.9}$ and free MTX in KB cells; **c** Effect of a competitive ligand (RF) on cell growth. PBS (control), **6** (30 nM), RF (30 μM), and **6** (30 nM) + RF (30 μM); **d** Effect of a RF-conjugated dendrimer on cell growth. PBS, **6** (30 nM), $G5(RF)_{2.5}$ (30 μM), and $G5(RF)_{2.5}$ (30 μM) + **6** (30 nM). *Asterisk* the *p* value for each of the data set is <0.005 compared to PBS. Reprinted with permission from [26]. Copyright © 2010, Elsevier

the dose response curve (at 4 h incubation) for the conjugate was 72 nM, which indicates slightly lower activity than that of free MTX of 48 nM.

In order to verify the mechanism of RF-mediated delivery by **6**, we performed a series of ligand competition experiments in RFR(+) KB cells with RF (30 μM, Fig. 7.5c) or $G5(RF)_{2.5}$ (30 μM, Fig. 7.5d). Here, the addition of RF or its dendrimer conjugate $G5(RF)_{2.5}$ (which has no MTX attached) alone showed no effect on cell growth. When $G5(RF)_{2.5}(MTX)_{3.9}$ **6** (30 nM) was co-incubated with an excess amount (30 μM) of $G5(RF)_{2.5}$ (a multivalent ligand competing for RFR), the cytotoxicity of **6** could be effectively blocked due to perhaps competitive occupation of RFRs by the added $G5(RF)_{2.5}$ which would contribute to the decrease of its intracellular uptake. As a result, the cell growth was restored to 90% from ~50% observed in the absence of $G5(RF)_{2.5}$.

Co-incubation with free RF failed to show such restoring effects on cell growth. This distinct difference between RF and $G5(RF)_{2.5}$ is attributable to the high avidity binding of the multivalent conjugate compared to the monovalent RF ligand [51, 52, 63]. Our results of ligand competition experiments are in agreement with a previous uptake study performed with ^{125}I-labeled, multivalent RF-conjugated bovine serum albumin (shortly, ^{125}I-$BSA(RF)_5$) in RFR(+) KB cells reported by Low et al. [21]. Thus, co-incubation of ^{125}I-$BSA(RF)_5$ with free RF (at 10–40 mol excess) resulted in almost no change in its cellular uptake relative to no RF addition, while co-incubation with an unlabeled $BSA(RF)_5$ (at 10 mol excess) led to significant blocking (~70%) of its uptake, evidence supportive of its multivalent tighter binding than monovalent RF.

All of these studies are supportive of the cellular uptake of **6** through a RFR-mediated mechanism and verify the activity of delivered MTX in the cytoplasm in inducing potent cytotoxicity. These studies also point to the potential application of RF-conjugated dendrimers in targeted delivery of a fluorescent imaging molecule and an anticancer therapeutic agent to malignant tumor cells overexpressing the RF receptor.

7.3.3 *Dendrimer Conjugates Designed for RFR-Targeted Gene Delivery*

We investigated the potential of applying RF-conjugated dendrimers as a new class of nonviral vectors for RFR-targeted gene delivery in tumor cells (Fig. 7.6) [42]. For this approach, we modified the conjugate $G5(RF)_{4.9}$ by co-attachment of multiple molecules of 3,8-diamino-6-phenylphenanthridinium (DAPP) which has the ability to intercalate into DNA, thus forming polyplexes with dsDNA. The resulting dendrimer $G5(RF)_{4.9}(DAPP)_{6.9}$ has dual functional motifs, one for targeting RFRs on the cell surface and the other for anchoring a DNA payload.

We selected a series of RF-conjugated dendrimers along with other targeted dendrimers that include **7** $G5(FA)_{8.6}$, **8** $G5(DAPP)_{5.4}$, **9** $G5(FA)_{8.6}(DAPP)_{5.4}$, **10** $G5(RF)_{4.9}$, and **11** $G5(RF)_{4.9}(DAPP)_{6.9}$. Each was used for preparing a series of

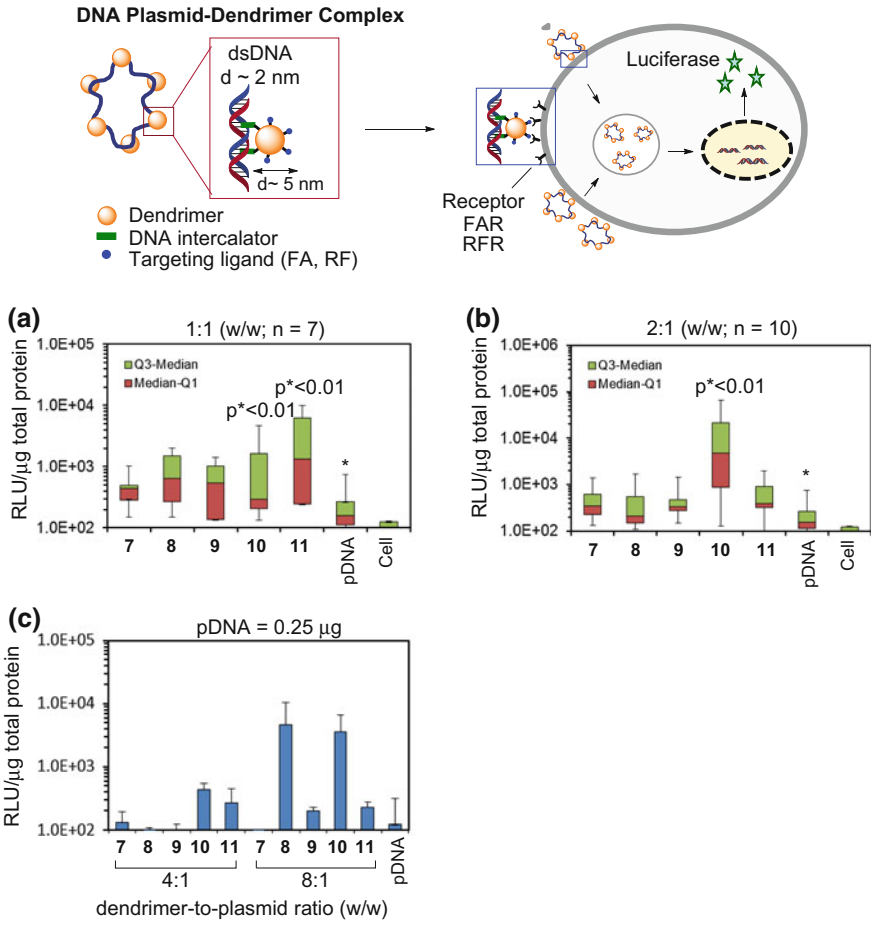

Fig. 7.6 A schematic illustrating the concept for dendrimer vectors with DNA intercalation motifs for RFR-targeted gene delivery. **a–c** Transfection of luciferase plasmid DNA (pLuc) in FAR(+) and RFR(+) KB cancer cells via dendrimer polyplexes, each made with **7** G5$(FA)_{8.6}$, **8** G5$(DAPP)_{5.4}$, **9** G5$(FA)_{8.6}(DAPP)_{5.4}$, **10** G5$(RF)_{4.9}$, and **11** G5$(RF)_{4.9}(DAPP)_{6.9}$. **a**, **b** *Box* and *whisker* plots showing the distribution of luminescence at dendrimer-to-plasmid (D/P) ratios of 1:1 (**a**) and 2:1 (**b**) at 1 µg of pLuc. Each *p* value was calculated against plasmid DNA alone (*Asterisk*). **c** Luciferase transfection at higher D/P ratio of 4:1 or 8:1. DAPP = 3,8-di-amino-6-phenylphenanthridine. *RLU* relative light unit. *Error bars* standard deviation (±SD). Adapted with permission from [42]. Copyright © 2011, American Chemical Society

polyplexes by complexation with plasmid DNA (pDNA) encoding a luciferase (pLuc) as a reporter gene. Several polyplexes containing DNA at various dendrimer-to-pDNA ratios (D/P) were made, and it was investigated whether such dendrimer polyplexes are effective for gene transfection by performing transfection experiments in FAR(+) and RFR(+) KB carcinoma cells in vitro.

As presented in Fig. 7.6a, b, each of the polyplexes prepared at the D/P ratios of 1:1 or 2:1 showed transfection activities greater than the pristine plasmid used as control. The transfection efficiency varied with dendrimer type such that polyplexes prepared with **10** G5$(RF)_{4.9}$ or **11** G5$(RF)_{4.9}(DAPP)_6$ gave the highest transfection efficiency at each ratio with statistical significance of $p < 0.01$ (F test). These were more effective than those polyplexes prepared with FA-conjugated dendrimers. It is notable that **10** G5$(RF)_{4.9}$ showed such high efficiency despite its lack of DAPP which was presumably needed for DNA anchoring. We postulate that RF alone attached to the dendrimer could play a dual functional role as both a targeting ligand and DNA anchor due to its previously demonstrated ability to intercalate its flat isoalloxazine head between two adjacent DNA base pairs in dsDNA [64, 65]. The efficiency of gene transfection also varied with the D/P ratios while a single best ratio applicable for all polyplexes was not observed. This variation is attributable to the mechanism of nonviral gene delivery [66] in which the ratio as well as nanoparticle type determine the shapes and charge properties of the polyplexes, each playing a critical role in the course of intracellular uptake, DNA release, and nuclear transport. This observation is indicative of the challenges in predicting the optimal structure and function of the polyplex which requires further studies in the future.

The cellular uptake of these polyplexes can occur through either FAR or RFR-mediated mechanism. By confocal microscopy, we imaged KB cells treated under the same conditions as in the transfection experiment. As shown in Fig. 7.7, cells treated with each polyplex showed significant fluorescence which is indicative of their cellular uptake. Most of the fluorescence intensity was predominantly localized in the cytoplasmic area rather than on the cell surface and with only minor fluorescence observed in the nuclei. This is supportive of their intracellular uptake possibly via a receptor-mediated mechanism, as well as the release of pDNA in the cytoplasm rather than nuclear uptake of the polyplex complex. As a comparison, **8** G5(DAPP) which lacks RF was taken up, but less effectively than **11** G5(RF)(DAPP), suggesting the possibility of other mechanisms of uptake such as macropinocytosis and phagocytosis which is dependent on nanoparticle shapes [67].

In summary, we investigated a new concept for targeted gene delivery using RF-conjugated multifunctional dendrimers. This novel platform was highly effective for facilitating gene transfection in specific for RFR(+) mammalian cells.

7.3.4 RFR-Targeted Imaging Methods

As shown above, imaging of RF-conjugated dendrimers in the cell can be performed by confocal microscopy by focusing on fluorescent dye molecules associated with the NP. However, these dye molecules are photounstable and rapidly bleach, leading to reduced resolution and detection capabilities. We developed another imaging modality for investigating the cellular association of RF-conjugated dendrimers [27]. It is based on a gold nanoparticle (AuNP) system

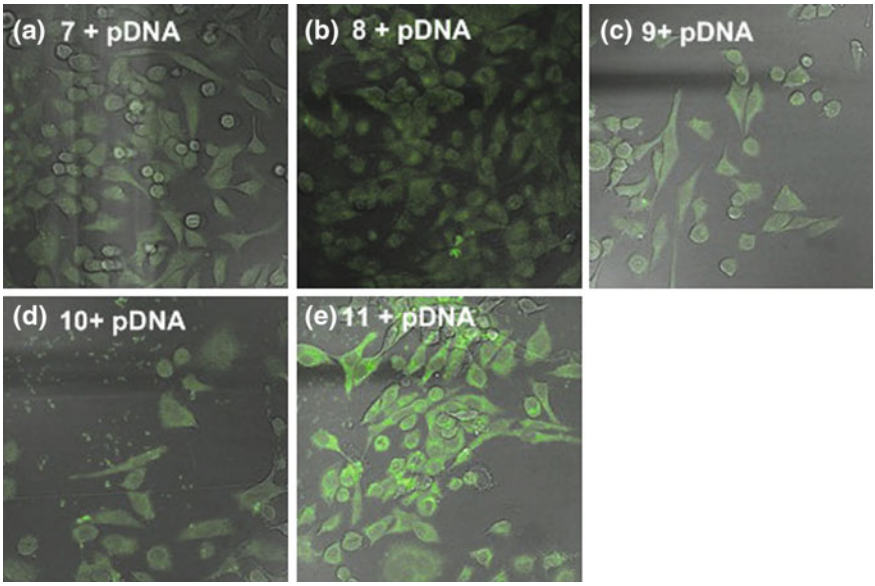

Fig. 7.7 **a**–**e** Fluorescence confocal microscopy of various polyplexes taken up by KB cells in vitro. Each sample was prepared using polyplexes made of luciferase plasmid (1 μg/mL) in complex with each of dendrimer conjugates **7** $G5(FA)_{8.6}$, **8** $G5(DAPP)_{5.4}$, **9** $G5(FA)_{8.6}(DAPP)_{5.4}$, **10** $G5(RF)_{4.9}$, or **11** $G5(RF)_{4.9}(DAPP)_{6.9}$ at a 2:1 ratio (w/w). In this imaging study, the localization of the dendrimer polyplex was detected by fluorescent emission that is attributed to excitation of dendrimer-attached ligands including folate (**a**), riboflavin (**d**), and/or DAPP (3,8-di-amino-6-phenylphenanthridine; **b**, **c**, **e**). Reprinted with permission from [42]. Copyright © 2011, American Chemical Society

which displays unique optophysical properties such as surface plasmon resonance (SPR) absorption, visible luminescence, and SPR scattering effects [68, 69]. With these modalities, the detection of AuNP does not require conjugation with any additional fluorescent labels, and it is conveniently performed under dark field light [70–72] and confocal microscopy [73].

The AuNPs used in this study [27] were spherical in shape and displayed a maximal absorption (λ_{max}) band at 520 nm. The size distribution of AuNPs was measured by atomic force microscopy (AFM), indicating a mean diameter of 13.5 ± 2.2 nm. Their hydrodynamic diameter as determined by dynamic light scattering (DLS) was as large as ~ 30 nm (Z_{ave}) which points to the contribution of the hydrated diffusion layer surrounding the AuNP core to the measured size. The AuNP was modified to form the core–shell nanocomposite AuNP@dendrimer by its surface modification with dendrimer conjugates **12**, **13** $G5(RF)_n$ ($n = 0, 4$) (Fig. 7.8). The surface modification was achieved through Au–S chemisorption between the surface Au and the cyclic disulfide moiety at the terminus of a lipoic amide branch of the dendrimer.

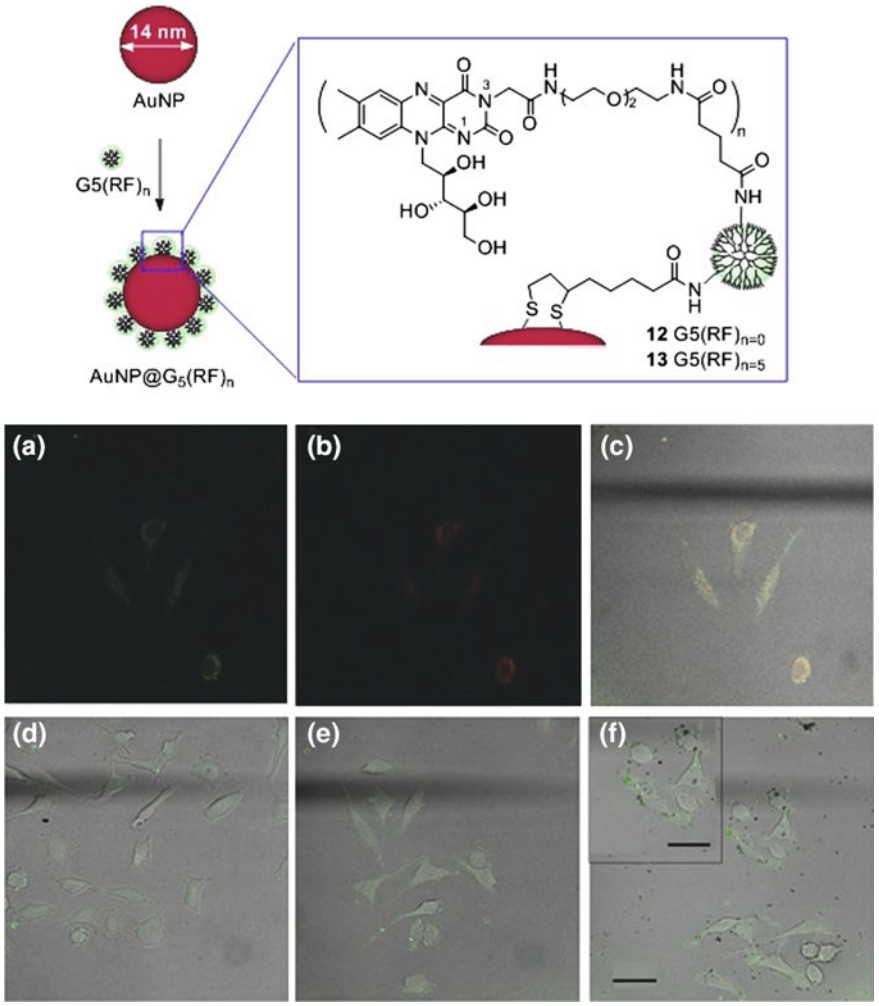

Fig. 7.8 SPR scattering imaging for the cellular uptake of dendrimer-coated gold nanoparticles AuNP@G5(RF)$_n$ in KB cells. **a–c** KB cells treated with 50 nM of unmodified AuNP for 2 h were imaged by **a** SPR scattering or **b** luminescence. **c** Co-localization of the signals was confirmed by the overlay. SPR scattering imaging was taken for KB cells treated for 4 h with 80 nM of **d** AuNP, **e** AuNP@G5(RF)$_{n=0}$ or **f** AuNP@G5(RF)$_{n=5}$, (*inset* is a magnified view of the adjacent cells). *Scale bar* 30.3 μm (*inset*, 28.8 μm). Signal from the SPR scattering was overlaid with differential interference contrast (DIC) images. Reprinted with permission from [27]. Copyright © 2014, American Chemical Society

We first validated two methods for detecting AuNPs which did not contain any fluorescent dyes or chemisorbed dendrimer. As shown in Fig. 7.8a–c, RFR(+) KB cells were incubated with citrate-stabilized AuNPs (50 nM) for 2 h, and were imaged by confocal microscopy via two detection modes including SPR scattering

(λ_{ex} 514 nm; λ_{em} 474–506 and 522–570 nm) and luminescence (λ_{ex} at 514 nm; λ_{em} at 550–650 nm). AuNPs associated with the cells were clearly detectable under both detection modes, SPR (Fig. 7.8a) and luminescence (Fig. 7.8b); however, their detection intensities were rather weak due to their low level of cellular uptake.

For enhanced uptake, KB cells were treated at a slightly higher concentration (80 nM) and incubated for a longer period (4 h) with AuNP and AuNP@G5(RF)$_n$ (n = 0, 5). Images of the treated cells were acquired in the SPR scattering mode, showing qualitatively clear differences between untargeted NPs (AuNP, AuNP@G5(RF)$_0$) and targeted AuNP@G5(RF)$_5$. The targeted AuNP@G5(RF)$_5$ showed more punctate and localized areas of signal, and their intensity was distinctly greater than those observed otherwise with the bare unmodified AuNP as well as with the AuNP@G5(RF)$_0$) treated cells (Fig. 7.8d–f). We attribute this scattering detection to large aggregates of AuNPs rather than individual AuNPs either bound on the cell surface or internalized.

In summary, our confocal microscopy studies demonstrated the utility of the dual detection modes of SPR scattering and luminescence for the determination of the cellular localization of dendrimer-chemisorbed AuNPs in tumor cells. As covalent modification with fluorophores for detection is sometimes not desirable due to the possible alteration of native activity, these nonfluorescent-based methods of detection may offer a better alternative for imaging applications.

7.4 Biophysical Basis of Multivalent High Avidity

The design principle of targeted NPs involves a multivalent ligand system in which each NP is conjugated with multiple targeting ligands. Thus, the multivalent NP recognizes and binds to a target cell with high specificity and strong binding affinity, which together are referred to as avidity [51, 52, 63, 74]. Unlike affinity which often refers to the strength of monovalent interaction between a single receptor and ligand pair, avidity is a collective property that measures the strength of simultaneous interactions between multiple receptor–ligand pairs [51, 56, 57] (Fig. 7.9).

Multivalent design factors have been extensively investigated by many laboratories including ours by conjugation of small molecule ligands such as carbohydrates [51, 63, 75, 76], folate [77, 78], methotrexate [79–83], vancomycin [84–87], and oligonucleotide [88] to NP scaffolds based on polymers [75, 89, 90], dendrimers [77, 79, 84, 88], and inorganic nanomaterials [78, 86, 87, 91]. These studies suggest that several factors play a significant role in conferring high avidity and selectivity. These include: (1) use of threshold ligand valence [77, 84, 88]; (2) presentation of two different ligands for co-targeting two distinct receptors on the same cell surface [78, 91]; (3) evaluation of NP sizes and shapes [92] for optimized conformal interactions [75, 93, 94]. It is also notable that an overcrowding or steric effect can occur [89, 95] when too many or bulky ligands are presented on the same surface of a NP which thus can interfere with high avidity

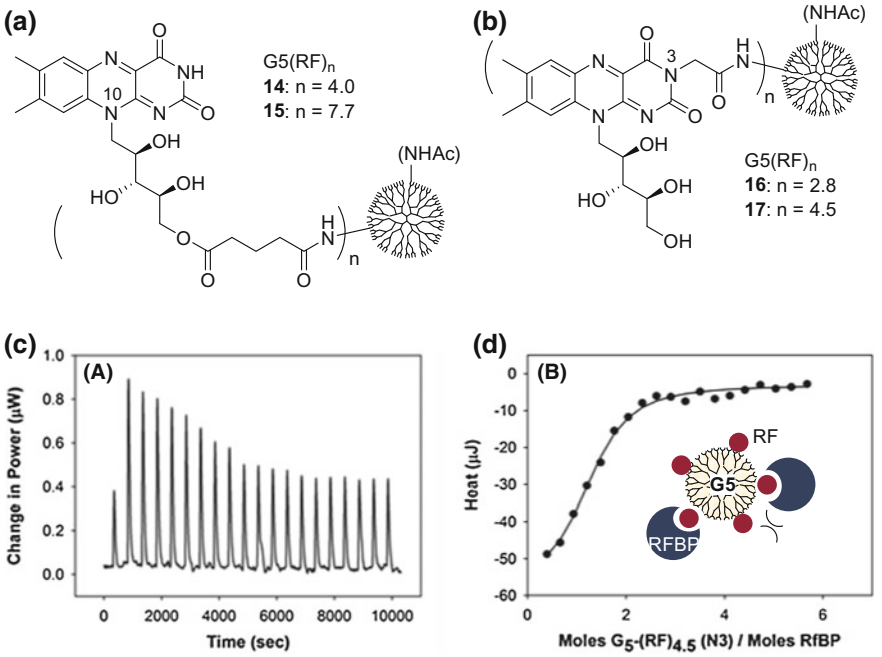

Fig. 7.9 **a**, **b** Structures of two RF-conjugated dendrimer series G5(RF)$_n$. In each, the RF ligand is tethered to the G5 PAMAM dendrimer through a linker located at either its *N*-10 or *N*-3 position with variable valency (*n*). **c** Representative raw ITC data for the interaction between **17** G5(RF)$_{4.5}$ with chicken RFBP (4 μM) at 25 °C in PBS buffer. **d** Plot of integrated area under each injection peak for **17**. The *solid line* is an independent model fit to data with parameters *n*, K_D, and ΔH. *Inset* a model for monovalent receptor–ligand association. Reprinted with permission from [28]. Copyright © 2012, American Chemical Society

binding. This steric interference is especially an issue with large molecule ligands such as antibodies [96]. Here, we investigated the biophysical basis for the specific and high avidity adsorption of RF-conjugated dendrimers to receptor expressing cell surfaces.

7.4.1 Ligand Affinity

We first investigated the thermodynamic basis of monovalent interactions between a receptor and a RF-conjugated dendrimer in solution [51]. One of the key design factors of this dendrimer conjugate is the RF valency which is known to play a significant role in controlling the avidity of the multivalent system. However, little is known about its role in monovalent affinity. Two series of RF-conjugated dendrimers G5(RF)$_n$ **14**–**19** were prepared by the covalent attachment of RF at either its *N*-10 or *N*-3 position to the dendrimer (Fig. 7.9). The linker used for RF attachment

in each series is composed of a three to five atom spacer. We chose this linker length as our previous cell binding [26] and SPR studies [25] suggested that it is long and flexible enough for the dendrimer-attached RF to be able to dock in the ligand site of RFBP. In each series, the average number (n = valency) of RF attached was varied in order to determine whether the ligand valency plays any role in the monovalent affinity (K_D) of the tethered RF ligand in solution.

Several binding parameters for the interaction between RF-conjugated dendrimers and soluble RFBP were determined by ITC in solution as summarized in Table 7.3 [28]. First, free RF binds to RFBP with a binding stoichiometry (n_b) of 1:1 (RFBP/ligand) [25]. Each of **14**–**16** G5(RF)$_n$ in the *N*-10 series showed an n_b of ~3–5:1 (RFBP/dendrimer), indicative of partial occupation of all the RF sites on the dendrimer by RFBP. This stoichiometry is in close agreement with the analysis based on a simple sphere model in which approximately six to seven RFBP (d = 4–5 nm) protein molecules can be theoretically accommodated around the surface of a G5 dendrimer nanoparticle (d = 5.4 nm) [55]. In contrast, **17**–**19** G5(RF)$_n$ in which each RF was tethered through a short spacer (3 atom) at its *N*-3 position showed only 1–2 RFBP occupation per dendrimer. These results suggest that ligand conjugation at the (D) ribose terminus via a longer glutarate linker provides more space and flexibility for more optimal protein accommodation.

Overall, this ITC analysis suggests a number of new insights in multivalent ligand design. First, we observed an upper limit in the maximal number of ligands that could engage in receptor binding. Control of this limit is dependent on design factors such as linkage position, spacer length, and ligand valency. However, it is notable that the RFBP used here is a monovalent system in solution, and thus different from RFRs presented on the cell surface. Accordingly, the remaining unoccupied ligands on the dendrimer are still available for making opportunistic receptor binding interactions to these RFRs, given their proximity [28].

Second, the dissociation constant (K_D) values determined for all dendrimer conjugates were greater by a factor of 93–1110 relative to the K_D value of RF (5 nM) [25]. This suggests that the mean affinity of each RF ligand to RFBP is significantly decreased once it is conjugated to the dendrimer surface. The K_D values determined for the *N*-3 linkage series also showed reduced affinity to RFBP, but overall higher affinity by a factor of ~5 than the *N*-10 series at a similar RF valency. These results clearly signify that contacts made in the binding pocket by the RF ligand with an unmodified (D) ribose moiety are important, and thus contribute to tighter binding in the binding pocket.

Third, the decrease in the affinity of the RF-dendrimer conjugates to RFBP is better understood by examination of thermodynamic parameters based on enthalpic (ΔH) and entropic ($-T\Delta S$) contributions. Enthalpically, the binding of the *N*-3 conjugates was much more favorable than the *N*-10 series. In contrast, the entropic penalty ($-T\Delta S$) was more severe for the *N*-3 conjugates. This implies that the binding of the *N*-3 conjugates is largely enthalpy driven, and the conjugation of more RF ligands per dendrimer likely results in the higher entropic penalty perhaps due to steric repulsion or congestion [97].

Table 7.3 Thermodynamic parameters for the monovalent binding of RF-conjugated dendrimers with RFBP in solution (phosphate buffered saline, pH 7.4) at 25 °C

System (versus RFBP)	Linkage position	n_b	K_D (nM)	ΔH^a (kJ mol^{-1})	ΔG (kJ mol^{-1})	$^{-}T\Delta S$ (kJ mol^{-1})
G5(RF)$_0$	–	NB	NB	NB	NB	NB
14 G5(RF)$_{4.0}$	*N*-10	2.88 ± 0.27	2671 ± 199	−15.7 ± 2.3	−31.9	−16.3
15 G5(RF)$_{7.7}$	*N*-10	5.16 ± 0.76	4049 ± 13	−9.0 ± 2.2	−30.8	−21.8
16 G5(RF)$_{2.8}$	*N*-3	1.76 ± 0.06	465 ± 12	−41.0 ± 2.7	−36.2	4.8
17 G5(RF)$_{4.5}$	*N*-3	1.24 ± 0.06	568 ± 95	−55.7 ± 3.8	−35.3	20.4

n_b = Binding stoichiometry (RFBP/dendrimer). NB = no binding. Errors are reported to two standard deviations (SD)

[a]Reported errors are from fitting data

7.4.2 *Multivalent Avidity*

Our thermodynamic studies above show that the monovalent interaction between the RF-dendrimer conjugate and the RFBP in solution is not enhanced, but is in fact weaker than that of free RF. We then investigated the avidity of the multivalent binding interactions between a RF-conjugated dendrimer and multiple RFBP molecules presented on a surface (a model system of the cell surface). We employed AFM because of its proven ability to quantify multivalent effects in biomolecules and synthetic model systems [98]. In particular, AFM-based dynamic force spectroscopy allows for the precise measurement of the physical forces involved in biomolecular interactions [98].

We hypothesized that the multivalent avidity, which results from multiple, cooperative interactions, should result in a force which is greater to break than the monovalent affinity [51, 52, 63, 99]. For this AFM study, a model system for the cell surface was generated by immobilization of RFBP onto a substrate (an ultra-flat gold surface) as illustrated in Fig. 7.10. Force experiments were performed through the contact approach of an AFM tip coated with $G5(RF)_n$ (n = 0, 3, 5) to the RFBP-immobilized substrate followed by retraction to measure the rupture force arising from the recognition interaction. Rupture events were observed over the course of the tip retraction, and the binding specificity was confirmed by addition of a competitive ligand (free RF) (not shown) which led to the block of the rupture events.

For data analysis, rupture forces were extracted by force–distance curves as illustrated for $G5(RF)_5$ in Fig. 7.10, and those forces measured for $G5(RF)_n$ were plotted as a function of loading rates as shown in Fig. 7.10D. $G5(RF)_0$ showed only nonspecific, weak interactions as most of its rupture events showed lack of loading rate dependency as typically expected for nonspecific events. However, some events showed a small loading rate dependency which is believed to arise from nonspecific global interactions such as electrostatic and/or van der Waals interactions between the dendritic residues and the RFBP protein. $G5(RF)_3$ showed a loading rate dependency that was markedly different from the nonspecific interactions observed in $G5(RF)_0$. Its rupture forces were in the range of 40–50 pN which may arise from a combination of mono, di- or trivalent interactions given its ligand distribution [100]. $G5(RF)_5$ also showed a loading rate dependency that was different from $G5(RF)_3$. The rupture forces observed from the $G5(RF)_5$-RFBP interactions are higher, and in the range of 70–110 pN, and the upper end of these forces are most likely arising from multivalent binding greater than those in $G5(RF)_3$. It is notable that the rupture forces measured in $G5(RF)_5$ are greater than those in $G5(RF)_3$, and even comparable to the force ($\sim$75 pN) reported for a biotin-avidin bond ($K_D \sim 10^{-15}$ M) [101] which constitutes one of the strongest non-covalent interactions.

In summary, this dynamic force spectroscopy study enabled us to quantitatively measure the physical forces involved in the adsorption of RF-conjugated dendrimers to the surface through multivalent receptor binding. RF valency is

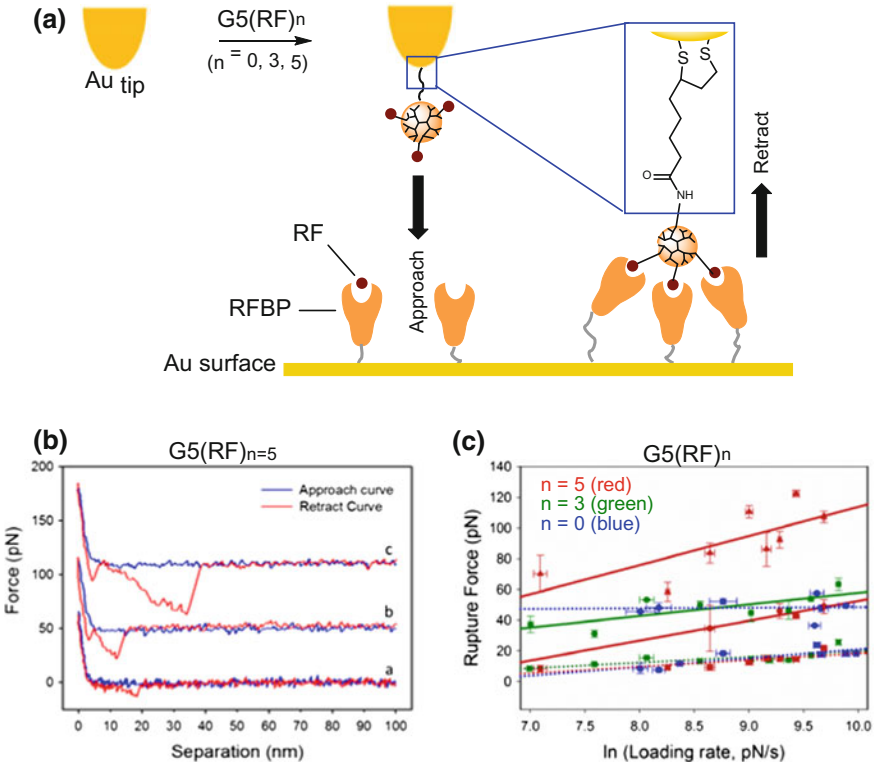

Fig. 7.10 **a** An AFM gold (Au) probe tip prepared by surface coating with G5(RF)$_n$ (n = 0, 3, 5; linkage at N-3 position), and schematic for dynamic force spectroscopy; **b** Representative force–distance curves between a G5(RF)$_5$ (**13**)-coated tip and RFBP covalently attached to an ultra-flat gold surface. Loading rate = 5.7 nN/s. Offset force curves depict rupture events in the **a** 10–20 pN, **b** 20–50 pN, and **c** 50–120 pN ranges; **c** Dynamic force spectra of G5(RF)$_n$ (n = 0, 3, 5) versus loading rate. *Square data* points represent rupture of unbinding event (**a**). *Circle* and *triangle* points represent unbinding events (**b**, **c**), respectively. Adapted with permission from [24]. Copyright © 2014, American Chemical Society

positively correlated with the magnitude of rupture force for dendrimer adhesion. These results were strongly supportive of its essential role in the design of RFR-targeted NPs.

7.5 Conclusion

RFR plays an essential role in cellular uptake of RF in normal physiology. Its overexpression is, however, observed in a number of cancer cell types and in cancer stem cells [19, 20, 43]. Here, we summarized the proof of concept studies reported

by our laboratories which demonstrated that RF or its homologous antagonists such as lumiflavin and quinacrine [25] have a strong potential to serve as ligands for selectively targeting RFRs, specific biomarkers in tumors and cancer stem cell biology. With a rational design approach based on an available RFBP crystal structure [45], we developed linker chemistry which enabled efficient conjugation of RF at its (D)-ribose unit and isoalloxazine head without loss of its binding activity [26, 28]. A series of multifunctional RF conjugates prepared with G5 PAMAM dendrimer were demonstrated as effective nanoplatforms for RFR-targeted delivery in RFR(+) KB cells in vitro using an anticancer therapeutic agent (MTX) and a reporter gene. Imaging methods based on AFM and confocal microscopy in combination with the SPR scattering modality of AuNPs conferred an ability to investigate the receptor-mediated uptake of RF-conjugated dendrimers by tumor cells [27, 42].

Development of nanotechnology for RFR-targeted applications has started only recently following early studies on receptor-mediated uptake of RF and its protein conjugates by tumor cells [21, 23]. Despite its early stage, a number of explorative studies which have been conducted in our laboratories [24–28] and others [29–31] are strongly supportive of multiple promising applications. These include delivery of antitumor agents (MTX [26], mitomycin C [31]) by RF-conjugated nanomaterials based on the PAMAM dendrimer [26, 28, 42], AuNP [27], *N*-(2-hydroxypropyl) methacrylamide (HPMA) copolymer [31], and human serum albumin [21]. In conclusion, we anticipate that RFR-targeted nanotechnology has a strong potential for playing a critical role in the development of new technology and effective nanodevices for tumor-specific delivery and imaging applications.

Acknowledgements The authors wish to acknowledge the support from the Michigan Nanotechnology Institute for Medicine and Biological Sciences, University of Michigan Medical School. SKC acknowledges partial support from the British Council and Department for Business Innovation and Skills through Global Innovation Initiative. KS acknowledges partial support from a Calvin College Research Fellowship.

References

1. Peer D, Karp JM, Hong S, Farokhzad OC, Margalit R, Langer R (2007) Nanocarriers as an emerging platform for cancer therapy. Nat Nanotechnol 2(12):751–760
2. Wong PT, Choi SK (2015) Mechanisms of drug release in nanotherapeutic delivery systems. Chem Rev (Washington, DC, US) 115(9):3388–3432
3. Kamaly N, Xiao Z, Valencia PM, Radovic-Moreno AF, Farokhzad OC (2012) Targeted polymeric therapeutic nanoparticles: design, development and clinical translation. Chem Soc Rev 41(7):2971–3010
4. Maeda H (2001) The enhanced permeability and retention (EPR) effect in tumor vasculature: the key role of tumor-selective macromolecular drug targeting. Adv Enzyme Regul 41(1):189–207
5. Zhu J, Shi X (2013) Dendrimer-based nanodevices for targeted drug delivery applications. J Mater Chem B 1(34):4199–4211

6. Esmaeili F, Ghahremani MH, Ostad SN, Atyabi F, Seyedabadi M, Malekshahi MR, Amini M, Dinarvand R (2008) Folate-receptor-targeted delivery of docetaxel nanoparticles prepared by PLGA–PEG–folate conjugate. J Drug Targ 16(5):415–423
7. Kelemen LE (2006) The role of folate receptor α in cancer development, progression and treatment: cause, consequence or innocent bystander? Int J Cancer 119(2):243–250
8. Yang W, Cheng Y, Xu T, Wang X, Wen L-P (2008) Targeting cancer cells with biotin-dendrimer conjugates. Eur J Med Chem 44:862–868
9. Yellepeddi VK, Kumar A, Palakurthi S (2009) Biotinylated poly(amido)amine (PAMAM) dendrimers as carriers for drug delivery to ovarian cancer cells in vitro. Anticancer Res 29 (8):2933–2943
10. Kok RJ, Schraa AJ, Bos EJ, Moorlag HE, Asgeirsdottir SA, Everts M, Meijer DKF, Molema G (2002) Preparation and functional evaluation of RGD-modified proteins as $\alpha_v\beta_3$ integrin directed therapeutics. Bioconj Chem 13(1):128–135
11. Pinto JT, Suffoletto BP, Berzin TM, Qiao CH, Lin S, Tong WP, May F, Mukherjee B, Heston WD (1996) Prostate-specific membrane antigen: a novel folate hydrolase in human prostatic carcinoma cells. Clin Cancer Res 2(9):1445–1451
12. Silver DA, Pellicer I, Fair WR, Heston WD, Cordon-Cardo C (1997) Prostate-specific membrane antigen expression in normal and malignant human tissues. Clin Cancer Res 3(1): 81–85
13. Ross JS, Fletcher JA (1998) The HER2/neu oncogene in breast cancer: prognostic factor, predictive factor, and target for therapy. Oncologist 3:237–252
14. Arteaga CL (2002) Epidermal growth factor receptor dependence in human tumors: more than just expression? Oncologist 7(suppl 4):31–39
15. Haugsten EM, Wiedlocha A, Olsnes S, Wesche J (2010) Roles of fibroblast growth factor receptors in carcinogenesis. Mol Cancer Res 8(11):1439–1452
16. Pollak M (2012) The insulin receptor/insulin-like growth factor receptor family as a therapeutic target in oncology. Clin Cancer Res 18(1):40–50
17. Herbison CE, Thorstensen K, Chua ACG, Graham RM, Leedman P, Olynyk JK, Trinder D (2009) The role of transferrin receptor 1 and 2 in transferrin-bound iron uptake in human hepatoma cells. Am J Physiol Cell Physiol 297(6):C1567–C1575
18. Bareford LM, Swaan PW (2007) Endocytic mechanisms for targeted drug delivery. Adv Drug Deliv Rev 59(8):748–758
19. Karande AA, Sridhar L, Gopinath KS, Adiga PR (2001) Riboflavin carrier protein: a serum and tissue marker for breast carcinoma. Int J Cancer 95:277–281
20. Johnson T, Ouhtit A, Gaur R, Fernando A, Schwarzenberger P, Su J, Ismail MF, El-Sayyad HI, Karande A, Elmageed ZA, Rao P, Raj M (2009) Biochemical characterization of riboflavin carrier protein (RCP) in prostate cancer. Front Biosci Landmark Ed 14:3634–3640
21. Holladay SR, Yang Z-F, Kennedy MD, Leamon CP, Lee RJ, Jayamani M, Mason T, Low PS (1999) Riboflavin-mediated delivery of a macromolecule into cultured human cells. Biochim Biophys Acta Gen Subj 1426(1):195–204
22. Phelps MA, Foraker AB, Gao W, Dalton JT, Swaan PW (2004) A novel rhodamine-riboflavin conjugate probe exhibits distinct fluorescence resonance energy transfer that enables riboflavin trafficking and subcellular localization studies. Mol Pharm 1(4):257–266
23. Huang S-N, Swaan PW (2000) Involvement of a receptor-mediated component in cellular translocation of riboflavin. J Pharmacol Exp Ther 294(1):117–125
24. Leistra AN, Han JH, Tang S, Orr BG, Banaszak Holl MM, Choi SK, Sinniah K (2015) Force spectroscopy of multivalent binding of riboflavin-conjugated dendrimers to riboflavin binding protein. J Phys Chem B 119(18):5785–5792
25. Plantinga A, Witte A, Li M-H, Harmon A, Choi SK, Banaszak Holl MM, Orr BG, Baker JR Jr, Sinniah K (2011) Bioanalytical screening of riboflavin antagonists for targeted drug delivery: a thermodynamic and kinetic study. ACS Med Chem Lett 2(5):363–367

26. Thomas TP, Choi SK, Li M-H, Kotlyar A, Baker JR Jr (2010) Design of riboflavin-presenting PAMAM dendrimers as a new nanoplatform for cancer-targeted delivery. Bioorg Med Chem Lett 20:5191–5194
27. Witte AB, Leistra AN, Wong PT, Bharathi S, Refior K, Smith P, Kaso O, Sinniah K, Choi SK (2014) Atomic force microscopy probing of receptor-nanoparticle interactions for riboflavin receptor targeted gold-dendrimer nanocomposites. J Phys Chem B 118(11): 2872–2882
28. Witte AB, Timmer CM, Gam JJ, Choi SK, Banaszak Holl MM, Orr BG, Baker JR, Sinniah K (2012) Biophysical characterization of a riboflavin-conjugated dendrimer platform for targeted drug delivery. Biomacromol 13:507–516
29. Beztsinna N, Solé M, Taib N, Bestel I (2016) Bioengineered riboflavin in nanotechnology. Biomaterials 80:121–133
30. Marlin F, Simon P, Bonneau S, Alberti P, Cordier C, Boix C, Perrouault L, Fossey A, Saison-Behmoaras T, Fontecave M, Giovannangeli C (2012) Flavin conjugates for delivery of peptide nucleic acids. ChemBioChem 13(17):2593–2598
31. Bareford LM, Avaritt BR, Ghandehari H, Nan A, Swaan PW (2013) Riboflavin-targeted polymer conjugates for breast tumor delivery. Pharm Res 30(7):1799–1812
32. Jayapaul J, Arns S, Bunker M, Weiler M, Rutherford S, Comba P, Kiessling F (2016) In vivo evaluation of riboflavin receptor targeted fluorescent USPIO in mice with prostate cancer xenografts. Nano Res 9(5):1319–1333
33. Lu Y, Low PS (2002) Folate-mediated delivery of macromolecular anticancer therapeutic agents. Adv Drug Deliv Rev 54(5):675–693
34. Low PS, Henne WA, Doorneweerd DD (2008) Discovery and development of folic-acid-based receptor targeting for imaging and therapy of cancer and inflammatory diseases. Acc Chem Res 41(1):120–129
35. Wang H-L, Wang S-S, Song W-H, Pan Y, Yu H-P, Si T-G, Liu Y, Cui X-N, Guo Z (2015) Expression of prostate-specific membrane antigen in lung cancer cells and tumor neovasculature endothelial cells and its clinical significance. PLoS ONE 10(5):e0125924
36. Shukla R, Thomas TP, Peters JL, Desai AM, Kukowska-Latallo J, Patri AK, Kotlyar A, Baker JR (2006) HER2 specific tumor targeting with dendrimer conjugated anti-HER2 mAb. Bioconj Chem 17(5):1109–1115
37. Mamot C, Drummond DC, Greiser U, Hong K, Kirpotin DB, Marks JD, Park JW (2003) Epidermal growth factor receptor (EGFR)-targeted immunoliposomes mediate specific and efficient drug delivery to EGFR- and EGFRvIII-overexpressing tumor cells. Cancer Res 63 (12):3154–3161
38. Foraker AB, Khantwal CM, Swaan PW (2003) Current perspectives on the cellular uptake and trafficking of riboflavin. Adv Drug Deliv Rev 55(11):1467–1483
39. Wu AML, Dedina L, Dalvi P, Yang M, Leon-Cheon J, Earl B, Harper PA, Ito S (2016) Riboflavin uptake transporter Slc52a2 (RFVT2) is upregulated in the mouse mammary gland during lactation. Am J Physiol Regul Integr Comp Physiol 310(7):R578–R585
40. Yonezawa A, Inui K-I (2013) Novel riboflavin transporter family RFVT/SLC52: identification, nomenclature, functional characterization and genetic diseases of RFVT/SLC52. Mol Aspects Med 34(2–3):693–701
41. White HB, Merrill AH (1988) Riboflavin-binding proteins. Annu Rev Nutr 8(1):279–299
42. Wong PT, Tang K, Coulter A, Tang S, Baker JR, Choi SK (2014) Multivalent dendrimer vectors with DNA intercalation motifs for gene delivery. Biomacromol 15(11):4134–4145
43. Miranda-Lorenzo I, Dorado J, Lonardo E, Alcala S, Serrano AG, Clausell-Tormos J, Cioffi M, Megias D, Zagorac S, Balic A, Hidalgo M, Erkan M, Kleeff J, Scarpa A, Sainz B Jr, Heeschen C (2014) Intracellular autofluorescence: a biomarker for epithelial cancer stem cells. Nat Methods 11(11):1161–1169
44. Zheng DB, Lim HM, Pène JJ, White HB (1988) Chicken riboflavin-binding protein. cDNA sequence and homology with milk folate-binding protein. J Biol Chem 263(23): 11126–11129

45. Monaco HL (1997) Crystal structure of chicken riboflavin-binding protein. EMBO J 16(7): 1475–1483
46. Huang S-N, Phelps MA, Swaan PW (2003) Involvement of endocytic organelles in the subcellular trafficking and localization of riboflavin. J Pharmacol Exp Ther 306(2):681–687
47. Mack M, Grill S (2006) Riboflavin analogs and inhibitors of riboflavin biosynthesis. Appl Microbiol Biotechnol 71(3):265–275
48. Chu CK, Bardos TJ (1977) Synthesis and inhibition analysis of 2(4)-imino-4(2)-amino-2,4-dideoxyriboflavin, a dual antagonist of riboflavin and folinic acid. J Med Chem 20(2):312–314
49. Musser EA, Heinle RW (1958) The effect of a riboflavin antagonist upon leukocytes of normal and shay myeloid chloroleukemic rats. Blood 13(5):464–474
50. Choi S-K (2004) Synthetic multivalent molecules: concepts and biomedical applications. Wiley, New Jersey
51. Mammen M, Choi SK, Whitesides GM (1998) Polyvalent interactions in biological systems: implications for design and use of multivalent ligands and inhibitors. Angew Chem Int Ed 37:2754–2794
52. Fasting C, Schalley CA, Weber M, Seitz O, Hecht S, Koksch B, Dernedde J, Graf C, Knapp E-W, Haag R (2012) Multivalency as a chemical organization and action principle. Angew Chem Int Ed 51(42):10472–10498
53. Caelen I, Kalman A, Wahlstrom L (2003) Biosensor-based determination of riboflavin in milk samples. Anal Chem 76(1):137–143
54. Wu FYH, MacKenzie RE, McCormick DB (1970) Kinetics and mechanism of oxidation-reduction reactions between pyridine nucleotides and flavins. Biochemistry 9(11):2219–2224
55. Tomalia DA, Naylor AM, Goddard WA (1990) Starburst dendrimers: molecular-level control of size, shape, surface chemistry, topology, and flexibility from atoms to macroscopic matter. Angew Chem Int Ed 29(2):138–175
56. Wong P, Tang S, Mukherjee J, Tang K, Gam K, Isham D, Murat C, Sun R, Baker JR, Choi SK (2016) Light-controlled active release of photocaged ciprofloxacin for lipopolysaccharide-targeted drug delivery using dendrimer conjugates. Chem Commun (Cambridge UK) 52:10357–10360
57. Wong PT, Chen D, Tang S, Yanik S, Payne M, Mukherjee J, Coulter A, Tang K, Tao K, Sun K, Baker JR Jr, Choi SK (2015) Modular integration of upconversion nanocrystal-dendrimer composites for folate receptor-specific near infrared imaging and light triggered drug release. Small 11(45):6078–6090
58. Cloninger MJ (2002) Biological applications of dendrimers. Curr Opin Chem Biol 6(6): 742–748
59. Esfand R, Tomalia DA (2001) Poly(amidoamine) (PAMAM) dendrimers: from biomimicry to drug delivery and biomedical applications. Drug Discov Today 6(8):427–436
60. Majoros I, Baker J Jr (eds) (2008) Dendrimer-based nanomedicine. Pan Stanford, Hackensack
61. Medina SH, El-Sayed MEH (2009) Dendrimers as carriers for delivery of chemotherapeutic agents. Chem Rev (Washington, DC, US) 109(7):3141–3157
62. Rosowsky A, Forsch RA, Wright JE (2004) Synthesis and in vitro antifolate activity of rotationally restricted aminopterin and methotrexate analogues. J Med Chem 47(27): 6958–6963
63. Kiessling LL, Gestwicki JE, Strong LE (2000) Synthetic multivalent ligands in the exploration of cell-surface interactions. Curr Opin Chem Biol 4(6):696–703
64. Horowitz ED, Hud NV (2006) Ethidium and proflavine binding to a 2′,5′-Linked RNA duplex. J Am Chem Soc 128(48):15380–15381
65. Sankaran NB, Nishizawa S, Seino T, Yoshimoto K, Teramae N (2006) Abasic-site-containing oligodeoxynucleotides as aptamers for riboflavin. Angew Chem Int Ed 45(10): 1563–1568
66. Luo D, Saltzman WM (2000) Synthetic DNA delivery systems. Nat Biotechnol 18(1):33–37

67. Herd H, Daum N, Jones AT, Huwer H, Ghandehari H, Lehr C-M (2013) Nanoparticle geometry and surface orientation influence mode of cellular uptake. ACS Nano 7(3):1961–1973
68. Giljohann DA, Seferos DS, Daniel WL, Massich MD, Patel PC, Mirkin CA (2010) Gold nanoparticles for biology and medicine. Angew Chem Int Ed 49(19):3280–3294
69. Daniel M-C, Astruc D (2004) Gold nanoparticles; assembly, supramolecular chemistry, quantum-size-related properties, and applications toward biology, catalysis, and nanotechnology. Chem Rev (Washington, DC, US) 104(1):293–346
70. El-Sayed IH, Huang X, El-Sayed MA (2005) Surface plasmon resonance scattering and absorption of anti-EGFR antibody conjugated gold nanoparticles in cancer diagnostics: applications in oral cancer. Nano Lett 5(5):829–834
71. El-Sayed IH, Huang X, El-Sayed MA (2006) Selective laser photo-thermal therapy of epithelial carcinoma using anti-EGFR antibody conjugated gold nanoparticles. Cancer Lett (NY, NY, US) 239(1):129–135
72. Qian W, Huang X, Kang B, El-Sayed MA (2010) Dark-field light scattering imaging of living cancer cell component from birth through division using bioconjugated gold nanoprobes. J Biomed Opt 15(4):46025–46029
73. Klein S, Petersen S, Taylor U, Barcikowski S, Rath D (2010) Quantitative visualization of colloidal and intracellular gold nanoparticles by confocal microscopy. J Biomed Opt 15(3):36015
74. Lee YC, Lee RT (1995) Carbohydrate-protein interactions: basis of glycobiology. Acc Chem Res 28(8):321–327
75. Choi S-K, Mammen M, Whitesides GM (1997) Generation and in situ evaluation of libraries of poly(acrylic acid) presenting sialosides as side chains as polyvalent inhibitors of influenza-mediated hemagglutination. J Am Chem Soc 119(18):4103–4111
76. Jayaraman N (2009) Multivalent ligand presentation as a central concept to study intricate carbohydrate-protein interactions. Chem Soc Rev 38(12):3463–3483
77. Hong S, Leroueil PR, Majoros IJ, Orr BG, Baker JR Jr, Banaszak Holl MM (2007) The binding avidity of a nanoparticle-based multivalent targeted drug delivery platform. Chem Biol (Oxford UK) 14(1):107–115
78. Li X, Zhou H, Yang L, Du G, Pai-Panandiker AS, Huang X, Yan B (2011) Enhancement of cell recognition in vitro by dual-ligand cancer targeting gold nanoparticles. Biomaterials 32 (10):2540–2545
79. Silpe JE, Sumit M, Thomas TP, Huang B, Kotlyar A, van Dongen MA, Banaszak Holl MM, Orr BG, Choi SK (2013) Avidity modulation of folate-targeted multivalent dendrimers for evaluating biophysical models of cancer targeting nanoparticles. ACS Chem Biol 8(9): 2063–2071
80. Li M-H, Choi SK, Thomas TP, Desai A, Lee K-H, Kotlyar A, Banaszak Holl MM, Baker JR Jr (2012) Dendrimer-based multivalent methotrexates as dual acting nanoconjugates for cancer cell targeting. Eur J Med Chem 47:560–572
81. Thomas TP, Huang B, Choi SK, Silpe JE, Kotlyar A, Desai AM, Gam J, Joice M Jr (2012) Polyvalent PAMAM-methotrexate dendrimer as a folate receptor-targeted therapeutic. Mol Pharm 9(9):2669–2676
82. Thomas TP, Joice M, Sumit M, Silpe JE, Kotlyar A, Bharathi S, Kukowska-Latallo J, Baker JR, Choi SK (2013) Design and in vitro validation of multivalent dendrimer methotrexates as a folate-targeting anticancer therapeutic. Curr Pharm Des 19(37): 6594–6605
83. Wong P, Choi SK (2015) Mechanisms and implications of dual-acting methotrexate in folate-targeted nanotherapeutic delivery. Int J Mol Sci 16(1):1772–1790
84. Choi SK, Myc A, Silpe JE, Sumit M, Wong PT, McCarthy K, Desai AM, Thomas TP, Kotlyar A, Banaszak Holl MM, Orr BG, Baker JR (2013) Dendrimer-based multivalent vancomycin nanoplatform for targeting the drug-resistant bacterial surface. ACS Nano 7(1): 214–228

85. Krishnamurthy VM, Quinton LJ, Estroff LA, Metallo SJ, Isaacs JM, Mizgerd JP, Whitesides GM (2006) Promotion of opsonization by antibodies and phagocytosis of gram-positive bacteria by a bifunctional polyacrylamide. Biomaterials 27(19):3663–3674
86. Qi G, Li L, Yu F, Wang H (2013) Vancomycin-modified mesoporous silica nanoparticles for selective recognition and killing of pathogenic gram-positive bacteria over macrophage-like cells. ACS Appl Mater Interfaces 5(21):10874–10881
87. Kell AJ, Stewart G, Ryan S, Peytavi R, Boissinot M, Huletsky A, Bergeron MG, Simard B (2008) Vancomycin-modified nanoparticles for efficient targeting and preconcentration of gram-positive and gram-negative bacteria. ACS Nano 2(9):1777–1788
88. Li M-H, Choi SK, Leroueil PR, Baker JR (2014) Evaluating binding avidities of populations of heterogeneous multivalent ligand-functionalized nanoparticles. ACS Nano 8(6): 5600–5609
89. Choi S-K, Mammen M, Whitesides GM (1996) Monomeric inhibitors of influenza neuraminidase enhance the hemagglutination inhibition activities of polyacrylamides presenting multiple C-sialoside groups. Chem Biol (Oxford UK) 3:97–104
90. Bhatia S, Dimde M, Haag R (2014) Multivalent glycoconjugates as vaccines and potential drug candidates. MedChemComm 5(7):862–878
91. Zhou H, Jiao P, Yang L, Li X, Yan B (2010) Enhancing cell recognition by scrutinizing cell surfaces with a nanoparticle array. J Am Chem Soc 133(4):680–682
92. Mintzer MA, Dane EL, O'Toole GA, Grinstaff MW (2011) Exploiting dendrimer multivalency to combat emerging and re-emerging infectious diseases. Mol Pharm 9(3): 342–354
93. Bromfield SM, Posocco P, Fermeglia M, Tolosa J, Herreros-López A, Pricl S, Rodríguez-López J, Smith DK (2014) Shape-persistent and adaptive multivalency: rigid transgeden (TGD) and flexible PAMAM dendrimers for heparin binding. Chem Eur J 20(31):9666–9674
94. Bhatia S, Camacho LC, Haag R (2016) Pathogen inhibition by multivalent ligand architectures. J Am Chem Soc 138(28):8654–8666
95. Hlavacek WS, Posner RG, Perelson AS (1999) Steric effects on multivalent ligand-receptor binding: exclusion of ligand sites by bound cell surface receptors. Biophys J 76(6):3031–3043
96. Howard M, Zern BJ, Anselmo AC, Shuvaev VV, Mitragotri S, Muzykantov V (2014) Vascular targeting of nanocarriers: perplexing aspects of the seemingly straightforward paradigm. ACS Nano 8(5):4100–4132
97. Choi SK, Leroueil P, Li M-H, Desai A, Zong H, Van Der Spek AFL, Baker JR Jr (2011) Specificity and negative cooperativity in dendrimer-oxime drug complexation. Macromolecules 44(11):4026–4029
98. Gomez-Casado A, Dam HH, Yilmaz MD, Florea D, Jonkheijm P, Huskens J (2011) Probing multivalent interactions in a synthetic host-guest complex by dynamic force spectroscopy. J Am Chem Soc 133(28):10849–10857
99. Roy R (1996) Syntheses and some applications of chemically defined multivalent glycoconjugates. Curr Opin Struct Biol 6(5):692–702
100. Mullen DG, Fang M, Desai A, Baker JR Jr, Orr BG, Banaszak Holl MM (2010) A quantitative assessment of nanoparticle-ligand distributions: implications for targeted drug and imaging delivery in dendrimer conjugates. ACS Nano 4(2):657–670
101. Teulon J-M, Delcuze Y, Odorico M, S-wW Chen, Parot P, Pellequer J-L (2011) Single and multiple bonds in (strept)avidin-biotin interactions. J Mol Recognit 24(3):490–502

Chapter 8
Nanomaterials in Cancer Theranostics

Lei Zhu, Lily Yang and Zhiyang Zhou

Abstract Recent advances in the development of novel nanomaterials and evaluation of their biomedical applications have shown promises of those multifunctional nanomaterials in the development of new approaches for cancer detection and therapy. The unique physicochemical properties of nanomaterials, small size, and large surface-area-to-volume ratio endow them with novel multifunctional capabilities for cancer imaging, drug delivery, and cancer therapy, referred to as theranostics, which are different from the traditional diagnosis and therapy approaches. To facilitate the translation of nanomaterials as imaging agents and drug delivery carriers into clinical applications, great efforts have been made on designing and improving biocompatibility, stability, safety, drug loading ability, targeted delivery, imaging signals, and thermal- or photodynamic responses. With the development of companion new imaging techniques and therapeutic approaches, several nanomaterials have demonstrated great theranostic potential in image-guided therapy of diseases, especially in cancer therapy. In this review, the current status and perspective of nanoparticles in the development of cancer theranostic agents will be discussed with a focus on several representative nanomaterials, including magnetic iron oxide nanoparticles, gold nanoparticles, silica nanoparticles, polymeric nanoparticles, and carbon nanomaterials.

Keywords Nanomaterials · Theranostics · Imaging-guide therapy

L. Zhu (✉) · L. Yang (✉)
Department of Surgery,
Emory University School of Medicine, Atlanta, GA 30322, USA
e-mail: lei.zhu@emory.edu

L. Yang
e-mail: lyang02@emory.edu

Z. Zhou
Xiangya School of Medicine, Central South University,
Changsha 410008, Hunan, China

B. Yan et al. (eds.), *Bioactivity of Engineered Nanoparticles*,
Nanomedicine and Nanotoxicology, DOI 10.1007/978-981-10-5864-6_8

8.1 Introduction

Cancer is characterized by the uncontrolled growth and spreading of abnormal cells. It has been a public health issue in many countries all over the world, including the US [1, 2]. Although progresses have been made in cancer diagnosis and treatment, the survival rate of cancer patients is still low, especially for those diagnosed at the later stage. Therefore, sensitive and specific diagnostic and effective therapeutic approaches are needed for the improvement of prognosis of cancer patients [3].

Nanoparticles, composed of different types of materials as the small particles in a nanoscale range, can be classified as organic and inorganic nanoparticles [4] (Fig. 8.1). Specifically, inorganic nanoparticles include metal nanoparticles, carbon nanoparticles, and quantum dots, while organic nanoparticles usually contain biocompatible materials, such as lipids, polymers, liposomes, polymeric micelles, dendrimers, and engineered peptides and nucleic acids. Nanoparticles have high ratio of the surface area-to-body volume, various chemical compositions, and biological characteristics that enable their ability of surface modification for conjugation or encapsulation of targeting, drug loading, and imaging contrast agents [5]. Moreover, surface characteristics play a vital role in metabolism and distribution of nanoparticles in the blood circulation. Various approaches have been developed to reduce nonspecific uptake by macrophages in the reticuloendothelial system (RES), such as polyethylene glycol (PEG) or antifouling polymer coating of the surface of nanoparticles [6, 7]. It is well accepted that after modification with PEG, nanoparticles could increase physiological stability, reduce nonspecific interaction with serum proteins and macrophages, and therefore prolong the half-life time in the blood circulation, which improve the passive targeting to tumor sites. Additionally, the shape of nanoparticles affects the blood half-life, macrophage uptake, extravasation, and internalization by cells. It has been reported that oblong-shaped nanoparticles can circulate in vivo for longer time than nanospheres due to the low level of macrophage uptake [8, 9].

A marked feature of nanoparticle-mediated drug delivery following systemic delivery is that small size nanoparticle drug carriers (<200 nm) can be delivered into and accumulated in tumors by the enhanced permeability and retention (EPR) effect through the leaking tumor vasculatures [10]. Drug delivery utilizing passively targeted nanoparticles have shown improved intratumoral delivery efficiency and therapeutic efficacy in preclinical and clinical studies. Most of the U.S. Food and Drug Administration (FDA) approved imaging and therapeutic nanoparticles that are currently used in cancer patients or in clinical trials are nontargeted nanoparticles (Table 8.1).

In human tumors, distribution, structure, and permeability of tumor vessels are highly heterogeneous [11]. To increase the efficiency of nanoparticle delivery and retention in tumors, targeting ligands to certain receptors that are highly expressed in tumor vasculatures, tumor stromal cells, and tumor cells have been conjugated onto the nanoparticles [12]. Those include antibodies or engineered antibody fragments, natural ligands, peptides, structured DNA and RNA molecules, and

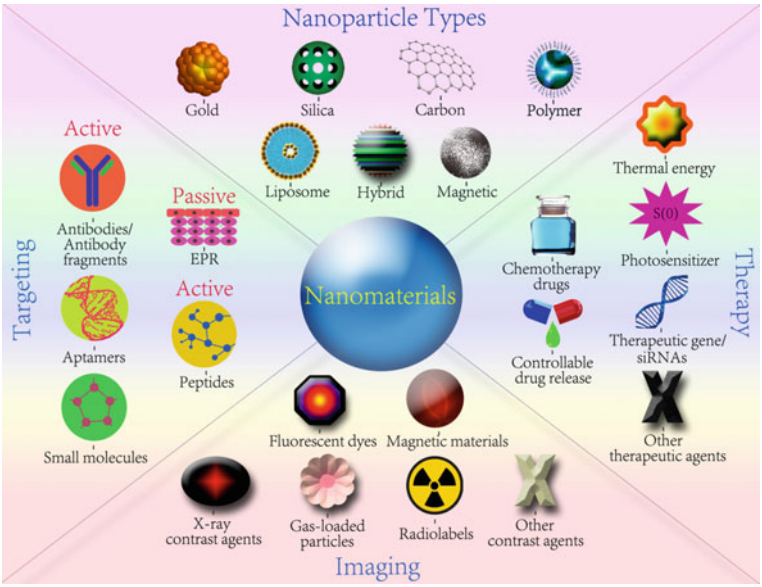

Fig. 8.1 Classification, modification, and functionalization of theranostic nanoparticles in biomedical applications

small molecules [12] (Fig. 8.1). Extensive preclinical studies have been conducted using different tumor targeting ligand conjugated nanoparticles, either as imaging probes or drug carriers [5, 13]. Improved drug delivery efficiency and therapeutic response have been demonstrated in various animal tumor models. Several targeted nanoparticle formulated drugs are currently in clinical trials to determine the therapeutic effect of targeted nanoparticles in human cancer patients (Table 8.1). Although theranostic nanoparticles have not been tested in human patients so far, preclinical studies have demonstrated the feasibility of further development of the nanoparticle platforms that have been tested in human patients into theranostic nanoparticles by conjugation or encapsulation of imaging contrasts, such as radioisotopes, optical dyes, gadolinium, or magnetic iron oxide nanoparticles [13–15]

For the development of effective targeted theranostic nanoparticles for cancer therapy, several major challenges are well recognized. First, it is important to identify an imaging and therapy suitable biomarker that is highly expressed in tumor cells but is absent or expressed at a low level in normal cells. There should also be an available corresponding targeting ligand that binds to the receptor with a high affinity and can be produced in large quantities for in vivo applications in the experimental animals and humans. For the development of a theranostic agent, it is critical for the nanoparticles to be stable, biocompatible, biodegradable, and low or no toxic. As a theranostic agent, it also requires the nanoparticle to have the capability of carrying and releasing therapeutic payloads after entering tumor

Table 8.1 Representative nanoparticle drug carriers in clinical trials or FDA-approved cancer nanotherapeutics

NP type	Name and formulation	Application	Status	Ref.
Iron oxide NP	Feridex® Sterile aqueous colloid of superparamagnetic iron oxide coated with dextran	MRI; focal hepatic lesions	FDA-approved	[16–18]
	Combidex® Ultrasmall superparamagnetic iron oxide covered with low molecular weight dextran	MRI; metastatic cancer lesions	Approved in Europe	[19, 20]
	Resovist® Superparamagnetic iron oxide nanoparticles coated with carboxyl dextran	MRI; focal hepatic lesions	Approved in Europe	[21–23]
	Gastromark® Aqueous suspension of silicone-coated, superparamagnetic iron oxide	MRI; gastrointestinal lumen imaging	FDA-approved	[15, 24]
Liposome NP	Doxil®, Lipodox® (Doxorubicin HCl liposome injection) DaunoXome® (Daunorubicin Citrate Liposome Injection)	Recurrent ovarian cancer, AIDS-related Kaposi's sarcoma, metastatic breast cancer	FDA-approved	[25–31]
	DepoCyt® Cytarabine liposome injection	Lymphomatous meningitis	FDA-approved	[32–34]
	Myocet® Liposomal doxorubicin	Metastatic breast cancer	Approved in Europe	[35, 36]
	LiPlaCis® Liposomal cisplatin	Solid tumors	Clinical trial	[37]
	DOTAP Liposomal transfection reagent	Gene transfer; lung cancer	Clinical trial	[38]
	Onivyde® Irinotecan liposome	Chemotherapy; metastatic pancreatic cancer	FDA-approved	[39]
Polymeric NP	Genexol® PM Cremophor EL-free polymeric micelle formulation of paclitaxel	Advanced non-small cell lung cancer, metastatic breast cancer	FDA-approved	[40–42]
	CALAA-01 Transferrin receptor-targeted anti-RRM2 siRNA	Solid malignancies	Clinical trial	[43, 44]
	DEP™ docetaxel Dendrimer-docetaxel	Solid tumors including breast, lung and prostate cancers	Clinical trial	[45, 46]
	Oncaspar® L-asparaginase (L-asparagine amidohydrolase) covalently conjugated to mono-methoxypolyethylene glycol (mPEG)	Acute lymphoblastic leukemia	FDA-approved	[47, 48]
	Opaxio® Polyglutamate polymer-paclitaxel	Lung cancer, ovarian cancer	Clinical trial	[49–51]

tissues or cancer cells. In addition to the all above criteria for a nanotherapeutic agent, theranostic nanoparticles should be able to generate stable and strong imaging signals or contrasts for noninvasive imaging of intratumoral nanoparticle drug delivery and tumor response to the therapy. To achieve this goal, specific and sensitive imaging techniques that are tailored to detect nanoparticle specific imaging signals will also be needed.

Theranostic nanoparticles can be engineered to have unique physicochemical properties that respond to external treatment to activate their antitumor effect. For example, in response to a laser irradiation, gold nanoparticles, carbon nanotubes, and near-infrared dye-conjugated nanoparticles are able to generate heat to kill surrounding tumor cells by photothermal therapy (PTT). Furthermore, photodynamic therapy (PDT) involves in nanoparticles conjugated with photosensitizers that can be activated by specific wavelength of light and then produces reactive oxygen species (ROS) to kill tumor cells.

8.2 Nanomaterials for the Development of Theranostic Nanoparticles

Theranostic nanomaterials are designed to contain both imaging and therapeutic agents. Up to date, various single or multiple imaging modality nanoparticles have been developed for optical, PET, SPECT, MRI, and photoacoustic imaging. In addition to the promising imaging property, theranostic nanoparticles have been produced to carry a single therapeutic agent or the combination of drugs [52], including chemotherapy drugs, small molecules, photosensitizers, and siRNAs. Significant advantages of nanoparticle formulated drug delivery include: (1) increasing in the drug dose by selective delivery of a large amount of drug molecules, especially highly insoluble drug-loaded nanoparticles, into the tumor while reducing systemic side effects [53]; (2) protecting drug molecules or biological therapeutic agents (siRNAs or peptides) from degradation before reaching target tissues and cells [43]; and (3) targeted delivery through cell receptors that bypasses multidrug-resistant mechanisms on tumor cell membrane [54]. For example, Doxil is a pegylated liposomal doxorubicin drug that is currently used in the clinic for cancer therapy. Liposomal formulated doxorubicin significantly reduced the risk for cumulative cardiac toxicity of the drug [55]. Abraxane is an FDA-approved cancer nanotherapeutic that contains 50–150 nm size nanoparticles composited of clusters of human albumin bound with paclitaxel. Paclitaxel is an effective antitumor drug but has a very poor water solubility that requires a special solvent, Cremophor EL (polyoxyethylated castor oil), in the drug formulation, which may induce inflammatory responses. Many patients had to be pretreated with steroid medications before administration of the anticancer drug. However, albumin-bound paclitaxel can be administrated into cancer patients at a higher dose (260 mg/m^2) with reduced systemic toxicity than the conventional paclitaxel with i.v. dose of

175 mg/m^2 [56]. A recent FDA-approved liposomal irinotecan formulation, Onivyde, in combination with conventional fluorouracil and leucovorin, to treat patients with metastatic pancreatic cancer that were resistant to gemcitabine treatment prolonged survival of the patients for 1.9 months [57].

Encouraged by clinical successes of nanodrugs, great efforts have been made toward the development of new and improved nanoparticle drugs or theranostic nanoparticles in preclinical and clinical studies. It is well known that human cancers are highly heterogeneous in their vascular structures and distribution, tumor stromal components, and tumor cells. To improve therapeutic efficacy, it is important to accurately assess the efficiency of intratumoral drug delivery, especially nanoparticle-mediated drug delivery, in individual patients using a noninvasive imaging. Such a precision oncology approach using image-guided drug delivery should allow timely assessment and adjustment of treatment strategies for cancer patients. Therefore, the development of theranostic nanoparticles with the ability of targeted drug delivery and imaging has the potential to contribute significantly to the personalized and effective cancer treatment. In the following sections, current status and results of the development of theranostic nanoparticles using different nanomaterials will be discussed.

8.2.1 Magnetic Nanomaterials

Magnetic nanomaterials refer to a class of nanocomplexes with a metal core, which can be iron, nickel, cobalt, gadolinium, or their oxide or chelated compounds [58]. The magnetism of magnetic nanomaterials makes them applicable as magnetic resonance imaging (MRI) contrast agents. One of the most widely applied magnetic nanomaterials is iron oxide nanoparticles that have been used as MRI contrasts in experimental animals and human patients [59, 60]. At present, magnetic iron oxide nanoparticles are one of the few FDA-approved nanomaterials that have been used in humans for clinical MRI applications (Table 8.1).

MRI has high imaging resolution, 3D-imaging capability, and anatomical information in soft tissues for the detection of intratumoral nanoparticle drug delivery and distribution. Extensive investigations have been done to develop targeted MRI contrast agents based on iron oxide nanoparticles to improve their tumor accumulation and imaging specificity and sensitivity. For example, peptides, antibodies, or antibody fragments that specifically bind to receptors overexpressed in tumor cells, such as MUC-1, αVβ3 integrin, epidermal growth factor receptor (EGFR), HER2/neu, urokinase plasminogen activator receptor (uPAR), and prostate specific membrane antigen (PSMA), were conjugated to the surface of polymer coated iron oxide nanoparticles. Systemic delivery of those MRI nanoparticle imaging probes led to the targeted accumulation and retention of the iron oxide nanoparticles in tumor tissues, enabling MRI T_2 contrast decreases and detection of tumors by MRI [61]. Furthermore, receptor-mediated endocytosis further increases intratumoral cell delivery of the nanoparticles and relative long-term retention of the

nanoparticles in tumors for imaging drug delivery and tumor responses to the therapy [62].

To improve MRI contrasts of the nanoparticles, various iron nanoparticle core sizes and surface modifications have been studied for their MR imaging properties. Although magnetic iron oxide nanoparticles have been generally considered as T_2 contrasts or dark effect MRI agents, the effect of the particle size on MRI contrast property is recognized by several studies. It has been shown that T_2 contrast increases as the size of iron oxide nanoparticles becomes larger [63]. When the nanoparticle core size is smaller (<5 nm), T_1 signal is dominant and gives rise to bright T_1 contrast. The production of strong T_1 MRI contrast from sub 5 nm core size iron oxide nanoparticles has been demonstrated in vitro in solution and in animal tumor models in vivo [6].

A recently study also showed that protein-coated iron oxide nanoparticles, such as milk casein protein, have prominent T_2 enhancing capability following intratumoral cell delivery of the nanoparticle MRI contrast [6]. Singe-chain anti-EGFR antibody-conjugated and milk casein protein-coated iron oxide nanoparticles showed targeted nanoparticle accumulation in a human breast cancer xenograft model in nude mice, producing strong T_2 MRI contrast [6].

To reduce nonspecific macrophage uptake and improve blood circulation time and biodistribution of the iron oxide nanoparticles, an anti-biofouling polymer-PEO-block-poly(γ-methacryloxypropyltrimethoxysilane) (PEO-b-PγMPS) has been developed to coat magnetic iron oxide nanoparticles [64]. Compared with other surface modified strategies for stabilizing the nanoparticles, PEO-b-PγMPS coated nanoparticles have enhanced cell targeting ability. In a recent study, HER2 antibody and ScFvEGFR were covalently conjugated to iron oxide nanoparticles. Both in vitro and in vivo results showed that anti-biofouling polymer coated iron oxide nanoparticles accumulated at a high level in breast tumors with reduced uptake in macrophages in the liver and spleen, suggesting the potential of using this system for improved tumor targeting and nanoparticle drug delivery tumor [65].

Iron oxide nanoparticles are promising drug carriers for the development of clinically applicable theranostic agents since they are biodegradable and have low toxicity. Furthermore, MRI is a commonly used clinical imaging modality, making the translation of MRI-guided drug delivery in cancer patients a feasible approach [12]. For example, to overcome the physical barrier of the stroma in drug delivery, theranostic nanoparticles targeting uPAR that is highly expressed in both pancreatic cancer cells and tumor associated stromal cells have been developed and their antitumor effects have been examined in a human pancreatic cancer xenograft model in nude mice. uPAR targeting ligands, derived from the amino-terminal fragment (ATF) peptides of urokinase plasminogen activator(uPA), were conjugated onto iron oxide nanoparticles (IONPs) carrying a conditional release chemotherapy drug, gemcitabine (Gem) (ATF-IONP-Gem) [66]. Systemic delivery of uPAR-targeted ATF-IONP-Gem resulted in a significant growth inhibition of pancreatic tumors. Nanoparticle drug delivery and changes in MRI contrasts and tumor sizes could be detected by MRI. To detect drug-resistant residual tumors, an

ultrashort TE MRI scan method was developed and produced MR images with bright T_1 contrasts in the resistant tumors containing delivered ATF-IONP-Gem [66]. Resistance to chemotherapy is a major and unmet challenge. Recent studies have demonstrated the ability of overcoming drug-resistant mechanism on the tumor cell membrane by nanoparticle-mediated internalization of nanoparticle drug complexes. It has been shown that hollow iron oxide nanoparticles (HIONPs) modified with human serum albumin (HSA) and incorporated with doxorubicin (DOX) had significantly higher level of intratumoral cell nanoparticle-DOX delivery compared to conventional DOX treatment in a multidrug-resistant human ovarian cancer OVCAR8-ADR cell line [54], which might be caused by decreased efflux of nanoparticle drugs by P-glycoprotein that located on the cellular membrane and transported free drugs out of cells.

Increasing evidence shows that insulin-like growth factor 1 receptor (IGF1R) is highly expressed in drug-resistant tumor cells and tumor stromal cells [67]. Recombinant human IGF1 has been used as a targeting ligand to be conjugated to theranostic IONPs carrying DOX. The effect of the theranostic IONPs was evaluated in an orthotopic human pancreatic cancer patient tissue derived xenograft model that recapitulated heterogeneous tumor cells and enriched tumor stroma in human pancreatic cancer [67]. Results of this study showed that IGF1R targeted IGF1-INOP-DOX theranostic nanoparticles efficiently targeted pancreatic tumors and were detectable by optical and MR imaging. Repeated delivery of IGF1-IONP-DOX led to breaking tumor stromal drug delivery barriers and significant tumor growth inhibition in this human pancreatic cancer tumor xenograft model in nude mice (Fig. 8.2). Histological analysis also revealed the inhibition of cell proliferation and induction of cell apoptosis in pancreatic cancer cells following IFG1-IONP-DOX treatment, suggesting that the IGF-1R-targeted theranostic IONP is a promising drug delivery system for further development of effective approaches for cancer treatment.

A. transmission electron microscopic (TEM) image of DOX capsulated NIR830-IGF1-IONPs. B. Pre- and post-24 h T_2-weighted MR images. Numbers shown are relative mean MRI signal intensities of the entire tumor. Pink arrows indicate the location of orthotopic pancreatic tumors. C. Tumor growth inhibition. The mean tumor weight (navy bar) and individual tumor weight distributions as color symbols after the treatment are shown. D. whole body NIR optical imaging 24 h after IONP administration. Optical images were overlaid with X-ray images of the mice. Red numbers shown are the mean signal intensities of tumor areas. E. Prussian blue staining of frozen tumor sections. Blue: IONP-positive cells. Red: nuclear fast red. Adapted with permission from [67]. Copyright 2015 American Chemical Society.

Unlike chemotherapy, hyperthermia induces cancerous cells undergoing apoptosis under high-temperature conditions. It also sensitizes cancer cells to radiation therapy or chemotherapy. In addition, external magnetic field induces superparamagnetism in magnetic nanoparticles, at the same time, could locally convert magnetic field energy to thermal energy, which is called magnetic hyperthermia [68–70]. For example, magnetic hyperthermia mediated by iron oxide nanoparticles

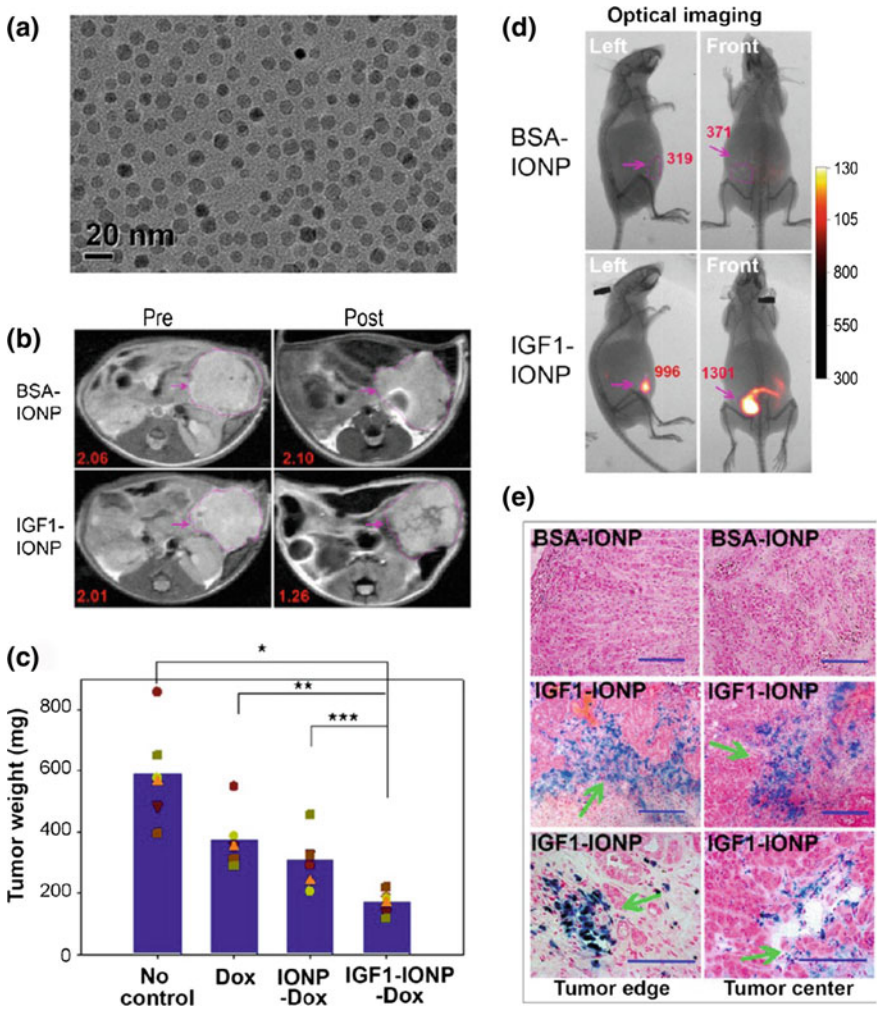

Fig. 8.2 Evaluation of the effect of IGF-1R targeted IONP carrying DOX for targeted and image-guided tumor therapy in a human pancreatic cancer patient tissue derived xenograft model. Reprinted with permission from [67]. Copyright © 2015, American Chemical Society

could increase temperature in the tumor center to >40 °C after exposed to alternating magnetic field [71], resulting in tumor growth inhibition in a human head and neck tumor xenograft model. Iron oxide nanoparticle-facilitated magnetic hyperthermia has been translated in human patients in clinical trails [72]. After receiving iron oxide nanoparticle-induced hyperthermia and low dosage radiotherapy, a significant increase in survival of the patients with recurrent glioblastoma was observed in the combination treatment group comparing to the control groups. No serious complications were found in the clinical trials, suggesting that the

combination of thermo- and radiotherapy is a safe and effective approach. As aforementioned, iron oxide nanoparticles mediated magnetic hyperthermia triggered by the external magnetic field not only ablated cancer cells, but also increased the effectiveness of other treatments. In comparison with laser-triggered photothermal therapy, magnetic hyperthermia therapy is more promising in translation due to the unlimited tissue penetration ability and the reduced skin damage. Although there may be some magnetic-thermal conversion efficient concern, it can be solved by the combined therapy, such as radiotherapy/magnetic hyperthermia or chemotherapy/magnetic hyperthermia.

Considering the potential and growing applications of MNPs, it is required to evaluate and clarify the toxicity of Magnetic nanoparticles. Typically, IONPs are internalized and degraded by Kupffer cells in liver and macrophages of spleen [73]. Once degraded, free iron will be released from IONP and participate in Fenton reaction to generate hydroxyl radicals. In addition, free irons will be stored in the form of protein complex, for example ferritin, for further applications. Unfortunately, the over amount of these iron–protein complex will induce an expression of ROS which is a major reason behind cell death [74]. A well design of shape, size, and surface charge of IONP will be a way of optimizing IONP in vivo behavior and reducing the potential systemic toxicity.

8.2.2 Gold Nanoparticles

Gold nanoparticles (GNPs), including gold nanorods, nanoshells, nanospheres, and nanocages, have been intensively studied for many years due to their unique surface plasmon resonance (SPR) effect, strong NIR light absorption, and the potential to integrate different entities at the same time for cancer diagnosis, and treatment.

GNPs with strong absorption and scattering intensity at a selected light wavelength [75] allow them as contrast agents for computed tomography (CT) imaging, optical imaging, photoacoustic imaging and surface-enhanced Raman spectroscopy imaging [76, 77] A folic acid (FA) targeting dendrimer stabilized gold nanoparticle (Au DSNPs) has shown the ability as a CT imaging contrast in a head and neck cancer xenograft model [78]. A notably higher CT value was observed in Au DSNPs treated tumor than that of a conventional CT contrast agent, Omnipaque. However, due to the fact that a large amount of the contrast agent is needed to produce a satisfying CT imaging, GNPs may not be the perfect choice clinically, considering the cost and safety. Alternatively, photoacoustic or Raman imaging has a higher sensitivity than CT imaging and can be used when GNPs will be used as the contrasts for imaging applications [79].

Besides the imaging ability, GNPs have been investigated as delivery scaffolds for tumor therapeutic agents. GNPs are feasible to encapsulate drug molecules to improve their solubility. Moreover, attachment of targeting ligands further improves the selective accumulation of therapeutic drugs into target sites. At present, GNPs carrying various therapeutic agents, including DOX, camptothecin,

irinotecan, topotecan, and paclitaxel [80–82], have been developed by many research groups and their antitumor effects have been reported in various mouse tumor models [83]. For example, You et al constructed a doxorubicin loaded hollow GNPs for tumor treatment. Significantly greater killing of the MDA-MB-231 breast cancer cells was observed after NIR laser triggered DOX release [84], suggesting that GNPs are promising carriers for chemotherapy drugs.

One of the theranostic functions of GNPs could be achieved by application of external activation laser sources. Photothermal therapy (PTT) induces tumor cell death in the tumor cells or tumor areas containing GNPs by converting photon energy into heat [76]. In the view of strong absorptions at different wavelength, GNPs were identified as superior PTT agents [85]. A study showed that intravenously injected 15 nm core GNPs conjugated with EGFR antibody induced effective tumor ablation but had minimal normal tissue damage in human squamous cell carcinoma A431 tumor xenografts in nude mice [86]. Besides antibodies, peptide and small molecules were both reported labeled on GNPs as recognition ligands for tumor targeting and PTT [87–89]. In addition to PTT, photodynamic therapy (PDT) is another emerging new cancer treatment approach that kills cancer cells through laser irradiation [90]. By modifications with photosensitizers, the efficiency of various GNPs in PTT or PDT has been investigated, including nanoshells [91], nanorods [92], nanocages [93], nanospheres [94], and nanostars [87]. Nearly all types of GNPs showed strong PDT or PTT effects. However, most gold nanomaterial based PTT/PDT therapeutic complexes required two wavelength laser for irradiation due to the absorbance differences between photosensitizer and gold nanoparticles. Recently, a monolayer of modified GNPs has been used to compose gold nanovesicles, which have capability to encapsulate photosensitizer, chlorin e6 (Ce6), in the interior hollow [79]. The gold vesicles hold a strong absorption at 671 nm, which is close to the absorbance of Ce6 for PDT. In this study, 671 nm laser radiation was used to excite gold vesicles for PTT and chlorin e6 for PDT, which solved the challenge of two different wavelengths laser for simultaneous PDT and PTT. Significantly improved tumor ablation efficacy of the multifunctional GNPs system was achieved under the fluorescence and photoacoustic imaging guidance (Fig. 8.3).

As described above, GNPs are excellent platforms for multimodal tumor imaging and various therapeutic approaches. Compared with the other nanomaterials, the inherent PTT ability and the controlled morphology suggested that GNPs are promising phototherapy agents. By clarification of the relationships between GNP shape and PTT effects, it is hopefully to apply this newly developed strategy for the treatment of human tumors located at relatively to the body surface, such as melanoma, head and neck cancer, breast cancer, and prostate cancer. With the development of endoscopic imaging devices, it is also feasible to treat tumors on the mucosal surface of the colon, esophagus, stomach, and bladder.

Although multifunctional GNPs have many potential applications for cancer imaging and therapy, a major challenge in the development of GNPs for human use is the concern of their biodegradability, long-term toxicity, and high cost [95]. Extensive investigations of these nanoparticle systems should be required to fully

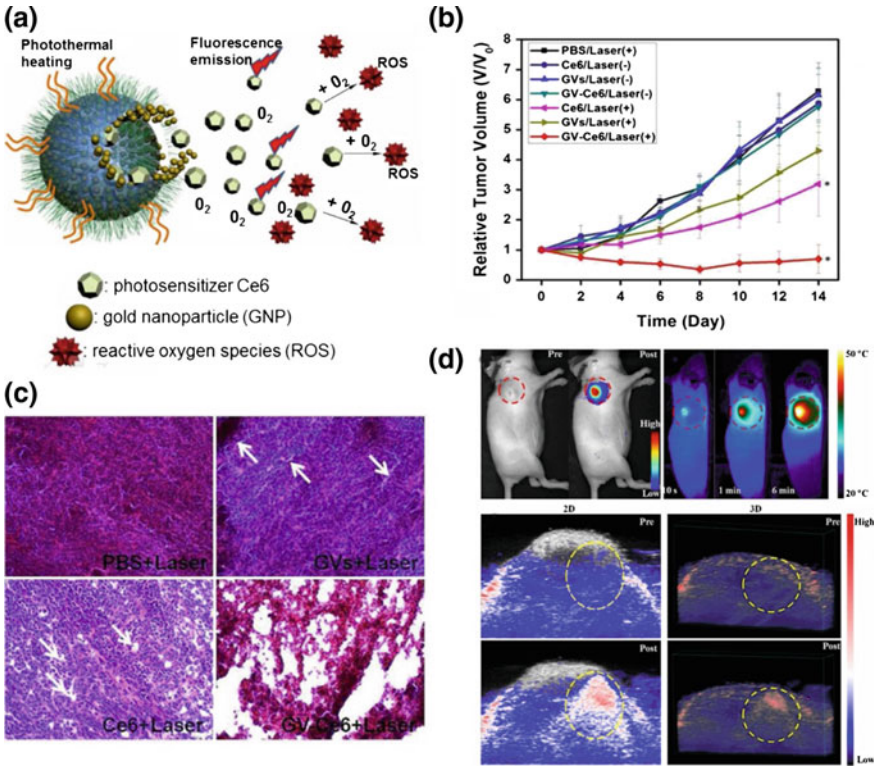

Fig. 8.3 Designed gold nanocomplex for tumor theranostic applications. **a** Schematic illustration of photosensitizer (Ce6)-loaded plasmonic gold vesicles. **b** Tumor growth curves of different groups in tumor-bearing mice after treatment. **c** H&E staining of tumors from different groups of mice 14 days post treatment. **d** NIR fluorescence images, thermal images and photoacoustic images of MDA-MB-435 tumor-bearing mice. Adapted with permission from [79]. Copyright © 2015 American Chemical Society

understand their pharmacokinetics, interactions with the immune system and other normal cells, the extent of cytotoxicity due to surface and size of the AuNPs, in vivo biodistribution and mechanisms of clearance. Appropriate surface tailoring and geometric manipulation may have an important role in improving the stabilities, biocompatibilities, and targeting ability with reduced toxicities of GNPs [96–99]. For example, it has been shown that GNPs smaller than 5 nm were able to be cleared out from the kidney. Novel GNPs that could disassemble themselves following in vivo delivery under specific conditions to allow in vivo clearance [100].

Additionally, most imaging devices for GNPs are still under preclinical development. For translation of gold-based theranostic nanoparticles for image-guided drug delivery, it is also important for translational development of imaging equipments that are tailored for the detection of imaging signals of GNPs.

8.2.3 Silica Nanoparticles

Silica nanoparticles (SNPs) have attracted great attentions due to the versatile exterior, interior surface chemistry, and highly tunable structures such as size and pore volume [101]. They are highly soluble in aqueous solutions due to a high concentration of silanol groups on their surface [102]. Generally, SNPs can be classified as mesoporous SNPs (MSNPs) and nonporous/solid SNPs [103–106].

A concern for the application of clinical MRI contrast agents like Gd-based compounds is the potential toxicity of the released Gd following in vivo delivery. Various attempts of developing new Gd- or Mn-based T_1 MRI contrast agents have been made to alleviate side effects and toxicities, but only few progresses were achieved. To address this issue, synthesized silica-coated iron oxide nanoparticles that exhibited excellent biocompatibility both in vitro and in vivo were used. Result of this study showed that the hybrid nanoparticles have high T_1-weighted MRI contrasts and could be promising imaging contrast agents for MRI [107]. More interestingly, a trimodality imaging agent, an iodinated oil-loaded fluorescent mesoporous silica-coated iron oxide nanoparticle, was prepared to integrate fluorescence, CT and MRI imaging approaches into a single nanoparticle platform. The trimodal imaging nanoparticle showed intensified fluorescence and enhanced CT and MRI contrasts [108].

Besides improving the in vivo behavior of imaging agents, SNPs are also applied as drug carriers for tumor ablations. To improve the ability of tumor targeting and reduce undesired accumulation, peptides or antibodies are usually used for modification of SNPs, which yield selective tumor targeting SNPs [109]. For example, a CD105 antibody modified SNP was recently reported by Cai group for successful PET/fluorescent imaging of a mouse breast tumor in the 4T1 mouse mammary tumor model [110].

MSNPs have the capability of loading large amounts of drug molecules and even different types of drugs. For example, camptothecin (CPT) was encapsulated into the inner pore and arsenic trioxide was coated onto the external surface of MSNPs [111]. MSNPs carry dual drugs significantly enhanced the inhibitory effect on tumor cell growth, and lowered the concentration of drugs that were required for the same treatment efficacy. Another approach of improving the treatment efficacy is to initiate treatment at desired locations, such as releasing drugs by certain stimuli when drugs accumulate mostly in tumors. MSNPs have the capabilities of loading targeting molecules on the external surfaces to enhance tumor selectivity, and placing diverse moieties on the outlets of pores to serve as gatekeeper to empower controllable drug release [112]. PEG modified MSNPs functionalized with folate acid and amino-β-cyclodextrin (β-CD) have been shown to be able to block DOX in the pores of SNPs (Fig. 8.4) [113]. This folate receptor-targeted SNP remarkably improved specific uptake of the nanoparticle by tumor cells, and showed stronger therapeutic efficacy in vivo compared with free drug or nontargeted groups. Acidic conditions or the presence of glutathione induced the chemical or physical change of β-CD that triggered the release of chemotherapeutic drugs, which considerably

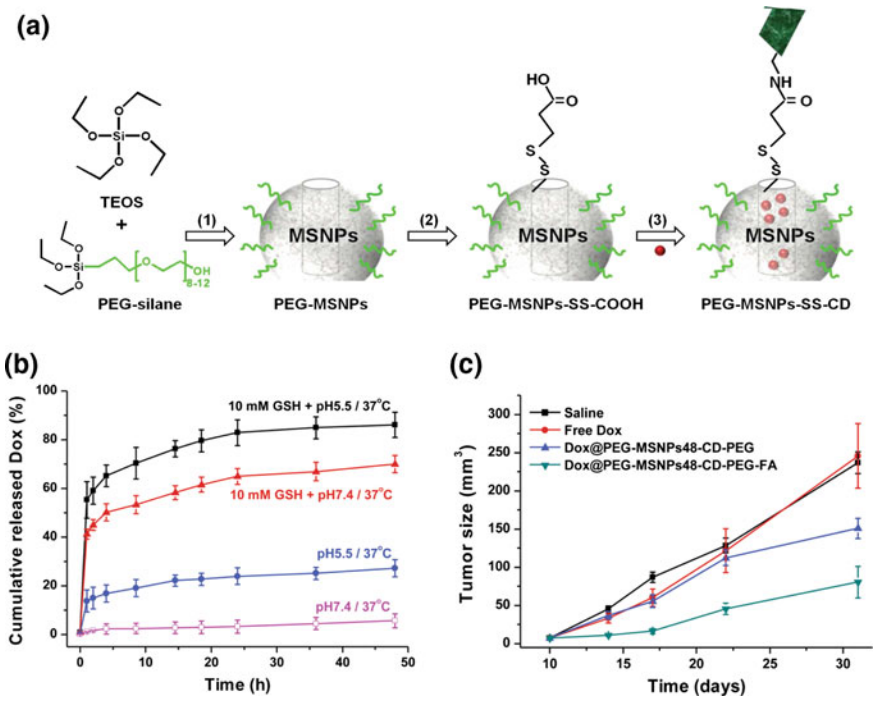

Fig. 8.4 Design of enzyme responsive SNP complex for tumor therapeutic. **a** The preparation of Cargo-encapsulated SNPs. **b** Drug release profile of SNP/drug complex under different conditions. **c** Tumor therapeutic effects of pH-sensitive SNPs. Adapted with permission from [113]. Copyright © 2015 John Wiley & Sons, Ltd.

improved the efficiency of drug delivery and ultimately enhanced tumor-inhibiting effect with reduced side effects.

In addition to chemotherapy, SNPs are also available for other promising therapeutic modalities such as gene therapy, PTT and PDT. MSNPs functionalized with cyclodextrin-grafted polyethylenimine (CP) have been shown to deliver siRNA targeting the M2 isoform of the glycolytic enzyme pyruvate kinase into tumors, resulting in inhibition of tumor cell growth, invasion, and migration, accompanying with effective knockdown of gene expression both in vitro and in vivo [114]. MSNPs coated with a photosensitizer, tetra-substituted carboxyl aluminum phthalocyanine, for PDT and small Pd nanosheets for PTT were developed for tumor phototherapy [111]. In vitro and in vivo studies indicated that simultaneous PDT and PTT had stronger effect on inhibition of tumor cell growth than either PDT or PTT alone. Therefore, results of those studies showed that SNPs are excellent nanoparticle platforms to integrate different types of therapeutic agents due to their tunable size and porosity. Some studies have demonstrated co-delivery of different moieties that can even overcome multidrug resistance, such as SNPs

functionalized with paclitaxel and tetrandrine [115] and SNPs coated with anti-CD44 antibody and chemotherapy drug, DOX [116].

Overall, SNPs are a class of nanomaterials with controllable size and morphology. Their biocompatibility and biodegradability make SNPs as widely applied nanomaterials in bioimaging and therapeutic fields in preclinical studies. With the capacities of receptor-mediated active targeting and controllable drugs release, SNP or SNP-hybrid nanoparticles demonstrated significantly enhanced tumor accumulation. However, safety of SNPs for human use as therapeutics is still a concern. Further preclinical studies on the toxicity, immunogenicity, pharmacokinetics, biodistribution, and clearance of SNPs should shade the light on the translational potential for future clinical theranostic applications.

8.2.4 Carbon Nanomaterials

The first report on fullerenes in 1985 opens the era of carbon nanomaterials, which mainly consist of sp^2 bonded graphitic carbon. Different from the above-mentioned nanomaterials, carbon nanomaterials exist in different low dimensionalities such as zero-dimensional fullerenes, one-dimensional carbon nanotubes (CNT), and two-dimensional graphemes. The nanoscale size (1 nm to 1 μm), extremely large surface area (2600 m^2/g) and unique optical properties make those promising nanomaterials for the development of nanoparticle-based biosensor, and imaging and therapy agents. Besides, some graphitic carbon nanomaterials, like graphene and CNT, hold strong optical absorptions ranging from 650 to 1000 nm, which allowed them to be utilized for photoacoustic imaging and in situ photothermal therapy. Interestingly, the characterized long fluorescent emission of single wall carbon nanotube (SWCNT) at so-called second near-infrared (NIR-II) window (1000–1700 nm) provided a new approach of optical imaging for the detection of tumors in deep tissues. Carbon nanomaterials were also used as tissue scaffolds and Raman scatter enhancers reviewed elsewhere [13, 117]. However, one of the key factors that affect the applications of carbon nanomaterials as nanoparticle drug carriers is their physiological compatibility, because unmodified carbon nanomaterials with a hydrophobic surface are very easily aggregated driven by the π–π interactions and van der Waals forces among themselves [118]. To make these carbon nanomaterials soluble in aqueous conditions, almost all carbon nanomaterials have to be surface modified with biocompatible moieties. Currently, covalently and non-covalently decorations of nanomaterials are two major categories of treating carbon materials, which simultaneously improve their biocompatibility and endow them specific biological functionalities. In this part, we covered the latest progresses of applications of carbon nanomaterials in diseases diagnosis and therapy by focusing on single-wall carbon nanotubes (SWCNTs).

SWCNT, composed of a single graphene sheet that is rolled into a tubular structure, is one of the more striking discoveries in the carbon nanomaterials. Typically, functional materials consisting of a hydrophilic head and hydrophobic

tail are broadly used for CNTs modifications. Through the designed modifications such as surfactants, polymers, gens, peptides/proteins, and other hydrophilic reagents, CNTs are reported advantageous for the development of new nanotechnologies for cancer detection and therapy. For example, PET imaging modality has high sensitivity and wide clinic applications for cancer diagnosis. A PEGylated SWCNT that chemically conjugated with ^{64}Cu-1,4,7,10-tetraazacyclododecane-N, N′, N″, N‴-tetraacetic acid (DOTA) and tumor-targeted arginine-glycine-aspartic acid (RGD) ligand was used for in vivo *detection of* glioblastoma (U87MG) by PET imaging [119]. SWCNT-PEG-RGD showed good tumor targeting with about 13% of injected dose per gram tumor (% ID/g) observed in the tumor. Due to a strong absorbance of CNTs, SWCNTs were also developed as photoacoustic imaging agents. Photoacoustic imaging is a sensitive imaging method that converts light into ultrasound by photoacoustic effect for the detection of tumors in deep tissues with fine spatial resolution. A highly sensitive photoacoustic imaging agent was developed by incorporation of indocyanine green (ICG) dye onto the surface of SWCNT/PL-PEG-RGD complex covalently [120]. After intravenous injection of ICG-SWCNT/PL-PEG-RGD, brain tumors in a human tumor xenograft model (U87MG) in nude mice were detected by photoacoustic imaging. Addition of ICG dye increased tumor specific photoacoustic signals by threefolds compared with the signal in the tumor of the mice that received SWCNT/PL-PEG-RGD without the ICG dye.

Although PL-PEG demonstrated satisfied dispersion of SWCNTs, the preparation procedures always require a long sonication time, which is proven significantly damaging to SWCNTs that causes low quantum yield and lowers imaging sensitivity [121]. A unique 'exchange' method was developed with less harm to SWCNTs and an order of magnitude higher quantum yield than direct sonication SWCNT modification [122]. In this aspect, an intrinsic near-infrared photoluminescence SWCNT has been developed for imaging of tumor vessels using whole body imaging [122]. Almost no autofluorescence background was observed, while a strong fluorescent signal was observed in the tumor, suggesting the great potential of using SWCNTs as biological fluorescent imaging agents. More recently, the NIR-II imaging has been successfully applied in hind limb imaging [123, 124], brain imaging, and endocarditis [125] in live animals. In addition, by changing the surface modification agents, SWCNTs are reported suitable for many imaging techniques not only as aforementioned but also for magnetic resonance imaging, ultrasound imaging, single-photon emission computed tomography (SPECT), Raman imaging and multimodalities imaging. All of these studies demonstrated that SWCNTs have the potential for further development of nanoparticle imaging and therapy agents for image-guided cancer therapy.

Because of their large surface area (2600 m^2/g) and unique shape, CNTs have the capacity to load drug molecules via different strategies. Small drug molecules such as paclitaxel, camptothecin, cisplatin, gemcitabine, methotrexate, and DOX [126] are loaded onto SWCNT by either chemically conjugated onto the well-dispersed SWCNTs or non-covalently attached onto the surface of SWCNT through π–π stack between aromatic drug molecules and SWCNT [127–129].

Targeted SWCNT/drug complex can recognize cancer biomarkers and enter into cells, subsequently triggering mechanisms for drug release or interacting with an external laser light to ablate cancer cells [118]. In addition, SWCNT has also been reported as a gene delivery vehicle to deliver DNA, small interfering RNA and micro-RNA to generate a therapeutic response in cancer cells. In comparison with other gene delivery systems, SWCNTs have a higher efficiency in penetrating cell membranes and therefore delivering genes into cells more effectively due to their unique shape and surface properties. For example, SWCNTs carrying siRNAs showed a good effect in the treatment of melanoma in a mouse tumor model by silence of Braf expression, an important signal molecule in the MAPK pathway for regulating cell growth and proliferation [130]. Polyethyleimine (PEI) functionalized SWCNTs that protected siRNA stability in vitro and in vivo demonstrated antitumor effect after SWCNT/siRNA complex treatment [130]. SWCNT has been an attractive nanoparticle system for PTT mediated cancer therapy. Success of NIR-II/MRI-guided PTT has been shown in tumor growth inhibition of primary tumor and cancer cells in lymph nodes. After administration of well-dispersed SWCNTs, primary tumor and metastasis tumor were identified by fluorescent imaging and MRI. PTT was then carried out and eliminated the primary tumor as well as cancer cells in lymph node [131]. The survival rates in treated mouse groups were significantly prolonged compared to the mice received control treatments [131]. By combination with chemotherapy, gene therapy or photodynamic therapy (PDT), SWCNTs have been designed as an effective agent for the generation of the synergistic antitumor effect. Albumin-bound paclitaxel was loaded to Evans blue molecule dispersed SWCNT mediated by the interaction of Evans blue molecule with albumin [118] (Fig. 8.5). The final complex, SWCNT/EB/Albumin/PTX, has dual functions of chemotherapy and photothermal therapy. A stronger tumor growth inhibition was demonstrated in the MDA-MB-435 breast tumor-bearing mice that received the combination treatment compared to chemotherapy or PTT alone. Additionally, photodynamic therapy is another noninvasive phototherapy approach that has been used in clinic. The multifunctional and PTT and PDT multimodal therapeutic approaches have been developed to enhance the treatment response in tumors. Various photosensitizers were chosen for functionalization of SWCNTs. For example, Ru(II) modified SWCNT was constructed for PTT and PDT combined therapy [118]. A greater cervical cancer tumor ablation effect was observed compared with PDT or PTT alone, highlighting the potential of using SWCNT carrying photosensitizers for the combination therapy. In summary, because of their large surface areas and specific surface properties, SWCNT is one of the promising nanoparticle systems for the development of theranostic agents. Through surface engineering, SWCNTs can be easily modified with diagnosis and therapy agents. So far, radioisotopes, dyes, magnetic nanoparticles, chemotherapy drugs, DNAs or RNAs, and photosensitizes all have been used to develop theranostic SWCNTs. Although promising results on theranostic applications have been achieved so far in experimental animal tumor models, future clinical applications of SWCNTs will still be challenging due to the concerns of biodegradability and the in vivo safety [132]. Currently, the mechanisms of clearance and long-term

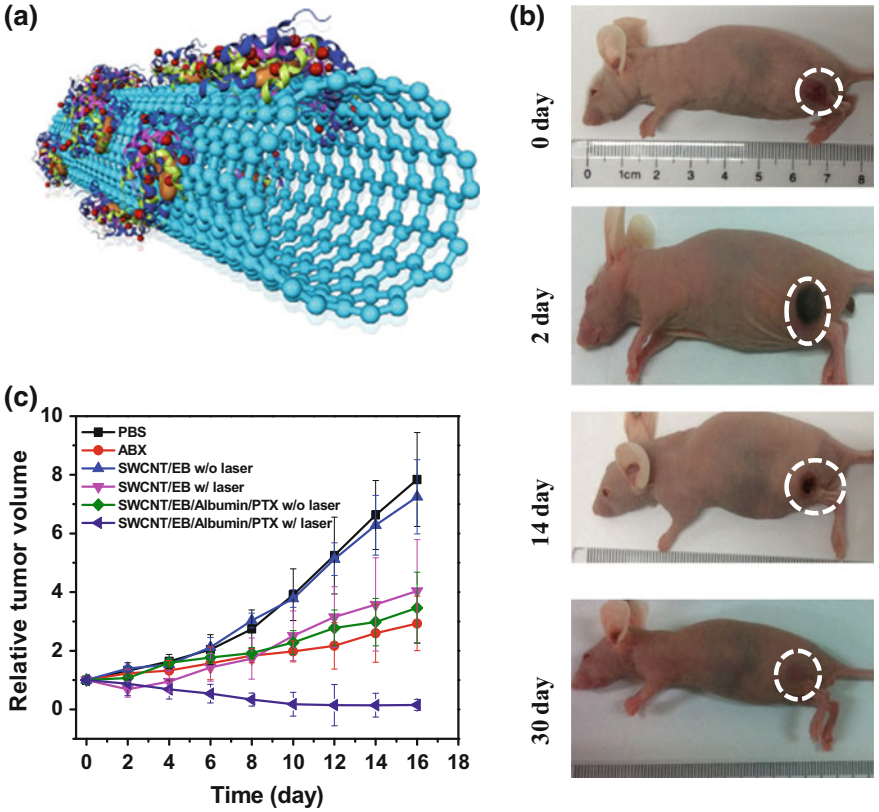

Fig. 8.5 A novel single-walled carbon nanotube (SWCNT) functionalization agent facilitated in vivo combined therapy. **a** The design of chemotherapy/PTT combined SWCNT. Paclitaxel (PTX) was encapsulated into albumin and bound with Evens Blue (EB) dispersed SWCNT. **b**, **c**. Antitumor effect of Evans blue functionalized SWCNT. Adapted with permission from [118] with permission from the Royal Society of Chemistry

systemic toxicity are largely unknown. Further preclinical studies will provide information on the feasibility of SWCNTs for human use as theranostic anti-cancer agents.

8.2.5 Polymeric Materials

Polymeric nanoparticles are the most commonly used nanoparticle drug carriers [133]. It has similar structures to lipid vesicles but different properties. Initially, polymeric materials are designed for drug delivery due to their biocompatibility, biodegradability, stability, and low toxicity. The polymeric drug formulation

significantly improved the drug solubility and stability with increased drug loading efficiency [134]. Polymeric materials have also been developed to carry imaging agents by encapsulation of different fluorescent dyes, magnetic nanoparticles, and radioisotopes. Recently, polymer nanoparticles have been produced as theranostic systems for further development of image-guided cancer therapy, targeted drug delivery as well as monitoring the therapeutic responses.

Polymeric nanomaterials can be structurally defined as solid nanoparticles, micelles, and dendrimers with diameters that are usually smaller than 300 nm [133]. Typically, polymeric nanoparticles are synthesized by assembling amphiphilic block copolymers, forming spheroidal architectures. A polymeric nanoparticle contains a hydrophilic shell and a hydrophobic inner core, where hydrophobic drugs can be encapsulated during the self-assembly process [134–136]. Interestingly, by adjusting the hydrophobic/hydrophilic ratio, chemical property or linkage of each polymer bock, it is now possible to generate specific stimuli-responsive polymeric nanoparticles, such as pH, enzyme, light, and temperature [135–137]. Under certain circumstances, designed polymeric nanoparticles will be active for imaging or releasing drugs, achieving a controlled theranostic function. In addition, polymeric nanoparticles can be easily functionalized with targeting moieties to improve specificity and delivery efficiency, because of their large surface and abundant surface functional groups. So far, a handful of successful polymeric nanoparticles on drug delivery and theranostic applications have been reported in the literatures. In this section, we will overview these state-of-the-art polymeric nanoparticles from tradition drug carriers to multifunctional polymer assemblies.

In the 1980s, a serial of polymeric drug delivery systems was reported by Speiser et al. Antitumor drugs were absorbed or loaded to polyalkylcyanoacrylate nanoparticles. Drug release mechanisms, distribution, and toxicity were also uncovered in vivo [138–140]. Since those reports brought attentions to polymeric nanoparticles, increasing efforts have been given to their biomedical applications. Although polymeric nanoparticles as delivery candidates for drugs, functional genes, and proteins were achieved, in most cases, clinical translation of polymeric nanoparticles was limited by a low drug loading efficiency (<5%) due to the fast drug aggregation kinetics in the hydrophilic core of polymeric nanoparicles [141]. Recently, a simply method for preparation of polymeric nanoparticles with over 50% drug loading was developed [141]. In this newly developed nanoparticle production protocol, two camptothecin (CPT) was covalently modified and formed a CPT dimer via carbonate linkage, which could be triggered by a reducing agent. The fast drug aggregation kinetics was then inhibited, resulting in small drug aggregates that could be used as cores for improving drug loading after interacting with amphiphilic polymers [141]. Polymeric nanoparticles are also widely used to improve drugs' solubility and reduce their side effects. For example, paclitaxel was encapsulated into poly (lactic-co-glycolic acid) (PLGA) nanoparticles. A small size (<200 nm) polymeric nanoparticle formation with homogeneous negatively charged anticancer drugs was produced and demonstrated stronger antitumor effect compared to conventional paclitaxel therapy [142–144]. Furthermore, hyaluronic

acid (HA) nanoparticle was developed with the capability of encapsulation of more than 30% (w/w) camptothecin [53]. Similarly, DOX could also be loaded into HA nanoparticles with a high loading efficiency [145, 146]. Resulting polymeric nanodrug showed nice aqueous solubility, physiological stability, and the ability of targeting cancer cells. Excellent antitumor efficiency was observed in vitro and in vivo [53]. It is well known that HA binds to CD44 that is a cellular receptor highly expressed in aggressive tumor cell populations with cancer-stem cell-like properties. Therefore, HA-based nanoparticles are also CD44 targeted drug delivery carriers that are able to target delivery of therapeutic agents into aggressive and invasive tumor cells [34, 135].

To effectively treat highly heterogeneous human tumors, efforts have been focused on the combination therapeutic approaches to overcome drug resistance. For example, cyclopamine (CPA) was loaded into polymeric micelle particles (M-CPA) to enhance radiation sensitivity of pancreatic cancer [147]. Combined M-CPA and Caesium-137 treatment showed enhanced toxicity to pancreatic cells. Another example is that DNA topoisomerase I inhibitor treated cancer cells become more sensitive to DNA topoisomerase II inhibitors [148]. Synergistic antitumor effect by combining therapeutic agents targeting different key pathways in tumor cells has, therefore, attracted great attentions. Although the combination of chemotherapy drugs is routinely used in cancer patients, the production of a synergistic antitumor effect has been limited by different pharmacokinetic, distribution, and clearance of different drugs following administrations. The advantage of co-delivery of multiple therapeutic agents using a single nanoparticle should ensure the therapeutic effect of different drugs occurring in the same tumor cells at the same time. A recently report demonstrated promising combined tumor therapy effects [148]. DNA topoisomerase I (CPT) and II (DOX) inhibitors were conjugated onto hyaluronic acid at an optimized ratio and then allowed assembling into HA-drug nanoparticles. A very low dose of the polymer drug complex (in equivalent to 2 mg/kg of CPT and 1.05 mg/kg of DOX) was able to inhibit tumor growth significantly with negligible side effects to normal organs, suggesting a great translational potential of HA polymeric nanoparticles. Besides the promising drug loading and delivery capacities, polymeric nanoparticles are ideal carriers for imaging contrast agents such as radioisotopes, fluorescent dyes, and magnetic reagents [14, 149]. The above-described HA nanoparticle drug carriers can also be converted into theranostic nanoparticles by conjugation with NIR dyes, radioisotopes, or encapsulation with ultrafine magnetic oxide nanoparticles [150].

A cyclodextrin polymer based nanoparticle, IT-101 (or CRLX101), modified with DOTA for ^{64}Cu coupling was conjugated with camptothecin, resulting in theranostic nanoparticles around 40 nm in diameter. It has a good water solubility and long circulation time (t1/2:13.3 h) in vivo. PET imaging in a Neuro2A tumor-bearing mouse model [151] revealed that the nanoparticle drug delivery by the passive targeting led to the accumulation of 11% injected dose per cm^3 in tumors at 24 h post injection, confirming the possibility of using polymeric nanoparticles for image-guided drug delivery assessment. Fluorescent dye labeled polymeric nanoparticles was developed as theranostic agents with optical imaging

ability [152–155]. By modification of designed fluorescent dyes, polymeric nanoparticles with tunable fluorescent emission wavelength can be prepared, facilitating optical imaging, or real-time imaging. Additionally, a fluorescent polymer, pDA-PEG, was prepared by conjugation of synthesized copolymer that is fluorescent at second near-infrared window with phospholipids–polyethylene glyco [156]. An ultrafast NIR-II window imaging of mouse hind limb was obtained immediately after intravenous injection of pDA-PEG, allowing visualization of blood flow moving inside the femoral artery. Because each imaging modality has different advantages and limitations, a multimodality polymeric imaging agent that is able to offer complementary information in a single matrix has become a new trend. Currently, polymeric multimodality imaging agents are also reported by several research groups, including SPECT/MRI, PET/CT, PET/fluorescent, fluorescent/MRI [157], and photoacoustic/fluorescent imaging [158] for potential clinical applications. Furthermore, γ-ray emitters, ^{11}C, ^{13}N, ^{15}O, ^{18}F, ^{64}Cu, and ^{111}In, all can be used for labeling of polymeric nanoparticles for imaging nanoparticle drug accumulation in tumors. In this aspect, ^{111}In labeled PPEGMA-b-PESPMA block copolymer has been shown to detect MDA-MB-468 breast cancer xenograft in nude mice by PET/optical imaging [159]. Long circulation and passive tumor accumulation behavior was observed following in vivo administration of those nanoparticles. A major concern for the application of radioactive agent as theranostic agents is that high therapeutic dose and repeated administrations of the theranostic nanoparticles will be required for effective cancer therapy in cancer patients. The use of radioactive therapeutics as imaging agents may cause systemic side effects and damages. It is unlikely that radioisotopes with short half lives (<4–6 h) can be effective imaging agents for monitoring drug delivery since it will take over 24 h to reach the maximal intratumoral accumulation of the nanoparticle drugs. However, such a long half-life radioactive agent limits the clinical use in cancer patients.

Another well-studied example is using bacteriochlorophyll-lipid as building blocks for optical imaging and metal chelating. By using filling in perfluorocarbon gas, a polymeric nanoparticle, named porphyrin microbubbles (pMB), with high photoacoustic and fluorescent imaging capabilities, was developed. The gas-encapsulated nanoparticle was able to be used as an ultrasound imaging agent. After ultrasound simulation, pMB was converted into porphyrin nanoparticles (pNP) with a good stability. A high level of intratumoral accumulation of pNPs after applying ultrasound was visualized by both photoacoustic and NIR imaging, suggesting the potential of using pMB for efficient drug delivery.

Encouraged by the excellent tumor targeting ability, imaging agents, as well as therapeutic drugs, were engineered into polymeric nanoparticles for simultaneous tumor imaging and therapeutic applications. A copper sulfide (CuS) encapsulated Cy5.5-conjugated hyaluronic acid nanoparticle (HANP) was developed for fluorescent/photoacoustic imaging guided tumor photothermal therapy [135] (Fig. 8.6). In this system, HANPs were delivered into tumors via the EPR effect as well as active CD44 targeting, which allowed HANPs to be delivered and bound to tumor cells more efficiently. Moreover, CuS with strong optical absorbance is an

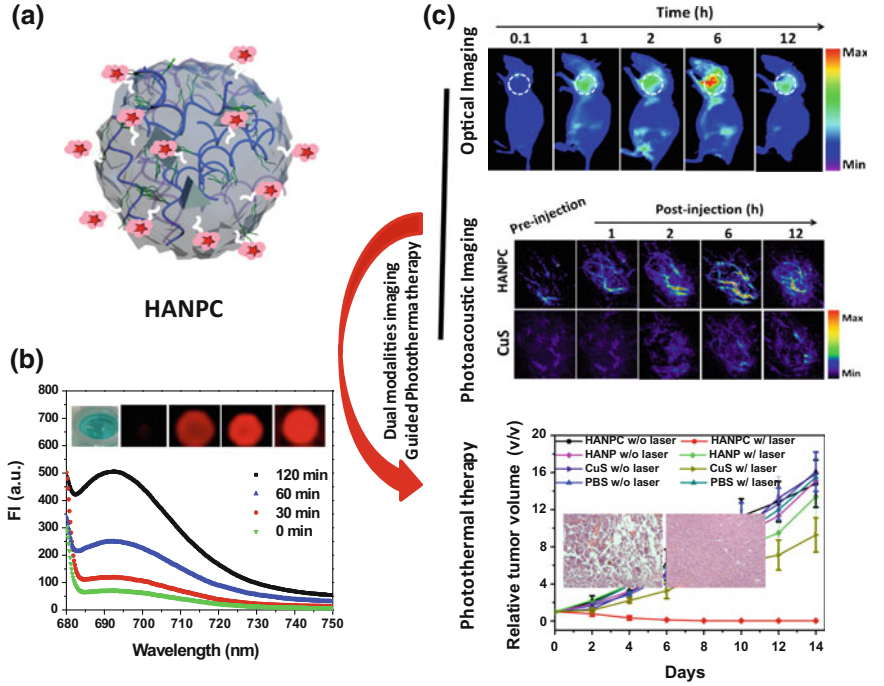

Fig. 8.6 Development of an activatable polymeric nanoparticle for image-guided tumor PTT. **a** Design of activatable hyaluronic acid nanoparticles (HANP) for photoacoustic/fluorescent image-guided PTT. **b** Fluorescent recovery of CuS encapsulated HANP utilizing high enzymatic activities in tumor. **c** Image-guided effective tumor ablation effects. Adapted with permission from Ref. [135]. Copyright © 2015 American Chemical Society

excellent photoacoustic agent. Effective quench of Cy5.5 fluorescent signals could be recovered after degradation of HANPs by hyaluronidase, resulting in NIR fluorescence signals for optical imaging of drug delivery. In the view of that CuS was able to convert proper light energy into heat, HA-based nanopolymer HANPC, and was capable of simultaneous imaging of tumor and ablation of tumor cells effectively. Aside from nice physiological stability and cancer cells targeting ability, HANPC demonstrated significant tumor ablation property by photothermal therapy with the guidance of optical and photoacoustic imaging. Therefore, results of this study support the possibility of using the polymeric nanoplatform for theranostic applications.

Polymeric micelles have also been used as MRI-guided cancer chemotherapeutic agents. Self-assembled pH-sensitive polymeric nanoparticle, TPTN, was produced using poly (lactic acid)-poly (ethylene glycol)-poly (L-lysine)-diethylenetriamine pentaacetic acid (PLA-PEG-PLL-DTPA) and pH-sensitive material, poly (L-histidine)-poly (ethylene glycol)-biotin (PLHPEG-biotin) [113]. After sorafenib and Gd loading, intratumoral TPTN delivery was evaluated by MRI to demonstrate

drug delivery into tumors. Breaking TPTN in tumor cells under low pH conditions led to drug release and resulted in tumor growth inhibition [113]. Recently, NIR fluorescent image-guided phototherapy was reported based on poly (ethylene glycol)-block-poly (ε-caprolactone) (PEG−PCL) [160]. Silicon naphthalocyanine (SiNc) was used to construct a polymeric nanoparticle that provided NIR fluorescent signals and phototherapeutic capabilities. The final product, SiNc-PNP, demonstrated good reactive oxygen generating ability and efficient photothermal property. After intravenous injection, tumor accumulation was observed 24 h post injection by optical imaging with a low body background. Phototherapy, composed of photothermal and photodynamic therapy, was conducted. Tumors were found effectively ablated without obvious toxicity to normal organs, suggesting that the reported polymeric nanoparticle is promising for precise treatment of tumor under fluorescent imaging guidance.

Overall, polymeric nanoparticles are excellent nanoparticle systems for the development of targeted theranostic agents, especially for those hydrophobic drug payloads. Fortunately, with the development of material chemistry, it is now possible to combine imaging and therapeutic capabilities in a single nanoparticle, allowing visualization of disease area by noninvasive imaging for evaluation of the delivery efficiencies and monitoring treatment responses. Due to their excellent biocompatibility, biodegradability, biostability, and easy surface chemistry, the polymeric nanoparticle is one of the most promising drug carriers for clinical translation. Nevertheless, several criteria have to be satisfied for an ideal polymeric nanoparticle drug carrier. For example, a polymeric imaging agent has to reach to the target fast enough with low imaging background. It has to be washed out body effectively without affecting next imaging. A long circulation time is necessary for drug delivery by polymeric nanoparticles for better tumor accumulation, which can be done through targeting ligand modification or the EPR effect. Collectively, novel polymeric designs with good tumor targeting ability, low immunogenicity, and controlled drug release are the future directions of the development of clinically translatable polymeric theranostic nanoparticles.

8.3 Prospects and Challenges

In this review, research advancements on the development of several nanoparticle systems for cancer theranostic applications were discussed. The ultimate goal of developing theranostic nanoplatform is to apply them to personalize cancer treatment through targeted and image-guided drug delivery, and assessment of tumor responses to the therapy by noninvasive imaging. We have discussed methods of surface modifications, functionalizations, and drug loading for different nanoparticle drug delivery systems. Imaging properties of various theranostic nanoparticles have also been presented in the review. By carrying different molecules, such as fluorescent dyes and radioisotopes, and the use of iron oxide or gold nanoparticles, intratumoral accumulation of theranostic nanoparticles could be detected using a

single or multimodal noninvasive imaging. Peptides, proteins, antibodies, and other small molecules are all suitable targeting ligands for conjugation onto the nanoparticles for improving tumor targeted drug delivery. Taking into consideration their small size and large surface area, nanomaterials have also been used for induction of antitumor therapeutic effects when loaded with chemotherapy drugs, antibodies, therapeutic genes, and/or photosensitizers. More interestingly, some nanomaterials with strong near-infrared absorbance can generate heat upon light irradiation for photothermal and photodynamic therapy. We have also discussed the advantages and limitations of each nanoparticle drug delivery carrier for the development and translation as theranostic agents for future clinical applications. It is believed that targeted cancer therapy in combination with image-guided drug delivery and monitoring tumor responses to therapy using the advanced theranostic nanoparticles offer a powerful and integrated cancer therapeutic approach for effective treatment of highly heterogeneous human cancers. The ability of noninvasive detection of tumor localization and accumulation of theranostic nanoparticles in tumors is extremely useful for image-guided cancer phototherapy. The therapy will be initiated precisely at the tumor site and the best time points by either laser irradiation or exogenous stimuli, resulting in an effective tumor ablation with minimum side effects. To obtain complementary tumor information in vivo, it may be necessary to combine more than one imaging modalities for visualization of interested tumors areas. For the development of theranostic nanoparticles, it is important to consider not only improving drug loading into nanoparticles, but also mechanisms of drug release. Various approaches, such as protease, pH, light, temperature, or reactive oxygen species (ROS) have been used to develop conditional activatable drug release nanoparticles. In addition to the efforts on incorporating diagnostic and therapeutic functions into single nanomaterial, nanoparticles particularly those containing two or more distinct components are also widely investigated. This type of nanomaterials, named hybrid nanoparticles, presents superior biomedical effects to that of single component due to the synergistic effect. Currently, carbon materials, magnetic nanoparticles, gold nanoparticles, and quantum dots are widely reported for the production of hybrid nanoparticles, providing improved theranostic property in a single platform. Although most reported nanoparticles or hybrid nanocomplex demonstrated exciting theranostic potentials in animal models, little were reported on the translation of these theranostic agents for human use. Collectively, it is still too early to predict the success of nanotechnology in cancer therapy and more investigations have to be conducted to answer some fundamental questions concerning the application of theranostic nanomaterials for clinical applications.

Until now, the most important issue is the potential toxicity of nanomaterials for biomedical applications in humans. Although the surface engineering is indeed helpful in improving physiological dispersion and stability of nanomaterials, only magnetic iron oxide nanoparticles have been approved by US FDA for clinical diagnostic radiology because most of the injected iron oxide nanoparticles can be endocytosed in the reticuloendothelial system and broken down in macrophages. The released iron can then be used as normal iron in red blood cells. However, the

potential long-term toxicity concern for many nanomaterials, particularly gold nanoparticle and carbon nanomaterials, is still the most important issue. More efforts are required to thoroughly investigate systemic toxicity, clearance, and distribution in not only rodent animals but also in bigger animals with different doses, injection routes, and intervals at different time periods. Most importantly, the effect of nanomaterials on the reproductive system has yet to be investigated seriously.

Besides the toxicity concern, the delivery efficiency is another major problem that has to be addressed before translating nanoparticles from bench to the clinic. First, the imaging efficiency of theranostic nanoparticles has to be considered since different imaging modalities have different specifications. For example, PET imaging is the most sensitive imaging modality with accurate quantification for data analysis but the resolution is relatively low. On the contrary, MRI imaging has excellent resolution but the sensitivity is not ideal. Optical imaging, which is less costly and nonradioactive, has high sensitivity and specificity, but tissue penetration depth and quantification remain concerns for clinic practice. At present, issues about how to take advantages of different imaging modalities in different theranostic nanoparticles have yet to be considered. In addition, the therapeutic efficiency is another factor that may hinder clinical applications of theranostic nanoparticles. Questions concerning how to effective delivery of nanoparticle drugs into a desired site rather than normal organs, and how to overcome tumor stromal barriers to deliver drug into tumor cells, remain to be answered by investigators in the cancer nanotechnology field.

It has to admit that nanoparticles can solve the traditional chemotherapy problems to some extent, such as the poor water solubility and the lack of a targeting ability of chemotherapy drugs. At the same time, nanoparticles bring new therapeutic approaches that allow attacking cancers using the combination of targeted and image-guided therapy. Although significant progresses have been made, numbers of issues remain to be addressed by multidisciplinary cooperation among biologist, chemist, engineers, and clinicians.

References

1. Anand P, Kunnumakara AB, Sundaram C, Harikumar KB, Tharakan ST, Lai OS, Sung BY, Aggarwal BB (2008) Cancer is a preventable disease that requires major lifestyle changes. Pharm Res Dord 25(9):2097–2116
2. Siegel RL, Miller KD, Jemal A (2015) Cancer statistics. Ca-Cancer J Clin 65(1):5–29
3. Johnson L, Gunasekera A, Douek M (2010) Applications of nanotechnology in cancer. Discov Med 47:374–379
4. Buzea C, Pacheco II, Robbie K (2007) Nanomaterials and nanoparticles: sources and toxicity. Biointerphases 2(4):17–71
5. Petros RA, DeSimone JM (2010) Strategies in the design of nanoparticles for therapeutic applications. Nat Rev Drug Discov 9(8):615–627

6. Huang J, Wang LY, Zhong XD, Li YC, Yang LL, Mao H (2014) Facile non-hydrothermal synthesis of oligosaccharide coated sub-5 nm magnetic iron oxide nanoparticles with dual MRI contrast enhancement effects. J Mater Chem B 2(33):5344–5351
7. Li YC, Lin R, Wang LY, Huang J, Wu H, Cheng GJ, Zhou ZY, MacDonald T, Yang L, Mao H (2015) PEG-b-AGE polymer coated magnetic nanoparticle probes with facile functionalization and anti-fouling properties for reducing non-specific uptake and improving biomarker targeting. J Mater Chem B 3(17):3591–3603
8. Toy R, Peiris PM, Ghaghada KB, Karathanasis E (2014) Shaping cancer nanomedicine: the effect of particle shape on the in vivo journey of nanoparticles. Nanomed UK 9(1):121–134
9. Liu Y, Tan J, Thomas A, Ou-Yang D, Muzykantov VR (2012) The shape of things to come: importance of design in nanotechnology for drug delivery. Ther Deliv 3(2):181–194
10. Aslan B, Ozpolat B, Sood AK, Lopez-Berestein G (2013) Nanotechnology in cancer therapy. J Drug Target 21(10):904–913
11. Matsumura Y, Maeda H (1986) A new concept for macromolecular therapeutics in cancer-chemotherapy—mechanism of tumoritropic accumulation of proteins and the antitumor agent smancs. Cancer Res 46(12):6387–6392
12. Markman JL, Rekechenetskiy A, Holler E, Ljubimova JY (2013) Nanomedicine therapeutic approaches to overcome cancer drug resistance. Adv Drug Deliv Rev 65(13–14):1866–1879
13. Wolfbeis OS (2015) An overview of nanoparticles commonly used in fluorescent bioimaging. Chem Soc Rev 44(14):4743–4768
14. Stockhofe K, Postema JM, Schieferstein H, Ross TL (2014) Radiolabeling of nanoparticles and polymers for PET imaging. Pharm (Basel) 7(4):392–418
15. Bonnemain B (1998) Superparamagnetic agents in magnetic resonance imaging: physicochemical characteristics and clinical applications a review. J Drug Target 6(3):167–174
16. Wen G, Zhang XL, Chang RM, Xia Q, Cang P, Zhang Y (2002) Superparamagnetic iron oxide (Feridex)-enhanced MRI in diagnosis of focal hepatic lesions. Di Yi Jun Yi Da Xue Xue Bao 22(5):451–452
17. Clement O, Siauve N, Cuenod CA, Frija G (1998) Liver imaging with ferumoxides (Feridex): fundamentals, controversies, and practical aspects. Top Magn Reson Imaging 9 (3):167–182
18. Johnson L, Pinder SE, Douek M (2013) Deposition of superparamagnetic iron-oxide nanoparticles in axillary sentinel lymph nodes following subcutaneous injection. Histopathology 62(3):481–486
19. Kernstine KH, Stanford W, Mullan BF, Rossi NP, Thompson BH, Bushnell DL, McLaughlin KA, Kern JA (1999) PET, CT, and MRI with Combidex for mediastinal staging in non-small cell lung carcinoma. Ann Thorac Surg 68(3):1022–1028
20. Harisinghani MG, Saini S, Hahn PF, Weissleder R, Mueller PR (1998) MR imaging of lymph nodes in patients with primary abdominal and pelvic malignancies using ultrasmall superparamagnetic iron oxide (Combidex). Acad Radiol 5(Supplement 1):S167–S169
21. Reimer P, Balzer T (2003) Ferucarbotran (Resovist): a new clinically approved RES-specific contrast agent for contrast-enhanced MRI of the liver: properties, clinical development, and applications. Eur Radiol 13(6):1266–1276
22. Vogl TJ, Hammerstingl R, Schwarz W, Kummel S, Muller PK, Balzer T, Lauten MJ, Balzer JO, Mack MG, Schimpfky C, Schrem H, Bechstein WO, Neuhaus P, Felix R (1996) Magnetic resonance imaging of focal liver lesions. Comparison of the superparamagnetic iron oxide resovist versus gadolinium-DTPA in the same patient. Invest Radiol 31(11):696–708
23. Reimer P, Rummeny EJ, Daldrup HE, Balzer T, Tombach B, Berns T, Peters PE (1995) Clinical results with Resovist: a phase 2 clinical trial. Radiology 195(2):489–496
24. Campbell JL, Arora J, Cowell SF, Garg A, Eu P, Bhargava SK, Bansal V (2011) Quasi-cubic magnetite/silica core-shell nanoparticles as enhanced MRI contrast agents for cancer imaging. PLoS ONE 6(7):e21857
25. Smith JA, Costales AB, Jaffari M, Urbauer DL, Frumovitz M, Kutac CK, Tran H, Coleman RL (2015) Is it equivalent? Evaluation of the clinical activity of single agent

Lipodox(R) compared to single agent Doxil(R) in ovarian cancer treatment. J Oncol Pharm Pract
26. Barenholz Y (2012) Doxil (R)—the first FDA-approved nano-drug: lessons learned. J Control Release 160(2):117–134
27. O'Brien ME, Wigler N, Inbar M, Rosso R, Grischke E, Santoro A, Catane R, Kieback DG, Tomczak P, Ackland SP, Orlandi F, Mellars L, Alland L, Tendler C, Group CBCS (2004) Reduced cardiotoxicity and comparable efficacy in a phase III trial of pegylated liposomal doxorubicin HCl (CAELYX/Doxil) versus conventional doxorubicin for first-line treatment of metastatic breast cancer. Ann Oncol 15(3):440–449
28. McTiernan A, Whelan J, Leahy M, Woll PJ (2006) A phase II nonrandomised open-label study of liposomal daunorubicin (DaunoXome) in advanced soft tissue sarcoma. Sarcoma 1:41080
29. Lowis S, Lewis I, Elsworth A, Weston C, Doz F, Vassal G, Bellott R, Robert J, Pein F, Ablett S, Pinkerton R, Frappaz D, United Kingdom Children's Cancer Study Group New A, Societe Francaise d'Oncologie Pediatrique Pharmacology G (2006) A phase I study of intravenous liposomal daunorubicin (DaunoXome) in paediatric patients with relapsed or resistant solid tumours. Br J Cancer 95(5):571–580
30. Rosenthal E, Poizot-Martin I, Saint-Marc T, Spano JP, Cacoub P, Group DNXS (2002) Phase IV study of liposomal daunorubicin (DaunoXome) in AIDS-related Kaposi sarcoma. Am J Clin Oncol 25(1):57–59
31. Chou H, Lin H, Liu JM (2015) A tale of the two PEGylated liposomal doxorubicins. Onco Targets Ther 8:1719–1720
32. Glantz MJ, Jaeckle KA, Chamberlain MC, Phuphanich S, Recht L, Swinnen LJ, Maria B, LaFollette S, Schumann GB, Cole BF, Howell SB (1999) A randomized controlled trial comparing intrathecal sustained-release cytarabine (DepoCyt) to intrathecal methotrexate in patients with neoplastic meningitis from solid tumors. Clin Cancer Res 5(11):3394–3402
33. Jaeckle KA, Batchelor T, O'Day SJ, Phuphanich S, New P, Lesser G, Cohn A, Gilbert M, Aiken R, Heros D, Rogers L, Wong E, Fulton D, Gutheil JC, Baidas S, Kennedy JM, Mason W, Moots P, Russell C, Swinnen LJ, Howell SB (2002) An open label trial of sustained-release cytarabine (DepoCyt) for the intrathecal treatment of solid tumor neoplastic meningitis. J Neurooncol 57(3):231–239
34. Phuphanich S, Maria B, Braeckman R, Chamberlain M (2007) A pharmacokinetic study of intra-CSF administered encapsulated cytarabine (DepoCyt®) for the treatment of neoplastic meningitis in patients with leukemia, lymphoma, or solid tumors as part of a phase III study. J Neurooncol 81(2):201–208
35. Mross K, Niemann B, Massing U, Drevs J, Unger C, Bhamra R, Swenson C (2004) Pharmacokinetics of liposomal doxorubicin (TLC-D99; Myocet) in patients with solid tumors: an open-label, single-dose study. Cancer Chemother Pharmacol 54(6):514–524
36. Leonard RC, Williams S, Tulpule A, Levine AM, Oliveros S (2009) Improving the therapeutic index of anthracycline chemotherapy: focus on liposomal doxorubicin (Myocet). Breast 18(4):218–224
37. de Jonge MJ, Slingerland M, Loos WJ, Wiemer EA, Burger H, Mathijssen RH, Kroep JR, den Hollander MA, van der Biessen D, Lam MH, Verweij J, Gelderblom H (2010) Early cessation of the clinical development of LiPlaCis, a liposomal cisplatin formulation. Eur J Cancer 46(16):3016–3021
38. Lu C, Stewart DJ, Lee JJ, Ji L, Ramesh R, Jayachandran G, Nunez MI, Wistuba II, Erasmus JJ, Hicks ME, Grimm EA, Reuben JM, Baladandayuthapani V, Templeton NS, McMannis JD, Roth JA (2012) Phase I clinical trial of systemically administered TUSC2 (FUS1)-nanoparticles mediating functional gene transfer in humans. PLoS ONE 7(4):e34833
39. Chen LT, Von Hoff DD, Li CP, Wang-Gillam A, Bodoky G, Dean AP, Shan YS, Jameson GS, Macarulla T, Lee KH, Cunningham D, Blanc JF, Hubner R, Chiu CF, Schwartsmann G, Siveke JT, Braiteh FS, Moyo VM, Belanger B, Bayever E (2015) Expanded analyses of napoli-1: Phase 3 study of MM-398 (nal-IRI), with or without

5-fluorouracil and leucovorin, versus 5-fluorouracil and leucovorin, in metastatic pancreatic cancer (mPAC) previously treated with gemcitabine-based therapy. J Clin Oncol 33(3):1
40. Ahn HK, Jung M, Sym SJ, Shin DB, Kang SM, Kyung SY, Park JW, Jeong SH, Cho EK (2014) A phase II trial of cremorphor EL-free paclitaxel (Genexol-PM) and gemcitabine in patients with advanced non-small cell lung cancer. Cancer Chemother Pharmacol 74(2):277–282
41. Kim TY, Kim DW, Chung JY, Shin SG, Kim SC, Heo DS, Kim NK, Bang YJ (2004) Phase I and pharmacokinetic study of Genexol-PM, a cremophor-free, polymeric micelle-formulated paclitaxel, in patients with advanced malignancies. Clin Cancer Res 10(11):3708–3716
42. Lee KS, Chung HC, Im SA, Park YH, Kim CS, Kim SB, Rha SY, Lee MY, Ro J (2008) Multicenter phase II trial of Genexol-PM, a Cremophor-free, polymeric micelle formulation of paclitaxel, in patients with metastatic breast cancer. Breast Cancer Res Treat 108(2):241–250
43. Zuckerman JE, Gritli I, Tolcher A, Heidel JD, Lim D, Morgan R, Chmielowski B, Ribas A, Davis ME, Yen Y (2014) Correlating animal and human phase Ia/Ib clinical data with CALAA-01, a targeted, polymer-based nanoparticle containing siRNA. Proc Natl Acad Sci USA 111(31):11449–11454
44. Davis ME, Zuckerman JE, Choi CH, Seligson D, Tolcher A, Alabi CA, Yen Y, Heidel JD, Ribas A (2010) Evidence of RNAi in humans from systemically administered siRNA via targeted nanoparticles. Nature 464(7291):1067–1070
45. Cheng J, Pun SH (2015) Polymeric biomaterials for cancer nanotechnology. Biomater Sci 3 (7):891–893
46. Leiro V, Garcia JP, Tomas H, Pego AP (2015) The present and the future of degradable dendrimers and derivatives in theranostics. Bioconjug Chem 26(7):1182–1197
47. Müller H-J, Beier R, da Palma J, Lanvers C, Ahlke E, von Schütz V, Gunkel M, Horn A, Schrappe M, Henze G, Kranz K, Boos J (2002) PEG-asparaginase (Oncaspar) 2500 U/m2 BSA in reinduction and relapse treatment in the ALL/NHL-BFM protocols. Cancer Chemother Pharmacol 49(2):149–154
48. Dinndorf PA, Gootenberg J, Cohen MH, Keegan P, Pazdur R (2007) FDA drug approval summary: pegaspargase (oncaspar) for the first-line treatment of children with acute lymphoblastic leukemia (ALL). Oncologist 12(8):991–998
49. Xu H, Ma H, Yang P, Zhang X, Wu X, Yin W, Wang H, Xu D (2015) Targeted polymer-drug conjugates: current progress and future perspective. Colloids Surf B Biointerfaces 136:729–734
50. Pang X, Du HL, Zhang HQ, Zhai YJ, Zhai GX (2013) Polymer-drug conjugates: present state of play and future perspectives. Drug Discov Today 18(23–24):1316–1322
51. Canal F, Sanchis J, Vicent MJ (2011) Polymer–drug conjugates as nano-sized medicines. Curr Opin Biotechnol 22(6):894–900
52. Choi KY, Liu G, Lee S, Chen XY (2012) Theranostic nanoplatforms for simultaneous cancer imaging and therapy: current approaches and future perspectives. Nanoscale 4 (2):330–342
53. Choi KY, Yoon HY, Kim JH, Bae SM, Park RW, Kang YM, Kim IS, Kwon IC, Choi K, Jeong SY, Kim K, Park JH (2011) Smart nanocarrier based on PEGylated hyaluronic acid for cancer therapy. ACS Nano 5(11):8591–8599
54. Xing R, Bhirde AA, Wang S, Sun X, Liu G, Hou Y, Chen X (2012) Hollow iron oxide nanoparticles as multidrug resistant drug delivery and imaging vehicles. Nano Res 6(1):1–9
55. Rafiyath SM, Rasul M, Lee B, Wei G, Lamba G, Liu D (2012) Comparison of safety and toxicity of liposomal doxorubicin vs. conventional anthracyclines: a meta-analysis. Exp Hematol Oncol 1(1):10
56. Vishnu P, Roy V (2011) Safety and efficacy of nab-paclitaxel in the treatment of patients with breast cancer. Breast Cancer (Auckl) 5:53–65
57. Chen LT, Von Hoff DD, Li CP, Wang-Gillam A, Bodoky G, Dean AP, Shan YS, Jameson GS, Macarulla T, Lee KH, Cunningham D, Blanc JF, Hubner R, Chiu CF,

Schwartsmann G, Siveke JT, Braiteh FS, Moyo VM, Belanger B, Bayever E (2015) Expanded analyses of napoli-1: Phase 3 study of MM-398 (nal-IRI), with or without 5-fluorouracil and leucovorin, versus 5-fluorouracil and leucovorin, in metastatic pancreatic cancer (mPAC) previously treated with gemcitabine-based therapy. J Clin Oncol 33(3)
58. Issa B, Obaidat IM, Albiss BA, Haik Y (2013) Magnetic nanoparticles: surface effects and properties related to biomedicine applications. Int J Mol Sci 14(11):21266–21305
59. Nandwana V, De M, Chu S, Jaiswal M, Rotz M, Meade TJ, Dravid VP (2015) Theranostic magnetic nanostructures (MNS) for cancer. Cancer Treat Res 166:51–83
60. Muthiah M, Park IK, Cho CS (2013) Surface modification of iron oxide nanoparticles by biocompatible polymers for tissue imaging and targeting. Biotechnol Adv 31(8):1224–1236
61. Tse BW, Cowin GJ, Soekmadji C, Jovanovic L, Vasireddy RS, Ling MT, Khatri A, Liu T, Thierry B, Russell PJ (2015) PSMA-targeting iron oxide magnetic nanoparticles enhance MRI of preclinical prostate cancer. Nanomedicine (Lond) 10(3):375–386
62. Peng XH, Qian XM, Mao H, Wang AY, Chen Z, Nie SM, Shin DM (2008) Targeted magnetic iron oxide nanoparticles for tumor imaging and therapy. Int J Nanomed 3(3):311–321
63. Bjornerud A, Johansson L (2004) The utility of superparamagnetic contrast agents in MRI: theoretical consideration and applications in the cardiovascular system. NMR Biomed 17 (7):465–477
64. Chen HW, Wang LY, Yeh J, Wu XY, Cao ZH, Wang YA, Zhang MM, Yang L, Mao H (2010) Reducing non-specific binding and uptake of nanoparticles and improving cell targeting with an antifouling PEO-b-P gamma MPS copolymer coating. Biomaterials 31 (20):5397–5407
65. Chen HW, Wang LY, Yu QQ, Qian WP, Tiwari D, Yi H, Wang AY, Huang J, Yang LL, Mao H (2013) Anti-HER2 antibody and ScFvEGFR-conjugated antifouling magnetic iron oxide nanoparticles for targeting and magnetic resonance imaging of breast cancer. Int J Nanomed 8:3781–3794
66. Lee GY, Qian WP, Wang LY, Wang YA, Staley CA, Satpathy M, Nie SM, Mao H, Yang LL (2013) Theranostic nanoparticles with controlled release of gemcitabine for targeted therapy and MRI of pancreatic cancer. ACS Nano 7(3):2078–2089
67. Zhou HY, Qian WP, Uckun FM, Wang LY, Wang YA, Chen HY, Kooby D, Yu Q, Lipowska M, Staley CA, Mao H, Yang L (2015) IGF1 receptor targeted theranostic nanoparticles for targeted and image-guided therapy of pancreatic cancer. ACS Nano 9 (8):7976–7991
68. Torres-Lugo M, Rinaldi C (2013) Thermal potentiation of chemotherapy by magnetic nanoparticles. Nanomed (Lond) 8(10):1689–1707
69. Hilger I (2013) In vivo applications of magnetic nanoparticle hyperthermia. Int J Hyperth 29 (8):828–834
70. Hilger I, Kaiser WA (2012) Iron oxide-based nanostructures for MRI and magnetic hyperthermia. Nanomed (Lond) 7(9):1443–1459
71. Zhao Q, Wang L, Cheng R, Mao L, Arnold RD, Howerth EW, Chen ZG, Platt S (2012) Magnetic nanoparticle-based hyperthermia for head and neck cancer in mouse models. Theranostics 2:113–121
72. Maier-Hauff K, Ulrich F, Nestler D, Niehoff H, Wust P, Thiesen B, Orawa H, Budach V, Jordan A (2011) Efficacy and safety of intratumoral thermotherapy using magnetic iron-oxide nanoparticles combined with external beam radiotherapy on patients with recurrent glioblastoma multiforme. J Neurooncol 103(2):317–324
73. Patil US, Adireddy S, Jaiswal A, Mandava S, Lee BR, Chrisey DB (2015) In vitro/in vivo toxicity evaluation and quantification of iron oxide nanoparticles. Int J Mol Sci 16 (10):24417–24450
74. Voinov MA, Pagan JOS, Morrison E, Smirnova TI, Smirnov AI (2011) Surface-mediated production of hydroxyl radicals as a mechanism of iron oxide nanoparticle biotoxicity. J Am Chem Soc 133(1):35–41

75. Jeong EH, Jung G, Hong CA, Lee H (2014) Gold nanoparticle (AuNP)-based drug delivery and molecular imaging for biomedical applications. Arch Pharm Res 37(1):53–59
76. Webb JA, Bardhan R (2014) Emerging advances in nanomedicine with engineered gold nanostructures. Nanoscale 6(5):2502–2530
77. Yuan H, Khoury CG, Hwang H, Wilson CM, Grant GA, Vo-Dinh T (2012) Gold nanostars: surfactant-free synthesis, 3D modelling, and two-photon photoluminescence imaging. Nanotechnology 23(7):075102
78. Liu H, Xu YH, Wen SH, Chen Q, Zheng LF, Shen MW, Zhao JL, Zhang GX, Shi XY (2013) Targeted tumor computed tomography imaging using low-generation dendrimer-stabilized gold nanoparticles. Chem Eur J 19(20):6409–6416
79. Lin J, Wang S, Huang P, Wang Z, Chen S, Niu G, Li W, He J, Cui D, Lu G, Chen X, Nie Z (2013) Photosensitizer-loaded gold vesicles with strong plasmonic coupling effect for imaging-guided photothermal/photodynamic therapy. ACS Nano 7(6):5320–5329
80. Khandekar SV, Kulkarni MG, Devarajan PV (2014) Polyaspartic acid functionalized gold nanoparticles for tumor targeted doxorubicin delivery. J Biomed Nanotechnol 10(1):143–153
81. Chen Y, Li N, Yang Y, Liu Y (2015) A dual targeting cyclodextrin/gold nanoparticle conjugate as a scaffold for solubilization and delivery of paclitaxel. RSC Adv 5(12):8938–8941
82. Li N, Chen Y, Zhang YM, Yang Y, Su Y, Chen JT, Liu Y (2014) d Polysaccharide-gold nanocluster supramolecular conjugates as a versatile platform for the targeted delivery of anticancer drugs. Sci Rep-Uk 4
83. Banu H, Stanley B, Faheem SM, Seenivasan R, Premkumar K, Vasanthakumar G (2014) Thermal chemosensitization of breast cancer cells to cyclophosphamide treatment using folate receptor targeted gold nanoparticles. Plasmonics 9(6):1341–1349
84. You J, Zhang R, Zhang GD, Zhong M, Liu Y, Van Pelt CS, Liang D, Wei W, Sood AK, Li C (2012) Photothermal-chemotherapy with doxorubicin-loaded hollow gold nanospheres: a platform for near-infrared light-trigged drug release. J Control Release 158(2):319–328
85. Rengan AK, Bukhari AB, Pradhan A, Malhotra R, Banerjee R, Srivastava R, De A (2015) In vivo analysis of biodegradable liposome gold nanoparticles as efficient agents for photothermal therapy of cancer. Nano Lett 15(2):842–848
86. Hainfeld JF, O'Connor MJ, Lin P, Qian L, Slatkin DN, Smilowitz HM (2014) Infrared-transparent gold nanoparticles converted by tumors to infrared absorbers cure tumors in mice by photothermal therapy. PLoS ONE 9(2):e88414
87. Wang SJ, Huang P, Nie LM, Xing RJ, Liu DB, Wang Z, Lin J, Chen SH, Niu G, Lu GM, Chen XY (2013) Single continuous wave laser induced photodynamic/plasmonic photothermal therapy using photosensitizer-functionalized gold nanostars. Adv Mater 25 (22):3055–3061
88. Yuan H, Fales AM, Vo-Dinh T (2012) TAT peptide-functionalized gold nanostars: enhanced intracellular delivery and efficient NIR photothermal therapy using ultralow irradiance. J Am Chem Soc 134(28):11358–11361
89. Oh MH, Yu JH, Kim I, Nam YS (2015) Genetically programmed clusters of gold nanoparticles for cancer cell-targeted photothermal therapy. ACS Appl Mater Interfaces 7 (40):22578–22586
90. Wang C, Cheng L, Liu Z (2013) Upconversion nanoparticles for photodynamic therapy and other cancer therapeutics. Theranostics 3(5):317–330
91. Vankayala R, Lin CC, Kalluru P, Chiang CS, Hwang KC (2014) Gold nanoshells-mediated bimodal photodynamic and photothermal cancer treatment using ultra-low doses of near infra-red light. Biomaterials 35(21):5527–5538
92. Kuo WS, Chang YT, Cho KC, Chiu KC, Lien CH, Yeh CS, Chen SJ (2012) Gold nanomaterials conjugated with indocyanine green for dual-modality photodynamic and photothermal therapy. Biomaterials 33(11):3270–3278

93. Gao L, Fei J, Zhao J, Li H, Cui Y, Li J (2012) Hypocrellin-loaded gold nanocages with high two-photon efficiency for photothermal/photodynamic cancer therapy in vitro. ACS Nano 6 (9):8030–8040
94. Chen R, Wang X, Yao X, Zheng X, Wang J, Jiang X (2013) Near-IR-triggered photothermal/photodynamic dual-modality therapy system via chitosan hybrid nanospheres. Biomaterials 34(33):8314–8322
95. Alkilany AM, Murphy CJ (2010) Toxicity and cellular uptake of gold nanoparticles: what we have learned so far? J Nanopart Res 12(7):2313–2333
96. Elci SG, Jiang Y, Yan B, Kim ST, Saha K, Moyano DF, Yesilbag Tonga G, Jackson LC, Rotello VM, Vachet RW (2016) Surface charge controls the suborgan biodistributions of gold nanoparticles. ACS Nano 10(5):5536–5542
97. Omlor AJ, Le DD, Schlicker J, Hannig M, Ewen R, Heck S, Herr C, Kraegeloh A, Hein C, Kautenburger R, Kickelbick G, Bals R, Nguyen J, Dinh QT (2017) Local effects on airway inflammation and systemic uptake of 5 nm PEGylated and citrated gold nanoparticles in asthmatic mice. Small 13(10)
98. Chithrani BD, Ghazani AA, Chan WCW (2006) Determining the size and shape dependence of gold nanoparticle uptake into mammalian cells. Nano Lett 6(4):662–668
99. Albanese A, Chan WCW (2011) Effect of gold nanoparticle aggregation on cell uptake and toxicity. ACS Nano 5(7):5478–5489
100. Wang YC, Liu YJ, Luehmann H, Xia XH, Brown P, Jarreau C, Welch M, Xia YN (2012) Evaluating the pharmacokinetics and in vivo cancer targeting capability of au nanocages by positron emission tomography imaging. ACS Nano 6(7):5880–5888
101. Vivero-Escoto JL, Huxford-Phillips RC, Lin W (2012) Silica-based nanoprobes for biomedical imaging and theranostic applications. Chem Soc Rev 41(7):2673–2685
102. Shirshahi V, Soltani M (2015) Solid silica nanoparticles: applications in molecular imaging. Contrast Media Mol Imaging 10(1):1–17
103. Tang L, Cheng J (2013) Nonporous silica nanoparticles for nanomedicine application. Nano Today 8(3):290–312
104. Wu X, Wu M, Zhao JX (2014) Recent development of silica nanoparticles as delivery vectors for cancer imaging and therapy. Nanomed UK 10(2):297–312
105. Baeza A, Colilla M, Vallet-Regi M (2015) Advances in mesoporous silica nanoparticles for targeted stimuli-responsive drug delivery. Expert Opin Drug Deliv 12(2):319–337
106. Douroumis D, Onyesom I, Maniruzzaman M, Mitchell J (2013) Mesoporous silica nanoparticles in nanotechnology. Crit Rev Biotechnol 33(3):229–245
107. Iqbal MZ, Ma X, Chen T, Le Z, Ren W, Xianga L, Wu A (2015) Silica-coated super-paramagnetic iron oxide nanoparticles (SPIONPs): a new type contrast agent of T1 magnetic resonance imaging (MRI). J Mater Chem B 3:5172–5181
108. Xue S, Wang Y, Wang M, Zhang L, Du X, Gu H, Zhang C (2014) Iodinated oil-loaded, fluorescent mesoporous silica-coated iron oxide nanoparticles for magnetic resonance imaging/computed tomography/fluorescence trimodal imaging. Int J Nanomed 9:2527–2538
109. Knezevic NZ, Durand JO (2015) Targeted treatment of cancer with nanotherapeutics based on mesoporous silica nanoparticles. ChemPlusChem 80(1):26–36
110. Chen F, Hong H, Shi S, Valdovinos HF, Barnhart TE, Cai W (2014) Engineering of hollow mesoporous silica nanoparticles for remarkably enhanced tumor active targeting efficacy. Eur J Nucl Med Mol I 41:S322–S322
111. Muhammad F, Zhao J, Wang N, Guo M, Wang A, Chen L, Guo Y, Li Q, Zhu G (2014) Lethal drug combination: arsenic loaded multiple drug mesoporous silica for theranostic applications. Colloids Surf B Biointerfaces 123:506–514
112. Baeza A, Colilla M, Vallet-Regi M (2015) Advances in mesoporous silica nanoparticles for targeted stimuli-responsive drug delivery. Expert Opin Drug Deliv 12(2):319–337
113. Liu Y, Feng L, Liu T, Zhang L, Yao Y, Yu D, Wang L, Zhang N (2014) Multifunctional pH-sensitive polymeric nanoparticles for theranostics evaluated experimentally in cancer. Nanoscale 6(6):3231–3242

114. Shen J, Kim HC, Su H, Wang F, Wolfram J, Kirui D, Mai J, Mu C, Ji LN, Mao ZW, Shen H (2014) Cyclodextrin and polyethylenimine functionalized mesoporous silica nanoparticles for delivery of siRNA cancer therapeutics. Theranostics 4(5):487–497
115. Jia L, Li Z, Shen J, Zheng D, Tian X, Guo H, Chang P (2015) Multifunctional mesoporous silica nanoparticles mediated co-delivery of paclitaxel and tetrandrine for overcoming multidrug resistance. Int J Pharm 489(1–2):318–330
116. Wang X, Liu Y, Wang S, Shi D, Zhou X, Wang C, Wu J, Zeng Z, Li Y, Sun J, Wang J, Zhang L, Teng Z, Lu G (2015) CD44-engineered mesoporous silica nanoparticles for overcoming multidrug resistance in breast cancer. Appl Surf Sci 332:308–317
117. Cha C, Shin SR, Annabi N, Dokmeci MR, Khademhosseini A (2013) Carbon-based nanomaterials: multifunctional materials for biomedical engineering. ACS Nano 7(4):2891–2897
118. Zhang P, Huang H, Huang J, Chen H, Wang J, Qiu K, Zhao D, Ji L, Chao H (2015) Noncovalent ruthenium(II) complexes-single-walled carbon nanotube composites for bimodal photothermal and photodynamic therapy with near-infrared irradiation. ACS Appl Mater Interfaces 7(41):23278–23290
119. Liu Z, Cai W, He L, Nakayama N, Chen K, Sun X, Chen X, Dai H (2007) In vivo biodistribution and highly efficient tumour targeting of carbon nanotubes in mice. Nat Nanotechnol 2(1):47–52
120. de la Zerda A, Liu Z, Bodapati S, Teed R, Vaithilingam S, Khuri-Yakub BT, Chen X, Dai H, Gambhir SS (2010) Ultrahigh sensitivity carbon nanotube agents for photoacoustic molecular imaging in living mice. Nano Lett 10(6):2168–2172
121. Wenseleers W, Vlasov II, Goovaerts E, Obraztsova ED, Lobach AS, Bouwen A (2004) Efficient isolation and solubilization of pristine single-walled nanotubes in bile salt micelles. Adv Funct Mater 14(11):1105–1112
122. Welsher K, Liu Z, Sherlock SP, Robinson JT, Chen Z, Daranciang D, Dai H (2009) A route to brightly fluorescent carbon nanotubes for near-infrared imaging in mice. Nat Nanotechnol 4(11):773–780
123. Hong G, Lee JC, Jha A, Diao S, Nakayama KH, Hou L, Doyle TC, Robinson JT, Antaris AL, Dai H, Cooke JP, Huang NF (2014) Near-infrared II fluorescence for imaging hindlimb vessel regeneration with dynamic tissue perfusion measurement. Circ Cardiovasc Imaging 7(3):517–525
124. Hong G, Lee JC, Robinson JT, Raaz U, Xie L, Huang NF, Cooke JP, Dai H (2012) Multifunctional in vivo vascular imaging using near-infrared II fluorescence. Nat Med 18 (12):1841–1846
125. Deng S, Zhang Y, Brozena AH, Mayes ML, Banerjee P, Chiou WA, Rubloff GW, Schatz GC, Wang Y (2011) Confined propagation of covalent chemical reactions on single-walled carbon nanotubes. Nat Commun 2:382
126. Liu Z, Sun X, Nakayama-Ratchford N, Dai H (2007) Supramolecular chemistry on water-soluble carbon nanotubes for drug loading and delivery. ACS Nano 1(1):50–56
127. Madani SY, Naderi N, Dissanayake O, Tan A, Seifalian AM (2011) A new era of cancer treatment: carbon nanotubes as drug delivery tools. Int J Nanomed 6:2963–2979
128. Liu Z, Chen K, Davis C, Sherlock S, Cao Q, Chen X, Dai H (2008) Drug delivery with carbon nanotubes for in vivo cancer treatment. Cancer Res 68(16):6652–6660
129. Liu Z, Robinson JT, Tabakman SM, Yang K, Dai HJ (2011) Carbon materials for drug delivery and cancer therapy. Mater Today 14(7–8):316–323
130. Siu KS, Chen D, Zheng X, Zhang X, Johnston N, Liu Y, Yuan K, Koropatnick J, Gillies ER, Min WP (2014) Non-covalently functionalized single-walled carbon nanotube for topical siRNA delivery into melanoma. Biomaterials 35(10):3435–3442
131. Liang C, Diao S, Wang C, Gong H, Liu T, Hong G, Shi X, Dai H, Liu Z (2014) Tumor metastasis inhibition by imaging-guided photothermal therapy with single-walled carbon nanotubes. Adv Mater 26(32):5646–5652
132. Liu Y, Zhao Y, Sun B, Chen C (2013) Understanding the toxicity of carbon nanotubes. Acc Chem Res 46(3):702–713

133. Cheng CJ, Tietjen GT, Saucier-Sawyer JK, Saltzman WM (2015) A holistic approach to targeting disease with polymeric nanoparticles. Nat Rev Drug Discov 14(4):239–247
134. Soppimath KS, Aminabhavi TM, Kulkarni AR, Rudzinski WE (2001) Biodegradable polymeric nanoparticles as drug delivery devices. J Control Release 70(1–2):1–20
135. Zhang LW, Gao S, Zhang F, Yang K, Ma QJ, Zhu L (2014) Activatable hyaluronic acid nanoparticle as a theranostic agent for optical/photoacoustic image-guided photothermal therapy. ACS Nano 8(12):12250–12258
136. Wang Z, Niu G, Chen XY (2014) Polymeric materials for theranostic applications. Pharm Res Dord 31(6):1358–1376
137. Schmaljohann D (2006) Thermo- and pH-responsive polymers in drug delivery. Adv Drug Deliver Rev 58(15):1655–1670
138. Couvreur P, Kante B, Roland M, Speiser P (1979) Adsorption of antineoplastic drugs to polyalkylcyanoacrylate nanoparticles and their release in calf serum. J Pharm Sci 68 (12):1521–1524
139. Couvreur P, Kante B, Lenaerts V, Scailteur V, Roland M, Speiser P (1980) Tissue distribution of antitumor drugs associated with polyalkylcyanoacrylate nanoparticles. J Pharm Sci 69(2):199–202
140. Kante B, Couvreur P, Dubois-Krack G, De Meester C, Guiot P, Roland M, Mercier M, Speiser P (1982) Toxicity of polyalkylcyanoacrylate nanoparticles I: free nanoparticles. J Pharm Sci 71(7):786–790
141. Cai K, He X, Song Z, Yin Q, Zhang Y, Uckun FM, Jiang C, Cheng J (2015) Dimeric drug polymeric nanoparticles with exceptionally high drug loading and quantitative loading efficiency. J Am Chem Soc 137(10):3458–3461
142. Fonseca C, Simoes S, Gaspar R (2002) Paclitaxel-loaded PLGA nanoparticles: preparation, physicochemical characterization and in vitro anti-tumoral activity. J Control Release 83 (2):273–286
143. Danhier F, Lecouturier N, Vroman B, Jerome C, Marchand-Brynaert J, Feron O, Preat V (2009) Paclitaxel-loaded PEGylated PLGA-based nanoparticles: in vitro and in vivo evaluation. J Control Release 133(1):11–17
144. Araki T, Kono Y, Ogawara K, Watanabe T, Ono T, Kimura T, Higaki K (2012) Formulation and evaluation of paclitaxel-loaded polymeric nanoparticles composed of polyethylene glycol and polylactic acid block copolymer. Biol Pharm Bull 35(8):1306–1313
145. Gao D, Gao L, Zhang C, Liu H, Jia B, Zhu Z, Wang F, Liu Z (2015) A near-infrared phthalocyanine dye-labeled agent for integrin alphavbeta6-targeted theranostics of pancreatic cancer. Biomaterials 53:229–238
146. Chen H, Zhang X, Dai S, Ma Y, Cui S, Achilefu S, Gu Y (2013) Multifunctional gold nanostar conjugates for tumor imaging and combined photothermal and chemo-therapy. Theranostics 3(9):633–649
147. Zhao J, Wu C, Abbruzzese J, Hwang RF, Li C (2015) Cyclopamine-loaded core-cross-linked polymeric micelles enhance radiation response in pancreatic cancer and pancreatic stellate cells. Mol Pharm 12(6):2093–2100
148. Camacho KM, Kumar S, Menegatti S, Vogus DR, Anselmo AC, Mitragotri S (2015) Synergistic antitumor activity of camptothecin-doxorubicin combinations and their conjugates with hyaluronic acid. J Control Release 210:198–207
149. Simone EA, Zern BJ, Chacko AM, Mikitsh JL, Blankemeyer ER, Muro S, Stan RV, Muzykantov VR (2012) Endothelial targeting of polymeric nanoparticles stably labeled with the PET imaging radioisotope iodine-124. Biomaterials 33(21):5406–5413
150. Huang J, Wang L, Lin R, Wang AY, Yang L, Kuang M, Qian W, Mao H (2013) Casein-coated iron oxide nanoparticles for high MRI contrast enhancement and efficient cell targeting. ACS Appl Mater Interfaces 5(11):4632–4639
151. Schluep T, Hwang J, Hildebrandt IJ, Czernin J, Choi CH, Alabi CA, Mack BC, Davis ME (2009) Pharmacokinetics and tumor dynamics of the nanoparticle IT-101 from PET imaging and tumor histological measurements. Proc Natl Acad Sci USA 106(27):11394–11399

152. Wu C, Bull B, Szymanski C, Christensen K, McNeill J (2008) Multicolor conjugated polymer dots for biological fluorescence imaging. ACS Nano 2(11):2415–2423
153. Capolla S, Garrovo C, Zorzet S, Lorenzon A, Rampazzo E, Spretz R, Pozzato G, Nunez L, Tripodo C, Macor P, Biffi S (2015) Targeted tumor imaging of anti-CD20-polymeric nanoparticles developed for the diagnosis of B-cell malignancies. Int J Nanomed 10:4099–4109
154. Park K, Kim JH, Nam YS, Lee S, Nam HY, Kim K, Park JH, Kim IS, Choi K, Kim SY, Kwon IC (2007) Effect of polymer molecular weight on the tumor targeting characteristics of self-assembled glycol chitosan nanoparticles. J Control Release 122(3):305–314
155. Qiu Y, Palankar R, Echeverria M, Medvedev N, Moya SE, Delcea M (2013) Design of hybrid multimodal poly(lactic-co-glycolic acid) polymer nanoparticles for neutrophil labeling, imaging and tracking. Nanoscale 5(24):12624–12632
156. Hong G, Zou Y, Antaris AL, Diao S, Wu D, Cheng K, Zhang X, Chen C, Liu B, He Y, Wu JZ, Yuan J, Zhang B, Tao Z, Fukunaga C, Dai H (2014) Ultrafast fluorescence imaging in vivo with conjugated polymer fluorophores in the second near-infrared window. Nat Commun 5:4206
157. Rolfe BE, Blakey I, Squires O, Peng H, Boase NR, Alexander C, Parsons PG, Boyle GM, Whittaker AK, Thurecht KJ (2014) Multimodal polymer nanoparticles with combined 19F magnetic resonance and optical detection for tunable, targeted, multimodal imaging in vivo. J Am Chem Soc 136(6):2413–2419
158. Huynh E, Leung BY, Helfield BL, Shakiba M, Gandier JA, Jin CS, Master ER, Wilson BC, Goertz DE, Zheng G (2015) In situ conversion of porphyrin microbubbles to nanoparticles for multimodality imaging. Nat Nanotechnol 10(4):325–332
159. Yang Z, Zheng S, Harrison WJ, Harder J, Wen X, Gelovani JG, Qiao A, Li C (2007) Long-circulating near-infrared fluorescence core-cross-linked polymeric micelles: synthesis, characterization, and dual nuclear/optical imaging. Biomacromol 8(11):3422–3428
160. Taratula O, Doddapaneni BS, Schumann C, Li XN, Bracha S, Milovancev M, Alani AWG, Taratule O (2015) Naphthalocyanine-based biodegradable polymeric nanoparticles for image-guided combinatorial phototherapy. Chem Mater 27(17):6155–6165

Chapter 9
Pluronic Nanotechnology for Overcoming Drug Resistance

Pallabita Chowdhury, Prashanth K.B. Nagesh, Santosh Kumar, Meena Jaggi, Subhash C. Chauhan and Murali M. Yallapu

Abstract Chemotherapy is one of the most conventionally used therapeutic interventions for treating various diseases. Chances of acquiring multidrug resistance in response to chemotherapeutic agents are exceedingly common among patients. Drug resistance arises mainly due to overexpression of efflux transporters such as P-glycoprotein and multidrug resistance-associated protein of the ATP-binding cassette superfamily of proteins, which significantly limits intracellular drug accumulation and drug activity. Although many approaches exist to overcome drug resistance, their uses are significantly limited in clinical practice. In this chapter, we demonstrate the superior functions of Pluronic-based technologies to overcome drug resistance. The present chapter highlights various aspects of Pluronic polymers, Pluronic conjugates, Pluronic nanotechnology, as well as their therapeutic implications for effective treatment strategies. We include the role of Pluronic polymers as a pharmaceutic excipient and drug delivery vehicle in this review. In addition, we highlight examples of Pluronic nanosystems that are currently in preclinical development, clinical trials, and clinically translatable formulations. Furthermore, a number of innovative Pluronic nano-designs of advanced therapeutics for future medicinal applications are presented. Collectively, the use of Pluronic-based nanoformulations discussed in this chapter suggests sensitization and prevention of drug resistance. Such an approach not only minimizes the dose required for treatment, but also minimizes the number of treatment cycles, which is useful in a clinical scenario.

Keywords Pluronics · Nanoparticles · Nanotechnology · Drug resistance

P. Chowdhury · P.K.B. Nagesh · S. Kumar · M. Jaggi · S.C. Chauhan · M.M. Yallapu (✉)
Department of Pharmaceutical Sciences, University of Tennessee Health Science Center, 881 Madison Ave, Memphis, TN 38163, USA
e-mail: myallapu@uthsc.edu

B. Yan et al. (eds.), *Bioactivity of Engineered Nanoparticles*, Nanomedicine and Nanotoxicology, DOI 10.1007/978-981-10-5864-6_9

9.1 Introduction

According to the National Institute of Allergy and Infectious Diseases (NIH), drug resistance (DR) or multidrug resistance (MDR) is defined as the ability of microbes, such as bacteria, viruses, parasites, or fungi to grow even in the presence of chemical(s) (therapeutic drug molecules) that would usually inhibit their growth. Paul Ehrlich, the father of modern chemotherapy, proposed that drug resistance was acquired by the biological system when there was "reduced avidity of the chemoreceptors so that they are no longer able to take up" the drugs [1]. Antimicrobial resistance has resulted in increased morbidity, mortality, and a waste of healthcare resources. Centers for Disease Control and Prevention (in April 2011) estimated that antibiotic resistance in the United States alone costs approximately $20 billion a year in excess healthcare costs [2].

Drug resistance or multidrug resistance in cancer therapy is frequently experienced. In fact, this is considered as one of the major impediments for the success of many forms of chemotherapy. In general, tumors consist of drug-sensitive and drug-resistant malignant cells. Conventional chemotherapy inhibits the drug-sensitive cells, leaving behind a considerable amount of drug-resistant cells. These cells have already acquired resistance and are not affected by chemotherapy. Additionally, cancer cells adopt and develop drug resistance to frequently administered drug molecules.

In chemotherapy, DR/MDR is governed by several factors. First, resistance occurs due to drug elimination from cells by the efflux ATP-binding cassette (ABC) transporters like P-glycoprotein (P-gp), ABCB1, MRP1, ABCC1, MCRP, ABCG2, BCRP, and ABCG2. Resistance inhibits the diffusion of drugs to the cells due to loss of receptors on the cell surface, loss of drug transporters, or the altercation in membrane lipid composition. Resistance can occur when the drug is compartmentalized in cellular vesicles. A change or alteration in drug targets can cause resistance. Extensive drug metabolism, a change in the cell cycle and the inhibition of apoptosis can cause resistance, as well. Finally, resistance can occur when active damage is repaired [3]. At times, cells undergo mutations, which change the cell's structure or biochemical pathway in a harmful way. These groups of growing cells are no longer affected by the presence or absence of drugs. Some mutations might even change the part of cells that are affected by drugs, creating a thriving resistance of the cell to the drug. Moreover, when drugs are no longer administered or not properly administered, the body's natural defenses fail to abolish the resistant survivors, allowing the ability to reproduce and pass the resistance to their descendants.

P-glycoprotein and multidrug resistance-associated protein (MDRP) are responsible for the efflux of drug molecules, and causing the development of resistance to drug action(s) [4]. Evidence of P-gp overexpression and mediated drug resistance was confirmed back in 1982 when deoxyribonucleic acid (DNA) from resistant cells transferred to nonresistant cell lines, which conferred resistance to the latter [3]. On the other hand, MRP was cloned in 1992 and found responsible for

drug resistance [4]. Subsequently, both ATP-binding cassette transporters (ABC transporters) have been extensively studied and are considered significant targets for anticancer drugs. Similarly, HIV is another disease that frequently develops resistance to known therapeutic drug molecules.

There have been many approaches to overcoming drug resistance. However, very few of these approaches could shift from research to bedside practice. A few of such investigations include co-delivery of gene therapy, such as adding siRNA, shRNA, DNA, or dsRNA with the drugs. One such combination was causing downregulation of cyclin B1 mRNA, thus creating a delay in growth of the tumor. Another approach was to develop a multifunctional carrier system to deliver both the drug and siRNA [5]. MicroRNA (miRNA) also plays an integral role in developing resistance and is shown to have various mechanisms involved in resistance development [6]. Synthetic analogue of dsRNA was exploited for combination therapy to develop a strategy against drug resistance [7]. On a similar attempt, various groups have investigated using mitochondria targeting for drug delivery [8].

Although many of these approaches help to some extent in overcoming drug resistance, their use is still unknown in clinical practice. An extensive literature search revealed that Pluronic-based technologies are highly successful when used to overcome drug resistance. Thus, we aim to present a review which highlights the novel role of Pluronics in chemotherapies. Poloxamer (Pluronics®) [9] is a nonionic triblock copolymer with surfactant properties that is amphiphilic in nature. These copolymers are also marketed as Synpersonic® or Tetronic®. It is believed that Pluronics consist of hydrophobic poly(propylene oxide) (PPO) chains, which has a tendency to be immersed in the hydrophobic core of the biomembrane, resulting in an altercation of the membrane and thus, sensitization of the MDR tumor cells to the anticancer drugs [10]. This function further aids in active drug transport across both blood–brain barriers and intestinal barriers, which can cause transcriptional activation of gene expression both in vitro and in vivo [11, 12].

9.2 Pluronic Polymers

Poloxamers were introduced in 1950 and are classified as nonionic copolymers. These polymers are *odorless, tasteless, white, waxy granules with free flow*ing properties. Amphiphilic in nature, *they are soluble in both polar and nonpolar solvents.* Pluronics are composed in a triblock fashion, consisting of a hydrophobic [poly(propylene oxide) (PPO)] unit in between two basic hydrophilic units [poly (ethylene oxide) (PEO)] with the basic sequence of A–B–A structure (PEO_a–PPO_b–PEO_a) (Fig. 9.1) [11]. The number and average size of PEO and PPO blocks are shown in Table 9.1. These polymers have the same chemical structure but differ in molecular weight. The hydrophilic–lipophilic balance (HLB) determines the amphiphilic property of Pluronic polymers, which is dependent on the number of PEO or PPO units. Pluronics are a major pharmaceutical excipient due to their

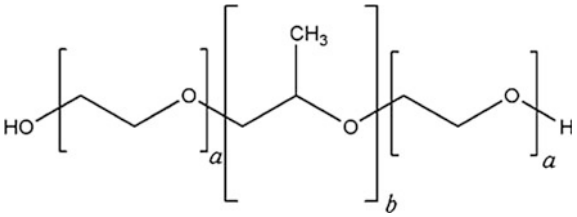

Fig. 9.1 General structure of poloxamers

Table 9.1 Different marketed brands of poloxamers [14, 15]

Name	Average molecular weight	No. of EO units	No. of PO units
Poloxamer 124 (Pluronic® L-44)	2090–2360	12	20
Poloxamer 188 (Pluronic® F-68)	7680–9510	80	27
Poloxamer 237 (Pluronic® F-87)	6840–8830	64	37
Poloxamer 338 (Pluronic® F-108)	12700–17400	141	44
Poloxamer 407 (Pluronic® F-127)	9840–14600	101	56
Poloxamer 401 (Pluronic® L121)	4400	10	68
Poloxamer 184 (Pluronic® L-64)	2900	26	30

superior stability in aqueous solutions in the presence of acid, alkali, or metals ions over other molecules. Pluronics are synthesized by sequential anionic polymerization by adding ethylene oxide (EO) or propylene oxide (PO) monomers in the presence of an alkaline catalyst, such as sodium or potassium hydroxide [13]. They exhibit a reversible thermodynamic property, which helps to convert the solution into a solid gel form by varying their chemical composition.

Pluronics are unstructured molecular solutions at low temperature. However, as the temperature rises and reaches the critical micelle temperature (CMT-also termed as Krafft temperature or Krafft point), the copolymers aggregate, resulting in the formation of spherical micelles. As the temperature increases above CMT, the micelles align in a uniform fashion, laying the hydrated and swollen PEO units at the outer lining, while the dehydrated PPO units occupy the inner core of the micelles. This self-assemble process is called micellization [11]. This leads to an increase in the hydrophobicity and a decrease in the degree of hydration. This critical micellar concentration (CMC), which influences the micellization process, is of prime importance. The possible dilution of the micelles by body fluids determines the stability of the solution, and is dependent on the CMC [16, 17]. CMC also determines the biological effect that the Pluronic® micelles have on the exposed cells [18].

The interactions of the PPO blocks are the primary driving force for the micellization. Depending on the type of Pluronic used, the micelles are about 20–80 nm in size [19]. In general, block copolymers have approximately $\geq 30\%$ PEO content,

especially in diluted solutions at body temperature [11]. The benefit of the hydrophobic core in the Pluronic micelles makes them an efficient carrier tool for delivering hydrophobic drugs and other therapeutic agents. The process of transferring lipophilic molecules to the core of the micelles is referred to as solubilization. Solubilization can be used to improve the metabolic stability, solubility, and pharmacokinetics of encapsulated therapeutic molecules at the physiological condition. The hydrophilic outer layer maintains the dispersed state of micelles and prevents undesirable interactions with cells and proteins [11]. Pluronics are capable of forming pores on cellular membranes [20], which gives them the added advantage of the ability to interact with the MDR cells and to develop sensitization of the cells causing apoptosis to anticancer drugs [11, 21]. Pluronics are much favored in drug delivery because of their ability to embody into the membrane, allowing translocation in cells, and thus changing cellular functions, such as mitochondrial respiration, ATP synthesis, activity of drug efflux transporters, apoptotic signal transduction, and gene expression [22]. Additionally, they have the ability to enhance the drug transport of various drugs through impervious barriers, such as blood–brain barrier and intestinal barriers, hence improving bioavailability [11, 12].

More importantly, Pluronic polymers have either a prevention or a reversal effect on MDR due to several associated mechanisms, which include but are not limited to:

(a) *Inhibition of P-gp drug efflux transport system*. As per literature review, Pluronics specifically inhibit the P-gp-dependent transport route in MDR cells and not in cells that do not express P-gp [18, 23].
(b) *Inhibiting the MDRPs* [24] *and breast cancer resistance protein (BCRP)* [25]. Significant accumulation and cytotoxic effect of MDRP substrate and MDRP-dependent drugs were observed in MDRP cells when compared to non-MDRPs cells using Pluronic-85, probably due to its ability to sensitize selected MDRP overexpressing cells. As demonstrated by Yamagata et al. [25] uptake of mitoxantrone was enhanced in BCRP-expressing cells and was less effective in green fluorescent protein (GFP)-expressing cells, suggesting that Pluronics could be a potent BCRP inhibitor in the small intestine. Although role of Pluronics on BCRP and P-gp inhibitory effects still remains unclear.
(c) *Eradicating drug sequestration inside the cytoplasmic vesicles*. [26, 27]. The MDR cells deter drug delivery by sequestrating the drugs within vesicles following drug release, to the cytoplasm, and accumulation in the nucleus [27–31]. This limits the potency of the drug before it can even implement any therapeutic action. The presence of H^+-ATPase, an ATP-dependent pump on the membranes, increases the pH gradients aiding drug sequestration in the resistant cells [32].
(d) *Significant ATP level depletion*. Mitochondria, where metabolic activities of the cell occur, may be a prospective site of action for the copolymer. As per Kabanov et al. [33], metabolic activities in the MDR cells are more responsive to Pluronics than the non-MDR cells, thus resulting in significant ATP inhibition by Pluronics in MDR expressed cells. Another hypothesis is that

Pluronics are supplements of K ionophores (lipid-soluble entities that transport ions across a cell membrane) [34–36] and are capable of uncoupling oxidative phosphorylation [37, 38], which may contribute to inhibit the metabolic activities on the mitochondria, reducing ATP level(s). It was reported that these copolymers directly target the hydrophobic site of NADH "nicotinamide adenine dinucleotide (NAD) + hydrogen (H)" dehydrogenase complex that are located in the mitochondrial membrane, which in turn inhibits the metabolic activity and the ATP depletion [37, 39].

(e) *Induction of membrane fluidization*. Pluronics can alter the structure of the lipid bilayer of the membrane leading to microviscosity. It is also important to note that both membrane fluidization and the ATP depletion are of critical importance for inhibiting the P-gp drug efflux transport system [10]. It is referred to as "double punch" effect, as the synergistic effect of both is important [11].

(f) *Inhibition of the Glutathione (GSH)/Glutathione S-transferase (GST) detoxification system*. Elimination of drug occurs due to the presence of GSH/GST detoxification system. It is believed that there is a complex and interrelated mechanism for drug elimination through the MRP and GSH/GST detoxification system in MDR cells when exposed to Pluronic polymers. Thus, it may be attributed that Pluronic® copolymers are responsible for the inhibition of the drug efflux transporter, causing accumulation of drugs in the resistant cells [11, 40].

(g) *Promoting release of cytochrome C*. Pluronics promote production of reactive oxygen species (ROS) in the cytoplasm due to the decreased potential of the mitochondrial membrane. This potential causes respiration deficiency in the mitochondria of the MDR cells [41].

(h) *Enhances drug-induced apoptosis*. Alterations in drug-induced apoptosis trigger pro-apoptotic signaling and prevent/minimize the activation of the anti-apoptotic defense in MDR cells [42].

A graphical representation of the working mechanism of Pluronic block copolymer is shown in Fig. 9.2.

To the best of our knowledge, Pluronic SP1049C (L61 and F127) is the first anticancer (doxorubicin) micellar formulation to reach clinical evaluation. Results of Phase I clinical trials in 26 advanced stage IV cancer patients reveal that the maximum tolerated dose (MTD) was 70 mg/m^2 and dose-limiting toxicities (DLT) was 90 mg/m^2 (neutropenia). It was considered as an acceptable safety profile and was efficacious against highly resistant oesophageal cancer [44]. In Phase II clinical trials on 19 patients evaluate SP1049C treatment, which showed a partial response (PR) in 9 patients and a minor response or stable disease in 8 patients. The median overall survival and Progression-free survival (PFS) were observed as 10 and 6.6 months [45]. In addition, various other Pluronic-based drug formulations are under pipeline for therapeutic evaluations.

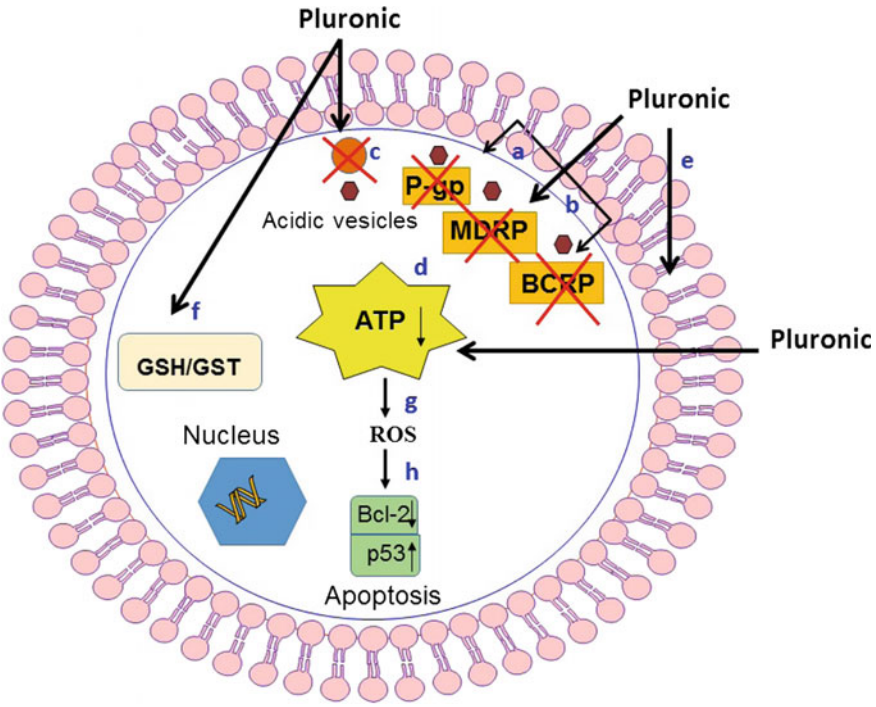

Fig. 9.2 Mechanism of action of Pluronics in MDR cells: (*a*) inhibition of drug efflux transporters (P-gp and MRP), (*b*) inhibition of other MDR protein (BCRP), (*c*) eradication of drug sequestration inside cytoplasmic vesicle, (*d*) ATP depletion, (*e*) decrease in the membrane microviscosity, (*f*) inhibition of the GSH/GST detoxification system, (*g*) increase in ROS level, (*h*) enhancement of pro-apoptotic and p53 signaling and decrease in anti-apoptotic signaling

9.3 Pluronic Conjugates

Pluronic copolymers owing it to their versatile nature for the hydrophilic and lipophilic block of PPO and PEO exhibited several advantages. The formed micelles (particles size, <100 nm) allowing significant accumulation in pathological tissues via the enhanced permeability and retention (EPR) effect, hence, they are capable of delivering drugs to tumors. Chemical or biomacromolecular conjugation with functional groups or drug(s) helps to enhance the property of the core-forming micelles and for drug delivery.

Kabanov et al. [43] developed a solution of haloperidol using P-85 in water, which was further conjugated with insulin or antibody. The resultant micelles could enhance the haloperidol delivery to the brain of mice almost 500-fold. This is due to the insulin moiety on the micelles surface, which could interact well with the insulin

receptors on the cell membrane. Coupling of micelles with the brain specific antibody could be target specific to the brain antigen. In contrast to this, haloperidol, when delivered using Pluronic solution without antibody conjugation, did not cross the hematoencephalic barrier (HEB) well, resulting in lower haloperidol concentration. In another study, a conjugate system using poloxamer 188 and grafting hydrophilic heparin leads to shell cross-linked micelles, which offers not only lowered CMC to the micelle system, but stabilized formulation [44, 45]. Additionally, such a heparin cross-linked poloxamer conjugate system could be a potential system to defy dilution in the body fluids and could enhance the stability of the micelles (in vivo), making it a potential temperature sensitive system for protein drug delivery [46].

Pluronic copolymer has shown promising results for delivering chemotherapeutic drugs, mainly because of their ability to reverse MDR effects in tumor cells. Song et al. [47] demonstrated that anti-human hypoxia inducible factor-1a (HIF-1a) antibody functionalized Pluronic P123 micelles for selective targetability and inhibition of cancer cells by releasing paclitaxel, and lowered the incidence of paclitaxel associated systemic toxicity. Similarly, synergistic action of doxorubicin was achieved when employing a combination of mixed/conjugated Pluronic micelle formulation [Pluronic P-105, PEG2000-diacylphospholipid, and poly(ethylene glycol)-*co*-poly(beta-benzyl-L-aspartate)] [44]. Li and Tan [48] demonstrated that Pluronic mixed micelles of P105 and PEG resulting in phosphatidyl ethanolamine conjugate (PEG-PE) could be much more efficacious when compared to P105 micelles. P105 and PE, when mixed in molar ratio less than 7:3, demonstrated higher stability and less adverse effects due to their low CMC value. This conjugate could also maintain the integrity, even when diluted in the blood. When tested on human breast carcinoma MCF-7 cells, this nanocomposite conjugate showed a higher cytotoxicity in contrast to the micelles with P105. This suggested that Pluronic, in conjugation with another polymer relative to one Pluronic, demonstrated better dilution stability (preventing dissociation of micelles into monomers) and efficacy.

Pluronics have gained considerable popularity in enhancing stability, solubility, and other added advantages. However, there are a few drawbacks associated with the use of Pluronic polymers, especially with reverse Pluronics (such as 10R5): high CMC, fast release/dissociation rates, and poor drug loading capacity. To overcome these innate shortcomings of Pluronics, F127 and 10R5 were conjugated with Folic acid (FA) and Quercitin (Q), respectively. Based on their structural characteristics, these two conjugated systems of F127-FA and 10R5-Q were mixed to form the final micelles. This final formulation was able to stabilize the doxorubicin in micelles, lower the CMC, and enhance loading capacity in contrast to mixed micelles of F127 and 10R5 [49]. Further, it was proposed previously that co-delivery of quercetin with doxorubicin enhances cytotoxicity to tumorous cells and minimized effects on healthy cells, which was also confirmed from this study.

Pluronics, being amphiphilic in nature, can co-deliver two anticancer drugs simultaneously to the tumor cells, one of which being hydrophobic (paclitaxel) and hydrophilic (doxorubicin). Both drugs being substrates of MRP, P-gp, and BCRP

have been used before to demonstrate efficient tumor regression [50, 51]. However, due to solubility differences of the two drugs, nanomicelles prepared from the amphiphilic Pluronic polymers F127 and P105 have been of significant help, aiding synergistic effects of both the drugs. As a result, enhanced cellular uptake, stronger growth inhibition, and better apoptosis in MDR cells were achieved. Results indicate that this dual drug loaded Pluronic micelles enhance drug accumulation in the tumor cells and in the plasma, thus achieving a higher incidence of antitumor efficiency with respect to single drug loaded Pluronic micelles or combined drug administration. This suggests that a combination of dual drugs with Pluronic micelles offers advantages of synergistic effects, passive tumor targeting, and reversed MDR effect, and therefore, could be a viable option for reversing MDR effect of cancer chemotherapy [52].

Apart from offering several advantages for cancer chemotherapy line of action, Pluronics have also been successful in offering anti-adhesive property when conjugated with protein lysozyme. The antibacterial lysozyme conjugate enables the lysozyme to stretch out more into the solution. This suggests that attaching the lysozyme to the PEO chain of the Pluronic could be better adsorbed to the attaching surface, as the free PPO chain adheres to the hydrophobic surface and the PEO lysozyme conjugate faces towards the hydrophilic solution. Therefore it is inferred that the PPO attached to the surface is an indication of the high stability that the Pluronic is capable of [53, 54], and the attachment of the antimicrobial lysozyme to the Pluronic provides resistance to particle deposition and selective lethal interaction with microorganisms, thus providing anti-adhesive activity [55].

9.4 Pluronic Nanotechnology

Nanotechnology in drug delivery research has gained significant attention for developing novel techniques and/or delivery of classic medicine to the body. The benefits of nanotechnology [56–58] include:

- The delivery of poorly soluble drugs, proteins, and peptides
- The delivery of macromolecules to the intracellular site of action
- The delivery of two or more drugs simultaneously to achieve synergistic effect
- Enhancing visibility at the site of drug action by combining therapeutic agents with imaging modalities
- Targeted delivery to cell or specific tissue
- Transcytosis of drugs across tight epithelial and endothelial barriers
- Enhancing therapeutic in vivo efficacy
- Controlled release of the therapeutic agent.

Pluronics, as mentioned earlier, are triblock copolymers with PEO and PPO units that exhibit surfactant properties, enabling them to interact with hydrophobic surfaces of biological membranes. Thus, Pluronics are an interesting candidate for

drug delivery across biological membrane, increasing drug solubility and drug stability, enhancing pharmacokinetics and biodistribution of drugs. These copolymers at concentrations above critical micelle concentration (CMC) can self-assemble into micelles, forming Pluronic micelles with diameters between 10 and 100 nm [16]. For example, Pluronic P85 was utilized in enhancing the cytotoxicity of daunorubicin in MDR cells [59]. This was achieved due to enhanced transport of daunorubicin into the cells, enhancing drug influx into the cytoplasm to enable a better binding with the DNA of the MDR cells. It is evident that with P85, an alternative delivery system can be developed to enhance the activity of the antineoplastic agents against MDR tumors [59]. The advantage of Pluronics is the ability to reverse MDR effects and to cross intestinal and blood–brain barriers, as well as gene expression in vitro and in vivo models, all of which have drawn interest of researchers globally.

Pluronic-based nanotechnology is making progressive advancements and is one of the fast flourishing fields in pharmaceutical research. Various nano-carriers, such as polymeric nanoparticles, metal nanoparticles, nano-suspensions, liposomes, dendrimers, nanogels, polymeric micelles, and solid lipid nanoparticles have been studied extensively over the past two to three decades. Recent trend follows modification/functionalization of nano-carriers with Pluronics in order to investigate their ability to reverse multidrug resistance in a precise manner, and is considered as a safe and more efficient delivery system for drugs, genes, and imaging molecules [60–62].

9.4.1 Pluronic Nanoparticles

Nanoparticles are colloidal systems with size ranging between 10 and 1000 nm. In nanoparticles, the drug can be dispersed, entrapped, encapsulated, or attached to a nanoparticle matrix. The unique structure of polymeric chain allows to achieve a specific shape, size, physical state, and surface. Due to their small size and uniform dispersion of drug molecules in polymer matrix, they provide a sustained drug release that avoids frequent administration. It can also help in attaining target specific delivery and intracellular penetration, and thereby a better absorption. Polymeric nanoparticles have the ability to target particular organs/tissues as carriers of drug, DNA, proteins, peptides, and genes. To prevent rapid elimination from human body system, they are often coated/conjugated with Pluronic polymers, polyethylene glycol, chitosan, and hyaluronic acid or even thermosensitive gels, to impart mucoadhesive property and thus improve the drug bioavailability [63]. Evidence of using polymeric nanoparticles in enhancing drug delivery often utilizes PLGA [64, 65], PEG [66, 67], PLGA–PEG [68–70], PCL [71, 72], and PLA [73] copolymers due to their biocompatibility and US-Food and Drug Administration (FDA) approved polymers for human use. To demonstrate the ability of Pluronics to cause immense sensitization of MDR tumors to several anticancer agents, Mei et al. [74] developed and characterized nanoparticles with PCL and Pluronic F68.

These nanoparticles increased the uptake in resistant breast cancer cells by 1.67-fold at all tested concentrations up to 500 μg/ml. Further, the cytotoxicity achieved on resistant breast cancer cell lines with PCL-F68 nanoparticles was significantly more ($p < 0.05$) than the PCL nanoparticles and a marketed formulation Taxotere. These findings confirm the potential of Pluronics to reverse MDR and achieve better therapeutic effects [74]. Similarly, nanoparticles prepared from Polyethyleneimine (PEI) and Pluronic P85 resulted in overcoming resistance in lung cancer cells. A conjugated nanoparticle of PEI-P85 was mixed with D-α-tocopheryl and polyethylene glycol 1000 succinate (TPGS) and survivin shRNA (ShSur) (which is used to down regulate the expression of survivin that is upregulated in resistant cancer cell lines). This complex nanoparticle of P85-PEI/TPGS/PTX/shSur was further loaded with paclitaxel. The complex nanoparticle demonstrated 87-fold higher cytotoxicity than free paclitaxel and enhanced cellular uptake by 36-fold, in contrast to blank nanoparticles. In addition, better antitumor efficacy was achieved on nude mice models with this complex nanoparticle conjugate due to the co-delivery of paclitaxel and shSur, both of which helped to overcome resistance in human lung cancer cell lines [75].

9.4.2 Dendrimers

Dendrimers are made up of polymeric chains with a highly branched star-shaped structure. Dendrimers are nanoconstructs with unique physical and chemical properties, such as high water solubility, encapsulation ability, monodispersity, and a large number of surface functionalizable groups. The ability to functionalize surface groups makes them suitable candidates for delivery of both hydrophilic and lipophilic drugs [76, 77]. They have been an immense help in delivering anticancer [78, 79], antibacterial, antiviral [80–83] drugs, as well as high molecular weight compounds [84, 85]. Dendrimer modification with Pluronic polymers, especially polyamidoamine (PAMAM) dendrimers, has attracted considerable interest, yielding a better product with improved reversion of MDR phenomenon. Highly lipophilic Pluronics (P123, F68, F127 and F108) that were conjugated on 4th generation of PAMAM dendrimer, i.e., PAMAMG4.0-Pluronics resulted in nanoformulations with a diameter of 60–180 nm [86]. PMMAMG4.0-P123 not only exhibited 76.25% of 5-fluorouracil (5FU) loading efficiency, but also promoted a highly anti-proliferative activity of 5-FU against MCF-7 breast cancer cells. Similarly, a F127 conjugated to the 5th generation PAMAM dendrimer showed a reduced hemolytic toxicity [87]. This formulation is efficient to encapsulate doxorubicin for a sustained release. While another PAMAM modified Pluronic (PAMAM:F127, 1:35.37 mole ratio) exhibited DOX complexation, which resulted in a pH-sensitive and sustained release behavior [88]. Additionally, this DOX-PAMAM-F127 complex showed stronger anticancer effects in MCF-7/ADR cells with a 33.15% resistance reversion index. Another PAMAM-F127 demonstrated formation of unimolecular micelles, and can be loaded with DOX, promoted

100% uptake in MCF-7/ADR cells and decreased cell viability even at 2 μg/ml concentration [89]. This implies a further superior role of dendrimer-Pluronic conjugates in the treatment of drug resistance cells.

9.4.3 Liposomes

Liposomes are lipid vesicles composed of one or more phospholipid bilayers with a central aqueous compartment [90]. They are capable of forming vesicles 25 nm to 10 μm in diameter and offers better encapsulation of both hydrophilic and lipophilic drugs due to the presence of a central aqueous compartment and lipid layer(s). Liposomes have a higher degree of biocompatibility than the polymer-based systems [91]. Commonly used polymers for liposome preparation are PEG, poly(vinyl pyrrolidone) (PVP), and poly(acrylic acid) (PAA). Pluronic P123 was conjugated with galactosyl (Gal), which is a specific ligand to target hepatocellular carcinoma (HCC) cells. The resultant Gal-P123 was used to develop liposomes (LPG) in order to enhance the ability of this molecule to reverse MDR effects by specifically targeting the HCC receptors. Mitoxantrone (MX) is the model drug for this study, which is a BCRP substrate that can overexpress BCRP in MDR cells. The MX loaded LPG had a good nanosize diameter of 100 nm. The in vitro capability of MX-LPG was evaluated using HCC Huh-7 cells, and then demonstrated a 2.3-fold increase in cytotoxicity by the MX-LPG over MX. Further, a 14.9-fold enhanced uptake of MX-LPG was reported in BCRP overexpressing MDCKII/BCRP cells over plain MX. Both in vitro data and in vivo study conducted on BALBc mice demonstrated improved uptake, target ability, and bioavailability of MX-LPG over LPG. The superiority of this formulation in reversing BCRP mediated MDR effect was clearly demonstrated [92]. Poloxamer P85 and F68 were modified into liposomes to overcome the effect of MDR. In this context, the group formulated modified poloxamers and tested it against normal cancer cells and MDR cells. Results demonstrate that Pluronic P85 at 50 μM enhanced the PML accumulation in MDR cells by 2-fold compared to control and 10-fold when compared to plain liposomes and Pluronic P68. This suggests that liposome modified Pluronic P85 is a potential carrier for anticancer drugs to reverse MDR cells [93].

9.4.4 Polymeric Micelles

Polymeric nanomicelles are synthesized from a block copolymer, which is generally biodegradable or biocompatible like PEG, PEO that forms amphiphilic monomeric units with distinct hydrophilic shell and hydrophobic core. They contain polymer chains, which are self-assembled due to hydrophobic or ion pair interactions between polymer segments [91]. The polymer blocks are arranged differently as diblock (A–B type), triblock (A–B–A type), or even grafted/branched

type copolymers, where A and B are different polymers used. If the core-forming block structures are efficiently monitored, the nanomicelles may have good thermodynamic and kinetic stability, and that increases the chance of a variety of drugs to be incorporated for drug loading, release, activation, and effective therapy. It is found that polymeric micelles are more stable than nanomicelles that are made from conventional surfactants [33]. Due to their low CMC values, they can retain drug molecules for longer periods of time, even in a diluted environment in systemic fluids. Moreover, polymeric micelles offer advantages like extended circulation time, sustained release, favorable biodistribution, reduced side effects, and lower toxicity [94–96]. Docetaxel was loaded in a polymeric micelle prepared with Pluronic F127 and P105 that was prepared by thin film hydration method. In vitro and in vivo data demonstrate superiority of this formulation over marketed Taxotere due to prolonged release by 1.85-fold. When tested on resistant human lung carcinoma, A549 anticancer efficacy and tumor inhibition were enhanced by 2-fold in contrast to Taxotere [97]. Additionally, when methotrexate was encapsulated into the same micelles of P105 and F127, they exhibited higher antitumor activity and increased cellular uptake over methotrexate injection. Also, higher cytotoxicity and lower systemic toxicity were induced by encapsulated methotrexate than methotrexate alone by injection on MDR cell lines. This confirms the ability of Pluronic as polymeric micelles to reverse MDR effects [98]. Pluronic P105 or P105 and L101 were used to formulate mixed micelles and were further attached to folic acid that was loaded with paclitaxel. This formulation exhibited enhanced targetability and uptake due to the presence of both Pluronic and folic acid, as there is an overexpression of folate receptors on MDR tumors. This caused enhanced internalization of the drug into the resistant tumor sites and prevented systemic toxicity at other bodily sites [99].

9.4.5 Ceramic Nanoparticles

Nanoscaled ceramics, such as Alumina (Al_2O_3) hydroxyapatite (HA), silica (SiO_2), and titanium oxide (TiO_2) [102, 103] are known to be biocompatible with biological environment and are utilized to form the ceramic nanoparticles ranging <100 nm. The ability to release the drug in a controlled fashion is the primary reason for its use in drug delivery. Apart from their porous nature, formation of sol-gel, enhanced stability in biological environment, high loading capacity, and water solubility, they have been advantageous in developing novel drug delivery systems. However, there is evidence of adverse effects by the use of ceramic materials to develop these nanoparticles [104]. They are primarily used to encapsulate proteins, DNA, gene delivery [105, 106], large molecular weight drugs, anticancer agents, as well as in photodynamic therapy [107]. In addition, a variety of organic groups, which may be incorporated on the surface of the outer matrix of ceramics, has shown to have direct effect on these nanoparticles [108], enhancing the ability to deliver hydrophilic drugs at the site of cancer cells specifically [109].

Ceramic particles are widely used for dental and orthopedic applications; however, the reactive nature of these ceramic particles can inhibit the drug release profile and stability of the particles. A well-suitable example of Pluronic modified nanoparticle, reported by Chan et al. [70], in which docetaxel was encapsulated with an amphiphilic hyaluronic acid/ceramide-conjugated Pluronic 85 forms polymeric nanoparticles, which exhibited ability to reverse multidrug resistance of docetaxel. From the in vitro cellular uptake study, it was clearly demonstrated that this formulation, in contrast to Taxotere®, has the ability to reverse MDR effects by reversing drug efflux due to the presence of Pluronic 85. Lastly, by using MTS assay, it was confirmed that their nanoparticle formulation can reverse MDR by lowering the IC_{50} significantly to Taxotere® (intravenously used concentrated docetaxel clinical formulation), thus suggesting that it was able to reverse MDR effects on resistant tumors. These results were in accordance to the in vivo data where NIR fluorescence imaging showed that the formulation was able to target specifically to the tumor region(s). Similarly, mesoporous silica nanoparticles were coated with a dual polymer lipid material, which was made from pH-sensitive phospholipid DOPE grafted Pluronic P123. The final mesoporous nanoparticle was loaded with irinotecan and its anticancer efficacy was checked against MCF-7/BCRP-resistant cells. It had an efficient intracellular activity due to cellular internalization, antitumor activity, and tumor targetability. Also, it showed the potential of reversing MDR by reducing the tumor growth at a low dose and preventing undesired effects [100].

9.4.6 Nanogels

Nanogels are swollen cross-linked polymeric particles composed of hydrophilic or amphiphilic polymer chains. They offer advantages such as high water content, biocompatibility, high stability, and nanometer size range, which enhance the loading capacity that serves as a carrier for the transport of drugs by multivalent biconjugation. Apart from these, their ability to be responsive to the environmental factors, such as ionic strength, pH, and temperature, makes them a remarkable nanocarrier system for drug delivery. The most common monomers used for the preparation of nanogels that are cross-linked to form the polymeric chain includes polymers such as polyethylenimine (PEI) [101], poly(ethylene glycol) (PEG) [102], poly(propylene glycol) (PPG) [103], poly(methacrylic acid) (PMA) [104], poly (acrylic acid) (PAA) [105]. Pluronic F68 and F127 were used to develop a PEI based nanogel that could sustain the drug stability of nucleoside 5′-triphosphate (NTP) to enzymatic hydrolysis, and were also less cytotoxic in comparison to PEG based nanogels due to 2–2.5 times enhanced interaction with the cellular membrane of the cancer cells. Also, these formulations possess a high loading capacity and thus, a high drug concentration could be achieved at the tumor site, minimizing both adverse toxicities at other sites and chances of developing resistance to the potent drug molecule [103].

9.4.7 Solid Lipid Nanoparticles

SLN can be defined as a solid lipid matrix in nanometer range accommodating a drug that is stabilized by one or more surfactants and/or co-surfactants such as Poloxamer 188, steric acid, Tween 80, and many more [106]. They offer advantages like controlling drug release, drug targeting, long-term stability, incorporation of lipophilic and hydrophilic drugs, and endless biotoxicity due to the use of physiological lipids [106]. However, SLN has a limited drug loading capacity (around 25% of lipid matrix) and leads to a burst release of hydrophilic drugs during the initial period [107]. SLN is used for delivering protein and antigens largely as it can be incorporated or absorbed into the lipid molecule of the SLN, which can further be administered into other conventional dosage forms such as oral, nasal, etc. Delivering proteins via SLN confirms protein stability, avoids proteolytic degradation, as well as sustained release of the incorporated molecules. SLN is used as a promising tool to deliver drugs that have a low bioavailability due to its inherent property of colloidal structure employed from both physiological lipids, as well as lipid molecules. To demonstrate the efficiency of SLN against MDR effects, Wong et al. developed and characterized a formulation of SLN using Pluronic F68. Doxorubicin was complexed with this SLN moiety and its cellular efficacy was investigated against MDR human breast cancer cell lines. In contrast to the doxorubicin solution with SLN, in vitro cytotoxicity was increased by 8-fold, cellular uptake was enhanced by 1.2-fold, and cellular retention was increased up to 2-fold, [108]. Further, SLN was used to embed human thymidylate synthase (hTS) inhibitor hydrophilic peptide (LRp) and was found to be effective against cDDP-resistant ovarian cancer cell line, thus extending the lifetime of the nanoparticles at the tumor site by the EPR effect and doubling the percentage of apoptosis [109].

9.4.8 Magnetic Nanoparticles

Magnetic nanoparticles are particles in a nanosized range with magnetic cores covered by a polymer or metal coating such as polyethylene glycol and polysaccharides, which can also be functionalized via cross-linkers [110]. In other words, these possible porous polymers may contain magnetic nanoparticles within its pores. These particles can then be functionalized by attaching carboxyl groups, amines, biotin, streptavidin, antibodies, or other cytotoxic drugs [111]. Magnetic nanoparticles offer the following advantages: it is easy to modulate the travel of the nanoparticles in vivo since they are guided by magnetic field; they can be heated for drug release; and they can be imaged simultaneously [112]. They have shown efficient targeted delivery and therapeutic effects on DNA. Magnetic nanoparticles were effectively used for delivering in vitro gene transfection [113]. Apart from that, magnetic nanoparticles can also be used as an anti-inflammatory agent by

maintaining the local concentrations at the required site and reducing the overall dosage and associated side effects [114]. Daunorubicin and 5-bromotetrandrin were encapsulated into Pluronic F127-iron oxide magnetic nanoparticle (MNP). This formulation was investigated against MDR leukemic cells, and is believed to have a sustained drug release and enhanced drug accumulation in K562/A02 cells after 48 h. Also, use of this formulation is believed to prevent the development of MDR effects in vitro due to the downregulation of MDR gene and P-gp expression [115]. Therapeutic benefit of various Pluronic-based drug nanoformulation with improved activity has been presented in Table 9.2.

Table 9.2 Therapeutic benefit of Pluronic drug nanoformulations

Type of Pluronic-based nanoparticle and composition	Therapeutic molecule	Improvement achieved
Alginate and chitosan polymeric nanoparticles coated with F127 polymer	Curcumin	Improved solubility of the lipophilic drug, achieved sustained release of the curcumin, and prolonged retention of curcumin in cancer cells [116]
PEO-modified poly(ε-caprolactone) nanoparticles and F68/F108 physical adsorption	Tamoxifen	90% drug encapsulation and increased accumulation of tamoxifen in the tumor cells, nonspecific endocytic process, followed by gradual release of the drug [117]
Poly(β-amino ester) F108 blend nanoparticles	Paclitaxel	Nanoparticles, when blended with Pluronic, showed rapid degradation at tumor cellular (acidic) environment and provided rapid tumoricidal effect in the cytosol when compared to PbAE [118]
Fe_3O_4 nanoparticles coated with β-cyclodextrin and F127 polymer	Curcumin	F127 coating improves stability in aqueous dispersion, haemo-compatibility, and excellent drug delivery, magnetic resonance imaging and hyperthermia formulation [119]
Fe_3O_4 nanoparticles coated with oleic acid and F127 polymer	Doxorubicin and Paclitaxel	The F127 impart steric stability, aqueous dispersity, and decreases uptake in macrophages thus slows down the rapid clearance by the reticuloendothelial system (RES). Comparative to the Feridex IV™ the clearance of the nanoparticles is slower thus aids imaging of the tumor [120]
Magnetic nanoparticles modified with oleic acid and L64 polymer	Enzyme	Pluronic coating stabilizes magnetic nanoparticles and offers adsorption

(continued)

Table 9.2 (continued)

Type of Pluronic-based nanoparticle and composition	Therapeutic molecule	Improvement achieved
		of lipase from *Candida cylindracea* via strong hydrophobic interactions and hence increases the enzymatic production and thus reusability [121]
Egg phosphatidylcholine, α-tocopherol and poloxamer 407 liposome	Ibuprofen	The liposomal poloxamer gel prolongs release and targeted permeation of ibuprofen [122]
Soybean phospholipids and F127 based liposome.	Paclitaxel	Liposomal serves as a reservoir for paclitaxel and improves anticancer efficiency [123]
Dipalmitoyl phosphatidylcholine and poloxamer 188 liposomes	Doxorubicin	Incorporation of P188 into DPPC liposome exhibits thermosensitive property, which results in controlled drug delivery for lung cancer [124]
Polyethylenimine (PEI)/ DNA/F127 complex nanogel	Thermo-responsive gene carrier	Inherent intracellular gene delivery and disrupting the endosome in the cell, retained even after F127 modification. The cytotoxicity of the nanogel increased as the temperature decreased from 37 to 20 °C, suggesting the Pluronic chain collapsed with temperature and plays a role in modulating cytotoxicity [125]
Heparin grafted F127 polymer nanogel	Vehicle for intracellular protein delivery	This formulation can be loaded up to 80–99% RNase A, maintain stability and offers significant cytotoxicity which suggests Heparin nanogel can be used as a high efficient delivery system for various proteins [126]
LMW heparin conjugated F127 nanogel	Low weight heparin	Minimize the adverse effects of Heparin and to enhance the therapeutic effect at fibrotic area [127]
Thiolated F127 polymeric micelles in combination with gold nanoparticle	Diagnostic	These cross-linked network micelles are used to immobilize various thiolated specific ligands and achieve specific targeting [128]
F127 polymeric micelles in combination with ceramic nanoparticles	Curcumin	This supramolecular complex helps to deliver intact drug in the presence of ceramic nanoparticle and can be used for drug delivery purpose in periodontal and orthopedic fields [129]

(continued)

Table 9.2 (continued)

Type of Pluronic-based nanoparticle and composition	Therapeutic molecule	Improvement achieved
Commercial Pluronic 188, F68, F127 and F407, polymer micelles	Itraconazole	These polymeric micelles favor corneal permeability and controlled release, which is very crucial in ocular drug delivery. Such penetration is facilitated due to Pluronic polymers [130]

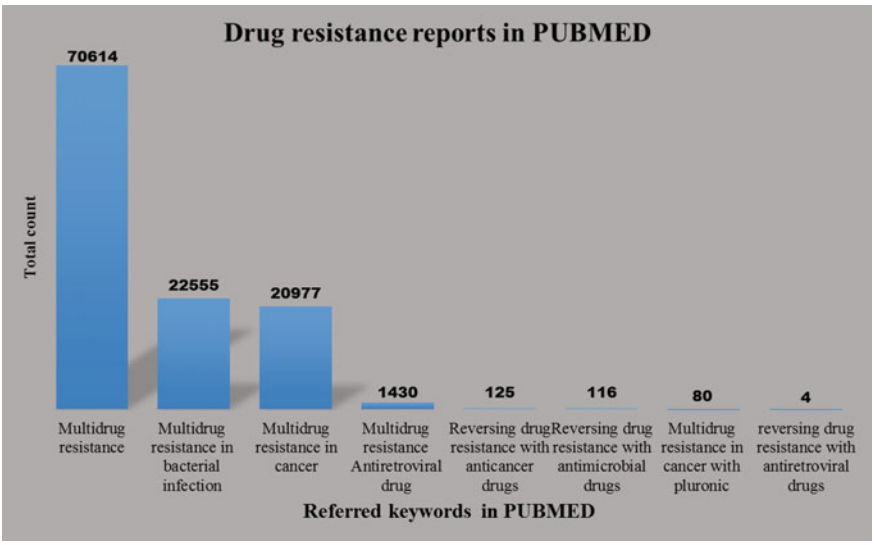

Fig. 9.3 PUBMED literature (between years 1965 and 2017) related to MDR in various diseases and use of Pluronics to reverse MDR

9.5 Role of Pluronic Nanotechnology in Reversing or Overcoming Drug Resistance

Pluronic® has been used extensively to enhance delivery of therapeutics and to improve bioavailability due to its ability to form pores, which can interact with the MDR cells and develop sensitization of these cells to anticancer drugs [7, 15]. Pluronic® has gained popularity in drug delivery system as it embodies into the membrane allowing translocation in cells and thus, changing cellular functions such as mitochondrial respiration, ATP synthesis, activity of drug efflux transporters, apoptotic signal transduction, and gene expression [16]. Pluronic polymers are used to improve drug transport of various drugs through the most favored routes and even through impervious barriers such as the blood–brain barrier and the intestinal barrier [7, 8]. The most common diseases where Pluronics are commonly used to inhibit MDR in cells have been presented in Fig. 9.3.

9.5.1 Cancer

Cancer is one of the leading causes of death worldwide and can be defined as a state of the body when the cells keep on dividing, to form tumors (solid tumors) and in some cases, leukemia (there is no solid tumor formed). The incidence of new cancer cases estimated in the US in 2016 was more than 1.6 million, as per the American Cancer Society (http://www.cancer.org/acs/groups/content/@resear-ch/documents/document/acspc-047079.pdf). It is highly challenging to remove tumor completely by conventional surgical procedures. Most often, reoccurrence of tumors and invasion in healthy tissues are observed with time. Therefore, chemotherapy is the necessary approach in cancer treatment [131, 132]. However, development of multidrug resistance is the most significant impediment encountered in the treatment of cancer. The most common drug efflux protein P-gp acts as an export "pump" for a wide variety of chemotherapeutic drugs such as vinca alkaloids, anthracyclines, epipodophyllotoxins, and taxanes [133]. A pluronic nanotechnology strategy to inhibit the P-gp-mediated drug efflux could be effective to enhance antitumor efficiency and to overcome MDR (Table 9.3).

Pluronic polymers are known to have low systemic cytotoxicity and weak immunogenicity [134]. Pluronics are known to decrease the membrane microviscosity by inserting in the plasma membrane to inhibit the P-gp efflux pump. Xiao et al. [135] investigated the ability of F127 to increase the therapeutic efficacy of camptothecin (CPT)-loaded poly(lactic-*co*-glycolic acid) (PLGA) nanoparticle by sensitizing tumor cells to apoptosis. It is also evident from in vivo studies, toxicity reduces and thus, reduces the adverse systemic effects of CPT, achieving better antitumor efficacy. Biodistribution study demonstrates longer retention of CPT nanoparticles in the body and also their tumor targetability. This was attributed to the functionalization with F127 which prolonged release when compared to the free drug, also improved cellular uptake in contrast to the non-functionalized nanoparticles. It is evident that F127 inhibits function of P-gp, increases the cellular uptake of CPT by the tumorous cells, thus improving the therapeutic efficacy [135]. Pluronic P85 successfully inhibits the P-gp drug efflux system, decreases ATP levels, and promotes apoptosis in MDR cells, Lewis lung carcinoma (3LL-M27), and T-lymphocytic leukemia (P388/ADR and P388) tumors [136] during doxorubicin treatments.

Another strategy of reversing MDR effects is to conjugate drug(s) chemically to Pluronic polymers. Upon conjugation of hydrophobic drug ruthenium (Ru) with Pluronics F127/folic acid, selective induction of intrinsic and extrinsic apoptosis in liver cancer cell apoptosis was achieved, while exhibiting minimal cytotoxicity towards human normal cells [137]. Poloxamers are utilized as a pore-forming agent and drug-releasing enhancer, which can induce drastic sensitization effects to various anticancer drugs. In a PLGA and d-α-Tocopheryl polyethylene glycol 1000 succinate (TPGS or vitamin E), poloxamer 235 stretches out from the aqueous phase and creates a porous structure on the surface of the nanoparticles [22]. This porousness enhances cellular uptake in docetaxel-resistant human breast cancer cell

line, MCF-7/TXT, and shows a higher cytotoxicity level in contrast to nanoparticle formed from PLGA, a TGPS nanoparticle, and the marketed formulation Taxotere® in vivo model.

Table 9.3 Selective P-gp and MDR inhibitory role of Pluronic drug nanoformulations in therapeutics

Formulation	Advantage
Pluronic P85-doxorubicin	Pluronics induces a selective inhibition of P-gp, which is a result of energy reduction in ATP levels (ATP depletion), particularly in MDR cells. The ability is accompanied by cytotoxic activity and sensitization in the MDR cells [10]
Pluronic P105 F127, c(RGDyK) (cyclic RGD [arginine-glycine-aspartic acid] peptide) with doxorubicin or paclitaxel	This study was evident that Pluronic P105/F127 mixed micelles have the ability to enhance drug accumulation in MDR tumor cells and c(RGDyK) play vital role for anti-angiogenesis which could be a potential delivery system for attaining superior tumor grown inhibition [139]
Pluronic P105 and P85 with doxorubicin	Pluronics are capable of inhibiting the respiration, as a result of which accumulation of reactive oxygen species occurs and release of cytochrome c which causes cell death via apoptosis [41]
Poly(ε-caprolactone)/Pluronic F68 with docetaxel	This formulation of Pluronics enhances drug transport across blood–brain barriers and intestinal barriers and enhances cellular accumulation in MDR MCF-7/TAX30 cells/tumors [74]
Poloxamer 407 (P407), d-α-tocopheryl polyethylene glycol succinate and folic acid with doxorubicin	Pluronics reduces the drug retention in the plasma, reverses MDR effect, induces apoptosis, and reduces antitumor activity. Due the conjugation of P407 to FA intracellular trafficking study shows that targeted and selective delivery is achieved in contrast to the unconjugated moiety [138]
Pluronic F-127, folic acid and doxorubicin	The presence of folic acid, along with Pluronics, targets and causes drastic sensitization of tumor cells, as well as inhibition of P-gp ATPase activity, and thus high therapeutic efficacy is attained [139]
Pluronic F-127, PAMAM dendrimers and doxorubicin	Conjugation of Pluronic F-127 to the PAMAM dendrimers forms unimolecular micelles, which is believed to have greater stability, thus preventing aggregation in the blood. The drug conjugate with dendrimer showed higher apoptosis and degraded nuclei of cancerous cells (MCF-7 and ADR) when compared to free drug Additionally, the conjugated formulation showed a higher cytotoxicity than the free drug, which is believed to have the potential ability to reverse MDR [89]

9.5.2 Bacterial Infection

Anti-microbial agents/drugs, used since the 1940s, are the first drug of choice for treating any bacterial infections. They can be defined as a strain of bacteria that is not killed or inhibited by the required concentration of antimicrobial agent that kills or inhibits the majority of strains of that organism [140]. When the anti-microbial agents/antibiotics that are used to treat the microorganisms are no longer effective, it is termed as antimicrobial resistance. According to World Health Organization (WHO) antimicrobial resistance develops when "Resistant microorganisms (including bacteria, fungi, viruses and parasites) that are able to withstand attack by antimicrobial drugs, such as anti-bacterial drugs (e.g. antibiotics), antifungals, antivirals, and antimalarials, so that standard treatments become ineffective and infections persist, increasing the risk of spread to others". As per the records by WHO, the higher proportion of antibiotic resistance in bacteria are common in infections like urinary tract infection, pneumonia, and bloodstream infections. One such highly resistant bacteria is Staphylococcus aureus (MRSA) or multidrug-resistant Gram-negative bacteria. Herein, antibiotics that are primarily used for treating bacterial infection mainly are discussed.

A highly refined poloxamer CRL-1072 has been used (alone or in combination) with antibiotics and was able to produce therapeutic efficacy against drug-sensitive and drug resistance organisms, especially *Mycobacterium tuberculosis* [141]. When CRL-1072 was used alone, it was found to be bactericidal to *M. tuberculosis*, but when used in combination with an antimycobacterial drug, the synergistic antibacterial effect was attained, even on the resistant strains of *M. tuberculosis* in macrophage culture and even in mice. These drugs include isoniazid (INH), rifampin, PAS, ethambutol, and ethionamide, which exhibited complete reverse resistance when used in combination with CRL-1072 against their respective *M. tuberculosis* resistant strains. However, CRL-1072, when used against streptomycin-resistant strain, indicated that it could partially overcome the resistance. Therefore, poloxamers were able to enhance the effectiveness of selected drugs against *M. tuberculosis* resistant strains.

Drug-resistant pathogens such as methicillin-resistant Staphylococcus aureus (MRSA) have become a serious impediment to drug delivery due to its acquired ability to develop high levels of resistance against several classes of antibiotics. Methicillin-resistant *Staphylococcus aureus* (MRSA) is treated with vancomycin. Lee et al. [142] demonstrated that vancomycin, when used with Pluronic F127 polymer (Pluronic hydrogel, 25% w/v), could enhance drug delivery to the infected inner ear, and also could inhibit the MRSA growth. It is believed to achieve a higher patient compliance due to prolonged release, and helps to attain complete therapeutic efficacy. The biodistribution study (in vivo) indicates no sign of inflammation, fibrosis or open space on day 50. Therefore, this Pluronic hydrogel had the potential not only to treat the resistant strain of *S. aureus,* but also was able to sustain drug release, and most importantly, inhibit the growth of the MRSA. Similarly, MRSA growth in *S. aureus* has been effectively controlled using

photodynamic therapy (PDT) and has been an effective alternative to treat antibiotic resistance. For enhanced efficacy, the photosensitizer-hematoporphyrin (Hp) was encapsulated in PEGylated liposomes and Pluronic P127 micelles [143]. With a low Hp concentration, Pegylated liposome/Pluronic micelle formulation exerted complete bactericidal activity in contrast to liposome, which is caused by prolonged action in the plasma membrane of the microbes.

9.5.3 Immunodeficiency

Human immunodeficiency virus (HIV) causing acquired immune deficiency syndrome (AIDS) was first detected back in the 1980s. Since the early discovery of AIDS, 35 million cases have been reported worldwide (UNAIDS 2014). Antiretroviral treatment (ART) has made a gradual progression in reducing the mortality rate. It is estimated that 12.9 million people living with AIDS worldwide are receiving the antiretroviral therapy. However, WHO had conducted a surveillance between 2004 and 2010 and has reported that drug resistance to HIV treatment has scaled up over the years [144]. This suggests that HIV-drug resistance research is of paramount importance. The potent antiretroviral drugs have limited access in the body, resulting in formation of virus reservoirs (like macrophages). These HGIV-infected macrophages enter into the brain and spread the HIV in perivascular macrophages, microglia, and astrocytes [145]. The blood–brain barrier forms a major barrier and hinders antiretroviral drugs to traverse through it, forming an immunologic and pharmacological sanctuary site for HIV in the brain [146]. Transport proteins, such as P-gp, are expressed on the surface of the BBB, further impeding antiretroviral drug delivery into the central nervous system [145]. It was suggested by Bendayan et al. [147] that the cellular membrane of the brain macrophages might be another additional barrier to drug permeability. Thus, the P-gp expressed on the surface of the BBB depletes the energy generated by ATP hydrolysis and effluxes the drug out of the brain, decreasing concentration of the therapeutic agent reaching the brain. Also, toxicity, adverse drug reactions, low bioavailability due to poor physicochemical properties, rapid drug metabolism in the liver, impaired biodistribution in HIV reservoirs, emergence of drug resistance, requirement of drug monitoring, and lifelong adherence are some of the associated problems with antiretroviral treatment [148]. In this context, Pluronic copolymer aids in the passage of drugs to the CNS by inhibiting P-gp substrates by two mechanisms of action. First, most of the Pluronics (especially P85) decrease ATP levels in the brain endothelial cell monolayers, which is crucial for the last stage processing of HIV-1 [149]. Second, the lipid structure of the Pluronic micelles is adsorbed in the membrane causing destabilization of the P-gp [10]. To demonstrate the effect, Pluronics have on the endothelial cells of the brain that form the BBB, BBMEC (bovine brain microvessel endothelial cells) an in vitro model was employed [150]. This study reports two points: (1) Pluronic, used at a concentration below the CMC by increasing the uptake of the drug through the P-gp dependent

pathway, enhances the drug delivery of neuroleptic agents that interact with the P-gp efflux system; and (2) P85, when used above the CMC drugs, is entrapped within the polymeric micelles, which is able to penetrate the BBB due to vesicular transport. Thus, interaction of P85 with the brain endothelial cells seems to be an energy dependent process with an inhibitory effect.

To develop a new approach to improve drug delivery to the CNS and BBB and enhance the efficacy of the ART target drug delivery is pivotal. Spitzenberger et al. [145] demonstrated that Pluronic P85 (alone) and a combination of P85 (0.2 and 1%) with ART (AZT, 3TC and nelfinavir) could suppress the viral replication significantly more (8–22% of control) than the ART alone (38% of control) when conducted on a severe combined immunodeficiency animal model of HIV-encephalopathy (HIVE) expressing monocyte-derived macrophages. Thus, this study was able to demonstrate that P85 was efficient in enhancing penetration of antiretroviral drugs through the BBB and also had a significant effect on cells (macrophages) that have a viral reservoir in the CNS. Protease inhibitors (PI) are drugs used for the treatment of HIV-1, when combined with ART. The development of resistance to PI is a very common issue and may even last after ART is discontinued. To investigate the ability of the Pluronics to interact with the PI and the P-gp substrates, MDCKII and LLC-PK1 cells transfected with human MDR1 were examined for drug transport [151]. The cell accumulation study and ATPase assay implied that Pluronic P85 was efficient in inhibiting the interaction of P-gp with PIs such as nelfinavir and saquinavir. Pluronics inhibit multiple transporters, thus reducing efficiency of PI efflux pumps and allowing proper distribution and therapeutic concentrations of antiretroviral drugs reaching the brain. Hence, P85 is efficient in suppressing viral replication and reducing production of drug-resistant mutants. It is also suggested that oral delivery of antiretroviral molecules, such as, saquinavir, where absorption is limited by the efflux of P-gp, use of P85 in the formulation at concentration less than the CMC leads to enhanced bioavailability.

9.6 Conclusion

Pluronic copolymers have proven to be a promising nanotechnology tool in reversing multidrug resistance in many diseases such as cancer chemotherapy, bacterial infection, and resistance to antiretroviral drugs. The ability of Pluronics to inhibit several associated mechanisms of drug resistance has reinforced its use in enhancing drug bioavailability and targeting. Further, researchers have combined inhibitory mechanisms of Pluronics with the sensitization effects, which indeed inhibit several multiple drug resistance mechanisms. Thus, it is apt to conclude that ongoing research with Pluronic copolymers has the potential to develop new progress in one of the major impediment of drug delivery to reverse and/or prevent multidrug resistance phenomenon. Clinically, such an intervention helps to minimize dose and number of cycles required for treatment.

References

1. Jacoby GA (2009) History of drug-resistant microbes. In: Antimicrobial drug resistance. Springer, Berlin, pp 3–7
2. Prevention CfDCa (2011) Antimicrobial resistance: no action today, no cure tomorrow
3. Alakhova DY, Kabanov AV (2014) Pluronics and MDR reversal: an update. Mol Pharm 11 (8):2566–2578
4. Persidis A (1999) Cancer multidrug resistance. Nat Biotechnol 17(1):94–95
5. Sakurai Y, Hatakeyama H, Akita H, Harashima H (2014) Improvement of doxorubicin efficacy using liposomal anti-polo-like kinase 1 siRNA in human renal cell carcinomas. Mol Pharm 11(8):2713–2719
6. Singh S, Narang AS, Mahato RI (2011) Subcellular fate and off-target effects of siRNA, shRNA, and miRNA. Pharm Res 28(12):2996–3015
7. Babu A, Wang Q, Muralidharan R, Shanker M, Munshi A, Ramesh R (2014) Chitosan coated polylactic acid nanoparticle-mediated combinatorial delivery of cisplatin and siRNA/Plasmid DNA chemosensitizes cisplatin-resistant human ovarian cancer cells. Mol Pharm 11(8):2720–2733
8. Fonseca SB, Pereira MP, Mourtada R, Gronda M, Horton KL, Hurren R, Minden MD, Schimmer AD, Kelley SO (2011) Rerouting chlorambucil to mitochondria combats drug deactivation and resistance in cancer cells. Chem Biol 18(4):445–453
9. Dumortier G, Grossiord JL, Agnely F, Chaumeil JC (2006) A review of poloxamer 407 pharmaceutical and pharmacological characteristics. Pharm Res 23(12):2709–2728
10. Batrakova EV, Li S, Vinogradov SV, Alakhov VY, Miller DW, Kabanov AV (2001) Mechanism of pluronic effect on P-glycoprotein efflux system in blood–brain barrier: contributions of energy depletion and membrane fluidization. J Pharmacol Exp Ther 299 (2):483–493
11. Kabanov AV, Batrakova EV, Alakhov VY (2002) Pluronic® block copolymers for overcoming drug resistance in cancer. Adv Drug Deliv Rev 54(5):759–779
12. Batrakova EV, Kabanov AV (2008) Pluronic block copolymers: evolution of drug delivery concept from inert nanocarriers to biological response modifiers. J Control Release 130 (2):98–106
13. Schmolka IR (1977) A review of block polymer surfactants. J Am Oil Chem Soc 54(3):110–116
14. Jeong B, Gutowska A (2002) Lessons from nature: stimuli-responsive polymers and their biomedical applications. Trends Biotechnol 20(7):305–311
15. Batrakova EV, Li S, Alakhov VY, Miller DW, Kabanov AV (2003) Optimal structure requirements for pluronic block copolymers in modifying P-glycoprotein drug efflux transporter activity in bovine brain microvessel endothelial cells. J Pharmacol Exp Ther 304 (2):845–854
16. Kabanov AV, Nazarova IR, Astafieva IV, Batrakova EV, Alakhov VY, Yaroslavov AA, Kabanov VA (1995) Micelle formation and solubilization of fluorescent probes in poly (oxyethylene-b-oxypropylene-b-oxyethylene) solutions. Macromolecules 28(7):2303–2314
17. Alakhov V, Lemieux P, Klinski E, Kabanov A, Pietrzynski G (2001) Block copolymeric biotransport carriers as versatile vehicles for drug delivery. Expert Opin Biol Ther 1(4):583–602
18. Batrakova E, Lee S, Li S, Venne A, Alakhov V, Kabanov A (1999) Fundamental relationships between the composition of pluronic block copolymers and their hypersensitization effect in MDR cancer cells. Pharm Res 16(9):1373–1379
19. Nagarajan R (1999) Solubilization of hydrocarbons and resulting aggregate shape transitions in aqueous solutions of Pluronic®(PEO–PPO–PEO) block copolymers. Colloids Surf B 16 (1):55–72

20. Yan F, Zhang C, Zheng Y, Mei L, Tang L, Song C, Sun H, Huang L (2010) The effect of poloxamer 188 on nanoparticle morphology, size, cancer cell uptake, and cytotoxicity. Nanomed Nanotechnol Biol Med 6(1):170–178
21. Moghimi SM, Hunter AC (2000) Poloxamers and poloxamines in nanoparticle engineering and experimental medicine. Trends Biotechnol 18(10):412–420
22. Tang X, Liang Y, Feng X, Zhang R, Jin X, Sun L (2015) Co-delivery of docetaxel and Poloxamer 235 by PLGA–TPGS nanoparticles for breast cancer treatment. Mater Sci Eng C 49:348–355
23. Venne A, Li S, Mandeville R, Kabanov A, Alakhov V (1996) Hypersensitizing effect of pluronic L61 on cytotoxic activity, transport, and subcellular distribution of doxorubicin in multiple drug-resistant cells. Can Res 56(16):3626–3629
24. Miller DW, Batrakova EV, Kabanov AV (1999) Inhibition of multidrug resistance-associated protein (MRP) functional activity with pluronic block copolymers. Pharm Res 16(3):396–401
25. Yamagata T, Kusuhara H, Morishita M, Takayama K, Benameur H, Sugiyama Y (2007) Effect of excipients on breast cancer resistance protein substrate uptake activity. J Control Release 124(1):1–5
26. van Veen HW, Margolles A, Putman M, Sakamoto K, Konings WN (1999) Multidrug resistance in lactic acid bacteria: molecular mechanisms and clinical relevance. In: Lactic acid bacteria: genetics, metabolism and applications. Springer, Berlin, pp 347–352
27. Altan N, Chen Y, Schindler M, Simon SM (1998) Defective acidification in human breast tumor cells and implications for chemotherapy. J Exp Med 187(10):1583–1598
28. Breuninger LM, Paul S, Gaughan K, Miki T, Chan A, Aaronson SA, Kruh GD (1995) Expression of multidrug resistance-associated protein in NIH/3T3 cells confers multidrug resistance associated with increased drug efflux and altered intracellular drug distribution. Can Res 55(22):5342–5347
29. Nooter K, Stoter G (1996) Molecular mechanisms of multidrug resistance in cancer chemotherapy. Pathol Res Pract 192(7):768–780
30. Clary I, Doherty G, Moran E, Clynes M (1997) The multidrug-resistant human lung tumour cell line, DLKP-A10, expresses novel drug accumulation and sequestration systems. Biochem Pharmacol 53(10):1493–1502
31. Shapiro AB, Fox K, Lee P, Yang YD, Ling V (1998) Functional intracellular P-glycoprotein. Int J Cancer 76(6):857–864
32. Benderra Z, Morjani H, Trussardi A, Manfait M (1998) Role of the vacuolar H+-ATPase in daunorubicin distribution in etoposide-resistant MCF7 cells overexpressing the multidrug-resistance associated protein. Int J Oncol 12(3):711–716
33. Kabanov AV, Batrakova EV, Alakhov VY (2002) Pluronic® block copolymers as novel polymer therapeutics for drug and gene delivery. J Control Release 82(2):189–212
34. Van Zutphen H, Merola A, Brierley G, Cornwell DG (1972) The interaction of nonionic detergents with lipid bilayer membranes. Arch Biochem Biophys 152(2):755–766
35. Atkinson TP, Smith T, Hunter R (1988) Histamine release from human basophils by synthetic block co-polymers composed of polyoxyethylene and polyoxypropylene and synergy with immunologic and non-immunologic stimuli. J Immunol 141(4):1307–1310
36. Atkinson TP, Smith TF, Hunter RL (1988) In vitro release of histamine from murine mast cells by block co-polymers composed of polyoxyethylene and polyoxypropylene. J Immunol 141(4):1302–1306
37. Brierley G, Jurkowitz M, Merola A, Scott K (1972) Ion transport by heart mitochondria: XXV. Activation of energy-linked K+ uptake by non-ionic detergents. Arch Biochem Biophys 152(2):744–754
38. Brustovetskiĭ N, Dedukhova V, Egorova M, Mokhova E, Skulachev V (1991) Uncoupling of oxidative phosphorylation by fatty acids and detergents suppressed by ATP/ADP antiporter inhibitors. Biokhimiia (Moscow, Russia) 56(6):1042–1048
39. Kirillova G, Mokhova E, Dedukhova V, Tarakanova A, Ivanova V, Efremova N, Topchieva I (1993) The influence of pluronics and their conjugates with proteins on the

rate of oxygen consumption by liver mitochondria and thymus lymphocytes. Biotechnol Appl Biochem 18(3):329–339
40. Su F, Hu X, Jia W, Gong C, Song E, Hamar P (2003) Glutathion S Transferase π indicates chemotherapy resistance in breast cancer. J Surg Res 113(1):102–108
41. Alakhova DY, Rapoport NY, Batrakova EV, Timoshin AA, Li S, Nicholls D, Alakhov VY, Kabanov AV (2010) Differential metabolic responses to pluronic in MDR and non-MDR cells: a novel pathway for chemosensitization of drug resistant cancers. J Control Release 142(1):89–100
42. Minko T, Batrakova EV, Li S, Li Y, Pakunlu RI, Alakhov VY, Kabanov AV (2005) Pluronic block copolymers alter apoptotic signal transduction of doxorubicin in drug-resistant cancer cells. J Control Release 105(3):269–278
43. Kabanov AV, Chekhonin V, Alakhov VY, Batrakova E, Lebedev A, Melik-Nubarov N, Arzhakov S, Levashov A, Morozov G, Severin E (1989) The neuroleptic activity of haloperidol increases after its solubilization in surfactant micelles: micelles as microcontainers for drug targeting. FEBS Lett 258(2):343–345
44. Gao Z-G, Fain HD, Rapoport N (2005) Controlled and targeted tumor chemotherapy by micellar-encapsulated drug and ultrasound. J Control Release 102(1):203–222
45. Yang T-F, Chen C-N, Chen M-C, Lai C-H, Liang H-F, Sung H-W (2007) Shell-crosslinked Pluronic L121 micelles as a drug delivery vehicle. Biomaterials 28(4):725–734
46. Tian J-L, Zhao Y-Z, Jin Z, Lu C-T, Tang Q-Q, Xiang Q, Sun C-Z, Zhang L, Xu Y-Y, Gao H-S (2010) Synthesis and characterization of Poloxamer 188-grafted heparin copolymer. Drug Dev Ind Pharm 36(7):832–838
47. Song H, He R, Wang K, Ruan J, Bao C, Li N, Ji J, Cui D (2010) Anti-HIF-1α antibody-conjugated pluronic triblock copolymers encapsulated with Paclitaxel for tumor targeting therapy. Biomaterials 31(8):2302–2312
48. Li L, Tan YB (2008) Preparation and properties of mixed micelles made of Pluronic polymer and PEG-PE. J Colloid Interface Sci 317(1):326–331
49. Hassanzadeh S, Feng Z, Pettersson T, Hakkarainen M (2015) A proof-of-concept for folate-conjugated and quercetin-anchored pluronic mixed micelles as molecularly modulated polymeric carriers for doxorubicin. Polymer 74:193–204
50. Ahmed F, Pakunlu RI, Brannan A, Bates F, Minko T, Discher DE (2006) Biodegradable polymersomes loaded with both paclitaxel and doxorubicin permeate and shrink tumors, inducing apoptosis in proportion to accumulated drug. J Control Release 116(2):150–158
51. Gustafson DL, Merz AL, Long ME (2005) Pharmacokinetics of combined doxorubicin and paclitaxel in mice. Cancer Lett 220(2):161–169
52. Chen Y, Zhang W, Huang Y, Gao F, Sha X, Fang X (2015) Pluronic-based functional polymeric mixed micelles for co-delivery of doxorubicin and paclitaxel to multidrug resistant tumor. Int J Pharm 488(1):44–58
53. Hellmich W, Regtmeier J, Duong TT, Ros R, Anselmetti D, Ros A (2005) Poly (oxyethylene) based surface coatings for poly (dimethylsiloxane) microchannels. Langmuir 21(16):7551–7557
54. Liu X, Wu D, Turgman-Cohen S, Genzer J, Theyson TW, Rojas OJ (2010) Adsorption of a nonionic symmetric triblock copolymer on surfaces with different hydrophobicity. Langmuir 26(12):9565–9574
55. Muszanska AK, Busscher HJ, Herrmann A, van der Mei HC, Norde W (2011) Pluronic–lysozyme conjugates as anti-adhesive and antibacterial bifunctional polymers for surface coating. Biomaterials 32(26):6333–6341
56. Farokhzad OC, Langer R (2009) Impact of nanotechnology on drug delivery. ACS Nano 3 (1):16–20
57. Liong M, Lu J, Kovochich M, Xia T, Ruehm SG, Nel AE, Tamanoi F, Zink JI (2008) Multifunctional inorganic nanoparticles for imaging, targeting, and drug delivery. ACS Nano 2(5):889–896
58. Ferrari M (2005) Cancer nanotechnology: opportunities and challenges. Nat Rev Cancer 5 (3):161–171

59. Alakhov VY, Moskaleva EY, Batrakova EV, Kabanov AV (1996) Hypersensitization of multidrug resistant human ovarian carcinoma cells by pluronic P85 block copolymer. Bioconjug Chem 7(2):209–216
60. Kabanov AV, Vinogradov SV, Suzdaltseva YG, Alakhov VY (1995) Water-soluble block polycations as carriers for oligonucleotide delivery. Bioconjug Chem 6(6):639–643
61. Kwon GS (2003) Polymeric micelles for delivery of poorly water-soluble compounds. Crit Rev Ther Drug Carrier Syst 20 (5)
62. Trentin D, Hubbell J, Hall H (2005) Non-viral gene delivery for local and controlled DNA release. J Control Release 102(1):263–275
63. Bu H-Z, Gukasyan HJ, Goulet L, Lou X-J, Xiang C, Koudriakova T (2007) Ocular disposition, pharmacokinetics, efficacy and safety of nanoparticle-formulated ophthalmic drugs. Curr Drug Metab 8(2):91–107
64. Panyam J, Labhasetwar V (2003) Biodegradable nanoparticles for drug and gene delivery to cells and tissue. Adv Drug Deliv Rev 55(3):329–347
65. Kim D-H, Martin DC (2006) Sustained release of dexamethasone from hydrophilic matrices using PLGA nanoparticles for neural drug delivery. Biomaterials 27(15):3031–3037
66. Riley T, Stolnik S, Heald C, Xiong C, Garnett M, Illum L, Davis S, Purkiss S, Barlow R, Gellert P (2001) Physicochemical evaluation of nanoparticles assembled from poly (lactic acid)-poly (ethylene glycol) (PLA-PEG) block copolymers as drug delivery vehicles. Langmuir 17(11):3168–3174
67. Gupta AK, Curtis AS (2004) Surface modified superparamagnetic nanoparticles for drug delivery: interaction studies with human fibroblasts in culture. J Mater Sci Mater Med 15 (4):493–496
68. Soppimath KS, Aminabhavi TM, Kulkarni AR, Rudzinski WE (2001) Biodegradable polymeric nanoparticles as drug delivery devices. J Control Release 70(1):1–20
69. Cheng J, Teply BA, Sherifi I, Sung J, Luther G, Gu FX, Levy-Nissenbaum E, Radovic-Moreno AF, Langer R, Farokhzad OC (2007) Formulation of functionalized PLGA–PEG nanoparticles for in vivo targeted drug delivery. Biomaterials 28(5):869–876
70. Chan JM, Zhang L, Yuet KP, Liao G, Rhee J-W, Langer R, Farokhzad OC (2009) PLGA–lecithin–PEG core–shell nanoparticles for controlled drug delivery. Biomaterials 30 (8):1627–1634
71. Pitt CG, Marks T, Schindler A (1980) Biodegradable drug delivery systems based on aliphatic polyesters: application to contraceptives and narcotic antagonists. Academic Press, New York
72. Pitt CG, Gratzl MM, Jeffcoat AR, Zweidinger R, Schindler A (1979) Sustained drug delivery systems II: factors affecting release rates from poly (ε-caprolactone) and related biodegradable polyesters. J Pharm Sci 68(12):1534–1538
73. Jackanicz TM, Nash HA, Wise DL, Gregory JB (1973) Polylactic acid as a biodegradable carrier for contraceptive steroids. Contraception 8(3):227–234
74. Mei L, Zhang Y, Zheng Y, Tian G, Song C, Yang D, Chen H, Sun H, Tian Y, Liu K (2009) A novel docetaxel-loaded poly (ε-caprolactone)/pluronic F68 nanoparticle overcoming multidrug resistance for breast cancer treatment. Nanoscale Res Lett 4(12):1530–1539
75. Shen J, Yin Q, Chen L, Zhang Z, Li Y (2012) Co-delivery of paclitaxel and survivin shRNA by pluronic P85-PEI/TPGS complex nanoparticles to overcome drug resistance in lung cancer. Biomaterials 33(33):8613–8624
76. Quintana A, Raczka E, Piehler L, Lee I, Myc A, Majoros I, Patri AK, Thomas T, Mulé J, Baker JR Jr (2002) Design and function of a dendrimer-based therapeutic nanodevice targeted to tumor cells through the folate receptor. Pharm Res 19(9):1310–1316
77. Ihre HR, Padilla De Jesús OL, Szoka FC, Fréchet JM (2002) Polyester dendritic systems for drug delivery applications: design, synthesis, and characterization. Bioconjug Chem 13 (3):443–452
78. Singh P, Gupta U, Asthana A, Jain NK (2008) Folate and folate–PEG–PAMAM Dendrimers: synthesis, characterization, and targeted anticancer drug delivery potential in tumor bearing mice. Bioconjug Chem 19(11):2239–2252

79. Kukowska-Latallo JF, Candido KA, Cao Z, Nigavekar SS, Majoros IJ, Thomas TP, Balogh LP, Khan MK, Baker JR (2005) Nanoparticle targeting of anticancer drug improves therapeutic response in animal model of human epithelial cancer. Cancer Res 65(12):5317–5324
80. Cheng Y, Qu H, Ma M, Xu Z, Xu P, Fang Y, Xu T (2007) Polyamidoamine (PAMAM) dendrimers as biocompatible carriers of quinolone antimicrobials: an in vitro study. Eur J Med Chem 42(7):1032–1038
81. Zhang L, Pornpattananangkul D, Hu C-M, Huang C-M (2010) Development of nanoparticles for antimicrobial drug delivery. Curr Med Chem 17(6):585–594
82. Chen CZ, Cooper SL (2002) Interactions between dendrimer biocides and bacterial membranes. Biomaterials 23(16):3359–3368
83. Rojo J, Delgado R (2004) Glycodendritic structures: promising new antiviral drugs. J Antimicrob Chemother 54(3):579–581
84. Gillies ER, Frechet JM (2005) Dendrimers and dendritic polymers in drug delivery. Drug Discov Today 10(1):35–43
85. Svenson S, Tomalia DA (2005) Dendrimers in biomedical applications—reflections on the field. Adv Drug Deliv Rev 57(15):2106–2129
86. Nguyen T, Nguyen C, Nguyend T, Trana N (2017) Highly lipophilic pluronics-conjugated polyamidoamine dendrimer nanocarriers as potential delivery system for hydrophobic drugs. Mater Sci Eng C. 70(2):992–999
87. Gu Z, Wang M, Fang Q, Zheng H, Wu F, Lin D, Xu Y, Jin Y (2015) Preparation and in vitro characterization of pluronic-attached polyamidoamine dendrimers for drug delivery. Drug Dev Ind Pharm 41(5):812–818
88. Gu ZJ, Wang M, Fang QY, Wang CR, Zheng HY (2014) Inhibition of MCF-7/ADR cells by DOX-loaded pluronic-attached PAMAM dendrimer conjugate. Yao xue xue bao = Acta Pharm Sin 49(8):1188–1193
89. Wang M, Han M, Li Y, Jin Y, Gao JQ (2016) Chemosensitization of doxorubicin in multidrug-resistant cells by unimolecular micelles via increased cellular accumulation and apoptosis. J Pharm Pharmacol
90. Ebrahim S, Peyman GA, Lee PJ (2005) Applications of liposomes in ophthalmology. Surv Ophthalmol 50(2):167–182
91. Cholkar K, Patel A, Vadlapudi AD, Mitra AK (2012) Novel nanomicellar formulation approaches for anterior and posterior segment ocular drug delivery. Recent Pat Nanomed 2 (2):82
92. Zhang X, Guo S, Fan R, Yu M, Li F, Zhu C, Gan Y (2012) Dual-functional liposome for tumor targeting and overcoming multidrug resistance in hepatocellular carcinoma cells. Biomaterials 33(29):7103–7114
93. Song CK, Balakrishnan P, Shim C-K, Chung S-J, Kim D-D (2011) Enhanced in vitro cellular uptake of P-gp substrate by poloxamer-modified liposomes (PMLs) in MDR cancer cells. J Microencapsul 28(6):575–581
94. Torchilin VP (2001) Structure and design of polymeric surfactant-based drug delivery systems. J Control Release 73(2):137–172
95. Kwon GS, Kataoka K (1995) Block copolymer micelles as long-circulating drug vehicles. Adv Drug Deliv Rev 16(2):295–309
96. Jones M-C, Leroux J-C (1999) Polymeric micelles–a new generation of colloidal drug carriers. Eur J Pharm Biopharm 48(2):101–111
97. Chen L, Sha X, Jiang X, Chen Y, Ren Q, Fang X (2013) Pluronic P105/F127 mixed micelles for the delivery of docetaxel against Taxol-resistant non-small cell lung cancer: optimization and in vitro, in vivo evaluation. Int J Nanomed 8:73
98. Chen Y, Sha X, Zhang W, Zhong W, Fan Z, Ren Q, Chen L, Fang X (2013) Pluronic mixed micelles overcoming methotrexate multidrug resistance: in vitro and in vivo evaluation. Int J Nanomed 8:1463

99. Wang Y, Yu L, Han L, Sha X, Fang X (2007) Difunctional Pluronic copolymer micelles for paclitaxel delivery: synergistic effect of folate-mediated targeting and Pluronic-mediated overcoming multidrug resistance in tumor cell lines. Int J Pharm 337(1):63–73
100. Zhang X, Li F, Guo S, Chen X, Wang X, Li J, Gan Y (2014) Biofunctionalized polymer-lipid supported mesoporous silica nanoparticles for release of chemotherapeutics in multidrug resistant cancer cells. Biomaterials 35(11):3650–3665
101. Vinogradov SV, Zeman AD, Batrakova EV, Kabanov AV (2005) Polyplex Nanogel formulations for drug delivery of cytotoxic nucleoside analogs. J Control Release 107 (1):143–157
102. Lin-Gibson S, Bencherif S, Antonucci JM, Jones RL, Horkay F (2005) Synthesis and characterization of poly (ethylene glycol) dimethacrylate hydrogels. In: Macromolecular symposia, vol 1. Wiley Online Library, Hoboken, pp 243–254
103. Vinogradov SV, Kohli E, Zeman AD (2006) Comparison of nanogel drug carriers and their formulations with nucleoside 5′-triphosphates. Pharm Res 23(5):920–930
104. Bontha S, Kabanov AV, Bronich TK (2006) Polymer micelles with cross-linked ionic cores for delivery of anticancer drugs. J Control Release 114(2):163–174
105. Bronich TK, Keifer PA, Shlyakhtenko LS, Kabanov AV (2005) Polymer micelle with cross-linked ionic core. J Am Chem Soc 127(23):8236–8237
106. Mehnert W, Mäder K (2001) Solid lipid nanoparticles: production, characterization and applications. Adv Drug Deliv Rev 47(2):165–196
107. Kaur IP, Rana C, Singh H (2008) Development of effective ocular preparations of antifungal agents. J Ocul Pharmacol Ther 24(5):481–494
108. Wong HL, Rauth AM, Bendayan R, Manias JL, Ramaswamy M, Liu Z, Erhan SZ, Wu XY (2006) A new polymer–lipid hybrid nanoparticle system increases cytotoxicity of doxorubicin against multidrug-resistant human breast cancer cells. Pharm Res 23 (7):1574–1585
109. Sacchetti F, Marraccini C, D'Arca D, Pelà M, Pinetti D, Maretti E, Hanuskova M, Iannuccelli V, Costi MP, Leo E (2015) Enhanced anti-hyperproliferative activity of human thymidylate synthase inhibitor peptide by solid lipid nanoparticle delivery. Colloids Surf B 136:346–354
110. Santra S, Tapec R, Theodoropoulou N, Dobson J, Hebard A, Tan W (2001) Synthesis and characterization of silica-coated iron oxide nanoparticles in microemulsion: the effect of nonionic surfactants. Langmuir 17(10):2900–2906
111. Dobson J (2006) Magnetic nanoparticles for drug delivery. Drug Dev Res 67(1):55–60
112. Arruebo M, Fernández-Pacheco R, Ibarra MR, Santamaría J (2007) Magnetic nanoparticles for drug delivery. Nano Today 2(3):22–32
113. McBain SC, Yiu HH, Dobson J (2008) Magnetic nanoparticles for gene and drug delivery. Int J Nanomed 3(2):169
114. Neuberger T, Schöpf B, Hofmann H, Hofmann M, Von Rechenberg B (2005) Superparamagnetic nanoparticles for biomedical applications: possibilities and limitations of a new drug delivery system. J Magn Magn Mater 293(1):483–496
115. Cheng J, Wang J, Chen B, Xia G, Cai X, Liu R, Ren Y, Bao W, Wang X (2011) A promising strategy for overcoming MDR in tumor by magnetic iron oxide nanoparticles co-loaded with daunorubicin and 5-bromotetrandrin. Int J Nanomed 6:2123–2131
116. Das RK, Kasoju N, Bora U (2010) Encapsulation of curcumin in alginate-chitosan-pluronic composite nanoparticles for delivery to cancer cells. Nanomed Nanotechnol Biol Med 6 (1):153–160
117. Shenoy DB, Amiji MM (2005) Poly (ethylene oxide)-modified poly (ε-caprolactone) nanoparticles for targeted delivery of tamoxifen in breast cancer. Int J Pharm 293(1):261–270
118. Shenoy D, Little S, Langer R, Amiji M (2005) Poly (ethylene oxide)-modified poly (β-amino ester) nanoparticles as a pH-sensitive system for tumor-targeted delivery of hydrophobic drugs. 1. In vitro evaluations. Mol Pharm 2(5):357–366

119. Yallapu MM, Othman SF, Curtis ET, Gupta BK, Jaggi M, Chauhan SC (2011) Multi-functional magnetic nanoparticles for magnetic resonance imaging and cancer therapy. Biomaterials 32(7):1890–1905
120. Jain TK, Richey J, Strand M, Leslie-Pelecky DL, Flask CA, Labhasetwar V (2008) Magnetic nanoparticles with dual functional properties: drug delivery and magnetic resonance imaging. Biomaterials 29(29):4012–4021
121. Mahmood I, Guo C, Xia H, Ma J, Jiang Y, Liu H (2008) Lipase immobilization on oleic acid —Pluronic (L-64) block copolymer coated magnetic nanoparticles, for hydrolysis at the oil/water interface. Ind Eng Chem Res 47(17):6379–6385
122. Paavola A, Kilpeläinen I, Yliruusi J, Rosenberg P (2000) Controlled release injectable liposomal gel of ibuprofen for epidural analgesia. Int J Pharm 199(1):85–93
123. Pan W, Yang Z (2011) Thermoreversible Pluronic® F127-based hydrogel containing liposomes for the controlled delivery of paclitaxel: in vitro drug release, cell cytotoxicity, and uptake studies. Int J Nanomed 6:151–166
124. Tagami T, Kubota M, Ozeki T (2015) Effective remote loading of doxorubicin into DPPC/poloxamer 188 hybrid liposome to retain thermosensitive property and the assessment of carrier-based acute cytotoxicity for pulmonary administration. J Pharm Sci
125. Im Lee J, Yoo HS (2008) Pluronic decorated-nanogels with temperature-responsive volume transitions, cytotoxicities, and transfection efficiencies. Eur J Pharm Biopharm 70(2):506–513
126. Choi JH, Jang JY, Joung YK, Kwon MH, Park KD (2010) Intracellular delivery and anti-cancer effect of self-assembled heparin-Pluronic nanogels with RNase A. J Control Release 147(3):420–427
127. Lee J-H, Lee H, Joung YK, Jung KH, Choi J-H, Lee D-H, Park KD, Hong S-S (2011) The use of low molecular weight heparin–pluronic nanogels to impede liver fibrosis by inhibition the TGF-β/Smad signaling pathway. Biomaterials 32(5):1438–1445
128. Bae KH, Choi SH, Park SY, Lee Y, Park TG (2006) Thermosensitive pluronic micelles stabilized by shell cross-linking with gold nanoparticles. Langmuir 22(14):6380–6384
129. Kamalasanan K, Deepa M, Sharma CP (2014) Supramolecular curcumin–barium prodrugs for formulating with ceramic particles. Colloids Surf B 122:301–308
130. Jaiswal M, Kumar M, Pathak K (2015) Zero order delivery of itraconazole via polymeric micelles incorporated in situ ocular gel for the management of fungal keratitis. Colloids Surf B 130:23–30
131. Zhang B, Zhang Y, Liao Z, Jiang T, Zhao J, Tuo Y, She X, Shen S, Chen J, Zhang Q (2015) UPA-sensitive ACPP-conjugated nanoparticles for multi-targeting therapy of brain glioma. Biomaterials 36:98–109
132. Ong BY, Ranganath SH, Lee LY, Lu F, Lee H-S, Sahinidis NV, Wang C-H (2009) Paclitaxel delivery from PLGA foams for controlled release in post-surgical chemotherapy against glioblastoma multiforme. Biomaterials 30(18):3189–3196
133. Gao Y, Chen L, Zhang Z, Chen Y, Li Y (2011) Reversal of multidrug resistance by reduction-sensitive linear cationic click polymer/iMDR1-pDNA complex nanoparticles. Biomaterials 32(6):1738–1747
134. Raveendran R, Bhuvaneshwar G, Sharma CP (2013) In vitro cytotoxicity and cellular uptake of curcumin-loaded Pluronic/Polycaprolactone micelles in colorectal adenocarcinoma cells. J Biomater Appl 27(7):811–827
135. Xiao B, Zhang M, Viennois E, Zhang Y, Wei N, Baker MT, Jung Y, Merlin D (2015) Inhibition of MDR1 gene expression and enhancing cellular uptake for effective colon cancer treatment using dual-surface-functionalized nanoparticles. Biomaterials 48:147–160
136. Batrakova EV, Li S, Brynskikh AM, Sharma AK, Li Y, Boska M, Gong N, Mosley RL, Alakhov VY, Gendelman HE (2010) Effects of pluronic and doxorubicin on drug uptake, cellular metabolism, apoptosis and tumor inhibition in animal models of MDR cancers. J Control Release 143(3):290–301

137. Liu T, Zeng L, Jiang W, Fu Y, Zheng W, Chen T (2015) Rational design of cancer-targeted selenium nanoparticles to antagonize multidrug resistance in cancer cells. Nanomed Nanotechnol Biol Med 11(4):947–958
138. Butt AM, Amin MCIM, Katas H (2015) synergistic effect of ph-responsive folate-functionalized poloxamer 407-TPgs-mixed micelles on targeted delivery of anticancer drugs. Int J Nanomed 10:1321
139. Nguyen DH, Lee JS, Bae JW, Choi JH, Lee Y, Son JY, Park KD (2015) Targeted doxorubicin nanotherapy strongly suppressing growth of multidrug resistant tumor in mice. Int J Pharm 495(1):329–335
140. Russell A, Hammond S, Morgan J (1986) Bacterial resistance to antiseptics and disinfectants. J Hosp Infect 7(3):213–225
141. Jagannath C, Emanuele MR, Hunter RL (2000) Activity of poloxamer CRL-1072 against drug-sensitive and resistant strains of *Mycobacterium tuberculosis* in macrophages and in mice. Int J Antimicrob Agents 15(1):55–63
142. Lee SH, Lee JE, Baek WY, Lim JO (2004) Regional delivery of vancomycin using pluronic F-127 to inhibit methicillin resistant Staphylococcus aureus (MRSA) growth in chronic otitis media in vitro and in vivo. J Control Release 96(1):1–7
143. Tsai T, Yang Y-T, Wang T-H, Chien H-F, Chen C-T (2009) Improved photodynamic inactivation of gram-positive bacteria using hematoporphyrin encapsulated in liposomes and micelles. Lasers Surg Med 41(4):316
144. WHO (2012) WHO HIV drug resistance report 2012. World Health Organization, Geneva
145. Spitzenberger TJ, Heilman D, Diekmann C, Batrakova EV, Kabanov AV, Gendelman HE, Elmquist WF, Persidsky Y (2007) Novel delivery system enhances efficacy of antiretroviral therapy in animal model for HIV-1 encephalitis. J Cereb Blood Flow Metab 27(5):1033–1042
146. Aweeka F, Jayewardene A, Staprans S, Bellibas ES, Kearney B, Lizak P, Novakovic-Agopian T, Price RW (1999) Failure to detect nelfinavir in the cerebrospinal fluid of HIV-1-infected patients with and without AIDS dementia complex. JAIDS J Acquir Immune Defic Syndr 20(1):39–43
147. Bendayan R, Lee G, Bendayan M (2002) Functional expression and localization of P-glycoprotein at the blood brain barrier. Microsc Res Tech 57(5):365–380
148. Sharma P, Garg S (2010) Pure drug and polymer based nanotechnologies for the improved solubility, stability, bioavailability and targeting of anti-HIV drugs. Adv Drug Deliv Rev 62 (4):491–502
149. Tritel M, Resh MD (2001) The late stage of human immunodeficiency virus type 1 assembly is an energy-dependent process. J Virol 75(12):5473–5481
150. Miller DW, Batrakova EV, Waltner TO, Alakhov VY, Kabanov AV (1997) Interactions of pluronic block copolymers with brain microvessel endothelial cells: evidence of two potential pathways for drug absorption. Bioconjug Chem 8(5):649–657
151. Shaik N, Pan G, Elmquist WF (2008) Interactions of pluronic block copolymers on P-gp efflux activity: experience with HIV-1 protease inhibitors. J Pharm Sci 97(12):5421–5433

Chapter 10
Silver Nanoparticles in Natural Environment: Formation, Fate, and Toxicity

Virender K. Sharma and Radek Zboril

Abstract In recent years, there has been growing interest in the existence of natural nanoparticles in the environment and their subsequent influence to the ecological health. This chapter presents the current status on thermally- and light-induced formation of silver nanoparticles (AgNPs) under environmentally relevant conditions. Influenced environmental parameters include temperature, pH, oxic/anoxic environment, and concentrations of precursors Ag^+ ions and natural organic matter (NOM). Surface-catalyzed reduction of Ag^+ could describe the formation of AgNPs under various conditions. The redox species of iron (Fe(II)/Fe(III)) in the thermally induced processes enhanced the formation of AgNPs. Moieties of NOM, Ag–NOM complexes, and reactive oxygen species, ROS (e.g., $O_2^{\cdot -}$) were provoked to explain the formation of AgNPs. Stability studies on formed AgNPs from Ag(I)–NOM reaction mixtures have shown their stability for days to several months. However, cations of the natural waters such as Na^+, K^+, Mg^{2+}, and Ca^{2+} can destabilize the AgNPs. A preliminary investigation on the toxicity of AgNPs, formed in the mixture of Ag^+-humic acid, suggests that lower minimum inhibition concentration against Gram-negative bacteria and Gram-positive bacteria compared to engineered AgNPs.

Keywords Noble metals · Natural nanoparticles · Organic matter · Stability · Toxicity

V.K. Sharma (✉)
Program for the Environment and Sustainability, Department of Environmental and Occupational Health, School of Public Health, Texas A&M University, College Station, TX 77843, USA
e-mail: vsharma@sph.tamhsc.edu

V.K. Sharma · R. Zboril
Regional Centre of Advanced Technologies and Materials, Departments of Experimental Physics and Physical Chemistry, Faculty of Science, Palacký University in Olomouc, 771 46 Olomouc, Czech Republic

B. Yan et al. (eds.), *Bioactivity of Engineered Nanoparticles*,
Nanomedicine and Nanotoxicology, DOI 10.1007/978-981-10-5864-6_10

10.1 Introduction

Engineered nanoparticles (ENPs) are widely used in development of technologies and in consumer products such as agriculture, electronic devices, and renewable energies [1–7]. ENPs synthesized in worldwide laboratories can be given as metals, metal oxides, metal sulfides, nonmetals, lipids, and polymers [8–10]. ENPs have been suggested to remediate polluted water [11, 12]. Iron-based nanoparticles are proposed in cancer treatment [13–15]. Because of many human health related applications of nanoparticles, synthesis of ENPs through reduction of metal salts with green chemistry reducing agents have been emphasized in order to protect the environment [5, 16–19]. Significantly, a role of environmental-friendly compounds to act as a stabilizing agent has also been investigated in detail [4, 10, 20]. Sugars and vitamins can act as both capping agents and thus represent examples of such compounds.

Among the category of metals, silver nanoparticles (AgNPs) have shown the most use in industrial and medical fields [1, 7, 21]. AgNPs have been found in more than 400 consumer products [22, 23]. After the intended use of AgNPs, the nanoparticles release into the environment [24–28]. Numerous investigations have been conducted on the fate and behavior of release of AgNPs into the aquatic environment, because of their effects on ecosystems and humans [8, 22, 26, 29, 30]. Comparatively, little is known on the mechanism of natural occurrence of AgNPs in different environmental conditions [31, 32]. Reactions in hydrothermal vents, surface water, and wastewater, and mining activities are possible processes that lead to natural formation of AgNPs in the environment [8, 33]. Significantly, the naturally formed AgNPs may also equally affect the ecological health of the environment [10, 34]. This chapter summarizes the results obtained on the formation of AgNPs under environmental conditions, followed by their fate and potential toxicity to the biological species.

10.2 Thermally Induced Formation of AgNPs

In this set of experiments, initial measurements on thermally induced formation of AgNPs were conducted at varied environmental conditions (Fig. 10.1) [35]. Solutions of Ag^+ were mixed with Suwannee River humic acid (SRHA) at different temperatures under different concentrations of SRHA and silver ions. It was observed that the color of the mixed solution changed with time from a light yellow color of the HA solution to strong yellow color. Spectra of the mixed solution were measured by UV–vis spectroscopy (Fig. 10.1a–c). The intense yellow color was from the surface plasmon resonance (SPR) of the AgNPs. The intensity of the SPR was dependent on the reaction conditions. When concentration of SRHA in mixed solution was increased by keeping concentration of Ag^+ at 90 °C, the intensity of SPR peak increased (Fig. 10.1a). An increase in temperature also enhanced the

growth of AgNPs (i.e., increase in the intensity of SPR) (Fig. 10.1b). When the level of Ag^+ in mixed solutions was increased by keeping the concentration of SRHA constant at 90 °C, the formation of AgNPs increased (Fig. 10.1c).

Figure 10.1a–c shows that the location of the peak wavelength and shape of the spectra depended on the initial concentration of SRHA and temperature. It seems that the location of the peak was a function of the diameter and agglomeration of the AgNPs. The peak was sharper with increased concentrations of SRHA at a constant Ag^+ concentration and temperature (Fig. 10.1a). This suggests that less polydisperse AgNP size distributions at high levels of SRHA. An increase in temperature of the mixed solution of Ag^+–SRHA enhanced growth of AgNPs and the peak became narrow (Fig. 10.1b). It was obvious that the formation mechanism of AgNPs was more likely operational at higher temperature. Low levels of Ag^+ also

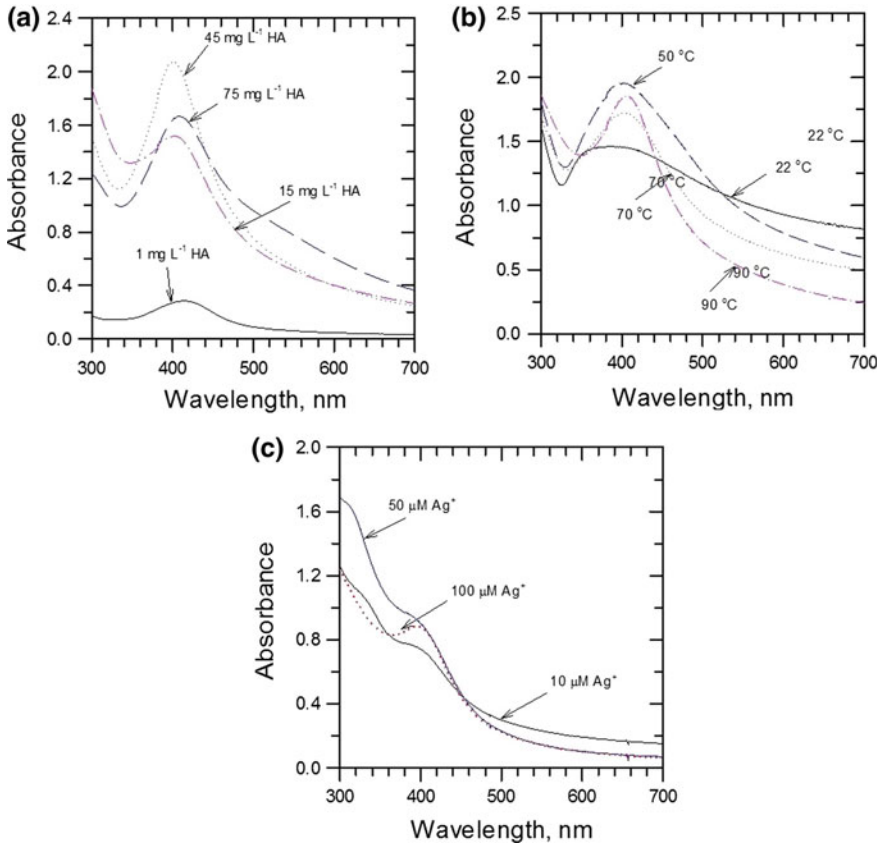

Fig. 10.1 UV-Vis absorption spectra of AgNPs. **a** Different [HA], $[Ag^+] = 1 \times 10^{-3}$ M, reaction time = 90–330 min, t = 90 °C; **b** different reaction temperatures, $[Ag^+] = 1 \times 10^{-3}$ M, [HA] = 100 mg L^{-1}; and **c** different $[Ag^+]$, t = 90 °C, [HA] = 100 mg L^{-1}. Adapted from [35] with the permission of American Chemical Society

showed the AgNPs (Fig. 10.1c). However, the peak of SPR was less defined (Fig. 10.1c).

In the next series of experiments, similar studies were conducted using Suwannee River fulvic acid (SRFA) [36]. Similar results, shown in Fig. 10.1, were observed. Increase in concentrations of Ag^+ and SRFA in mixed solutions and temperature resulted in the increase in intensity of SPR peak of the AgNPs. At high temperature of 90 °C, formation of AgNPs occurred in hours (or minutes) with well-defined SPR peak. Comparatively, it takes days to result in AgNPs at room temperature (25 °C). The SPR peaks were much broader at room temperature because of considerable polydispersity in size and local dielectric environment of the AgNPs [36]. Additional experiments were performed by varying the pH of the mixed solution [36]. Results demonstrated the increase in the formation of AgNPs with increase in pH (Fig. 10.2) [36]. With increase in pH, the shape of the SPR peaks of AgNPs was also broadened.

Results of Figs. 10.1 and 10.2 were understood by monitoring of the SPR peak of the AgNPs as a function of time intervals (Fig. 10.3) [36]. The shape of the curve seen in Fig. 10.3 suggests an autocatalytic process for the growth of AgNPs. Equation 10.1 was used to explain the process of the formation of AgNPs. Basically, Ag^+ ions from the bulk solution first adsorb onto a small cluster Ag_n before reduction by SRFA (or SRHA) to catalyze the growth of AgNPs.

$$Ag^+ + Ag_n + \text{SRFA(or SRHA)} \rightarrow Ag_{n+1} + \text{SRFA(ox)(or SRHA(ox))} \quad (10.1)$$

The autocatalytic process is described by Eq. 10.2.

$$\ln(a/(1-a)) = (k[Ag^+])t - \ln([Ag^+]/n[Ag_n]), \quad (10.2)$$

where $a = A_t/A_\infty$, and A_t and A_∞ are the absorbance values at time t and ∞, respectively. A linear relationship between ln $(a/(1-a))$ and the reaction time support that the formation of AgNPs results from an autocatalytic reaction in the Ag^+–SRHA or Ag^+–FA mixtures mixture solutions of Figs. 10.1 and 10.2.

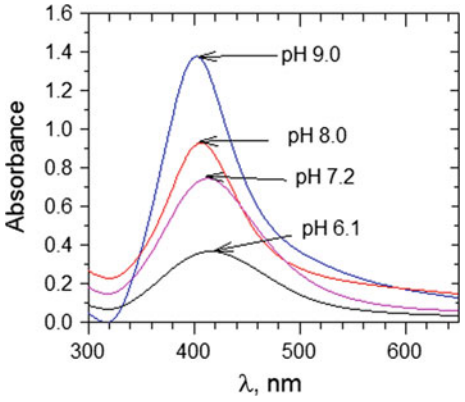

Fig. 10.2 UV-Vis absorption spectra of AgNPs in SRFA at different pH in 2 h heating at 90 °C. $[Ag^+] = 1 \times 10^{-3}$ mol L^{-1}, 100 mg L^{-1} SRFA. Adapted from [36] with the permission of American Chemical Society

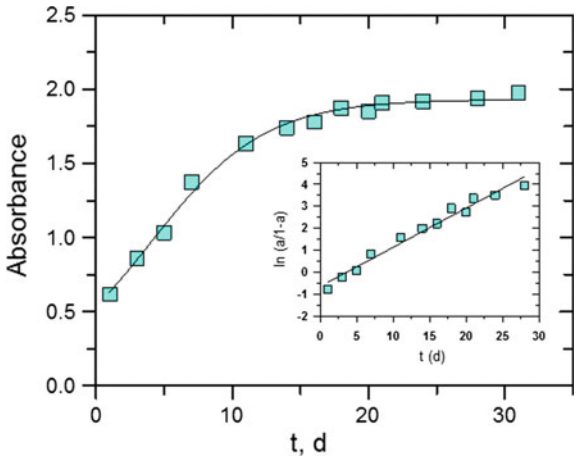

Fig. 10.3 Plot of absorbance versus time for the formation of AgNPs at 22 °C. $[Ag^+] = 1 \times 10^{-3}$ mol L^{-1}, 100 mg L^{-1} SRFA. *Inset* Plot of $\ln(\alpha/1 - \alpha)$ versus time. Adapted from [36] with the permission of American Chemical Society

The formation of AgNPs through the autocatalytic process was also confirmed by determining the thermodynamic feasibility of the reaction of Ag^+ ion and SRFA (or SRHA) under homogeneous solutions. The redox potentials for FA and HA are −0.5 and −0.7 V, respectively (Table 10.1) [37–43], which are not sufficient to overcome the highly negative redox potential of Ag^+ ions to isolated silver ($Ag^+ + e^- \rightarrow Ag^o$; $E^o = -1.8$ V vs. NHE) [38]. Therefore, direct reduction of Ag^+ ion by either SRFA or SRHA in solution mixture is not possible. However, it is likely that Ag^+ ions deposited on solid surfaces are being reduced by SRFA (or SRHA) due to a more positive redox potential. This idea stimulated from the known redox potential for reducing Ag^+ onto a Ag electrode is +0.8 V [37]. The steps of the mechanism of the formation of AgNPs may be written by Reactions (10.3–10.7).

$$2Ag^+ + 2OH^- \rightarrow Ag_2O + H_2O \quad \text{fast} \tag{10.3}$$

$$Ag_2O + (Ag^+)_n \rightarrow Ag_2O - (Ag^+)_n \quad \text{fast} \tag{10.4}$$

$$Ag_2O - (Ag^+)_n + FA \rightleftharpoons Ag_2O - (Ag^+)_n - FA \quad K_{ad} \tag{10.5}$$

$$Ag_2O - (Ag^+)_n - FA \rightarrow Ag_2O - (Ag^+)_{n-1} + Ag^o + FA^-(ox) k_{red} \tag{10.6}$$

$$Ag^o + Ag^o \rightarrow Ag_2 \quad \text{fast} \tag{10.7}$$

In this proposed mechanism, initial formation of colloidal Ag_2O occurred from the reaction between Ag^+ and OH^- ions (Reaction 10.3). The solid surface of Ag_2O thus adsorbed Ag^+ ion (Reaction 10.4), which could satisfy the thermodynamic feasibility condition of reduction of Ag^+ ion by SRFA (or SRHA) (Reactions 10.5 and 10.6). According to the mechanism, SRFA was adsorbed first onto colloidal particle of Ag_2O before reducing Ag^+ ion to metallic silver. The formation of

Table 10.1 Redox potentials of possible reactions in the Ag^+–NOM–Fe system

Reaction	E^0 versus NHE (V)	References
$Ag^+ + e^- \rightleftharpoons Ag^o$	−1.8	[37]
$Ag^+ + Ag^o_\infty + e^- \rightleftharpoons Ag^o_\infty$	0.8	[38]
$Fe^{3+} + e^- \rightleftharpoons Fe^{2+}$	0.77	[40]
$Q + 2H^+ + 2e^- \rightleftharpoons HQ$	−0.699	[38]
$FA_{(ox)} + e^- \rightleftharpoons FA_{(Red)}$	~0.5	[42]
$HA_{(ox)} + e^- \rightleftharpoons HA_{(Red)}$	~0.7	[43]
$Fe^{III}(HS) + e^- \rightleftharpoons Fe^{II}(HS)$	−0.20 to 0.30	[40]

FA fulvic acid, *HA* humic acid, *HS* humic substances

dimers (Reaction 10.7) was proposed prior to stabilization of larger clusters [44]. The autocatalytic reduction of Ag^+ may represent the driving force to reach metastable (or "magic-sized") Ag_n clusters that are thermodynamically far more favored than smaller entities. In the growth period, the metastable silver clusters agglomerate to generate the characteristic yellow color of AgNPs.

It is clear that reaction step (10.6) is the rate-determining step of the mechanism. The reduction capacity of organic matter (FA or HA) derives the formation of AgNPs. The amount of AgNPs (or growth of AgNPs) is directly related to the concentrations of both Ag^+ ions and SRHA (Fig. 10.1) [35]. An increase in the pH (or more concentration of OH^- ions) in solution would increase the amount of colloidal Ag_2O that enhanced the rate of formation of Ag_2O–$(Ag^+)_n$ particles. This process thus ultimately yielded increase in amount of AgNPs with increase in pH of the solution. Other possibility is that the functional groups of aromatic fractions of FA generally are deprotonated species at higher pH. The deprotonated species have relatively higher electron density than functional groups of protonated species. The initial binding and complexation of Ag^+ ions by FA species is expected to increase with increase in pH. This process may increase the rate of the formation of AgNPs with increase in pH (Fig. 10.2) [36].

Next, the formation of AgNPs was investigated using HA, obtained or isolated from different sources, which include aquatic, sedimentary, and soil. Details of procedures to obtain HA are given elsewhere [35]. Figure 10.4 shows the results of the formation of AgNPs under different HA at RT and 90 °C while keeping concentrations of Ag^+ and HA constant [35]. SUWHA was from Suwannee River HA from an aquatic source. SR, LD, and M2 represent HA are from sediments while MB, FITJ, S1, and WM belong to sources of HA from soil. As expected, a distinct yellow color of AgNPs was observed at RT was in days (Fig. 10.4a). At 90 °C, the formation of AgNPs was seen within 90 min (Fig. 10.4b). The intensity of the peak of the AgNPs varied with the source of the HA. The organic content and moieties of the organic matter present in HA determine the variation in growth of the AgNPs. Interestingly, soil HAs had sluggish or no formation of AgNPs. It appears that the predominant aliphatic-based SHA and aquatic HA were more easily able to reduce Ag^+ to yield AgNPs than did aromatic-dominated soil HA. The difference in growth

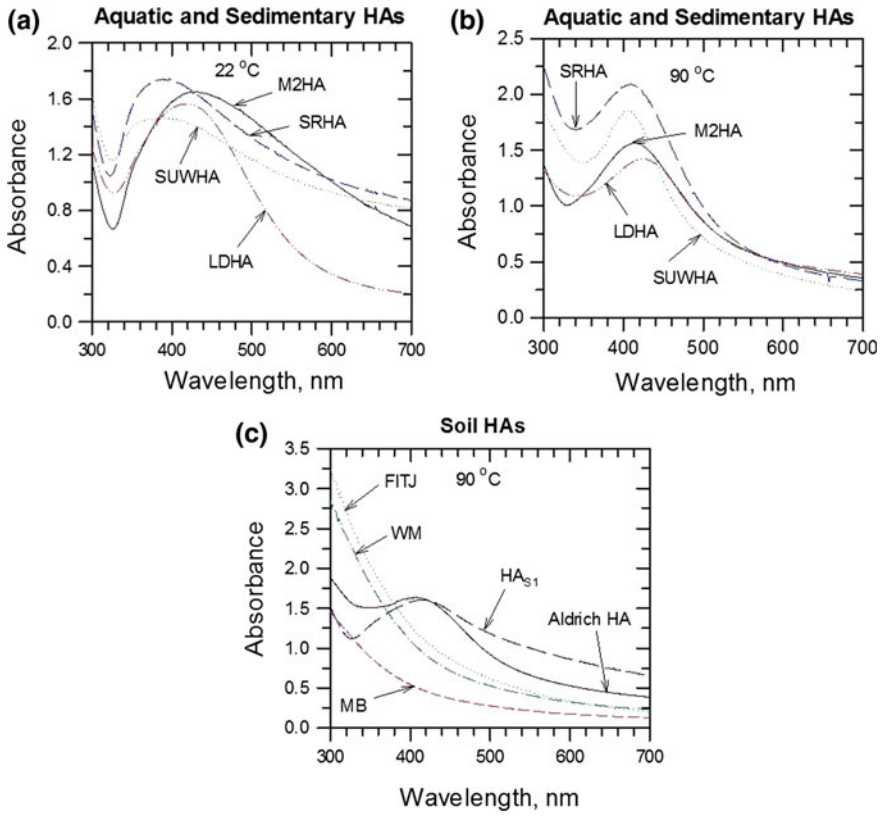

Fig. 10.4 UV-Vis absorption spectra of AgNPs. **a** Different aquatic/sedimentary HAs. $[Ag^+] = 1 \times 10^{-3}$ M, reaction time = 60–180 min, t = 22 °C, and [HA] = 100 mg L^{-1}; **b** different aquatic/sedimentary HAs. $[Ag^+] = 1 \times 10^{-3}$ M, reaction time = 60–180 min, t = 90 °C, and [HA] = 100 mg L^{-1}; and **c** different soil HAs, reaction time = 60–180 min, [HA] = 100 mg L^{-1}, $[Ag^+] = 1 \times 10^{-3}$ M, and t = 90 °C. Adapted from [35] with the permission of American Chemical Society

of AgNPs in sedimentary and soil samples may be described by the presence of the dominant form of reduced organic sulfides (thiols) in sedimentary HAs relative to the more oxidized form of organic sulfur present in soil HAs [45].

AgNPs obtained by the interaction of Ag^+ and HA were characterized by transmission electron microscopy, selected area electron diffraction (SAED), and atomic force microscopy (AFM) (Fig. 10.5) [35]. The shapes of the AgNPs were usually spherical with a very broad size distribution, ranging from diameters greater than 50 nm to less than 5 nm (Fig. 10.5a–d). The agglomeration of AgMPs was relatively more in the larger size AgNPs. The images of the AFM support the presence of crystalline AgNPs in the samples. Figure 10.3b demonstrates the [111] growth direction of the formed AgNPs. The high-resolution TEM (HRTEM) images in Fig. 10.5c indicates the presence of crystallites AgNPs. The SAED

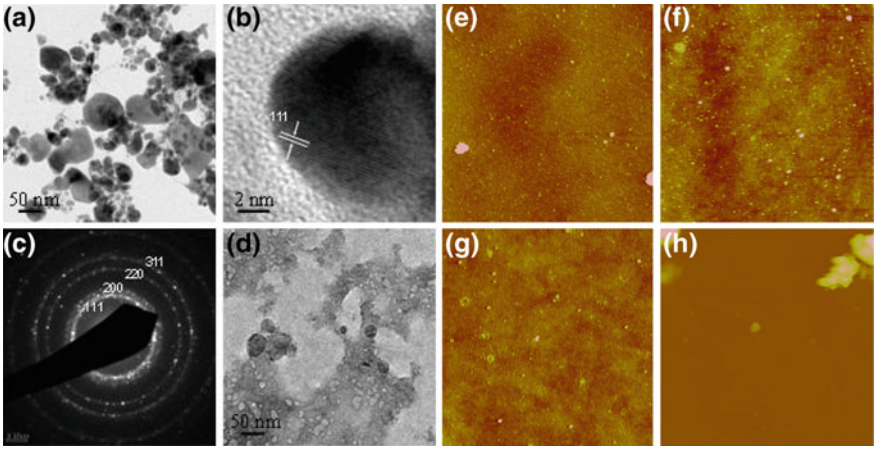

Fig. 10.5 Low resolution (**a**) and high resolution (**b**) TEM images of the AgNPs produced in the M2HA solution with the corresponding SAED pattern (**c**) of the Ag nanoparticles. Low-resolution TEM image of the as prepared M2HA solution is shown for comparison, and (**d**). The diffraction patterns can be precisely indexed to the face-centered cubic phase of Ag. AFM image of AgNPs formed by mixing $AgNO_3$ at room temperature with **e** M2HA, **f** SRHA, and **g**, **h** SUWHA for 6–13 days. *Scale bars* represent 400 nm, z-scale is 10 nm in (**e**–**g**) and 250 nm in (**h**). Adapted from [35] with the permission of the American Chemical Society

patterns and lattice planes seen can be indexed to face-centered cubic silver metal (Fig. 10.5c). Significantly, an abundance of amorphous natural colloids with equivalent electron density was observed (Fig. 10.5d). According to AFM images, AgNPs were singly dispersed spherical particles, mostly less than 10 nm in diameter (Fig. 10.5e–h). Significantly, images contained larger diameter particles that were less spherical (e.g., Fig 10.5f) or large agglomerates of many particles (e.g., Fig 10.5h).

The effect of iron species was explored by heating the mixture of Ag^+ with SRHA with and without Fe(II)/Fe(III) in solution at pH 6.0 and heated at 90 °C for 4 h [46]. The characteristic intense yellow color due to SRP of AgNPs appeared in mixed solutions (Fig. 10.6a). However, Fe^{2+} and Fe^{3+} species enhanced absorbance of SPR of AgNPs (Fig. 10.6a). Importantly, a mixed solution of only Ag^+ and Fe^{2+} without SRHA had no SPR of AgNPs (Fig. 10.6a). Significantly, there was no further enhancement in the SPR absorbance of AgNPs when the concentration of Fe^{2+} was increased (Fig. 10.6a). Similar results were observed at room temperature. However, the growth of AgNPs happened in several days, similar to results observed in Fig. 10.1.

The formation of AgNPs by the reduction of Ag^+ ion by either Fe^{2+} or SRHA is not thermodynamically possible due to the high negative potentials of the reactions (Eqs. 10.7 and 10.8) [37, 38, 40, 42, 43]. Surface auto-catalysis processes, described in Eqs. 10.3–10.7, were provoked to explain the formation of AgNPs.

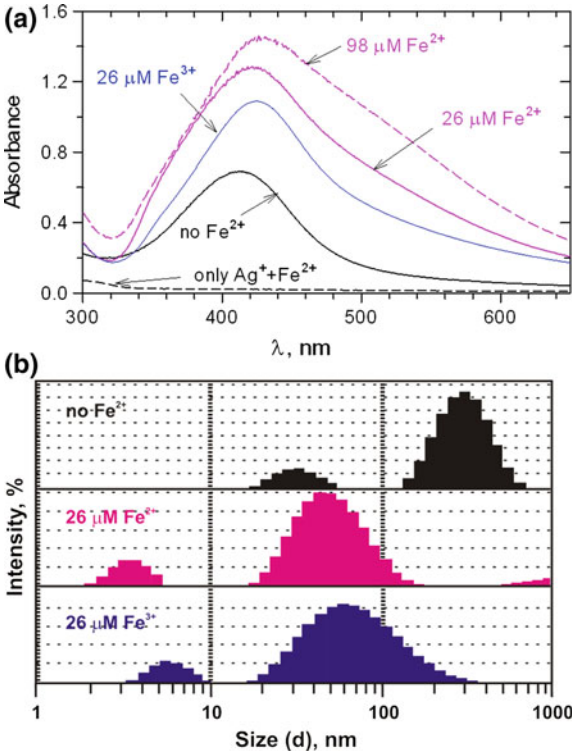

Fig. 10.6 UV-vis absorption spectra and DLS determined size distributions based on intensity fluctuation of AgNPs in Ag^+–SRHA solutions with and without Fe^{2+} and Fe^{3+} at pH 6.0. **a** UV-vis spectra and **b** DLS measurements. $[Ag^+] = 1 \times 10^{-3}$ mol L^{-1}, 40 mg L^{-1} SRHA. Adapted from [46] with the permission of American Chemical Society

$$Ag^+ + Fe^{2+} \rightleftharpoons Ag^o + Fe^{3+} \quad E^0 = -2.57\ V \tag{10.8}$$

$$Ag^+ + HA_{(Red)} \rightleftharpoons Ag^o + HA_{(Ox)} \quad E^0 = -2.50\ V \tag{10.9}$$

The presence of Fe^{2+} in the reaction mixture of Ag^+ and SRHA leading to a number of reactions can lead to number of reactions, which include the formation and dissociation of Fe(II)/Fe(III)-SRHA complexes and the formation of reactive oxygen species (ROS) $O_2^{\cdot-}$, H_2O_2, and $^{\cdot}OH$ [47–49]. These additional reactions helped to generate more amount of AgNPs in Ag^+–SRHA–Fe(II)/Fe(III) mixtures than in Ag^+–SRHA mixed solutions. For example, the complex formation of Fe^{2+} with NOM gave additional driving force to form AgNPs and thus enhanced the formation of AgNPs in the Ag^+–Fe^{2+}–SRHA mixed solution. This can be seen in positive redox potential of the Reaction (10.9). The reaction includes the redox potential of Fe(II)-HA/Fe(III)-HA system. The Reaction (10.9) provides additional step of the formation of AgNPs besides Reaction (10.7) without involvement of iron species to cause the increased formation of AgNPs (see Fig. 10.6a)

$$Ag^{+} + Ag^{o}_{\infty} + Fe^{II}(HS) \rightleftharpoons Ag^{o}_{\infty} + Fe^{III}(HS) \quad E^{0} \sim 0.5 - 1.0\ V \qquad (10.10)$$

The $O_2^{\cdot-}$ species, possibly formed in the reaction system, can also react with Ag^+ to yield an additional reaction to result in AgNPs.

Figure 10.6b shows the DLS measurements (intensity-based size distributions) of AgNPs in the absence and presence of iron in the Ag^+–SRHA system. The mean hydrodynamic diameter (HDD) of the AgNPs in the absence of iron was 201 nm. The HDD of AgNPs in the presence of consistent with faster growth of AgNPs in Ag^+–SRHA–Fe^{2+}/Fe^{3+} mixture solution than in Ag^+–SRHA. A polydisperse size distribution was seen in the polydispersity index (PI) of ~0.5 of the AgNPs (Fig. 10.6b).

The nature of natural organic matter (NOM) greatly influenced the growth of the formation of AgNPs in the Ag^+–NOM and Ag^+–NOM–Fe^{3+} systems (Fig. 10.7) [46]. In agreement with results of Fig. 10.6a, the presence of Fe^{3+} had higher amount of AgNPs formation than that in the absence of Fe^{3+} (Fig. 10.7). In the absence of Fe^{3+}, the relative ordering of the formation of AgNPs was NLFA > SRHA > SRFA (Fig. 10.7a). The composition of individual NOM, given in Table 10.2, was considered to understand the ordering of the growth of AgNPs. The carbon distribution and the content of functional groups did not provide clues of the ordering of growth rates of AgNPs (Fig. 10.7a and Table 10.2). Interestingly, the rate of the formation of AgNPs could be correlated with the free radical content order: NLFA, SRHA, and SRFA (see Table 10.2). It was suggested that the free radical species was involved in the initial formation of metallic silver (Reaction 10.6).

In the case of Ag^+–HA/FA–Fe^{3+} system, an increase in the growth of AgNPs for all HA and FAs was observed compared to Ag^+–HA/FA (Fig. 10.7a vs. 10.7b). However, the trend of the growth of AgNPs was SRHA > NLFA > SRFA, which

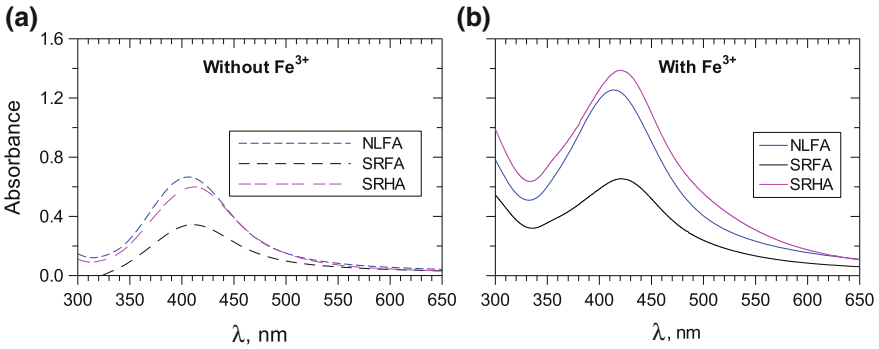

Fig. 10.7 UV-Vis absorption spectra of AgNPs in reduction of Ag^+ by different organic matter with and without Fe^{2+} at pH 6.0. A-without Fe^{2+} and B-with Fe^{3+} ($[Ag^+] = 1 \times 10^{-3}$ mol L^{-1}, [SRHA] = [SRFA] = [NLFA] = 40 mg L^{-1}, $[Fe^{3+}] = 13$ μM). Adapted from [46] with the permission of American Chemical Society

Table 10.2 Components present in different samples of FAs and HS

Sample	Function groups				^{13}C NMR estimates of carbon distribution content				Free radical
	Carboxyl	Phenolic	Carbonyl	Carboxyl	Aromatic	Acetal hetroaliphatic aliphatic			
	220–190 ppm	190–165 ppm	165–110 ppm	110–90 ppm	90–60 ppm	60–0 ppm			
SRHA	9.13	3.72	6	15	31	7	13	29	0.64[a]
SRFA	11.44	2.91	7	20	24	5	11	33	0.54
NLFA	11.16	3.18	10	24	31	7	12	18	1.14

SRHA Suwannee River II Humic Acid, *SRFA* Suwannee River I Fulvic Acid, *NLFA* Nordic Lake Fulvic Acid
[a]Reported for Suwannee River I Humic Acid

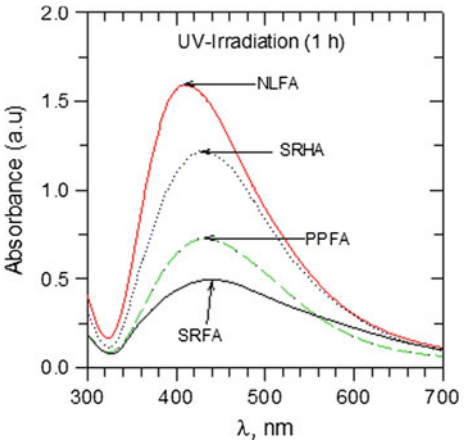

Fig. 10.8 UV-Vis absorption spectra of AgNPs for MRHW synthetic freshwater under UV irradiation for 1 h at pH 8.0. [Ag^+] = 1×10^{-3} mol L^{-1}, FA or HA = 45 mg L^{-1}). Adapted from [36] with the permission of the American Chemical Society

was different from the trend in the absence of Fe^{3+}. The Fe^{3+}-ligands complexation may have roles in the Ag^+–HA/FA–Fe^{3+} system. The complexation is usually driven by the nature and functional groups of the ligands [47]. Overall, reactions responsible to reduce Ag^+ to metallic silver are influenced by the nature of ligands to cause the trend seen in Fig. 10.7a.

10.3 Light-Induced Formation of AgNPs

Photochemical reactions involving metal species and natural organic matter represent a potential source for the natural formation of nanoscale particles in the environment [10, 50]. In our initial study, the UV light-induced formation of AgNPs was investigated (Fig. 10.8) [36]. The formation of the characteristic yellow color of AgNPs was clearly seen. The literature reports the photochemical formation of AgNPs under photosensitizers containing solution [51, 52]. Both fulvic and humic acids in the reaction mixtures may behave like photosensitizers to result in

the formation of AgNPs. Other possibility is that the formed Ag_2O in the reaction mixture (see Reaction 10.3) may act like a semiconductor [53]. The mechanism may involve the reduction of Ag^+ adsorbed onto Ag_2O by the photochemically generated reactive species such as hydrated electrons and $O_2^{-\cdot}$ in solution to yield AgNPs [48, 54]. The $O_2^{-\cdot}$ species can react with Ag^+ ions to form AgNPs [55]. It seems that the interactions among Ag^+, AgNPs and reactive species are causing the formation of AgNPs.

Significantly, the nature of organic matter was found to be important. For example, the use of different fulvic acids and humic acid showed the following order for the rate of formation: NLFA > SRHA > PPFA > SRFA [36]. This order is similar to the one seen in thermally induced formation of AgNPs using different sources of organic matter [35]. A few other studies have also shown the formation of AgNPs under UV and visible light irradiation [56]. The presence of Cl^- may enhance the formation of AgNPs from solid AgCl(s) in the presence of visible light. This is important considering natural levels of Cl^- ions in water. An earlier work on the formation of AgNPs from Ag(I)-NOM mixtures under UV light suggested the role of superoxide [56]. However, later work on sunlight-driven formation of AgNPs from the mixture of Ag(I)-NOM ruled out the possibility of superoxide to reduce Ag(I) ions [57]. The Ag(I)-NOM binding may be responsible in the sunlight-driven photoreduction of Ag(I) ions to AgNP [57].

More recently, the role of oxygen was probed by irradiating the mixed solution of Ag^+–HA at pH 6.0 under oxic and anoxic conditions. The formation of AgNPs nanoparticles at different time intervals is demonstrated in Fig. 10.9 [58]. The characteristic yellow color from the SPR of AgNPs had a broader peak features

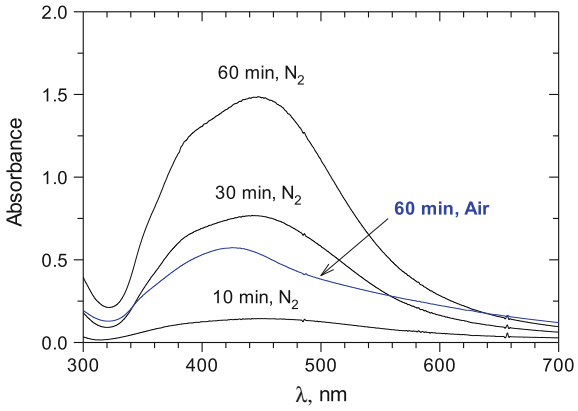

Fig. 10.9 Formation of silver nanoparticles from silver(I)-humic acid mixtures in 2-(*N*-morpholino)ethanesulfonic acid buffer at pH 6.0 under ultraviolet irradiation and nitrogen or air. This data shows that a process involving silver(I) ions binding to organic matter is suggested in the photoreduction of silver ion for silver particle in the environment. Experimental conditions: $[Ag^+] = 1.0 \times 10^{-3}$ mol L^{-1}, [HA] = 40 mg L^{-1}. Adapted from [58] with the permission of Springer Inc.

between 420 and 460 nm. The intensity of the peak increased gradually with time (Fig. 10.9). Significantly, the peak intensity under N_2 (i.e., anoxic condition) at 60 min was much more than the corresponding intensity under air (i.e., oxic conditions) at 60 min. This indicates dissolved oxygen may not be playing a dominant role in the formation of AgNPs under UV irradiation.

The effect of iron species (Fe(II)/Fe(III) on the UV-induced formation was studied by mixing 26 μM Fe(II) ion to a Ag^+–HA solution (Fig. 10.10) [46]. With Fe(II) solution in the anoxic solution, a sharp decrease in the AgNPs was observed (Fig. 10.10a). Other interesting feature was a much broader and more intense SPR of the AgNPs under anoxic conditions. This indicates that Fe(II) decreased the growth of AgNPs in the mixed solution, which caused the large particle size distribution and broad spectrum under anoxic conditions of Ag^+–HA–Fe(II) system. Furthermore, Fe(II) ions may be inhibiting the ligand-to-metal-charge transfer process to photoreduce silver ions to yield AgNPs (Fig. 10.10a). When a similar study was performed under oxic conditions, iron ions had almost no influence on giving AgNPs; in contrast to the thermally induced Fe(II) enhanced AgNPs formation [46]. This was not surprising because different mechanisms are generally involved in thermal- and photo-induced formation of AgNPs from the reduction of Ag^+ ion to metallic silver.

The influence of the valence state of iron (i.e., Fe(II) versus Fe(III) ion) on the formation of AgNPs was also explored by adding 26 μM Fe(II) and 26 μM Fe(III) ions into Ag^+–FA mixed solution, followed by UV irradiation. This study was carried out under anoxic conditions. The presence of Fe(II) caused broadening of the SPR peaked of the formed AgNPs. Also, no change in the intensity of SPR peak due to the presence of Fe(II) in the Ag^+–FA solution was seen (Fig. 10.10b). Comparatively, a decrease in the intensity of the AgNPs in the Ag^+–HA–Fe(II)

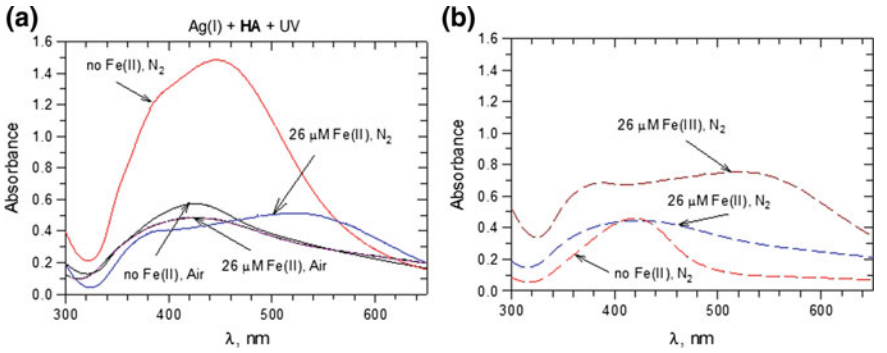

Fig. 10.10 Formation of silver nanoparticles during the ultraviolet irradiation of **a** silver(I)-humic acid-iron(II) purged with nitrogen and air at pH 6.0 and **b** silver(I)-fulvic acid-iron(II)/iron(III) purged with nitrogen at pH 6.0. The data shows that the influence of iron ions on the formation of silver particles from photoreduction of silver ions depends on the nature of the organic matter. Experimental conditions: $[Ag^+] = 1.0 \times 10^{-3}$ mol L^{-1}, [FA] = [HA] = 40 mg L^{-1}. Adapted from [58] with the permission of Springer Inc.

solution was observed (Fig. 10.10a). Humic and fulvic acids have different moieties, which would result in distinguished effects due to Fe(II) on the formation of AgNPs. In the case of Fe(III) ions in the mixture of Ag^+–FA solution, the formation of AgNPs had broader peak in comparison with no Fe(III) in the mixed solution of Ag^+ and FA. Further investigations are needed to comprehend the effect of iron species on the UV-induced formation of AgNPs in the mixture of Ag^+ and NOM.

10.4 Fate of AgNPs

In the beginning of our work on the syntheses of AgNPs, we focused on stabilization of the particles using surfactants, saccharides, and polymers [16]. These AgNPs were classified as engineered AgNPs. In recent years, we are interested in learning the fate of AgNPs formed from the interaction of Ag^+ with NOM under conditions of environmental relevance [35, 36, 46, 59]. Results of AgNPs formed from the reduction of Ag(I) by HA and FA with and without iron species in solution are presented in Fig. 10.11. Figure 10.11a shows the stability of AgNPs formed from the thermally induced reduction of Ag^+ by sedimentary and river HA. River HA had a decrease in stability of AgNPs up to 25% in 7 days. However, sediments HA showed only 7% in the same time period of 70 days. A blueshift in the SPR peak from 423 to 410 nm was noticeable (Fig. 10.11a). A similar stability trend of AgNPs resulted from the interaction of Ag^+ with FA was observed (Fig. 10.11b). Repulsive forces between negatively charged AgNPs (zeo potential varied only from −40 to −33 mV during seven months) was largely responsible for preventing the aggregation of particles and thus AgNPs were stable even for 7 months (Fig. 10.11b). More importantly, Fe^{3+} ions in the reaction mixtures of Ag^+–FA did not alter the stability of AgNPs (Fig. 10.11c). Interestingly, increase in SPR of AgNPs was noticed during 7-month period. In the presence and absence of Fe^{3+} ions, the values of zeta potential were −18 and −23 mV, respectively, in Ag^+–FA reaction mixture. This indicates that Fe^{3+} ion did not cause any significant change in the organic matter coated surfaces of AgNPs. It is likely that the coating of organic matter on AgNPs inhibits the dissolution of the nanoparticles, which ultimately result in increased stability of the AgNPs.

The presence of ions in solutions decreased the stability of AgNPs [29, 60]. The decreases in the stability of AgNPs were less in chloride salts of monovalent ions (Na^+ and K^+) than those of divalent cations (e.g., Mg^{2+} and Ca^{2+}) in solutions of Ag^+-organic matter [59]. An increase in ionic strength of solution also destabilized the AgNPs. This could be seen in decrease in the value of zeta potential of AgNPs from ~ -32 mV at 1 mM to ~ -15 mV at 10 mM $CaCl_2$ solution. Furthermore, the hydrodynamic diameter (HDD) of AgNPs increased from nm to μm in this ionic strength range, which showed that the agglomeration of the AgNPs increased with ionic strength of the electrolyte solution. The major finding of these results was that the natural organic matter stabilized AgNPs may become less stable as they move from freshwater to estuarine water and finally to seawater.

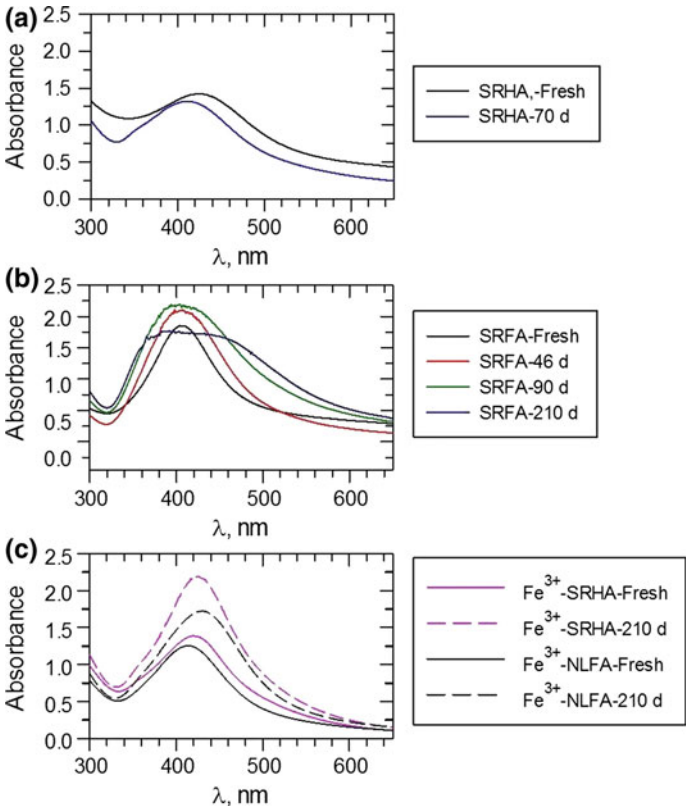

Fig. 10.11 UV-Vis measurements of aging of AgNPs formed at 90 °C. Days represent time after the formation of particles. **a** 100 mg L^{-1} SRHA, pH 8.0, **b** 100 mg L^{-1} SRFA; pH 8.0, and **c** Fe^{3+}–FA reaction mixtures, [SRHA] = [NLFA] = 40 mg L^{-1} SRFA. [Fe^{3+}] = 13 µM; pH 6.0) ([Ag^{+}] = 1 × 10^{-3} mol L^{-1}). Adapted from [36, 46, 59] with the permission of American Chemical Society

10.5 Toxicity

An investigation in our laboratory on the toxicity of thermally induced formation of AgNPs from the reduction of Ag^{+} by HA was conducted [46]. The minimum inhibitory concentrations (MIC) of HA-coated AgNPs against Gram-positive (GP) and Gram-negative (GN) bacteria were determined [46]. Selection of two kinds of bacteria was based on their distinct toxic effects against GP and GN bacterial species. Figure 10.12 shows the comparison of naturally formed AgNPs (i.e., HA-coated AgNPs) with ENPs (poly vinylpyrrolidone coated silver nanoparticles (AgNPs-PVP) and sodium dodecyl sulfate coated silver nanoparticles (AgNPs-SDS) [10, 16, 46]. Differences in toxicity of AgNPs against GN bacteria from GP bacteria species could be seen in Fig. 10.12. ENPs (AgNPs-PVP and

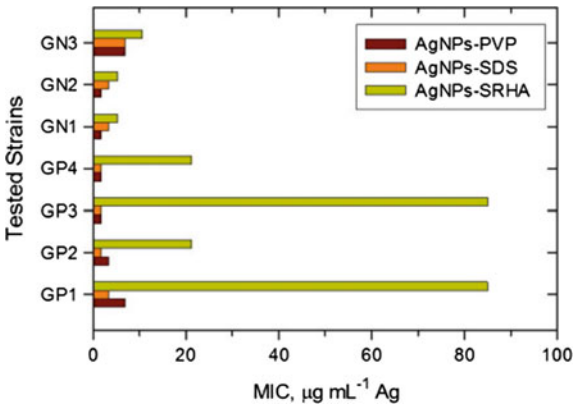

Fig. 10.12 Minimum inhibitory concentrations of engineered NPs (AgNPs-PVP and AgNPS-SDS) and natural AgNPs (AgNPs-SRHA) against Gram-positive (GP) and Gram-negative (GN) bacteria. *PVP* Poly vinylpyrrolidone; *SDS* Sodium dodecyl sulfate; *SRHA* Suwanee River humic acid; *GP1 Enterococcus faecalis* CCM 4224; *GP2 Staphylococcus aureus* CCM 3953; *GP3 Staphylococcus aureus* (MRSA); *GP4 Staphylococcus epidermidis* 1; *GN1 Pseudomonas aeruginosa* CCM; *GN2 Pseudomonas aeruginosa*; *GN3 Klebsiella pneumoniae* (ESBL). Adapted from [10] with the permission of the Royal Chemical Society

AgNPs-SDS) were more toxic than HA-coated AgNPs) (i.e., values of MIC were less in engineered AgNPs than MIC values obtained in naturally formed AgNPs). This difference in toxicity between ENPs and natural AgNPs was less pronounced for GN than GP species (Fig. 10.12). The organic coating produced on the AgNPs under conditions of natural environment may result in decreasing toxicity.

10.6 Conclusions

Several researchers have performed studies on the fate and behavior of the released engineered AgNPs into the environment in order to learn their health effects to humans and ecology. Comparatively, the formation and fate of naturally occurring AgNPs is rather sparse. AgNPs are formed by reduction of Ag^+ by NOM under thermal and photochemical conditions, followed by capping to ensure the stability of formed AgNPs. The surface-capped by NOM would be affected by pH, ions, and light. The interaction of naturally formed AgNPs, which are covered with bulky components of natural organic matter (NOM), with cell surface to cause toxicity is very likely different from the engineered AgNPs. The toxic mechanism may include the generation of ROS by AgNPs and direct and indirect damage to DNA by AgNPs and/or released Ag^+ ions. Genomic and proteomic approaches may be applied to comprehend ecotoxicological impacts of naturally formed AgNPs. Overall, more studies are needed to fully understand the formation and fate of

AgNPs under various environmental conditions (e.g., oxicic and anoxic) as well as their true toxic potential to ecological systems.

Acknowledgements V.K. Sharma and R. Zboril acknowledge the support by the Operational Program Research and Development for Innovations-European Regional Development Fund (CZ.1.05/2.1.00/03.0058). V.K. Sharma thanks the Program for the Environment and Sustainability.

References

1. Soenen SJ, Parak WJ, Rejman J, Manshian B (2015) (Intra)cellular stability of inorganic nanoparticles: effects on cytotoxicity, particle functionality, and biomedical applications. Chem Rev 115:2109–2135
2. Mu Q, Jiang G, Chen L, Zhou H, Fourches D, Tropsha A, Yan B (2014) Chemical basis of interactions between engineered nanoparticles and biological systems. Chem Rev 114:7740–7781
3. Bandyopadhyay S, Peralta-Videa JR, Gardea-Torresdey JL (2013) Advanced analytical techniques for the measurement of nanomaterials in food and agricultural samples: a review. Environ Eng Sci 30:118–125
4. Mohammadinejad R, Karimi S, Iravani S, Varma RS (2015) Plant-derived nanostructures: types and applications. Green Chem 18:20–52
5. Varma RS (2012) Greener approach to nanomaterials and their sustainable applications. Curr Opin Chem Eng 1:123–128
6. Rizzello L, Pompa PP (2014) Nanosilver-based antibacterial drugs and devices: mechanisms, methodological drawbacks, and guidelines. Chem Soc Rev 43:1501–1518
7. Stark WJ, Stoesset PR, Wohlleben W, Hafner A (2015) Industrial applications of nanoparticles. Chem Soc Rev 44:5793–5806
8. Philippe A, Schaumann GE (2014) Interactions of dissolved organic matter with natural and engineered inorganic colloids: a review. Environ Sci Technol 48:8946–8962
9. Quigg A, Chin WC, Chen CS, Zhang S, Jiang Y, Miao AJ, Schwehr KA, Xu C, Santschi PH (2013) Direct and indirect toxic effects of engineered nanoparticles on algae: role of natural organic matter. ACS Sustain Chem Eng 1:686–702
10. Sharma VK, Filip J, Zboril R, Varma RS (2015) Natural inorganic nanoparticles: formation, fate, and toxicity in the environment. Chem Soc Rev 44:8410–8423
11. Noubactep C, Caré S, Crane R (2012) Nanoscale metallic iron for environmental remediation: prospects and limitations. Water Air Soil Pollut 223:1363–1382
12. Sánchez A, Recillas S, Font X, Casals E, González E, Puntes V (2011) Ecotoxicity of, and remediation with, engineered inorganic nanoparticles in the environment. Trends Anal Chem 30:507–516
13. Zhang Y, Bai Y, Jia J, Gao N, Li Y, Zhang R, Jiang G, Yan B (2014) Perturbation of physiological systems by nanoparticles. Chem Soc Rev 43:3762–3809
14. Pati SS, Singh LH, Guimarães EM, Mantilla J, Coaquira JAH, Oliveira AC, Sharma VK, Garg VK (2016) Magnetic chitosan-functionalized Fe_3O_4@Au nanoparticles: synthesis and characterization. J Alloys Compd 684:68–74
15. Lohse SE, Murphy CJ (2012) Applications of colloidal inorganic nanoparticles: from medicine to energy. J Am Chem Soc 134:15607–15620
16. Panáček A, Kvítek L, Prucek R, Kolář M, Večeřová R, Pizúrová N, Sharma VK, Nevěčná T, Zbořil R (2006) Silver colloid nanoparticles: synthesis, characterization, and their antibacterial activity. J Phys Chem B 110:16248–16253

17. Sharma VK, Yngard RA, Lin Y (2009) Silver nanoparticles: green synthesis and their antimicrobial activities. Adv Colloid Interface Sci 145:83–96
18. Batley GE, Kirby JK, McLaughlin MJ (2013) Fate and risks of nanomaterials in aquatic and terrestrial environments. Acc Chem Res 46:I854–I862
19. Nadagouda MN, Iyanna N, Lalley J, Han C, Dionysiou DD, Varma RS (2014) Synthesis of silver and gold nanoparticles using antioxidants from blackberry, blueberry, pomegranate, and turmeric extracts. ACS Sustain Chem Eng 2:1717–1723
20. Virkutyte J, Varma RS (2011) Green synthesis of metal nanoparticles: biodegradable polymers and enzymes in stabilization and surface functionalization. Chem Sci 2:837–846
21. Alexander JW (2009) History of the medical use of silver. Surg Infect 10:289–292
22. Tang S, Wang M, Germ KE, Du HM, Sun WJ, Gao WM, Mayer GD (2015) Health implications of engineered nanoparticles in infants and children. World J Pediatr 11:197–206
23. Guo H, Zhang Z, Xing B, Mukherjee A, Musante C, White JC, He L (2015) Analysis of silver nanoparticles in antimicrobial products using surface-enhanced raman spectroscopy (SERS). Environ Sci Technol 49:4317–4324
24. Mitrano DM, Motellier S, Clavaguera S, Nowack B (2015) Review of nanomaterial aging and transformations through the life cycle of nano-enhanced products. Environ Int 77:132–147
25. Wigger H, Hackmann S, Zimmermann T, Köser J, Thöming J, von Gleich A (2015) Influences of use activities and waste management on environmental releases of engineered nanomaterials. Sci Total Environ 535:160–171
26. Lowry GV, Espinasse BP, Badireddy AR, Richardson CJ, Reinsch BC, Bryant LD, Bone AJ, Deonarine A, Chae S, Therezien M, Colman BP, Hsu-Kim H, Bernhardt ES, Matson CW, Wiesner MR (2012) Long-term transformation and fate of manufactured Ag nanoparticles in a simulated large scale freshwater emergent wetland. Environ Sci Technol 46:7027–7036
27. Krzyzewska I, Kyziol-Komosinska J, Rosik-Dulewska C, Czupiol J, Antoszczyszyn-Szpicka P (2016) Inorganic nanomaterials in the aquatic environment: behavior, toxicity, and interaction with environmental elements. Arch Environ Prot 42:87–101
28. Holden PA, Nisbet RM, Lenihan HS, Miller RJ, Cherr GN, Schimel JP, Gardea-Torresdey J (2013) Ecological nanotoxicology: Integrating nanomaterial hazard considerations across the subcellular, population, community, and ecosystems levels. Acc Chem Res 46:813–822
29. Sharma VK, Siskova K, Zboril R, Gardea-Torresdey J (2014) Organic-coated silver nanoparticles in biological and environmental conditions: Fate, stability and toxicity. Adv Colloid Int Sci 204:15–34
30. Ellis LJA, Valsami-Jones E, Lead JR, Baalousha M (2016) Impact of surface coating and environmental conditions on the fate and transport of silver nanoparticles in the aquatic environment. Sci Total Environ 568:95–106
31. Arturo Gómez-Caballero J, Guadalupe Villaseñor-Cabral M, Santiago-Jacinto P, Ponce-Abad F (2010) Hypogene Ba-rich todorokite and associated nanometric native silver in the San Miguel Tenango mining area, Zacatlán, Puebla, Mexico. Can Mineral 48:1237–1253
32. Wen LS, Santschi PH, Gill GA, Paternostro CL, Lehman RD (1997) Colloidal and particulate silver in river and estuarine waters of Texas. Environ Sci Technol 31:723–731
33. Gartman A, Findlay AJ, Luther GW (2014) Nanoparticulate pyrite and other nanoparticles are a widespread component of hydrothermal vent black smoker emissions. Chem Geol 366:32–41
34. Furtado LM, Bundschuh M, Metcalfe CD (2016) Monitoring the fate and transformation of silver nanoparticles in natural waters. Bull Environ Contam Toxicol 97:1–7
35. Akaighe N, MacCuspie RI, Navarro DA, Aga DS, Banerjee S, Sohn M, Sharma VK (2011) Humic acid-induced silver nanoparticle formation under environmentally relevant conditions. Environ Sci Technol 45:3895–3901
36. Adegboyega NF, Sharma VK, Siskova K, Zbořil R, Sohn M, Banerjee S (2013) Interactions of aqueous Ag^{+} with fulvic acids: mechanisms of silver nanoparticle formation and investigation of stability. Environ Sci Technol 47:757–764
37. Henglein A (1989) Non-metallic silver clusters in aqueous solution: stabilization and chemical reactions. Chem Phys Lett 154:473–476

38. Gentry ST, Fredericks SJ, Krchnavek R (2009) Controlled particle growth of silver sols through the use of hydroquinone as a selective reducing agent. Langmuir 25:2613–2621
39. Rose AL, Waite TD (2003) Kinetics of iron complexation by dissolved natural organic matter in coastal waters. Mar Chem 84:85–103
40. Rose AL, Waite TD (2003) Effect of dissolved natural organic matter on the kinetics of ferrous iron oxygenation in seawater. Environ Sci Technol 37:4877–4886
41. Rose AL, Waite TD (2003) Kinetics of hydrolysis and precipitation of ferric iron in seawater. Environ Sci Technol 37:3897–3903
42. Wilson SA, Weber JH (1977) A comparative study of number-average dissociation-corrected molecular weights of fulvic acids isolated from water and soil. Chem Geol 19:285–293
43. Struyk Z, Sposito G (2001) Redox properties of standard humic acids. Geoderma 102:329–346
44. Takesue M, Tomura T, Yamada M, Hata K, Kuwamoto S, Yonezawa T (2011) Size of elementary clusters and process period in silver nanoparticle formation. J Am Chem Soc 133:14164–14167
45. Kvítek L, Prucek R, Panáček A, Novotný R, Hrbáč J, Zbořil R (2005) The influence of complexing agent concentration on particle size in the process of SERS active silver colloid synthesis. J Mater Chem 15:1099–1105
46. Adegboyega NF, Sharma VK, Siskova KM, Vecerova R, Kolar M, Zboril R, Gardea-Torresdey JL (2014) Enhanced formation of silver nanoparticles in Ag^+–NOM–iron (II, III) systems and antibacterial activity studies. Environ Sci Technol 48:3228–3235
47. Jones AM, Pham AN, Collins RN, Waite TD (2009) Dissociation kinetics of Fe(III)- and Al (III)-natural organic matter complexes at pH 6.0 and 8.0 and 25 °C. Geochim Cosmochim Acta 73:2875–2887
48. Jones AM, Garg S, He D, Pham AN, Waite TD (2011) Superoxide-mediated formation and charging of silver nanoparticles. Environ Sci Technol 45:1428–1434
49. Rose AL, Waite TD (2002) Kinetic model for Fe(II) oxidation in seawater in the absence and presence of natural organic matter. Environ Sci Technol 36:433–444
50. Liu Z, Xie P, Ma J (2016) Aqueous photoproduction of Au nanoparticles by natural organic matter: effect of $NaBH_4$ reduction. Environ Sci Nano 3:707–714
51. Stamplecoskie KG, Scaiano JC (2012) Silver as an example of the applications of photochemistry to the synthesis and uses of nanomaterials. Photochem Photobiol 88:762–768
52. Sudeep PK, Kamat PV (2005) Photosensitized growth of silver nanoparticles under visible light irradiation: a mechanistic investigation. Chem Mater 17:5404–5410
53. Tselepis E, Fortin E (1986) Preparation and photovoltaic properties of anodically grown Ag_2O films. J Mater Sci 21:985–988
54. Wang W, Zafiriou OC, Chan IY, Zepp RG, Blough NV (2007) Production of hydrated electrons from photoionization of dissolved organic matter in natural waters. Environ Sci Technol 41:1601–1607
55. He D, Jones AM, Garg S, Pham AN, Waite TD (2011) Silver nanoparticle-reactive oxygen species interactions: application of a charging-discharging model. J Phys Chem C 115:5461–5468
56. Yin Y, Liu J, Jiang G (2012) Sunlight-induced reduction of ionic Ag and Au to metallic nanoparticles by dissolved organic matter. ACS Nano 6:7910–7919
57. Hou WC, Stuart B, Howes R, Zepp RG (2013) Sunlight-driven reduction of silver ions by natural organic matter: formation and transformation of silver nanoparticles. Environ Sci Technol 47:7713–7721
58. Adegboyega NF, Sharma VK, Cizmas L, Sayes CM (2016) UV light induces Ag nanoparticle formation: roles of natural organic matter, iron, and oxygen. Environ Chem Lett 14:353–357

59. Akaighe N, Depner SW, Banerjee S, Sharma VK, Sohn M (2012) The effects of monovalent and divalent cations on the stability of silver nanoparticles formed from direct reduction of silver ions by Suwannee River humic acid/natural organic matter. Sci Total Environ 441:277–289
60. El Badawy AM, Luxton TP, Silva RG, Scheckel KG, Suidan MT, Tolaymat TM (2010) Impact of environmental conditions (pH, ionic strength, and electrolyte type) on the surface charge and aggregation of silver nanoparticles suspensions. Environ Sci Technol 44:1260–1266

Chapter 11
Experimental Research into Metallic and Metal Oxide Nanoparticle Toxicity In Vivo

Boris A. Katsnelson, Larisa I. Privalova, Marina P. Sutunkova, Ilzira A. Minigalieva, Vladimir B. Gurvich, Vladimir Y. Shur, Ekaterina V. Shishkina, Oleg H. Makeyev, Irene E. Valamina, Anatoly N. Varaksin and Vladimir G. Panov

Abstract We studied purposefully produced silver, gold, iron oxide, copper oxide, nickel oxide, manganese oxide, lead oxide, and zinc oxide nanoparticles using two experimental models: (a) a single intratracheal (IT) instillation in low doses 24 h before the bronchoalveolar lavage to obtain a fluid for cytological and biochemical assessment; (b) repeated intraperitoneal (IP) injections during 6–7 weeks in non-lethal doses to assess the thus induced subchronic intoxication by a lot of functional and morphological indices and by the distribution and elimination of respective nanoparticles. Along with assessing the toxicity of these metallic nanoparticles (Me-NPs) acting separately, we also studied the same effects of some practically relevant Me-NP combinations. Besides, we carried out a 10-month inhalation experiment with an iron oxide (Fe_2O_3) nano-aerosol. We demonstrated that Me-NPs are much more noxious as compared with their fine micrometric counterparts although physiological mechanisms of their elimination from lungs proved highly active. At the same time, the in situ cytotoxicity, organ-systemic toxicity and in vivo genotoxicity of Me-NPs having a given geometry strongly depends on their chemical nature as well as on the specific mechanisms of action characteristic of a given metal. Even though being water-insoluble, Me-NPs are

B.A. Katsnelson (✉) · L.I. Privalova · M.P. Sutunkova · I.A. Minigalieva · V.B. Gurvich
The Ekaterinburg Medical Research Center for Prophylaxis and Health Protection in Industrial Workers, 30 Popov Str, Ekaterinburg 620014, Russia
e-mail: bkaznelson@etel.ru; bkaznelson@ymrc.ru

V.Y. Shur · E.V. Shishkina
School of Natural Sciences and Mathematics, The Ural Federal University, Ekaterinburg, Russia

O.H. Makeyev · I.E. Valamina
The Ural State Medical University, Ekaterinburg, Russia

A.N. Varaksin · V.G. Panov
The Institute of Industrial Ecology, The Ural Branch of the Russian Academy of Sciences, Ekaterinburg, Russia

B. Yan et al. (eds.), *Bioactivity of Engineered Nanoparticles*, Nanomedicine and Nanotoxicology, DOI 10.1007/978-981-10-5864-6_11

significantly solubilized in some biological milieus, and this process plays an important part in their biokinetics in vivo. In toto, Me-NPs are one of the most dangerous occupational and environmental hazards due to their cytotoxicity and genotoxicity, and therefore standards or recommended values of presumably safe Me-NP concentrations in the workplace and ambient air should be significantly lower as compared with those established for their micrometric counterparts. At the same time, the toxicity and even genotoxicity of Me-NPs can be significantly attenuated by background or preliminary administration of adequately composed combinations of some bioactive agents in innocuous doses.

Keywords Nanoparticles of metals and metal oxides · In vivo toxicity on cell · Organ-systemic and organism levels · Combined impacts · Safe exposure levels

11.1 Introduction

Nanoparticles (NPs) of metals and especially of their oxides are of special interest in the light of health risk assessment and management challenges because, along with engineered metallic NPs (Me-NPs),[1] there usually is a substantial fraction of

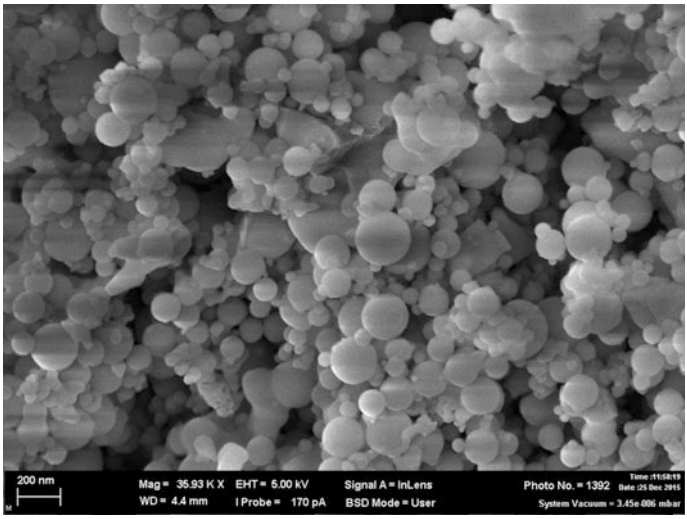

Fig. 11.1 Particles collected from emissions of an ore-thermal furnace for producing metallurgical grade silicon (SEM, magnification ×36,000)

[1]In this chapter, we use this term collectively for particles of elemental metals and of their oxides not only because many of the important mechanisms of their toxicity are similar but also taking into consideration that "most metal nanoparticles (NPs), except noble metal NPs, rapidly form a thin surface oxide in ambient conditions" [1].

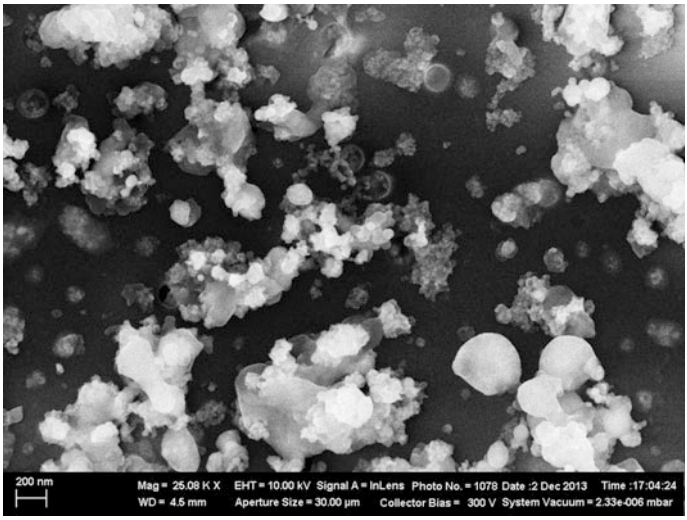

Fig. 11.2 Particles sampled from copper smelter workplace air (SEM, magnification ×25,080)

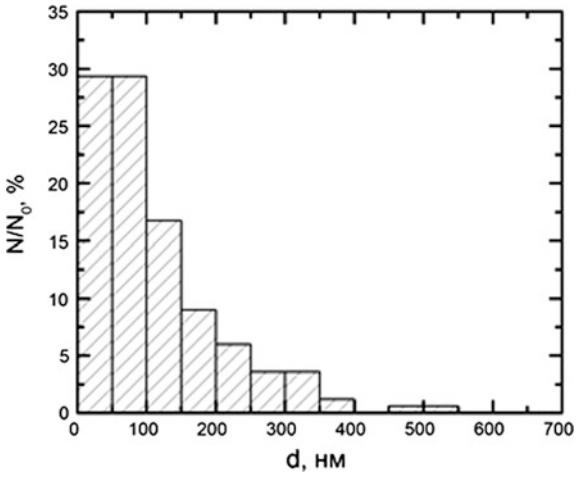

Fig. 11.3 Percentage distribution of submicron particles by size on filters sampled from the workplace air of a copper smelting and casting facility. *N* is the number of particles of a given diameter; No is the total number of particles (programmed statistical processing of 500 measurements). First published in [12]

nanoscale ("ultrafine") particles of the same substances in the particle size distribution of condensation aerosols generated by arc-welding and metallurgical technologies. Some examples illustrating this statement are given in Figs. 11.1, 11.2, 11.3 and 11.4.

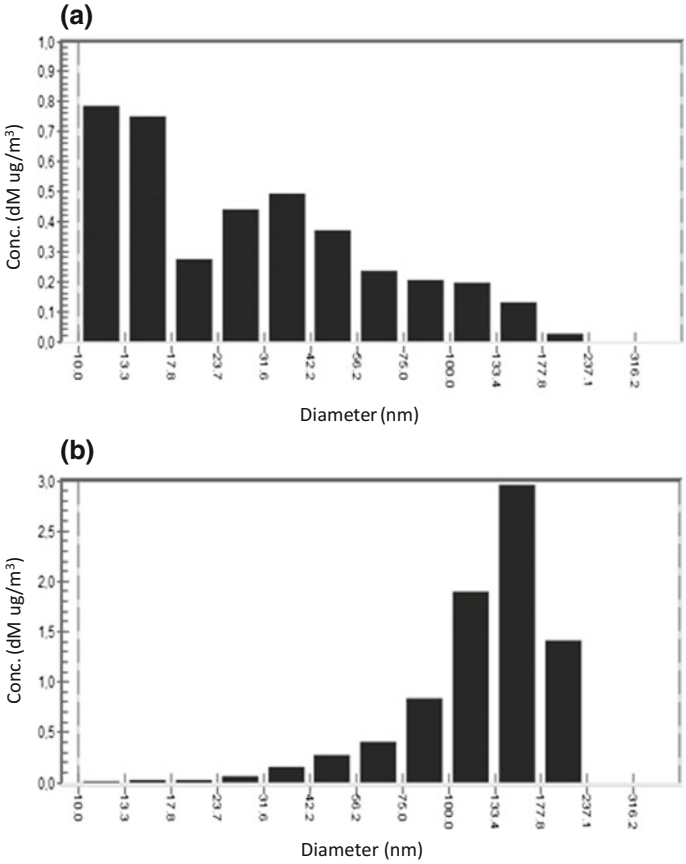

Fig. 11.4 Submicron particle size distribution as measured with a NANOSCAN SMPS 3910 in lead refinery workplace air **a** by number of particles per mL, **b** by mg per m^3

As can be seen from the same examples, however, such industrial aerosols contain micrometer particles (MPs) as well, including submicron ones measuring >100 nm, although their number is usually lower than that of <100 nm particles (Figs. 11.3 and 11.4a). It is true that these MPs can even prevail over NPs in the mass concentration of airborne particles but the contribution of the latter to this mass is, nevertheless, quite important (Fig. 11.4b). In such cases, the question is which fraction gives the most important input into worker's health risk: Me-MPs because they prevail in overall mass terms, or Me-NPs because they are presumably far more toxic per unit mass? To answer this important question in general terms it is necessary, first of all, to understand whether Me-NPs are always (or, at least, mostly) more dangerous compared to their micrometric and even submicron counterparts.

The situation becomes even more complicated if we take into consideration how rare in such industries the workroom air is polluted by particles of only one chemical composition. Indeed, most Me-NP-generating metallurgical and welding

technologies are bound to produce and do produce multi-component mixtures of chemically different particles of similar or dissimilar geometry. For instance, in arc-welding and alloyed steel making one usually finds different combinations of iron, chromium, nickel, manganese and silicon oxides in the form of NPs and MPs, while in crude copper smelting and refining—those of copper, lead, cadmium, zinc, and arsenic oxides.

Thus, solving some general problems in relation to Me-NPs that nanotoxicology faced from the very beginning of its evolution as a special branch of the toxicological science was not only theoretically challenging but also very urgent for the everyday practice of occupational health risks assessment and management.

The most important questions of this kind were as follows:

(1) Are Me-NPs recognized and dealt with by the organism's key defenses far less efficient compared with respective MPs, or was this widely proclaimed defenselessness just a fallacy of some experimental and theoretical works?
(2) Are Me-NPs really much more toxic than respective Me-MPs on both cellular and systemic levels?
(3) Is there a definite dependence of defense and adverse responses to Me-NP impacts on their dimensions within the conventional nanometer range?
(4) For a given nano-size, do these responses significantly depend on the chemical identity of Me-NP species and on some characteristics associated with it?
(5) When the human organism is being simultaneously or intermittently exposed to Me-NPs of different metals, are there any essential differences between their combined toxicity typology and that of the combined toxicity of respective metals in an ionic-molecular state?
(6) Last but not least, is it possible to protect the health of people exposed to either engineered or "spontaneous" Me-NPs by establishing low but still practicable permissible exposure levels and by enhancing organism's resistance to the especially high toxicity of Me-NPs?

In 2009–2016, our experimental work was focused on attempts to find answers to these questions [2–17].

In the vast nanotoxicological literature of the last decade, studies concerned with the assessment of Me-NP toxicity are quite numerous. To illustrate this, let us refer but to several works devoted to the same Me-NPs that were the subject-matter of our own studies considered in this chapter: iron oxides [18–27], silver [28–52], gold [33, 41, 53–65], copper and copper oxide [52, 66–75], nickel oxide [70, 76–80], manganese oxides [81–83], zinc oxide [84–88], lead oxide [89, 90]. It would be easy to notice, however, that the prevailing majority of these researchers assessed adverse effects of Me-NPs in vitro on stable cell lines while the in vivo studies were implemented mostly on small animals like daphnia or zebrafish larvae and only rarely on laboratory mammals.

No doubt, in vitro experiments feature a number of well-known advantages relating, in particular, to the analysis of primary toxicity mechanisms on cellular

and sub-cellular levels. At the same time, any extrapolation of the results of these experiments to the organism level and even the organ-systemic level is associated with a number of uncertainties and assumptions. Moreover, some important aspects (in particular¸ organism-level toxicokinetics, relationships between doses and systemic responses, the functioning, and efficiency of supracellular self-regulatory and protective mechanisms, etc.) can generally be addressed only through experiments on the whole mammalian organism.

Let us consider just one relevant example. In one of the earliest nanotoxicological studies, it was demonstrated that nano-sized manganese oxide particles induced dopamine depletion in cultured neuronal cells, similar to a free ionic manganese effect [81]. Later on, the same researchers showed that these NPs affected in vitro not only neuronal but also astrocyte cell lines [91]. Then Ngwa et al. [92] found, again in vitro, that manganese nanoparticles activated mitochondrial dependent apoptotic signaling and autophagy in dopaminergic neuronal cells.

The well-known specific neurotoxicity of manganese in different chemical forms renders these results (as well as similar data from other researchers) quite important, provided one is sure that under an in vivo impact of Mn-NPs these particles (or Mn-ions released by their solubilization, or the products of subsequent binding of these ions by metallothionein or by other proteins) really reach specific brain structures (in particular, *corpus striatum* and *hippocampus*) and, most importantly, provided factual damage to these structures and respective neurons has been demonstrated in animals under an Mn-NP in vivo exposure. As far as we know, it had not been done until we obtained such in vivo results for M_3O_4-NP subchronic intoxication [13].

We believe that such in vivo demonstration of any specific outcome of Me-NP toxicity should precede in vitro mechanistic studies, not vice versa, but in the relatively young field of nanotoxicology, this natural sequence of research was mostly inverted. Whatever explanation of this paradoxical reversal might be given, it is now a past history since in recent years in vivo nanotoxicology of metals has regained its course, and there is growing recognition that a synthesis of both approaches as complementary ones is necessary. Although different researchers usually tend to employ one of them depending on what expertise they may have gained or equipment and knowhow available to them, still such synthesis should be achieved through information exchange and coordination of collaborative effort.

Starting from the very first nanotoxicological work carried out in 2008–2009 [2–4] up until now, our team has been conducting only in vivo animal experiments involving Me-NPs and has thus accumulated a certain wealth of relevant knowledge, so we believe that this chapter, summarizing mostly our own experience, may be of interest as a contribution to this synthesis. That is why it is largely a self-overview with occasional references to other researchers' results, mostly for discussion's sake.

11.2 Preparation and Characterization of Me-NPs for Toxicological Experiments

We experimented with NPs of various compositions and sizes: (i) iron oxide Fe_3O_4 (magnetite) with a mean diameter of 10, 50 nm and 1 μm, (ii) gold, (4 and 50 nm), (iii) silver, (4, 49 nm and 1.1 μm), (iv) copper oxide CuO (20 and 340 nm), (v) nickel oxide NiO (30 nm), (vi) manganese oxide Mn_3O_4 (32 nm), (vii) zinc oxide ZnO (25 nm), and (viii) lead oxide PbO (62 nm).

Keeping in mind the theoretical premises and practical implications of our research outlined in the Introduction, we used accurately prepared and characterized water suspensions of NPs of pure metals and their oxides rather than commercial nanomaterials. Only magnetite NPs were synthesized chemically [2–4]. All other NPs were produced by laser ablation in liquid. According to this method, a target of pure metal was ablated in deionized water by a focused beam from a fiber laser. The process was followed, where necessary, by laser beam fragmentation for improving the suspension stability and by partial water evaporation for concentrating the suspension to a level convenient for toxicological purposes.

The laser ablation yields the partial surface oxidation of the generated metal nanoparticles with the consequent attraction of hydroxyl ions from water, which generally yields a partially negative surface charge. The charged nanoparticles are dispersed in water, attract counter ions [O^+] and form an electrical double layer. The most critical criterion for colloidal stability is whether the electrical double layer extends far enough to keep the nanoparticles at the appropriate distance and prevent their aggregation and agglomeration. In our experience, with laser ablation technique it is quite often so.

11.2.1 NP Production

The suspensions of NPs were produced by laser ablation of metal targets (99.99% purity, 1-mm thick) placed on the bottom of a glass vessel with 5–30 mL of deionized water (Fig. 11.5). The laser system used was a Fmark-20RL (LTC, Russia) device based on an Yb fiber laser with a wavelength of 1080 nm, pulse duration of 100 ns, pulse energy of 1 mJ, and a repetition rate of 21 kHz. The target's surface, cleaned with deionized water in an ultrasonic bath, was irradiated by a spot of laser irradiation with a fixed diameter of 40 μm and a fluence ranging from 15 to 80 J/cm^2. The thickness of the water layer covering the target ranged from 2 to 10 mm. The scanning velocity was about 270 mm/s, and the scanned area ranged from 25 to 300 mm^2. A motor-driven agitator was used to reduce the scattering of the laser beam on cavitation bubbles and to remove the ablated nanoparticle cloud from the irradiated area during ablation. The duration of the ablation process ranged from 1 to 60 min. The value of the ablated mass was

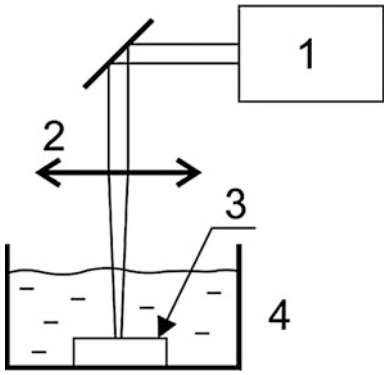

Fig. 11.5 Diagram of laser ablation in liquid: *1*—laser, *2*—focusing lens, *3*—metal target, *4*—cuvette with deionized water

measured by weighing the target before and after ablation using an analytical balance, ME 235 S (Sartorius).

This technique provides suspensions with a sufficiently narrow NP size distribution, and although singlet Me-NPs always tend to stick together, the resulting aggregates are usually loose and rather small (examples are shown in Figs. 11.6 and 11.7). These suspensions are highly stable, maintaining their characteristics without any significant increase in particle aggregation over periods sufficient for carrying out experiments as described below. In no experiment did we add any chemical stabilizer to the suspension; however, in experiments with some Me-NPs we had to use an ultrasonic dispersion of the suspensions just before instillations or injections to split NP aggregates.

Suspension stability was characterized by the value of Zeta potential as measured by means of electrophoretic light scattering with the help of a Zetasizer

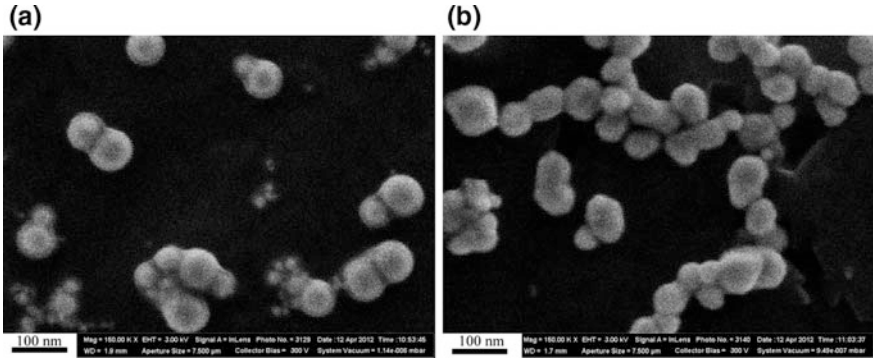

Fig. 11.6 Typical SEM images of NPs obtained by laser ablation in water: **a** gold, **b** silver. First published in [8]

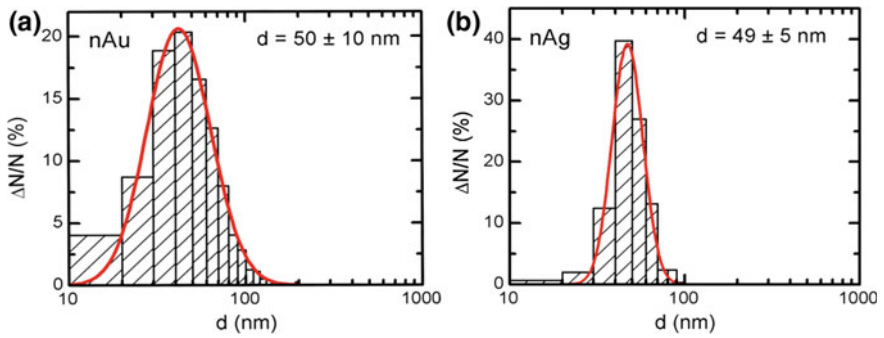

Fig. 11.7 Size distribution functions of noble metal NPs in the suspensions shown in Fig. 11.6. Results of statistical analysis of SEM images: **a** gold (800 NP images) and **b** silver (650 NP images). First published in [8]

Nano ZS analyzer (Malvern, UK). The high suspension stability achieved (Zeta potential up to 42 mV) allowed us to increase the concentration of NPs by partial water evaporation at 50 °C on a heat plate. The suspensions, with a concentration of 0.5 g/L, remained stable without any appreciable change in the NP size distribution and chemical composition.

The size distribution function of the NPs was measured by two methods, firstly, dynamic light scattering (DLS) using a Zetasizer Nano ZS, and, secondly, statistical analysis of high-resolution images obtained with a scanning electron microscope (SEM), CrossBeam Workstation Auriga (Carl Zeiss, Germany).

The elemental composition of the NPs was measured by energy dispersive X-ray analysis using a CrossBeam Workstation Auriga SEM equipped with an X-ray detector X-Max (Oxford, UK) at an accelerating voltage of 5 kV with averaging over an area of 100 × 100 μm^2.

The chemical composition of NP surface layer was analyzed by recording the Raman spectra with a confocal Raman microscope, Alpha 300 AR WiTec+ (WiTec GmbH, Germany) under irradiation by a solid state laser with a wavelength of 488 nm.

It should be noted that although laser ablation in liquid yields NPs with various non-spherical geometries, such as needle, spindle, and discus, we always chose a technological regime that provided near-spherical NP shapes. There were two reasons for this choice. Firstly, according to our experience, primary metal and metal oxide NPs in industrial condensation aerosols are mostly spherical or ovoid. Secondly, in order to ensure that comparative experiments reveal the dependence of Me-NP toxicity on their size, chemical composition or solubility, their shape (assuming that it also has a role to play) had to be constant. However interesting it could be to find out whether NP shape is indeed an important toxicity factor, this would require a special comparative study in which all other relevant characteristics of NPs should be fixed.

11.2.2 Solubility

The solubility of NPs in deionized water and biological liquids, including bronchoalveolar lavage fluid (BALF) supernatant, blood serum, normal saline, was studied using electron paramagnetic resonance spectroscopy (EPR) for paramagnetic NPs (Fe_3O_4, Mn_3O_4, NiO) and optical spectrometry by means of an Agilent Cary 5000 (Agilent Technologies, USA) spectrophotometer for other NPs (Au, Ag, CuO, ZnO, PbO).

We used two experimental protocols for solubility measurements. For paramagnetic NPs, the filters with NPs were placed into the liquid studied and then taken out and examined by EPR at certain time intervals. For non-paramagnetic NPs, the liquid studied was added to the original water suspension of NPs in a one-to-one ratio. At certain time intervals, transmission optical spectra were recorded after short-term ultrasonic dispersion. Relative changes in the integral intensity of the EPR spectra or in the integral of the optical absorption in a spectral range from 400 to 800 nm provided information on NP solubility in time.

11.2.3 Determination of Tissue Metal Content

The total metal content of liver, kidneys, spleen and brain samples from NP-exposed rats was measured using an atomic emission spectrometer with inductively coupled plasma, iCAP 6500 Duo (Thermo Fisher Scientific, USA). The samples of freeze-dried homogenized tissue were subjected to acid ignition by means of a MARS 5 Microwave Accelerated Reaction System.

Paramagnetic metals (Fe_3O_4, Mn_3O_4, NiO) were also studied by the EPR method using an electron paramagnetic resonance spectrometer, EMX Plus Bruker (Bruker, Germany). This method enabled us to measure the metal contents in the form of NPs.

The impact of NPs on alveolar macrophages in vivo was studied by Atomic Force Microscopy (AFM) and Transmission Electron Microscopy (TEM).

NP phagocytosis was found to lead to changes in the cell surface morphology in the nanoscale. The “pits” on cell surfaces revealed by AFM had diameters close to those of the NPs studied. It should be noted that such pits were virtually absent on the reference cells.

The localization of NPs in the rat tissue samples and ultrastructural damage associated with them were revealed by scanning transmission electron microscopy.

11.3 General Design of Animal Experiments

All experiments were carried out on outbred white female rats from our own breeding colony with an initial body mass of 150–220 g, with a minimum of 12 animals in different exposed and control groups. Rats were housed in conventional

conditions, breathed unfiltered air, and were fed standard balanced food. The experiments were planned and implemented in accordance with the "International guiding principles for biomedical research involving animals" developed by the Council for International Organizations of Medical Sciences (1985) and approved by the Committee on Ethics of the Ekaterinburg Medical Research Center for Prophylaxis and Health Protection in Industrial Workers.

11.3.1 Experimental Modeling of Immediate Pulmonary Responses

As a rule, a single intratracheal (i.t.) instillation of 1 mL of Me-NP or Me-MP water suspension (or of sterile deionized water from the same batch, without any particles) served as an experimental model for the response of the lower airways to particle deposition. It is well known that important qualitative and quantitative patterns of the response displayed by the pulmonary free cell population (in particular, its dependence on the cytotoxicity of deposited particles) observed in inhalation exposures to different mineral dust MPs are essentially the same as in the case of their i.t. administration. As for Me-NPs, we saw the same homology when comparing the pulmonary responses to the i.t. instillation and low-level inhalation exposures of Fe_2O_3-NPs in a nose-only inhalation chamber [17].

At the same time, the i.t. model provides cellular material for assessing the in vivo phagocytic activity of pulmonary macrophages and polymorphonuclear leukocytes, as well as intracellular localization of Me-NPs engulfed by them and ultrastructural damage caused to the cell by those NPs. The results thus obtained may be compared with the data reported by researchers experimenting with NP-exposed cell cultures, being a valuable addition to the latter because in vivo interaction between cells and particles occurs in a microenvironment which is not completely reproducible by artificial cell culture media and, besides, under the influence of many direct and feedback cellular interactions.

A cell population of bronchoalveolar lavage fluid (BALF) obtained 24 h after intratracheal instillation of NP or MP suspensions to rats was studied with optical (OM), transmission electron (TEM) and semi-contact atomic force microscopy (sc-AFM).

11.3.2 Experimental Modeling of Subchronic Me-NP Intoxications

The subchronic toxicity of the Me-NPs used in our study was investigated by means of repeated intraperitoneal (i.p.) injections of the same suspensions in sub-lethal doses 5 times a week during 5–7 weeks. This approach to modeling systemic intoxication (which in real conditions can be induced by long-term exposure of

humans to NPs, either inhaled, or engulfed with contaminated water and food, or absorbed through the skin) needs some justification. It is well known that "nanoparticles deposit with high efficiency in the entire respiratory tract, from the head airways to the alveoli, due to diffusion" [93]. For instance, the widely used Human Respiratory Tract Model (HRTM) of the International Commission of Radiological Protection (ICRP) [94, 95] predicts 100% total deposition of 0.001 μm (i.e., I nm) and ~90% for 0.01 μm (i.e., 10 nm) particles for a normal mouth-breathing adult male human subject. There are, however, various anatomical, functional and aerodynamic differences between human and rodent airways suggesting the possibility of interspecies distinctions in regional particle deposition and, thus, in the kinetics of their elimination from the airways to the GIT and/or their absorption. Thus the authors of a comprehensive review of nanotoxicological assessment techniques [96] maintain that "rodents, the commonly used species for toxicology testing, are … not representative models for human respiratory inhalation exposure." In other words, NP inhalation by laboratory rodents is not as ideal a model of real human exposures as it is often deemed to be.

The intraperitoneal animal model circumvents these interspecies differences in inhaled NP deposition, being adequate enough when one wants to look into the body distribution and elimination of Me-NPs, and into organism's reactions to Me-NPs *after* they have penetrated into the blood—directly under a "natural" exposure such as mentioned above or from a primary deposit—as well as to metal ions released as a result of Me-NP dissolution. Like any model (a necessary simplification of a complicated system deliberately omitting some sub-systems and some material or informational flows and feedbacks), it has both drawbacks and virtues. One of the latter is the fact that dosing by injection is much more accurate, reliable and reproducible compared with the more "natural" experimental methods. This consideration is crucial for experiments of comparative design, such as ours. Intraperitoneal modeling of subchronic intoxications is well known and recognized in general experimental toxicology. Moreover, it has been used by other researchers as well, just in experimental nanotoxicological studies ([97, 98] and others).

After the exposure period, the following was performed for both exposed and sham-exposed (control) rats: body weighing; estimation of the CNS ability to perform temporal summation of sub-threshold impulses in a variant of the withdrawal reflex and its facilitation by repeated electrical stimulations in an intact, conscious rat [99]; recording of the number of head dips into the holes of a hole-board, which is frequently used for studying the behavioral effects of toxicants and drugs (e.g. [100, 101]); collection of daily urine for analysis of its density, urine output, and coproporphyrin, delta-aminolevulinic acid (δ-ALA), creatinine and relevant toxic element contents.

Then the rats were sacrificed by decapitation and their blood was collected by exsanguination. The liver, spleen, kidneys, and brain were weighed. The blood biochemical indices studied usually included total serum protein, albumin, globulin, triglycerides, cholesterol, high and low density lipoproteins, bilirubin, ceruloplasmin, reduced glutathione (GSH), malonyldialdehyde (MDA), alkaline phosphatase, alanine- and asparate-transaminases (ALT, AST), catalase, gamma glutamyl

transferase, creatinine, and, in some experiments, also thyrotropic hormone of hypophysis, thyroxin, and triiodothyronine, follicle-stimulating and luteinizing hormones, progesterone, dehydroepiandrosterone, estradiol, and neuron-specific enolase. We used an MYTHIC-18 auto-hematology analyzer for determining the hemoglobin content, hematocrit, thrombocrit, mean erythrocyte volume, and RBC, WBC and thrombocyte counts. The proportion of reticulocytes was counted using the routine technique. Cytochemical determination of succinate dehydrogenase (SDH) activity in lymphocytes was based on the reduction of nitrotetrazolium violet to formazane, the number of granules of which in a cell was counted under immersion microscopy. Genomic DNA fragmentation was assessed in cells of several tissues using the RAPD test.

In all experiments, histological changes were described and estimated morphometrically in the liver, spleen, and kidneys; and additionally in the brain in the experiments with copper manganese and nickel oxide NPs and in rat lungs after chronic inhalation exposure to iron oxide NPs. Thin sections of different organs were prepared for histological examination by hematoxilin-eosine stain and, where necessary, PAS, Nissl and Perl's stains. We used a planimetric ocular grid for the morphometry of the spleen and an image recognition programmed system for that of the liver, kidneys, and brain.

The total number of quantitative indices the shifts in which served as indicators of Me-NP effect on the organism thus amounted to 30–50.

The metal content of the liver, spleen, kidneys, and brain was determined by atomic emission or atomic absorption spectrometry (AES, AAS) and, for iron, nickel, manganese oxide particles, also by the electron paramagnetic resonance (EPR) method.

11.4 The Most Important Features of Metallic Nanoparticle In Vivo Bioactivity

In this section, we propose to summarize and discuss the main results of our research in light of the first five questions suggested in the Introduction, starting from the one that was and still is the most disputable and, on the other hand, one of the most important.

11.4.1 Are Metallic Nanoparticles Recognized and Dealt with by the Organism Worse, as Efficiently as, or Even Better than Respective Microparticles?

The practical implications of this theoretical question would hardly need any explanation. Indeed, if the physiological defenses against Me-NPs are of low

effectiveness, one should assume that any non-harmful levels of exposure to them would, in principle, be hardly feasible. In other words, it would be impossible to establish safe (permissible) exposure levels for nanoparticles in the environment.

At the beginning of the "nanotoxicological boom," many reputed authors (for instance [102, 103]) maintained that the physiological protective mechanisms enabling animals and humans to exist in an atmosphere unavoidably polluted with suspended particles of a wide range of sizes and chemical compositions are, for whatever reasons, less than effective in relation to airborne NPs. It was thought, specifically, that NPs deposited in the pulmonary region are not efficiently phagocytized by alveolar macrophages (AMs) due either to the inability of these cells to recognize the finest particles or to the failure of the latter to generate a chemotactic signal at the site of their deposition. For instance, a top ranking group of experts [103] maintained that "very small particles … may not be detected by the normal phagocytic defenses." Even seven years later, a comprehensive review on the interaction of engineered NPs with the immune system presented this problem as still unresolved: "Macrophages engulf microbes and apoptotic debris, but the question is: are nanoparticles recognized by phagocytes or do such particles fly under the radar and escape immune recognition?" [104].

We started off our own research into this field [2] with some criticism of the research data seemingly corroborating those pessimistic views and with skepticism based on evolutionary considerations. We stressed that terrestrial vertebrates had to inhale ultrafine nanoscale particles (such as volcanic ash, airborne particles of dispersed seawater, forest fire smoke, sulfates generated in the atmosphere as a result of sulfur dioxide oxidation) for as long as they inhaled fine MPs. We reminded that the main physiological mechanisms of pulmonary clearance (engulfment of particles by phagocytes and their removal by the so-called mucociliary transport) had been present already in the amphibians [105], that is even before the morphological structuring of the lungs was complete. We maintained that it would be difficult to understand why these ancient defenses, highly efficient in relation to MPs, should have been selected and fixed by the Evolution had they been ineffective in relation to NPs against which a defense is even more necessary since they are presumably more noxious (see Sect. 11.4.2).

From the very first experiment, however, our data suggested that the organism is not defenseless when confronted with Me-NP exposures. In particular, we have found that the pulmonary phagocytosis response to the deposition of Me-NPs is quite potent. In several experiments, it was found that, given equal mass doses and identical chemical composition, NPs induced more intensive recruitment of phagocytes, manifested as an increased cell count in the BALF, than respective MPs. One example illustrating this is given in Table 11.1.

Moreover, such recruitment and, especially, increase in the neutrophil leukocyte (NL) to alveolar macrophage (AM) ratio in the BALF cell count is more pronounced, the smaller the particle *within* the nanoscale range as illustrated by Fig. 11.8.

The recruitment of neutrophil leukocytes (NL) towards the lower airways in response to the deposition of cytotoxic particles, including nanoscale ones, (e.g.

Table 11.1 Number of cells in the bronchoalveolar lavage fluid (BALF) 24 h after intratracheal instillation of silver nano- or microparticles to rats at a dose of 0.2 mg per rat ($x \pm$ s.e)

Substance administered i. t.	Number of cells $\times 10^6$			NL/AM
	Total	Alveolar macrophages (AM)	Neutrophil leukocytes (NL)	
Ag-NP (49 nm)	4.25 ± 0.77*°	1.16 ± 0.14	2.99 ± 0.71*°	2.47 ± 0.33*°
Ag-MP (1.1 μm)	1.99 ± 0.25	1.24 ± 0.19	0.73 ± 0.15*	0.66 ± 0.13*
Water (controls)	1.41 ± 0.33	0.89 ± 0.18	0.13 ± 0.04	0.14 ± 0.023

Note Statistically significant difference *from control group; °from microsilver group ($P < 0.05$ by Student's t-test)

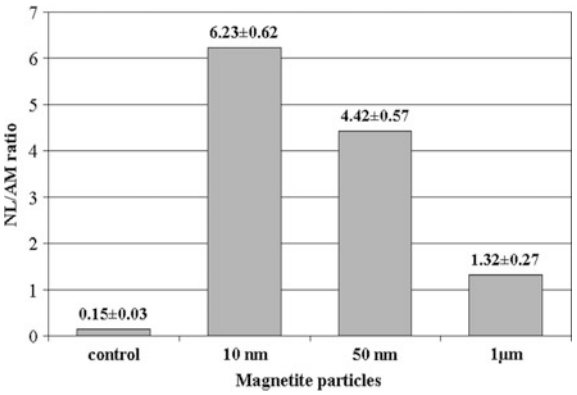

Fig. 11.8 The ratio of the number of neutrophil leukocytes (NL) to the number of alveolar macrophages (AM) in the BALF of rats 24 h after the instillation of magnetite particles of different sizes at a dose of 2 mg in 1 mL of distilled water ($x \pm s_x$)

[106–110]) has been traditionally described as "inflammation" caused by such particles without discussing or even mentioning the role these cells play in pulmonary particle clearance. Meanwhile, there are fairly strong reasons for considering this recruitment, even if it is indeed one of the acute inflammation components, as an important mechanism of partial functional compensation for the damage caused by cytotoxic particles to AMs, the main effector of low-soluble particle pulmonary clearance. A multi-compartmental mathematical model of pulmonary region clearance incorporating this compensatory mechanism was developed and identified by [111–115]. This model simulated very well experimental data on the retention of virtually insoluble dust particles of varying degrees of cytotoxicity (quartzite rock, titanium dioxide, standard quartz DQ12) in the lungs under long-term inhalation exposures and the decrease in this retention under the effect of such potent protector of the macrophage against particle cytotoxicity as glutamate.

Recently we have successfully adjusted it [17] to the results of a long-term experiment with a low-level inhalation exposure to 14 nm Fe_2O_3-NPs, although in this case we had to include into this model additional elimination flows associated

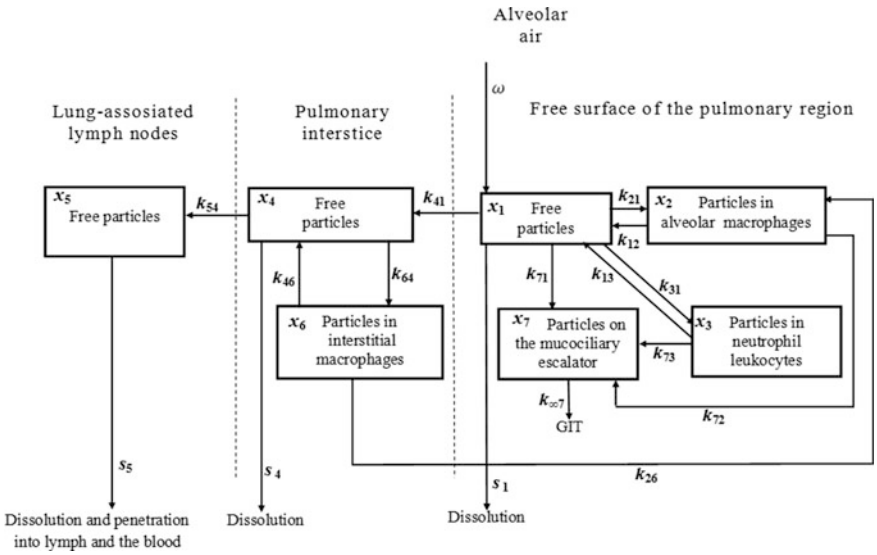

Fig. 11.9 Structure of the multi-compartmental model for the kinetics of retention and elimination of Fe_2O_3-NPs deposited in the pulmonary region of the lung, where: ω is a function of particle deposition in the pulmonary region, k_{ji} is a rate constant of particle translocation from compartment x_i into compartment x_j, s_i is an NP dissolution rate constant. The *dotted lines* are conventional boundaries between anatomical regions. First published in [17]

with NP solubilization rather than with the physiological mechanisms under consideration (Fig. 11.9).

Many other data obtained in our experiments with Me-NPs also demonstrate that the enhanced NL recruitment, be it a manifestation of inflammation or a normal physiological pulmonary particle clearance mechanism, plays an important part in this cleaning process. It should be stressed that both types of recruited phagocytes engulf NPs much more avidly compared with MPs of the same chemical nature, and the smaller the diameter of the particles, the more active their phagocytosis by these cells. We illustrate these relationships with an example of Fe_3O_4 (magnetite) MPs and NPs of various diameters (Fig. 11.10).

Semi-contact Atomic Force Microscopy (sc-AFM) reveals multiple "pits" on the surfaces of both AMs and NLs, their diameter being bigger, the bigger the particle (see Fig. 11.11). At the same time, the smaller the particle, the higher the surface concentration of these pits (Fig. 11.12). We consider the pits to represent fixed moments of cell membrane invagination at the first stage of active particle endocytosis rather than mere "footprints" of particles passively penetrating through the cell membrane and leaving a hole in it. Indeed, although the mean diameter of these pits correlates with that of i.t. instilled NPs, the former is not equal to but usually greater or smaller than the latter. For instance, under exposure to 49 nm silver particles and 50 nm gold particles, the average diameter of the pits was 75.2 ± 0.3 and 77.6 ± 1.5 nm, respectively [8].

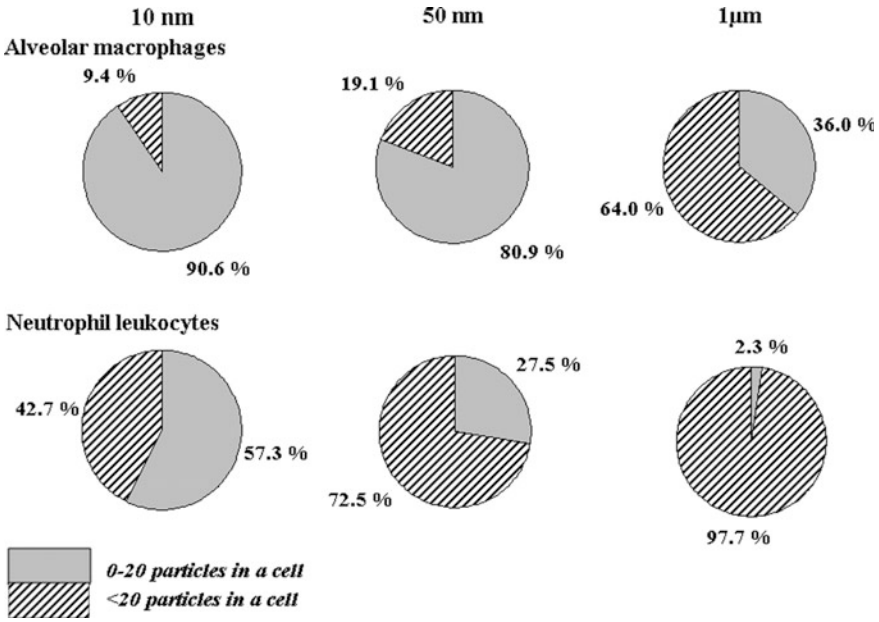

Fig. 11.10 Percentages of phagocytic cells with different particle burdens in rat BALF 24 h after an i.t. instillation of Fe_3O_4 particles having different diameters

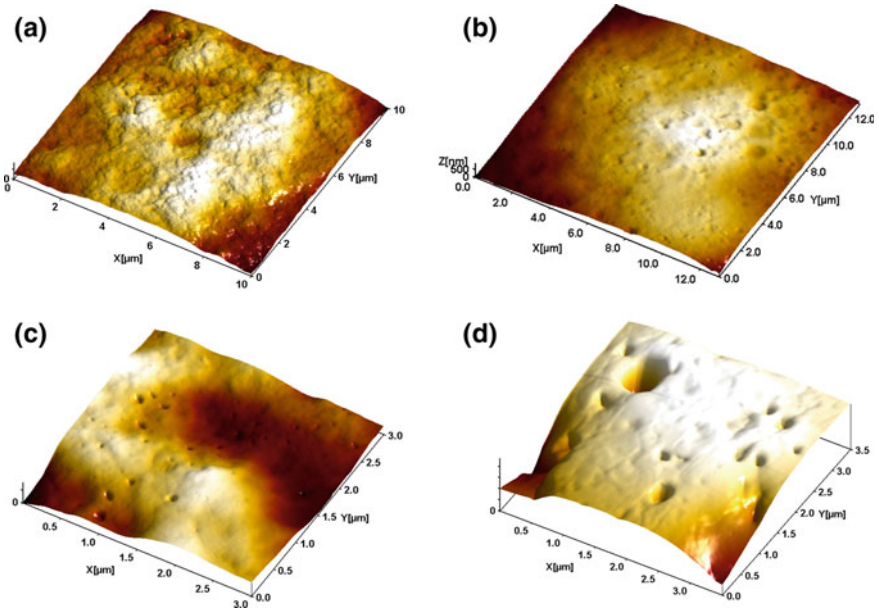

Fig. 11.11 Alveolar macrophage surface topography visualized by semi-contact AFM **a** control; **b** after instillation of 10 nm Fe_3O_4-NPs; **c** after instillation of 50 nm Fe_3O_4-NPs; **d** after instillation of 1 µm Fe_3O_4-MPs

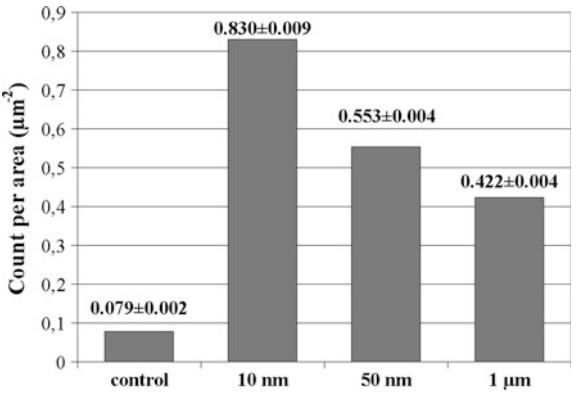

Fig. 11.12 Average ($x \pm$ s.e.) surface concentration of pits of all transverse dimensions detected on the surfaces of cells in each group of rats administered Fe_3O_4 particles of different diameters and in control rats

The transmission electron microscopy (TEM) images [6] revealing the formation of phagosomes with centrally located one or several NPs in the vicinity of the cell membrane (Fig. 11.13) also testify to the physiological endocytosis of nanoparticles by AMs as opposed to their direct penetration through the cell membrane by diffusion.

The latter mechanism is, however, also possible, and even probable, for the smallest Me-NPs. Our systemic model of pulmonary particle toxicokinetics (Fig. 11.9) describes exactly such diffusion by presumably passive NP transfer from compartment *X1* to compartment *X4* with transfer rate constant k_{41}. However, in real lungs this transfer through the alveolar membrane involves temporary internalization of particles by alveolocytes forming this membrane. Indeed, the TEM images (Fig. 11.14) did reveal such internalization in rats exposed inhalationally to 14 nm Fe_2O_3-NPs [17].

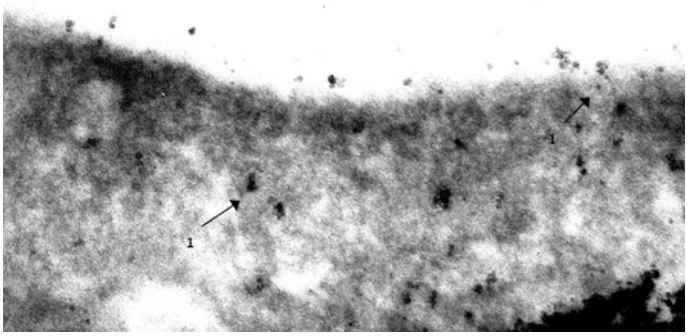

Fig. 11.13 Engulfment of 10 nm magnetite particles by an AM (phagosomes—*arrows 1*). TEM, magnification ×140,000

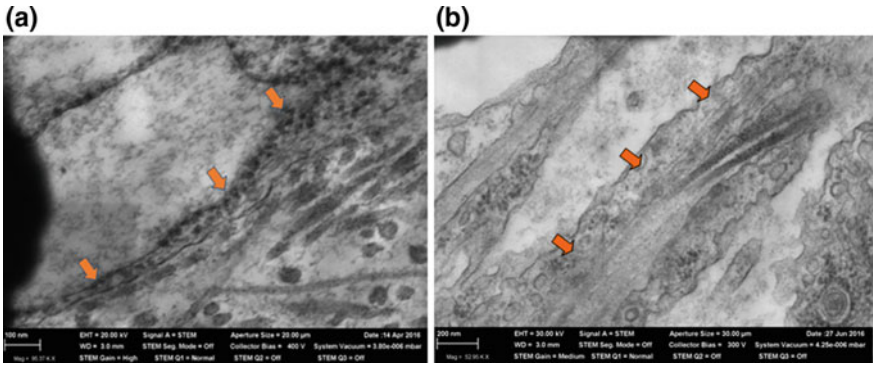

Fig. 11.14 Type I alveolocytes (pointed by *arrows*) in the lung of: **a** a rat after 6-month inhalation exposure to Fe_2O_3-NPs (1.09 ± 0.10 mg/m^3, 4 h a day, 5 days a week) with a lot of internalized NPs (TEM, magnification ×95,370); **b** a sham-exposed rat without discernible NPs (TEM, magnification ×52,950). First published in [17]

For a given size of Me-NPs, the pulmonary phagocytosis response strongly depends on their chemical nature. For instance, as can be seen from Table 11.2, the total cell, NL and AM counts of the BALF increased more in response to silver NPs than to virtually equidimensional gold NPs. A similar dependence of both AM and NL recruitment on the chemical nature of NPs was shown in a comparative experiment with nano-suspensions of NiO and Mn_3O_4 [9] or with CuO, PbO, and ZnO (Table 11.2) [116].

Judging from the sc-AFM images, nanosilver particles were engulfed by phagocytic cells twice more avidly than nanogold ones since the average number of invagination "pits" per square micrometer was 18.0 and 9.0, respectively [8]. The TEM images show that the intracellular distribution of the internalized silver and gold NPs was also different, the most significant difference being a more pronounced affinity of Ag-NPs for mitochondria and their lesser ability to penetrate into cell nuclei as compared with Au-NPs (Figs. 11.15 and 11.16) [8].[2]

In another experiment, we compared responses to i.t. instillation of 20 nm CuO-NPs or of submicron (340 nm) particles of elemental Cu covered with a layer of Cu_2O and found again that NPs evoked a more significant recruitment of NLs compared with MPs even of submicron diameters ($9.41 \pm 2.01 \times 10^6$ and $3.64 \pm 0.90 \times 10^6$, respectively, the control value being $0.05 \pm 0.01 \times 10^6$). The respective NL/AM ratio values were 4.76 ± 1.39, 1.39 ± 0.16 and 0.06 ± 0.01. Semi-contact AFM again revealed pits on the cell surface (Fig. 11.17) with an

[2]The most probable explanation of this fact is that particles which are more cytotoxic for AMs due to a smaller diameter (as in the abovementioned case of Fe_3O_4—see Fig. 11.5) or to a specific chemical nature (as in case of nanoAg vs. nanoAu) produce a higher mass of the macrophage breakdown products which as we demonstrated long ago [113] stimulate dose-dependently the macrophageal phagocytosis. Let us remind that the more avid is the latter, the higher surface concentration of plasma membrane invaginations (i.e., of "pits").

Table 11.2 Number of cells in the bronchoalveolar lavage fluid (BALF) 24 h after intratracheal instillation of suspension of equidimensional Me-NPs of different chemical nature to rats at a dose of 0.2 mg per rat ($x \pm$ s.e.)

Substance administered	Number of cells $\times 10^6$			NL/AM
	Total	Alveolar macrophages (AM)	Neutrophil leukocytes (NL)	
Comparing nanoparticles of silver and gold				
Ag-NP	4.25 ± 0.77	1.16 ± 0.14	2.99 ± 0.71*	2.47 ± 0.33*
Au-NP	2.30 ± 0.93$^{\bullet}$	0.94 ± 0.09	0.63 ± 0.15*$^{\bullet}$	0.63 ± 0.13*$^{\bullet}$
Water (controls)	1.41 ± 0.33	0.89 ± 0.18	0.13 ± 0.04	0.14 ± 0.02
Comparing nanoparticles of copper, lead, and zinc oxides				
CuO-NP	2.10 ± 0.36	1.54 ± 0.28	0.69 ± 0.24*	0.49 ± 0.17*
PbO-NP	3.49 ± 0.54*	1.88 ± 0.30	1.62 ± 0.37*	0.96 ± 0.24*
ZnO-NP	4.57 ± 0.72*	2.21 ± 0.36	2.36 ± 0.60*	1.25 ± 0.38*
Water (control)	1.40 ± 0.07	1.30 ± 0.07	0.09 ± 0.03	0.08 ± 0.02

Note Statistically significant difference *from the respective control group; $^{\bullet}$Au-NP group from Ag-NP group ($P < 0.05$ by Student's t-test)

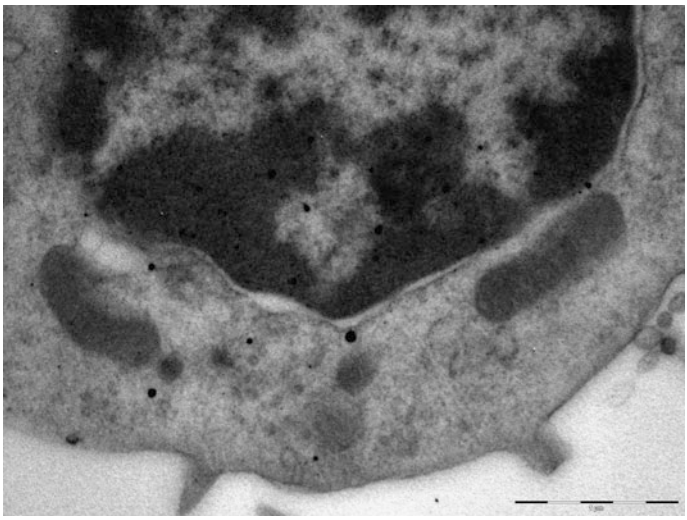

Fig. 11.15 Gold nanoparticles uniformly distributed throughout the cytoplasm and nucleus of an alveolar macrophage from the BALF of a rat instilled i.t. with Au-NPs The two-contour organization of the nucleus membrane is intact throughout. TEM, magnification ×22,000. First published in [8]

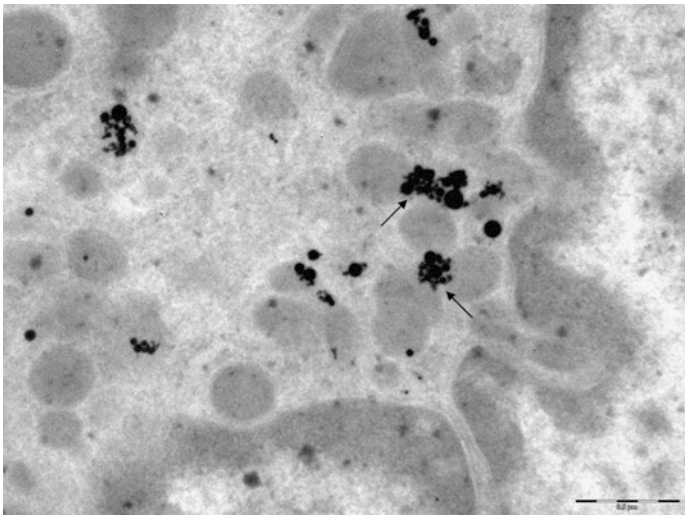

Fig. 11.16 An alveolar macrophage from the BALF of a rat instilled i.t. with Ag-NPs. Penetration of silver nanoparticles into mitochondria from aggregates (pointed out by *arrows*) lying seemingly free in the cytoplasm. No silver nanoparticles are discovered in the nucleus. TEM, magnification ×28,000. First published in [8]

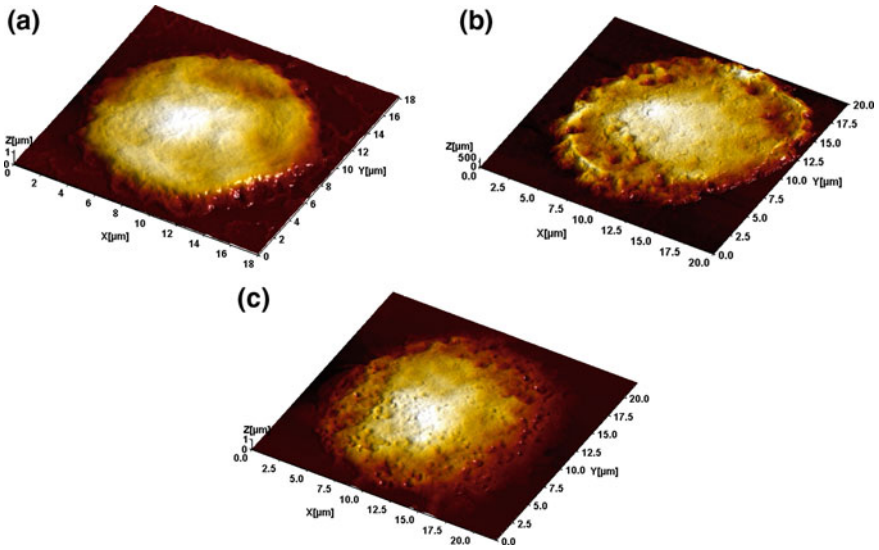

Fig. 11.17 Alveolar macrophage surface topography visualized by semi-contact AFM: **a** controls; **b** after instillation of 340 nm Cu/Cu_2O-MPs; **c** after instillation of 20 nm CuO-NPs. First published in [11]

average diameter of 25 ± 1 nm under exposure to NPs and 290 ± 14 nm under exposure to MPs, the average surface density of these pits were 32.6 and 1.9 per μm^2, respectively. A hypothetical explanation of the positive rank correlations between the NL/AM ratio and phagocytosis activity as judged by sc-AFM will be discussed below.

To sum up the data discussed in this sub-section, it seems evident that:

(a) the pulmonary phagocytosis response to Me-NP deposition (namely, phagocyte recruitment towards the free surface of the lower airways and the phagocytic activity of these cells) is even more pronounced than such response to the deposition of respective MPs,
(b) both aspects of this response depend on Me-NP size and, for a given size, on the chemical identity of the metal.

Most importantly, we found that pulmonary tissue was liberated from deposited nanoparticles quicker indeed than from their micrometric counterparts, this process being quicker, the smaller the nanoparticles [2, 4]. We believe this to be due to not only quicker dissolution but also more active phagocytosis of the smallest NPs. However, both the physicochemical and the physiological mechanisms of NP pulmonary clearance, while attenuating the harmful impact of nanoparticles on lungs, serve as premises to the toxic action of NPs on other organs either through the GIT (where they are transferred to in a free or cell-internalized state by the normal mucociliary transport) or directly through the blood (as a result of their dissolution/absorption or penetration/diffusion).

11.4.2 Are Metallic Nanoparticles Really Much More Toxic as Compared with Microparticles of the Same Chemical Nature on Both Cellular and Systemic Level? If They Are, Is There a Definite Dependence of Organism's Adverse Responses to NP Exposure on Their Dimensions Within the Conventional Nanometer Range and/or on Their Chemical Nature?

The paradigm of a considerably higher biological aggressiveness of Me-NPs as compared with particles of the same substance in the micrometric range first emerged as a theoretically sound perception [102, 103, 117]. Very soon afterward, some experimental facts corroborating this perception were obtained by different researchers, but that corroboration was, for some time, neither unanimous nor absolutely reliable due to some drawbacks and lack of comparability between different experimental designs. Thus, very reputable authors would justifiably state that "this common perception of greater nanoparticle toxicity is based on a limited

number of studies" [110], and still less was known about the comparative toxicity of chemically identical particles having different sizes *within* the conventional nanometric range.

Eventually, however, the situation changed substantially. Today's body of facts allows one to say without qualification that, given identical exposure pathways and similar chemistry, the toxic effects of metal and metal oxide NPs are much higher than those of their micrometric counterparts, even of minimal (including submicron) sizes. For a given size, the toxicity of NPs depends on their chemical nature and related properties, including solubility. Along with the latter property, quite often causing "the Trojan horse effect" (intracellular release of toxic metal ions by engulfed Me-NPs), there is another, now widely recognized major mechanism of their cytotoxicity and, especially, genotoxicity, which is the generation of reactive oxygen species on the Me-NP surface [118].

The toxic impact of particles on lung phagocytes is of special significance not only per se as an important unfavorable factor influencing the pulmonary clearance but also as an in vivo estimate of comparative particle cytotoxicity in a broader sense of the term. As mentioned above, the recruitment of new echelons of neutrophil leukocytes (beginning with enhanced differentiation of stem cells) in greater numbers compared with macrophages is a mechanism of compensation, even if partial, for the breakdown of alveolar macrophages damaged by cytotoxic particles. This recruitment was found to be controlled by the mass of macrophage breakdown products (MBP) and, especially, by their lipid fraction [114, 115, 119–121]. Therefore, the more cytotoxic the particles deposited in the lungs are for AMs (or the higher the i.t. dose of MBPs obtained by aseptic freezing-thawing or ultrasonic destruction of nonactivated peritoneal macrophages and then instilled i.t.), the higher the count ratio of neutrophile leukocytes (NLs) to alveolar macrophages (AMs) in the bronchoalveolar lavage fluid (BALF). This ratio (NL/AM) can, therefore, be used as an indirect but highly informative comparative in vivo index for the cytotoxic action of any low-soluble particle. Thus, it was demonstrated that the ranking of mineral MPs by this index correlated well with the ranking of their cytotoxicity based on the trypan blue exclusion test for cell viability in vitro. All these earlier revealed facts permitted us to use the BALF NL/AM ratio as an in vivo estimate of comparative cytotoxicity for NPs as well.

Using this index, we showed that the Me-NPs studied were far more cytotoxic compared with even the smallest Me-MPs of the same metal (see examples in Table 11.1 for silver nano- vs. micrometer particles, as well as the values are given in the text above for copper oxide nano- versus submicron particles). Moreover, within the nanoscale range, the smaller the particle, the more cytotoxic it was (see Fig. 11.18 for Fe_3O_4-NPs with different dimensions). Given a virtually equal nanoscale size, the cytotoxicity of particles can be quite different depending on their chemical nature. Thus, we found (see Table 11.2) that, judging by the NL/AM index, Ag-NPs were far more cytotoxic as compared with Au-NPs, while in the experiment comparing CuO-NPs, PbO-NPs and ZnO-NPs their cytotoxicity was found to increase in the order of listing. Likewise, NiO-NPs were found to be more cytotoxic in comparison with Mn_3O_4–NPs [9]. Differences were also discovered in

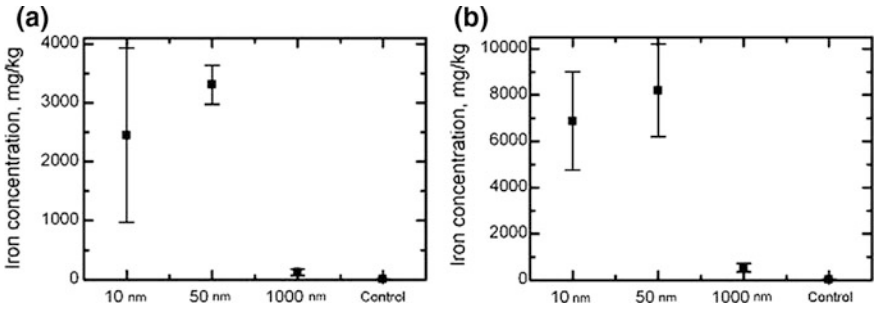

Fig. 11.18 Fe_3O_4 iron concentration (measured by EPR spectrometry) in rat tissues of **a** liver and **b** spleen after repeated i.p. injections of magnetite particles of various sizes. First published in [4]

the ultrastructural damage to the macrophage caused by different nanometals. For instance, we found that nanosilver was more likely to damage mitochondrial membranes and cristae than nanogold [8].

Comparison of the absolute BALF cell counts and "pit" numbers per unit cell surface area revealed by the sc-AFM with the NL/AM ratio values suggests that the more cytotoxic the nanoparticles are (because of either their smaller dimensions or their chemical nature, or both), the more active the pulmonary phagocytosis response is and the more avidly these NPs are engulfed by phagocytes. This phenomenon can be easily explained since macrophage breakdown products stimulate not only the recruitment but also the phagocytic activity of viable macrophages judging by the results of an in vitro test with I μm polystyrene beadles [112].

It stands to reason, however, that such compensation for AM breakdown cannot be complete and, in the final analysis, the especially high cytotoxicity of nanoparticles can be regarded as their very dangerous characteristic, increasing as their diameter decreases.

The relationship between particle dimensions and their toxicity is not so unequivocal on the organ and organism levels. For instance, judging by our results [2, 4], the subchronic toxicity of Fe_3O_4 (magnetite) nanoparticles was higher when compared to that of one-micrometer particles, but within the nanoscale range, the relationship under consideration proved inverse for some effects. Such seemingly paradoxical dependence of adverse effects of nanoparticles on their diameter is quite characteristic of target organs rich in RES cells and thus capable of actively accumulating nanoparticles from the blood—such as the liver and spleen.

This fact should be attributed to the differences of nanoparticle toxicokinetics. The latter is controlled, first of all, by their more or less easy penetration through the biological barriers into the bloodstream from the sites of their primary deposition, to be then captured by RES cells (resident macrophages) of this or that organ. It may be assumed that this biphasic mechanism of particle translocation should be more effective for smaller nanoparticles because of both their higher penetrability and more avid engulfment by macrophages. However, the smaller the particle, the quicker it dissolves from these secondary depots due to its immense specific

surface. Besides, the smallest NPs are presumably more cytotoxic for any cells, resident macrophages included, and thus cause their destruction (with the eventual release of NPs back into the bloodstream) more effectively. The balance between these oppositely acting mechanisms of nanoparticle retention in different tissues depends on many variables. That the result can be a greater burden of larger nanoparticles, as opposed to smaller ones, on the organ (but, at the same time, both of them creating a much greater burden as compared with microparticles) is illustrated for Fe_3O_4 NPs and MPs by Fig. 11.18. Judging by the percentage of akaryotic hepatocytes (equal to 13.1 ± 0.9 in control rats, 19.6 ± 1.7 in those injected with 1 mcm Fe_3O_4—MPs, 44.4 ± 1.3—with 50 mcm Fe_3O_4—NPs and 37.0 ± 1.6—with 10 mcm Fe_3O_4 –NPs), it is no wonder that the toxic damage to the liver was more prominent in rats exposed to 50 nm magnetite particles than to 10 nm ones, and nanoparticles of both sizes proved to be more hepatotoxic as compared with microparticles.

The systemic toxicity of equidimensional nanoparticles depends, beyond any reasonable doubt, on the toxic properties of a particular metal and can differ very much between different metals. For instance, nanosilver is more toxic than nanogold when tested in parallel and specifically, nanosilver is more genotoxic in vivo compared with nanogold judging by the results of the RAPD test performed on cells of different rat tissues under subchronic intoxication (Table 11.3) [8]. Why these differences in the genotoxicity of the nanometals compared are not seen in the kidneys may, most probably, be explained by the fact that silver NPs, judging by their considerably higher solubility in a model bio-milieu in vitro as compared with gold NPs [8], release substantially higher ion concentrations into the blood in vivo as well and, therefore, possess higher nephrotoxicity. We believe that the marked toxic damage to kidney epithelial cells can mask this metal's genotoxic effect. This hypothesis found confirmation in an experiment with copper oxide NPs [11, 12], which are even more soluble in vivo and thus even more nephrotoxic compared to silver NPs. In that experiment, the kidneys proved to be the only organ in which the DNA fragmentation coefficient was not elevated in response to the subchronic intoxication with copper oxide NPs in comparison with the controls. Meanwhile, in a parallel group in which animals were exposed to the same CuO-NPs but with the background administration of bio-protectors (see Sect. 11.5), the morphometric data revealed a considerably lower death rate of tubular epithelial cells, while it was just against this background that a significant genotoxic effect of CuO-NPs became quite manifest.

It should be stressed in this context that in each subchronic experiment involving any of the Me-NPs investigated by us so far, the RAPD test was performed on at least one type of nucleated cells, namely those of circulating blood—and we have not yet found a Me-NP that would not be genotoxic in vivo. Moreover, concerning this effect, the difference between the effects of chemically different particles was not always statistically significant and usually not very big.

A typical example illustrating the latter statement is given in Fig. 11.19, which also suggests the additivity of genotoxic effects when more than one kind of

Table 11.3 Coefficients of genomic DNA fragmentation in rats exposed to subchronic impact of silver or gold nanoparticles (based on the results of the RAPD test), $x \pm$ s.e

Group of rats exposed to	Tissues				
	Liver	Bone marrow	Spleen	Kidney	Nucleated cells of circulating blood
Water (controls)	0.399 ± 0.001	0.385 ± 0.003	0.379 ± 0.002	0.385 ± 0.003	0.383 ± 0.001
Au-NPs	0.392 ± 0.010°	0.412 ± 0.014*	0.397 ± 0.008°	0.422 ± 0.009*	0.403 ± 0.018
Ag-NPs	0.461 ± 0.002*	0.455 ± 0.032*	0.462 ± 0.001*	0.423 ± 0.008*	0.413 ± 0.012*

Note Statistically significant difference *from the control group; °between the group receiving Au-NPs and the group receiving Ag-NPs ($P < 0.05$ by Student's *t*-test)

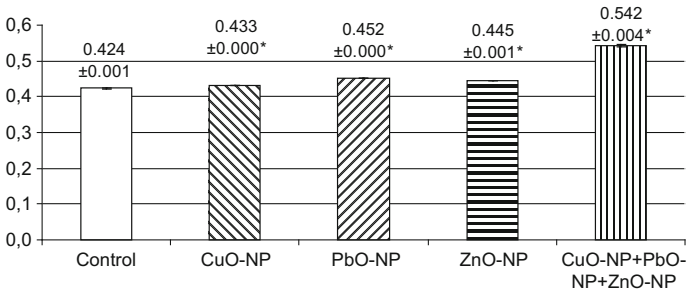

Fig. 11.19 Genomic DNA fragmentation coefficients (based on the results of the RAPD test) in rats exposed to subchronic administration of CuO-NPs, PbO-NPs and ZnO-NPs in equal doses separately or in combination ($x \pm$ s.e.). *Asterisk* designates values that are statistically significantly different from the controls ($p < 0.05$ by Student's *t*-test)

Me-NPs are acting together (the issue of combined Me-NP toxicity will be specially discussed in the next sub-section).

On the other hand, differences between some non-genetic (somatic) adverse effects of distinct Me-NPs can be rather pronounced, not only quantitatively (easily explainable in some instances by different in vivo solubilities, though hardly by this factor alone) but also qualitatively, being explicitly associated with the toxicological specificity of different metals in whatever chemical form.

Indeed, one of the physicochemical properties of metal and, in particular, metal oxide nanoparticles is that being virtually insoluble in vitro in deionized water, they do (depending on chemical composition) get more or less solubilized, sometimes even in normal saline, but much more so in real or artificial (model) biological milieus [17, 122]. As one of our own examples, Fig. 11.20 presents the comparative kinetics of 14 nm Fe_2O_3-NP dissolution in water, blood serum and cell-free BALF supernatant.

These data suggest that Me-NPs are most likely to be similarly solubilized in vivo. In the foregoing, we discussed the probable role of this mechanism in Me-NP elimination from lungs (and thus in the transfer of dissolved substances with blood to target organs). When discussing the role of Me-NPs' more or less ready solubilization in biological milieus as a probable determinant of the above-mentioned quantitative differences in toxicity between different Me-NPs, we may not only recall the higher nephrotoxicity of Ag-NPs compared with that of Au-NPs but also turn back to the pulmonary cell responses. In particular, the especially high pulmonary cytotoxicity of ZnO-NPs shown by us may be juxtaposed with the 100% in vitro dissolution of the same NPs in artificial lysosomal fluid and transient increase in the Zn^{2+} concentration in the BALF of mice after a period of inhalation exposures to these particles as demonstrated by Adamcakova-Dodd et al. [86].

However, this seemingly simple overall dependence of comparative cyto= or target organ toxicity of different Me-NPs on their comparative in vivo solubilization can be masked by some toxicokinetic and/or toxicodynamic peculiarities specific to this or that metal in different chemical forms. For instance, Minigalieva et al. [13]

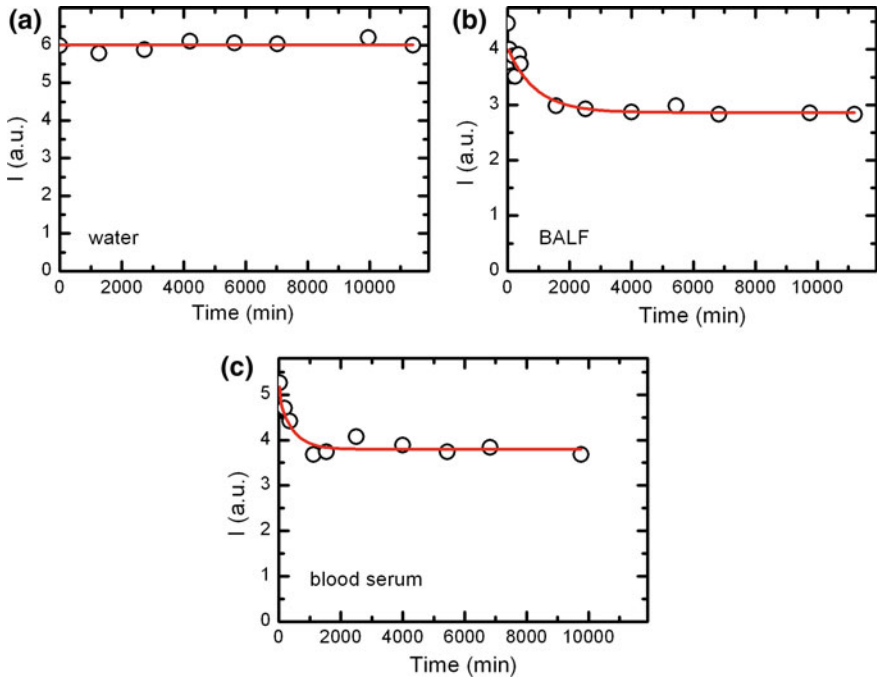

Fig. 11.20 Decay kinetics of the Fe^{3+} EPR signal from a filter on which Fe_2O_3-NPs had deposited from the inhalation exposure chamber exhaust air **a** in deionized water, **b** in rat BALF supernatant, **c** in sterile fetal bovine blood serum

demonstrated that Mn_3O_4-NPs solubilized in vivo much more readily compared with NiO-NPs and, thus, one might expect greater damage to be caused to kidneys by the former. However, renal tubular epithelium degeneration to the extent of destruction was highest in rats exposed to NiO-NPs or to a combination of these two Me-NPs (Fig. 11.21). This fact can be explained by the data presented in Table 11.4: whereas the NiO-NP exposure drastically increased Ni renal excretion (and, presumably, the impact of Ni on the kidneys), the Mn_3O_4-NP exposure did not enhance the urinary excretion of Mn over the background level. The predominantly renal route of nickel excretion in contrast to the elimination of manganese predominantly through the hepato-biliary system under exposures to soluble salts of these metals is a well-known fact. We have demonstrated that this fundamental difference in their toxicokinetic patterns is also present where in vivo solubilization of respective Me-NPs takes place.

Turning now to the metal-associated *specific* (qualitative) differences between the patterns of adverse health effects displayed by different nanoparticles, we may refer as an example to the much higher damage to the brain striatum and hippocampus caused by manganese oxide nanoparticles (compared with nickel oxide

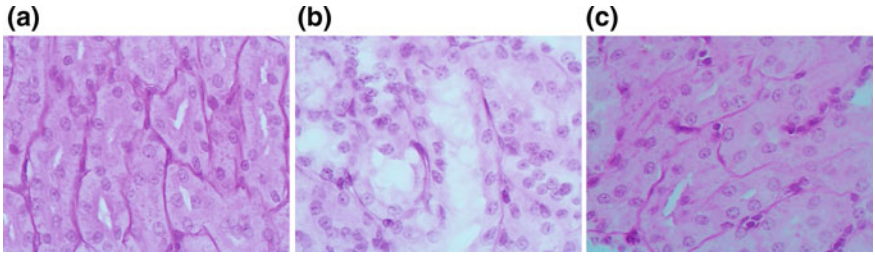

Fig. 11.21 **a** Kidney of a control rat (proximal convoluted tubules with an intact brush border). **b** Kidney of a rat exposed to NiO-NPs and Mn_3O_4-NPs together (marked degenerative and necrobiotic changes in tubular epithelial cells up to their disappearance; partial destruction of the brush border). **c** Kidney of a rat exposed to NiO-NPs and Mn_3O_4-NPs together against background administration of bio-protectors (see Sect. 11.5 for explanation). Periodic Acid Shiff (PAS) stain, magnification ×400. First published in [13]

Table 11.4 Manganese and nickel renal excretion in rats after repeated intraperitoneal injections of NiO or Mn_3O_4 nanoparticles, mcg per 24 h ($x \pm$ s.e.)

Groups injected i.p. with	Metal	
	Manganese	Nickel
Water (control)	0.06 ± 0.05	2.9 ± 0.2
NiO-NPs	0.008 ± 0.006	37.9 ± 5.3*°
Mn_3O_4-NPs	0.06 ± 0.01	0.63 ± 0.3*

Note Statistically significant difference *from the control group; °from the group given Mn_3O_4-NPs; ($P < 0.05$ by Student's *t*-test)

ones), which may be considered as an experimental counterpart of occupational Parkinsonism in arc-welders or steel-makers exposed to similar NPs [13].

Very similar damage to the brain (Fig. 11.22) was induced by the subchronic toxicity of metallic nanoparticles of another kind—those of copper oxide [11].

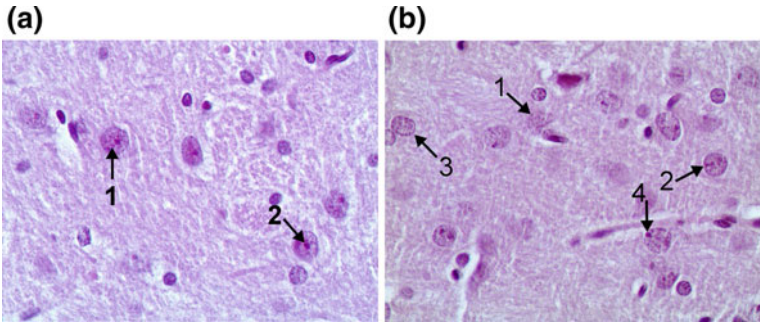

Fig. 11.22 Rat brain in the nucleus caudatus area (hematoxylin-eosine stain, magnification ×400). **a** A control rat. The neuron nuclei are predominantly spherical, with well-visible eosinophilic granulosity (*arrow 1*), and notable nucleoli in the center (*arrow 2*). **b** A rat exposed to subchronic i.p. intoxication with CuO-NPs. Arrows point to: poorly stained neuron nuclei, with an indistinct membrane (*1*), nucleoli that are pycnotic (*2*), often absent (*3*) or shifted towards the nuclear membrane (*4*). First published in [12]

Table 11.5 Some morphometric indices for the status of the rat's brain after repeated intraperitoneal injections of NiO or Mn_3O_4 nanoparticles, together or separately ($x \pm$ s.e.)

Neurons (%%)	Control	Mn_3O_4-NPs	NiO-NPs	NiO-NPs + Mn_3O_4-NPs
Nucleus caudatus				
Without a nucleolus	30.5 ± 2.8	69.9 ± 1.8*$^+$	47.4 ± 2.5*$^+$	60.3 ± 2.3*
With a distinct centrally located nucleolus	25.1 ± 1.2	9.3 ± 0.90*$^+$	17.0 ± 1.0*$^+$	12.4 ± 0.95*
Hippocampus (CA 1)				
Without a nucleolus	30.5 ± 2.3	70.5 ± 2.3*	35.8 ± 2.2$^+$	70.4 ± 3.8*
With a distinct centrally located nucleolus	46.4 ± 2.9	13.4 ± 1.5*	31.6 ± 1.8*$^+$	11.0 ± 1.1*

Note Statistically significant difference *from the control group; $^+$from the group given NiO-NPs + Mn_3O_4-NPs ($P < 0.05$ by Student's *t*-test). First published in [14]

In this experiment, very similar neurotoxic effects were observed in a group of rats exposed to submicron Cu/Cu_2O-MPs. Along with such damage to brain basal nuclei neurons, the toxicological syndrome comprised an accumulation of Cu in the liver and brain, some decrease in the serum ceruloplasmin level, and anemia. All these are characteristic of Wilson's disease in humans associated with genetically determined disturbances of copper metabolism. We believe that in our animal experiments this syndrome may be considered specific to the chronic toxicity of exogenous copper (in the form of NPs or ultrafine MPs) (Table 11.5).

Yet another example of metal-specific systemic nano-toxicity was found by us [116] in the aforementioned comparative subchronic experiment with CuO-, ZnO- and PbO-NPs. As can be seen from Table 11.6, rats exposed to PbO-NPs were found to have the highest (even though not statistically significantly different from the control) urine concentration of coproporphyrins, and only in this group was the urine concentration of the δ-aminolevulinic acid (δ-ALA) elevated compared with the control level ($p < 0.05$). These two effects are typical of lead's toxic action on

Table 11.6 Some toxic effects of repeated Me-NP i.p. injections to rats at a dose of 0.5 mg, 3 times a week, during 6 weeks ($x \pm$ s.e.)

Toxicity index	Me-NPs injected i.p.			
	(control)	CuO-NPs	PbO-NPs	ZnO-NPs
Coproporphyrins in urine (nMol/L)	63.5 ± 11.3	53.0 ± 13.4	122.2 ± 56.3	106.6 ± 29.2
Δ-ALA in urine (mg/L)	8.1 ± 2.7	5.3 ± 1.3	17.4 ± 2.8*	6.6 ± 1.8
Reticulocytes in blood (‰)	10.2 ± 1.4	11.6 ± 1.0	24.7 ± 2.7*	19.3 ± 1.7*

Note Statistically significant difference *from control group ($P < 0.05$ by Student's *t*-test)

porphyrin metabolism (and, thus, on hem synthesis). Given low doses used in this experiment, neither hemoglobin levels nor erythrocyte counts were decreased in any of the Me-NP exposed groups, however one of the earliest hematological indices of lead intoxication, namely, increased proportion of reticulocytes, was again highest in the PbO-NP exposed rats.

Besides, it is hardly by chance that among the 46 other functional indices for the organism's status used in that experiment, the only two that also testified to the higher toxicity of the same PbO-NPs compared with both CuO-NPs and ZnO-NPs were the indices characterizing exploratory activity inhibition. This effect may be tentatively interpreted as manifesting lead's well-known toxicity for the brain. The genotoxic effect as measured in the RAPD test on blood nucleated cells was also somewhat higher in the PbO-NP exposed rats compared with those exposed to CuO-NPs or ZnO-NPs, although this difference was not significant statistically (Fig. 11.19).

In all other respects, the systemic toxicity of PbO-NPs was either the same or even lower than that of either or both other Me-NPs. Moreover, the acute pulmonary toxicity of the same PbO-NPs instilled i.t., as judged from all cell counts and BALF biochemistry, was significantly lower compared with ZnO-NPs but higher as opposed to CuO.

By way of summarizing the main inferences from the data discussed in this sub-section, we may conclude that:

(1) Me-NP in vivo toxicity on the cellular and organ-systemic levels depends on both their size and chemical nature;
(2) generally speaking, it is much higher compared with the in vivo toxicity of their micrometric (even submicron) chemical counterparts;
(3) unequal solubilization in biological milieus (which, in turn, depends on Me-NP size and chemistry) is one of the most probable but not necessarily the most important explanation of the quantitative difference between qualitatively the same outcomes of exposures to different Me-NPs;
(4) besides, these exposures may result in just qualitatively different outcomes as manifestations of certain *specific* features pertinent to the toxicokinetics and toxicodynamics of the NP-forming metal;
(5) in a real toxicological process, one virtually always sees a complicated interplay of these dependencies which makes straightforward and definitive comparative assessment of health risks associated with different Me-NPs a rather difficult task.

This task is even more difficult where one has to deal with frequently encountered realistic situations in which humans are being exposed to combined impacts of more than one Me-NP species.

11.4.3 Are There Any General Patterns of Combined Action of Me-NPs Having Different Chemical Compositions?

However extensive the advancements and developments in general and specific nanotoxicology have been over the recent decade, one cannot help noticing a virtually complete lack of studies devoted to comparative and *combined* toxicity of different substances in the nanoscale range [123]. Meanwhile, the broader the use of nanomaterials in various industries, science, and medicine, the higher the probability that humans would be exposed, either simultaneously or successively, to the multi-component impact of these materials. Moreover, if we consider not only purposely engineered Me-NPs but, as we do it in this chapter, also those generated as by-products in many traditional technologies (see the Introduction), such multiple factor nano-impacts appear to be a general rule. Indeed, Me-NPs generated by arc-welding and alloyed steel metallurgy and contaminating workplace air and ambient air usually have a complex chemical composition comprising oxides of iron, manganese, nickel, chrome, vanadium, silicon and other elements. Both the chemical identity of these NPs and quantitative relationships between them vary broadly depending on a specific technology or its phase, the composition of the alloy being molten or welded and of the welding electrodes being used, the melting temperature, etc. One of the urgent challenges for the nanotoxicologist is, therefore, the need to assess not only the comparative toxicity of various Me-NPs but also their combined effects.

In a series of papers [9, 13, 124, 125], we have discussed the state of the art in the complicated domain of the combined toxicity theory and its mathematical modeling. The mainstream philosophy dominating in the relevant scientific literature and in some official guidelines or recommendations as well as its controversies have been critically overviewed by us, mainly in the first article [124]. Our own first substantial contribution to this problem presented by those articles concerned subchronic intoxications induced by repeatedly injecting IP pre-made solutions of some non-particulate inorganic chemicals (binary combinations: Pb–Cd, Pb–F, Cr–Ni, Cr–Mn, Ni–Mn; a three-factorial combination, Cr–Ni–Mn). Later on, similar subchronic experiments and experiments involving combined single-shot intratracheal instillations helped us reveal essentially the same patterns of combined toxicity as in the above combinations of salts for several other binary combinations of Me-NPs: NiO-NP + Mn_3O_4-NP [13]; PbO-NP + CuO-NP, PbO-NP + ZnO-NP, ZnO-NP + CuO-NP [116] and for a triple combination of PbO-NP + CuO-NP + ZnO-NP acting together [116].

We first analyzed our experimental results using different mathematical models based on (a) ANOVA and (b) Mathematical Theory of Experimental Design, which corresponds to the well-known paradigms of effect additivity and dose additivity (Loewe additivity), respectively. Later on, we used mostly the Response Surface Methodology, which generalizes these traditional paradigms [126–129].

In this methodology, an Eq. (11.1) describing the response surface $Y = Y(x_1, x_2)$ can be constructed by fitting its coefficients to experimental data.

$$Y = f(x_1, x_2), \tag{11.1}$$

where Y is a quantitative effect (outcome) of a toxic exposure; x_1 and x_2 are the doses of the toxicants participating in the combination; $f(x_1, x_2)$ is a regression equation with some numeric parameters. In the case of two-level exposures (even if one of the levels is equal to zero), the response surface may have one possible shape (hyperbolic paraboloid)

$$Y = b_0 + b_1 x_1 + b_2 x_2 + b_{12} x_1 x_2 \tag{11.2}$$

Myers et al. [129] noted the special importance of two-level experiments in response surface works. Moreover, in many other cases model (11.2) is quite consistent and useful. Below, we will use model (11.2) throughout to show the principal points of the approach considered, as it demonstrates a reasonable compromise between the complexity of the model and its ability to interpret the results.

It is inferred that two agents produce a unidirectional effect on response Y if both one-way response functions $Y(x_1, 0)$ and $Y(0, x_2)$ either increase or decrease with an increase in x_1 or x_2; on the contrary, two agents are assumed to be acting contra-directionally (oppositely) if one function increases while the other decreases. This mathematical model enables one to predict the magnitude of response Y for any combination of toxicant doses within the experimental range for each of them (rather than at two factual points only). The sectioning of the response surface on different levels corresponding to different meanings of the outcome **Y** or of the doses **x** provides a family of Loewe isoboles that may have the same or a different form and/or different slopes and thus render the interpretation of binary combined toxicity types both easy and illustrative. Here we, therefore, discuss an analysis presented just in this form.

In all cases of binary toxic combinations that we have considered so far, the analysis has led us to the following principal postulates:

(1) the abovementioned paradigms are virtually interchangeable and so they might be regarded as different methods for modeling combined toxicity rather than as concepts reflecting fundamentally differing processes;
(2) within both paradigms, there exist more than three traditionally recognized types of combined toxicity (additivity, subadditivity, and superadditivity), and we have found at least 10 variants of it depending on exactly which effect is considered and what its level is, as well as on dose levels and their ratios.

(3) when one deals with the multiple-outcome characterization of combined intoxications, both unidirectional (additive, subadditive, or superadditive) and oppositely directed action of one and the same pair of toxics is usually found in respect to even one and the same effect but at a different dose or effect levels.

Indeed, even without a sophisticated mathematical analysis, judging merely by the intergroup differences between different intoxication indices, it might be usually surmised that the type of combined Me-NP toxicity is different for different effects. However, thanks to the abovementioned analysis, this hypothesis has become a proven general pattern of combined nano-metal toxicity.

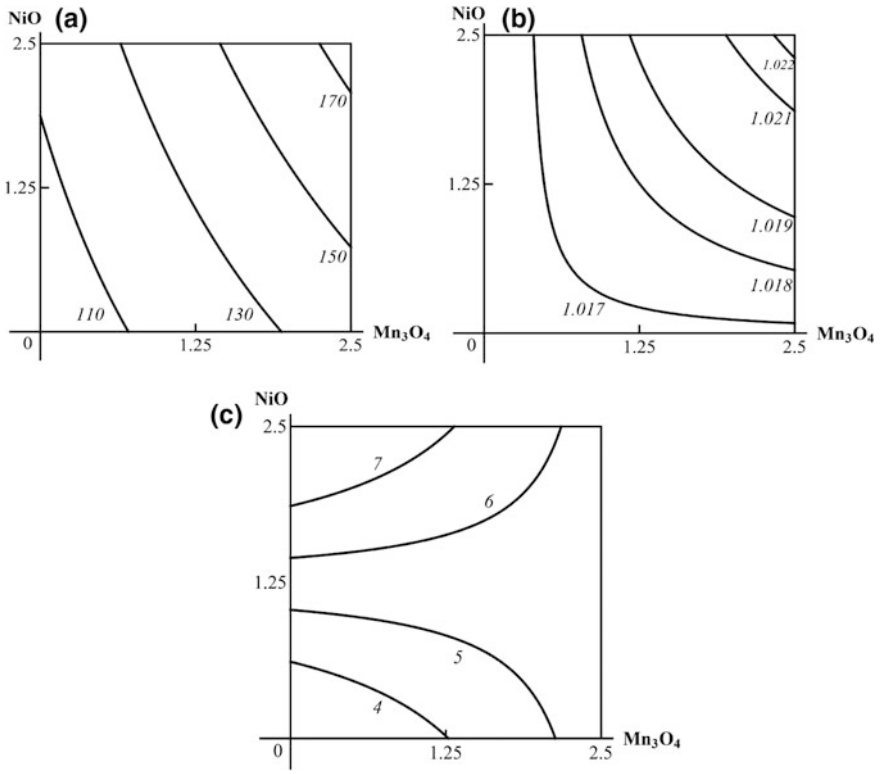

Fig. 11.23 Examples of isoboles characterizing NiO-NP + Mn_3O_4-NP combined subchronic toxicity: **a** for uric acid concentration in blood serum (additivity); **b** for urine density (synergism at low effect levels and additivity at high effect levels); **c** for akaryotic hepatocyte percentage (subadditivity of unidirectional action at low effect levels and oppositely directed action at high effect levels). The doses of Mn_3O_4 and NiO are plotted on the axes in mg per rat. The *numbers at the lines* of the isoboles show the values of the effect *Y* (uric acid in mcMol/L)

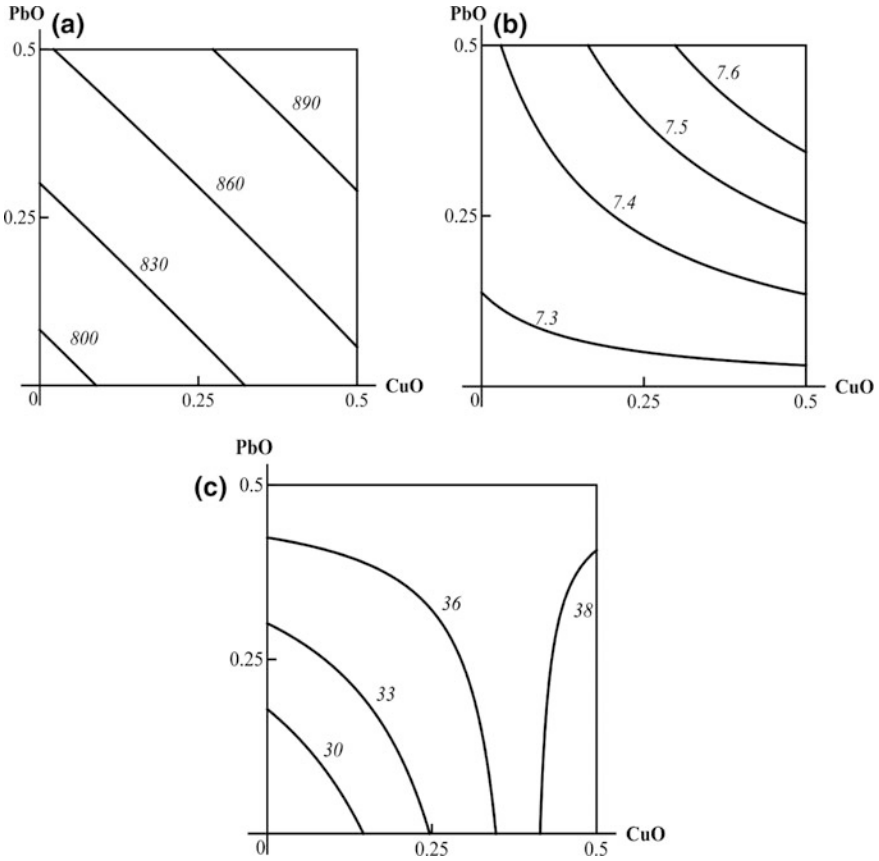

Fig. 11.24 Examples of isoboles characterizing CuO-NP + PbO-NP combined subchronic toxicity: **a** for thrombocyte count (additivity); **b** for erythrocytes (synergism at low effect levels and additivity at high effect levels); **c** for diuresis (subadditivity of unidirectional action at low effect levels and oppositely directed action at high effect levels. The doses of CuO and PbO are plotted on the axes in mg per rat. The *numbers at the lines* of the isoboles show the values of the effect Y (thrombocytes $\times$ 10^9/L; erythrocytes $\times$ 10^{12}/L; diuresis in mL per 24 h)

Some examples demonstrating such outcome-dependent diversity of Me-NP combined toxicity types are presented in Figs. 11.23, 11.24, 11.25 and 11.26.

Essentially the same effect-dependent diversity of the binary combined toxicity type was revealed when analyzing acute pulmonary responses to Me-NPs instilled i. t. as illustrated in Fig. 11.27.

As concerns the combined toxicity of three metals acting together, we [16] proposed a new health risk-oriented approach based on the consideration whether

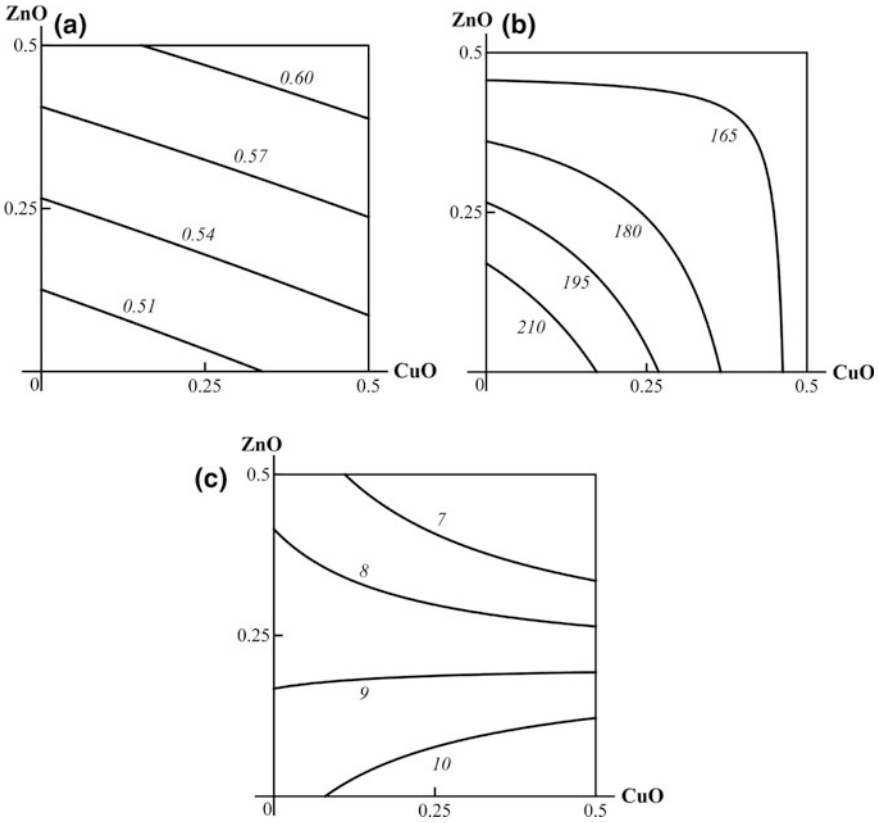

Fig. 11.25 Examples of isoboles characterizing CuO-NP + ZnO-NP combined subchronic toxicity: **a** for thrombocrit; **b** for alkaline phosphatase (AF) in blood serum (subadditivity); **c** for testosterone (superadditivity of unidirectional action at low effect levels and oppositely directed action at high effect levels). The doses of CuO and ZnO are plotted on the axes in mg per rat. The *numbers at the lines* of the isoboles show the values of the effect *Y* (AF in IU/L; testosterone in nMol/L)

the addition of a third toxic to the other two leads to the type of binary combined action becoming either more or less adverse (Classes A and B, respectively) or remaining basically unchanged (Class C). This approach has been successfully tested with reference to subchronic intoxication with nickel, chromium(VI) and manganese salts. We have revealed some stable patterns of classification fully or partly reproduced when considering, one by one, various metals as the third component of the combination and have found that, for the absolute majority of outcomes, the classification appears to be inherently consistent. Again, this approach has proven to be adequate for analyzing three-factorial Me-NP toxicity as

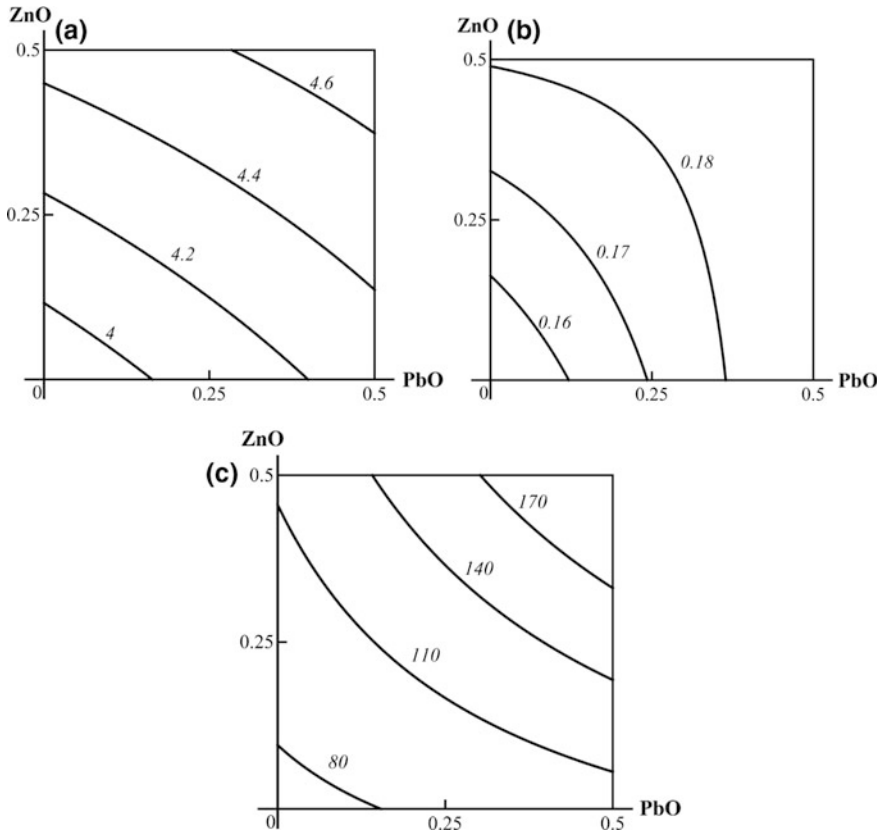

Fig. 11.26 Examples of isoboles characterizing PbO-NP + ZnO-NP combined subchronic toxicity: **a** for the De Ritis coefficient (additivity); **b** for follicle-stimulating hormone (FSH) (subadditivity); **c** for coproporphyrin in urine (superadditivity of unidirectional action). The doses of CuO and ZnO are plotted on the axes in mg per rat. The *numbers at the lines* of the isoboles show the values of the effect *Y* (FSH in IU/L, coproporphyrin in nMol/L)

well [116]. Examples of the isobolograms typical of each class are given in Figs. 11.28, 11.29 and 11.30.

The toxicodynamic and toxicokinetic mechanisms explaining this or that type of combined toxicity are complicated and not always fully understood. Taking into consideration what was said in the previous sub-section in relation to the metal-dependent specificity of some important effects displayed by one-factor Me-NP toxicity, it stands to reason that the mechanisms of their interaction should be hypothesized and discussed with reference to a particularly toxic combination

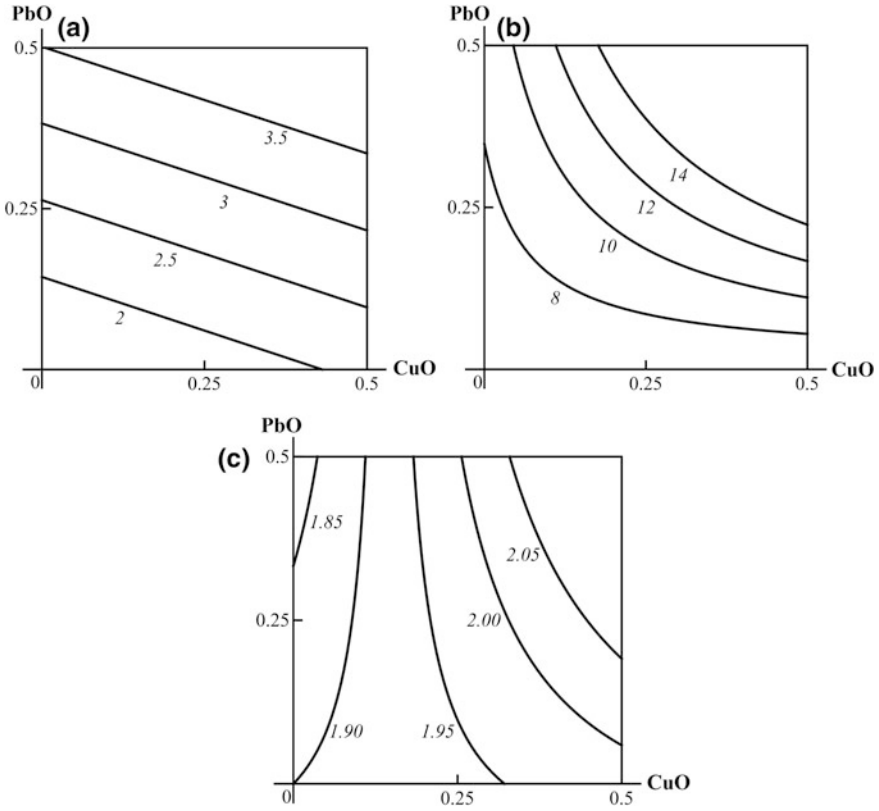

Fig. 11.27 Examples of isoboles characterizing CuO-NP + PbO-NP combined pulmonary toxicity: **a** for BALF total cell count (additivity); **b** for BALF supernatant amylase activity (superadditivity); **c** for BALF albumin content (oppositely directed action at a low effect and superadditivity of unidirectional action at a high effect). The doses of CuO-NP and PbO-NP are plotted on the axes in mg per rat. The *numbers at the lines* of the isoboles show the values of the effect Y (cell counts in $\times 10^6$, amylase in IU/L, albumin in g/L)

rather than in general terms. At any rate, at the present stage of the research into this problem, one knows too little for such generalization.

Nevertheless, although we found that the toxicokinetic interactions of Me-NPs did not always correspond to the functional effects of combined toxicity and often were not easy to explain, these interactions do take place. Thus, Table 11.7 demonstrates that exposure to NiO and Mn_3O_4 nanoparticles in combination resulted in much higher retention of Ni in the liver (but not in the spleen, kidneys or brain) than to NiO-NPs alone, while the same combination of Me-NPs decreased

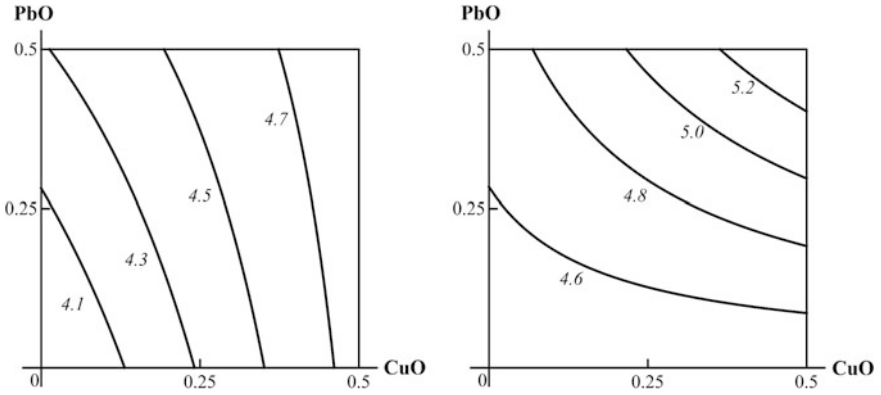

Fig. 11.28 An example of three-factorial toxicity effects classified as "A": an additive action of PbO-NP and CuO-NP on the De Ritis coefficient in the absence of any other toxic exposure is transformed into the synergism of the same two Me-NPs against concomitant background exposure to ZnO-NP. The doses of PbO and CuO are plotted on the axes in mg per rat. The *numbers at the lines* of the isoboles show the values of the effect

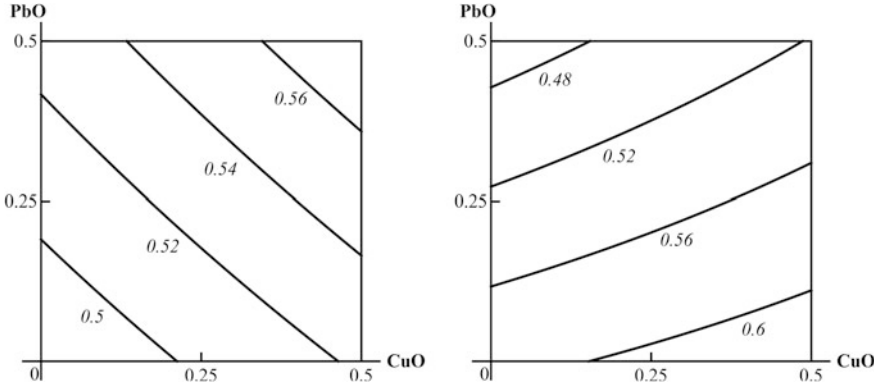

Fig. 11.29 An example of three-factorial toxicity effects classified as "B": the additivity of a PbO-NP and CuO-NP unidirectional action on the thrombocrit index in the absence of any other toxic exposure transforms into a contra-directional action of the same two Me-NPs against concomitant background exposure to ZnO-NP. The doses of PbO and CuO are plotted on the axes in mg per rat. The *numbers at the lines* of the isoboles show the values of the effect

Mn retention significantly in the kidneys and insignificantly, although noticeably, in the brain compared with separate Mn_3O_4-NP exposure.

Paradoxically, however, the urinary excretion of Mn in the combined exposure group was significantly higher, while that of Ni significantly lower as compared with respective separate exposure groups (Table 11.8), but the morphometric indices presented in Table 11.9 testify to a higher nephrotoxicity of this combination compared to that of separate Me-NPs.

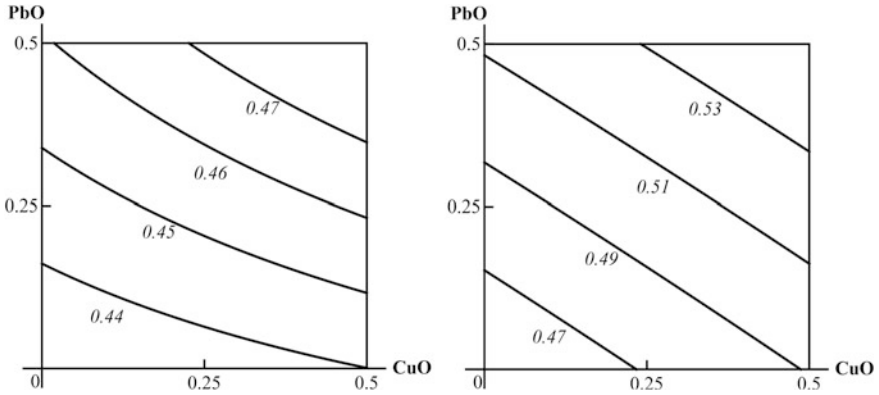

Fig. 11.30 An example of three-factorial toxicity effects classified as "C": the additivity of a PbO-NP and CuO-NP unidirectional action on the DNA fragmentation coefficient both with and without concomitant background exposure to ZnO-NP. The doses of PbO and CuO are plotted on the axes in mg per rat. The *numbers at the lines* of the isoboles show the values of the effect

Table 11.7 Total manganese and nickel contents of rat's organs after repeated intraperitoneal injections of NiO and/or Mn_3O_4 nanoparticles at a dose of 0.50 mg per rat, mcg per g of dried tissue ($x \pm$ s.e.)

Metal	Groups of rats given			
	Control	NiO-NPs	Mn_3O_4-NPs	NiO-NPs + Mn_3O_4-NPs
Liver				
Manganese	7.33 ± 0.56	6.33 ± 0.49	7.20 ± 0.73	6.80 ± 0.20
Nickel	3.17 ± 0.65	16.40 ± 3.26*$^{+\circ}$	2.80 ± 0.20^{+}	38.00 ± 2.80*$^{+\circ}$
Spleen				
Manganese	28.80 ± 1.74	32.00 ± 4.15	25.00 ± 1.87	25.83 ± 4.23
Nickel	25.60 ± 1.89	46.75 ± 8.44*	32.50 ± 4.63	36.17 ± 7.21
Kidneys				
Manganese	13.75 ± 0.95	10.00 ± 0.63*$^{\circ}$	20.50 ± 1.45*$^{+}$	10.80 ± 1.11
Nickel	18.20 ± 1.56	20.60 ± 3.23	16.00 ± 1.58	17.60 ± 1.29
Brain				
Manganese	6.00 ± 0.45	7.17 ± 0.98	10.75 ± 1.70*	7.60 ± 1.08
Nickel	14.67 ± 0.96	12.83 ± 1.20	15.75 ± 2.46	15.80 ± 2.65

Note *Statistically significant difference from the control group; $^{+}$from the group given NiO-NPs + Mn_3O_4-NPs; $^{\circ}$from the group given Mn_3O_4-NPs ($P < 0.05$ by Student's t-test). First published in [14]

Table 11.8 Total manganese and nickel renal excretion in rats after repeated intraperitoneal injections of NiO and/or Mn_3O_4 nanoparticles at a dose of 0.50 mg per rat, mcg per 24 h ($X \pm$ s.e.)

Metal	Groups of rats given			
	Control	NiO-NPs	Mn_3O_4-NPs	NiO-NPs + Mn_3O_4-NPs
Manganese	0.06 ± 0.05	0.008 ± 0.006$^{+\circ}$	0.06 ± 0.01^{+}	0.52 ± 0.1*
Nickel	2.9 ± 0.2	37.9 ± 5.3*$^{+\circ}$	0.63 ± 0.3*$^{+}$	16.7 ± 2.9*

Note *Statistically significant difference from the control group; $^{+}$from the group given NiO-NPs + Mn_3O_4-NPs; °from the group given Mn_3O_4-NPs ($P < 0.05$ by Student's *t*-test). First published in [14]

Table 11.9 Morphometric indices for tubular epithelium damage in rat kidneys after repeated intraperitoneal injections of NiO and/or Mn_3O_4 nanoparticles at a dose 0.50 mg per rat ($x \pm$ s.e.)

Groups of rats given	Brush border loss (% lengthwise)	Epithelial desquamation (% lengthwise)
Water (control)	5.44 ± 0.9	0.00 ± 0
NiO-NPs	10.3 ± 1.7*	0.48 ± 0.36
Mn_3O_4-NPs	9.02 ± 1.17*	0.28 ± 0.32^{+}
NiO-NPs + Mn_3O_4-NPs	12.33 ± 2.3*	2.43 ± 1.0*

Note *Statistically significant difference from the control group; $^{+}$from the group given NiO-NPs + Mn_3O_4-NPs ($P < 0.05$ by Student's *t*-test)

11.5 Are There Ways to Protect the Organism from an Especially Harmful Bioactivity of Metallic Nanoparticles?

Beyond any reasonable doubt, the most protectively effective (although not always cost-effective) way to manage occupational health risks associated with any hazardous impact would be to decrease the latter to a presumably safe level. Whatever term a country or its various agencies may use to denote safe exposure standards, the philosophy underlying such standard setting would be basically the same: it is assumed that at some low level of potentially dangerous exposure, a balance between a toxic's adverse biological activity and the organism's natural defensive mechanisms can prevent the development of any identifiable disease or condition or even mild subclinical anomalies. Is such a balance possible for nanoparticles (NPs) and, specifically, for Me-NPs?

Obviously, the answer depends on the assumption whether or not these defenses are sufficiently effective in this case too, and we argue that they are (see Sect. 11.4.1). We, therefore, believe that establishing permissible exposure levels for Me-NPs that would be sufficiently safe in the just formulated sense of this term is theoretically justifiable and practically feasible. Nevertheless, the opposite scale of the abovementioned balance is so "overloaded" with the especially high toxicity

and seemingly obligatory genotoxicity of Me-NPs that the presumably safe levels of exposure to Me-NPs proposed so far are so much lower than those for respective Me-MPs (e.g. [5, 130, 131]) that they are hardly attainable in reality.

We, therefore, reasoned that it would be worthwhile to try and tip this balance from the other end, that is to enhance the natural resistance to the adverse health effects of Me-NPs [16]. This idea was based on our long-term experience of successful bioprotection of the organism against various other toxics, including some mineral microparticles [8, 10, 132].

11.5.1 Theoretical Premises

The organism-level mechanisms of what we designate as bioprotection or bio-prophylaxis are schematically presented in the flowchart in Fig. 11.31.

In general terms, we maintain that the mammalian organism can be protected against occupational or environmental toxic impacts using:

(a) bio-protectors aimed primarily at increasing the effectiveness of the natural mechanisms of bio-transformation and/or elimination of toxics, and thus, at reducing the inner dose of a harmful substance retained in the organism and especially in the target organs (designated in our chart as "toxicokinetic effects");
(b) bio-protectors aimed at enhancing the functional reserves at all levels of the organism affected by a toxic substance; at increasing the effectiveness of repair and compensatory processes; and at employing physiological and toxicological antagonisms (designated in the chart collectively as "toxicodynamic effects").

However, these two modes of action are usually interrelated and interdependent, as it is schematically shown with reciprocally directed arrows. Indeed, by reducing the retention of a toxic substance in the organism and especially in target organs, a bio-protector inhibits the development of a pathological process (thus, a

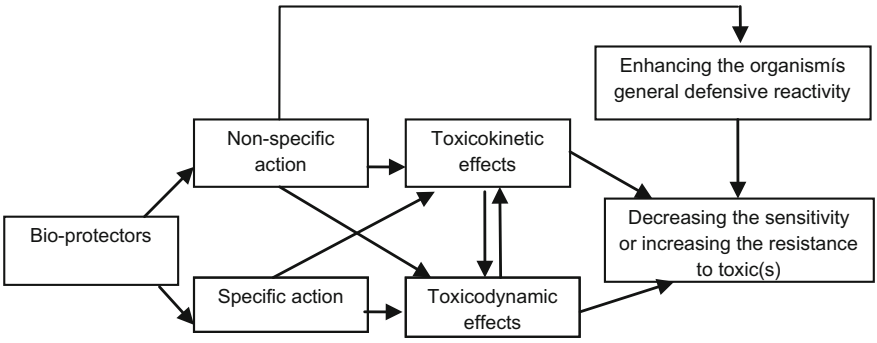

Fig. 11.31 Schematic presentation of anti-toxic biological prophylaxis. First published in [16]

bio-protector of a primarily toxicokinetic type of action produces a beneficial toxicodynamic effect). On the other hand, primary enhancement of resistance to the damaging impact of a toxic on the cells and organs that control the processes of its elimination or detoxication (pulmonary macrophages, liver, kidneys) maintains the effectiveness of these processes and, thus, reduces the retention of this toxic in the organism (so we see a beneficial toxicokinetic effect of a toxicodynamic bio-protector). Such bilateral interdependence of toxicokinetic and toxicodynamic effects is pronounced to a varying degree in response to the action of different harmful substances but, on the whole, can be considered as a consistent pattern.

The flowchart shows also that both toxicokinetic and toxicodynamic bio-protectors can be:

- more or less specific with regard to a particular toxic or a particular range of toxics if bioprotection interferes with the mechanisms of toxicokinetics and toxicodynamics pertaining just to these toxics or to a class of similarly acting ones;
- predominantly non-specific, if their effect is realized through such integral responses at the organism level as Selye's general adaptation syndrome or a related but still distinct concept of "non-specifically enhanced resistance" developed by the school of late Nikolay Lazarev, an outstanding Russian toxicologist and pharmacologist.

However, one and the same bio-protector may, in different cases. either render a largely specific effect or help the organism mainly as an agent enhancing its non-specific defenses and thus decreasing its sensitivity or increasing its resistance to harmful exposures (see respective boxes and links in the same chart).

In our experiments, bio-protectors employing mechanisms that are not fully identical proved to be most effective when administered not separately but in combinations which we call "bioprotective complexes," or BPCs [8, 10, 132].

With a view to further possible usage of bio-protectors for humans, we test in animal experiments only substances which, acting alone, are innocuous when taken for a long time in preventively effective doses. We have been able to demonstrate through our more than three-decades-long research work on a lot of chronic or subchronic experimental intoxications with different inorganic and organic chemicals acting separately or in different combinations (modeling actual occupational and environmental combined chemical exposures of industrial workers and industrially polluted area dwellers) the bioprotective efficacy of:

- some amino acids (e.g., glutamate, glycine, cysteine);
- vitamins (such as A, B1, E, C) and essential trace elements (selenium, iodine, copper, etc.) or multivitamin-multimineral preparations;
- fish oils rich in polyunsaturated fatty acids, predominantly of the omega 3 class;
- pectin enterosorbents;
- calcium and iron supplements.

In many instances, the beneficial effects and intrinsic safety of the experimentally tested BPCs were then confirmed in field investigations on volunteers as a prerequisite to wider prophylactic usage. (For the latest overview of all these scientific and medico-social activities, see [10]).

Concerning bioprotection against the adverse effects of metallic nanoparticles described in Sect. 11.4, we have so far chosen, based on the above formulated theoretical premises, and experimentally tested four BPCs protecting from nanosilver [8], nano-copper oxide [12], and combinations of NiO-NP + Mn_3O_4-NP [13–15] and PbO-NP + CuO-NP + ZnO-NP [116]. Being different in some important details depending on specific toxicodynamic and toxicokinetic mechanisms underlying the toxic action of the different metals, the compositions of all three BPCs still have much in common. We believe that similar BPCs to be further examined for bioprotection against other metallic nanoparticles should comprise most of the same components. These components of choice are:

(1) Glutamate as an effective cell membrane stabilizer acting through the intensification of ATP synthesis under exposure to the damaging effect of various cytotoxic particles (e.g. [133]) and, at the same time, as one of the precursors of glutathione, which is a powerful cell protector against oxidative stress as, presumably, one of the key mechanisms underlying the cytotoxicity and genotoxicity of virtually all metallic NPs [118]. In addition to these non-specific and almost universal bioprotective effects, the administration of glutamate, as we thought, might specifically increase resistance to the neurotoxicity of manganese, lead and some other metallic nanoparticles due to its major role in the transmission of excitatory signals in the mammalian central nervous system and thus its involvement in most aspects of normal brain functioning. Indeed, it is known, for instance, that manganese impairs the expression and function of the main glutamate transporters in astrocytes [134] and that lead interferes with glutamate release in the hippocampus [135]. We thought that additional glutamate supply to the brain might partly compensate for these adverse effects of the respective Me-NPs.
(2) The other two glutathione precursors: glycine and cysteine (the latter in a highly active and metabolically well available form of *N*-acetylcysteine), taking into consideration both the abovementioned general important role played by oxidative stress as a mechanism of Me-NP toxicity and some experimental data demonstrating that glutathione deficiency potentiates metal toxicity—e.g., manganese-induced damage to the rat striatum and brainstem [136].
(3) Other agents of the organism's anti-oxidant system (vitamins A, E, and C, and selenium).
(4) Omega-3 polyunsaturated fatty acids whose intracellular derivatives—eicosanoids—activate DNA replication and thus play an important part in its repair.
(5) Iodine, taking into consideration the well-known disturbances of the thyroid function caused by lead, manganese, and some other metallic intoxication.
(6) Trace elements are known to be antagonists of the metal that forms Me-NPs under study.

(7) Pectin enterosorbent as an agent that hinders the re-absorption of toxic metals excreted into the intestines with bile (which, again, is of special importance for metals that are excreted predominantly by this route (e.g., manganese and copper) or released within the GIT by Me-NPs translocated there after deposition in the airways (see Fig. 11.9).

In all the studies we have found that, as was expected, the toxicity and even genotoxicity of Me-NPs could be really attenuated against the background administration of adequately composed BPCs. It should be understood that we do not claim to be the first to have shown a possibility of inhibiting some metallic nanoparticles' toxicity with the help of this or that agent targeted at a certain mechanism of such toxicity. However, other researchers would demonstrate this possibility in experiments in vitro as a rule, using it as evidence of the importance of this mechanism (e.g. [37]) rather than as the foundation of a holistic bioprotective system. In the meantime, it is just such a prevention-oriented system ("biological prophylaxis" in our terminology) that is the goal of our mechanistically substantiated approach, and we believe we were the first indeed who began to investigate the effects of bio-protectors against metallic nanoparticles on the whole mammalian organism in animal experiments.

11.5.2 Examples of Experimental Bioprotection

We have demonstrated the high beneficial efficacy of anti-Me-NP bioprotection in our experiments using a lot of indices, but here we present only some of them to illustrate this efficacy with several typical examples.

Thus, virtually all Me-NPs studied by us prove to be markedly nephrotoxic, causing, in particular, significant damage to the epithelial cells of proximal convoluted renal tubules. As was stated in Sect. 11.4.2, histological preparations of kidneys in rats exposed intraperitoneally to these nanoparticles during 6–7 weeks revealed marked degenerative and necrotic changes in these cells up to their disappearance with partial destruction of the brush border, while rats exposed to the same nanoparticles against background BPC administration demonstrated marked alleviation of such tubular damage. Figure 11.21 presents as typical example the microscopic pictures of kidneys from rats exposed to a combination of NiO-NPs and Mn_3O_4-NPs with or without concomitant oral administration of a BPC comprising pectin, glutamate, glycine, *N*-acetylcysteine, vitamins A, C, E, selenium, iodide, and omega-3 PUFA. Table 11.10 provides respective morphometric results obtained in this experiment with nickel oxide and manganese oxide nanoparticles [13] and quite similar results of an earlier experiment involving copper oxide nanoparticles [11, 12]. In the latter, we tested a BPC of a similar composition plus vitamin B12 and biotic doses of iron, zinc, molybdenum, and manganese.

Another well established adverse effect of virtually all Me-NPs is damage to the organs rich in RES cells, in particular, to the spleen and liver, which accumulate

Table 11.10 Some morphometric indices for tubular epithelium damage in the kidneys of rats after repeated intraperitoneal injections of some metallic oxide nanoparticles with or without background oral administration of a BPC ($x \pm$ s.e.)

Groups of rats given	Brush border loss (% lengthwise)	Epithelial desquamation (% lengthwise)
NiO nanoparticles + Mn_3O_4 nanoparticles		
Water (control)	5.44 ± 0.90	0.00 ± 0.00
Nanoparticles	12.33 ± 2.30*	2.43 ± 1.00*
Nanoparticles + BPC	7.08 ± 1.70	0.00 ± 0.00+
CuO nanoparticles		
Water (control)	5.39 ± 0.42	0.33 ± 0.13
Nanoparticles	8.36 ± 0.76*	1.16 ± 0.38*
Nanoparticles + BPC	5.98 ± 0.46+	0.98 ± 0.35

Note *Statistically significant difference from the control group; +from the group given nanoparticles without the BPC ($P < 0.05$ by Student's *t*-test)

them more avidly than any other organs. Indeed, in both of these organs, we observed an explicit pathology the type of which virtually did not depend on the chemical nature of the Me-NPs, and this pathology was also alleviated by background BPCs administration as exemplified in Table 11.11 by the results of an experiment with Ag-NPs [8].

A more specific adverse effect characterizing the toxicity of Mn_3O_4-NPs (acting either with or without NiO-NPs) and CuO-NPs was marked damage to some

Table 11.11 Some morphometric indices of the cell structure of liver and spleen in rats exposed to Ag-NPs with or without background BPC[a] administration ($x \pm$ s.e.)

Index	Rats injected with water (control)	Rats injected with nanoparticles	Rats injected with nanoparticles and administered a BPC
Liver			
Akaryotic hepatocytes per 100 cells	17.6 ± 0.6	18.5 ± 1.3	13.0 ± 1.0*+
Kupffer cells per 100 liver cells	16.5 ± 0.5	25.0 ± 0.8*	20.0 ± 0.6*+
Average particle load of Kupffer cells, score[#]	0	0.91 ± 0.7	0.51 ± 0.09+
Spleen			
White to red pulp ratio[†]	0.59 ± 0.036	0.37 ± 0.035*	0.59 ± 0.086+

[a]In this case, the BPC comprised pectin, glutamate, glycine, *N*-acetylcysteine, vitamins A, C, E, selenium, copper, calcium, and omega-3 PUFA

Note *Statistically significant difference from the control group; +from the group given nanoparticles without the BPC ($P < 0.05$ by Student's *t*-test); [#]the particle burden of a cell is visually estimated as a score of points from 0 to 4. The weighted average index is calculated allowing for the percentage ratio between cells given different scores (the total number of scored cells = 100); [†]Measured with the help of a planimetric grid

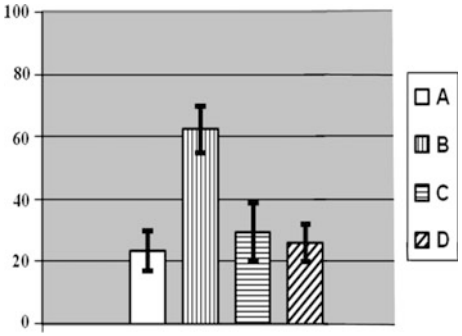

Fig. 11.32 Number of cells without a nucleolus per 100 Golgi cells in nucleus caudatus of rats exposed **a** to water (Control); **b** to water suspension of copper oxide nanoparticles; **c** to the same against background administration of the bioprotective complex (BPC), **d** to the BPC only (average values with 95% CI). Differences are statistically significant between (**b**) and (**a**); (**c**) and (**b**) ($P < 0.05$ by Student's *t*-test). First published in [16]

specialized structures of the brain (to the striatum and the hippocampus especially). In both cases, this damage was also significantly attenuated by the respective BPCs [11, 13]. Examples are given in Fig. 11.32 and Table 11.12.

Still another metal-specific outcome of subchronic Me-NP intoxications considered by us in Sect. 11.4.2 (Table 11.6) was an increased reticulocyte percentage under the impact of PbO-NPs (24.7 ± 2.7 against 10.2 ± 1.4‰ in control rats, $P < 0.05$). This effect was even more pronounced under a combined impact of PbO-NPs + CuO-NPs + ZnO-NPs (29.7 ± 3.2‰) but was significantly attenuated against background BPC administration (18.00 ± 1.6‰, $P < 0.05$). Similar

Table 11.12 Some morphometric indices for the state of rat's brain after repeated intraperitoneal injections of NiO and Mn_3O_4 nanoparticles with or without background oral administration of a BPC ($x \pm$ s.e.)

Golgi neurons (%%)	Rats injected with water (control)	Rats injected with nanoparticles	Rats injected with nanoparticles and administered BPC
Nucleus caudatus			
Without a nucleolus	30.50 ± 2.77	60.30 ± 2.26*	37.15 ± 2.89^{+}
With a distinct centrally located nucleolus	25.12 ± 1.16	12.35 ± 0.95*	23.28 ± 1.09^{+}
Hippocampus (CA 1)			
Without a nucleolus	30.50 ± 2.30	70.40 ± 3.75*	41.30 ± 2.14*$^{+}$
With a distinct centrally located nucleolus	46.4 ± 2.92	11.0 ± 1.13*	30.5 ± 1.96*$^{+}$

Note *Statistically significant difference from the control group; $^{+}$from the group given nanoparticles without the BPC ($P < 0.05$ by Student's *t*-test). First published in [14]

Table 11.13 Some functional indices for the condition of the rat after repeated intraperitoneal injections of NiO and Mn_3O_4 nanoparticles and/or oral administration of a BPC ($x \pm$ s.e.)

Index	Groups given			
	Water (control)	Nanoparticles	Nanoparticles and BPC	BPC
Leukocytes ($10^3/\mu L$)	8.6 ± 0.8	12.2 ± 1.0*	11.4 ± 1.2$^+$	8.6 ± 0.8
Bilirubin in blood serum (μmol/L)	2.02 ± 0.40	1.15 ± 0.10*	1.5 ± 0.1$^+$	1.7 ± 0.1
Albumin in blood serum (g/L)	46.6 ± 0.8	38.6 ± 0.8*	41.8 ± 1.1$^+$	47.3 ± 1.2
Diuresis (mL)	32.7 ± 1.8	17.9 ± 2.9*	30.2 ± 2.7$^+$	31.2 ± 4.5
Urine relative density	1.017 ± 0.001	1.023 ± 0.001*	1.019 ± 0.001$^+$	1.019 ± 0.001
Creatinine in urine (mmol/L)	1.09 ± 0.10	1.8 ± 0.20*	1.2 ± 0.1$^+$	1.2 ± 0.1
δ-ALA in urine (μmol/day)	0.23 ± 0.07	0.54 ± 0.13	0.22 ± 0.02	0.25 ± 0.08

Note *Statistically significant difference from the control group; $^+$from the group given NiO-NPs + Mn_3O_4-NPs (without the BPC) ($P < 0.05$ by Student's t-test with Bonferroni correction)

attenuation (although statistically non-significant) was observed in respect to the decrease in the hemoglobin level (165.5 ± 10.7 g/L against 145.5 ± 4.0 g/L in the group exposed without bio-protectors and 158.8 ± 5.6 g/L in the control group) and to the increase in the δ-ALA urine concentration (11.1 ± 4.3, 15.2 ± 25 and 8.1 ± 2.7 mcg/mL, respectively).

To illustrate the efficacy of bioprotection against less specific systemic toxic effects of Me-NPs, we may once again provide some results of the experiment involving nickel oxide in combination with manganese oxide nanoparticles. Table 11.13 presents the values of one those indices for which the difference between the groups exposed to Me-NPs with versus without BPC administration proved statistically significant, but there were even more indices in the protected group that lost their statistically significant distinction from the control values. In general, the group exposed to the Me-NPs combination without protection had a statistically significant adverse deviation from the control value in 25 out of the 50 functional and biochemical indices for the organism's status, whereas only one index (decrease in the number of head dips into holes) was observed to have such deviation in the group so exposed along with background BPC administration [13]. This table also demonstrates that the BPC, which significantly attenuated the adverse effects caused by nanoparticles, had by itself no effect on the respective indices. This is quite typical of all our experiments.

It should also be stressed that significant attenuation in the toxic effects was not necessarily associated with a decrease in the target organ's burden of toxic metal (including in the form of nanoparticles), although this beneficial toxicokinetic effect of the BPCs was also observed in some cases, as illustrated by Table 11.14 [12]. In the experiment with a combined exposure to NiO-NPs plus Mn_3O_4-NPs [13], BPC

Table 11.14 Copper content of some organs (mcg/g of dry-frozen tissue) in rats after repeated intraperitoneal injections of copper oxide nanoparticles and/or oral administration of a BPC ($x \pm$ s.e.)

Group of rats given	Kidneys	Liver	Spleen	Brain
Water (control)	42.4 ± 2.9	12.2 ± 2.4	22.5 ± 2.1	18.9 ± 0.7
CuO-NPs	62.5 ± 7.1*	28.8 ± 6.3*	24.2 ± 1.5	21.5 ± 1.7
CuO-NPs and BPC	59.4 ± 10.0	22.1 ± 3.5*	18.0 ± 2.5^{+}	18.8 ± 1.4
BPC	50.4 ± 5.6	10.6 ± 0.3	25.3 ± 2.2	20.8 ± 1.5

Note *Statistically significant difference from the control group; $^{+}$from the group given nanoparticles without the BPC ($P < 0.05$ by Student's *t*-test)

administration significantly decreased the retention of nickel, though not of manganese, in the liver, spleen, and brain. Under exposure to Ag-NPs, the retention of silver in the liver, spleen, and kidneys over the control levels was very significant but did not depend at all on BPC administration [8]. We believe that this seeming inconsistency is due to the predominance of toxicodynamic bioprotection mechanisms over toxicokinetic ones.

All of the above-described results demonstrate the attenuating effects of the bio-protectors on the subchronic systemic toxicity of Me-NPs. Could it be similarly demonstrated that such bio-protectors also beneficially influence the immediate pulmonary response to the deposition of such NPs in the lower airways? An affirmative answer to this question was obtained with the help of a single intratracheal instillation model. To this end, we carried out two experiments with BPC premedication during 4 weeks before the instillation of NiO-NPs + Mn_3O_4-NPs [9] or PbO-NPs + CuO-NPs + ZnO-NPs [115] and assessed this response by total and differential cell counts and by some biochemical BALF indices.

As can be seen from the results presented in Table 11.15, in both experiments we observed the usual prevalence of neutrophil leukocyte (NL) recruitment over that of alveolar macrophages (AMs), which is the most characteristic feature of the immediate pulmonary reaction to an impact of cytotoxic particles, including all Me-NPs studied by us up until now. In both experiments, the increase in the BALF NL count and NL/AM ratio over the respective control values was significantly lower in rats exposed to the same Me-NPs after a premedication with BPCs.

The interpretation of this NL-shift in the BALF free cell population was briefly discussed in the foregoing (see Sect. 11.4), but whatever the interpretation, this shift is an index of particles' pulmonary toxicity. Thus, the effect of the BPCs tested in these experiments may be considered as increasing resistance to the latter.

Taking the experiment with PbO-NPs + CuO-NPs + ZnO-NPs as an example, Table 11.16 demonstrates that all biochemical BALF indices for AM damage (such as the release of lysosomal enzymes) or for inflammation with increased vascular permeability (increased albumin content) were also lower in rats exposed after BPC premedication. Although the intergroup difference for each index is not significant statistically, the probability of a unidirectional chance difference between the groups in all 4 indices is <0.1 (0.0625).

Table 11.15 Influence of bioprotective premedication on the cell counts in the bronchoalveolar lavage fluid (BALF) of rats exposed to different metallic nanoparticles ($x \pm$ s.e.)

Exposure to	Number of cells $\times 10^6$			NL/AM count ratio
	Total	Neutrophil leukocytes (NL)	Alveolar macrophages (AM)	
24 h after the intratracheal instillation of NiO-NPs and Mn_3O_4 + NPs				
Me-NPs	9.6 ± 1.6*	7.17 ± 1.24*	2.3 ± 0.43	3.44 ± 0.62*
Me-NPs after 4 weeks BPC administration	5.7 ± 1.49	3.36 ± 1.38*$^+$	2.3 ± 0.29	1.46 ± 0.54*$^+$
Water after 4 weeks BPC administration	3.8 ± 0.75	0.67 ± 0.21	3.09 ± 0.64	0.23 ± 0.07
Water (control)	3.8 ± 0.9	0.34 ± 0.12	3.4 ± 0.86	0.12 ± 0.05
24 h after the intratracheal instillation of PbO-NPs + CuO-NPs + ZnO-NPs				
Me-NPs	7.93 ± 0.62*	5.86 ± 1.52*	2.07 ± 0.21	2.83 ± 0.77
Me-NPs after 4 weeks BPC administration	3.30 ± 0.53*$^+$	1.47 ± 0.36$^+$*	1.82 ± 0.40	1.11 ± 0.30$^+$
Water after 4 weeks BPC administration	2.18 ± 0.41	1.20 ± 0.35*	0.98 ± 0.25	1.59 ± 0.55*
Water (control)	1.40 ± 0.07	0.094 ± 0.029	1.30 ± 0.07	0.075 ± 0.024

Note *Statistically significant difference from the control group; $^+$from the group given nanoparticles without the BPC ($P < 0.05$ by Student's *t*-test)

Table 11.16 Influence of bioprotective premedication on the biochemistry of the bronchoalveolar lavage fluid (BALF) of rats exposed i.t. to a Me-NP combination ($x \pm$ s.e.)

Indices	Exposure to			
	Water (control)	Me-NPs	Me-NPs after 4 weeks BPC administration	Water after 4 weeks BPC administration
Albumin (g/L)	1.90 ± 0.08	2.50 ± 0.16*	2.20 ± 0.06*	1.99 ± 0.05
Amylase (IU/L)	6.56 ± 1.20	49.09 ± 15.46*	27.75 ± 7.86*	9.81 ± 1.47
γ-Glutamyl transpeptidase (IU/L)	1.01 ± 0.52	4.02 ± 0.93*	3.64 ± 1.10	1.15 ± 0.43
Lactate dehydrogenase (IU/L)	54.60 ± 10.74	91.10 ± 18.96	57.36 ± 6.59	36.20 ± 7.14

Note *Statistically significant difference from the control group ($P < 0.05$ by Student's *t*-test)

In the same context of pulmonary anti-NP protection, of interest are also some data obtained by us in a chronic inhalation experiment with iron oxide nano-aerosol. Airborne Fe_2O_3-NPs with a mean diameter of 14 ± 4 nm obtained by sparking from 99.99% pure iron rods were fed during 4 months, 5 times a week, 4 h per day into a nose-only exposure chamber for rats, while an analogous

chamber was used for sham exposures. The mean (±s.e.) concentration of Fe_2O_3-NPs was equal to 1.21 ± 0.17 mg/m^3. When being out of the chambers, half of the animals were given to drink 1.5% sodium glutamate solution (which is an obligatory component of all our BPCs) instead of water. It had been repeatedly demonstrated that drinking this solution increased dramatically organism's resistance to the cytotoxicity, pulmotoxicity and fibrogenicity of inhaled quartz dust and even decreased respective indices in control rats as well (e.g. [133]).

As follows from the results of this experiment (Table 11.17), glutamate proved to be an effective bio-protector against inhaled Fe_2O_3-NPs even if administered alone. Its protective efficacy was demonstrated in the same rats also when assessing the influence of iron oxide inhalation, with or without drinking the glutamate solution, by the activity of well-known marker enzymes in the BALF. Thus, for lactate dehydrogenase activity, the average values (x ± s.e.) were 33.80 ± 2.78 IU in control (sham-exposed) rats and 43.00 ± 7.39 IU in those inhaling NPs, while the same inhalation exposure with glutamate drinking provided only 26.40 ± 2.96 IU ($P < 0.05$). For γ-glutamyl transpeptidase, the respective values were 4.08 ± 0.28, 6.09 ± 0.87 and 4.02 ± 0.44 IU ($P < 0.05$).

The last, but not the least, the result of bioprotection we would like to demonstrate is as follows: while all the Me-NPs studied by us so far are more or less genotoxic, all the BPCs tested up until now significantly attenuated this most worrying effect. For instance, in one of the experiments [8], the coefficient of genomic DNA fragmentation calculated based on the results of the RAPD test (x ± s.e.) was equal to 0.40 ± 0.001 in the liver of control rats and to 0.46 ± 0.002* in the liver of rats exposed to subchronic intoxication with silver nanoparticles. In similarly exposed rats with background BPC administration, it was equal to just 0.41 ± 0.011$^+$; 0.39 ± 0.003, 0.46 ± 0.032*, 0.37 ± 0.003*$^+$ in the bone marrow; 0.38 ± 0.002, 0.46 ± 0.001*, 0.42 ± 0.003*$^+$ in the spleen;

Table 11.17 Influence of glutamate solution drinking on the cell counts in the bronchoalveolar lavage fluid (BALF) of rats chronically exposed to Fe_2O_3-NPs in the inhaled air (x ± s.e.)

Exposure	Number of cells × 10^6			NL/AM count ratio
	Total	Neutrophil leukocytes (NL)	Alveolar macrophages (AM)	
Sham (drinking water)	2.16 ± 0.22	0.22 ± 0.05	1.93 ± 0.19	0.12 ± 0.02
Sham (drinking glutamate)	1.52 ± 0.13*	0.11 ± 0.02	1.40 ± 0.13	0.09 ± 0.05
Fe_2O_3-NPs (drinking water)	1.96 ± 0.18	0.43 ± 0.07	1.51 ± 0.18	0.32 ± 0.07*
Fe_2O_3-NPs (drinking glutamate)	1.76 ± 1.53	0.24 ± 0.04$^+$	1.52 ± 0.09	0.15 ± 0.02$^+$

Note *Statistically significant difference from the control group; $^+$from the group inhaling nanoparticles without the glutamate drink ($P < 0.05$ by Student's t-test)

0.39 ± 0.003, 0.42 ± 0.008*, 0.40 ± 0.006*$^{+}$ in the kidneys; 0.38 ± 0.001, 0.41 ± 0.012*, 0.39 ± 0.007 in nucleated blood cells, respectively, (in both exposed groups, the values differing statistically significantly from respective control ones are tagged with an asterisk, in the group exposed to NPs and administered the BPC, the values differing from respective ones in the group exposed without the BPC are marked with a cross). As additional illustration, here are the results of this test for nucleated blood cells in the experiment with NiO-NPs + Mn_3O_4-NPs [13]: 0.42 ± 0.00, 0.50 ± 0.01*, 0.45 ± 0.01*$^{+}$, respectively, and the results for spleen cells in the experiment with CuO-NPs [11]: 0.37 ± 0.002, $0.46 \pm 0.002^{*}$, 0.42 ± 0.002*$^{+}$, respectively.

11.6 Conclusions

Metal and metal oxide NPs are of special interest in the light of health risk assessment and management because they are not only commercially engineered but are also commonly present in substantial proportions as nanoscale ("ultrafine") particles of the same substances in the particle size distribution of condensation aerosols generated by arc-welding, metallurgical processes, and some chemical technologies. Several examples illustrating this statement have been given in this chapter.

In a series of experiments on outbred white rats of our own breading, we have compared the toxicity of spherical metallic particles in the nanometer and micrometer ranges. We have studied iron oxide (Fe_3O_4) nanoparticles produced by a chemical technique and nanoparticles of silver, gold, copper oxide, nickel oxide, manganese oxide, lead oxide, and zinc oxide produced by laser ablation of respective 99.99% pure metals in deionized water. In some experiments, we compared particles of one and the same chemical composition having different diameters, while in others—equidimensional nanoparticles of different metals or metal oxides. Nanoparticles were produced as water suspensions (either quite stable or, in some cases, ultrasonicated before injection/instillation but never stabilized by a chemical).

Each kind of nano-suspension was tested using two experimental models:

(a) a single intratracheal (IT) instillation in low doses 24 h before the bronchoalveolar lavage to obtain a fluid (BALF) for cytological and biochemical assessment;
(b) repeated intraperitoneal (IP) injections during 6–7 weeks in non-lethal doses to assess the thus induced subchronic intoxication by a lot of functional and morphological indices and by the distribution and elimination of respective nanoparticles.

In both types of experiment, we tested the effects of the above-listed nanoparticles not only acting alone but some of them also in combinations (NiO + Mn_3O_4; CuO + PbO; CuO + ZnO; PbO + ZnO; PbO + CuO + ZnO).

In several experiments, a special group of rats was being given per as a complex of innocuous bioactive substances along with IP exposure or during one month before IT exposure to nanoparticles.

Besides, we carried out a 10-month inhalation experiment with an iron oxide (Fe_2O_3) aerosol produced by a sparking nanoparticle generator and fed to rats in a "nose-only" inhalation system.

Our research has demonstrated that metallic nanoparticles are much more noxious as compared with their fine micrometric or even submicron counterparts. Moreover, metallic nanoparticles are generally more toxic, the smaller their dimensions *within* the nanoscale range. However, for the RES-rich organs, this dependence is not so unique due to intricate and often contra-directional influences of this parameter on toxicodynamics and toxicokinetics.

At the same time, the in situ cytotoxicity, organ-systemic toxicity, and in vivo genotoxicity of nanoparticles having a given geometry strongly depends on their chemical nature and on the properties associated with the latter (in vivo solubility included) as well as on the specific mechanisms of action characteristic of a given metal in any chemical form. A mathematical analysis has shown that for the nanoparticles studied, as well as for soluble salts of the respective metals, there exist not merely three traditionally acknowledged types of binary combined toxicity (additivity, subadditivity and superadditivity) but up to 10 variants of them depending on exactly which effect is considered, on its level, as well as on dose levels and their ratio. Where a 3rd component is present in a combination, these variants can change more or less significantly.

All water-insoluble nanoparticles of metals and, especially, of metal oxides are significantly solubilized in some biological milieus, and this process plays an important part in the biokinetics. This role of Me-NP solubilization can even prevail over that of the physiological mechanisms controlling their distribution, retention, and elimination. On the other hand, we have proved that thanks to the high activity of these mechanisms (pulmonary phagocytosis in the first place) the animal organism is not as defenseless against the impact of nanoparticles as many researchers thought it to be. Moreover, the smaller the particles, the higher this defensive physiological activity.

Nevertheless, we maintain that even though the defense mechanisms may be highly active, metallic nanoparticles are one of the most dangerous occupational and environmental hazards due to their especially high toxicity and virtually obligatory genotoxicity. That is why the standards or recommended values of presumably safe nanoparticle concentrations in the workplace and ambient air should be significantly lower as compared with those established for their micrometric counterparts.

At the same time, we have shown that the toxicity and even genotoxicity of metallic nanoparticles could be markedly attenuated by background administration of adequately composed combinations of some bioactive agents in innocuous doses.

We, therefore, believe that, along with decreasing exposures to nanoparticles, enhancing the organism's resistance to their adverse effects with the help of such bio-protectors can be an efficient auxiliary tool of health risk management in related occupations.

References

1. Hedberg YS, Pradhan S, Cappellini F, Karlsson ME, Blomberg E, Karlsson HL, Odnevall Wallinder I, Hedberg JF (2016) Electrochemical surface oxide characteristics of metal nanoparticles (Mn, Cu and Al) and the relation to toxicity. J Electrochim Acta 212:360–371
2. Katsnelson BA, Privalova LI, Degtyareva TD, Sutunkova MP, Minigalieva IA, Kireyeva EP, Khodos MY, Kozitsina AN, Shur VY, Nikolaeva EV, Vazhenin VA, Potapov AP, Morozova MV, Valamina IE, Tulakina LG, Pichugova SV, Beikin JB (2010) Experimental estimates of the toxicity of iron oxide Fe_3O_4 (magnetite) nanoparticles. Cent Eur J Occup Environ Med 16:47–63
3. Katsnelson BA, Privalova LI, Kuzmin SV, Degtyareva TD, Sutunkova MP, Yeremenko OS, Minigalieva IA, Kireyeva EP, Khodos MY, Kozitsina AN, Malakhova NA, Glazyrina JA, Shur VY, Shishkin EI, Nikolaeva EV (2010) Some peculiarities of pulmonary clearance mechanisms in rats after intratracheal instillation of magnetite (Fe_3O_4) suspensions with different particle sizes in the nanometer and micrometer ranges: are we defenseless against nanoparticles? Int J Occup Environ Health 16:503–519
4. Katsnelson BA, Degtyareva TD, Minigalieva IA, Privalova LI, Kuzmin SV, Yeremenko OS, Kireyeva EP, Sutunkova MP, Valamina II, Khodos MY, Kozitsina AN, Shur VY, Vazhenin VA, Potapov AP, Morozova MV (2011) Sub-chronic systemic toxicity and bio-accumulation of Fe_3O_4 nano- and microparticles following repeated intraperitoneal administration to rats. Int J Toxicol 30:59–68
5. Katsnelson BA, Privalova LI, Kuzmin SV, Gurvich VB, Sutunkova MP, Kireyeva EP, Minigalieva IA (2012) An approach to tentative reference levels setting for nanoparticles in the workroom air based on comparing their toxicity with that of their micrometric counterparts: a case study of iron oxide Fe_3O_4. ISRN Nanotechnol 143613
6. Katsnelson BA, Privalova LI, Sutunkova MP, Khodos MY, Shur VY, Shishkina EV, Tulakina LG, Pichugova SV, Beikin JB (2012) Uptake of some metallic nanoparticles by, and their impact on pulmonary macrophages in vivo as viewed by optical, atomic force, and transmission electron microscopy. J Nanomed Nanotechnol 3:1–8
7. Katsnelson BA, Privalova LI, Sutunkova MP, Tulakina LG, Pichugova SV, Beykin JB, Khodos MJ (2012) The "in vivo" interaction between iron oxide Fe_3O_4 nanoparticles and alveolar macrophages. J Bull Exp Biol Med 152:627–631
8. Katsnelson BA, Privalova LI, Gurvich VB, Makeyev OH, Shur VY, Beikin YB, Sutunkova MP, Kireyeva EP, Minigalieva IA, Loginova NV, Vasilyeva MS, Korotkov AV, Shuman EA, Vlasova LA, Shishkina EV, Tyurnina AE, Kozin RV, Valamina IE, Pichugova SV, Tulakina LG (2013) Comparative in vivo assessment of some adverse bio-effects of equidimensional gold and silver nanoparticles and the attenuation of nanosilver's effects with a complex of innocuous bioprotectors. Int J Mol Sci 14:2449–2483
9. Katsnelson BA, Minigalieva IA, Privalova LI, Sutunkova MP, Gurvich VB, Shur VY, Shishkina EV, Varaksin AN, Panov VG (2014) Lower airways response in rats to a single or combined intratracheal instillation of manganese and nickel nanoparticles and its attenuation with a bio-protective pre-treatment. J Toksicol Vestn 6:8–14
10. Katsnelson BA, Privalova LI, Gurvich VB, Kuzmin SV, Kireyeva EP, Minigalieva IA, Sutunkova MP, Loginova NV, Malykh OL, Yarushin SV, Soloboyeva JI, Kochneva NI (2014) Enhancing population's resistance to toxic exposures as an auxilliary tool of

decreasing environmental and occupational health risks (a self-overview). J Environ Prot 5:1435–1449
11. Privalova LI, Katsnelson BA, Loginova NV, Gurvich VB, Shur VY, Beikin YB, Sutunkova MP, Minigalieva IA, Shishkina EV, Pichugova SV, Tulakina LG, Beljayeva SV (2014) Some characteristics of free cell population in the airways of rats after intratracheal instillation of copper-containing nano-scale particles. Int J Mol Sci 15:21538–21553
12. Privalova LI, Katsnelson BA, Loginova NV, Gurvich VB, Shur VY, Valamina IE, Makeyev OH, Sutunkova MP, Minigalieva IA, Kireyeva EP, Rusakov VO, Tyurnina AE, Kozin RV, Meshtcheryakova EY, Korotkov AV, Shuman EA, Zvereva AE, Kostykova SV (2014) Subchronic toxicity of copper oxide nanoparticles and its attenuation with the help of a combination of bioprotectors. Int J Mol Sci 15:12379–12406
13. Minigalieva IA, Katsnelson BA, Privalova LI, Sutunkova MP, Gurvich VB, Shur VY, Shishkina EV, Valamina IE, Makeyev OH, Panov VG, Varaksin AN, Grigoryeva EV, Meshtcheryakova EY (2015) Attenuation of combined nickel(II) oxide and manganese(II, III) oxide nanoparticles' adverse effects with a complex of bioprotectors. Int J Mol Sci 16 (9):22555–22583
14. Katsnelson BA, Privalova LI, Sutunkova MP, Privalova LI, Varaksin AN, Gurvich VB, Sutunkova MP, Shur VY, Shishkina EV, Valamina IE, Makeyev OH (2015) Some patterns of metallic nanoparticles' combined subchronic toxicity as exemplified by a combination of nickel and manganese oxide nanoparticles. J Food Chem Toxicol 86:351–364
15. Katsnelson BA, Panov VG, Minigaliyeva IA, Varaksin AN, Privalova LI, Slyshkina TV, Grebenkina SV (2015) Further development of the theory and mathematical description of combined toxicity: an approach to classifying types of action of three-factorial combinations (a case study of manganese–chromium–nickel subchronic intoxication). Toxicology 334:33–44
16. Katsnelson BA, Privalova LI, Sutunkova MP, Minigalieva IA, Gurvich VB, Shur VY, Makeyev OH, Valamina IE, Grigoryeva EV (2015) Is it possible to enhance the organism's resistance to toxic effects of metallic nanoparticles? Toxicology 337:79–82
17. Sutunkova MP, Katsnelson BA, Privalova LI, Gurvich VB, Konysheva LK, Shur VY, Shishkina EV, Minigalieva IA, Solovjeva SN, Grebenkina SV, Zubarev IV (2016) On the contribution of the phagocytosis and the solubilization to the iron oxide nanoparticles retention in and elimination from lungs under long-term inhalation exposure. Toxicology 363:19–28
18. Zhu MT, Feng WY, Wang B, Wang TC, Gu YQ, Wang M, Wang Y, Ouyang H, Zhao YL, Chai ZF (2008) Comparative study of pulmonary responses to nano- and submicron ferric oxide in rats. Toxicology 247:102–111
19. Mahmoudi M, Simchi A, Milani AS, Stroeve P (2009) Cell toxicity of superparamagnetic iron oxide nanoparticles. J Colloid Interface Sci 336(2):510–518
20. Naqvi S, Samim M, Abdin MZ, Ahmed FJ, Maitra A, Prashant C, Dinda AK (2010) Concentration-dependent toxicity of iron oxide nanoparticles mediated by increased oxidative stress. Int J Nanomed 5:983–989
21. Singh N, Jenkins GJS, Asadi R, Doak SH (2010) Potential toxicity of superparamagnetic iron oxide nanoparticles (SPION). J Nano Rev 1:5358
22. Wu X, Tan Y, Mao H, Zhang M (2010) Toxic effects of iron oxide nanoparticles on human umbilical vein endothelial cells. Int J Nanomed 5:385–399
23. Mahmoudi M, Laurent S, Shokrgozar MA, Hosseinkhani M (2011) Toxicity evaluations of superparamagnetic iron oxide nanoparticles: cell "vision" versus physicochemical properties of nanoparticles. J ACS Nano 5(9):7263–7276
24. Markides H, Rotherham M, El Haj AJ (2012) Biocompatibility and toxicity of magnetic nanoparticles in regenerative medicine. J Nanomater 2012:1–11
25. Soenen SJ, De Cuyper M, De Smedt SC, Braeckmans K (2012) Investigating the toxic effects of iron oxide nanoparticles. J Methods Enzymol 509:195–224

26. Barhoumi L, Dewez D (2013) Toxicity of superparamagnetic iron oxide nanoparticles on green alga *Chlorella vulgaris*. BioMed Res 647974
27. Liu G, Gao J, Ai H, Chen X (2013) Applications and potential toxicity of magnetic iron oxide nanoparticles. J Small 9(9–10):1533–1545
28. Ahamed M, Karns M, Goodson M, Rowe J, Hussain SM, Schlager JJ, Hong Y (2008) DNA damage response to different surface chemistry of silver nanoparticles in mammalian cells. J Toxicol Appl Pharmacol 233:404–410
29. Arora S, Jain J, Rajwade JM, Paknikar KM (2009) Interactions of silver nanoparticles with primary mouse fibroblasts and liver cells. J Toxicol Appl Pharmacol 236:310–318
30. Ahamed M, AlSalhi MS, Siddiqui MKJ (2010) Silver nanoparticles applications and human health. J Clin Chim Acta 411:1841–1848
31. Choi JE, Kim S, Ahn JH, Youn P, Kang JS, Park K, Yi J, Ryu DY (2010) Induction of oxidative stress and apoptosis by silver nanoparticles in the liver of adult zebrafish. J Aquat Toxicol 100:151–159
32. Kim YS, Song MY, Park JD, Song KS, Ryu HR, Chung YH, Chang HK, Lee JH, Oh KH, Kelman BJ, Hwang IK, Yu IJ (2010) Subchronic oral toxicity of silver nanoparticles. J Part Fibre Toxicol 7(1):20
33. Li T, Albee B, Alemayehu M, Diaz R, Ingham L, Kamal S, Rodriguez M, Bishnoi SW (2010) Comparative toxicity study of Ag, Au, Ag-Au bimetallic nanoparticles on *Daphnia magna*. J Anal Bioanal Chem 398:689–700
34. Park EJ, Bae E, Yi Y, Kim Y, Choi K, Lee SH, Yoon J, Lee BC, Park K (2010) Repeated-dose toxicity and inflammatory responses in mice by oral administration of silver nano-particles. J Environ Toxicol Pharmacol 30:162–168
35. Trickler WJ, Lantz SM, Murdock RC, Schrand AM, Robinson BL, Newport GD, Schlager JJ, Oldenburg SJ, Paule MG, Slikker W Jr, Hussain SM, Ali SF (2010) Silver nanoparticle induced blood-brain barrier inflammation and increased permeability in primary rat brain micro vessel endothelial cells. J Toxicol Sci 118:160–170
36. Ahmadi F, Kordestany AH (2011) Investigation on silver retention in different organs and oxidative stress enzymes in male broiler fed diet supplemented with powder of nano silver. Amer-Eurasian J Toxicol Sci 3:28–35
37. Foldbjerg R, Dang DA, Autrup H (2011) Cytotoxicity and genotoxicity of silver nanoparticles in the human lung cancer cell line, A549. J Arch Toxicol 85:743–750
38. Hackenberg S, Scherzed A, Kessler M, Hummel S, Technau A, Froelich K, Ginzkey C, Koehler C, Hagen R, Kleinsasser N (2011) Silver nanoparticles: evaluation of DNA damage, toxicity and functional impairment in human mesenchymal stem cell. J Toxicol Lett 201:27–33
39. Kim HR, Kim MJ, Lee SY, Oh SM, Chung KH (2011) Genotoxic effects of silver nanoparticles stimulated by oxidative stress in human normal bronchial epithelial (BEAS-2B) cells. J Mutat Res 726:129–135
40. Park MV, Neigh AM, Vermeulen JP, de la Fonteyne LJ, Verharen HW, Briedé JJ, van Loveren H, de Jong WH (2011) The effect of particle size on the cytotoxicity, inflammation, developmental toxicity and genotoxicity of silver nanoparticles. Biomaterials 32:9810–9817
41. Singh S, D'Britto V, Prabhune AA, Ramana CV, Dhawan A, Prasad BLV (2011) Cytotoxic and genotoxic assessment of glycolipid-reduced and -capped gold and silver nanoparticles. New J Chem 34:294–301
42. Srivastava M, Singh S, Self WT (2011) Exposure to silver nanoparticles inhibits selenoprotein synthesis and the activity of thioredoxin reductase. J Environ Health Perspect 120:56–61
43. Stebounova LV, Adamcakova-Dodd A, Kim JS (2011) Nanosilver induces minimal lung toxicity or inflammation in a subacute murine inhalation model. J Part Fibre Toxicol 8(1):5
44. Asare N, Instanes C, Sandberg WJ, Refsnes M, Schwarze P, Kruszewski M, Brunborg G (2012) Citotoxic and genotoxic effects of silver nanoparticles in testicular cell. Toxicology 291:65–72

45. Flower NAL, Brabu B, Revathy M, Gopalakrishnan C, Raja SV, Murugan SS, Kumaravel TS (2012) Characterization of synthesized silver nanoparticles and assessment of its genotoxicity potentials using the alkaline comet assay. J Mutat Res 742:61–65
46. Karlsson HL, Gliga AR, Kohonen P, Wallberg A, Fadeel B (2012) Genotoxic and epigenetic effects of silver nanoparticles. J Toxicol Lett 211S:S35–S42
47. Li Y, Chen DH, Yan J, Chen Y, Mittelstaedt RA, Zhang Y, Biris AS, Heflich RH, Chen T (2012) Genotoxicity of silver nanoparticles evaluated using the Ames test and in vitro micronucleus assay. J Mutat Res 745:4–10
48. Lim DH, Jang J, Kim S, Kang T, Lee K, Choi IH (2012) The effects of sub-lethal concentrations of silver nanoparticles on inflammatory and stress in human macrophages using cDNA microarray analysis. Biomaterials 33:4690–4699
49. Tavares P, Balbino F, de Oliveira HM, Fagundes GE, Venâncio M, Ronconi JVV, Merlini A, Streck EL, da Silva Paula MM, de Andrade VM (2012) Evaluation of genotoxic effect of silver nanoparticles (Ag-NPs) in vitro and in vivo. J Nanopart Res 14(4):1–7
50. Beer C, Foldbjerg R, Hayashi Y, Sutherland DS, Autrup H (2012) Toxicity of silver nanoparticles—nanoparticle or silver ion? J Toxicol Lett 208:286–292
51. Cronholm P, Karlsson HL, Hedberg J, Lowe TA, Winnberg L, Elihn K, Wallinder IO, Möller L (2013) Intracellular uptake and toxicity of Ag and CuO nanoparticles: a comparison between nanoparticles and their corresponding metal ions. J Small 8:970–982
52. Gomes T, Araújo O, Pereira R, Almeida AC, Cravo A, Bebianno MJ (2013) Genotoxicity of copper oxide and silver nanoparticles in the mussel *Mytilus galloprovincialis*. J Mar Environ Res 84:51–59
53. Bakri SJ, Pulido JS, Mukerjee P, Marler RJ, Mukhopadhyay D (2008) Absence of histologic retinal toxicity of intravitreal nanogold in a rabbit model. J Retina 28:147–149
54. Chen YSh, Hung YCh, Huang GS (2009) Assessment of the in vivo toxicity of gold nanoparticles. J Nanoscale Res Lett 4:858–864
55. Pan Y, Leifert A, Ruau D, Neuss S, Bornemann J, Schmid G, Brandau W, Simon U, Jahnen-Dechent W (2009) Gold nanoparticles of diameter 1.4 nm trigger necrosis by oxidative stress and mitochondrial damage. J Small 5:2067–2076
56. Balasurbamanian SK, Jittiwat J, Manikandan J, Ong CN, Yu LE, Ong WY (2010) Biodistribution of gold nanoparticles and gene expression changes in the liver and spleen after intravenous administration in rats. J Biomater 31:2034–2042
57. Zhang Q, Hitchins VM, Schrand AM, Hussain SM, Goering PL (2010) Uptake of gold nanoparticles in murine macrophage cells without cytotoxicity or production of proinflammatory mediators. Nanotoxicology 5:284–295
58. Glazer ES, Zhu C, Hamir AN, Borne A, Thompson CS, Curley SA (2011) Biodistribution and acute toxicity of naked gold nanoparticles in a rabbit hepatic tumor model. Nanotoxicology 5:459–468
59. Li JJ, Lo SL, Ng CT, Gurung RL, Hartono D, Hande MP, Ong CN, Bay BH, Yung LY (2011) Genomic instability of gold nanoparticle treated human lung fibroblast cells. J Biomater 32:5515–5523
60. Mustafa T, Watanabe F, Monroe W, Mahmood M, Xu Y, Saeed LM, Karmakar A, Casciano D, Ali S, Biris AS (2011) Impact of gold nanoparticle concentration on their cellular uptake by MC3T3-E1 mouse osteoblastic cells as analyzed by transmission electron microscopy. J Nanomed Nanotechnol 2:1–8
61. Trickler WJ, Lantz SM, Murdock RC, Schrand AM, Robinson BL, Newport GD, Schlager JJ, Oldenburg SJ, Paule MG, Slikker W Jr, Hussain SM, Ali SF (2011) Brain microvessel endothelial cells responses to gold nanoparticles: in vitro pro-inflammatory mediators and permeability. J Nanotoxicol 5:479–492
62. Choi SY, Jeong S, Jang SH, Park J, Park JH, Ock KS, Lee SY, Joo SW (2012) In vitro toxicity protein-adsorbed citrate-reduced gold nanoparticles in human lung adenocarcinoma cells. J Toxicol In Vitro 26:229–237
63. Dykman L, Khlebtsov N (2012) Gold nanoparticles in biomedical applications: recent advances and perspectives. J Chem Soc Rev 41:2256–2282

64. Rudolf R, Friedrich B, Stopic S, Anzel I, Tomic S, Colic M (2012) Cytotoxicity of gold nanoparticles prepared by ultrasonic spray pyrolysis. J Biomater Appl 26:595–612
65. Shulz M, Ma-Hock L, Brill S, Strauss V, Treumann S, Gröters S, van Ravenzwaay B, Landsiedel R (2012) Investigation on the genotoxicity of different sizes of gold nanoparticles administered to the lungs of rats. J Mutat Res 745:51–57
66. Chen Z, Meng H, Xing G, Chen C, Zhao Y, Jia G, Wang T, Yuan H, Ye C, Zhao F, Chai Z, Zhu C, Fang X, Ma B, Wan L (2006) Acute toxicological effects of copper nanoparticles in vivo. J Toxicol Lett 25:109–120
67. Karlsson H, Cronholm P, Gustafsson J, Moller L (2008) Copper oxide nanoparticles are highly toxic: a comparison between metal oxide nanoparticles and carbon nanotubes. J Chem Res Toxicol 21:1726–1732
68. Studer AM, Limbach LK, Van Duc L, Krumeich F, Athanassiou EK, Gerber LC, Moch H, Stark WJ (2010) Nanoparticle cytotoxicity depends on intracellular solubility: comparison of stabilized copper metal and degradable copper oxide nanoparticles. J Toxicol Lett 1:169–174
69. Bondarenko O, Ivask A, Käkinen A, Kahru A (2012) Sub-toxic effects of CuO nanoparticles on bacteria: kinetics, role of Cu ions and possible mechanisms of action. J Environ Pollut 169:81–89
70. Magaye R, Zhao J, Bowman L, Ding M (2012) Genotoxicity and carcinogenicity of cobalt-, nickel- and copper-based nanoparticles. J Exp Ther Med 4:551–561
71. Pang C, Selck H, Misra SK, Berhanu D, Dybowska A, Valsami-Jones E, Forbes VE (2012) Effects of sediment-associated copper to the deposit-feeding snail, *Potamopyrgus antipodarum*: a comparison of Cu added in aqueous form or as nano- and micro-CuO particles. J Aquat Toxicol 15:114–122
72. Akhtar MJ, Kumar S, Alhadlaq HA, Alrokayan SA, Abu-Salah KM, Ahamed M (2013) Dose-dependent genotoxicity of copper oxide nanoparticles stimulated by reactive oxygen species in human lung epithelial cells. J Toxicol Ind Health 32:5
73. Alarifi S, Ali D, Verma A, Alakhtani S, Ali BA (2013) Cytotoxicity and genotoxicity of copper oxide nanoparticles in human skin keratinocytes cells. Int J Toxicol 32:296–307
74. Cuillel M, Chevallet M, Charbonnier P, Fauquant C, Pignot-Paintrand I, Arnaud J, Cassio D, Michaud-Soret I, Mintz E (2014) Interference of CuO nanoparticles with metal homeostasis in hepatocytes under sub-toxic conditions. J Nanoscale 16:1707–1715
75. Xu J, Li Z, Xu P, Xiao L, Yang Z (2013) Nanosized copper oxide induces apoptosis through oxidative stress in podocytes. J Arch Toxicol 87:1067–1073
76. Zhang Q, Yukinori K, Sato K, Nakakuki K, Kohyama N, Donaldson K (1998) Differences in the extent of inflammation caused by intratracheal exposure to three ultrafine metals: role of free radicals. J Toxicol Environ Health 53:423–438
77. Morimoto Y, Hirohashi M, Ogami A, Oyabu T, Myojo T, Hashiba M, Mizuguchi Y, Kambara T, Lee BW, Kuroda E, Tanaka I (2011) Pulmonary toxicity following an intratracheal instillation of nickel oxide nanoparticle agglomerates. J Occup Health 53 (4):293–295
78. Magaye R, Zhao J (2012) Recent progress in studies of metallic nickel and nickel-based nanoparticles' genotoxicity and carcinogenicity. Environ Toxicol Pharmacol 34(3):644–650
79. Capasso L, Camatini M, Gualtieri M (2014) Nickel oxide nanoparticles induce inflammation and genotoxic effect in lung epithelial cells. Toxicol Lett 226(1):28–34
80. Pang H, Zhang B, Du J, Chen J, Zhanga J, Lia S (2012) Porous nickel oxide nanospindles with huge specific capacitance and long-life cycle. J RSC Adv 2:2257–2261
81. Hussain SM, Javorina AK, Schrand AM, Duhart HM, Ali SF, Schlager JJ (2006) The interaction of manganese nanoparticles with PC-12 cells induces dopamine depletion. J Toxicol Sci 92(2):456–463
82. Singh SP, Kumari M, Kumari SI, Rahman MF, Mahboob M, Grover P (2013) Toxicity assessment of manganese oxide micro and nanoparticles in Wistar rats after 28 days of repeated oral exposure. J Appl Toxicol 33(10):1165–1179
83. Bellusci M, La Barbera A, Padella F, Mancuso M, Pasquo A, Grollino MG, Leter G, Nardi E, Cremisini C, Giardullo P, Pacchierotti F (2014) Biodistribution and acute toxicity

of a nanofluid containing manganese iron oxide nanoparticles produced by a mechanochemical process. Int J Nanomed 9:1919–1929
84. Wang B, Fen WY, Wang TC, Jia G, Wang M, Shi JW, Zhang F, Zhao YL, Chai ZF (2006) Acute toxicity of nano- and micro-scale zinc powder in healthy adult mice. J Toxicol Lett 161(2):115–123
85. Cho WS, Duffin R, Howie S, Scotton CJ, Wallace WA, Macnee W, Bradley M, Megson IL, Donaldson K (2011) Progressive severe lung injury by zinc oxide nanoparticles; the role of Zn^{2+} dissolution inside lysosomes. J Part Fibre Toxicol. 8:27
86. Adamcakova-Dodd A, Stebounova LV, Kim JS, Vorrink SU, Ault AP, O'Shaughnessy PT, Grassian VH, Thorne PS (2014) Toxicity assessment of zinc oxide nanoparticles using sub-acute and sub-chronic murine inhalation models. J Part Fibre Toxicol. 11:15
87. Jacobsen NR, Stoeger T, van den Brule S, Saber AT, Beyerle A, Vietti G, Mortensen A, Szarek J, Budtz HC, Kermanizadeh A, Banerjee A, Ercal N, Vogel U, Wallin H, Møller P (2015) Acute and subacute pulmonary toxicity and mortality in mice after intratracheal instillation of ZnO nanoparticles in three laboratories. Food Chem Toxicol 85:84–95
88. Gao F, Ma NJ, Zhou H, Wang Q, Zhang H, Wang P, Hou H, Wen H, Li L (2016) Zinc oxide nanoparticles induced epigenetic change and G2/M arrest are associated with apoptosis in human epidermal keratinocytes. Int J Nanomed 11:3859–3874
89. Shaikh SM, Shyama SK, Desai PV (2015) Absorption, LD50 and effects of CoO, MgO and PbO nanoparticles on mice "*Mus musculus*". IOSR-JESTFT 9(2):32–38
90. Amiri A, Mohammadi M, Shabani M (2016) Synthesis and toxicity evaluation of lead oxide (PbO) nanoparticles in rats. Electron J Biol 12(2):110–114
91. Ali SF, Boulton MC, Braydish-Stolle LK, Murdock RC, Jiang H, Rongzhu L, Miltatovic D, Aschner M, Schlager JJ, Hussain SM (2009) Cytotoxic effects of manganese nanoparticles using different solvent system in astrocytes and neuronal cultured cell. FASEB 23(1), suppl.759.3
92. Ngwa H, Kanthasamy A, Gu Y, Fang N, Anantharam V, Kanthasamy AG (2011) Manganese nanoparticle activates mitochondrial dependent apoptotic signaling and autophagy in dopaminergic neuronal cells. J Toxicol Appl Pharmacol 256(3):227–240
93. Geiser M, Kreyling WG (2010) Deposition and biokinetics of inhaled nanoparticles. J Part Fibre Toxicol 7(1):2
94. ICRP (1994) Human respiratory tract model for radiological protection. A report of a Task Group of the International Commission on Radiological Protection. Ann. ICRP, vol 24, pp 1–482
95. Kreyling WG, Geiser M (2009) Dosimetry of inhaled nanoparticles. In: Marijnissen JCM, Gradon L (eds) Nanoparticles in medicine and environment, inhalation and health effects. Springer, Dordrecht
96. Fröhlich E, Salar-Behzadi S (2014) Toxicological assessment of inhaled nanoparticles: role of in vivo, ex vivo, in vitro, and in silico studies. Int J Mol Sci 15:4795–4822
97. Sadauskas E, Wallin H, Stolenberg M, Vogel U, Doering P, Larsen A, Danscher G (2007) Kupffer cells are central in the removal of nanoparticles from the organism. J Part Fibre Toxicol 4:10–16
98. Lasagna-Reeves C, Gonzalez-Romero D, Barria MA, Olmedo I, Clos A, Sadagopa Ramanujam VM, Urayama A, Vergara L, Kogan MJ, Soto C (2010) Bioaccumulation and toxicity of gold nanoparticles after repeated administration in mice. J Biochem Biophys Res Commun 393:649–655
99. Rylova ML (1964) Methods of investigating long-term effects of noxious environmental agents in animal experiments. Meditsina, Leningrad
100. Abeyemi OO, Yemitan OK, Taiwo AE (2006) Neurosedative and muscle-relaxant activities of ethyl acetate extract of *Baphianitida nitida* AFZEL. Ethnopharmacology 106:312–316
101. Fernandez SP, Wasowski C, Loscalzo LM, Granger RE, Johnston GA, Paladini AC, Marder M (2006) Central nervous system depressant action of flavonoid glycosides. Eur J Pharmacol 539:168–176

102. Donaldson K, Stone V, Tran CK, Kreyling W, Borm PJ (2004) Nanotoxicology (editorial). J Occup Environ Med 61:727–728
103. Oberdörster G, Oberdörster E, Oberdörster J (2005) Nanotoxicology: an emerging discipline evolving from studied of ultrafine particles. J Environ Health Perspect 113:823–839
104. Fadeel B (2012) Clear and present danger? Engineered nanoparticles and the immune system. J Swiss Med Wkly 142(24):w13609
105. Kilburn KH (1969) Alveolar clearance of particles. A bullfrog lung model. J Arch Environ Health 18:556–563
106. Renwick L, Brown D, Clouter K, Donaldson K (2004) Increased inflammation and altered macrophage chemotactic responses caused by two ultrafine particle types. J Occup Environ Med 61:442–447
107. Stoeger T, Reinhard C, Takenaka Sh, Schroeppel A, Karg E, Ritter B, Heyder J, Schulz H (2006) Instillation of six different ultrafine carbon particles indicates a surface area threshold dose for acute lung inflammation in mice. J Environ Health Perspect 114(3):328–333
108. Sager TM, Porter DW, Robinson VA, Lindsley WG, Schwegler-Berry DE, Castranova V (2007) Improved method to disperse nanoparticles in vitro and in vivo investigation of toxicity. Nanotoxicology 1:118–129
109. Grassian VH, O'Shaughnessy PT, Adamcakova-Dodd A, Pettibone JM, Thorne PS (2007) Inhalation exposure study of titanium dioxide nanoparticles with a primary particle size of 2 to 5 nm. J Environ Health Perspect 115:397–402
110. Warheit DB, Reed KL, Sayes CM (2009) A role fore surface reactivity in TiO_2 and quartz-related nanoparticle pulmonary toxicity. Nanotoxicology 3:181–187
111. Privalova LI (1990) Hygienic dimensions of non-specific action of low-soluble dust particles. Dissertation, The Medical Research Center for Prophylaxis and Health Protection in Industrial Workers
112. Privalova LI, Katsnelson BA, Sharapova NY, Kislitsina NS (1995) On the relationship between activation and the breakdown of macrophages in pathogenesis of silicosis. Med Lav 86:511–521
113. Katsnelson BA, Konysheva LK, Privalova LY, Morosova KI (1992) Development of a multicompartmental model of the kinetics of quartz dust in the pulmonary region of the lung during chronic inhalation exposure of rats. Brit J Ind Med 49:172–181
114. Katsnelson BA, Konyscheva LK, Sharapova NY, Privalova LI (1994) Prediction of the comparative intensity of pneumoconiotic changes caused by chronic inhalation exposure to dusts of different cytotoxicity by means of a mathematical model. J Occup Environ Med 51:173–180
115. Katsnelson BA, Konysheva LK, Privalova LY, Sharapova NY (1997) Quartz dust retention in rat lungs under chronic exposure simulated by a multicompartmental model: further evidence of the key role of the cytotoxicity of quartz particles. J Inhalation Toxicol 9:703–715
116. Minigalieva IA, Katsnelson BA, Panov VG, Privalova LI, Varaksin AN, Gurvich VB, Sutunkova MP, Shur VY, Shishkina EV, Valamina IE, Makeyev OH, Grigoryeva EV, Klinova SV (2017) In vivo toxicity of copper oxide, lead oxide and zinc oxide nanoparticles acting in different combinations and its attenuation with a complex of innocuous bio-protectors. Toxicology 380:72–93
117. Bastus NG, Casals E, Socorro VC, Puntes V (2008) Reactivity of engineered inorganic nanoparticles and carbon nanostructures in biological media. Nanotoxicology 2(3):99–112
118. Fröhlich E (2013) Cellular targets and mechanisms in the cytotoxic action of non-biodegradable engineered nanoparticles. J Curr Drug Metab 14:976–988
119. Privalova LI, Katsnelson BA, Osipenko AB, Yushkov BN, Babushkina LG (1980) Response of a phagocyte cell system to products of macrophage breakdown as a probable mechanism of alveolar phagocytosis adaptation to deposition of particles of different cytotoxicity. J Environ Health Perspect 35:205–218

120. Katsnelson BA, Privalova LI (1984) Recruitment of phagocytizing cells into the respiratory tract as a response to the cytotoxic action of deposited particles. J Environ Health Perspect 55:313–325
121. Privalova LI, Katsnelson BA, Yelnichnykh LN (1987) Some peculiarities of the pulmonary phagocytotic response, dust kinetics, and silicosis development during long term exposure of rats to high quartz levels. Brit J Ind Med 44:228–235
122. Utembe W, Potgieter K, Stefaniak AB, Gulumian M (2015) Dissolution and biodurability: important parameters needed for risk assessment of nanomaterials. J Part Fibre Toxicol 12(1):11
123. Tong T, Wilke CM, Wu J, Binh CT, Kelly JJ, Gaillard JF, Gray KA (2015) Combined toxicity of nano-ZnO and nano-TiO_2: from single- to multinanomaterial systems. Environ Sci Technol 49(13):8113–8123
124. Varaksin AN, Katsnelson BA, Panov VG, Privalova LI, Kireyeva EP, Valamina IE, Beresneva OY (2014) Some considerations concerning the theory of combined toxicity: a case study of subchronic experimental intoxication with cadmium and lead. Food Chem Toxicol 64:144–156
125. Panov VG, Katsnelson BA, Varaksin AN, Privalova LI, Kireyeva EP, Sutunkova MP, Valamina IE, Beresneva OYu (2015) Further development of mathematical description for combined (a case study of lead–fluoride combination). Toxicol Rep 2:297–307
126. Box GEP, Draper NR (2007) Response surfaces, mixtures, and ridge analyses. Wiley, Hoboken
127. Tallarida RJ (2001) Drug synergism: its detection and applications. J Pharmacol Exp Ther 298(3):865–872
128. Euling S, Gennings C, Wilson EM, Kemppainen JA, Kelce WR, Kimmel CA (2002) Response-surface modeling of the effect of 5α-dihydrotestosterone and androgen receptor levels on the response to the androgen antagonist vinclozolin. Toxicol Sci 69(2):332–343
129. Myers JP, vom Saal FS, Akingbemi BT, Arizono K, Belcher S, Colborn T, Chahoud I, Crain DA, Farabollini F, Guillette LJ Jr, Hassold T, Ho SM, Hunt PA, Iguchi T, Jobling S, Kanno J, Laufer H, Marcus M, McLachlan JA, Nadal A, Oehlmann J, Olea N, Palanza P, Parmigiani S, Rubin BS, Schoenfelder G, Sonnenschein C, Soto AM, Talsness CE, Taylor JA, Vandenberg LN, Vandenbergh JG, Vogel S, Watson CS, Welshons WV, Zoeller RT (2009) Why public health agencies cannot depend on good laboratory practices as a criterion for selecting data: the case of bisphenol A. J Environ Health Perspect 117 (3):309–315
130. CDC and NIOSH: Current Intelligence Bulletin 63: (2011) Occupational exposure to titanium dioxide. US Department of Health and Human Services, NIOSH, Cincinnati
131. Safe Work Australia (2010) Hazardous Substances Information System (HSIS). http://hsis.safeworkaustralia.gov.au/. Accessed 1 Nov 2009
132. Katsnelson BA, Privalova LI, Kuzmin SV, Degtyareva TD, Soloboyeva JI (2008) "Biological prophylaxis"—One of the ways to proceed from the analytical environmental epidemiology to the population health protection. Cent Eur J Occup Environ Med 14:41–42
133. Morosova KI, Aronova GV, Katsnelson BA, Velichkovski BT, Genkin AM, Elnichnykh LN, Privalova LI (1982) On the defensive action of glutamate on the cytotoxicity and fibrogenicity of quartz dust. Brit J Ind Med 39:244–252
134. Karki P, Webb A, Smith K, Lee K, Son DS, Aschner M, Lee E (2013) CREB and NF-kappaB mediate the tamoxifen-induced up-regulation of GLT-1 in rat astrocytes. J Biol Chem 288(40):28975–28986
135. White LD, Cory-Slechta DA, Gilbert ME, Tiffany-Castiglioni E, Zawia NH, Virgolini M, Rossi-George A, Lasley SM, Qian YC, Basha MR (2007) New and evolving concepts in the neurotoxicology of lead. J Toxicol Appl Pharmacol 225(1):1–27
136. Desole MS, Esposito G, Migheli R, Sircana S, Delogu MR, Fresu L, Miele M, de Natale G, Miele E (1997) Glutathione deficiency potentiates manganese toxicity in rat striatum and brainstem and in PC12 cells. J Pharmacol Res 36(4):285–292

Chapter 12
Hepatic Injuries Induced by Engineered Nanomaterials

Jianbo Jia and Bing Yan

Abstract The production, usage, and disposal of engineered nanomaterial (ENM)-based products inevitably increased their environmental accumulation and human exposures. Liver is the major organ for deposition of ENMs after their clearance from the circulation system. Accumulation of ENMs in liver may cause hepatic oxidative stress, inflammation, DNA damage, hepatocyte death, as well as liver fibrosis in healthy populations. In subpopulations with various liver diseases, such effects may be aggravated. Critical factors such as properties of ENMs, animal experimental protocols, and status of liver are discussed, as well as possible future directions.

Keywords ENMs · Hepatic injury · Environmental exposures · Physicochemical properties · Oxidative stress · Inflammation

12.1 Introduction

Liver is the major organ for xenobiotic chemicals metabolism and excretion. Liver injury induced by therapeutic drugs (troglitazone, bromfenac and pemoline for instance) and industrial chemicals (such as carbon tetrachloride and vinyl chloride) and the underlying mechanisms have been discussed [1–5]. With the global production, usage, and disposal of engineered nanomaterials (ENMs) and ENM-based products, the release of ENMs into the environment is inevitable. Therefore, ENMs have become a new environmental threat that may cause both acute and chronic hepatotoxicity.

J. Jia · B. Yan (✉)
School of Chemistry and Chemical Engineering, Shandong University, Jinan 250100, China
e-mail: drbingyan@yahoo.com

B. Yan
School of Environment, Jinan University, Guangzhou 510632, China

B. Yan et al. (eds.), *Bioactivity of Engineered Nanoparticles*, Nanomedicine and Nanotoxicology, DOI 10.1007/978-981-10-5864-6_12

12.1.1 Liver Function

Liver is a multifunctional organ involved in nutrient metabolism, proteins synthesis, hormone production, glycogen storage and release, and detoxification (Table 12.1). Blood coming from the stomach and the intestine flows through the liver prior to entering the systemic circulation. Therefore, liver is the first organ encountering absorbed nutrients. In liver, nutrients absorbed by intestines were metabolized into forms that can be utilized by human body. Liver also stores some nutrients such as vitamins (including vitamin A, vitamin D, and vitamin B12) and minerals (including iron and copper). Moreover, liver is the major organ involved in detoxification where toxic substances, such as drugs, alcohol, and environmental toxins, are broken down to less harmful or sometimes more toxic metabolites [6, 7].

12.1.2 Liver as the Major Organ for ENM Accumulation

As an important part of mononuclear phagocyte system, also known as reticuloendothelial system, liver is a major organ for xenobiotic ENMs accumulation and clearance. Gold NPs (Au NPs) can be accumulated in liver in a size-dependent manner. After intravenous (*i.v.*) injection into rats, about 50% of Au NPs with a diameter of 1.4 nm are accumulated in liver, while >99% of Au NPs with a

Table 12.1 Major functions of the liver

Type of function	Examples
Metabolism	Carbohydrate metabolism Lipid metabolism Amino acid metabolism Mineral metabolism Vitamin metabolism
Synthesis	Albumin Clotting factors Transport proteins Binding proteins
Detoxification	Xenobiotics Steroids hormones Thyroid hormones Endogenous metabolites
Storage	Glycogen Vitamins
Secretory	Bile acid Bilirubin and cholesterol Metals Xenobiotics
Filtration of particulates	Products of intestinal bacteria (e.g., endoxin)

diameter of 200 nm are accumulated [8]. Amorphous silica particles of 70 nm accumulate mainly in liver regardless of surface modifications [9]. Entering liver, ENMs may be taken up by hepatocytes or Kupffer cells. The selectivity may depend on the properties of the nanoparticles. For example, positively charged nanoparticles are accumulated more in hepatocytes, whereas negatively charged nanoparticles are rapidly taken up by Kupffer cells in liver sinusoids (Fig. 12.1) [10, 11]. Purposeful liver accumulation of nano-drug carrier or diagnostic agents may facilitate development of passive liver-targeting nanomedicines [12].

Inert ENMs such as Au NPs, fullerenes, and carbon nanotubes (CNTs) can hardly be metabolized effectively [13]. Biliary route is a pathway for ENM excretion from the liver. ENMs in the liver that are not immediately internalized by Kupffer cells are translocated through the fenestrated vascular endothelium into the Dissé spaces where they are taken up by hepatocytes and processed into biliary canaliculi [14]. Then, ENMs are drained through the biliary duct and excreted in feces [15, 16].

Even though ENMs may be cleared from the liver via the biliary pathway, their long-term retention increases the risk of hepatotoxicity. For example, ENMs such

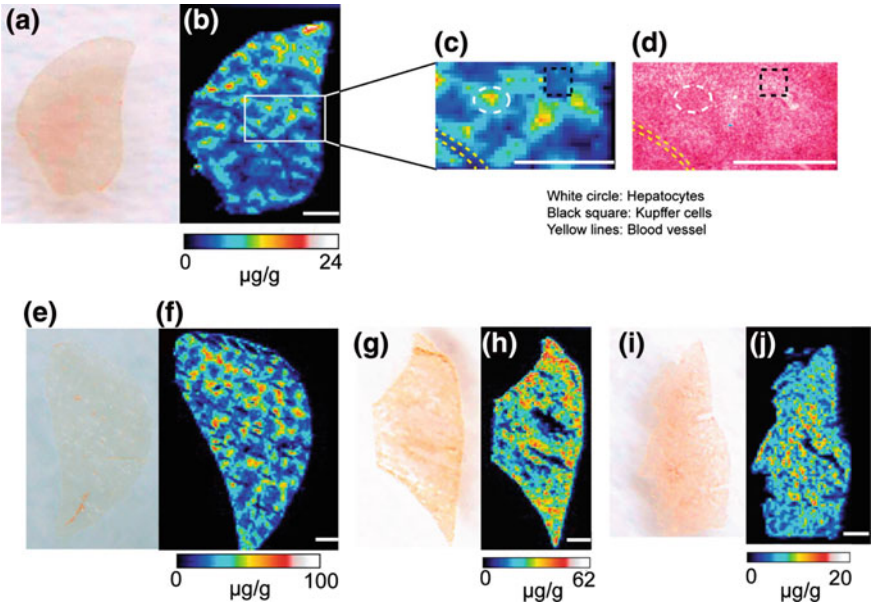

Fig. 12.1 Imaging results for the liver tissues. **a** Optical and **b** quantitative LA-ICP-MS images of AuNP 1; **c** zoomed-in area illustrating the amount of AuNP 1 in a selected area of the liver tissue with a blood vessel, hepatoctyes, and Kupffer cells indicated in *yellow*-, *white*-, and *black-dotted lines*, respectively; **d** optical image after H&E staining of the same region shown in (**c**), indicating the blood vessel, hepatoctyes, and Kupffer cells in *yellow*-, *white*-, and *black-dotted lines*. **e** Optical and **f** quantitative LA-ICP-MS images of AuNP 2; **g** optical and **h** quantitative LA-ICP-MS images of AuNP 3; **i** optical and **j** quantitative LA-ICP-MS images of AuNP 4. All *scale bars* correspond to 0.5 mm. Reprinted with permission from [11]. Copyright (2016) American Chemical Society

as SWCNTs (a single *i.v.* injection of ~0.02 mg per mouse) [15] and superparamagnetic iron oxide nanoparticles (a single injection at a dose of 50 μmol/kg via a retro-orbitary route) [17] could still be detected in the liver of mouse models after 3 months.

12.2 ENM-Induced Hepatic Injuries in Healthy Population

Long-term ENM accumulation in the liver may affect its functions in various aspects as discussed below.

12.2.1 Hepatic Oxidative Stress

ENMs induce excess reactive oxygen species (ROS) via several mechanisms [18]. A low level of ROS in cells plays an important role in various physiological processes including antibacterial, anti-inflammatory, and tumor suppression. Meanwhile, excessive ROS could break the balance of the oxidant/antioxidant system in the liver, resulting in lipid peroxidation damage and hepatocyte toxicity.

Hepatic ROS level is reflected by malondialdehyde (MDA) activity, levels of several antioxidant enzymes such as glutathione peroxidase (GSHPx), catalase (CAT), and superoxide dismutase (SOD), as well as non-enzyme antioxidant, e.g., glutathione (GSH). In human liver cancer cells (HepG2), exposure of zinc oxide nanoparticles (ZnO NPs, 30 nm) [19], silver nanoparticles (Ag NPs, 5–10 nm) [20], silica nanoparticles (15 nm) [21], titanium dioxide nanoparticles (TiO_2 NPs, 30–70 nm) [22], and single-walled carbon nanotubes (SWCNTs, 1–8 nm in diameter and 2000–6000 nm in length) [23] can induce oxidative cell damage, as indicated by increased ROS production, reduced level of GSH, increased MDA content, hydroperoxide level, as well as level of lipid peroxidation. Similar ENM-induced production of ROS was also observed in BRL 3A rat liver cells [24]. Ag NP (15 and 100 nm) exposure induces ROS-mediated cytotoxicity with depletion of GSH level and reduced mitochondrial membrane potential in these cells. In a murine hepatocyte cell line AML 12, cadmium telluride quantum dots (CdTe QDs) induce a dose-dependent generation of ROS. An antioxidant, *tert*-butyl Hydroquinone, can reduce intracellular ROS production [25].

ENM administration can also increase the production of ROS in liver tissues of animal models. For instance, subacute oral exposure of ZnO NPs (30 nm) for 14 consecutive days at a daily dose of 300 mg/kg induces hepatic oxidative stress in male Swiss albino mice, as indicated by an increase in lipid peroxidation [19]; Dermal exposure of TiO_2 NPs (10 nm, 400 μg TiO_2 per cm^2) for 60 days caused oxidative stress-mediated liver injury with an increased MDA content and a

reduced SOD activity in liver tissues of BALB/c hairless mice [26]; Intraperitoneal (*i.p.*) injection of TiO_2 NPs (5 nm) daily for 14 days increases hepatic lipid peroxidation and O_2^- and H_2O_2 generation, and reduced activities of hepatic antioxidative enzymes such as SOD, CAT, GSHPx, and ascorbic acid peroxidase (APx) in CD-1 (ICR) mice [27]; *I.v.* administration of Na-oleate-coated Fe_3O_4 nanoparticles (8 nm) at a dose equivalent to 10% of the LD_{50} (3.64 mg/kg) significantly increases hepatic mitochondrial respiration in female outbred Wistar rats [28].

On the contrast, several ENMs including fullerene [29, 30] and cerium oxide nanoparticles [31, 32] are able to efficiently scavenge ROS, protecting the liver from chemical-induced hepatic injury.

12.2.2 Liver Inflammation

The absorption and deposition of ENMs in the liver may stimulate the activation of immune responses. Besides, excessive ROS could activate ROS-sensitive pathways such as the mitogen-activated protein kinase (MAPK) and nuclear factor κB (NF-κB) cascades, resulting in pro-inflammatory responses [18].

Kupffer cells are resident liver macrophages responsible for removal of nanoparticles from the system [33]. They are major immune effector cells in the liver. Liver accumulation of ENMs activates Kupffer cells, resulting in hepatic inflammation. Single *i.v.* injection of silica NPs (15 nm) at a dose of 50 mg/kg caused Kupffer cell hyperplasia and hepatic inflammation in male Sprague Dawley (SD) rats [34]. A single *i.v.* administration of hydroxyapatite nanoparticles (HA NPs, needlelike, long diameter of 80 nm and short diameter of 20 nm) at a dose of 50 mg/kg induced oxidative stress-associated inflammatory cell infiltration at the portal area in the liver of SD rats [35]. Oral administration of Ag NPs (60 nm, 300 or 1000 mg/kg) for 28 days also induces hepatic inflammation in SD rats, as indicated by an increased level of alkaline phosphatase and infiltration of inflammatory cells in the liver [36].

Similar ENM-induced hepatic inflammation was also observed in mice. A single oral dose of Ag NPs (13 nm, 2.5 g per mouse) induced acute liver inflammation in male BALB/c mice, as evidenced by altered expression of genes related to inflammation and lymphocyte infiltration [37]. Anatase TiO_2 NPs (21 nm) administrated (150 mg/kg/day) orally for 2 weeks triggered an inflammatory response in the liver of male albino mice, as indicated by the activation of Kupffer cells and increased production of TNF-α and interleukin-6 [38]. Moreover, these NPs upregulated the mRNA expression of Nrf2 and NF-κB. In female ICR mice, *i.p.* administration of Eu^{3+}-doped gadolinium oxide nanotubes (Gd_2O_3:Eu^{3+} nanotubes, 400 mg/kg daily) for 35 days induced oxidative stress-related liver injury and increased the production of several inflammatory cytokines including TNF-α, interleukin-1β (IL-1β), and interleukin-8 (IL-8) [39]. In another study, intragastric administration of TiO_2 NPs (5 nm, 5, 10, and 50 mg/kg) for 60 days increased the mRNA and protein levels of Toll-like receptor-2 (TLR2) and TLR-4, as well as

several inflammatory cytokines, such as IKK1, IKK2, NF-κB, NF-κBP52, NF-κBP65, TNF-α, and NIK [40]. Meanwhile, TiO_2 NPs exposure decreases the mRNA and protein expression of IκB and IL-2. This suggested a potential TiO_2 NPs-stimulated TLRs- and NF-κB-mediated hepatic inflammation.

12.2.3 Hepatic DNA Damage

ENMs may impact DNA molecules directly by forming covalent linkages with them. By computational modeling, $Al_{12}X$ (X = Al, C, N, and P) nanoparticles are able to tightly bind to Watson–Crick DNA base pairs to form stable complexes, suggesting the potential adverse impacts of Al nanoparticles on the structure and stability of DNA [41]. *I.p.* injection of TiO_2 NPs (5 nm) for 14 days resulted in a dose-dependent accumulation of NPs in the liver of ICR mice [42]. TiO_2 NPs were able to bind DNA base pairs by interacting with three oxygen or nitrogen atoms and two phosphorous atoms on the DNA molecules. Lengths of Ti–O(N) and Ti–P bonds were 1.87 and 2.38 Å, respectively. The combination of TiO_2 NPs with DNA altered the secondary structure of DNA, resulting in perturbations of genetic information transmission.

To induce genotoxicity, ENMs do not need to bind DNA directly. ENMs exposure may cause genotoxicity by interacting with nuclear proteins [44] or disturbing cell cycle checkpoint functions [45]. In most cases, ENM-induced oxidative stress leads to hepatic DNA damage indirectly (Fig. 12.2). ROS generated in cells may cause oxidative DNA damage through free radicals. For example, metal oxide NPs such as TiO_2 NPs (30–70 nm) [22], ZnO NPs (30 nm) [19, 46], and nickel oxide nanoparticles (NiO NPs, 44 nm) [47] induce DNA damage in HepG2 cells through ROS generation. Furthermore, ZnO NPs [19], TiO_2 NPs [48], CuO NPs [49], C60 fullerenes, and SWCNTs [50] induce oxidative DNA damage in the liver of rodents. Ag NPs (5–20 nm) administration induced hepatic DNA damage in adult zebrafish [51].

12.2.4 Hepatocyte Death

Death of hepatocytes typically follows one of two patterns: necrosis and apoptosis [52]. Necrosis is the consequence of acute metabolic injury with ATP depletion. ENMs could induce necrotic cell death of hepatocytes both in vitro and in vivo. For instance, ZnO NPs (47–106 nm) increase the number of necrotic catfish primary hepatocytes in a dose-dependent manner [53]; Chitosan nanoparticle (18 nm) exposure induces a dose-dependent increase in CYP3A4 enzyme activity and necrotic or autophagic cell death of human liver cells [54]; Administration of several ENMs including MWCNTs (20–30 nm in diameter, 5–50 μm in length) [55], Ag NPs (<100 nm) [56], Au NPs (10 and 20 nm) [57], TiO_2 NPs (42 nm) [58],

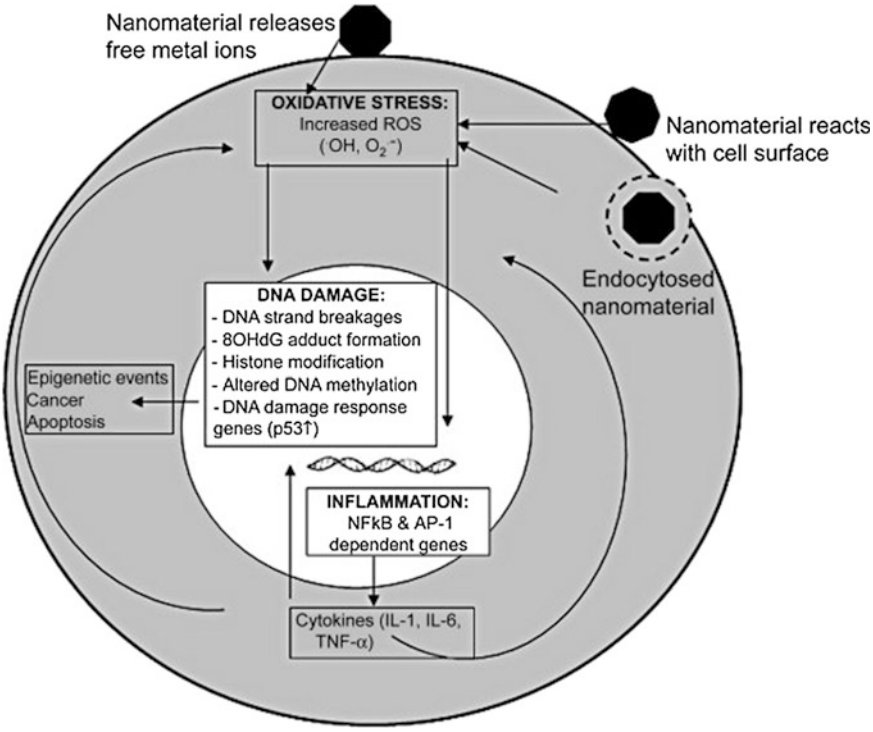

Fig. 12.2 Indirect mechanisms that can lead to genotoxicity. Nanomaterials may result in oxidative stress or inflammatory responses that in turn have the potential to damage DNA and alter transcriptional patterns. Reprinted with permission from [43]. Copyright © 2009 Elsevier Ltd.

and silica NPs (20 and 80 nm) [59] all induce hepatocyte necrosis in livers of various animal models.

Apoptosis, on the other hand, is a form of programmed cell death. Apoptosis is initiated through one of the two main pathways: the extrinsic pathway (death receptor pathway) or the intrinsic pathway (mitochondrial pathway) [60]. ENM-induced apoptosis in hepatocytes is more likely through a mitochondrial pathway. For example, ENMs, such as copper oxide NPs (CuO NPs, 22 nm) [61], silica NPs (15 nm) [21], HA NPs (26, 45 and 78 nm) [62], CdTe QDs (2.2 nm) [25], and Ag NPs (5–10 nm) [20], can induce mitochondria-dependent apoptosis of hepatocytes, as shown by upregulated expression of apoptotic genes (*caspase-3*, *p53*, *Bax*, *Bid*, *p21,* etc.), downregulated expression of anti-apoptotic gene (*Bcl-2*), decreased mitochondrial membrane potential, and the release of cytochrome *c* from mitochondria into cytoplasm. Ag NPs (5–20 nm) induce oxidative stress and apoptosis in the liver of adult zebrafish by the upregulation of p53-related pro-apoptotic genes *Bax*, *Noxa*, and *p21* [51].

12.2.5 Hepatic Fibrosis

Hepatic fibrosis is an excessive deposition of extracellular matrix (ECM) proteins including glycoproteins, collagen, and proteoglycans [63]. It is a response of the liver to chronic damages. The cellular mechanisms of liver fibrosis are highly complex and sophisticated, with several different hepatic cell types involved. ENMs can induce liver fibrosis in mouse models. Repeated *i.v.* injection of silica NPs (70 nm, 10 or 30 mg/kg) twice a week for 4 weeks causes hepatic fibrosis in male BALB/c mice, as evidenced by elevated hepatic hydroxyproline levels 1.6- or 3.5-fold over the control value [64]. Significant hepatic fibrosis around the central vein in ICR mice can be observed 7 days after a single *i.p.* injection of TiO_2 NPs (100 nm) at a dose of 1944 mg/kg [65]. When female ICR mice are *i.p.* injected with silica NPs (110 nm, 10, 25, and 50 mg/kg) twice a week for 6 weeks [66], a dose-dependent hepatocyte fibrosis and collagen fibers accumulation around silicotic nodular-like lesions in the liver will occur. Activation of Kupffer cells may play a key role in these injuries.

In brief, various ENMs are able to cause hepatic DNA damage, necrosis, apoptosis of hepatocytes, and liver fibrosis. ENMs induce liver injuries by producing ROS and activating pro-inflammatory responses in the liver (Fig. 12.3). Excess ROS and pro-inflammatory cytokines disturb the oxidant/antioxidant equilibrium as well as the balance between pro-inflammatory and anti-inflammatory cytokines, resulting in hepatic toxicity.

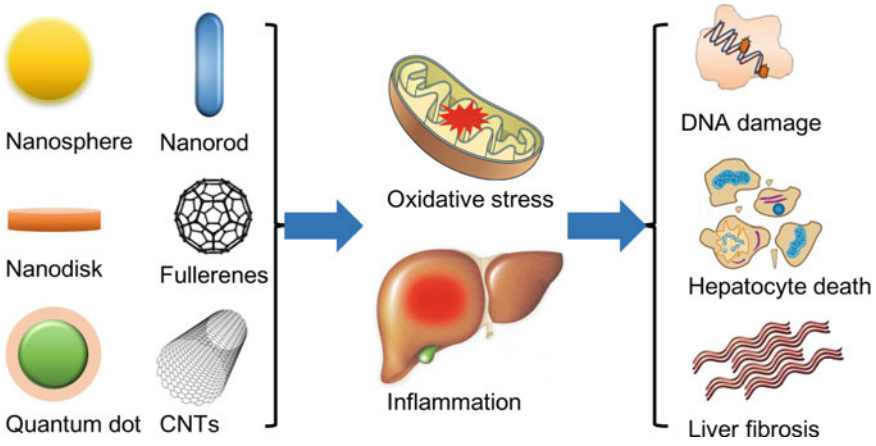

Fig. 12.3 A schematic showing the ENM-induced hepatic injuries. ENMs accumulated in the liver induce hepatic oxidative stress and inflammation, which further cause liver DNA damage, hepatocyte death, and liver fibrosis

12.3 ENM-Induced Hepatic Injuries in Diseased Populations

Liver diseases of both acute and chronic nature are common and the rate of liver diseases is steadily increasing over the years. Liver diseases are recognized as the fifth most common cause of death in the UK [42]. They are ranked as the second leading cause of death (after colorectal cancer) among all digestive diseases in the US [67]. In China, liver diseases affect approximately 300 million people, exerting a significant impact on the global burden of liver diseases [68]. The three major aetiologies of liver failure are nonalcoholic fatty liver disease (NAFLD), viral hepatitis, and alcoholic liver disease. It has been well known that populations with liver diseases were more susceptible to environmental pollutants [69, 70]. The potentially more severe toxicity of ENMs to hepatic diseased population needs to be addressed.

12.3.1 Chemical-Induced Hepatitis Animal Models

Hepatitis is an inflammation of the liver caused by virus, drugs, or other factors. Animal models of both acute and chronic hepatitis have been established for the investigation of the pathogenesis of liver disease and development of novel diagnostic, and therapeutic tools [71, 72]. Several hepatitis animal models were used to study the toxicity of ENMs. These models include concanavalin A (ConA)-induced hepatic injury model [73], carbon tetrachloride (CCl_4)-induced hepatitis animal model [32], monocrotaline-induced liver injury model [31], and alcohol-induced liver injury model [30].

Gold nanorods (AuNR) exposure at a dose showing no toxicity in healthy mice (12 μg/kg body weight via *i.v.* administration) causes exacerbated liver damage by inducing pre-activation of hepatic macrophages in ConA-induced acute C57BL/6 hepatitis mouse model [73]. Meanwhile, such AuNR shows no effects on liver scarring or termed fibrosis in CCl_4-induced chronic hepatic injury model.

As mentioned above, some ENMs exhibit efficient ROS scavenging. They may protect the liver from ROS-related liver injury. For example, C_{60} accumulated in the liver of Wistar rats efficiently scavenges radicals including $CCl_3^{\cdot}$ and $CCl_3OO^{\cdot}$ and improved the antioxidant status of rats [29]. As a result, C_{60} protects liver in a dose-dependent manner against CCl_4-induced free-radical damage. C_{60} nanoparticles also exhibit potential hepatoprotective effects against alcohol-induced liver injuries by scavenging intracellular ROS induced by ethanol [30]. Similarly, cerium oxide nanoparticles also protect the liver from CCl_4- [32] or monocrotaline-induced [31] liver injury by reducing oxidative stress in vivo. Besides, *i.v.* injected graphene quantum dots (40 nm, 50 mg/kg) are accumulated in the liver and reduced Con A-induced mouse hepatitis by interfering with T cell and macrophage activation [74].

12.3.2 Diet-Induced Fatty Liver Animal Models

Among various liver diseases, the most prevalent liver condition is fatty liver disease, which affects one-third of the population in the United States [75]. *I.v.* injection of Au NPs (5 mg/kg) in methionine- and choline-deficient diet-fed mice results in a higher level of liver injury, as evidenced by elevated the serum ALT and AST levels, severe hepatic cell damage, acute inflammation, and increased apoptosis and ROS production, compared to that in mice fed a normal chow diet [76]. In a high-fat diet (HFD)-induced overweight mouse model, HFD feeding results in hepatic steatosis. Oral administration of Ag NPs (30 nm) daily for 14 days at a dose (300 mg/kg) showing no toxicity to normal weight mice aggravates the progression of fatty liver disease in overweight mice, as evidenced by focal inflammation, hydropic degeneration, and enhanced steatosis [77]. Ag NPs, rather than Ag^+ ions, are responsible for such a disease progression because Ag^+ ions are reduced to Ag NPs in the liver of overweight mice and the liver doses of Ag NPs, not Ag ions are correlated to the toxic effects. Further mechanistic study reveals that pro-inflammatory activation of Kupffer cells and suppression of fatty acid oxidation play critical roles in the Ag NP-induced fatty liver disease progression. Meanwhile, orally co-exposure of ZnO NPs (14 or 58 nm, 200 mg/kg) and Pb^{2+} (150 mg/kg) for 14 days increases the Pb deposition in various organs (the liver, the kidneys, and the spleen) in overweight mice, compared to that in normal weight mice [78]. The ZnO NP-enhanced liver deposition of Pb causes hepatic ROS and increases the release of pro-inflammatory cytokines, resulting in enhanced liver injury in overweight mice.

ROS and inflammation play vital roles in the progression of various liver diseases including alcoholic liver disease, nonalcoholic fatty liver disease, virus hepatitis, and cirrhosis [79, 80]. When the liver is under diseased conditions, it is more sensitive to environmental toxicants including ENMs. ENM-induced additional oxidative stress and inflammation would definitely aggravate the disease progression.

12.4 Critical Factors in ENM-Induced Liver Injuries

ENMs can cause hepatic injuries in both healthy population and population with liver diseases. Even though our understanding of ENMs-induced liver injury is incomplete, several factors are of obvious importance, according to recent studies.

12.4.1 Physicochemical Properties of ENMs

Physicochemical properties of ENMs determine what the cells see and how the cells interact with them. These properties mainly refer to the primary characters of an ENM including composition [49], crystal structure [81], size [82], shape [83], surface coating [84], and agglomeration state [85], which further determine their secondary characters (protein adsorption and in situ characterization in cells or tissues, etc.). Physicochemical properties of ENMs not only affect their cellular uptake and sub-organ distribution and clearance [11], but also altered their hepatic toxicity. For example, surface chemical modifications are able to alter the interaction between CNTs and CYP450 enzymes in human liver microsomes, resulting in various perturbations on CYP3A4 (Fig. 12.4) [86]. Certain surface chemical structures responsible for inducing the inhibitory effects of CNTs are identified using a cheminformatics analysis.

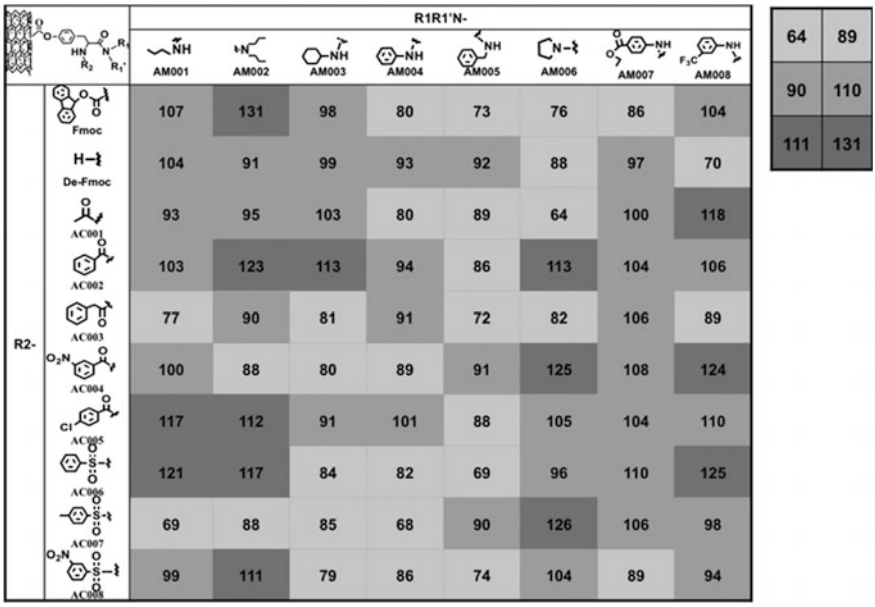

Fig. 12.4 CYP3A4 activity is modulated by f-MWCNTs from a combinatorial MWCNT library. The CYP3A4 activity in the HLM-only group was defined as 100%, and that in the ketoconazole group was defined as 0%. The activity of CYP3A4 in f-MWCNT-treated groups was calculated according to the following equation: f-MWCNT's effect on CYP3A4 activity = (peak area of NFP in ketoconazole group—peak area of NFP in f-MWCNT group)/(peak area of NFP in ketoconazole group—peak area of NFP in HLM-only group). Reprinted with permission from [86]. Copyright © 2015 WILEY-VCH Verlag GmbH & Co. KGaA, Weinheim

12.4.2 Administration Procedures

Various administration methods such as dermal [26], intragastric (or oral) [40], *i.v.* [87], *i.p.* [66], or respiratory [88] exposure routes have been used in nanotoxicity investigations, mimicing the different ways of human exposures. Administration routes influence the amount of absorption and deposition of ENMs in animal models, resulting in different toxicities. For instance, the blood Ag content in lactating mice *i.v.* administrated with Ag NPs is twice as high as that exposed orally, even though the dose in the former is only 15% of the latter [89]. *I.p.* exposure causes greater hepatic accumulation of Ag NPs than *i.v.* administration, resulting in disordered hepatic cord alignment and enlarged central veins in livers of BALB/c mice [90]. Dosing and duration of exposure, on the other hand, are more direct factors determining ENM-induced hepatic injuries. In rat models, oral administration of Ag NPs at a dose >125 mg/kg for 90 days [91], or >300 mg/kg for 28 days [36] induces slight liver damages. Meanwhile, Ag NPs administration causes no hepatotoxicity or immunotoxicity after orally exposed for 28 days at a dose of 90 mg/kg [92].

12.4.3 Physiology of the Liver

The liver is the major organ for metabolism of xenobiotic chemicals and detoxification. A good redox and immunological status of the liver is essential for the operation of normal functions. Knowing that populations with hepatic diseases may be more sensitive to ENM exposures, hepatic toxicity of ENMs to aged population characterized by reduced metabolic activity, oxidative stress, and chronic inflammation is reported recently. Oral administration of ZnO NPs at 300 mg/kg for 14 days increases the liver accumulation of Zn in aged mice, which may be mainly attributed to the increased intestinal permeability and decreased hepatic metabolic capability [93]. Together with higher levels of oxidative stress and inflammation in livers of aged mice, ZnO NPs cause additional hepatic oxidative stress and inflammation and result in acute liver injury.

12.5 Concluding Remarks

In conclusion, ENMs can induce hepatic ROS and inflammation, resulting in hepatotoxicity in both healthy and diseased populations. Generally, populations with liver diseases are more susceptible to nanotoxicity because the additional ROS and inflammation induced by ENMs accelerate the progression of various liver diseases. Relating factors include the properties of the ENMs, amounts of liver deposition of ENMs, and the physiological state of the liver.

Investigations on hepatic nanotoxicity still need to be continued and intensified. A better characterization of ENMs is crucial. Both primary (composition, crystal structure, size, shape, surface coating, agglomeration state, etc.) and secondary (protein adsorption and in situ characterization in cells or tissues) characterizations of tested ENMs are very important for toxicity investigations. Hepatic toxicity assessment of ENMs should mimic the environmental exposure scenarios. Current studies use much higher doses of ENMs and quite different exposure periods. Therefore, low-dose and long-term exposures of ENMs will be much more helpful for the determination of the hepatic toxicity of ENMs. Furthermore, only limited studies have been carried out on ENM-induced hepatic injuries in diseased populations. Such understandings are very important for the safe applications of nanomaterial-based therapy and products. Toxicological data should be analyzed by computational and modeling approaches to uncover the general regularity of ENM-induced hepatic injuries. This will also guide ENMs' safe applications in advanced biomedical fields, as well as many other applications.

Acknowledgments This work was supported by the National Key Research and Development Program of China (2016YFA0203103), the National Natural Science Foundation of China (91543204 and 91643204), the Strategic Priority Research Program of the Chinese Academy of Sciences (XDB14030401) and the Natural Science Foundation of Shandong Province (ZR2014BM026).

References

1. Kaplowitz N (2005) Idiosyncratic drug hepatotoxicity. Nat Rev Drug Discov 4(6):489–499
2. Lee WM (2003) Medical progress: drug-induced hepatotoxicity. N Engl J Med 349(5):474–485
3. Navarro VJ, Senior JR (2006) Current concepts—drug-related hepatotoxicity. N Engl J Med 354(7):731–739
4. Recknagel RO (1967) Carbon tetrachloride hepatotoxicity. Pharmacol Rev 19(2):145–208
5. Thomas LB, Popper H, Berk PD, Selikoff I, Falk H (1975) Vinyl-chloride-induced liver disease. From idiopathic portal hypertension (Banti's syndrome) to Angiosarcomas. N Engl J Med 292(1):17–22
6. Percival M (1997) Phytonutrients and detoxification. Clin Nutr Insights 5(2):1–4
7. Vander A, Sherman J, Luciano D (1994) Nonimmune metabolism of foreign chemicals. Hum Physiol 738–740
8. Hirn S, Semmler-Behnke M, Schleh C, Wenk A, Lipka J, Schäffler M, Takenaka S, Möller W, Schmid G, Simon U (2011) Particle size-dependent and surface charge-dependent biodistribution of gold nanoparticles after intravenous administration. Eur J Pharm Biopharm 77 (3):407–416
9. Lu X, Ji C, Jin T, Fan X (2015) The effects of size and surface modification of amorphous silica particles on biodistribution and liver metabolism in mice. Nanotechnology 26 (17):175101
10. Cheng S-H, Li F-C, Souris JS, Yang C-S, Tseng F-G, Lee H-S, Chen C-T, Dong C-Y, Lo L-W (2012) Visualizing dynamics of sub-hepatic distribution of nanoparticles using intravital multiphoton fluorescence microscopy. ACS Nano 6(5):4122–4131
11. Elci SG, Jiang Y, Yan B, Kim ST, Saha K, Moyano DF, Yesilbag Tonga G, Jackson LC, Rotello VM, Vachet RW (2016) Surface charge controls the sub-organ biodistributions of gold nanoparticles. ACS nano

12. Wang H, Thorling CA, Liang X, Bridle KR, Grice JE, Zhu Y, Crawford DH, Xu ZP, Liu X, Roberts MS (2015) Diagnostic imaging and therapeutic application of nanoparticles targeting the liver. J Mater Chem B 3(6):939–958
13. Hamidi M, Azadi A, Rafiei P, Ashrafi H (2013) A pharmacokinetic overview of nanotechnology-based drug delivery systems: an ADME-oriented approach. Critical Reviews™ in Therapeutic Drug Carrier Systems 30(5)
14. Johnston HJ, Hutchison G, Christensen FM, Peters S, Hankin S, Stone V (2010) A review of the in vivo and in vitro toxicity of silver and gold particulates: particle attributes and biological mechanisms responsible for the observed toxicity. Crit Rev Toxicol 40(4):328–346
15. Liu Z, Davis C, Cai W, He L, Chen X, Dai H (2008) Circulation and long-term fate of functionalized, biocompatible single-walled carbon nanotubes in mice probed by Raman spectroscopy. Proc Natl Acad Sci USA 105(5):1410–1415
16. Wang H, Wang J, Deng X, Sun H, Shi Z, Gu Z, Liu Y, Zhaoc Y (2004) Biodistribution of carbon single-wall carbon nanotubes in mice. J Nanosci Nanotechnol 4(8):1019–1024
17. Levy M, Luciani N, Alloyeau D, Elgrabli D, Deveaux V, Pechoux C, Chat S, Wang G, Vats N, Gendron F, Factor C, Lotersztajn S, Luciani A, Wilhelm C, Gazeau F (2011) Long term in vivo biotransformation of iron oxide nanoparticles. Biomaterials 32(16):3988–3999
18. Nel A, Xia T, Madler L, Li N (2006) Toxic potential of materials at the nanolevel. Science 311(5761):622–627
19. Sharma V, Anderson D, Dhawan A (2012) Zinc oxide nanoparticles induce oxidative DNA damage and ROS-triggered mitochondria mediated apoptosis in human liver cells (HepG2). Apoptosis 17(8):852–870
20. Piao MJ, Kang KA, Lee IK, Kim HS, Kim S, Choi JY, Choi J, Hyun JW (2011) Silver nanoparticles induce oxidative cell damage in human liver cells through inhibition of reduced glutathione and induction of mitochondria-involved apoptosis. Toxicol Lett 201(1):92–100
21. Ahmad J, Ahamed M, Akhtar MJ, Alrokayan SA, Siddiqui MA, Musarrat J, Al-Khedhairy AA (2012) Apoptosis induction by silica nanoparticles mediated through reactive oxygen species in human liver cell line HepG2. Toxicol Appl Pharmacol 259(2):160–168
22. Shukla RK, Kumar A, Gurbani D, Pandey AK, Singh S, Dhawan A (2013) TiO_2 nanoparticles induce oxidative DNA damage and apoptosis in human liver cells. Nanotoxicology 7(1):48–60
23. Yuan J, Gao H, Sui J, Chen WN, Ching CB (2011) Cytotoxicity of single-walled carbon nanotubes on human hepatoma HepG2 cells: an iTRAQ-coupled 2D LC–MS/MS proteome analysis. Toxicol In Vitro 25(8):1820–1827
24. Hussain SM, Hess KL, Gearhart JM, Geiss KT, Schlager JJ (2005) In vitro toxicity of nanoparticles in BRL 3A rat liver cells. Toxicol In Vitro 19(7):975–983
25. Zhang T, Hu Y, Tang M, Kong L, Ying J, Wu T, Xue Y, Pu Y (2015) Liver toxicity of cadmium telluride quantum dots (CdTe QDs) due to oxidative stress in vitro and in vivo. Int J Mol Sci 16(10):23279–23299
26. Wu J, Liu W, Xue C, Zhou S, Lan F, Bi L, Xu H, Yang X, Zeng F-D (2009) Toxicity and penetration of TiO_2 nanoparticles in hairless mice and porcine skin after subchronic dermal exposure. Toxicol Lett 191(1):1–8
27. Liu H, Ma L, Liu J, Zhao J, Yan J, Hong F (2010) Toxicity of nano-anatase TiO_2 to mice: liver injury, oxidative stress. Toxicol Environ Chem 92(1):175–186
28. Volkovova K, Handy RD, Staruchova M, Tulinska J, Kebis A, Pribojova J, Ulicna O, Kucharská J, Dusinska M (2015) Health effects of selected nanoparticles in vivo: liver function and hepatotoxicity following intravenous injection of titanium dioxide and Na-oleate-coated iron oxide nanoparticles in rodents. Nanotoxicology 9(sup1):95–105
29. Gharbi N, Pressac M, Hadchouel M, Szwarc H, Wilson SR, Moussa F (2005) [60] fullerene is a powerful antioxidant in vivo with no acute or subacute toxicity. Nano Lett 5(12):2578–2585
30. Li Y, Luo HB, Zhang HY, Guo Q, Yao HC, Li JQ, Chang Q, Yang JG, Wang F, Wang CD, Yang X, Liu ZG, Ye X (2016) Potential hepatoprotective effects of fullerenol nanoparticles on alcohol-induced oxidative stress by ROS. RSC Adv 6(37):31122–31130

31. Amin KA, Hassan MS, Awad E-ST, Hashem KS (2011) The protective effects of cerium oxide nanoparticles against hepatic oxidative damage induced by monocrotaline. Int J Nanomed 6:143–149
32. Hirst SM, Karakoti A, Singh S, Self W, Tyler R, Seal S, Reilly CM (2013) Bio-distribution and in vivo antioxidant effects of cerium oxide nanoparticles in mice. Environ Toxicol 28 (2):107–118
33. Sadauskas E, Wallin H, Stoltenberg M, Vogel U, Doering P, Larsen A, Danscher G (2007) Kupffer cells are central in the removal of nanoparticles from the organism. Part Fibre Toxicol 4(1):10
34. Chen Q, Xue Y, Sun J (2013) Kupffer cell-mediated hepatic injury induced by silica nanoparticles in vitro and in vivo. Int J Nanomed 8:1129–1140
35. Chen Q, Xue Y, Sun J (2014) Hepatotoxicity and liver injury induced by hydroxyapatite nanoparticles. J Appl Toxicol 34(11):1256–1264
36. Kim YS, Kim JS, Cho HS, Rha DS, Kim JM, Park JD, Choi BS, Lim R, Chang HK, Chung YH (2008) Twenty-eight-day oral toxicity, genotoxicity, and gender-related tissue distribution of silver nanoparticles in Sprague–Dawley rats. Inhalation Toxicol 20(6):575–583
37. Cha K, Hong H-W, Choi Y-G, Lee MJ, Park JH, Chae H-K, Ryu G, Myung H (2008) Comparison of acute responses of mice livers to short-term exposure to nano-sized or micro-sized silver particles. Biotechnol Lett 30(11):1893–1899
38. Azim SAA, Darwish HA, Rizk MZ, Ali SA, Kadry MO (2015) Amelioration of titanium dioxide nanoparticles-induced liver injury in mice: possible role of some antioxidants. Exp Toxicol Pathol 67(4):305–314
39. Liu H, Jia G, Chen S, Ma H, Zhao Y, Wang J, Zhang C, Wang S, Zhang J (2015) In vivo biodistribution and toxicity of Gd_2O_3: Eu^{3+} nanotubes in mice after intraperitoneal injection. RSC Adv 5(90):73601–73611
40. Cui Y, Liu H, Zhou M, Duan Y, Li N, Gong X, Hu R, Hong M, Hong F (2011) Signaling pathway of inflammatory responses in the mouse liver caused by TiO_2 nanoparticles. J Biomed Mater Res, Part A 96(1):221–229
41. Jin P, Chen Y, Zhang SB, Chen Z (2012) Interactions between $Al_{12}X$ (X = Al, C, N and P) nanoparticles and DNA nucleobases/base pairs: implications for nanotoxicity. J Mol Model 18(2):559–568
42. Li N, Ma L, Wang J, Zheng L, Liu J, Duan Y, Liu H, Zhao X, Wang S, Wang H (2009) Interaction between nano-anatase TiO_2 and liver DNA from mice in vivo. Nanoscale Res Lett 5(1):108
43. Singh N, Manshian B, Jenkins GJS, Griffiths SM, Williams PM, Maffeis TGG, Wright CJ, Doak SH (2009) NanoGenotoxicology: the DNA damaging potential of engineered nanomaterials. Biomaterials 30(23–24):3891–3914
44. Baweja L, Gurbani D, Shanker R, Pandey AK, Subramanian V, Dhawan A (2011) C60-fullerene binds with the ATP binding domain of human DNA topoiosmerase II alpha. J Biomed Nanotechnol 7(1):177–178
45. Huang S, Chueh PJ, Lin Y-W, Shih T-S, Chuang S-M (2009) Disturbed mitotic progression and genome segregation are involved in cell transformation mediated by nano-TiO_2 long-term exposure. Toxicol Appl Pharmacol 241(2):182–194
46. Sharma V, Anderson D, Dhawan A (2011) Zinc oxide nanoparticles induce oxidative stress and genotoxicity in human liver cells (HepG2). J Biomed Nanotechnol 7(1):98–99
47. Ahamed M, Ali D, Alhadlaq HA, Akhtar MJ (2013) Nickel oxide nanoparticles exert cytotoxicity via oxidative stress and induce apoptotic response in human liver cells (HepG2). Chemosphere 93(10):2514–2522
48. Trouiller B, Reliene R, Westbrook A, Solaimani P, Schiestl RH (2009) Titanium dioxide nanoparticles induce DNA damage and genetic instability in vivo in mice. Cancer Res 69 (22):8784–8789
49. Song M-F, Li Y-S, Kasai H, Kawai K (2012) Metal nanoparticle-induced micronuclei and oxidative DNA damage in mice. J Clin Biochem Nutr 50(3):211–216

50. Folkmann JK, Risom L, Jacobsen NR, Wallin H, Loft S, Møller P (2009) Oxidatively damaged DNA in rats exposed by oral gavage to C60 fullerenes and single-walled carbon nanotubes. Environ Health Perspect 117(5):703
51. Choi JE, Kim S, Ahn JH, Youn P, Kang JS, Park K, Yi J, Ryu D-Y (2010) Induction of oxidative stress and apoptosis by silver nanoparticles in the liver of adult zebrafish. Aquat Toxicol 100(2):151–159
52. Malhi H, Gores GJ, Lemasters JJ (2006) Apoptosis and necrosis in the liver: a tale of two deaths? Hepatology 43(S1)
53. Wang Y, Aker WG, H-m H, Yedjou CG, Yu H, Tchounwou PB (2011) A study of the mechanism of in vitro cytotoxicity of metal oxide nanoparticles using catfish primary hepatocytes and human HepG2 cells. Sci Total Environ 409(22):4753–4762
54. Loh JW, Yeoh G, Saunders M, Lim L-Y (2010) Uptake and cytotoxicity of chitosan nanoparticles in human liver cells. Toxicol Appl Pharmacol 249(2):148–157
55. Awasthi KK, John PJ, Awasthi A, Awasthi K (2013) Multi walled carbon nano tubes induced hepatotoxicity in Swiss albino mice. Micron 44:359–364
56. Korani M, Rezayat S, Gilani K, Bidgoli SA, Adeli S (2011) Acute and subchronic dermal toxicity of nanosilver in guinea pig. Int J Nanomed 6(1):855–862
57. Abdelhalim MAK, Jarrar BM (2011) Gold nanoparticles induced cloudy swelling to hydropic degeneration, cytoplasmic hyaline vacuolation, polymorphism, binucleation, karyopyknosis, karyolysis, karyorrhexis and necrosis in the liver. Lipids Health Dis 10(1):166
58. Xu J, Shi H, Ruth M, Yu H, Lazar L, Zou B, Yang C, Wu A, Zhao J (2013) Acute toxicity of intravenously administered titanium dioxide nanoparticles in mice. PLoS ONE 8(8):e70618
59. Xie G, Sun J, Zhong G, Shi L, Zhang D (2010) Biodistribution and toxicity of intravenously administered silica nanoparticles in mice. Arch Toxicol 84(3):183–190
60. Elmore S (2007) Apoptosis: a review of programmed cell death. Toxicol Pathol 35(4):495–516
61. Siddiqui MA, Alhadlaq HA, Ahmad J, Al-Khedhairy AA, Musarrat J, Ahamed M (2013) Copper oxide nanoparticles induced mitochondria mediated apoptosis in human hepatocarcinoma cells. PLoS ONE 8(8):e69534
62. Yuan Y, Liu C, Qian J, Wang J, Zhang Y (2010) Size-mediated cytotoxicity and apoptosis of hydroxyapatite nanoparticles in human hepatoma HepG2 cells. Biomaterials 31(4):730–740
63. Bataller R, Brenner DA (2005) Liver fibrosis. J Clin Invest 115(2):209–218
64. Nishimori H, Kondoh M, Isoda K, S-i T, Tsutsumi Y, Yagi K (2009) Silica nanoparticles as hepatotoxicants. Eur J Pharm Biopharm 72(3):496–501
65. Chen J, Dong X, Zhao J, Tang G (2009) In vivo acute toxicity of titanium dioxide nanoparticles to mice after intraperitioneal injection. J Appl Toxicol 29(4):330–337
66. Liu T, Li L, Fu C, Liu H, Chen D, Tang F (2012) Pathological mechanisms of liver injury caused by continuous intraperitoneal injection of silica nanoparticles. Biomaterials 33 (7):2399–2407
67. Everhart JE, Ruhl CE (2009) Burden of digestive diseases in the United States part III: liver, biliary tract, and pancreas. Gastroenterology 136(4):1134–1144
68. Wang F-S, Fan J-G, Zhang Z, Gao B, Wang H-Y (2014) The global burden of liver disease: the major impact of China. Hepatology 60(6):2099–2108
69. Ruzzin J, Petersen R, Meugnier E, Madsen L, Lock E-J, Lillefosse H, Ma T, Pesenti S, Sonne SB, Marstrand TT (2010) Persistent organic pollutant exposure leads to insulin resistance syndrome. Environ Health Perspect 118(4):465
70. Wahlang B, Falkner KC, Gregory B, Ansert D, Young D, Conklin DJ, Bhatnagar A, McClain CJ, Cave M (2013) Polychlorinated biphenyl 153 is a diet-dependent obesogen that worsens nonalcoholic fatty liver disease in male C57BL6/J mice. J Nutr Biochem 24(9):1587–1595
71. Rahman TM, Hodgson HJF (2000) Animal models of acute hepatic failure. Int J Exp Pathol 81(2):145–157
72. Liu Y, Meyer C, Xu C, Weng H, Hellerbrand C, ten Dijke P, Dooley S (2013) Animal models of chronic liver diseases. Am J Physiol Gastrointest Liver Physiol 304(5):G449

73. Bartneck M, Ritz T, Keul HA, Wambach M, Jr B, Gbureck U, Ehling J, Lammers T, Heymann F, Gassler N (2012) Peptide-functionalized gold nanorods increase liver injury in hepatitis. ACS Nano 6(10):8767–8777
74. Volarevic V, Paunovic V, Markovic Z, Simovic Markovic B, Misirkic-Marjanovic M, Todorovic-Markovic B, Bojic S, Vucicevic L, Jovanovic S, Arsenijevic N (2014) Large graphene quantum dots alleviate immune-mediated liver damage. ACS Nano 8(12):12098–12109
75. Ogden CL, Carroll MD, Kit BK, Flegal KM (2014) Prevalence of childhood and adult obesity in the United States, 2011–2012. JAMA 311(8):806–814
76. Hwang JH, Kim SJ, Kim Y-H, Noh J-R, Gang G-T, Chung BH, Song NW, Lee C-H (2012) Susceptibility to gold nanoparticle-induced hepatotoxicity is enhanced in a mouse model of nonalcoholic steatohepatitis. Toxicology 294(1):27–35
77. Jia J, Li F, Zhou H, Bai Y, Liu S, Jiang Y, Jiang G, Yan B (2017) Oral exposure to silver nanoparticles or silver ions may aggravate fatty liver disease in overweight mice. Environ Sci Technol
78. Jia J, Li F, Zhai S, Zhou H, Liu S, Jiang G, Yan B (2017) Susceptibility of overweight mice to liver injury as a result of the ZnO nanoparticle-enhanced liver deposition of Pb^{2+}. Environ Sci Technol 51(3):1775–1784
79. Cichoż-Lach H, Michalak A (2014) Oxidative stress as a crucial factor in liver diseases. World J Gastroenterol: WJG 20(25):8082–8091
80. Dirchwolf M, Ruf AE (2015) Role of systemic inflammation in cirrhosis: from pathogenesis to prognosis. World J Hepatol 7(16):1974–1981
81. PetkoviĆ J, Žegura B, StevanoviĆ M, Drnovšek N, UskokoviĆ D, Novak S, FilipiČ M (2011) DNA damage and alterations in expression of DNA damage responsive genes induced by TiO_2 nanoparticles in human hepatoma HepG2 cells. Nanotoxicology 5(3):341–353
82. Mu Q, Su G, Li L, Gilbertson BO, Yu LH, Zhang Q, Sun Y-P, Yan B (2012) Size-dependent cell uptake of protein-coated graphene oxide nanosheets. ACS Appl Mater Interfaces 4 (4):2259–2266
83. Zhang Y, Tekobo S, Tu Y, Zhou Q, Jin X, Dergunov SA, Pinkhassik E, Yan B (2012) Permission to enter cell by shape: nanodisk vs nanosphere. ACS Appl Mater Interfaces 4 (8):4099–4105
84. Wu L, Zhang Y, Zhang C, Cui X, Zhai S, Liu Y, Li C, Zhu H, Qu G, Jiang G (2014) Tuning cell autophagy by diversifying carbon nanotube surface chemistry. ACS Nano 8(3):2087–2099
85. Lankoff A, Sandberg WJ, Wegierek-Ciuk A, Lisowska H, Refsnes M, Sartowska B, Schwarze PE, Meczynska-Wielgosz S, Wojewodzka M, Kruszewski M (2012) The effect of agglomeration state of silver and titanium dioxide nanoparticles on cellular response of HepG2, A549 and THP-1 cells. Toxicol Lett 208(3):197–213
86. Zhang Y, Wang Y, Liu A, Xu SL, Zhao B, Zou H, Wang W, Zhu H, Yan B (2016) Modulation of carbon nanotubes' perturbation to the metabolic activity of CYP3A4 in the liver. Adv Funct Mater 26(6):841–850
87. Bai Y, Zhang Y, Zhang J, Mu Q, Zhang W, Butch ER, Snyder SE, Yan B (2010) Repeated administrations of carbon nanotubes in male mice cause reversible testis damage without affecting fertility. Nat Nanotechnol 5(9):683–689
88. Adamcakova-Dodd A, Stebounova LV, Kim JS, Vorrink SU, Ault AP, O'Shaughnessy PT, Grassian VH, Thorne PS (2014) Toxicity assessment of zinc oxide nanoparticles using sub-acute and sub-chronic murine inhalation models. Part Fibre Toxicol 11(1):1
89. Morishita Y, Yoshioka Y, Takimura Y, Shimizu Y, Namba Y, Nojiri N, Ishizaka T, Takao K, Yamashita F, Takuma K (2016) Distribution of silver nanoparticles to breast milk and their biological effects on breast-fed offspring mice. ACS Nano 10(9):8180–8191
90. Wang Z, Qu G, Su L, Wang L, Yang Z, Jiang J, Liu S, Jiang G (2013) Evaluation of the biological fate and the transport through biological barriers of nanosilver in mice. Curr Pharm Des 19(37):6691–6697

91. Kim YS, Song MY, Park JD, Song KS, Ryu HR, Chung YH, Chang HK, Lee JH, Oh KH, Kelman BJ (2010) Subchronic oral toxicity of silver nanoparticles. Part Fibre Toxicol 7(1):1
92. van der Zande M, Vandebriel RJ, Van Doren E, Kramer E, Herrera Rivera Z, Serrano-Rojero CS, Gremmer ER, Mast J, Peters RJ, Hollman PC (2012) Distribution, elimination, and toxicity of silver nanoparticles and silver ions in rats after 28-day oral exposure. ACS Nano 6 (8):7427–7442
93. Wei Y, Li Y, Jia J, Jiang Y, Zhao B, Zhang Q, Yan B (2016) Aggravated hepatotoxicity occurs in aged mice but not in young mice after oral exposure to zinc oxide nanoparticles. NanoImpact 3:1–11

Chapter 13
Silicon Quantum Dots: From Synthesis to Bioapplications

Miruna Silvia Stan, Cornelia Sima and Anca Dinischiotu

Abstract Silicon quantum dots (Si QDs) represent a special class of nanomaterials with distinctive properties, being used in different applications such as photovoltaics, optoelectronics devices, and biomedical ones. They have excellent luminescence at UV irradiation, tunable band gap, and resistance against photobleaching compared to standard dyes. Being less toxic in comparison with conventional metal-containing QDs, they received growing research interest in the last decade as a more biocompatible alternative to which displayed toxicological concerns. There are several physical and chemical methods for Si QDs synthesis, each of them involving advantages and disadvantages. In physical methods, the experimental setup is very simple and parameters can be adjusted from outside in order to obtain the desired size of nanoparticles. Chemical methods seem to be attractive due to the huge scale of productions, but the purity control of the material and experimental setup are more complicated. For biomedical applications, many techniques have been established to achieve water-soluble Si QDs and for their conjugation with biomolecules that render them to specific biological targets. Si QDs have become powerful nanomaterials in various biomedical applications, a promising approach for in vivo imaging, tumor biology investigation, and cancer treatment. Besides of all these advantages, their characteristics can also trigger cytotoxicity in healthy cells by different mechanisms that have been in vitro and in vivo investigated in the last years. This chapter summarizes the major methods of synthesis and recent advances in bioconjugation strategies for preparing high-quality Si QDs, with a focus on their toxicity evaluation and bioapplications.

Keywords Silicon quantum dots · Semiconductors · Self-fluorescence · Biocompatibility · Biomedical applications

M.S. Stan · A. Dinischiotu (✉)
Department of Biochemistry and Molecular Biology, University of Bucharest, 91-95 Splaiul Independentei, 050095 Bucharest, Romania
e-mail: anca.dinischiotu@bio.unibuc.ro

C. Sima
Laser Department, National Institute of Laser, Plasma and Radiation Physics, 409 Atomistilor, 077125 Bucharest, Magurele, Romania

B. Yan et al. (eds.), *Bioactivity of Engineered Nanoparticles*, Nanomedicine and Nanotoxicology, DOI 10.1007/978-981-10-5864-6_13

13.1 Si QDs Synthesis

13.1.1 Quantum Dots Versus Organic Dyes

Silicon is a chemical element widely used in many industrial and biomedical applications. Compared with other semiconductor materials, silicon is found in a large quantity in the earth's crust. Although it is an indirect band-gap semiconductor material, in the bulk form is less used for optoelectronics and biological applications. However, by decreasing the size of the particles (usually less than 5 nm), silicon acquires special properties exhibiting luminescence due to the existence of quantum confinement effect [1–5]. Several parameters influence the quantum confinement, such as particle size and size distribution, particle density, and surface properties [6, 7].

Crystalline silicon nanoparticles show emission from infrared to blue when their size is less than 5 nm meaning an increasing of the band gap: blue (2.64–3.0 eV), green (2.25 eV), orange (2.05 eV), red (1.70–1.80 eV) and infrared (1.2–1.6 eV) [8, 9]. It is assumed that the quantum confined effect appears in quantum dots (QDs) when their size becomes comparable with the exciton Bohr radius (4 nm for silicon) [9–11].

Wei-Wi et al. [12] noticed that photoluminescence of silicon quantum dots (Si QDs) at room temperature, in an atmosphere type dependent manner. So in hydrogen or in a vacuum, the emission was from infrared to ultraviolet with a blue shift observed with the decreasing of nanocrystal size, whereas in oxygen, air or nitrogen a stronger emission in a narrower wavelength range occurred [12].

Over the years, several semiconductor QDs were studied: CdS, CdSe, CdTe, InP, InAs, GaAs, and PbSe, PbS. One of the main disadvantages of these standard QDs is that they use heavy metal elements and are not suitable for in vivo applications being very toxic for biological systems [1].

In order to surpass these drawbacks, extensive researches were developed to synthesize reliable QDs with less toxicity, for use in optoelectronic and bioimaging applications [13–15]. In this context, silicon proved to be one of the ideal candidates having significant advantages over standard QDs (PbS(Se) and CdSe(Te)): less toxic, increased photostability, emission in near infrared range, and not at least their compatibility with biological medium [14, 16].

In the biological experiments, conventional fluorophores used are organic substances composed of either chemically synthesized fluorescent dyes or genetically encoded fluorescent proteins that have some limitations such as short fluorescence duration, narrow excitation, and broad bandwidth emission [17]. In contrast, QDs have broad absorption and at the same time a narrow wavelength-tunable emission peak. The molar absorption coefficients are larger than 100,000,000 M^{-1} cm^{-1} at the excitation peak wavelength compared to organic fluorophores which is less than 250,000 M^{-1} cm^{-1} [1]. Additionally, the emission peak of QDs is also tunable by varying size of the particles, which is not possible for organic dyes that have often the emission bands unsymmetrical [1–4]. Moreover, the quantum yield of QDs is

high, in the range of 60–80%, in visible and near infrared domains, whereas in the case of organic dye it is less than 20% in the near infrared region [1].

The fluorescence lifetime of the Si QDs is longer (tens of ns or μs), while in the case of organic dye it is shorter (5 ns in the visible region and 1 ns in the near infrared) [1, 4]. On the other hand, it was shown that "short fluorescence lifetime in Si QDs is often associated with core-related recombination and longer lifetime is due to the existence of ultrafast trapping of excited carriers in surface states, preventing core recombination" [1].

The emission properties of QDs are dependent on the particle size, morphology, composition, surface architecture, as well as shell ligands.

In consequence, QDs are more convenient than conventional dye for bioimaging applications due to strong stability to photobleaching, high quantum yield, broad absorption profile, and size-tunable emission [18–20].

13.1.2 Physical, Morpho-Structural, Optical and Surface Properties

QDs are semiconductor nanocrystals with size smaller than the exciton Bohr radius that present quantum size effect [1, 11, 13, 21]. They present special and unique properties due to quantum confinement phenomenon [20]. More exactly, the quantum confinement in the case of QDs consists of limitation of few electrons inside of a semiconductor that when are excited, emit a light with a specific wavelength which depends on the dot size [22].

It is well known that silicon has a very weak absorption in the visible range due to its indirect band gap. As a result of the quantum confinement phenomenon, optical band gap of the QDs can be adjusted as a function of size [14]. They have wavelength-tunable visible light emission, which depends on the core size of the nanoparticles [23].

There are many studies concerning the photoluminescence properties, on the nanoparticles size and size distribution, surface functionalization (surface passivation), crystallinity, shape of the nanoparticles, temperature, aging, etc. [21].

Studies regarding the variation of photoluminescence depending on the nanoparticle size revealed that larger nanoparticles (8 nm) exhibited luminescence toward longer wavelengths while those with size about 2 nm presented luminescence at higher energy (blue region) [24, 25].

The advantage of the Si QDs compared to other materials is mainly due to the low toxicity of silicon and possibility of modifying the nanoparticle size in a wide range [26, 27]. Other characteristics such as rates of radiative recombination, lifetimes, and quantum efficiency strongly depend also on the size of QDs.

In the synthesis process, nature of *the ambient gas* had a strong influence on the crystallization state. Due to this fact, Si QDs grown in NH_3 with plasma enhanced chemical vapor deposition (PECVD) had a crystalline structure, whereas those

synthesized in N_2 gas were amorphous, suggesting that hydrogen present in gaseous NH_3 favored the crystallinity [28]. Analyzing the photoluminescence intensity of Si QDs prepared in SiH_4/N_2, it was observed that the highest intensity was noticed for those prepared in SiH_4/NH_3, and the lowest was observed in the case of the ones prepared in SiH_4/N_2, probably due to the effect of hydrogen passivation on reducing dangling bonds and nonradiative species [28, 29]. The decrease of size by increasing of N_2 flow rate resulted in an enhancement of quantum confinement and appearance of a blue shift [30, 31].

A clear dependence between band gap, size, and shape of QDs was reported [32]. Also, it was demonstrated that "cubic Si QDs exhibit larger wavelengths while octahedral nanoparticles exhibit smaller wavelengths and truncated Si QDs exhibit wavelengths between cubic and octahedral" [32]. It was also proved that plasma-based methods produced cubic shapes which are advantageous for "maximization of amount surface hydrogen absorption" while the other synthesis methods generated pseudospherical shapes which, after annealing, leaded to faceted shapes [32].

In the chemical etching synthesis method, the *etching time* also influences the photoluminescence; therefore, increasing the etching time, reduces the size of nanoparticles leading to a blue shifting in the photoluminescence peak [33].

Previous studies revealed that Si QDs with average size of about 3.6 nm did not present any photoluminescence immediately after synthesis. But, after about 20 min in air, they exhibited a weak photoluminescence at about 1.72 eV; by increasing the aging time in air to 25 days, the photoluminescence peak was at about 1.87 eV. It was concluded that the photoluminescence peak shifted toward shorter wavelengths, in an oxidation time dependent manner, probably due to the decrease of the core size and the increase of the oxide layer [24]. Also, the full width at half maximum (FWHM) after 20 min of aging was about 0.23 eV, and increased to 0.31 eV after 25 days. After 1 month, the peak intensity increased by about 16 times [24]. After 6 months of aging in air after SiO_2 removal, the luminescence peak position did not change, but FWHM returned to approximately the same value before oxidation. Additionally, the intensity strongly increased by about 70-fold [24]. Similar observations have been done by Ledoux et al. [25].

One of the most important parameters which influences the photoluminescence are the *surface properties* of Si QDs as well. Absence of a semiconductor shell reduces the degree of exciton confinement in the core and broadnesses the emission peak. It was demonstrated that Si QDs prepared via colloidal solution method have emission in blue–green while the red emission could be observed when Si QDs are prepared at high temperature. Also the crystallinity and size of the core of Si QDs are influenced by the oxidation of dots; therefore, by adding an organic monolayer on the Si QDs surface, oxidation of the surface could be avoided leading to stable photoluminescence properties [1].

Taking into account that surface of Si QDs is very active, several ways to modify the surface properties for improvement of the photoluminescence were studied [34]. So the surface of Si QDs (4.9–6 nm) was covered with an oxide layer by gradual

oxidation for 2 years in the air. After dispersion in ethanol, they exhibited a luminescence at about 763 nm, while the freshly prepared QDs had no photoluminescence [34].

It was assumed that the presence of dangling bonds on the silicon surface is a disadvantage for the photoluminescence occurrence and a passivation of Si QDs surface by hydrofluoric acid (HF) has been done in order to remove the oxide layer leading to a narrow band from 0.4 eV (before HF treatment) to 0.26 eV (after HF treatment) [35].

It was demonstrated that the dangling bonds (nonradiative defect) could be passivated using NH_3 instead of N_2. Furthermore, photoluminescence was very strong and the peak position was strongly influenced by the flow rate of NH_3 being shifted to lower wavelengths (blue shift) when the flow gas rate increased from 10 to 900 sccm at a fixed SiH_4 flow rate of 400 sccm. On the other hand, when the NH_3 flow rate was maintained at 30 sccm and SiH_4 flow rate was varied in the range 100–900 sccm, the photoluminescence peak shifted toward longer wavelengths [28].

When the Si QDs were capped with SH, NH_2, OH, photoluminescence spectra presented significant modifications, whereas when alky groups (–Si–C–) were added low alterations appeared in the photoluminescence spectrum [36].

The halogenation of the Si QDs strongly influenced the optical properties of QDs. So under direct UV irradiation of the halide attached on the Si QDs, no any photoluminescence was detected; but after oxidation it was noticed. Therefore, a blue photoluminescence was observed in the case of chlorine terminated silicon quantum dots surface, while for bromide and iodide, yellow–orange photoluminescence was observed. It was assumed that blue photoluminescence is due to oxychloride defects while the yellow orange is generated by oxide defects [37].

The photoluminescence of Si QDs is also influenced by *temperature.* A shifting toward red after an increase of temperature between 110 and 350 K, when the silicon sample was excited with 266 nm wavelength occurred [38]. Also after heating from 700 to 1000 °C the photoluminescence peak was shifted toward longer wavelengths due to the fact of the increase of the grain size at high temperatures [39].

The optical properties of the Si QDs are dependent on their *electronic structure* [40]. Theoretically, a strong correlation between the split of the energy level in the dot and the dot size, crystallographic directions, and shape exist [40]. Therefore, Zianni et al. [40] assumed that "for [001] level, the lifetime is not influenced by the crystallographic direction" and in the case of small dots (2 nm), it is of μs order while "for [100] level the lifetime is strongly influenced by the crystallographic direction" being about ms order [40].

It is considered that the photoluminescence lifetime is a result of radiative and nonradiative recombination processes. The study of Wu and Lin [41] on Si QDs revealed that "non-radiative recombination rate is much lower than radiative recombination rate," that means that the photoluminescence lifetime of these is the result of radiative recombination only [41].

13.1.3 Synthesis Methods

The synthesis methods of Si QDs are various being both physical and chemical ones. Each of them has advantages and disadvantages.

Physical methods produce high purity particles, the experimental setup being very simple and parameters can be adjusted from outside in order to obtain the desired size of nanoparticles; on the other hand, the particles have a lower yield [4].

Chemical methods seem to be attractive due to the huge scale of production, but the purity control of the material and experimental setup are more complicated. Unlike the physical methods, in order to enhance the QDs luminescence, additional treatment, such as annealing is necessary; moreover, multistep procedures are required [4].

There are several synthesis methods such as: laser ablation [6, 12, 26, 27, 42–52], magnetron sputtering [13, 53–55], solution phase oxidation/reduction [1, 4, 19, 56], thermolysis/laser pyrolysis [1, 4, 24, 25, 34, 35], electrochemical etching (anodic oxidation) [4, 5, 33, 38, 57, 58], microwave-assisted method [8, 11, 59–61], atmospheric pressure plasma [7, 62].

13.1.3.1 Laser Ablation

First experiments for preparing silicon nanoparticles by laser ablation have been done by Okada and Iijima [4, 42]. The method is advantageous due to the fact that no chemical precursors which could contaminate the nanoparticles is used (therefore, it is considered a very clean method); the experimental setup is very simple without the requirement of high temperatures or pressures; it is versatile, giving the possibility to vary from outside any experimental parameters [10].

There are two types of environments to prepare nanoparticles by laser ablation: in liquid or gas. Laser ablation in liquid demonstrated a good capability to produce pure nanoparticle colloidal solution. The photoluminescence of the silicon nanoparticles obtained in liquid is dependent of laser wavelength and pulse duration [43]. Intartaglia et al. [43] synthesized silicon nanoparticles in aqueous solution (deionized water) using a Ti: sapphire femtosecond laser, (110 fs pulse duration, 800 nm wavelength, 1 kHz repetition rate) at two different energies/pulse (0.15 and 0.4 mJ). In the case of high energy (0.4 mJ), the nanoparticles were in the range of 10–120 nm with an average size of about 65 nm. On the other hand, at low energy of 0.15 mJ, the size of the silicon nanoparticles was in the range of 1–8 nm with average size of about 5.5 nm. In both cases, the nanoparticles were crystalline. After synthesis, they were excited with 400 nm wavelength; the small nanoparticles (obtained at low energy) exhibited a blue green emission; the large ones (synthesized at high energy) exhibited a luminescence peak at 575 nm and decreased intensity [43].

Vaccaro et al. [44] evidenced also the versatility of the laser ablation in water, offering the possibility to control each parameter during the experiments

(wavelength, energy, fluency, pulse duration, liquid) leading to the desired properties of the silicon nanoparticles (crystallinity, composition, size). A nanosecond Nd:YAG laser (1064 nm, 10 Hz, 5 ns, 0.6 J/cm^2 energy density) was used. The nanoparticles were in the range of 2–10 nm with the mean size of about 4 nm. Concerning the photoluminescence, it was observed an emission peak at about 1.95 eV, being in accordance with quantum confinement. Therefore, decreasing the size of nanoparticle, the emission peak is shifted toward shorter wavelength and increasing the band gap. The measured photoluminescence lifetime was in the range of μs. It was demonstrated that the photoluminescence peak depends on the size of nanoparticle according to expression:

$$E_{\mathrm{PL}} = E_0 + \left(3.73/d^{1.39}\right), \tag{13.1}$$

where E_0 = 1.17 eV (the band gap energy of bulk silicon) and d = size of nanoparticle in nm [44].

Starting from a *p*-type silicon wafer, with a nanosecond Nd:YAG laser (532 nm, 13 ns, 10 Hz), Chewchinda et al. [45] synthesized silicon nanoparticles in ethanol, energy density from 0.15 to 0.45 J/cm^2. The nanoparticles were spherical, and their size was in the range of 2–30 nm, the average size decreasing with increasing of energy density. So at highest energy density of 0.45 J/cm^2, the average size was about 6 nm. In this case, the photoluminescence peak increases with increasing the energy density when small nanoparticles are generated and at the same time are blue shifted [45].

Eroshova et al. [26] studied the influence of the pulse duration on the nanoparticle characteristics. So, a picosecond laser (Nd:YAG, 1064 nm, 34 ps, 10 Hz, 1 mJ) was used for the ablation of a silicon wafer in distilled deionized water and femtosecond laser (1250 nm, 120 fs, 10 Hz, 300 μJ) in liquid nitrogen. The average size of nanoparticles obtained using picosecond laser was about 18 nm and these were crystalline. On the other hand, using fs laser for ablation in liquid nitrogen, the average size of the silicon nanoparticles was about 5 nm. In this case, the photoluminescence spectrum exhibited an emission peak at about 750 nm (1.65 eV).

Concerning the synthesis of Si QDs in a gas atmosphere, it was studied the temperature dependence of these nanoparticles produced by laser ablation in helium atmosphere [46]. Using a Nd:YAG laser (532 nm, 210 mJ, 10 Hz) a silicon wafer target was irradiated in an atmosphere of 7 Torr. Spherical nanoparticles with a very narrow lognormal distribution (6–8 nm) and average size about 7 nm were obtained. Additionally, it was observed that the silicon nanoparticles were covered with an amorphous silicon oxide shell due to the oxidation after exposure to the ambient atmosphere. From the photoluminescence spectra measured at different temperatures from 300 to 4 K, Orii et al. observed a "gradually increasing of the luminescence intensity, peaked at about 60 K and then decreasing rapidly. The photoluminescence intensity at 60 K was increased relative to the value of 300 K by a factor of 5 and that at 4 K decreased roughly to the value at 300 K" [46].

Another study used a KrF excimer laser (248 nm, 20 ns, 2 J/cm^2 fluency, 10 Hz), starting from a silicon target. The experiments were made in helium atmosphere at 10^{-1} mbar. All the silicon samples were almost spherical. The mean size of the nanoparticles was in the range of 1–5 nm. At room temperature, a UV–VIS photoluminescence attributed to direct band recombination from quantum confinement of silicon was observed. The photoluminescence lifetime was about 1.5 ns [6].

Laser ablation experiments in two different inert gases (helium and argon with pressure in the range of 250–550 mbar) were also made by Grigoriu et al. [47, 48]. A Nd:YAG laser (532/355 nm, 5 ns, 10 Hz and 4–8 J/cm^2) was used.

The synthesis of Si QDs by laser ablation in reactive gases was also done in oxygen atmosphere, using a KrF excimer laser (248 nm, 17 ns, 20 Hz, 5 J/cm^2) [49]. It was observed a strong dependence of the photoluminescence intensity on oxygen pressure and size of crystals. It was observed that increasing the oxygen pressure leads to a decreasing of the intensity photoluminescence. Additionally, the position and shape of the photoluminescence spectrum depend on the crystal size and size distribution; the crystal size decreases with increasing of oxygen pressure [49].

Wei-Qi et al. prepared Si QDs using infrared radiation, 1064 nm, 60–80 ns pulse duration, and 1000–3000 s^{-1} repetition rate [12]. They prepared Si QDs in different atmospheres: oxygen, nitrogen, air. A *p*-type silicon wafer was used as target. After synthesis, the samples were annealed at 1000 °C for 5–30 min in oxygen, nitrogen or air, in order to eliminate dangling bonds from the surface of Si QDs; the annealing produced a narrowing of the size range. Another method to reduce the dangling bonds was "the passivation of hydrogen in HF liquid" [12].

Concerning the correlation between pulse duration and nanoparticle characteristics, it is considered that laser ablation with picosecond pulses is more advantageous in comparison with nanosecond laser pulses. Therefore, when a laser with nanosecond pulse duration impinges the target, due to the high energies/pulse and low repetition rates, the ejected macroparticles interact with the gas leading to the formation of large particles. Conversely, using picosecond pulses, low energies/pulse and high repetition rates, a fine material is ejected from the target creating particles with small size [50].

13.1.3.2 Magnetron Sputtering

The method consists of bombardment of a target with energetic ions that come from gaseous plasma. Following the interaction between the ions and the atoms from target surface, the individual atoms condensed onto a substrate [53]. The method is very fast, simple, with high productivity, being similar with laser technique. The shape and size of the particles depend on the "distance between magnetron and exit aperture" [54]. Also, the aggregation of the particles is dependent on the distance between magnetron and exit aperture, gas pressure, and time [54].

By this method, Fujioka et al. obtained Si QDs with mean diameter about 6.5 nm and a core structure of silicon with average size of about 2.5 nm. At excitation wavelength of 300 nm, the photoluminescent emission was at 414 nm [13].

Ohta et al. synthesized Si QDs with diameter about 3 nm exhibiting luminescence at 450 nm after irradiation with 360 nm wavelength [55]. Generally, use of QDs in biological environments requires their dipping in aqueous medium thus leads to aggregation of the nanoparticles. In order to avoid the interaction between particles, it was necessary to modify their surface. For biomedical applications, their surfaces were modified by allylamine and amphiphilic block copolymers that did not modify the photoluminescence emission peak [55].

13.1.3.3 Solution Phase Oxidation/Reduction

The first experiment using this method has been performed by Heath in 1992 [56]. This is a simple method due to the flexibility of choosing different reducing agents [4, 56]. Ghosh et al. described in 2014 the synthesis method as consisting of a "reduction of $SiCl_4$ and $RSiCl_3$ (where R could be hydrogen or octyl group) by sodium metal in a non-polar organic solvent at high temperature of 385 °C and pressure higher than 100 atmosphere" [4]. The obtained silicon nanoparticles were in the range between 5 nm and 3 μm with hexagonal shapes in trichlorosilane or about 5.5 nm in the presence of trichlorooctylsilane [4]. On the other hand, this method is considered disadvantageous due to the difficulty of controlling or adjusting the nanoparticle size.

13.1.3.4 Thermolysis/Laser Pyrolysis

This method generates freestanding nanoparticles and was first demonstrated by Cannon et al. in silane gas, using a CO_2 laser [1, 4]. It consists in dissociation of SiH_4 and nucleation of the silicon nanoparticles [4]. Several authors investigated the Si QDs produced by laser pyrolysis [24, 25, 34, 35]. Ledoux et al. explained the principle method as follows: "a conical nozzle is placed near the pyrolysis "flame" and the clusters and nanoparticles are extracted from the flow reactor" [25]. "They are skimmed into a low-pressure vacuum chamber and form a "molecular beam" of noninteracting clusters." "In this molecular beam, the cluster velocity is mass dependent; the smaller the particles, the faster they are; therefore, a rotating chopper synchronized with the pulsed pyrolysis laser, the size distribution of the clusters can be significantly narrowed" [25]. This method can produce high quantities comparing with other methods; by laser pyrolysis about 200 mg/h particles with size less than 3 nm could be obtained [34]. The disadvantage is that is more complicated to obtain pure QDs and not at least silane is very explosive and should be taken additionally adequate protections which generate other supplementary costs.

13.1.3.5 Electrochemical Etching/Anodic Oxidation

Generally, the method consists in dissolving of the material which is subjected for obtaining of nanoparticles using some acids, basis, or several chemical agents. It could use different semiconducting materials (in this case silicon), metals or glass. Thus, after the interaction between the material and the respective chemical agents, the target is corroded and finally the material is removed. In order to adjust the size of the nanoparticles, the etching time could be varied as well as the etching solutions. One can be concluded that the characteristics of the nanoparticles depend on these parameters. Examples of etching solution could be considered nitric acid (HNO_3) and hydrofluoric acid (HF) [58]. More exactly, silicon wafer is etched and the resulted materials are dispersed in different solvents leading to a suspension with Si QDs of irregular shapes, with size from few nm to microns [4]. Wang and his coworkers [5], synthesized photoluminescent (red–orange) silicon nanoparticles (about 2.7 nm size) by electrochemical etching, starting from a silicon *n*-type or *p*-type wafer. Both wafers were etched in a mixture of HF/H_2O/ethanol [5]. This method is a promising one but it should be mentioned that the size of nanoparticles cannot be easy controlled "at the single nanoscale" [4].

13.1.3.6 Microwave-Assisted Synthesis Method

One experimental setup for obtaining silicon nanoparticles is reported by Chinnathambi et al. [11]. The method is based on a heating mechanism being known as "microwave dielectric heating" [60]. Baretto et al. [59] and Atkins et al. [60] give some explanation of the synthesis method with their advantages as follows. The heating takes place through two processes: dipolar polarization and ionic conduction. Thus, after the electromagnetic field is applied to the sample, the electrical component produces "dipols and ions which try to align with the electric field." Procedure of the alignment of the dipols with electric field involves "energy which is lost as generation of heat" [60].

The microwave-assisted synthesis method proved to be advantageous being a very fast and simple method. So, 0.1 g Si QDs of 4 nm size are obtained in about 15 min [61]. These have shown excellent aqueous dispersibility and a strong fluorescence. The spherical shape, high crystallinity and average size of about 3.1 nm were obtained. The emission peak of Si QDs was at 660 nm. Under UV irradiation, it could be seen a very strong red luminescence [61].

13.1.3.7 Atmospheric Pressure Plasma

Synthesis of Si QDs by atmospheric pressure plasma is considered one recent method with high capabilities for different applications.

An experimental setup of synthesis of Si QDs by plasma was described by Yu et al. [62]. Between two parallel aluminum electrodes covered with quartz as

dielectric barrier vertically in the reaction chamber, plasma was generated. As working gases, argon, silane, and hydrogen flow through the electrodes conducted at a discharge. Thus, the electrons from plasma dissociate the silane resulting into silicon clusters and after about several milliseconds generated few nanometers particles which were collected onto a substrate when an RF power is attached. The photoluminescence of the nanoparticles remain unchanged more than 1 month [62].

One of the main drawbacks of this method is that it takes long time for obtaining important quantities. The aim is to have a continuous flow-through process; therefore it was demonstrated that RF frequencies were more suitable from production rate point of view, comparing with DC excitation [7].

13.2 Si QDs Bio-Interaction

13.2.1 Si QDs Biocompatibility and Cytotoxicity

As stated before, Si QDs have proved an increased in vitro biocompatibility and low cytotoxicity, or even the absence of it [61, 63–66]. Compared with the heavy metal-based QDs, the toxicity of Si QDs was not observed at 112 μg/ml, and these proved to be more than ten times safer than CdSe QDs [13]. Despite the biocompatibility observed for low doses of nanoparticles, a reduced viability was noticed when the concentration was increased in respect with the type of synthesis which certainly influences the toxicity [13, 61, 63, 67–70]. Erogbogbo et al. considered that residual chloroform used in synthesis could be responsible for the toxic effects. The mechanism of toxicity suggested by the group of Fujioka pointed out that Si QDs can generate reactive oxygen species (ROS) which could be associated with membrane damage [63]. Similar, Stan et al. revealed the absence of toxicity in human lung cells for doses up to 200 μg/ml after 24 h of exposure, but toxic effects appeared for high concentrations after 48 and 72 h [70]. Similarly, HepG2 hepatic cells tolerated high doses of Si QDs without suffering significant damage [71]. The negative influence of Si QDs on redox homeostasis of pulmonary fibroblasts was reflected by increased levels of ROS, lipid peroxidation and oxidized proteins, together with decreased glutathione content, the intracellular distribution of GSH being altered during longer incubation intervals [70]. Taking into account all these in vitro data, it could be suggested that cell death induced by high doses of Si QDs is mediated by oxidative stress, a common key factor involved in the cytotoxicity of various types of nanoparticles, which disturbs protein functions and cell signaling [72]. In addition, an inflammatory response in lung cells characterized by the release of pro-inflammatory cytokines was triggered by Si QDs which modulated also the expression and activity of matrix metalloproteinases [69]. A schematic representation of the most important effects induced by Si QDs is depicted in Fig. 13.1.

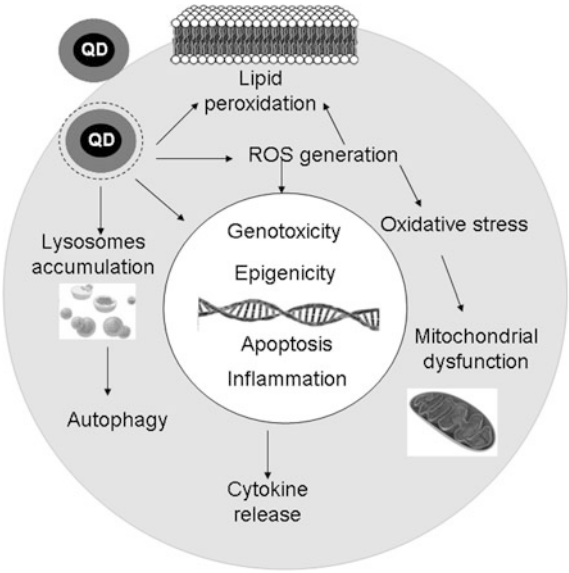

Fig. 13.1 A schematic representation of the most important effects induced by Si QDs

The surface chemistry of Si QDs can modulate their cytotoxicity, nanoparticles capped with polar molecules being less toxic than QDs with more relative functionalities [73]. In addition, our group considered that toxic effects of Si QDs could be related to the siloxane rings formed through the condensation of silanol groups which were expected to appear due to the hydroxylation of SiO_2 surface consecutively to laser ablation synthesis [69].

Studies over the past decade have shown that autophagy is part of the biological effects triggered by different nanoparticles, including QDs [69, 74], highlighting an increased expression of LC3-II and ATG7 proteins, and the possibility that autophagy could be triggered by the oxidized environment created after the exposure, and not directly by the nanoparticles [75]. Induction of autophagy could be seen as a cellular survival mechanism which allows self-clearance of nanoparticles which were frequently detected in lysosomes upon internalization, although their biopersistence could cause lysosomal disfunction [76]. Moreover, the degree of cellular uptake QDs might determine the cytotoxic potential.

The in vivo biocompatibility of Si QDs has been previously assessed especially to provide the confirmation for a future safety use in humans of these nanoparticles in biomedical applications [2, 77, 78]. The results obtained suggested that systemic reactions were specific to each type of model organism used and cytotoxicity appeared mostly at higher doses [77–83].

In addition, complex investigations were performed on gibel and crucian carp to establish the effects induced in fish on short and long terms because fish represent attractive alternative models to mammalian species for the analysis of toxicity mechanism induced by nanoparticles. Oxidative stress induced in fish liver by Si QDs was revealed 1-week post-administration [80]. Further, the profile of oxidative

stress markers and of heat shock proteins after 3 weeks post-injection indicated liver recovery after Si QDs-induced redox imbalance, suggesting that a longer period of time was necessary to overcome the harmful effects of QDs [81]. Besides degenerative processes, nephrogenesis was initiated after a week post-injection which indicated the ability of kidney to regenerate after the Si QDs-induced injury hallmarked by the increased lipid peroxidation and decreased level of reduced glutathione and of glutathione reductase and glutathione peroxidase activities [82]. Interestingly, an effective adaptative response was activated in the white muscle of gibel fish, and thus the oxidative stress induced by QDs did not cause any permanent damage in this tissue [83].

13.2.2 Si QDs Internalization and Accumulation

The typical pathway described for in vitro Si QDs uptake was endocytosis as reviewed by Cheng et al. [1]. Differences on the uptake rate were reported between normal and cancer cells, many more Si nanocrystals being found in the neoplastic cells after the internalization via cholesterol-dependent endocytosis [84]. Time course observations of Si QDs uptake revealed their transport to late endosomes/lysosomes, the number of internalized nanoparticles increasing with time and reaching a plateau value [69, 85]. Consequently, the removal of Si QDs from endothelial cells was reported via exocytosis, a kinetic model based on the mass balance of QDs and cell receptors being proposed [85]. Tu et al. showed a receptor-mediated accumulation of manganese-doped Si QDs in macrophages due to the dextran sulfate coating [68].

Although blue- and green-emitting Si QDs synthesized by atmospheric plasma method were visualized manly in the cytoplasm, along with a significant fraction inside the nucleus of the monocytes [2], our group observed the red-emitting Si QDs obtained by laser ablation only in the cytoplasm of lung fibroblasts [69]. These differences are most probably based on the QDs synthesis method, concentration and cellular type used in the experiments. Anyway, a concentration-dependent increase in LDH level and in the number of apoptotic and necrotic cells was noticed in both studies, underling the cytotoxicity of high doses of Si QDs.

Regarding the Si QDs accumulation in animals, studies showed the presence of high levels in liver and spleen of mice after three months of treatment investigated by Liu et al. [78]. However, these effects were not noticed in monkeys, suggesting that some systemic reactions could be dependent on the animal model [78]. A recent study on zebrafish model revealed a distribution of blue and green fluorescence of Si QDs mainly in the yolk-sac region, probably due to their interaction with lipid-rich yolk cells during embryonic development [2]. Although the authors stated that Si QDs induced a low toxicity in zebrafish, abnormalities, such as yolk-sac edema, head edema, and tail truncation, were observed, possibly due to a miss-regulation of certain genes, as it was noticed also for silver nanoparticles [2].

Furthermore, Tu et al. evaluated the biodistribution in mice of ^{64}Cu-DO3A derivative four labeled dextran-coated Si_{Mn} QDs (1% manganese-doped Si QDs) by in vivo positron emission tomography (PET) imaging [77]. The main sites of accumulation were urinary bladder and liver during the first hour after injection, and via gamma counting of ex vivo tissues after 48 h PET scan the liver was found to be the major organ where QDs accumulated. Regarding the nanoparticle excretion, it was demonstrated that the particles smaller than 7 nm are rapidly eliminated through renal filtration, and the larger ones are taken up by the reticuloendothelial system being excreted into the biliary system [77].

Tissue fluorescence microscopy revealed a gradual accumulation of Si QDs in gibel carp liver during the next 7 days post-injection which induced important histological changes in the hepatic tissue [80]. Also the presence of Si QDs in the liver of crucian carp was evidenced after 2 weeks post-administration and significantly disappeared after 3 weeks [81]. Regarding the biodistribution of Si QDs in the fish kidney, a progressive loading of renal tubular epithelial cells with nanoparticles was noticed along with their accumulation in the macrophages [82]. Visualization of Si QDs in the white skeletal muscle of gibel fish showed a localization pattern in the subsarcolemmal space and inside muscle fibers which generated degenerative changes [83].

13.3 Bioapplications of Si QDs

Their special optical properties make Si QDs a promising material for a large variety of applications ranging from optoelectronic devices, solar cells, energy storage materials to in vivo imaging labels, therapy, and contrast agents in bioimaging (Fig. 13.2). Due to their large emission in the infrared region are very useful for deep-tissue penetration [11, 20, 43]. Also, they can be used as photoluminescence probes in photodynamic diagnostics and therapy [26].

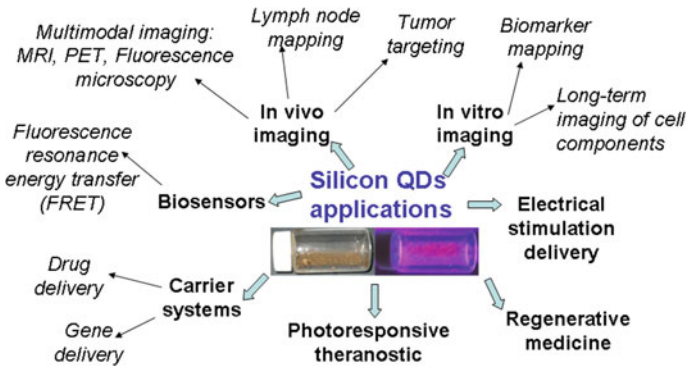

Fig. 13.2 The most important biomedical applications of Si QDs

It was proved that they could be used as drug and gene carriers for different treatments and imaging agents in magnetic resonance imaging (MRI), ultrasound (US), computed tomography (CT), photoacoustic (PA), and fluorescence imaging. For these applications, the particles should be nontoxic with increased photostability and highly resistant to the enzymatic degradation in physiological medium. Consequently, semiconductor QDs have been successfully demonstrated as in vitro and in vivo imaging probes in the field of medicine because they do not damage upon continuous light exposure [2, 45].

Since 2004 when Li and Ruckenstein [86] opened the research of Si QDs fluorescence imaging, several recent reports have illustrated the applicability of highly luminescent Si QDs as nontoxic in vitro and in vivo bioimaging probes. First, Erogbogbo et al. published in 2008 the preparation of biocompatible micelle-encapsulated Si QDs used for imaging pancreatic cancer cells [63]. Later on, water dispersible Si QDs of low toxicity coated with Pluronic F127 block copolymer were developed by Shen et al. for a long-term real-time observation of endoplasmic reticulum in live cells [64]. Other biocompatible and photostable Si QDs suitable for long-term imaging of cell nuclei for up to 60 min were described by Zhong et al. [65]. The use of Si QDs synthesized by one-step hydrothermal method as probes for fluorescent imaging was also illustrated by Wu et al. [66].

The excellent photophysical features of Si QDs have permitted the combination of their surface chemistry with optical microscopy in the context of bioimaging. Nanocrystalline Si QDs were used in fluorescence lifetime imaging microscopy (FLIM), which was successfully combined with Förster resonance energy transfer (FRET) studies where QDs revealed an enhanced performance as biosensors over conventional molecular fluorophores [18]. In this case, organic dye acceptors were conjugated onto the nanoparticle surface and contributed to the color tuning of nanoparticles [18]. Also, an energy transfer micelle platform was created in order to improve the QD emission yield for biological applications [67]. By combining Si QDs with an anthracene-based dye in the hydrophobic core of 1,2-distearoyl-sn-glycero-3-phosphoethanolamine-*N*-[methoxy(polyethylene glycol)-2000] (DSPE-PEG) micelles the luminescence was enhanced by more than 80% [67].

Nanostructured multimodal imaging probes can be achieved by combining the MRI technique and the optical imaging methods. Although Si QDs do not exhibit paramagnetic properties, the dual character can be obtain through their co-encapsulation with paramagnetic Fe_3O_4 nanoparticles in phospholipids [87], being doped with manganese [68] or by direct attachment of DOTA-chelated Gd^{3-} to the PEGylated micelles with hydrophobic Si QDs in their core [88], resulting a prolonged T1 relaxation time for an improved contrast while the fluorescence intensity was maintained. Also, Tu et al. demonstrated the efficiency of ^{64}Cu-DO3A derivative four labeled dextran-coated Si_{Mn} QDs (1% manganese-doped Si QDs) as a new biomedical candidate for in vivo positron emission tomography (PET) imaging [77]. Moreover, luminescent Si QDs functionalized with 2-vinylpyridine were developed by Klein et al. in 2009 as self-tracking vehicle for siRNA delivery in tumor cells. The biocompatible and water-soluble luminescent Si QDs were internalized by endocytosis, and the Si QDs-siRNA complexes formed via electrostatic interactions,

were internalized by endocytosis [89]. Prasad and his team succeeded to encapsulate Si QDs in Pluronic® block copolymers (PSiQDs). These were water dispersible, protected against oxidation and aggregation and with preserved optical properties [90]. Their surface modification with anti-claudin-4 and anti-mesothelin in order to target pancreatic cancer cells led to an improved uptake of these nanoconstructs compared to folate-conjugated PSiQDs, being competitive for tumor targeting in cancer applications without exhibiting toxicity. Moreover, the same group of Prasad developed a nanoplatform with both plasmonic and luminescent properties for multimodal imaging by incorporating multiple Si QDs into the core of a micelle and depositing plasmonic gold on its surface [91].

The potential of Si QDs as carriers in drug-delivery systems was evaluated after their conjugation with alminoprofen, a non-steroid anti-inflammatory drug for rheumatism [92]. The results revealed a lower toxicity of the "silicon drug" compared to the parental alminoprofen due to a condensed surface integration of ligand/receptor-type drugs which might reduce the adverse interaction between the cells and ligants, and also an enhanced functionality of the anti-inflammatory drug [92]. In addition, doxorubicin-loaded Si QD aggregates were designed for the intracellular release of drug in response to endosomal pH decrease [85]. Recently, a drug-delivery system based on amine functionalized Si QDs and covalently conjugated phototrigger *o*-nitrobenzyl with caged anticancer drug chlorambucil onto it, was designed as a photoresponsive theranostic which combines multiple functions [93]. Besides the nanocarrier role for drug delivery and the controlled drug release under one- and two-photon excitation, these photoswitchable fluorescent nanoparticles allowed the real-time monitoring of drug release based on the photoinduced electron transfer process [93].

The in vivo imaging using QDs was reported especially for lymph node mapping, blood vessel visualization, and tumor targeting. Si QDs with a hydrodynamic size of 20 nm, injected subcutaneously to mice were observed in the axillary lymph nodes and a long tumor accumulation time in vivo, without any important adverse effects which suggest their biocompatibility compared with cadmium containing QDs [79]. This opportunity to track the lymphatic flow in real time and to guide the nodal resection given by the noninvasive fluorescence detection of sentinel lymph nodes using QDs is very useful.

Recently, Erogbogbo and his coworkers managed to translate the metabolomic and proteomic data obtained in a human model of cardiac ischemia into a potential therapeutic diagnostic (theranostic) containing Si QDs. The fabrication of such theranostic nanoconstruct represents an important step which should be adopted in the pathway to a personalized medicine [94].

Besides fluorescence imaging and drug-delivery applications, the large variety of biomedical purposes of Si QDs includes also the regenerative medicine. In this way, the group of Olson has investigated the capability of intravitreal Si QDs to deliver electrical stimulation to the retinal cells and the effects on retinal electrophysiology and anatomy [95]. The use of Si QDs in the rat model of retinal photoreceptor degeneration was safe, providing a prolonged cell survival rate and increased

amplitude of the b-wave, mainly in the rod's response. This great opportunity of nanotechnology to deliver electrical stimulation at molecular level should represent a priority for future biomedical research on Si QDs to raise the cure rate of various diseases.

References

1. Cheng X, Lowe SB, Reece PJ, Gooding JJ (2014) Colloidal silicon quantum dots: from preparation to the modification of self-assembled monolayers (SAMs) for bio-applications. Chem Soc Rev 43:2680–2700
2. Fan JW, Vankayala R, Chang CL, Chang CH, Chiang CS, Hwang KC (2015) Preparation, cytotoxicity and in vivo bioimaging of highly luminescent water-soluble silicon quantum dots. Nanotechnology 26:215703
3. Alima D, Estrin Y, Rich DH, Bar I (2012) The structural and optical properties of supercontinuum emitting Si nanocrystals prepared by laser ablation in water. J Appl Phys 112:114312
4. Ghosh B, Shirahata N (2014) Colloidal silicon quantum dots: synthesis and luminescence tuning from the near-UV to the near-IR range. Sci Technol Adv Mater 15:014207
5. Hwang J, Jeong Y, Lee KH, Seo Y, Kim J, Hong JW, Kmaloo E, Camesano TA, Choi J (2015) Simple preparation of fluorescent silicon nanoparticles from used Si wafers. Ind Eng Chem Res 54:5982–5989
6. Chaturvedi A, Joshi MP, Rani E, Ingale A, Srivastava AK, Kukreja LM (2014) On red-shift of UV photoluminescence with decreasing size of silicon nanoparticles embedded in SiO_2 matrix grown by pulsed laser deposition. J Lumin 154:178–184
7. Askari S, Macias-Montero M, Velusamy T, Maguire P, Svrcek V, Mariotti D (2015) Silicon-based quantum dots: synthesis, surface and composition tuning with atmospheric pressure plasmas. J Phys D Appl Phys 48:314002
8. Gupta A, Wiggers H (2011) Freestanding silicon quantum dots: origin of red and blue luminescence. Nanotechnology 22:055707
9. Shcherbyna L, Torchynska T (2013) Si quantum dot structures and their applications. Physica E 51:65–70
10. Huan C, Shu-Qing S (2014) Silicon nanoparticles: preparation, properties, and applications. Chin Phys B 23:088102
11. Chinnathambi S, Chen S, Ganesan S, Hanagata N (2014) Silicon quantum dots for biological applications. Adv Healthc Mater 3:10–29
12. Huang WQ, Miao XJ, Huang ZM, Liu SR, Qin CJ (2012) Activation of silicon quantum dots for emission. Chin Phys B 21:094207
13. Fujioka K, Hiruoka M, Sato K, Manabe N, Miyasaka R, Hanada S, Hoshino A, Tilley RD, Manome Y, Hirakuri K, Yamamoto K (2008) Luminescent passive-oxidized silicon quantum dots as biological staining labels and their cytotoxicity effects at high concentration. Nanotechnology 19:415102
14. Zhou T, Anderson RT, Li H, Bell J, Yang Y, Gorman BP, Pylypenko S, Lusk MT, Sellinger A (2015) Bandgap tuning of silicon quantum dots by surface functionalization with conjugated organic groups. Nano Lett 15:3657–3663
15. Chatterjee S, Mukherjee TK (2013) Size-dependent differential interaction of allylamine-capped silicon quantum dots with surfactant assemblies studied using photoluminescence spectroscopy and imaging technique. J Phys Chem C 117:10799–10808
16. Joo J, Liu X, Kotamraju VR, Ruoslahti E, Nam Y, Sailor MJ (2015) Gated luminescence imaging of silicon nanoparticles. ACS Nano 9:6233–6241
17. Lee KH (2007) Quantum dots for molecular imaging. J Nucl Med 48:1408–1410

18. Cheng X, Hinde E, Owen DM, Lowe SB, Reece PJ, Gaus K, Gooding JJ (2015) Enhancing quantum dots for bioimaging using advanced surface chemistry and advanced optical microscopy: application to silicon quantum dots (SiQDs). Adv Mater 27:6144–6150
19. Wang Y, Wang H, Guo J, Wu J, Gao LJ, Sun YH, Zhao J, Zou GF (2015) Water-soluble silicon quantum dots with quasi-blue emission. Nanoscale Res Lett 10:300
20. Cheng X, Lowe SB, Ciampi S, Magenau A, Gaus K, Reece PJ, Gooding JJ (2014) Versatile "Click Chemistry" approach to functionalizing silicon quantum dots: applications toward fluorescent cellular imaging. Langmuir 30:5209–5216
21. Chen X, Yang P (2015) Preparation and photovoltaic properties of silicon quantum dots embedded in a dielectric matrix: a review. J Mater Sci Mater Electron 26:4604–4617
22. Barbadikar D, Gautam R, Sahare S, Patrikar R, Bhatt J (2013) Optimization of process parameter for synthesis of silicon quantum dots using low pressure chemical vapour deposition. Bull Mater Sci 36:483–490
23. DeBenedetti WJI, Chiu SK, Radlinger CM, Ellison RJ, Manhat BA, Zhang JZ, Shi J, Goforth AM (2015) Conversion from red to blue photoluminescence in alcohol dispersions of alkyl-capped silicon nanoparticles: insight into the origins of visible photoluminescence in colloidal nanocrystalline silicon. J Phys Chem C 119:9595–9608
24. Huisken F, Ledoux G, Guillois O, Reynaud C (2002) Light-emitting silicon nanocrystals from laser pyrolysis. Adv Mater 14:1861–1865
25. Ledoux G, Guillois O, Porterat D, Reynaud C (2000) Photoluminescence properties of silicon nanocrystals as a function of their size. Phys Rev B 62:15942–15951
26. Eroshova OI, Perminov PA, Zabotnov SV, Gongal'skii MB, Ezhov AA, Golovan LA, Kashkarov PK (2012) Structural properties of silicon nanoparticles formed by pulsed laser ablation in liquid media. Crystallogr Rep 57:831–835
27. Xin Y, Nishio K, Saitow K (2015) White-blue electroluminescence from a Si quantum dot hybrid light-emitting diode. Appl Phys Lett 106:201102
28. Kim BH, Cho CH, Kim TW, Park NM, Sung GY, Park SJ (2005) Photoluminescence of silicon quantum dots in silicon nitride grown by NH_3 and SiH_4. Appl Phys Lett 86:091908
29. Wu Q, Wang X, Li QS, Zhang RQ (2013) Excited state relaxation and stabilization of hydrogen terminated silicon quantum dots. J Clust Sci 24:381–397
30. Park NM, Kim SH, Sung GY, Park SJ (2002) Growth and size control of amorphous silicon quantum dots using SiH_4/N_2 plasma. Chem Vap Depos 8:254–256
31. Someno K, Usami K, Kodera T, Kawano Y, Hatano M, Oda S (2012) Photoluminescence of nanocrystalline silicon quantum dots with various sizes and various phosphorus doping concentrations prepared by very high frequency plasma. Jpn J Appl Phys 51:115202
32. Barnard AS, Wilson HF (2015) Optical emission of statistical distributions of silicon quantum dots. J Phys Chem C 119:7969–7977
33. Le TH, Jeong HD (2014) Characterization of band gaps of silicon quantum dots synthesized by etching silicon nanopowder with aqueous hydrofluoric acid and nitric acid. Bull Korean Chem Soc 35:1523–1528
34. Vincent J, Maurice V, Paquez X, Sublemontier O, Leconte Y, Guillois O, Reynaud C, Herlin-Boime N, Raccurt O, Tardif F (2010) Effect of water and UV passivation on the luminescence of suspensions of silicon quantum dots. J Nanopart Res 12:39–46
35. Ledoux G, Gong J, Huisken F (2001) Effect of passivation and aging on the photoluminescence of silicon nanocrystals. Appl Phys Lett 79:4028–4030
36. Li QS, Zhang RQ, Lee ST, Niehaus TA, Frauenheim T (2008) Optimal surface functionalization of silicon quantum dots. J Chem Phys 128:244714
37. Dasog M, Bader K, Veinot JGC (2015) Influence of halides on the optical properties of silicon quantum dots. Chem Mater 27:1153–1156
38. Amans D, Guillois O, Ledoux G, Porterat D, Reynaud C (2002) Influence of light intensity on the photoluminescence of silicon nanostructures. J Appl Phys 91:5334–5340
39. Kim BH, Davis RF, Park SJ (2010) Optical property of silicon quantum dots embedded in silicon nitride by thermal annealing. Thin Solid Films S18:1744–1746

40. Zianni X, Nassiopoulou AG (2006) Photoluminescence lifetimes of Si quantum dots. J Appl Phys 100:074312
41. Wu CL, Lin GR (2012) Inhomogeneous linewidth broadening and radiative lifetime dispersion of size dependent direct bandgap radiation in Si quantum dot. AIP Adv 2:042162
42. Okada R, Iijima S (1991) Oxidation property of silicon small particles. Appl Phys Lett 58:1662–1663
43. Intartaglia R, Bagga K, Scotto M, Diaspro A, Brandi F (2012) Luminescent silicon nanoparticles prepared by ultra short pulsed laser ablation in liquid for imaging applications. Opt Mater Express 2:510–518
44. Vaccaro L, Sciortino L, Messina F, Buscarino G, Agnello S, Cannas M (2014) Luminescent silicon nanocrystals produced by near-infrared nanosecond pulsed laser ablation in water. Appl Surf Sci 302:62–65
45. Chewchinda P, Odawara O, Wada H (2014) The effect of energy density on yield of silicon nanoparticles prepared by pulsed laser ablation in liquid. Appl Phys A 117:131–135
46. Orii T, Hirasawa M, Seto T, Aya N, Onari S (2003) Temperature dependence of photoluminescence from mono-dispersed Si nanoparticles. Eur Phys J D 24:119–122
47. Grigoriu C, Nicolae I, Ciupina V, Prodan G, Suematsu H, Yatsui K (2004) Influence of the experimental parameters on silicon nanoparticles produced by laser ablation. J Optoelectron Adv Mater 6:825–830
48. Grigoriu C, Kuroki Y, Nicolae I, Zhu X, Hirai M, Suematsu H, Takata M, Yatsui K (2005) Photo and cathodoluminescence of Si/SiO_2 nanoparticles produced by laser ablation. J Optoelectron Adv Mater 7:2979–2984
49. Riabinina D, Durand C, Chaker M, Rosei F (2006) Photoluminescent silicon nanocrystals synthesized by reactive laser ablation. Appl Phys Lett 88:073105
50. Wu MH, Mu R, Ueda A, Henderson DO, Vlahovic B (2005) Production of silicon quantum dots for photovoltaic applications by picosecond pulsed laser ablation. Mater Sci Eng B 116:273–277
51. Mahdieh MH, Momeni A (2015) From single pulse to double pulse ns laser ablation of silicon in water: photoluminescence enhancement of silicon nanocrystals. Laser Phys 25:015901
52. Nakamura T, Yuan Z, Adachi S (2014) High-yield preparation of blue emitting colloidal Si nanocrystals by selective laser ablation of porous silicon in liquid. Nanotechnology 25:275602
53. Kelly PJ, Arnell RD (2000) Magnetron sputtering; a review of recent developments and applications. Vacuum 56:159–172
54. Tang W, Eilers JJ, van Huis MA, Wang D, Schropp REI, Di Vece M (2015) Formation and photoluminescence of "cauliflower" silicon nanoparticles. J Phys Chem C 119:11042–11047
55. Ohta S, Shen P, Inasawa S, Yamaguchi Y (2012) Size- and surface chemistry-dependent intracellular localization of luminescent silicon quantum dot aggregates. J Mater Chem 22:10631–10638
56. Heath JR (1992) A liquid solution phase synthesis of crystalline silicon. Science 258:1131
57. Belomoin G, Therrien J, Smith A, Rao S, Twesten R (2002) Observation of a magic discrete family of ultrabright Si nanoparticles. Appl Phys Lett 80:841–843
58. Sato K, Tsuji H, Hirakuri K, Fukata N, Yamauki Y (2009) Controlled chemical etching for silicon nanocrystals with wavelength-tunable photoluminescence. Chem Commun 25:3759–3761
59. Baretto GP, Morales G, Lopez Qintanilla ML (2013) Microwave assisted synthesis of ZnO nanoparticles: effect of precursor reagents, temperature, irradiation time and additives on nano-ZnO morphology development. J Mater 2013. Article ID 478681
60. Atkins TM, Louie AY, Kanzlarich SM (2012) An efficient microwave-assisted synthesis method for the production of water soluble amine-terminated Si nanoparticles. Nanotechnology 23:294006
61. He Y, Zhong Y, Peng F, Wei X, Su Y, Lu Y, Su S, Gu W, Liao L, Lee ST (2011) One-pot microwave synthesis of water-dispersible, ultraphoto- and pH-stable, and highly fluorescent silicon quantum dots. J Am Chem Soc 133:14192–14195

62. Yu W, Xu Y, Li H, Zhan X, Lu W (2013) Synthesis of full-visible-spectrum luminescent silicon nanocrystals and the origin of the luminescence. Appl Phys A 111:501–507
63. Erogbogbo F, Yong KT, Roy I, Xu GX, Prasad PN, Swihart MT (2008) Biocompatible luminescent silicon quantum dots for imaging of cancer cells. ACS Nano 2(5):873–878
64. Shen P, Ohta S, Inasawa S, Yamaguchi Y (2011) Selective labeling of the endoplasmic reticulum in live cells with silicon quantum dots. Chem Commun (Camb) 47:8409–8411
65. Zhong Y, Peng F, Bao F, Wang S, Ji X, Yang L, Su Y, Lee ST, He Y (2013) Large-scale aqueous synthesis of fluorescent and biocompatible silicon nanoparticles and their use as highly photostable biological probes. J Am Chem Soc 135:8350–8356
66. Wu J, Dai J, Shao Y, Sun Y (2015) One-step synthesis of fluorescent silicon quantum dots (Si-QDs) and their application for cell imaging. RSC Adv 5:83581–83587
67. Erogbogbo F, Chang CW, May J, Prasad PN, Swihart MT (2012) Energy transfer from a dye donor to enhance the luminescence of silicon quantum dots. Nanoscale 4:5163–5168
68. Tu CQ, Ma XC, Pantazis P, Kauzlarich SM, Louie AY (2010) Paramagnetic, silicon quantum dots for magnetic resonance and two-photon imaging of macrophages. J Am Chem Soc 132:2016–2023
69. Stan MS, Sima C, Cinteza LO, Dinischiotu A (2015) Silicon-based quantum dots induce inflammation in human lung cells and disrupt extracellular matrix homeostasis. FEBS J 282:2914–2929
70. Stan MS, Memet I, Sima C, Popescu T, Teodorescu VS, Hermenean A, Dinischiotu A (2014) Si/SiO_2 quantum dots cause cytotoxicity in lung cells through redox homeostasis imbalance. Chem Biol Interact 220:102–115
71. Stanca L, Sima C, Petrache Voicu SN, Serban AI, Dinischiotu A (2015) In vitro evaluation of the morphological and biochemical changes induced by Si/SiO_2 QDs exposure of HepG2 cells. Rom Rep Phys 67:1512–1524
72. De Stefano D, Carnuccio R, Maiuri MC (2012) Nanomaterials toxicity and cell death modalities. J Drug Deliv. Article ID 167896
73. Shiohara A, Hanada S, Prabakar S, Fujioka K, Lim TH, Yamamoto K, Northcote PT, Tilley RD (2010) Chemical reactions on surface molecules attached to silicon quantum dots. J Am Chem Soc 132:248–253
74. Stern ST, Zolnik BS, McLeland CB, Clogston J, Zheng J, McNeil SE (2008) Induction of autophagy in porcine kidney cells by quantum dots: a common cellular response to nanomaterials? Toxicol Sci 106:140–152
75. Luo YH, Wu SB, Wei YH, Chen YC, Tsai MH, Hp CC, Lin SY, Yang CS, Lin P (2013) Cadmium-based quantum dot induced autophagy formation for cell survival via oxidative stress. Chem Res Toxicol 26:662–673
76. Stern ST, Adiseshaiah PP, Crist RM (2012) Autophagy and lysosomal dysfunction as emerging mechanisms of nanomaterial toxicity. Part Fibre Toxicol 9:20
77. Tu C, Ma X, House A, Kauzlarich SM, Louie AY (2011) PET imaging and biodistribution od silicon quantum dots in mice. ACS Med Chem Lett 2:285–288
78. Liu J, Erogbogbo F, Yong KT, Ye L, Liu J, Hu R, Chen H, Hu Y, Yang Y, Yang J, Roy I, Karker NA, Swihart MT, Prasad PN (2013) Assessing clinical prospects of silicon quantum dots: studies in mice and monkeys. ACS Nano 7:7303–7310
79. Erogbogbo F, Yong KT, Roy I, Hu R, Law WC, Zhao W, Ding H, Wu F, Kumar R, Swihart MT, Prasad PN (2011) In vivo targeted cancer imaging, sentinel lymph node mapping and multi-channel imaging with biocompatible silicon nanocrystals. ACS Nano 5:413–423
80. Stanca L, Petrache SN, Serban AI, Staicu AC, Sima C, Munteanu MC, Zărnescu O, Dinu D, Dinischiotu A (2013) Interaction of silicon-based quantum dots with gibel carp liver: oxidative and structural modifications. Nanoscale Res Lett 8:254
81. Serban AI, Stanca L, Sima C, Staicu AC, Zarnescu O, Dinischiotu A (2015) Complex responses to Si quantum dots accumulation in carp liver tissue: beyond oxidative stress. Chem Biol Interact 239:56–66

82. Petrache SN, Stanca L, Serban AI, Sima C, Staicu AC, Munteanu MC, Costache M, Burlacu R, Zarnescu O, Dinischiotu A (2012) Structural and oxidative changes in the kidney of crucian carp induced by silicon-based quantum dots. Int J Mol Sci 13:10193–101211
83. Stanca L, Petrache SN, Radu M, Serban AI, Munteanu MC, Teodorescu D, Staicu AC, Sima C, Costache M, Grigoriu C, Zarnescu O, Dinischiotu A (2012) Impact of silicon-based quantum dots on the antioxidative system in white muscle of Carassius auratus gibelio. Fish Physiol Biochem 38:963–975
84. Alsharif NH, Berger CEM, Varanasi SS, Chao Y, Horrocks BR, Datta HK (2009) Alkyl-capped silicon nanocrystals lack cytotoxicity and have enhanced intracellular accumulation in malignant cells via cholesterol-dependent endocytosis. Small 5:221–228
85. Ohta S, Yamura K, Inasawa S, Yamaguchi Y (2015) Aggregates of silicon quantum dots as a drug carrier: selective intracellular drug release based on pH-responsive aggregation/dispersion. Chem Commun 51:6422–6425
86. Li ZF, Ruckenstein E (2004) Water-soluble poly(acrylic acid) grafted luminescent silicon nanoparticles and their use as fluorescent biological staining labels. Nano Lett 4:1463–1467
87. Erogbogbo F, Yong KT, Hu R, Law WC, Ding H, Chang CW, Prasad PN, Swihart MT (2010) Biocompatible magnetofluorescent probes: luminescent silicon quantum dots coupled with superparamagnetic iron (III) oxide. ACS Nano 4:5131–5138
88. Erogbogbo F, Chang CW, May JL, Liu L, Kumar R, Law WC, Ding H, Yong KT, Roy I, Sheshadri M, Swihart MT, Prasad PN (2012) Bioconjugation of luminescent silicon quantum dots to gadolinium ions for bioimaging applications. Nanoscale 4:5483–5489
89. Klein S, Zolk O, Fromm MF, Schrodl F, Neuhuber W, Kryschi C (2009) Functionalized silicon quantum dots tailored for targeted siRNA delivery. Bioch Biophys Res Commun 387:164–168
90. May JL, Erogbogbo F, Yong KT, Ding H, Law WC, Swihart MT, Prasad PN (2012) Enhancing silicon quantum dot uptake by pancreatic cancer cells via pluronic® encapsulation and antibody targeting. J Solid Tumors 2:24–37
91. Erogbogbo F, Liu X, May JL, Narain A, Gladding P, Swihart MT, Prasad PN (2013) Plasmonic gold and luminescent silicon nanoplatforms for multimode imaging of cancer cells. Integr Biol 5:144–150
92. Hanada S, Fujioka K, Futamura Y, Manabe N, Hoshino A, Yamamoto K (2013) Evaluation of anti-inflammatory drug-conjugated silicon quantum dots: their cytotoxicity and biological effect. Int J Mol Sci 14:1323–1334
93. Paul A, Jana A, Karthik S, Bera M, Zhao Y, Singh NDP (2016) Photoresponsive real time monitoring silicon quantum dots for regulated delivery of anticancer drugs. J Mater Chem B 4:521–528
94. Erogbogbo F, May J, Swihart M, Prasad PN, Smart K, Jack SE, Korcyk D, Webster M, Stewart R, Zeng I, Jullig M, Bakeev K, Jamieson M, Kasabov N, Gopalan B, Liang L, Hu R, Schliebs S, Villas-Boas S, Gladding P (2013) Bioengineering silicon quantum dot theranostics using a network analysis of metabolomic and proteomic data in cardiac ischemia. Theranostics 3:719–728
95. Olson JL, Velez-Montoya R, Mandava N, Stoldt CR (2012) Intravitreal silicon-based quantum dots as neuroprotective factors in a model of retinal photoreceptor degeneration. Invest Ophthalmol Vis Sci 53:5713–5721

Chapter 14
Quantitative Nanostructure–Activity Relationships: Methods, Case Studies, and Perspectives

Denis Fourches and Ryan Lougee

Abstract In this chapter, we discuss the development and application of molecular modeling methods to analyze and forecast the experimental properties of nanomaterials. We mainly focus on Quantitative Nanostructure—Activity Relationships (QNAR) to evaluate the extent of biological activities potentially induced by various types of nanomaterials. First, we present the basic principles of QNAR modeling that uses machine-learning techniques to establish quantified links between the biological endpoint of interest (e.g., cytotoxicity, cell death, ROS production) and nanomaterials' characteristics. Second, we briefly review recently published studies reporting on the QNAR modeling of the largest and most significant datasets of nanomaterials available in the public domain. Third, we discuss some perspectives for the use of molecular modeling on nanomaterials. Overall, we show how molecular modeling can represent a key element for enabling the rational design of nanomaterials with the desired activity and safety profile.

Keywords Molecular modeling · Cheminformatics · QNAR · Machine learning · Virtual screening

14.1 Introduction

Nanotechnology [1] represents the final frontier for advanced material manufacturing at the atomic resolution. Manufactured nanoparticles (MNPs) are materials with at least one dimension varying from 1 to 100 nm. At that scale, such materials are characterized by unique optical, thermal, electrical, magnetic, and biological properties [2]. As a consequence, this is no surprise that the research on novel MNPs has led to a wide interest in many areas of research and industrial applications. Thus, nanotechnology is now seen as a global, multi-purpose technology [3].

D. Fourches (✉) · R. Lougee
Department of Chemistry, Bioinformatics Research Center,
North Carolina State University, 1 Lampe Dr, Raleigh, NC 27695, USA
e-mail: dfourch@ncsu.edu

B. Yan et al. (eds.), *Bioactivity of Engineered Nanoparticles*,
Nanomedicine and Nanotoxicology, DOI 10.1007/978-981-10-5864-6_14

Its worldwide impact is expected to be as big as that of plastics with a global market reaching three trillion dollars as early as 2020 [4, 5]. As of mid-2013, more than 1800 consumer products from 622 companies and 32 countries have already been inventoried [6].

One area of great interest for the use of nanotechnology is nanomedicine. As potential medical devices, MNPs are already capable of being used on various surfaces as antimicrobials, water purifying agents, or as electrochemical biosensors [7, 8]. Other nanomedicine-relevant applications have also been explored in which MNPs are directly interacting with biological systems. For instance, we can highlight the use of MNPs for achieving fluorescent labeling, drug delivery, detection of pathogens, detection of proteins, probing of DNA structure, tissue engineering, tumor destruction, purification of biomolecules and cells, or MRI contrast enhancement [9]. Furthermore, nature actually relies on complex nanoparticles in many organisms: e.g., cephalopods fabricate reflective protein platelet nanostructures [10], fireflies generate nanostructured cuticles on their abdomen, which enhance the emission of bioluminescent light [11]. We could also underline *Geobacter sulfurreducens,* a sulfur-reducing proteobacterium, which utilizes protein-based nanowires to transfer electron in the extracellular environment [12]. Thus, the potential of nanomaterials for medical applications with therapeutically relevant outcomes is tremendous. However, this objective is only valid as long as the MNP-based nanodevices have controlled and safe bioprofiles.

One particularly well-studied class of nanomedicine-relevant MNP is carbon nanotube (CNT). These cylindrical structures entirely composed of carbon are considered the quintessential nanomaterial. A varied list of properties and morphologies makes CNTs useful in many applications, especially when it comes to their mechanical strength, high thermal conductivity, optical properties, and outstanding field emission properties. As CNTs are increasingly considered in next-generation microelectronics (e.g., CNTs used as key components for the upcoming generation of 3-D microprocessors), they are also seen as a promising platform for carrying and delivering drugs in the human body [13–15]. However, up to this date, the lack of biocompatible CNTs has dramatically slowed down their development as devices for nanomedicine.

With MNPs being used in medicine, cosmetics, clothing, food, and even goods for children, it is of high importance to study and understand whether and how exposure to these highly diverse nanoparticles could impact their environment as well as human health. Are the unique properties of MNPs a potential source of short-term and/or long-term toxicity [6] for living organisms? Indeed, one important drawback of MNPs (and in particular CNTs) is their known toxicity potential due to their complex (and mostly unknown) bioprofiles as shown in various assays, cell lines, and organisms [16, 17]. For instance, even though CNTs are entirely made of carbon, these MNPs are not inert. In fact, they resist biological degradation and can potentially accumulate and induce toxicity in organs like lungs [18]. Moreover, not only humans are directly concerned but the whole environment including aquatic ecosystems due to industrial waste waters [19]. Therefore, eco- and human toxicological assessments are

increasingly needed as the number and diversity of consumer-oriented MNPs continue to follow a sustained rise.

When considering the outcome of federal screening efforts [20–22] such as Toxcast and Tox21, it is rather accurate to hypothesize that testing all the MNP-including products currently available on the market following similar experimental toxicological protocols would literally and optimistically take decades and cost several billion dollars. With the skyrocketing rate at which MNPs are being generated and incorporated into everyday products, there is a strong rationale for mainly relying on computational chemistry techniques to speed up the assessment of MNPs characteristics.

In this chapter, we discuss the development and application of cheminformatics methods to analyze and assess the experimental properties of nanomaterials. We focus on a family of techniques entitled Quantitative Nanostructure—Activity Relationships (QNAR or nano-QSAR) for evaluating the biological events induced by nanomaterials based on their chemical, physical, and structural characteristics. In Sect. 14.2, we present the basic principles of QNAR modeling that employs machine-learning techniques (e.g., logistic regression, support vector machines, artificial neural network) to establish quantified links between the biological endpoint of interest (e.g., cytotoxicity, cell death, ROS production) and a selected pool of experimentally measured physical chemical properties and/or nanomaterials' characteristics computed from their structures. In Sect. 14.3, we briefly review a couple of recently published studies reporting on the QNAR modeling of datasets of nanomaterials, especially for carbon nanotubes. In Sect. 14.4, we discuss some perspectives for the use of molecular modeling on nanomaterials, especially the use of predictive molecular docking and molecular dynamics simulations in the complement of QNAR models.

14.2 Quantitative Nanostructure—Activity Relationships (QNAR)

14.2.1 Definitions and General Principles

Nanotechnology has been defined by the National Nanotechnology Initiative as "*the ability to control and restructure the matter at the atomic and molecular levels in the range of approximately 1–100 nm, and exploiting the distinct properties and phenomena at that scale as compared to those associated with single atoms or molecules or bulk behavior*" [23]. MNPs are nanoparticles that have been designed and manufactured through either top-down or bottom-up approaches, i.e., top-down approaches are processes where NPs are created from bulk materials through processes such as milling, repeated quenching, or photolithography [24, 25]; bottom-up approaches are based on molecular-sized components as starting materials and complex clusters are created through chemical reactions, nucleation,

and growth process [26]. Importantly, functionalization is the process of adding surface modifications to a material. In the case of nanomaterials, functionalization is used to modulate the bioprofiles of MNPs by decorating their surface with small molecules (see Sect. 14.3). Nanotoxicology is the field that seeks to understand how the unique characteristics and properties of nanomaterials can induce, modulate, and/or impact a potential detrimental and toxic effect in the human body and/or the environment.

The main cheminformatics method used to model MNPs is actually based on Quantitative Structure–Activity Relationships (QSAR). Based on the general principle that similar compounds should induce similar biological effects, Puzyn et al. [27] introduced the term "nano-QSAR" (which is equivalent to the term QNAR) referring to the use of QSAR models for nanoparticles. Puzyn et al. [27] proposed that "nano-QSAR" models would be capable of establishing key links between MNPs features and their biological properties. QSAR primarily relies on machine-learning algorithms (e.g., random forests, support vector machines, artificial neural networks) to generate prediction models using subsets of parameters (called *descriptors*) describing MNPs' chemical, physical, constitutional, and structural characteristics. QSAR methods have a long history of providing valuable and robust models used to identify and help designing drugs [28, 29]. For more technical details about the exact nature of a QSAR model, how to train and validate it, how to assess the domain of applicability, and how to screen a set of molecules using a QSAR model, we highly recommend the recent state-of-the-art review by Cherkasov et al. [30].

Again, Quantitative Nanostructure–Activity Relationships (QNAR) are based on the same principle as QSAR, i.e., nanomaterials with similar chemical, physical, and structural characteristics are likely to induce similar biological effects. Thus, QNAR models [29] involve the use of molecular descriptors that characterize the structures and other chemical physical properties of MNPs. Here, we should underline the fact that these descriptors can be either computed using dedicated software taking as input the chemical structures of the nanomaterials, or experimentally measured (e.g., zeta potential, size distribution) according to the same protocols and conditions. Some of the latter measured descriptors are sometimes referred as biological descriptors when MNPs are tested in a range of in vitro biochemical assays. Each QNAR model establishes quantified relationships between nanomaterials' descriptors and a particular endpoint (e.g., cytotoxicity). To do so, modelers use the exact same machine-learning techniques they employ when building more traditional QSAR models for small organic molecules [29].

14.2.2 Data Sources

Publicly available sources and repositories for MNP datasets suitable for QNAR modeling are slowly emerging. In this paragraph, we cite some of the most well-known repositories for MNP-related data:

- The DaNa$^{2.0}$ database (*Data and Knowledge on Nanomaterials*—accessible at www.nanopartikel.info/en/) incorporates key information on MNPs, exposure, uptake, and behavior in both the human body and environment. The information is organized first by the field of application of a given product, then by the type of nanoparticle.
- The Nanowerk nanomaterials database (accessible at www.nanowerk.com) currently contains almost 4000 unique nanomaterials. The information contained in this database is primarily originating from supplier information. Key physical characteristics (e.g., purity, size distribution) are available for the MNPs included in the dataset.
- The Nanodatabase (accessible at nanodb.dk) is a search engine containing a collection of 2340 different consumer nanomaterials. The collection contains information on the product category, year, type of nanomaterial, country of origin, country of production, manufacturer, waste products, and potential exposure pathways.
- Nano is a searchable database (accessible at https://nano.nature.com) of nanoscience data created by Springer. The database offers more than 200,000 curated profiles on nanomaterials and nanodevices. Each entry comes from high impact journals and patents, which are all evaluated by nanotechnology experts. Precise search tools help to categorize the structures, size, composition, properties, characterization methods, toxicity, other biological effect, synthesis methods, applications, and patent claims of these nanomaterials.
- The Nanomaterial Registry (accessible via https://nanohub.org/groups/nanomaterialregistry) contains information from many publicly available sources. This dataset contains several thousands of records, the most populated entry being for silver-based MNPs (ca. 200 records). Particles' size, size distribution, zeta potential, aggregation properties, and purity values are generally available for the records. The data quality control, MNPs' naming and description ontology, and storing protocols are state of the art by following the Nano-Tab recommendations [31, 32].
- The Nanomaterial–Biological Interactions Knowledgebase (accessible at nbi.oregonstate.edu) compiles experimental data on various types of MNPs and their effects on biological systems. The now famous weighted EZ metric scores are calculated from a panel of assays to characterize the bioprofiles of each MNP and can represent valuable biological descriptors to train nano-QSAR models [33].

14.2.3 QNAR Modeling

QNAR modeling workflow is strictly similar to the classical predictive QSAR workflow [30, 34]. Therefore, we refer the readers to these papers for more details regarding the exact procedures for training, validating, and selecting the best models using a particular set of molecules, a machine-learning technique, and one

(or several) endpoint(s) to assess. Importantly, QNAR models need to account for the unique properties arising with MNPs.

There are many features and other specificities that contribute to the diversity and uniqueness of MNPs [35]. For instance, we can underline the molecular shape (e.g., cubes, cylinders, platelets, hollow spheres), the dispersion medium (e.g., liquids, gels, solid matrix), or the surface modifications (e.g., pristine, polymer grafting, biomolecules, surface coatings). These aforementioned features should thus be characterized either by the computational descriptors or the experimentally measured properties [27]. Therefore, modelers should consider various types and combinations of descriptors (such as chemical composition, size distribution, zeta potential, agglomeration state, porosity, overall molecular shape, surface chemistry) in order to build their nano-QSAR models.

This structural diversity of MNPs makes the choice of descriptors very challenging and so critical when it comes to prediction performances and the interpretability of the QNAR models built with these descriptors [27]. For instance, the chemical descriptors used for quantum dots will likely not be the same as the ones used for functionalized multiwalled carbon nanotubes. Therefore, we proposed to distinguish two categories of nanomaterials: (1) those with different cores and surface chemistry and (2) those possessing the same core but different surface functionalization. In order to afford high-performing QNAR models, the descriptors used to characterize MNPs need to be well-chosen. In case of MNPs with different cores, descriptors need to describe the whole MNP taking into account both the cores and the surface modifiers (if any). In the case of a mono-core with different functionalization, the descriptors can either describe the whole MNP or simply the surface modifiers. In the latter case, the nano-QSAR model is simply a traditional QSAR model of the surface decorators.

The chemical data curation workflow we published [36, 37] is also critical for MNPs. While each dataset of MNPs should theoretically undergo its own customized curation procedure, curation should always involve the removal of certain records (e.g., mixtures), structural cleaning (e.g., neutralization, removal of counterions), normalization of specific chemotypes, treatment of tautomeric forms, analysis and removal of duplicates, and a final manual inspection of the curated dataset of structures.

Once the chemical datasets has been compiled and curated, a set of chemical descriptors needs to be obtained for each MNP. Among the computed descriptors, we can mention: 0D/1D descriptors are a single number parameter usually referring to a global property of the MNP (e.g., presence of carbon atoms, average molecular weight, number of oxygen atoms). 2-D descriptors are computed from the 2-D molecular representations of the MNPs or its surface modifier. 2-D descriptors traditionally encompass molecular fragments, topological indices, and other graph-derived parameters [30]. 3-D descriptors refer to parameters and indices computed from the three-dimensional structure of the MNP and/or its surface decorators [30]. Quantum descriptors computed from semiempirical or ab initio quantum chemistry software are also very useful for characterizing the distinct properties of MNPs [30].

Similarly to classical QSAR models, QNAR can be either continuous or classification models. Classification QNAR models relate the predictor variables to a categorical value (binary or multi-class) of the response variable, while regression models have continuous response variables. QNAR models can not only be utilized to forecast the properties of MNPs, but also to understand which functional groups, physical characteristics, or quantum parameters have significant effects in the modulation of those experimental properties. This is crucial when it comes to the rational design of new MNPs.

14.3 Recent Case Studies of Nano-QSAR Modeling

Gajewicz et al. [38] developed nano-QSAR models for a set of 18 metal oxide nanoparticles to evaluate their toxicity on cells. Quantum descriptors used in this study included ΔH_f^c (related to the band gap width) and X^c (related to Fermi level of the oxide). The authors showed these computer-selected descriptors could help the understanding of the mechanism of action for these MNPs when tested against HaCat keratinocyte human cells and *Escherichia coli* cell lines.

Interestingly, this paper echoes another study [39] published in Nanotoxicology regarding the nano-QSAR models based on a set of 70 oxide nanoparticles and their oxidative stress potential. The authors showed those MNPs were capable of inducing oxidative stress in vitro because of their specific band energy characteristics similar to redox potentials of antioxidants or radical formation reactions.

Recently, Puzyn and coworkers [40, 41] further demonstrated the usefulness of characterizing the physicochemical features of metal oxide nanoparticles, especially for predicting the zeta potential of such MNPs, a determining factor of their aggregation properties and ultimate behavior once released in the environment.

As illustrated by the three aforementioned examples, the compendium of studies regarding the development of QNAR and nano-QSAR models is growing fast. We recommend reading the excellent reviews by Kar et al. [42], Puzyn et al. [27, 43], or Tantra et al. [44] One should also note the growing interest in the modeling of gold-based nanomaterials [45].

In this mini-chapter, we specially focus on the papers reporting on QNAR models for carbon nanotubes (CNT) as the current knowledge is still limited regarding CNTs' in vivo bioprofiles and potential induced toxicity. Indeed, a significant range of negative effects caused by pristine CNTs has been reported in the literature for various assays, cell lines, and organisms [16, 17]. Interestingly, recent studies have proven these detrimental effects can be noticeably reduced by functionalizing CNTs' surface with organic molecules [46]. Therefore, the rational design of CNTs' surface chemistry could lead to safe and controlled bioprofiles for industrial CNTs, and obviously a more appropriate biocompatibility for CNTs potentially relevant for medical applications.

To allow a safe and optimal use of CNTs in medical applications, CNTs can be functionalized to optimize blood circulation and biocompatibility [47].

On a practical point of view, the nanotube surface is drastically modified by adding biocompatible organic compounds. These surface modifications can lead to improved interactions with biological components, altered homeostasis, and improved permeability with plasma membranes [48].

In 2006, Dumortier et al. [49] studied the effects of functionalized carbon nanotubes (f-CNTs) on immune system cells. T lymphocytes, B lymphocytes, and macrophages were shown to take up four different types of f-CNTs and the authors did not observe any detrimental effects on cell viability.

In another study, Liu et al. [50] studied the biodistribution of radio-labeled f-CNTs in mice by in vivo positron emission tomography and Raman spectroscopy. They found that CNT functionalized with poly ethylene-glycol phospholipids were stable in vivo. These f-CNTs exhibited relatively long blood circulation times with a half-life of $\sim$2 h for longer phospholipid chains, and $\sim$0.5 h for the shortest chains. Also, the authors showed these f-CNTs exhibited surprisingly low uptake into the liver and kidneys. Additionally, these f-CNTs efficiently showed significant uptakes in various tumor types giving a strong indication of their potential abilities in cancer nanomedicine. In a follow-up publication, Liu et al. [51] increased blood circulation to 24 h and showed complete clearance of CNTs from major organ systems in about two months. Since f-CNTs were detected in feces, kidneys, and bladder, the study of Liu et al. [51] demonstrated that clearance is possible via the biliary and renal pathways.

In the context of structure–toxicity relationships, Sayes et al. [52] analyzed the effects of the density of functionalization for f-CNTs. The authors showed that the type and density of functionalization were correlated with CNTs' cytotoxicity observed in cultures of human dermal fibroblasts. Interestingly, the authors found that when the degree of sidewall functionalization increases, the cytotoxicity induced by the f-CNTs decreases. These results illustrate how CNTs can be rendered less toxic to cells. A complementary study by Chen et al. [53] showed that polymer-coated CNTs could be better interfaced with living cells.

As shown by the aforementioned studies, the experimental testing of pristine and functionalized CNTs is well underway and has now led to more knowledge on the actual bioprofiles of some compounds. However, are these preliminary results sufficient to start building predictive models to assess the induced effects of new CNTs? Or help in designing CNTs with the desired biocompatibility?

There are many challenges in developing and using computational chemistry methods to evaluate the biological effects induced by CNTs. The ultimate objective is to develop techniques that are effective and accurate in identifying biological effects (harmful or beneficial) for the various forms of CNTs being synthesized. The current experimental methods to characterize CNTs experimentally are expensive and time-consuming. Therefore, high-throughput computational methods with the ability to assess biological outcomes for hundreds of thousands of virtual f-CNTs in a time-effective manner would dramatically reduce overhead cost and allow for the exploration of the chemical space of f-CNTs.

Modern cheminformatics methods such as QNAR and nano-QSAR models utilize biological and chemical data including physical and geometric properties in order to

create statistically significant and externally predictive models capable of accurately forecasting the adverse and therapeutic biological effects of f-CNTs [29]. Although interest in the predictive modeling of MNPs is increasing in the computational chemistry community, literature specifically related to the cheminformatics modeling of f-CNTs for the purpose of understanding and forecasting their biological activity is still scarce. Below are recapitulated some of the most recent studies:

Monajjemi and Mollaamin [54] conducted molecular dynamics simulations of f-CNTs in different solvents. The functionalization was based on the anti-cancer drug cisplatin. The authors explored the potential of those f-CNTs for drug delivery.

Puzyn et al. [43] developed a robust nano-QSAR model based on ensemble learning regression methods in order to predict the biological effects of diverse nanomaterials including CNTs. Based on CDK molecular descriptors, these models were tested against *in vitro* assays to determine their reliability and underwent fivefold cross validation. The prediction performances of the nano-QSAR model for f-CNTs were as high as $R^2 = 0.922$ for the full set.

Fourches et al. [29, 55, 56] developed a series of QNAR models based on a dataset of 83 f-CNTs tested in in vitro toxicological assays. Four protein-binding assays (bovine serum albumin, carbonic anhydrase, chymotrypsin, and haemoglobin) were conducted as well as acute and immune toxicity assays. External prediction accuracy of the QNAR models based on 2-D descriptors and support vector machines were shown to be as high as 74% ($n = 73$, sensitivity = 79%, specificity = 69%) for the cytotoxicity models. Protein-binding classification QNAR models afforded 77% external prediction accuracy. Importantly, these models were used to screen a large library of 240,000 potential surface modifiers. The modifiers predicted to lead to f-CNTs with low toxicity and low protein affinity were identified and recommended for experimental synthesis. Ten putatively active and 10 putatively inactive CNTs were synthesized and tested. We found that all 10 putatively inactive and 7 of 10 (*6 of 10*) putatively active CNTs were confirmed in the protein-binding (*cytotoxicity*) assay. These results suggested that QNAR models can be employed for predicting biological activity profiles of novel nanomaterials, and prioritizing the design and manufacturing of nanomaterials toward better and safer products.

New studies are under way to build QNAR models for even larger sets of f-CNTs tested in more diverse assays. The progress of machine-learning techniques (e.g., deep learning) will enable the prediction performances to afford higher levels of accuracy and allow the rational design of f-CNTs with perfectly controlled bioprofiles. This is the only way to achieve a fast and robust screening of millions of hypothetical f-CNTs and to prioritize the experimental testing to the most interesting compounds.

14.4 Perspectives

As modelers, we should recognize that the current QNAR modeling technology is still in its infancy. In that regard, there are multiple ways QNAR models will evolve in the coming years. Not too surprisingly, these evolutions will mostly follow the

directions taken by the more traditional QSAR models for small organic molecules, and we describe those potential evolutions in the section below. Not only the actual prediction performances of these models will improve, but more generally the overall robustness and interpretability of cheminformatics methods we rely on when it comes to the modeling of nanomaterials.

However, it is important to emphasize the fact that the QNAR modeling field has completely different types of challenges comparing to the QSAR modeling field. The latter deals with very large sets of well-defined and characterized molecules tested against multiple and diverse of biochemical and cell-based assays. There is no lack of small molecule datasets to be modeled by QSAR models due to the efforts of the research community to deposit and maintain experimental data in freely accessible online repositories (such as PubChem, ChEMBL, or Chemspider). On the contrary, the field of QNAR modeling faces a severe paucity of nanomaterial datasets available in the public domain, and this lack of experimental data limits the type, quality, and applicability domain of the current generation of QNAR models.

Below, we underline several approaches regarding the future evolution of QNAR and nano-QSAR modeling:

- **Consensus QNAR models**: the vast majority of QNAR and nano-QSAR modeling studies rely on the use of one single type of machine-learning technique and one type of chemical descriptors per study. However, the benefits of using a collection of independent models based on various learning algorithms and chemical descriptors have been shown and established in several key community benchmarks [57, 58]. Therefore, it is likely that future QNAR and nano-QSAR models will, in fact, be consensus models, i.e., *an* ensemble of individual models averaging their predictions to assess the bioactivity of a given compound. The averaging procedure can be complex with a weighting scheme based on models' individual characteristics and/or performances. The two main advantages of using a consensus QNAR models are the gain of prediction performances and an assessment of the models' concordance allowing a better estimation of the prediction reliability for a particular compound. Importantly, methods like read-across [59, 60] can also be considered for taking part in such types of consensus models.
- **Use of biological descriptors**: hybrid QSAR models involving both computed molecular descriptors and experimentally measured biological properties have been shown to afford higher prediction performances [30, 61–63]. For instance, concentration-response curves can be used as descriptors in a QSAR model [64]. Datasets including hundreds or thousands of chemicals fully tested against tens or hundreds of biological assays are still rare in the public domain, but one could note several recent examples of such screening efforts [21, 65]. Due to the critical lack of MNP-related data in the public domain, it is way more difficult to obtain and use biological descriptors for training a QNAR model. The largest datasets of MNPs in the public domain contain ca. 150 compounds and are generally tested in one single biological assay. Therefore, the use of biological

descriptors for QNAR models will certainly intensify as soon as more experimental screens are conducted for larger sets of MNPs.

- **Mixtures of nanomaterials:** Slurries are stable suspensions of abrasive nanomaterials (e.g., alumina, silica, and/or ceria) dispersed in water with other chemicals. They are notably employed for polishing tasks in the manufacturing of semi-conductors (e.g., chemical mechanical planarization process). These types of suspensions represent a real challenge for molecular modelers as they involve complex mixtures of different nanomaterials and various organic molecules in solution. As their bioprofiles are difficult to assess, it is likely more cheminformatics studies will be done to create simpler "*model systems*" for attempting the modeling of such types of mixtures of nanomaterials.
- **Quantum mechanics**: QM represents one of the cornerstones of computational chemistry. As shown by the work of Puzyn and coworkers [40], QM-based calculations are essential in enabling the characterization of the electronic, physical, and chemical properties of nanomaterials. With the development of new DFT functionals adapted for subtypes of nanomaterials, the use of QM calculations for computing MNPs' descriptors in order to build QNAR models will skyrocket in the coming years. This is especially true for challenging series of analogous MNPs with subtle structural variations, for which QM-based descriptors will help in discriminating.
- **Molecular docking**: Three-dimensional molecular docking [66] is a popular technique used for screening large libraries of molecules in drug discovery [67, 68]. Docking allows modelers to forecast the binding mode of small molecule ligands in the active site of a biological target (e.g., protein, DNA). Obviously, the 3-D structure of the target is needed. Molecular docking not only predicts the binding mode of the ligand but also scores the actual molecular interactions to estimate the free energy of binding. These docking scores can be used to rank ligands in virtual screening studies [69, 70]. These methods can be applied to estimate the binding modes of carbon nanotubes with small proteins. Since the scoring functions used by molecular docking programs have not been designed and trained for that purpose, the docking of f-CNTs is still very prototypical and not ready for reliable virtual screening.
- **Molecular dynamics**: Another computational methodology utilized in cheminformatics is molecular dynamic simulations (MDS) [71]. MDS allows modelers to simulate the dynamic motions of molecules by solving Newton's equations of motions for every single atom in the system. A force field [72] is used to compute all intra- and intermolecular forces so that the full-atom system with the explicit solvent can evolve over several hundreds of nanoseconds of biological time in a "realistic" manner. There are several examples of MDS for nanomaterials and CNTs [73–76]. These simulations can give clear insight into the intermolecular forces of f-CNTs interacting with biological targets in an explicit solvent as well as the effects of different functionalization. In the future, these MDS trajectories are likely to be used in complement to nano-QSAR models.

Overall, QNAR modeling represents a reliable and potentially disrupting way we assess the properties of nanomaterials. This is obviously critical from a chemical risk assessment standpoint and thus for regulators that need to fully evaluate the potentially detrimental effects induced by a given MNP in a particular organism. But QNAR modeling is also essential for enabling the rational design of new MNPs with a defined list of characteristics and controlled bioprofiles. In fact, developing reliable QNAR models to help identifying those highly valuable MNPs is critical for the future of nanotechnology. Nanomedicine-oriented MNPs are requiring enormous amounts of costly and time-consuming rounds of structural optimization to make them efficient and safe *by design*. Thus, we posit that any new computational technique enabling or facilitating that MNP design process is relevant and worth investigating as part of establishing the future toolbox of next-generation chemists.

References

1. Drexler KE (2004) Nanotechnology: from feynman to funding. Bull Sci Technol Soc 24:21–27
2. Gogotsi Y, Presser V (2014) Carbon nanomaterials, 2nd edn. Taylor & Francis Group LLC, Abingdon
3. Helpman E (1998) General purpose technologies and economic growth. MIT Press, Cambridge
4. Berube D (2006) Nano-hype: the truth behind the nanotechnology buzz. Prometheus Books, Amherst, N.Y. ISBN 978-1-59102-351-7
5. Roco MC (2011) The long view of nanotechnology development: the national nanotechnology initiative at 10 Years. In: Nanotechnology research directions for societal needs in 2020. Science Policy Reports, vol 1. Springer, Dordrecht. ISBN 978-94-007-1167-9
6. Vance ME, Kuiken T, Vejerano EP, McGinnis SP, Hochella MF, Rejeski D, Hull MS (2015) Nanotechnology in the real world: redeveloping the nanomaterial consumer products inventory. Beilstein J. Nanotechnol 6:1769–1780
7. Li Q, Mahendra S, Lyon DY, Brunet L, Liga MV, Li D, Alvarez PJJ (2008) Antimicrobial nanomaterials for water disinfection and microbial control: potential applications and implications. Water Res 42:4591–4602
8. Wang J (2005) Carbon-nanotube based electrochemical biosensors: a review. Electroanalysis 17:7–14
9. Salata O (2004) Applications of nanoparticles in biology and medicine. J Nanobiotechnol 2:3
10. Crookes WJ, Ding LL, Huang QL, Kimbell JR, Horwitz J, McFall-Ngai MJ (2004) Reflectins: the unusual proteins of squid reflective tissues. Science 303(5655):235–238
11. Kim JJ, Lee Y, Kim HG, Choi KJ, Kweon HS, Park S, Jeong KH (2012) Biologically inspired LED lens from cuticular nanostructures of firefly lantern. Proc Natl Acad Sci USA 109:18674–18678
12. Reguera G, McCarthy KD, Mehta T, Nicoll JS, Tuominen MT, Lovley DR (2005) Extracellular electron transfer via microbial nanowires. Nature 435:1098–1101
13. Franklin AD (2013) Electronics: the road to carbon nanotube transistors. Nature 498:443–444
14. Singh RK, Patel KD, Kim JJ, Kim TH, Kim JH, Shin US, Lee EJ, Knowles JC, Kim HW (2014) Multifunctional hybrid nanocarrier: magnetic CNTs ensheathed with mesoporous silica for drug delivery and imaging system. ACS Appl Mater Interfaces 6:2201–2208

15. Song W, Zheng Z, Tang W, Wang X (2007) A facile approach to covalently functionalized carbon nanotubes with biocompatible polymer. Polymer (Guildf) 48:3658–3663
16. Kumar A, Kumar P, Anandan A, Fernandes TF, Ayoko GA, Biskos G (2014) Engineered nanomaterials: knowledge gaps in fate, exposure, toxicity, and future directions. J Nanomater 2014:1–16
17. Qu G, Bai Y, Zhang Y, Jia Q, Zhang W, Yan B (2009) The effect of multiwalled carbon nanotube agglomeration on their accumulation in and damage to organs in mice. Carbon 48:2060–2069
18. Ryman-Rasmussen JP, Cesta MF, Brody AR, Shipley-Phillips JK, Everitt JI, Tewksbury EW, Moss OR, Wong BA, Dodd DE, Andersen ME, Bonner JC (2009) Inhaled carbon nanotubes reach the subpleural tissue in mice. Nat Nanotechnol 4:747–751
19. Moore MN (2006) Do nanoparticles present ecotoxicological risks for the health of the aquatic environment? Environ Int 32:967–976
20. Dix DJ, Houck KA, Martin MT, Richard AM, Setzer RW, Kavlock RJ (2007) The ToxCast program for prioritizing toxicity testing of environmental chemicals. Toxicol Sci 95:5–12
21. Sipes NS, Martin MT, Kothiya P, Reif DM, Judson RS, Richard AM, Houck KA, Dix DJ, Kavlock RJ, Knudsen TB (2013) Profiling 976 ToxCast chemicals across 331 enzymatic and receptor signaling assays. Chem Res Toxicol 26:878–895
22. Thomas RS, Black MB, Li L, Healy E, Chu TM, Bao W, Andersen ME, Wolfinger RD (2012) A comprehensive statistical analysis of predicting in vivo hazard using high-throughput in vitro screening. Toxicol Sci 128:398–417
23. Roco M, Chen H (2009) Mapping nanotechnology innovations and knowledge. Springer, Boston
24. Niemeyer CM (2001) Nanoparticles, proteins, and nucleic acids: biotechnology meets materials science. Angew Chemie Int Ed 40:4128–4158
25. Ju-Nam Y, Lead JR (2008) Manufactured nanoparticles: an overview of their chemistry, interactions and potential environmental implications. Sci Total Environ 400:396–414
26. Rotello V (2004) Nanoparticles: building blocks for nanotechnology. Nanostructure Science and Technology. Springer US. ISBN 978-1-4613-4770-5
27. Puzyn T, Leszczynska D, Leszczynski J (2009) Toward the development of "nano-QSARs": advances and challenges. Small 5:2494–2509
28. Verhaar HJM, van Leeuwen CJ, Hermens JLM (1992) Classifying environmental pollutants. Chemosphere 25:471–491
29. Fourches D, Pu D, Tropsha A (2011) Exploring quantitative nanostructure-activity relationships (QNAR) modeling as a tool for predicting biological effects of manufactured nanoparticles. Comb Chem High Throughput Screen 14:217–225
30. Cherkasov A, Muratov EN, Fourches D, Varnek A, Baskin II, Cronin M, Dearden J, Gramatica P, Martin YC, Todeschini R, Consonni V, Kuz'min VE, Cramer R, Benigni R, Yang C, Rathman J, Terfloth L, Gasteiger J, Richard A, Tropsha A (2014) QSAR modeling: where have you been? Where are you going to? J Med Chem 57:4977–5010
31. Thomas DG, Pappu RV, Baker NA (2011) NanoParticle Ontology for cancer nanotechnology research. J Biomed Inform 44:59–74
32. Thomas DG, Klaessig F, Harper SL, Fritts M, Hoover MD, Gaheen S, Stokes TH, Reznik-Zellen R, Freund ET, Klemm JD, Paik DS, Baker NA (2011) Informatics and standards for nanomedicine technology. Wiley Interdiscip Rev Nanomed Nanobiotechnol 3(5):511
33. Harper B, Thomas D, Chikkagoudar S, Baker N, Tang K, Heredia-Langner A, Lins R, Harper S (2015) Comparative hazard analysis and toxicological modeling of diverse nanomaterials using the embryonic zebrafish (EZ) metric of toxicity. J Nanopart Res 17:250
34. Tropsha A (2010) Best practices for QSAR model development, validation, and exploitation. Mol Inform 29:476–488
35. Nagarajan R (2008) Nanoparticles: building blocks for nanotechnology. ACS Symp Ser 996:2–14

36. Fourches D, Muratov E, Tropsha A (2010) Trust, but verify: on the importance of chemical structure curation in cheminformatics and QSAR modeling research. J Chem Inf Model 50:1189–1204
37. Fourches D, Muratov E, Tropsha A (2015) Curation of chemogenomics data. Nat Chem Biol 11:535
38. Gajewicz A, Schaeublin N, Rasulev B, Hussain S, Leszczynska D, Puzyn T, Leszczynski J (2014) Towards understanding mechanisms governing cytotoxicity of metal oxides nanoparticles: hints from nano-QSAR studies. Nanotoxicology 1–13
39. Burello E, Worth AP (2011) A theoretical framework for predicting the oxidative stress potential of oxide nanoparticles. Nanotoxicology 5:228–235
40. Mikolajczyk A, Gajewicz A, Rasulev B, Schaeublin N, Maurer-Gardner E, Hussain S, Leszczynski J, Puzyn T (2015) Zeta potential for metal oxide nanoparticles: a predictive model developed by a nano-quantitative structure-property relationship approach. Chem Mater 27:2400–2407
41. Wyrzykowska E, Mikolajczyk A, Sikorska C, Puzyn T (2016) Development of a novel in silico model of zeta potential for metal oxide nanoparticles: a nano-QSPR approach. Nanotechnology 27:445702
42. Kar S, Gajewicz A, Puzyn T, Roy K (2014) Nano-quantitative structure-activity relationship modeling using easily computable and interpretable descriptors for uptake of magnetofluorescent engineered nanoparticles in pancreatic cancer cells. Toxicol In Vitro 28:600–606
43. Puzyn T, Rasulev B, Gajewicz A, Hu X, Dasari TP, Michalkova A, Hwang HM, Toropov A, Leszczynska D, Leszczynski J (2011) Using nano-QSAR to predict the cytotoxicity of metal oxide nanoparticles. Nat Nanotechnol 6:175–178
44. Tantra R, Oksel C, Puzyn T, Wang J, Robinson KN, Wang XZ, Ma CY, Wilkins T (2015) Nano(Q)SAR: challenges, pitfalls and perspectives. Nanotoxicology. 9:636–642
45. Bigdeli A, Hormozi-Nezhad MR, Parastar H, Rother J, Sunnick E, Rosman C, Pierrat S, Sönnichsen C, Wegener J, Janshoff A, Sperling R, Schmid G, Simon U, Parak WJ, Semmler-Behnke M (2015) Using nano-QSAR to determine the most responsible factor(s) in gold nanoparticle exocytosis. RSC Adv 5:57030–57037
46. Zhou H, Mu Q, Gao N, Liu A, Xing Y, Gao S, Zhang Q, Qu G, Chen Y, Liu G, Zhang B, Yan B (2008) A nano-combinatorial library strategy for the discovery of nanotubes with reduced protein-binding, cytotoxicity, and immune response. Nano Lett 8:859–865
47. Singh R, Pantarotto D, Lacerda L, Pastorin G, Klumpp C, Prato M, Bianco A, Kostarelos K (2006) Tissue biodistribution and blood clearance rates of intravenously administered carbon nanotube radiotracers. Proc Natl Acad Sci USA 103:3357–3362
48. Vardharajula S, Ali SZ, Tiwari PM, Eroğlu E, Vig K, Dennis VA, Singh SR (2012) Functionalized carbon nanotubes: biomedical applications. Int J Nanomed 7:5361–5374
49. Dumortier H, Lacotte S, Pastorin G, Marega R, Wu W, Bonifazi D, Briand JP, Prato M, Muller S, Bianco A (2006) Functionalized carbon nanotubes are non-cytotoxic and preserve the functionality of primary immune cells. Nano Lett 6:1522–1528
50. Liu Z, Cai W, He L, Nakayama N, Chen K, Sun X, Chen X, Dai H (2007) In vivo biodistribution and highly efficient tumour targeting of carbon nanotubes in mice. Nat Nanotechnol 2:47–52
51. Liu Z, Davis C, Cai W, He L, Chen X, Dai H (2008) Circulation and long-term fate of functionalized, biocompatible single-walled carbon nanotubes in mice probed by Raman spectroscopy. Proc Natl Acad Sci USA 105:1410–1415
52. Sayes CM, Liang F, Hudson JL, Mendez J, Guo W, Beach JM, Moore VC, Doyle CD, West JL, Billups WE, Ausman KD, Colvin VL (2006) Functionalization density dependence of single-walled carbon nanotubes cytotoxicity in vitro. Toxicol Lett 161:135–142
53. Chen X, Tam UC, Czlapinski JL, Lee GS, Rabuka D, Zettl A, Bertozzi CR (2006) Interfacing carbon nanotubes with living cells. J Am Chem Soc 128:6292–6293
54. Monajjemi M, Mollaamin F (2011) Molecular modeling study of drug-DNA combined to single walled carbon nanotube. J Clust Sci 23:259–272

55. Mu Q, Jiang G, Chen L, Zhou H, Fourches D, Tropsha A, Yan B (2014) Chemical basis of interactions between engineered nanoparticles and biological systems. Chem Rev 114 (15):7740–7781
56. Fourches D, Pu D, Tassa C, Weissleder R, Shaw SY, Mumper RJ, Tropsha A (2010) Quantitative nanostructure-activity relationship modeling. ACS Nano 4:5703–5712
57. Zhu H, Tropsha A, Fourches D, Varnek A, Papa E, Gramatica P, Oberg T, Dao P, Cherkasov A, Tetko IV (2008) Combinatorial QSAR modeling of chemical toxicants tested against *Tetrahymena pyriformis*. J Chem Inf Model 48:766–784
58. Sushko I, Novotarskyi S, Körner R, Pandey AK, Cherkasov A, Li J, Gramatica P, Hansen K, Schroeter T, Müller KR, Xi L, Liu H, Yao X, Öberg T, Hormozdiari F, Dao P, Sahinalp C, Todeschini R, Polishchuk P, Artemenko A, Kuz'min V, Martin TM, Young DM, Fourches D, Muratov E, Tropsha A, Baskin I, Horvath D, Marcou G, Muller C, Varnek A, Prokopenko VV, Tetko IV (2010) Applicability domains for classification problems: benchmarking of distance to models for Ames mutagenicity set. J Chem Inf Model 50:2094–2111
59. Gajewicz A, Cronin MTD, Rasulev B, Leszczynski J, Puzyn T (2015) Novel approach for efficient predictions properties of large pool of nanomaterials based on limited set of species: nano-read-across. Nanotechnology. 26:15701
60. Low Y, Sedykh A, Fourches D, Golbraikh A, Whelan M, Rusyn I, Tropsha A (2013) Integrative chemical-biological read-across approach for chemical hazard classification. Chem Res Toxicol 26:1199–1208
61. Rusyn I, Sedykh A, Low Y, Guyton KZ, Tropsha A (2012) Predictive modeling of chemical hazard by integrating numerical descriptors of chemical structures and short-term toxicity assay data. Toxicol Sci 127:1–9
62. Low Y, Uehara T, Minowa Y, Yamada H, Ohno Y, Urushidani T, Sedykh A, Muratov E, Kuz'min V, Fourches D, Zhu H, Rusyn I, Tropsha A (2011) Predicting drug-induced hepatotoxicity using QSAR and toxicogenomics approaches. Chem Res Toxicol 24:1251–1262
63. Zhu XW, Sedykh A, Liu SS (2013) Hybrid in silico models for drug-induced liver injury using chemical descriptors and in vitro cell-imaging information. J Appl Toxicol 34(3): 281–288
64. Sedykh A, Zhu H, Tang H, Zhang L, Richard A, Rusyn I, Tropsha A (2011) Use of in vitro HTS-derived concentration-response data as biological descriptors improves the accuracy of QSAR models of in vivo toxicity. Environ Health Perspect 119:364–370
65. Elkins JM, Fedele V, Szklarz M, Abdul Azeez KR, Salah E, Mikolajczyk J, Romanov S, Sepetov N, Huang XP, Roth BL, Al Haj Zen A, Fourches D, Muratov E, Tropsha A, Morris J, Teicher BA, Kunkel M, Polley E, Lackey KE, Atkinson FL, Overington JP, Bamborough P, Müller S, Price DJ, Willson TM, Drewry DH, Knapp S, Zuercher WJ (2015) Comprehensive characterization of the published kinase inhibitor set. Nat Biotechnol 34:95–103
66. Sousa SF, Fernandes PA, Ramos MJ (2006) Protein-ligand docking: current status and future challenges. Proteins. 65:15–26
67. Shoichet BK (2004) Virtual screening of chemical libraries. Nature 432:862–865
68. Kitchen DB, Decornez H, Furr JR, Bajorath J (2004) Docking and scoring in virtual screening for drug discovery: methods and applications. Nat Rev Drug Discov 3:935–949
69. Damm-Ganamet KL, Smith RD, Dunbar JB, Stuckey JA, Carlson HA (2013) CSAR benchmark exercise 2011-2012: evaluation of results from docking and relative ranking of blinded congeneric series. J Chem Inf Model 53:1853–1870
70. Fourches D, Muratov E, Ding F, Dokholyan NV, Tropsha A (2013) Predicting binding affinity of CSAR ligands using both structure-based and ligand-based approaches. J Chem Inf Model 53:1915–1922
71. Mortier J, Rakers C, Bermudez M, Murgueitio MS, Riniker S, Wolber G (2015) The impact of molecular dynamics on drug design: applications for the characterization of ligand–macromolecule complexes. Drug Discov Today 20:686–702

72. Shivakumar D, Williams J, Wu Y, Damm W, Shelley J, Sherman W (2010) Prediction of absolute solvation free energies using molecular dynamics free energy perturbation and the OPLS force field. J Chem Theory Comput 6:1509–1519
73. Oliveira OV (2009) Atomistic molecular dynamics simulation of the CeO_2 nanoparticle aggregation. International conference on advanced materials, Rio de Janeiro, Brazil
74. Argyris D, Ho T, Cole DR, Striolo A (2011) Molecular dynamics studies of interfacial water at the alumina surface. J Phys Chem C 115:2038–2046
75. Sayle TXT, Molinari M, Das S, Bhatta UM, Möbus G, Parker SC, Seal S, Sayle DC (2013) Environment-mediated structure, surface redox activity and reactivity of ceria nanoparticles. Nanoscale 5:6063–6073
76. Proctor EA, Yin S, Tropsha A, Dokholyan NV (2012) Discrete molecular dynamics distinguishes nativelike binding poses from decoys in difficult targets. Biophys J 102:144–151